NATIONAL CENTER FOR EARTHQUAKE
ENGINEERING RESEARCH
State University of New York at Buffalo

Proceedings from the Fourth Japan-U.S. Workshop on Earthquake Resistant Design of Lifeline Facilities and Countermeasures for Soil Liquefaction

Volume I

Edited by

M. Hamada and T. D. O'Rourke

Technical Report NCEER-92-0019

August 12, 1992

This workshop was conducted at the Tokai University Pacific Center in Honolulu, Hawaii. It was partially supported by the National Science Foundation under Grant No. BCS 90-25010 and the New York State Science and Technology Foundation under Grant No. NEC-91029.

NOTICE

This report was prepared by the National Center for Earthquake Engineering Research (NCEER). Neither NCEER, associates of NCEER, its sponsors, nor any person acting on their behalf:

a. makes any warranty, express or implied, with respect to the use of any information, apparatus, method, or process disclosed in this report or that such use may not infringe upon privately owned rights; or

b. assumes any liabilities of whatsoever kind with respect to the use of, or the damage resulting from the use of, any information, apparatus, method or process disclosed in this report.

Any opinions, findings, and conclusions or recommendations expressed in this publication are those of the author(s) and do not necessarily reflect the views of the National Science Foundation, the New York State Science and Technology Foundation, or other sponsors.

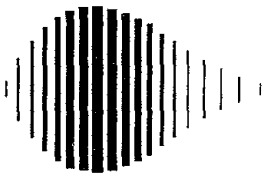

Proceedings
from the
Fourth Japan-U.S. Workshop
on Earthquake Resistant Design of Lifeline Facilities
and Countermeasures for Soil Liquefaction

Volume 1

held at the
Tokai University Pacific Center
Honolulu, Hawaii
May 27-29, 1992

Technical Report NCEER-92-0019

Edited by: M. Hamada[1] and T.D. O'Rourke[2]
August 12, 1992

NCEER Project Number 90-3008

NSF Master Contract Number BCS 90-25010
and
NYSSTF Grant Number NEC-91029

1 Professor, Faculty of Marine Science and Technology, Tokai University
2 Professor, School of Civil and Environmental Engineering, Cornell University

NATIONAL CENTER FOR EARTHQUAKE ENGINEERING RESEARCH
State University of New York at Buffalo
Red Jacket Quadrangle, Buffalo, NY 14261

PREFACE

The Fourth Japan-U.S. Workshop on Earthquake Resistant Design of Lifeline Facilities and Countermeasures Against Soil Liquefaction was held on May 27-29, 1992 at the Tokai Pacific Center of Tokai University in Honolulu, Hawaii. The Tokai Pacific Center was established in 1991. One of the major purposes of the Center is to provide facilities for international academic meetings and to encourage research developments in various fields. The conference organizers and members of Tokai University are pleased to have participated in the Fourth Japan-U.S. Workshop and to have utilized the conference resources available through the Pacific Center.

The Fourth Japan-U.S. Workshop is the most recent in a series of workshops, of which the first was hosted by the Japanese research team in Tokyo and Niigata. The second and third workshops were hosted by the U.S. research team in Buffalo and Ithaca, NY and in San Francisco, CA respectively. The fourth workshop was hosted by the Japanese research team.

There has been a steady increase in workshop participants and technical papers, progressing from the first to fourth workshops. These meetings have not only emphasized bilateral cooperation between Japan and the U.S., but have involved substantial international contributions. Participants in the workshops have come from many different countries, covering six continents. In addition, workshop participants have come from many different sectors, including governmental organizations, universities, utility companies, construction firms, and engineering consultants. Accordingly, there has been representation from virtually all segments of the earthquake engineering community, including significant interaction with practicing engineers.

M. Hamada

T.D. O'Rourke
May 20, 1992

TABLE OF CONTENTS

V PERFORMANCE OF LIFELINE FACILITIES AND FOUNDATIONS DURING LIQUEFACTION

VI DYNAMIC RESPONSE OF UNDERGROUND STRUCTURES

VII MODELING FOR SEISMIC BEHAVIOR OF GROUND

VIII PERFORMANCE OF LIFELINE SYSTEMS

JAPAN-U.S. COOPERATIVE RESEARCH PROGRAM AND WORKSHOPS

The Japan-U.S. Research Program on Earthquake Resistant Design of Lifeline Facilities and Countermeasures for Soil Liquefaction focuses on the earthquake performance of lifelines, with emphasis on liquefaction-induced large ground deformations. Large ground deformations are known to be the most troublesome source of subsurface structural damage during previous earthquakes. Currently, there is a growing recognitition in the civil and earthquake engineering communities of the importance of large ground deformations. However, our understanding of the mechanism of the large ground deformations and their effects on lifeline facilities, and our ability to predict magnitude and distribution of displacements are limited and necessitate substantial improvement. Both Japanese and U.S. researchers have been working on this topic, and it was recognized that considerable benefits will result from cooperative effort to collect case history data and recommend analytical methods and design procedures on the basis of a careful data review.

The program was initiated formally in November, 1988 with the signing of a Memorandum of Understanding between the Japanese and U.S. sides. The document was signed at a ceremony during a workshop in Tokyo, Japan by K. Kubo, Professor Emeritus of Tokyo University, and M. Shinozuka, Sollenberger Professor of Civil Engineering of Princeton University. Professor Kubo signed on behalf of the Association for the Development of Earthquake Prediction (ADEP), the Japanese sponsoring agency. Professor Shinozuka signed on behalf of Robert L. Ketter, the Director of the National Center for Earthquake Engineering Research (NCEER), the U.S. sponsoring agency. A second Memorandum of Understanding was signed in December, 1990 to continue the cooperative program of research. The signatures were K. Kubo, representing ADEP, and M. Shinozuka, the Director of NCEER.

The research program has concentrated on case histories of ground deformations and their effects on lifeline facilities. The case histories were collected in two volumes and published in May, 1992 as a joint Japan-U.S. effort by NCEER. The earthquakes included in the Japanese case histories are: 1923 Kanto, 1948 Fukui, 1964 Niigata, 1983 Nihonkai-Chubu, and 1990 Luzon, Philippines earthquakes. The earthquakes included in the U.S. case histories are: 1906 San Francisco, 1964 Alaska, 1971 San Fernando, 1979 Imperial Valley, and 1989 Loma Prieta earthquakes. The Japanese and U.S. case history studies were coordinated by Professor T.D. O'Rourke of Cornell University and Professor M. Hamada of Tokai University.

In addition to the publication of the case history volumes, the products of the cooperative research include Japan-U.S. workshops and associated publications of the proceedings covering case history data, analytical modeling, experimental studies and recommendations for improved practices, and a technical summary and recommendations for improved modeling, siting, design, and construction of lifeline facilities.

The Japan-U.S. Workshop program is a major instrument for collaboration and cooperative exchange. To date, there have been four workshops. The first was held in Tokyo and Niigata, Japan on November 16-19, 1988. The proceedings of this workshop were published by ADEP, and are available from NCEER. The second and the third workshops were held in Buffalo and Ithaca,

NY on September 26-29, 1989, and in San Francisco, CA on December 17-19, 1990, respectively. The fourth workshop was held in Honolulu, Hawaii on May 27-29, 1992. This volume contains the proceedings of the fourth workshop.

Cooperative research between Japanese and U.S. earthquake engineers has resulted in significant new findings about liquefaction and its effects on lifeline facilities, assessment of liquefaction potential, modeling of liquefaction-induced large ground displacements, performance of lifeline facilities and foundations, dynamic response of underground structures, and countermeasures and earthquake resistant design against liquefaction.

It is hoped that the spirit of cooperation fostered by these workshops and research program will contribute to a strong and enduring relationship among U.S. and Japanese engineers. It is believed that the research accomplishments of this collaborative activity will encourage additional joint projects and lead to improved understanding and mastery in the field of earthquake engineering.

T.D. O'Rourke
Professor, Cornell University

M. Hamada
Professor, Tokai University

ACKNOWLEDGEMENTS

The organizers of the workshop thank the Association for the Development of Earthquake Prediction(ADEP) and the National Center for Earthquake Engineering Research(NCEER) for sponsoring the research program and workshop activities. In particular, we express our gratitude to M. Shinozuka, the Director of NCEER and Sollenberger Professor of Civil Engineering, Princeton University, and to K. Kubo, Vice President of ADEP and Professor Emeritus of the University of Tokyo, who provided oversight on the coorperative research work and support for the workshop.

Our special thanks is extended to H. Yano, President of Tokai University at Honolulu, for his encouragement for the workshop activity and for his exellent arrangement of the conference facility.

We are very pleased that K. Ishihara, Professor of the University of Tokyo and A.S. Furumoto, Professor of the University of Hawaii, were able to give special invited lectures at the workshop. Professor Ishihara lectured on "Steady State Deformation Characteristics of Sand", and Professor Furumoto lectured on "Hawaiian Volcanoes, Birth to Disappearance".

We extend our sincere thanks to the members of the steering committee of the workshop, who helped to organize the workshop and assisted during the technical meetings to facilitate the exchange of information and execution of the program. In particular, we thank Miss N. Konagaya of Tokai University, Prof. F. Miura of Yamaguchi University, Dr. N. Yoshida of Sato Kogyo Company and Mr. H. Suzuki of Tokyo Electric Power Company for their dedication and excellent service in developing a successful workshop.

Special recognition is extended to the staff of Tokai University at Honolulu: Mrs. W.T. Sako and Mr. Y. Naito, whose help and excellent support were indispensable for this successful event.

T.D. O'Rourke
Professor, Cornell University

M. Hamada
Professor, Tokai University

Conference Organizers

I Plenary Session

Retrofitting Lifeline Facilities on Liquefied Deposits

Alexis A. Acacio
Dept. of Civil Engineering
University of the Philippines
Quezon City, Philippines

ABSTRACT

Liquefaction was widespread in Northern Luzon during the recent 16 July 1990 Philippine Earthquake which registered a magnitude of 7.7 on the Richter scale. Dagupan City, located approximately 200 kilometers north of Manila, suffered most of the liquefaction damages within the region.

The lifeline facilities of Dagupan City were devastated but due to the combined efforts of the residents of the area and the government, remedial measures were done.

Retrofitting the lifeline facilities of the city consisted mainly of 3 basic steps namely: 1 - identifying the damage and assigning an order of priority; 2 - providing a temporary facility to make the lifeline functionable ; and, 3 - constructing a facility which is properly designed to handle the effects of liquefaction.

This paper describes in detail the pre-earthquake and post-earthquake condition of the existing lifeline facilities of Dagupan City and discusses the various retrofitting procedures employed for the facilities lying on the liquefied deposits.

Key words : Liquefaction, Lifelines, Retrofitting Methods

I. INTRODUCTION

1.1 General

This paper provides an assessment of the lifeline facilities of Dagupan City which were badly damaged by soil liquefaction during the recent 16 July 1990 Philippine Earthquake.

The extent of the damage and the retrofitting procedures are analyzed to show the remedial measures used in arresting the damage in the city.

Almost 2 years have passed since the devastating earthquake happened and Dagupan city is slowly but steadily rebuilding its lifeline facilities.

1.2 Earthquake Data

The earthquake was felt in Northern Philippines on 16 July 1990 at about 4:26 in the afternoon and lasted for about 60 seconds which registered a magnitude of 7.7 on the Richter scale.

The main cause of the earthquake was due to the movement of the Philippine fault which was followed by a series of ruptures on the Digdig fault and the surrounding areas.

1.3 Geology of Dagupan City

Dagupan city lies at the locus of the Lingayen Gulf and the deposits form that of a delta. The soil of the area is composed of fine sand with occassional traces of silt and clay. Most of the soil found in the area were either transferred, reclaimed or deposited by the movement of water in the rivers. Dagupan soil consists of Quarternary Alluvium with very large deposits of sand coming from the coastline. As seen in river maps, the river channels are meandering with very sharp bends which indicate that these channels are relatively young.

Dagupan soil, from the engineering point of view is highly liquefiable. Unfortunately, liquefaction was still not known during the time in which the city of Dagupan was built.

II. DAMAGES TO LIFELINES

Lifeline facilities of the city were badly damaged during the recent earthquake causing economic dislocation of many residents. Slowly but steadily, these lifeline facilities are being reconstructed. As a basis, each

facility will be discussed in detail in the following sections.

2.1 Water Supply

Pre - Earthquake Condition and Damages

The Dagupan City Waterworks System (DCWS) is the main water source for the city. However, not all the 31 barangays were served and these barangays utilized artesian wells as source of water supply.

At the commercial business district, about 98 percent of the population is being served by the waterworks system and the remaining derives their water supply from government artesian systems built at strategic locations.

Due to the earthquake, the water distribution system of the city was badly damaged. Main lines were sheared off and water supply in the city was cut - off. The immediate solution was that water was brought to Dagupan City from Manila by fire trucks. The travel time was about 5 hours covering a distance of about 200 kilometers per truck. This scheme was very expensive to operate and caused the government millions of pesos.

Another solution was the establishmment of temporary artesian wells at various points (at least 3) all over the city. These artesian wells derived their water from the underlying aquifers of the city. The water being expelled was not treated and was used mainly for cleaning purposes and not for drinking.

Solutions / Retrofitting Procedures

At present, the water distribution system of the city is fully restored supplying most of the residents. Also, the vulnerability of the city being totally cut again from water supply is now greatly reduced due to the establishment of several artesian wells in the city. In short, the population derives their water now from 2 sources - from the waterworks system and from the individual artesian wells.

2.2 Power and Electrification

Pre - Earthquake Condition and Damages

The Dagupan Electric Corporation thru the National Power Corporation provides the power requirements of the city. As of 1989, all the 31 barangays and 100 percent of the 19,952 potential houses in the city were already supplied

with electrical power.

But due to the recent earthquake, the city was affected especially the whole of A. B. Fernandez and the whole of Perez Boulevard and other side streets of the commercial business district. The city suffered a total loss of power for about 2 weeks causing the population to rely mainly on standby generators and on individual house lamps. Since power loss is not a rare occurence in the Philippines as it occurs frequently during the summer, most commercial establishments have their own diesel or gasoline fed standby power generators. The residential houses suffered mostly from total power loss.

Solutions / Retrofitting Procedures

Power was restored on some areas of the city after 4 days but it took about 2 weeks to fully restore electricity in the city. Most of the electric posts were damaged due to liquefaction and a lot of live electric wires hanging from tilted electrical posts were extending on the streets. The Dagupan Electric Corporation had to verify the safety of all electrical connections before fully restoring power.

Unfortunately, most of the electrical lines are attached to the old and partially damaged electrical lines of the city. To date, very few lamp posts have been totally replaced. Since the main damage on electric posts was simply due to tilting, the old lamp posts were simply re-aligned and used again.

2.3 Communication

Pre Earthquake Condition and Damages

The available telecommunication facilities of the city consist of the telephone, the telegraph and the telex.

As of 1989, the city had 4 telegraph stations serving the city resulting in a ratio of one telegraph office to 19,000 persons. A total of 3650 telephone subscribers are reported to cover the area.

The communication lines for the telephone and telegraph is usually attached to the power lines (in the Philippines). During the earthquake, the tilting of electric posts also brought about damage to the communication facilities of the city. Dagupan city was totally cut off from communicating with the surrounding regions for at least 2 weeks after the earthquake.

At present, underground cables are now being placed as transmission lines for the telephone. This provides better flexibility of the cables. While exposed cables on vertical posts can be damaged when toppled over or when objects fall during an earthquake, underground cables are safer.

Damages to the Postal System

There is only one post office serving the city's 110,000 population which is unacceptable considering the standard of one post office for every 6,000 citizens. The postal situation was badly affected due to the closing of the postal office. The post office tilted due to soil liquefaction.

At present, the postal office is now transferred to the McAdore complex. On the average, there are 27 letter carriers in the city in which one carrier serves about 4,100 persons which is better than the standard of one carrier for every 5,000.

2.4 Flood Control and Drainage

Pre Earthquake Condition and Damages

A total aggregate length of 17,970 linear meters exists for the flood control and drainage system of the city. This consists of concrete revetments, closed pipes, open canals and earthdikes. Along the commercial business district, most of the drainage facilities consist of circular closed pipes embedded into the ground.

The drainage system of the central business district was badly damaged especially along Perez Boulevard and A.B. Fernandez Avenue. Since most of the drainage pipes of the city were buried under ground with no signs on the surface into where they are, great difficulty was experienced in identifying the location of these sheared off pipes. The main steets of the commercial business district were flooded with water coming out of the drainage and sewer lines.

The earthquake occured during the rainy season and as soon as the drainage ducts were damaged, most of the run-off passed the pavements causing heavy flooding especially in the commercial district of the city. Also, the performance of these drainage ducts are below standard since a lot of refuse material clogs these pipes.

Solutions / Retrofitting Methods

The new drainage system of Dagupan City now consists of open canals with removable upper slabs for easy maintenance since these can easily be clogged. The failure of drainage facilities in the Philippines is due to lack of maintenance. This system however does not take into consideration that the ground is liquefiable and still is very rigid.

2.5 Roads and Bridges

Dagupan city has a total road network of 92 kilometers in which about one half consists of barangay roads. The total road system of the city represents a mere 0.7 % of the regions total of 12,738 km.

Due to the earthquake, the city's road system was badly damaged and is tabulated as follows:

Type of Road	Length (km)	% of Total	Damaged (km)	% of Total
National	22.300	24.22	11.920	12.95
City	17.800	19.34	6.840	7.43
Barangay	51.960	56.44	17.550	19.10
TOTAL	92.060	100.00	36.310	39.48

Due to the earthquake, the main trunkline of the road was badly damaged.

34 % of the total bridge length for the city was damaged. The damaged bridges are as follows:

Magsaysay Bridge	527 meters	- unpassable
Manguragday Bridge	80 meters	- partially damaged
Mariposa Bridge	16 meters	- partially damaged
Bolosan\ Tebeng Balani Carael\ Bacayao Sur\ Don Maximo	54 meters	- unpassable
	39 meters	- partially damaged

2.6 Seaports

Dagupan city has a seaport, the Sual Fishing Port but activities are very limited due to inadequate facilities.

III. CONCLUSIONS

As shown in the above discussions, retrofitting the lifeline facilities of Dagupan City is not an easy task. Various considerations have to be taken into account in rebuilding structures in liquefiable ground. The repair of the lifeline facilities of Dagupan City is generally very slow in pace.

In rebuilding damaged lifeline facilities due to soil liquefaction, special attention should be focused on the vulnerability and interdependence of these facilities should an earthquake happen again. In order to formulate a design guide, the following considerations should be considered.

1. Liquefiable areas should be identified by the conventional and accepted methods of liquefaction analysis. Once this is done, structures to be built can be designed to mitigate against liquefaction damage.

2. As much as possible, structures should take into account the detrimental effects of uneven settlements caused by liquefaction.

3. The population of an area should not be solely dependent on a single facility. Should damage occur, at least a few of these facilities should still be functioning. Distribution of risks should be done.

4. Back-up facilites should always be ready to support the population after an earthquake.

5. In the planning of cities, the vulnerability and interdependence of lifeline facilities should always be considered.

6. Finally, these considerations should be placed properly on government guidelines for strict implementation. Building regulations at present strictly require soil investigation before detailed design.

References

1. Acacio, A. A. , Liquefaction Damages Due to the Recent Philippine Earthquake, Proceedings, International Seminar on Earthquake Prediction and Hazard Mitigation Technology, March 1991

2. Rehabilitation Plan of Dagupan City, City Engineers Office, Department of Public Works and Highways.

3. Various local publications, reports and seminar proceedings in the Philippines after the 16 July 1990 Earthquake.

Acknowledgements

The author would like to thank ADEP for the invitation to participate in this workshop, the University of the Philippines, UPERDFI, and to Engr. Frederick Parayno for providing information on the retrofitting methods of Dagupan City.

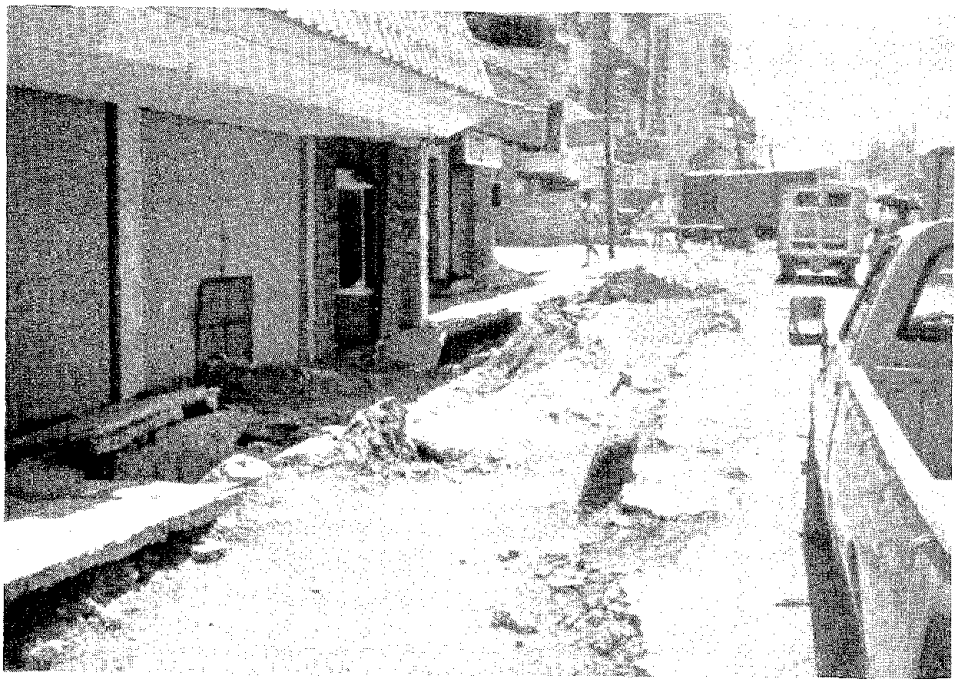

Photo 1 : Damaged Drainage Pipe

Photo 2 : Damaged Drainage System , Note Tilted Electric Post

Photo 3 : Road Reconstruction

Photo 4 : Fully Reconstructed Roadway

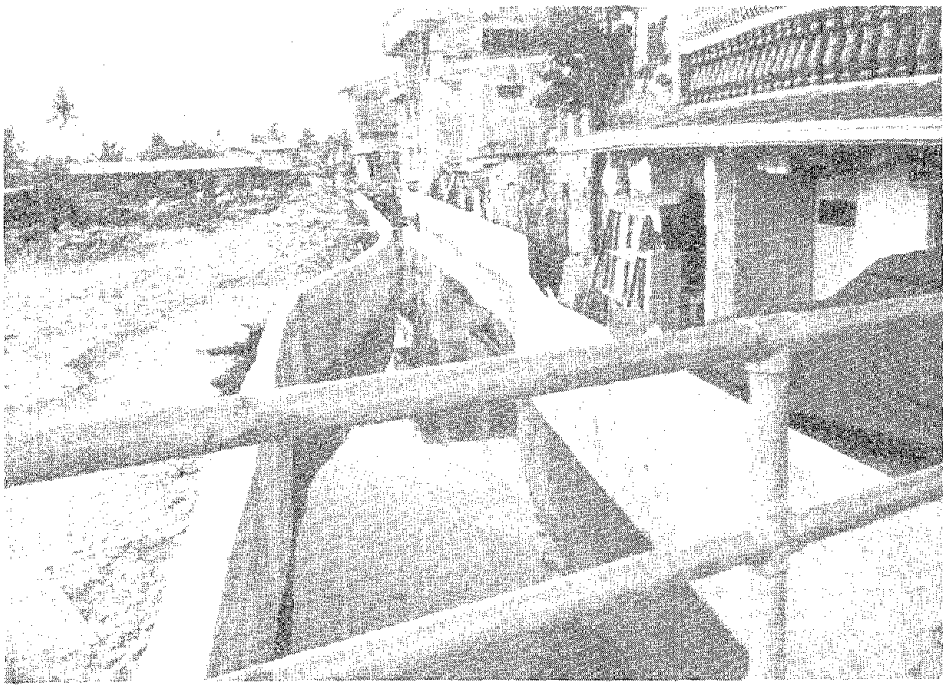

Photo 7 : Slope Protection for a Small Creek

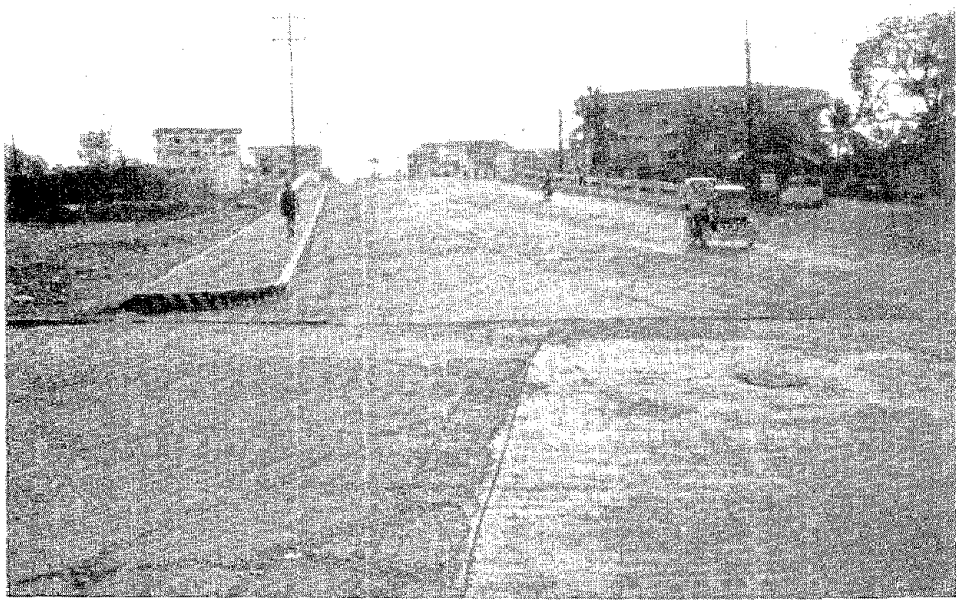

Photo 8 : The New Magsaysay Bridge

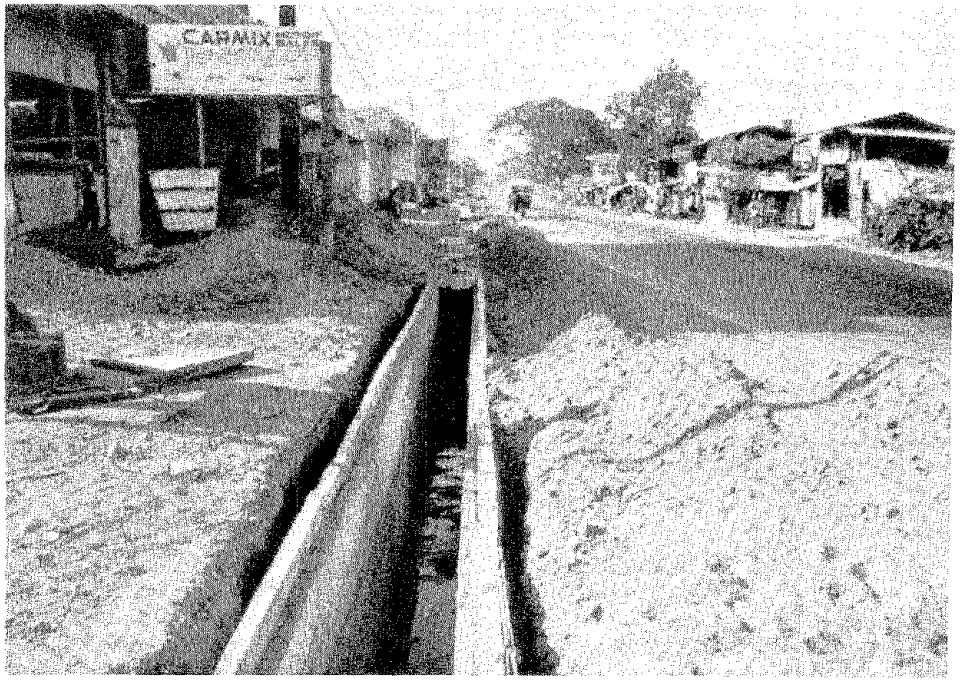

Photo 5 : Open Canal Under Construction

Photo 6 : Covered Canal, Note Replaced Circular Pipes

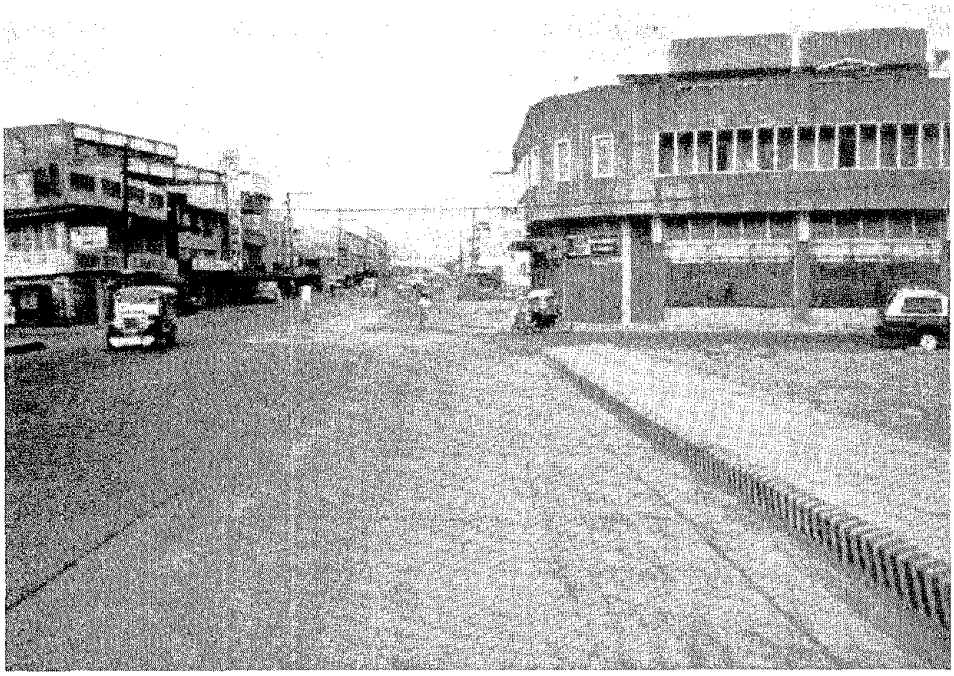

Photo 9 : Full View of a Fully Reconstructed Intersection

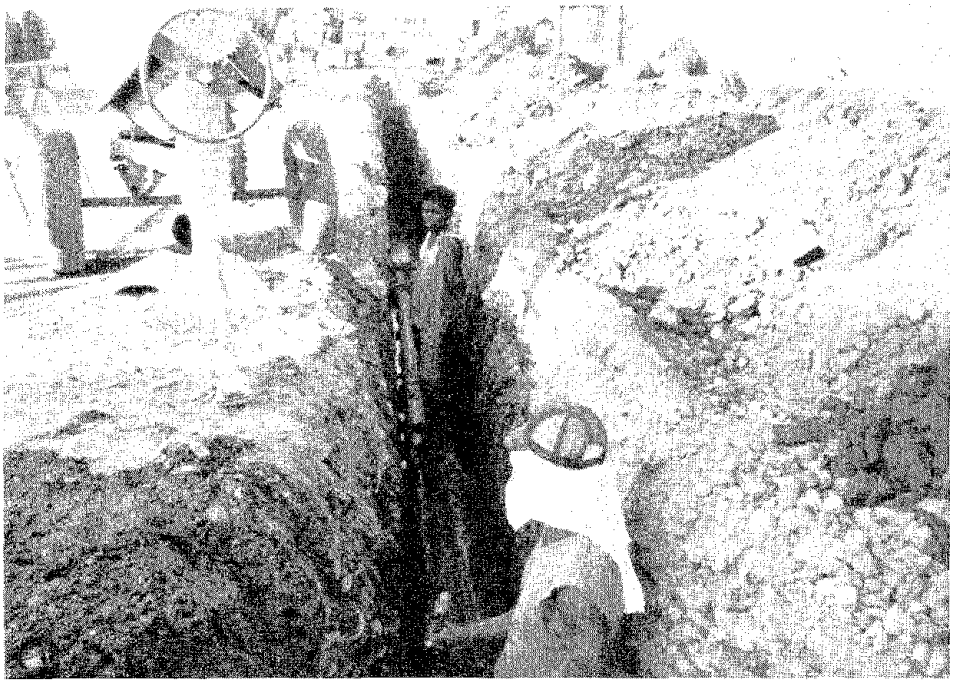

Photo 10 : Laying Out Underground Communication Cables

An Investigation into the Erzincan (Turkey) Earthquake of March 13, 1992

Ömer AYDAN and Masanori HAMADA

Dept. of Marine Civil Engineering
Tokai University, Shimizu, JAPAN

ABSTRACT

An earthquake of magnitude 6.8 on the Richter Scale occured at 19:19 on local time on March 13, 1992 in Erzincan (Turkey), which was subjected to big earthquakes in the past and situated on the famous *NORTH ANATOLIAN FAULT*. Following the earthquake on March 13, there were numerous aftershocks of intensive ones. The earthquake caused the loss of lives more than 590 and destroyed or heavily damaged buildings totaling more than 17000 and made 35000 people homeless. Landslides, avalanches and snow-slides occured during or soon after the earthquake shook the city of Erzincan and its environment. This report will outline the investigation undertaken by the authors on various aspects of the earthquake (Hamada and Aydan 1992).

DESCRIPTION OF THE MARCH 13 EARTHQUAKE AND AFTER SHOCKS

The earthquake occured at 19:19 on local time on March 13, 1992 near the city of Erzincan with a population of 93,000. The intensity of the earthquake was 6.8 on the Richter scale. According to the official announcements the numbers of dead and injured peoples are 590 and 1300, respectively. The epicenter of the earthquake has been estimated as 12 km deep but its exact location has not been officially announced yet. Erzincan is located on the eastern flank of the NORTH ANATOLIAN FAULT (NAFZ) which is a strike-slip fault (Fig. 1).

During this earthquake a 12-16 km long rupture zone has developed although the scarps of the fault were not easily distinguished on site (Photo 1). Since the motion of the NAFZ is right lateral stike-slip, the surface en-echelon tension cracks coincide with the expected directions (Fig. 2).

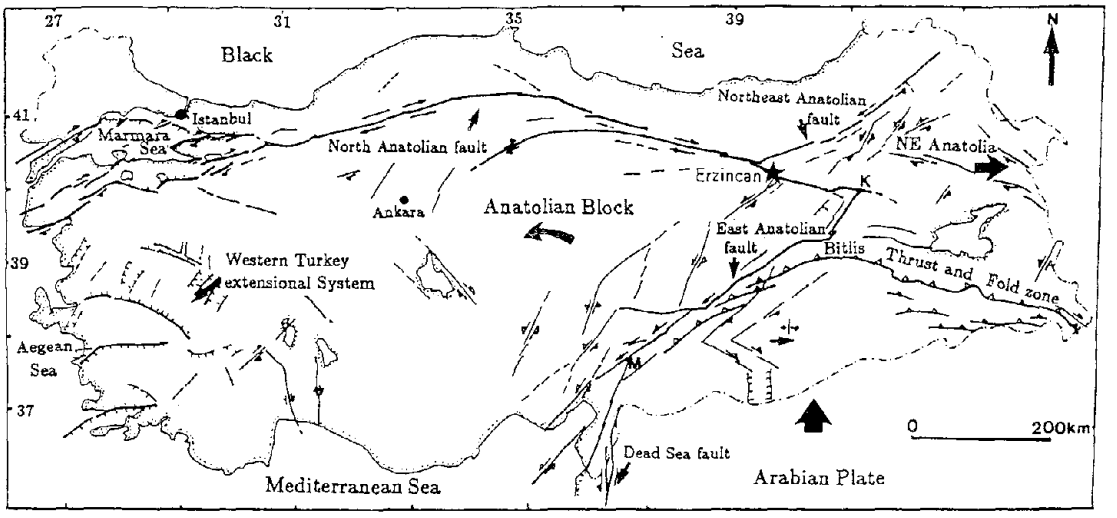

Fig. 1 Main fault system of Turkey

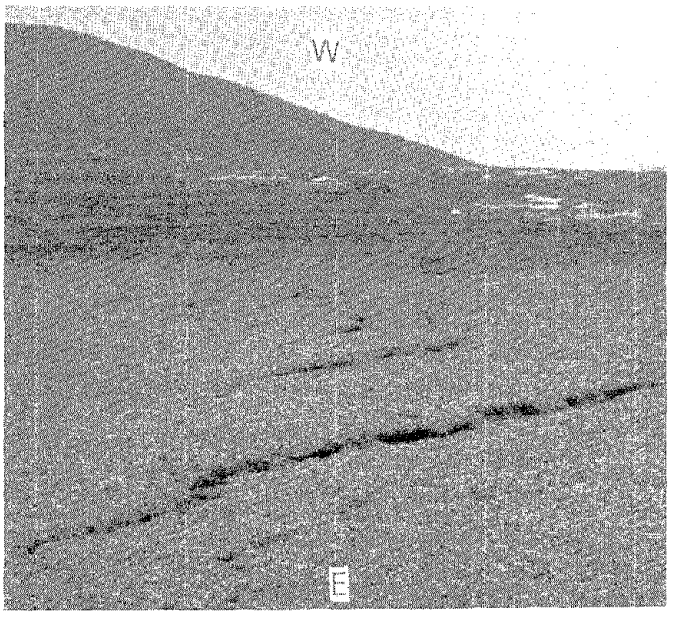

Photo 1 En-echelon cracks on the ground surface at Ekşisu

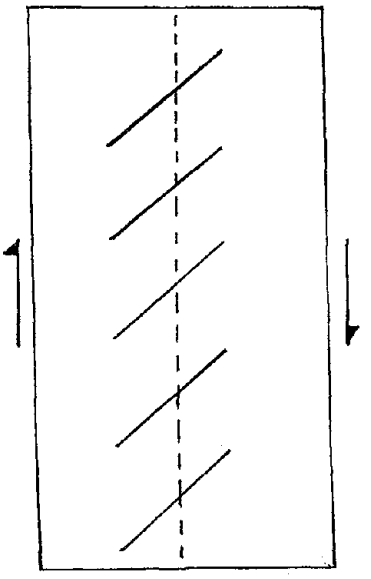

Fig. 2 En-echelon tension gashes during shearing

There are SMA-type accelographs positioned at the Meteorological stations at Erzincan, Tercan and Refahiye near the epicenter. The stations are all located on the sedimentary deposites of basins. Fig. 3 shows accelographs for the directions of N-S, E-W and UD during the March 13 earthquake at Erzincan Meteorological Station. It is noted the E-W component of the waves is the maximum The maximum E-W component at Erzincan is probably a natural consequence of the alignement of the NAFZ, which has a strike N70W in Erzincan Ovası (Basin) and its motion is of strike-slip type. The UD acceleration was recorded as 249.32 gal at Erzincan and it is almost half of the maximum accelerations of the horizontal component.

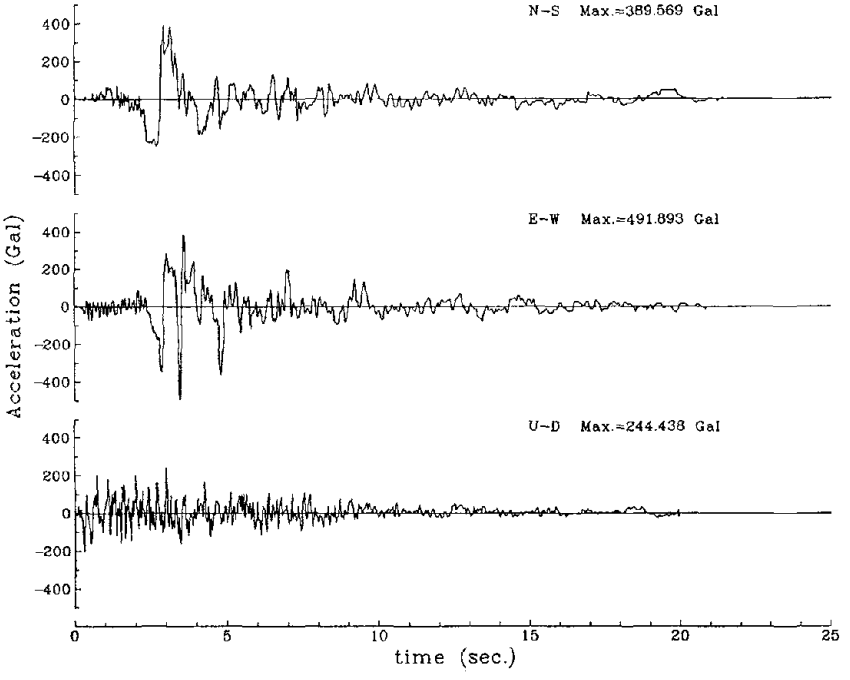

Fig. 3 Accelegraphs recorded at the Erzincan Meteorological station (Main shock)

The response spectra of the main shock is shown in Fig. 4. The UD spectra indicates natural periods of 0.11s, 0.17s and 0.58s (Fig. 4(a)). The N-S spectra indicates natural periods of 0.2s - 0.33s and 0.72s (Fig. 4(b)). The E-W spectra analysis shows natural periods of 0.3s, 0.86s and 1.19s (Fig. 4(c)).

The accelographs, recorded at the Erzincan Meteorological Station, of the earthquake occured at Pülümür at 18:17 on local time on March 15, 1992 is shown in Fig. 5. The response spectra analyses shown in Fig. 6 are very similar to the results as shown in Fig. 4. The UD spectra indicates natural periods of 0.17s, 0.28s and 0.44s. The N-S spectra indicates natural periods of 0.19s - 0.32s and 0.54s. The E-W spectra analysis shows natural period of 0.50s.

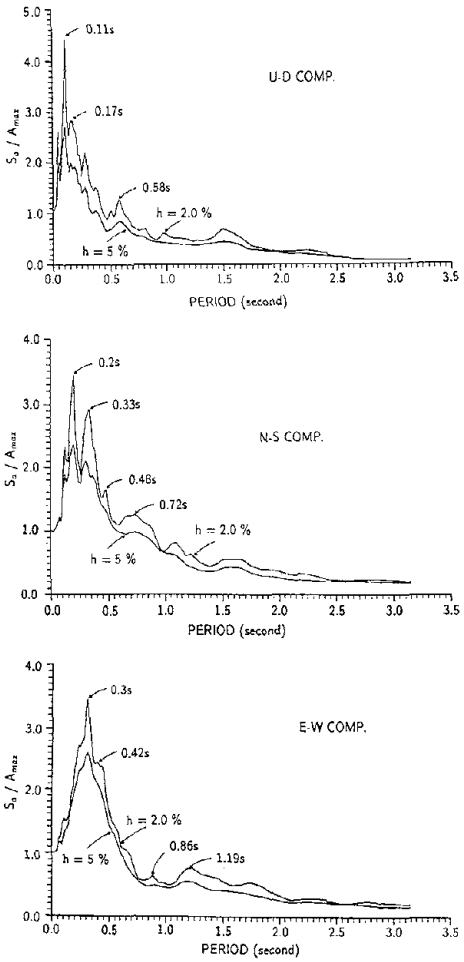

Fig. 4 Response spectra of main shock

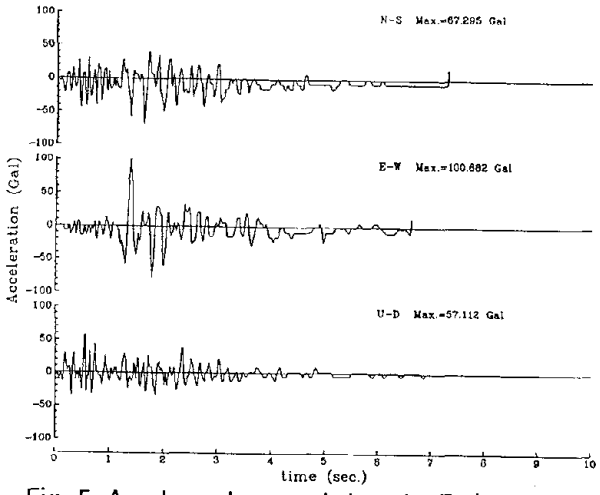

Fig. 5 Accelegraphs recorded at the Erzincan Meteorological station (aftershock)

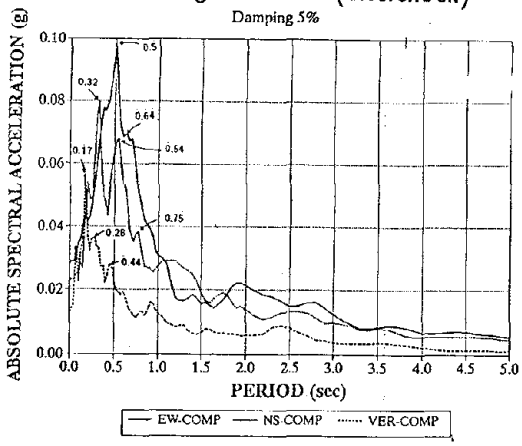

Fig. 6 Response spectra of aftershock

GEOLOGY, TECTONIC SETTING AND SEISMICITY OF ERZİNCAN OVASI

Geology

There is not any boring data deeper than 250 m for Erzincan Ovası (Basin), but the geological information is available from geophysical explorations and shallow borings by Devlet Su İşleri (D.S.İ) (State Hydraulic Works Directorate of the Ministry of Energy and Natural Resources) and outcrop surveying of the region. Fig. 7 shows a stratigraphical column and the geology of Erzincan Ovası. An alluvial sedimentary layer of 300 m thick overlays a layer consisting of conglemerate, volcaniclastics and probably fault brecia. The base and sides of the valley consists of ofiolitic melange overlaid by a limestone formation. On the northern side of the valley it is interesting to note that volcanic cones

exist which are probably consequences of the creation of tension gashes due to the shear motions of NAFZ in the geologic past. Volcanics ranges from rhyolite to basaltic series. It is also said according to geophysical explorations that the crust beneath the NAFZ is thinner than the both sides of the fault.

According to the borings of D.S.İ, the alluvial deposit consists of various layers of clay, sand and gravel. Fig. 8 shows typical borehole logs (L1, L2, L3, L4) at Güllüce (the southern side of the basin), near the Erzincan railway station (the center of the basin) and the down-town of the new city (northward) and Üzümlü (the northern side of the basin), respectively. Among all boring data, the only boring L4 at the Northern side of the basin near Üzümlü crosses rock formations. The borings near the northern side of the valley, indicates very thick layers of sand and gravel, and clay layers are generally thin. On the other hand, the thickness of clay layers increases on the southern side. In the old Erzincan city, which was completely destroyed during the great 1939 earthquake, the thickness of the clay layers is very thick and it is more than 100 m. The formations under the new Erzincan city consists of mostly gravel and sandy layers, intercalated with silty sand layers of 4-10 meters thick.

Tectonic Setting

As stated previously, the Erzincan Ovası is on the eastern flank of the NORTH ANATOLIAN FAULT ZONE (NAFZ). According Barka and Gülen (1987), the Erzincan Ovası is a junction point of various faults as shown in Fig. 7. It is presumed that during the March 13, 1992 earthquake, the motions along the NAFZ and Ovacık faults took place, and the epicenters of aftershocks have migrated toward Pülümür, which is situated on the Ovacık fault and an earthquake of 6.2 took place on March 15, 1992 along that fault two days after the Erzincan earthquake.

Seismicity of Erzincan Ovası

Erzincan Ovası is a well known location of high seismic activity all over the world. Barka et al. (1987) have compiled data on the seismic activity of Erzincan Ovası for about 1000 years. Fig. 9 shows a plot of the seismic activity in the space of time and the intensity of earthquakes.

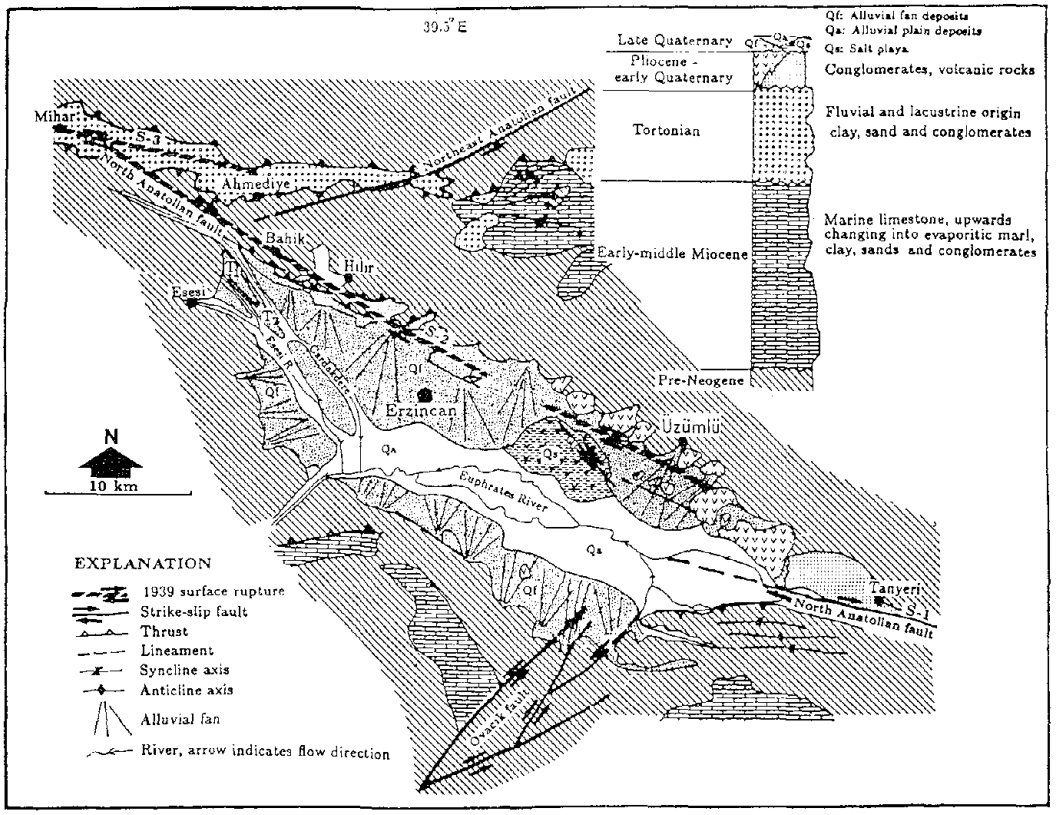

Fig. 7 Geology and faults of Erzincan Ovası

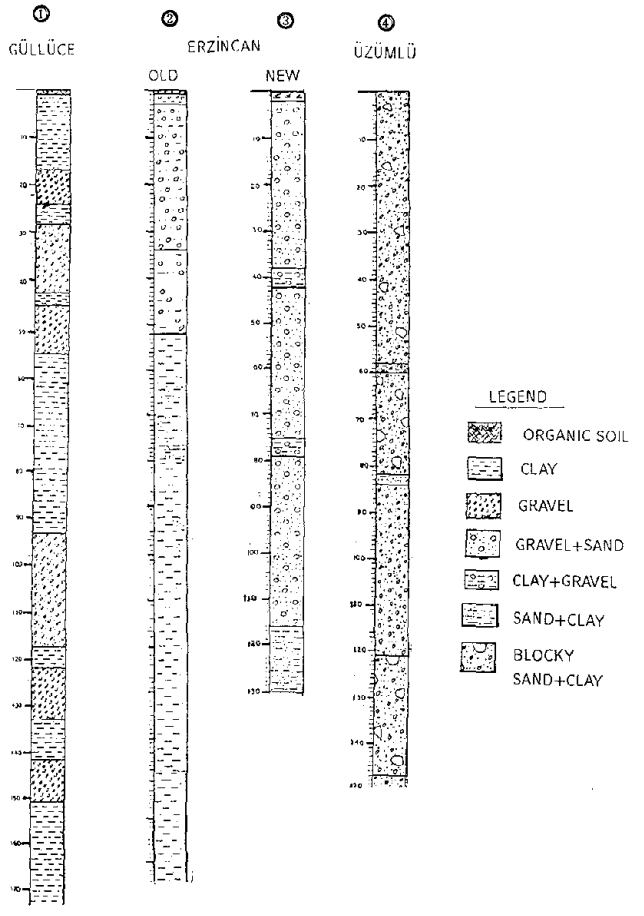

Fig. 8 Boring logs by D.S.İ

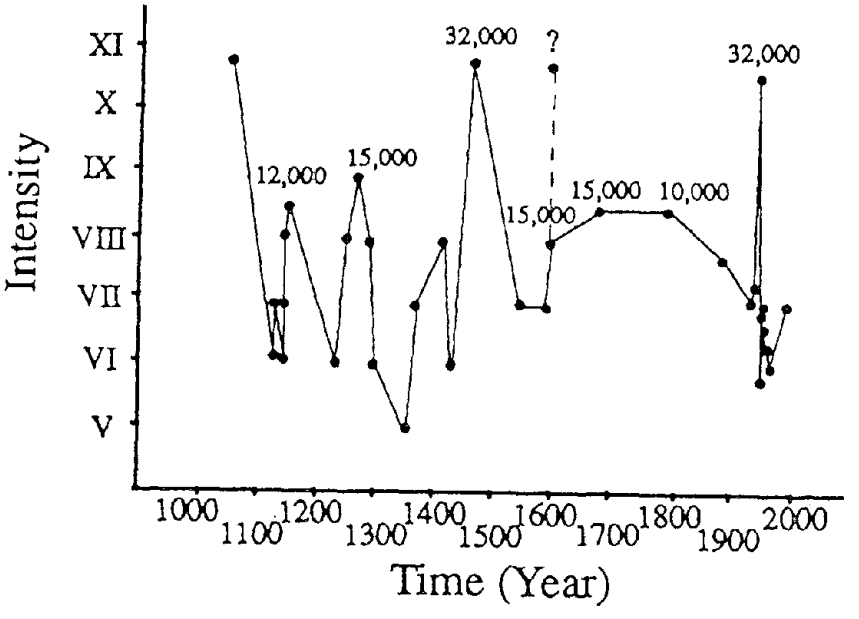

Fig. 9 Earthquake activity histogram of Erzincan region. Numbers above the dots are the number of casualties resulting from each particular event.

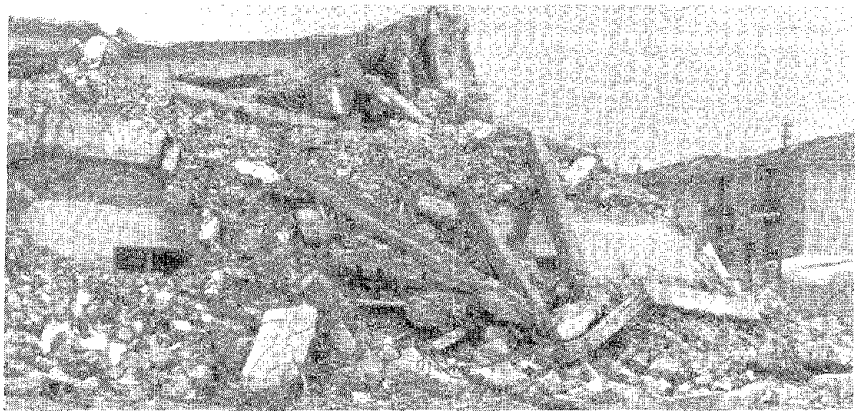

Photo 2 Collapsed 5 story Akşemsettin İmam Hatip Okulu

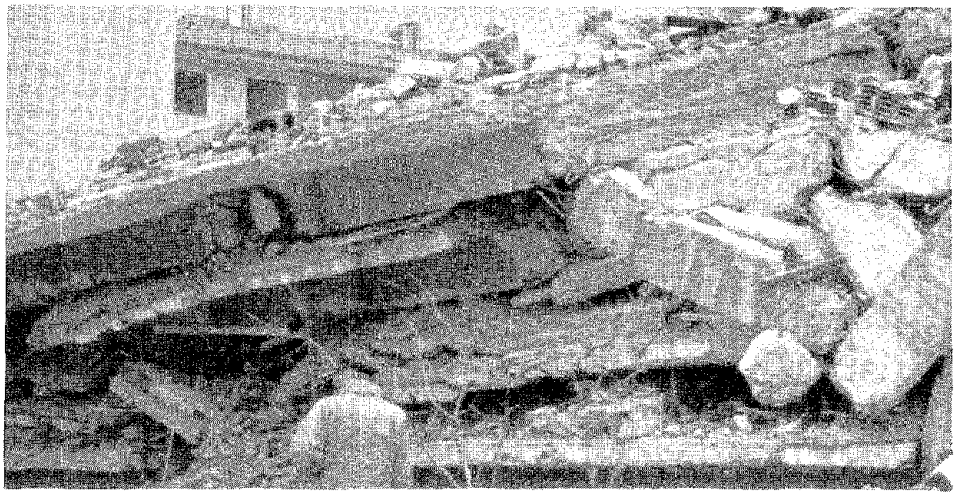

Photo 3 Collapsed 4 story building (Fatih Mah.)

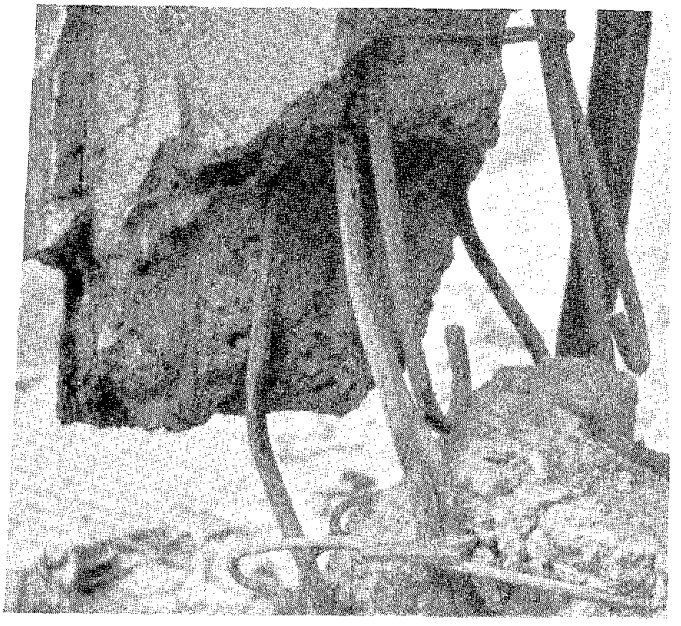

Photo 4 Unproper column-slab connections

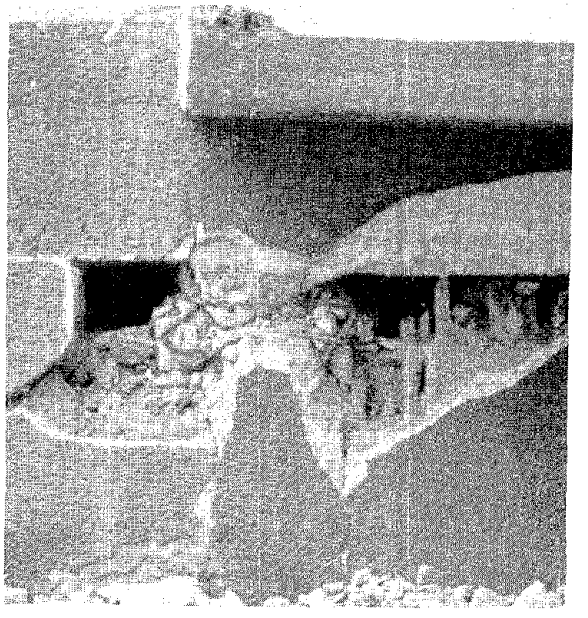

Photo 5 Buckled steel bars

type with some anchorages put tangentially between blocks of rocks. However, there were no anchorage between layers of rock blocks.

Table 1: Damage state in Erzincan City and Erzincan Province

LOCATION	TOTAL	HEAVY	MEDIUM	LIGHT
ERZİNCAN (CITY)	28007	2169	3290	4061
ERZİNCAN (VILLAGES)	9717	1492	1557	2507
ÜZÜMLÜ (TOWN)	1000	23	130	294
ÜZÜMLÜ (VILLAGES)	2009	406	346	623

Photo 6 Failure of the top of a column

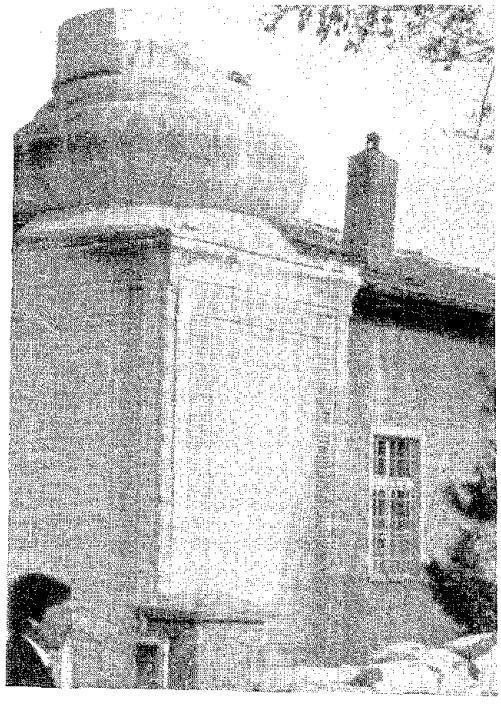

Photo 7 Fallen minaret (Akyazı)

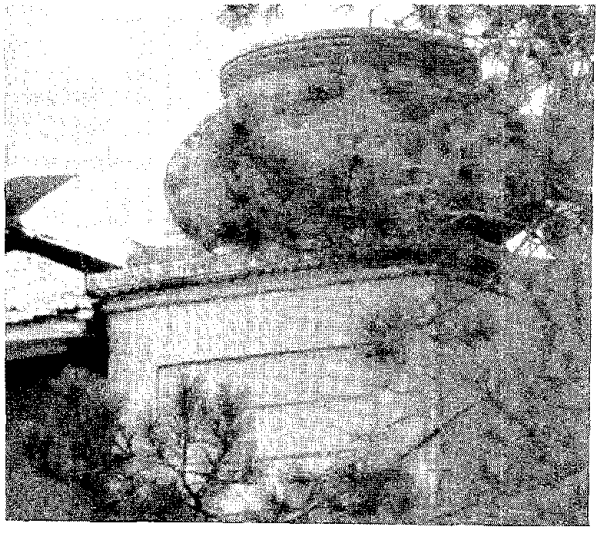

Photo 8 Fallen minaret (Erzincan)

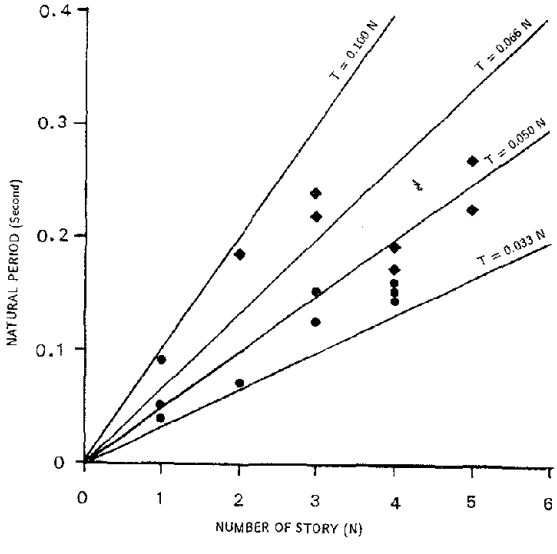

Fig. 10 Natural period of structures in Turkey

DAMAGE TO STRUCTURES

The earthquake on March 13, 1992 has killed more than 590 people and destroyed or damaged buildings more than 17000. Table 1 gives global figures on the number of collapsed or damaged structures. From these figures, the heavily damaged or collapsed buildings are 8-20 % of the total figure.

Our site-investigation has revealed that reinforced concrete buildings suffered the most, particularly those which have 4 and 5 stories. The second type of heavily damaged or collapsed structures are masonry made of kerpiç (adobe).

There was only one heavily damaged bridge on the highway to Kemah from Erzincan. At other locations slight damage to bridges were observed.

Only 5 mosques of more than 300 were reported to have suffered heavy damages. Two of them lost their minarets.

Reinforced Concrete Structures

Since a month was already past over the earthquake at the time of the visit of the authors, most of the collapsed or heavily damaged buildings were cleared away. According to the video recording of Istanbul Technical University, the collapsed reinforced structures had 4 or 5 stories. The structures such as hotels, schools and the hospital in the down-town were completely were destroyed. Photos 2-3 shows damaged reinforced concrete buildings in Akşemsettin and Fatih wards. The cause of damage are various and classified in the following order:

1-) Natural periods of structures mostly coincided with those of the input waves and this resulted in the resonance of structures and their subsequent collapses. Bayülke (1978) reports that his experimental investigations indicates that the following relation approximately holds between the natural period T of the building and the number N of stories (Fig. 10):

$$T = 0.05N \tag{1}$$

For a 4 or 5 stories buildings, the natural period will be between 0.2 and 0.25 s. Since these values are close to those of input waves (see Fig 4(b) and (c)), the collapse of buildings on the basis of resonance phenomenon is satisfactory.

2-) Poor workmanship: There are two kinds of poor workmanship. One is that the connections of columns and beams were very weak as the connections of steel bars were not properly done and detritus materials at such locations were not cleaned (Photo 4). The second one is that the granulometry of the sand and gravels of concrete was very poor and the range was wide. While very fine sand caused the low strength concrete, the big gravels blocked the concrete during casting at locations where steel connections were dense and this resulted in very porous and weak connections. During the up and down motion of buildings, it seems that concrete at the connections first failed and this subsequently caused the buckling of steel bars at such locations. Photo 5 show an example of buckling failure of bars.

3-) Design mistakes: One of the most striking design mistake was the confinement of concrete at the beam-column connections (Photo 6, see also Photo 4). As stir-ups were very few at such locations, the failure of concrete was very brittle and it could not absorb the work done by the earthquake forces.

Domes and Minarets

Most of the mosques having domes were intact or suffered very slight damage. Minarets, which are generally 25 to 30 m high and made of reinforced concrete, were intact and no damage was visible.

On the other hand, two minarets designed and constructed by the same person collapsed, one of which fell down over the mosque and killed 25 people who were at the pray of Teravih of Ramadan at that time in Erzincan. The direction of the collapse was N50W. In a village in the east of the Erzincan, the minaret fell down in the direction of S50W. Luckily, the building of the mosque was on the other direction. Photographs of fallen minarets are shown in Photos 7 & 8. The minerates were masonry

Masonry Structures

1-) Kerpiç (adobe) Masonry Structures

Kerpiç bricks are made of sandy-clay and bio fibres (straw) by casting in moulds and baked under the sun-light. The uniaxial strength of these bricks are reported as about 4-5 kgf/cm^2 (Bayülke 1978). The reason that local people prefer to use this type of bricks is that it is cheap and has a low heat conductivity which is quite important in the cold regions such as Erzincan. The interblock friction angle is between 35-40°. Observations on several houses indicated that when the quality of such bricks were poor and the roof of houses was earthen, the houses collapsed and people were killed by the weight of roofs rather than the collapse of the kerpiç walls (Photo 9). In some houses, which are reinforced by concrete and having light roofs, no cracking and no damage were observed.

2-) Tuğla (brick) Masonry Structures

The most severe damage to houses made with tuğla and concrete floors and roofs was observed near Üzümlü (Photo 10). Nevertheless, the damage was restricted to the houses on the lower elevations of the site. Although it is still difficult to say without a proper knowledge of the local ground conditions, the structures were failed by translation towards the corners and subsequent compressive failures of bricks. According of the site investigations by Bayülke (1978) at various earthquakes, the houses failed in a mode, which he calls as the corner mode.

3-) Taş (Rock) Masonry Structures

Angular and rough surfaced rock masonry structures, adhered by a mortar and with some concrete layers suffered almost no damages during the earthquake. However, such structures are few in the region. At one location near Karasu, there was a masonry structure with earthen mortar. The Western side of this structure only failed although the ground nearby sites was liquefied.

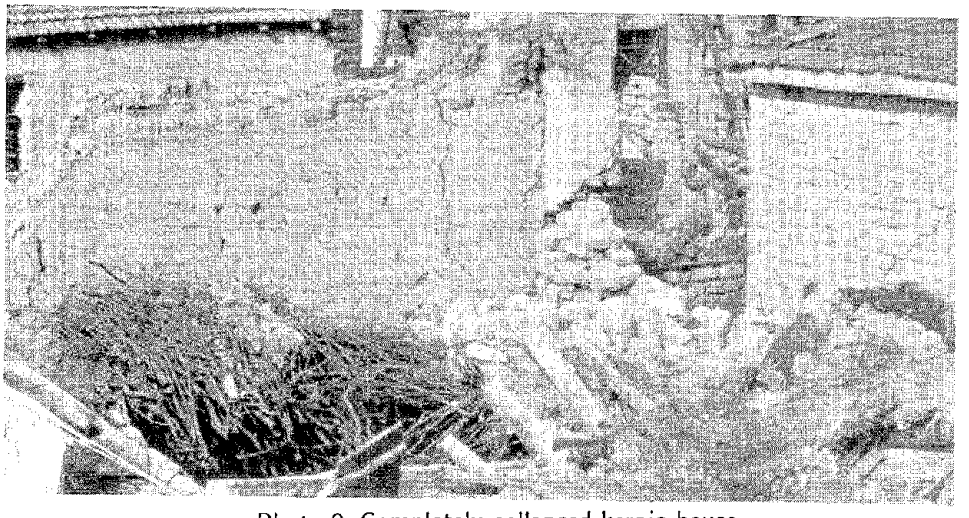

Photo 9 Completely collapsed kerpiç house

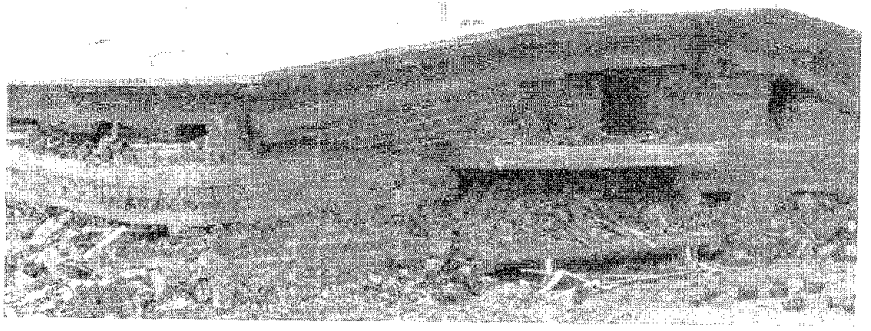

Photo 10 Completely collapsed tuğla house

Electricity Towers, Poles and Chimneys

During the earthquake, no electricity towers was broken except some transformer units were fell down from the poles. The electricity towers are of two kinds: i-) Pylons; ii-) Reinforced concrete poles. Main electricity towers are pylons while distribution towers (poles) are reinforced concrete structures. No damage to steel structure towers was reported. The reinforced concrete poles also suffered no damage or very slight damage. Photo 11 shows such a pole which had some cracks due to bending at Üzümlü. The observations indicated that the damage at the bottom of the pole was caused by bending.

Chimneys of some buildings which were either under construction or constructed were damaged. Photo 12 shows a toppled chimney.

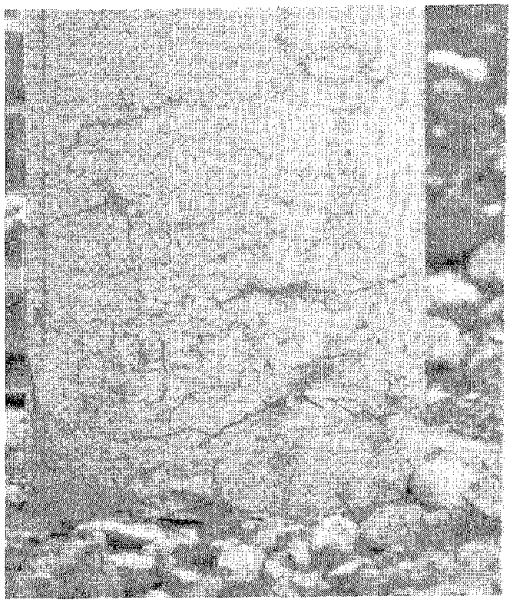

Photo 11 Bending cracks at the toe of the pole

Photo 12 Toppled chimney (Erzincan Sanayi Sitesi)

Dams and Underground Structures

The nearest dam to the earthquake location is 60 km far in Tercan. The dam is a rock-fill dam and no-damage was reported for this dam.

There are also some tunnels mainly for the Ankara-Kars railway line of Türkiye Cumhuriyeti Devlet Demiryolları (TCDD, Turkish State Railway Lines). There was no damage at the nearest tunnel which is 20 km far from the earthquake epicenter. But the damage was mainly at portals due to slope failures (Photo 13).

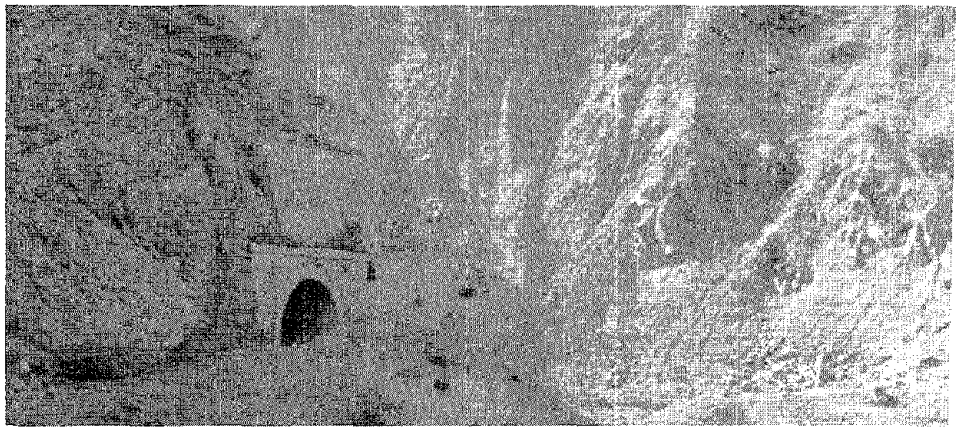

Photo 13 Slope failures at portals of a railway tunnel

The nearest mining site was the Aşkale Coal Mine of Doğu Linyitleri İşletmesi (DLİ, State East Lignite Mine), and no damage was reported.

There was an underground market just below the collapsed hotel complex. There was almost no visible damage to the underground market.

The reservoirs of the water supply systems were of buried-type. During the earthquake these reservoirs did not suffer any damage at all.

Roadways and Railways

Damages to roadways and railways were observed on various locations. The most severe damages were observed at a locality called KARASU (Fig. 11).

There were lateral and longitudinal cracks on roadways, which generally run parallel to the valley. The roadway *Route 23* was displayed by 200 mm towards the Fırat river (Euphrates), which is on the south side of the roadway and settled by approximately 100 mm (Photo 14). This place is thought to be the junction point of the NAFZ and Ovacık fault zone (Koçyiğit 1992, Barka and Gülen (1987)). There were also severe ground failures and liquefaction in this locality.

The Ankara-Kars railway line of TCDD was buckled at the several places at the same locality (Photo 15). There were no reports on damage at other sections of the line.

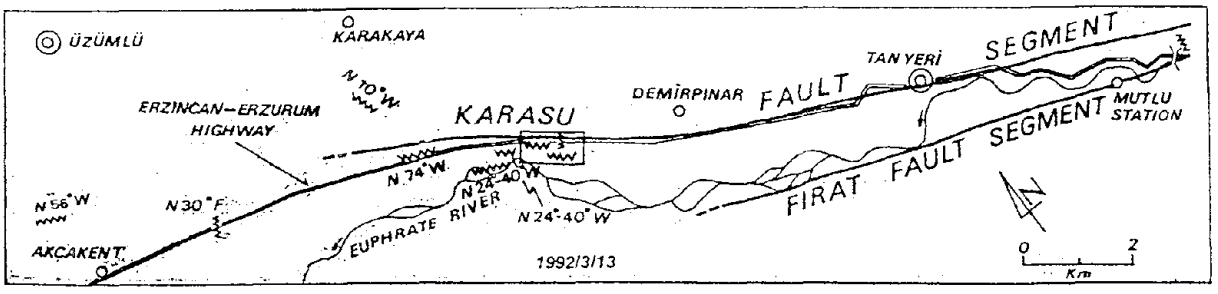

Fig. 11 Map of the location where the highway and the railway line severely damaged

Photo 14 Displayed highway for Erzurum & Erzincan at Karasu

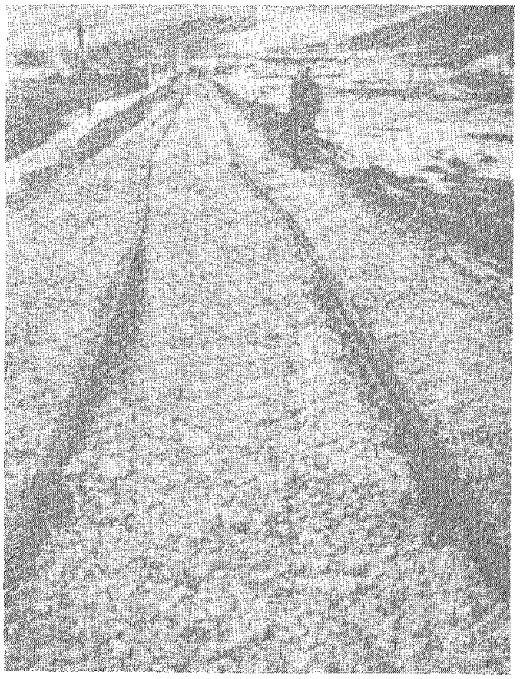

Photo 15 Buckled and deformed railway

Bridges

The most severe damage was observed at a bridge which is a cross-over bridge on the roadway for Kemah over the railway line. Photo 16 shows the severely damaged bridge. The walls of the eastern embankment of the bridge was ruptured and moved westwardly and struck the adjacent piers (Photo 17). As a result, the piers cracked at the top by bending (Photo 18). Piers in the middle of the bridge were also fractured by bending. Girders were damaged due to collison at joints (Photo 19).

Settlement of the piers were observed at a bridge crossing an unlined canal on the highway between Erzurum and Erzincan at a location just east of Erzincan in a weak ground (see Photo 23). The piers were slightly inclined towards the south by approximately 3° and there were slight spalling at the connections between beams and girders. It was of great interest that simple beam bridges of low height were not damaged at all.

In addition, a stone arch bridge, which also endured the great Erzincan Earthquake of 1939, was not damaged at all. There were also no damages to modern reinforced concrete bridges over Fırat river.

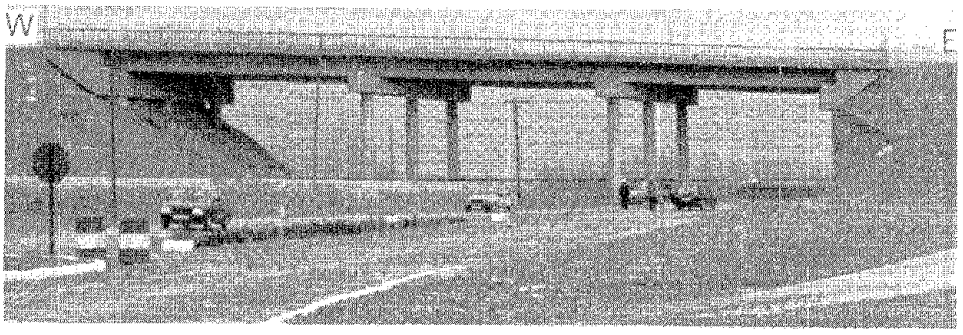

Photo 16 Severly damaged cross-over bridge on a highway for Erzincan-Kemah

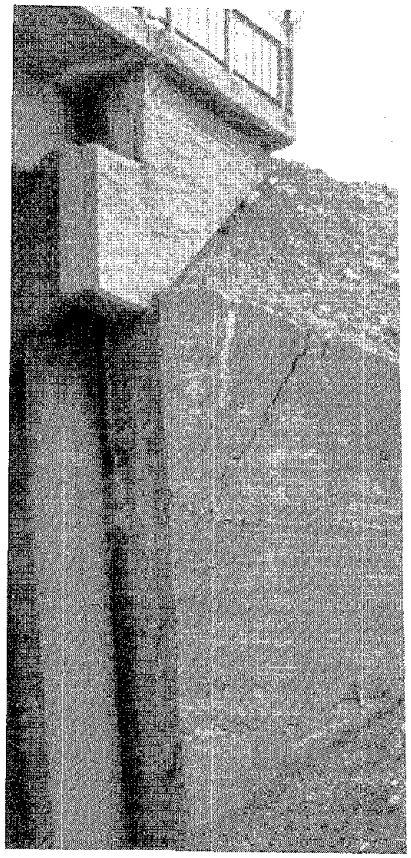

Photo 17 Fractured and displayed embankment wall

Photo 18 Fractured pier hit by the failed embankment wall

Photo 19 Fractured RC concrete bridge girders

Canals

In Erzincan Ovası, there is a canal system for the water supply for agricultural purposes. The canals have a inverted trapezoidal shape and were generally lined with lightly reinforced concrete panels, and some of them were unlined.

During the investigation at several locations, no severe damage to the system was observed. At one location where the canal had a alignment of EW direction and next to a bridge, some concrete panels were ruptured (Photo 20).

Near the same bridge, a concrete pipe under the bridge embankment was translated in EW direction for about 10 cm which resulted in the washing-out of the soil above and the opening of a hole in the embankment (Photo 21).

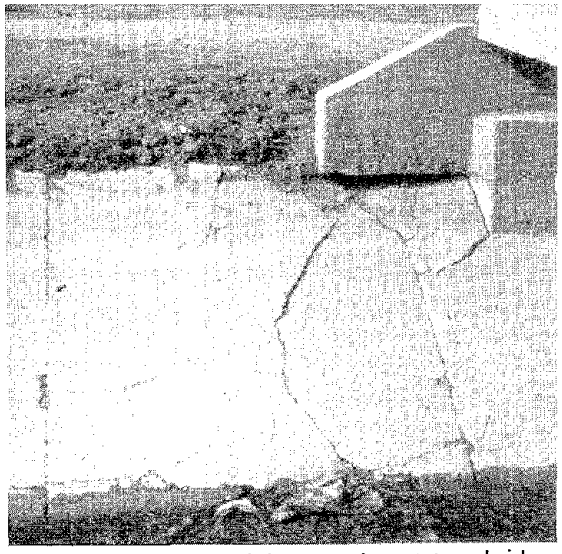

Photo 20 Fractured lining panel next to a bridge

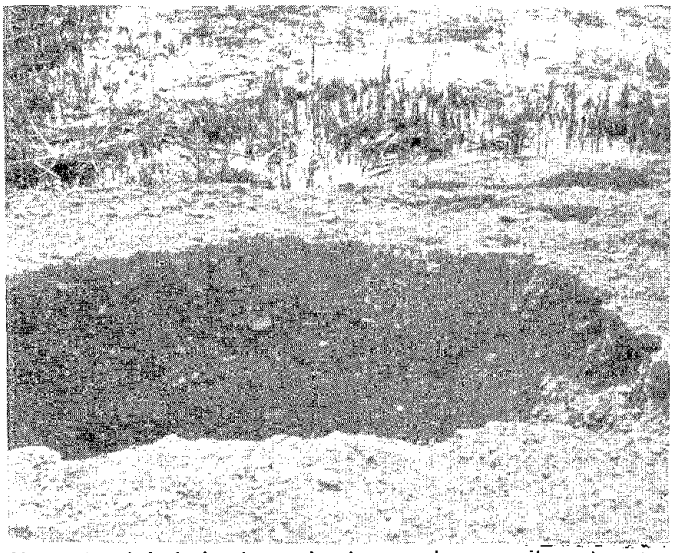

Photo 21 A hole in the embankment due to soil wash-out

Embankments

At several places, embankment failures of roadways, railways, bridges and canals were observed as shown in Photos 22-23. The embankment failures are similar to soil slope failures having a curved failure surfaces and scarps of failures were observable.

Photo 22 Failure of the embankment of an unlined canal under a bridge

Photo 23 Translational failure of a bridge embankment

Lifelines

The damages to lifelines will be grouped into four groups and will be described as follows:

1-) Electricity system

As indicated in the previous section, there were no damage to transmission lines and substation facilities except some transformer units on poles were fallen down. Fig. 12 shows the electricity system. Most of the damage were on the distribution lines and insulators. The total length of buried cables was 32 km and only 1.8 km part was damaged. The length of damaged cable in the air was 4 km. Most of the damage was in the city of Erzincan. Electricity perfectly came back 3 days after the occurence of the earthquake.

2-) Water Supply system

The water supply system consists of two sub-systems (Fig. 13). The upper part system has two pumping stations and buried reservoir facilities at two locations Karasu and Kurutelek. The lower level system has 5 pumping facilities and a buried reservoir of 1000 m^3 capacity. The water is pumped to two upper level buried reservoirs of 8000 m^3 and 5000 m^3 capacity.

The pipeline of the lower system used for pumping the water from wells to the upper level reservoirs is made of steel and has a diameter of 800 mm. The pipes of main distribution system are made of cast iron and have a diameter of 600 mm. The distribution system pipes are made of cast iron, plastic (PVC) and asbestos and their diameter ranges between 200 mm to 600mm.

There were no damage to buried reservoirs and to pumping equipments and facilities. However, the transformer units on electricity towers were fallen down during the earthquake. As a result of such incident, the water supply system was distrupted by the stopage of electricity. The repair work on electricity was completed on March 14 (second day).

In the meantime, the upper system was checked and no damage was found and the upper water system was activated on March 15. However, the damage to the joints of the pipes of the main distribution system of the upper system at three locations were found and repaired on the same day.

On March 15 (third day), the water was also pumped to the upper level reservoirs of the lower level system. But some ruptures at some junctions occured as the water in pipes were frozen. After having repaired these junctions, the water was again pumped and the damage was found on the second part of the pipeline at welding points of the pipes at 6 locations. After having repaired these parts, the water was again pumped to the upper reservoirs. Then, the water supply to the main distribution system was carried out district by district and street by street in order to take into account possible breaks in the distribution system. Total number of breaks on the main distribution system were 25 event. The whole work was completed on March 27, 1992 after 14 days following the earthquake.

For the urgent need of water for the people of Erzincan and its vicinity 60 rollies were readied.

Sewage system

Sewage system is approximately 250 km long and the 90 % of the buildings connected to this system. The sewage system is checked systematically through water flow states at man-holes. During the whole check-up process, it was reported that as there were no blocking in the system. It was presumed that the sewage system was undamaged during the earthquake. The diameter of the main pipes of the sewage system is 1200 mm and made of concrete. However, the authorities are aware that it is difficult to check the system throughly since they are buried structures. It is urgently felt that a remote sensing system is necessary to check the damages and leakage to sewage systems.

Telephone system

The telephone in Turkey is run by Posta Telgraf Telefon (PTT, State Post Telegraph and Telephone Directorate) and the telephone lines of the system are buried in concrete conduits as illustrated in Fig. 14. The total length of the system is 18 km. There were some damages at the connection points between the distribution system and buildings. Some parts were also damaged due to rescue operations. The switching units and the energy back-up system worked perfectly against the 3 days stopage of electricity.

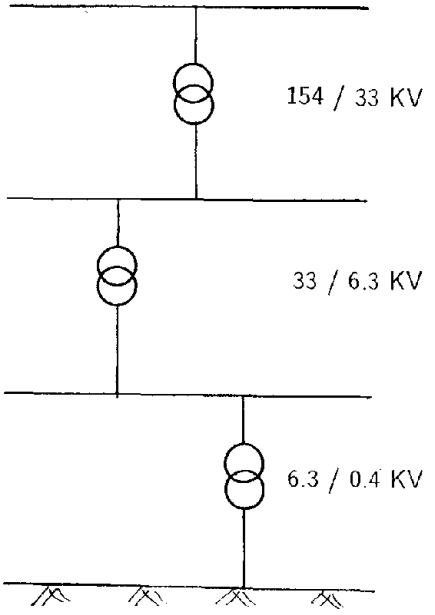

Fig. 12 Electricity system

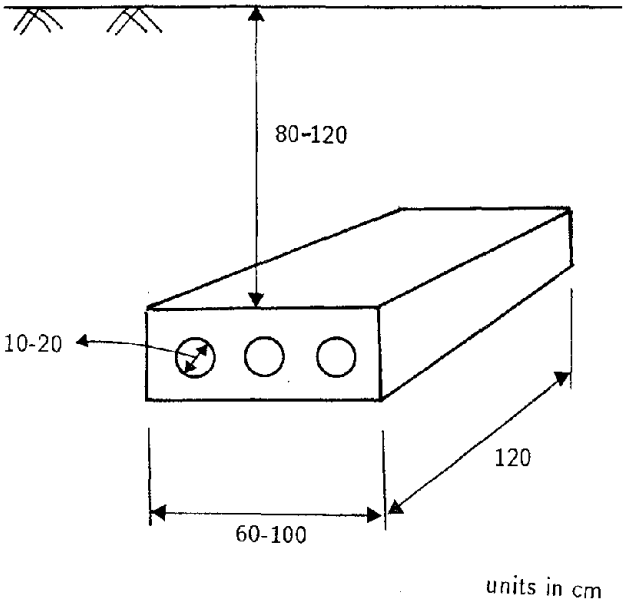

Fig. 14 Underground conduit system for telephone cables

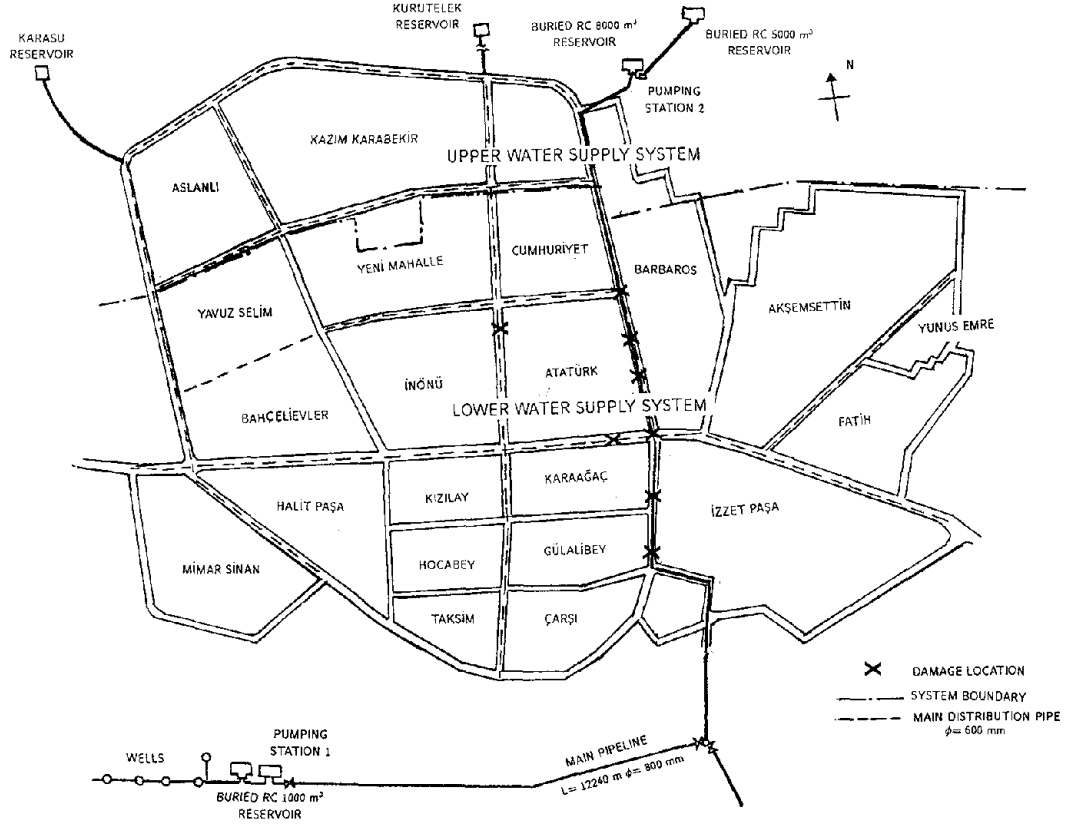

Fig. 13 Water supply system

SLOPE FAILURES AND AVALANCHES

Soil and Rock Slope Failures

There were some soil slope failures on the banks of Fırat river (Fig. 11). At several locations on the northern slope of the valley, where the rock mass shows up and is highly fractured, there were some rock slope failures (Photo 25). In addition to these, there were some rock falls weighting about 2-3 tonf at maximum. However, the soil or rock slope failures were of limited scale and did not have any major impact on roadways or railways or damage on villages located next to mountain sides.

Photo 24 Failure of soil slope on the bank of Fırat river

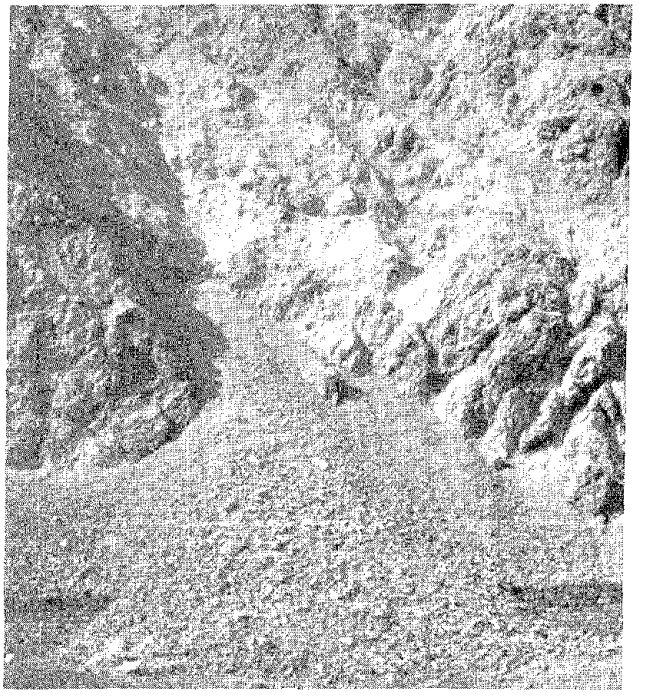

Photo 25 Failure of rock slope on the bank of Fırat river

Avalanches and snow slides

It was earlier reported that there were some avalanches and snow slides in mountainous villages and at a locality called Tanyeri where there is a roadway junction (Fig. 11). The roadway was closed for about one day at this point. At the time of the investigation of authors, the snow melted at lower levels and no trace of such an incident could be observed. However, at higher levels, the authors spotted small scale avalanches.

LIQUEFACTION AND GROUND FAILURES

There were no liquefaction failures in the city of Erzincan. However, at several places such as Ekşisu, Karasu and Altınbaş, severe liquefactions were observed (Photo 26). Although more than one month was already passed over the earthquake, the incidents of sand volcanos, sand blows were still clearly visible at the above localities. Fig. 15 shows particle size distribution curves of liquified ground at various locations. It should be noted that old Erzincan city was located on a liquifiable ground and it was completely destroyed by the great earthquake of 1939 (M 8.0). As a result, the city was moved northwardly and relocated at its present place.

At Ekşisu and Karasu, the ground failures as a result of liquefaction were observed and the ground were displaced more than 1 m. Photo 27 shows ground failure at Karasu.

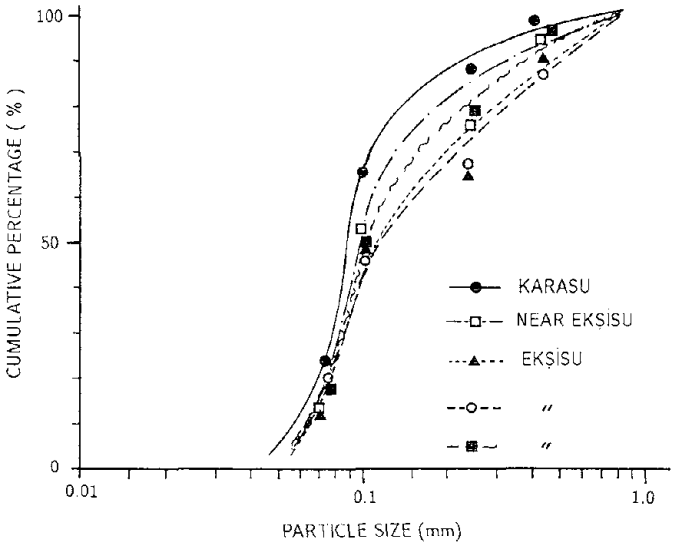

Fig. 15 Particle size distribution curves for liquified ground

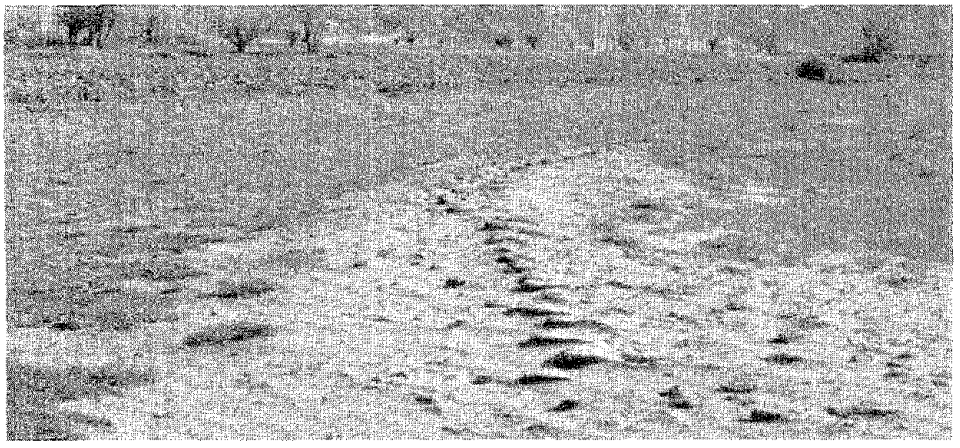

Photo 26 Liquifaction of ground near Fırat river (Karasu)

Photo 27 Ground failure at Karasu (note 1000 mm separations and partial subsidence)

CONCLUSIONS

The authors have described in this report their site observations and information they have gathered during their investigation. There is no need to repeat the conclusions drawn in each sections or subsections herein. However, there is one thing to say that we should do our utmost efforts to predict the earthquakes beforehand on the basis of scientific knowledges, which is as important as trying to solve out the genesis of the universe and to develop methods to minimise the devastating and killing effects of earthquakes.

Turkey and Japan has a long history of cooperation in the field of seismology and earthquake engineering. Japan should share the knowhow and technology for the earthquake resistant reinforced concrete (RC) design to Turkey by taking this chance as an indication of the historical cooperation between two countries. Furthermore, there were many people killed by the collapse of masonry structures. A fundamental research program should be initiated to increase the earthquake resistance of these structures by developing new reinforcing materials, which are cheap and easily obtainable. This would be in accordance with with the spirit of "INTERNATIONAL DECADE FOR NATURAL DISASTER REDUCTION"

ACKNOWLEDGEMENTS

The authors would like to sincerely express their thanks and gratitudes to Prof. Dr. R. Yarar and his colleauges in Faculty of Civil Engineering, Istanbul Technical University, in particular to Assoc. Prof. Dr. Z. Hasgür (who also joined the authors in the field trip), Mr. Muzaffer Dikili of Bayındırlık Bakanlığı Afet İşleri Genel Müdürlüğü (Housing Ministry of Turkey) and his staff, Mr. F. Civelek, Director of the 14th Division of İller Bankası, Engineers of Devlet Su İşleri 8. Bölge Müdürlüğü (State Hydraulic Department) who provided the logs of borings in Erzincan Ovası. Finally, we would like also to express our condolences to the people of ERZİNCAN.

REFERENCES

A.A.Barka and L. Gülen (1987): Age and total displacement of the North Anatolian Fault zone and its significance for the better understanding of the tectonic history and present day dynamics of the Eastern Mediterranean region, Melih Tokay Geol. Symp., METU, Geol. Dept., Ankara, Turkey, pp.57-58.

A.A. Barka and K. Kadinsky-Cade (1988): Strike-slip fault geometry in Turkey and its influence on earthquake activity, Tectonics, 7, pp.663-684.

N. Bayülke (1978): Tuğla yığma yapıların depremlerdeki davranışı, Deprem Araştırma Enstitüsü Bülteni, 6(22), pp.26-41.

D.S.İ Hydrological Reports for Erzincan Ovası.

M. Hamada and Ö. Aydan (1992): The site investigation of the March 13 Earthquake of Erzincan, Turkey. Published by the Association for the Development of Earthquake Prediction (ADEP), Tokyo.

A. Koçyiğit 1992: Kuzey Anadolu Fay kuşağı ve 1939-1992 Erzincan depremleri, Cumhuriyet Gazetesi, Bilim-Teknik, No: 265, April 11.

A.M.C. Şengör (1979): The North Anatolian transform fault: its age, offset and tectonic significance, J. Geol. Soc. London, 136, pp. 269-282.

II Liquefaction and its Related Damage During Past Earthquakes

Liquefaction-Induced Ground Failure and Related Damage to Structures during 1991 Telire-Limon, Costa Rica, Earthquake

N. Yoshida[1], H. Watanabe[2], S. Yasuda[3], and S.Mora C.[4]

[1] Research Head, Engineering Research Institute
Sato Kogyo Co., Ltd.
[2] Professor of Civil Engineering
Saitama University
[3] Associate Professor of Civil Engineering
Kyushu Institute of Technology
[4] Jefe Departamento de Geologia
Instituto Costarricense de Electricidad

ABSTRACT

An earthquake of magnitude 7.5 occurred on April 22, 1991, in Costa Rica, which caused significant damage in Costa Rica and Panamá. Soil liquefaction occurred widely in the east coast of Costa Rica and Panamá. Landslides occurred in the Talamanca Mountain area for over 2000 km^2. Several tens km of main road from San José to Panamá through Limón was damaged mainly due to soil liquefaction, along which five bridges totally collapsed. Two reinforced concrete buildings fell down due to strong shaking. The authors conduced reconnaissance 2 months after the earthquake for about a week. This paper describes the damage during the earthquake focusing upon the liquefaction based on the reconnaissance.

INTRODUCTION

An earthquake of magnitude 7.4 occurred in Costa Rica at 15:57 local time on April 22, 1991. The earthquake caused widespread and significant damage in the area in the Talamanca Mountain area and the Caribbean low land and Panamá. Totally 53 people were killed, and the damage in Costa Rica is estimated to be over $500 million in Costa Rica.

The authors conducted reconnaissance on the damage caused by the earthquake 2 months after the earthquake for a week. This paper focuses on the liquefaction-induced ground failure and related damage to the road and bridges due to the earthquake.

OVERVIEW OF EARTHQUAKE AND DAMAGE

Costa Rica and adjacent area lies at the interface of 3 tectonic plates, namely the Caribbean, Nazca, and Cocos plates. Very active seismicity occurs along the Middle America Trench in the Pacific Ocean, interface between the Caribbean plate and the Cocos plate; past earthquakes concentrated in the areas along the Pacific Ocean. The Telire-Limón earthquake, however, occurred in the Caribbean Sea side, the seismicity of which is not so active.

The general features of the main shock were as follows:

Origin time	: 15:57, April 22, 1991
Epicenter	: 9°36.60' N, 98°9.20' W
Depth	: 16.44 km
M_S	: 7.5
M_L	: 7.2 (EQE, 1991)

The fault was a shallow angle thrust fault; the upper block, east coast of Costa Rica, moved toward the northwest direction. It is not sure whether the plane of this fault rupture reached the surface or not. If a fault trace appeared in the surface, its location is some distance offshore in the Caribbean Sea as shown in Figure 1. The tectonic uplift of the sea floor was observed along the east Costa Rica shoreline (Astorga, 1991). The uplift at Limón reached over 2 m. The amount of the uplift decreases gradually in the south, about 1 m at Cahuita and about 0.5 m at Puerto Viejo, whereas it decreases rapidly to the north. A tsunami, with 3.5 m high, hit Limón.

Figure 1 shows seismic intensity in MM scale in Costa Rica. In general, the intensity in the coastal area is larger than that in the mountain area. The areas, with intensity IX, are located only in the coastal area.

The main shock was recorded by more than 20 strong motion stations in Costa Rica by UCR (University of Costa Rica) and by ICE (Institute Costarricense de Electricidad). The closest station to the epicenter is Siquirres dam construction site (epicentral distance = 61 km) where peak accceleration was 0.76 g. The station at San Isidro is also close to the epicenter (epicentral distance = 76 km), but in this case the peak accelcration was 0.20 g. The difference of the peak accelerations between these two stations is recognized from the fact that a directivity of ways took place during the rupture process and hence that San Isidro is located in the transverse

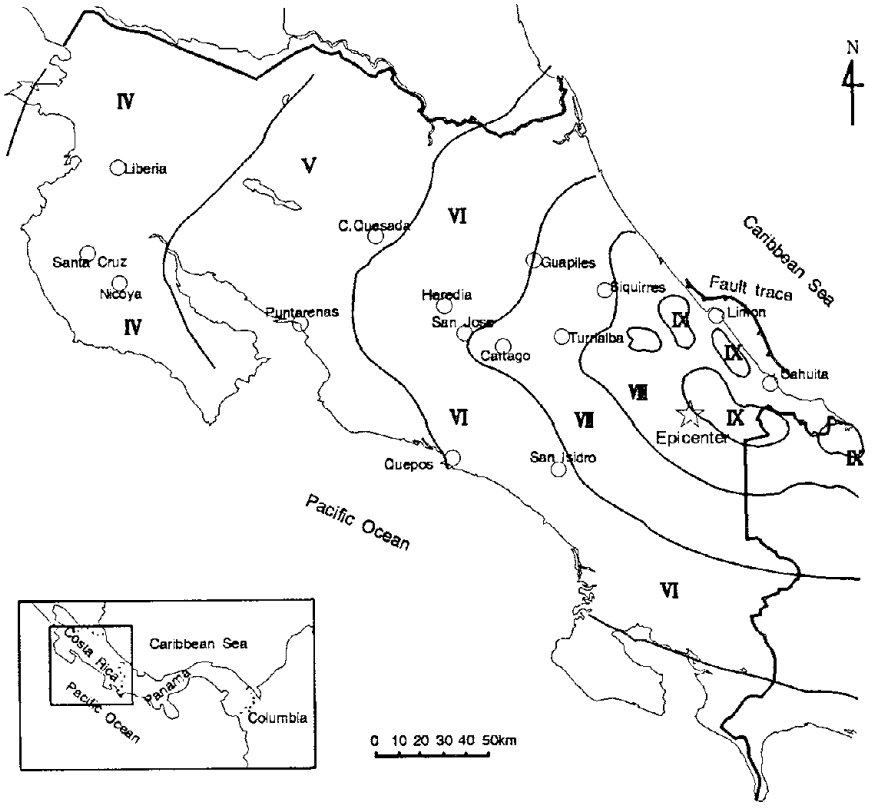

Figure 1 Map showing the location of epicenter, fault trace and seismic intensity in MM scale

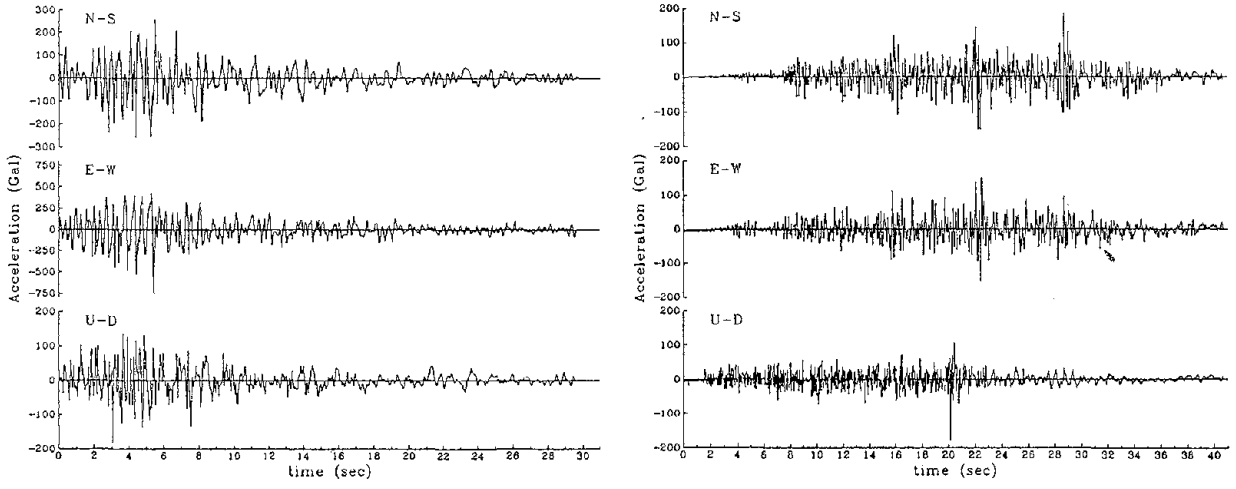

(a) Siquirres (recorded by ICE) (b) San Isidro (recorded by UCR)

Figure 2 Digitized acceleration records

direction to the fault trace whereas Siquirres is located along the longitudinal direction or on the fault rupture plane. The authors digitized these records, which are shown in Figure 2. Figure 3 shows peak accelerations of the records by UCR in terms of the epicentral distance. The peak acceleration is larger on the soft ground than hard deposit and rocks, which is supposed to be the reason why seismic intensity is larger in the coastal region than in the mountain area in Figure 1.

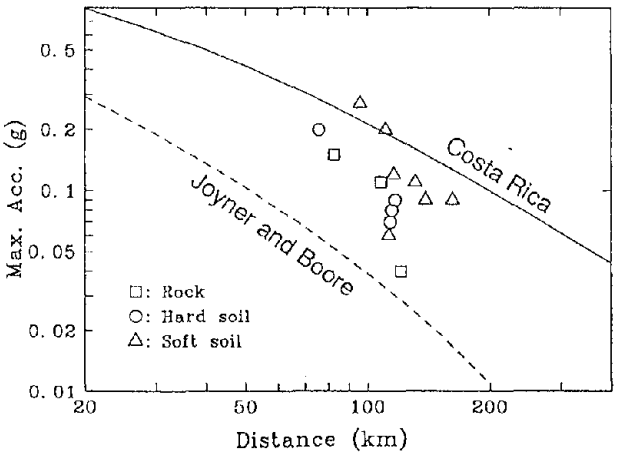

Figure 3 Peak acceleration versus epicentral distance relationships

The empirical equation by Joyner and Boore and equation based on the records in Costa Rica (Climent, 1991) is also shown in Figure 3. The former equation is derived from rock site records in the North America, and it is observed that peak accelerations are larger in Costa Rica. Peak accelerations are, in general, smaller than the ones from the records in Costa Rica indicating the effect of mountain areas on the passage of earthquake waves.

Figure 4 shows areas affected by the earthquake in Costa Rica. Landslides occurred in the areas north from the epicenter for about 2000 km^2, among which the ratio of slid area to the global area is larger than 60 % in 75 km^2, and that is between 15 to 60 % in 375 km^2. The difference of the slid area between the north and the south from the epicenter is recognized to be the difference of slope angles. Relief is steeper in the north than that in the south. Soil liquefaction occurred in the Caribbean low lands, which is described in detail in the following sections. Road suffered heavy damage for several tens km and five bridges fell down along the main road from San José, capital of Costa Rica, to Panamá through Limón city. Two reinforced concrete buildings were totally collapsed at Limón. An oil refinery facility at Port of Moin suffered significant damage such as oil leakage, fire, etc.

OVERVIEW OF SOIL LIQUEFACTION

Soil liquefaction occurred widely in the low lying area in eastern Costa Rica, as shown in Figure 4, which caused significant damage to the embankment, bridges, and houses, etc. The maximum distance from the epicenter to the liquefied site is read off from Figure 4 as 92 km. This data was plotted in terms of the magnitude of the earthquake in Figure 5 as a solid circle. Data for other earthquakes derived by Kuribayashi et al. (1975), Wakamatsu (1991) and Youd (1977) are also shown in the figure, with the boundary line derived by Wakamatsu(1991). The data of this earthquake is within the range of the past earthquakes, hence the maximum distance to the liquefied site is not very large in comparison.

The authors investigated mainly the areas along Route 32 which runs from San José to Limón, along Route 36 which runs from Limón to Panamá, and the road running to the north from Limón along the shoreline. Liquefied sites, damage, and grain sizes of the sand are summarized

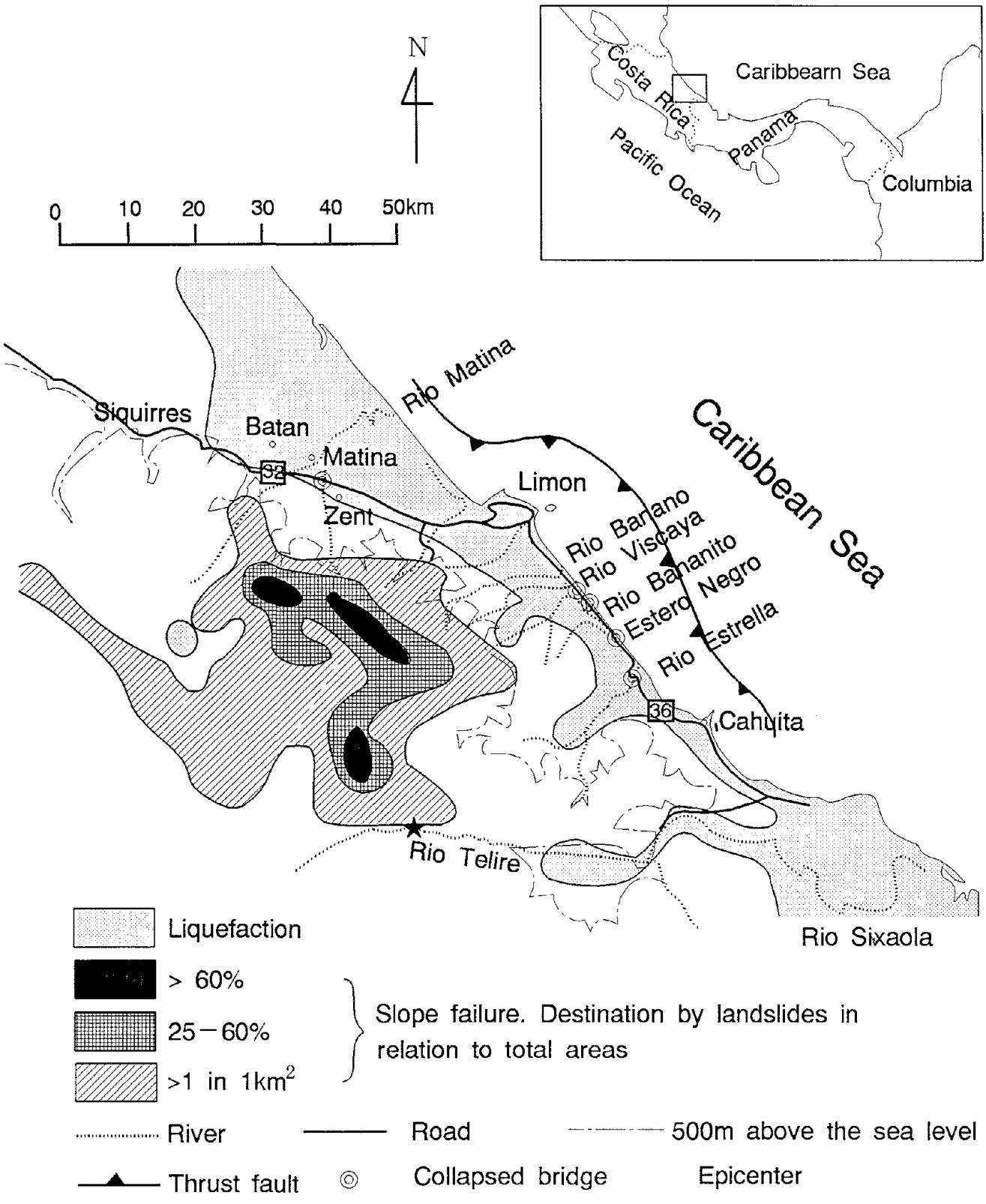

Figure 4 Map showing the affected area in Costa Rica, from the April 22, 1992 Telire–Limón earthquake (M_l=7.5, z=16.5km)

Table 1 Summary of liquefied sites

Location	Damage description	Sand
Area along Route 32, low lying land between San José and Limón	Slide and lateral spreading of the road embankment in the low lying area east from the Chirripó river	Fine sand
	Tilting of electric steel truss tower at Zent	
	Lateral spreading of river bank at the Cuba river	
	Lateral spreading of river bank at the Blanco River	Fine Sand
Community of Matina	Settlement and tilting of houses, sand boiling, soil liquefaction, lateral spread at Matina River	
Area along the road running the Caribbean sea shoreline from Limón to the mouth of the Matina River	Fissure and lateral spreading of the road at Cem Plaza	Medium sand
	Sinking of road at the south of the mouth of the Matina river	
	Channel like subsidence at the inland side from the road at the south of the mouth of the Matina river	
	Slide and lateral spreading of the embankment constructed for oil survey	Silty sand
	Settlement and tilting of houses, sand boils, soil fractures	Medium sand
Area along Route 36, from Limón to the Estrella River	Fissure at the runway of the airport at Limon	
	Lateral spreading of the river bank at the Banano river	
	Lateral flow of the river bank at the Vizcaya river	
	Fissure, subsidence, and lateral flow toward the inland side in the road between the Vizcaya and the Estero Negro rivers	
	Lateral flow of the river bank at the Bananito River	Medium Sand
	Lateral flow of the river bank at the Estero Negro river	
	Lateral spreading of the river bank at the Estrella river (?)	

in Table 1. Soils were sampled at four sites, the grain size distribution curves of which are shown in Figure 6, where D_{50} denotes mean diameter of soil particle and FC denotes fine contents in %. The liquefied sites are classified into 3 categories:

1) Inland areas along the river which are located up to several km from the Caribbean Sea shore into the alluvial plain developed by the rivers.
2) Sand bars along the beach and areas from sand bar to the low lying marsh at the back of the sand bar.
3) Coastal areas along the rivers.

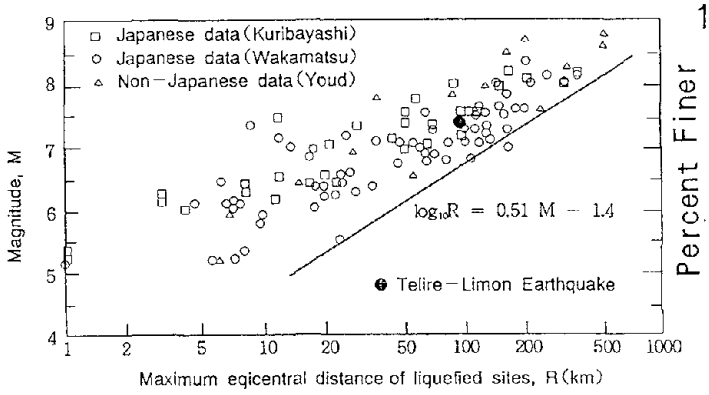

Figure 5 Maximum epicentral distance to liquefied site versus Magnitude relationships

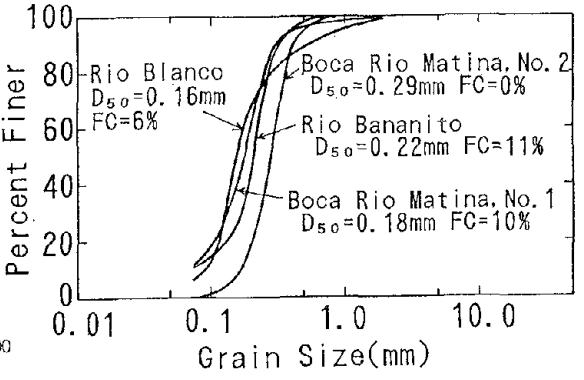

Figure 6 Grain size distribution curves

LIQUEFACTION IN THE INLAND ALLUVIAL PLAIN

On the way from San José to the Limón city, Route 32 enters the Caribbean low land a little before Siquirres. Road embankment was damaged for about 35 km from Siquirres to Limón. Photo 1 shows damage of the road embankment, in which fissures parallel to the road and lateral spreading are observed. Figure 7 schematically shows the mechanism of the damage to the road embankment; liquefaction beneath the embankment caused loss of sustain strength of the ground. Sand boils are observed near the road (Photo 2).

Lateral spreading of the river bank was also observed. The with of the river became narrow due to lateral spreading at the Cuba, Toro and Blanco rivers.

LIQUEFACTION AT THE SAND BAR AND MARSH

Port of Moin is located about 5 km west from the Limón city. An unpaved road runs toward the north from there on the sand bar besides the Caribbean Sea shore. Liquefaction occurred at the sand bars and marsh at the back of the sand bar along the road. Photo 3 shows typical damage to the road due to liquefaction, and Figure 8 shows a cross section and the mechanism of the damage there schematically. The road is constructed on the sand bar besides which there is a channel or marsh in the inland side. Liquefaction occurred in the areas between the channel and the sand bar, in which the ground moved toward the channel, causing fissures in the sand bar as shown in Photo 3. The height of the sand bar is about 2 to 3 m from the sea level. Boiled sand is clean medium sand.

Photo 1 Fissures and lateral spreading of the road embankment on Route 32 near Siquirres

Photo 2 Sand boils near the Rio Blanco bridge

Photo 3 Fissures parallel to the road at Cem Plaza

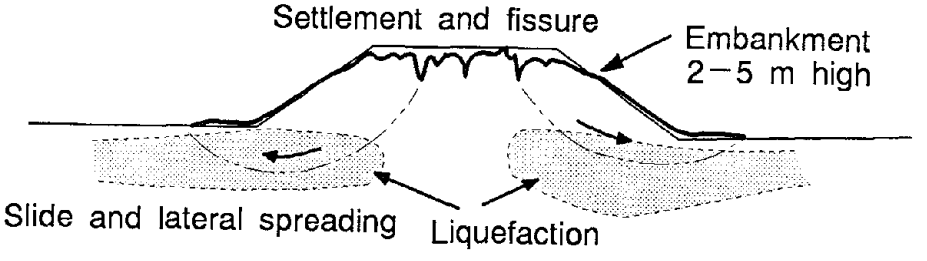

Figure 7 Schematic figure on the damage to road embankment

At the community near the mouth of the Matina river a 2 meters wide grabben runs parallel to the shoreline and settled about 50 cm. According to an interview to the resident, the settlement occurred about 2 minutes after the main shock and the ground was soft like a jelly when walking after the earthquake. Houses were damaged due to the ground deformation.

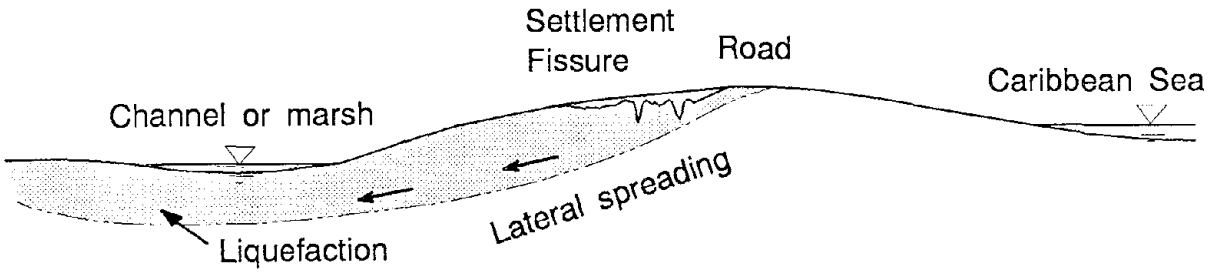

Figure 8 Schematic figure showing the cross section and the mechanism of the damage to the road on the sand bar

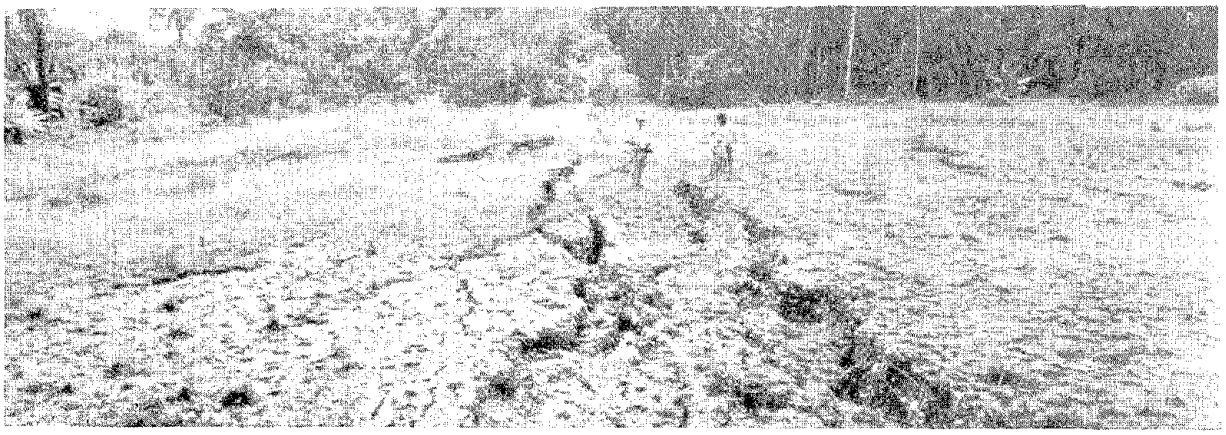

Photo 4 Ground failure of the embankment for the oil survey

A few hundreds of meters to the northwest of the community, there is a fill with about 100 x 100 m^2 area which was constructed for the oil survey. The embankment was composed of gravel and the height is about 1.5 m. Many wide fissures parallel to the shoreline are seen at the embankment as shown in Photo 4; silty sand boiled up from one of the fissures. The mechanism of the damage is supposed to be similar to the one shown in Figure 8; liquefaction at the marsh and under the embankment caused lateral spreading of the ground toward the marsh causing fissures. The weight and rigidity of the embankment is supposed to aggravate the damage.

Traces of liquefaction are also observed just south of the mouth of Matina river.

As described preceding, there exist always a marsh and/or channels in the inland side of the road; whenever fissures due to lateral spreading are observed in the areas along the shoreline in the north of Limón. Since the height of the sand bar is the same in these area, a few meters from the sea level, the existence of the channel and/or marsh is supposed to be the main factor causing lateral spreading.

In the south of Limón, a primary road, Route 36, runs on the sand bar beside the shoreline to the neighboring country, Panamá. The same kind of damage described above is seen along the road, too. Damage is significant at the mouth of the Banano river where the river flows into the sea after flowing parallel to the shoreline for more than 1 km. The ground flows laterally at the

sand pit between the shore and the river, and fissures with large width run parallel to the river. Fissures are also observed along the temporary road for the collapsed Rio Bananito bridge. The same kind of damage also occurred at the sand pit about 3 km south from the mouth of the Estero Negro river.

LIQUEFACTION AT MOUTHS OF RIVERS FLOWING INTO THE CARIBBEAN SEA

Since Route 36 runs along the Caribbean sea, it crosses several middle or small rivers at their river mouths. The bridges from Limón to the Estrella river suffered significant damage and four bridges totally collapsed.

The Rio Banano bridge, first bridge along Route 36 south from Limón, is located several km inland from the mouth of the Banano river. According to the interview, sand and water boiled at the river bank during the earthquake, and the boiled water was as hot as several ten degrees Centigrade. The river bank flowed laterally and the approach fill subsided, but the bridge itself was not damaged.

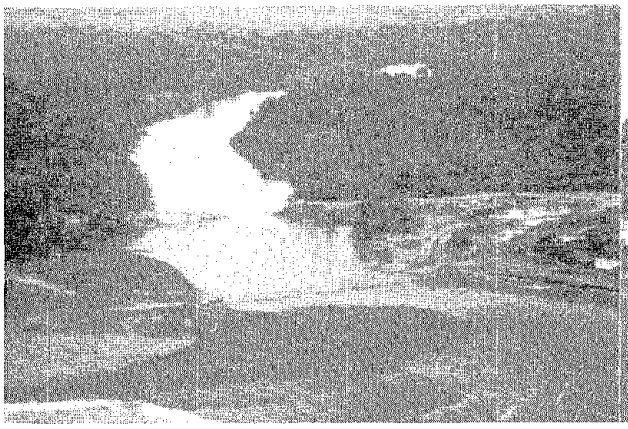

Photo 5 Bridge over the Vizcaya river

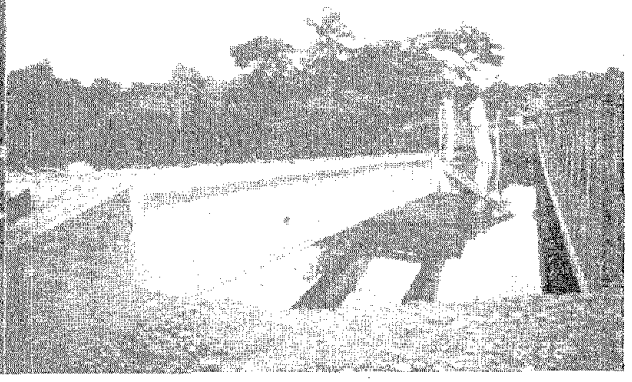

Photo 6 Bridge over the Vizcaya River

The Rio Vizcaya bridge, a 3-span prestressed concrete I-beam bridge, collapsed completely (Photos 5 and 6). Figure 9 schematically shows damage of the bridge. One internal support is missing and was supposed to settle down due to liquefaction. The south abutment rotated 8 degrees and was pushed towards the center of the river due to lateral flow of river bank.

The Rio Bananito bridge, a 2-span prestressed concrete I-beam bridge, also completely collapsed as shown in Photo 7

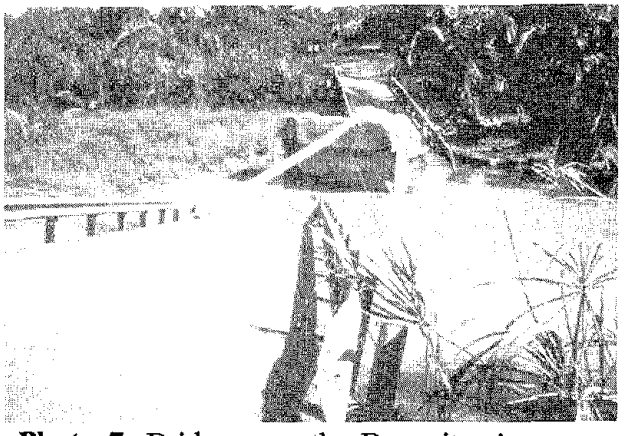

Photo 7 Bridge over the Bananito river

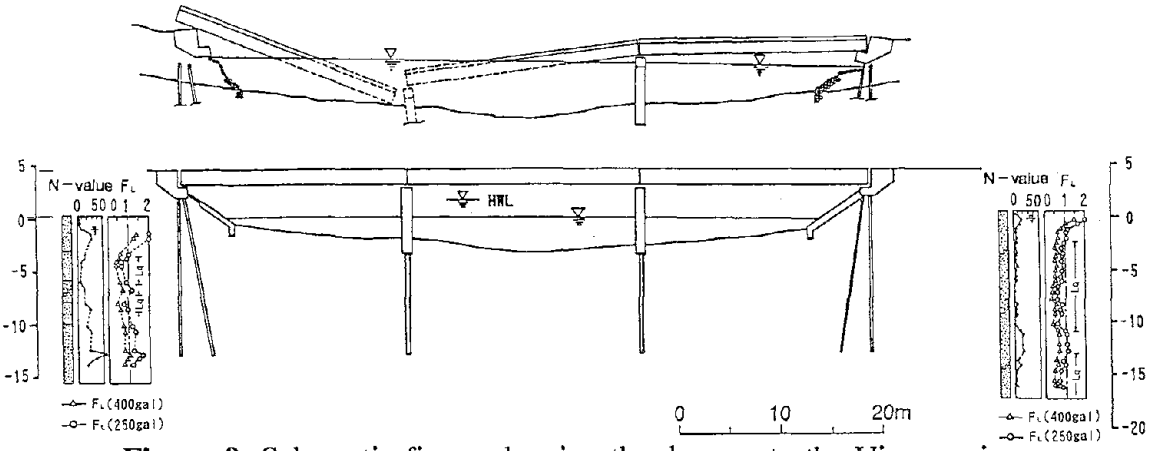

Figure 9 Schematic figure showing the damage to the Vizcaya river

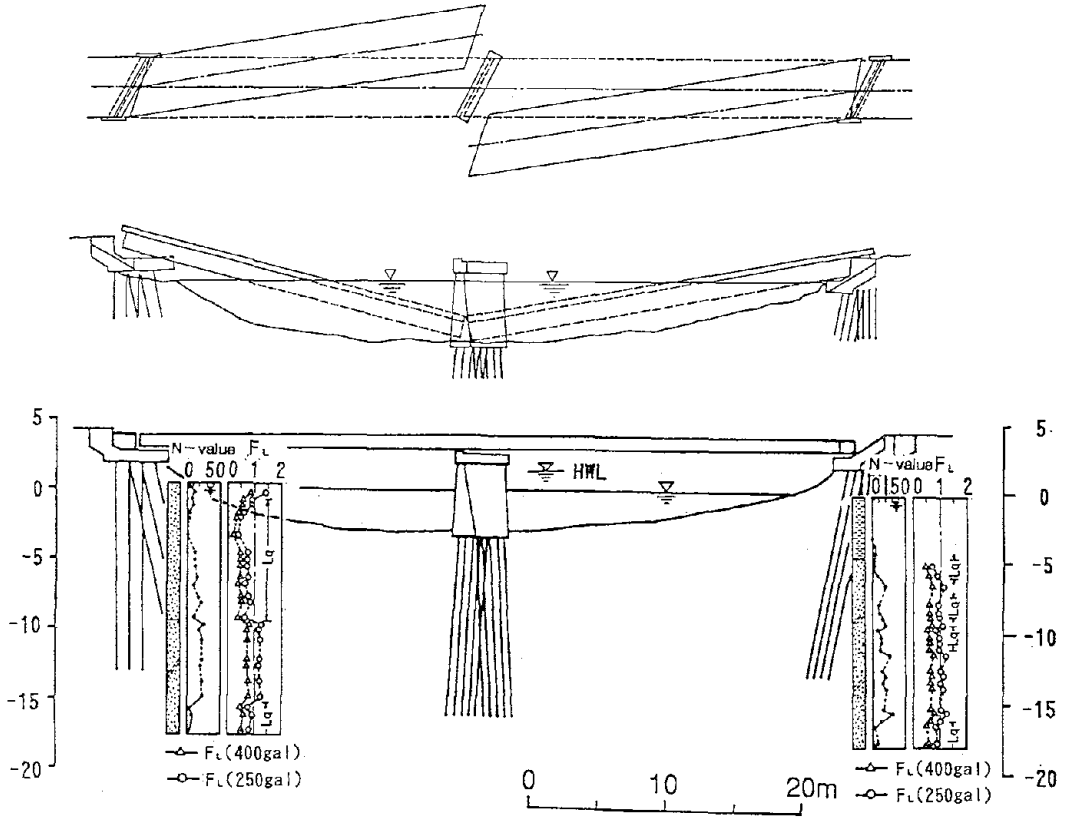

Figure 10 Schematic figure showing the damage to the Bananito bridge

and Figure 10. The Bananito river flows into the Caribbean sea after running parallel to the shoreline for about 4 km. Since the bridge crosses the river at the parallel portion, Route 36 bends in S-shape near the bridge; the road runs on the sand bar in the north and on the marsh in the south. Lots of fissures parallel to the river were observed along the river bank (Photo 8), and the approach roadway slumped. The southern abutment rotated about 15 degrees due to lateral flow of the ground towards the river center.

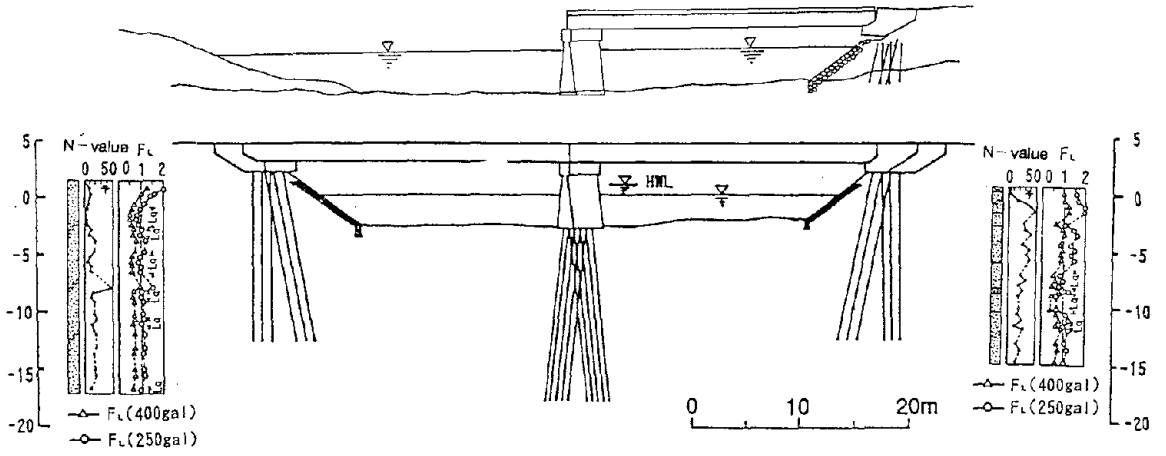

Figure 11 Schematic figure showing the damage to the Estero Negro bridge

Photo 8 Fissures and subsidence along the right bank of the Bananito river caused by the lateral flow of the ground

The same kind of ground failure occurred near the bridge over the Estero Negro river. One span of the 2-span prestressed concrete I-beam bridge fell down as shown in Photo 9 and Figure 11, which was already taken off at the time of the reconnaissance. The lateral flow of the ground at the right river bank was supposed to push the abutment and the remaining span, which resulted in the falling down of the missing span.

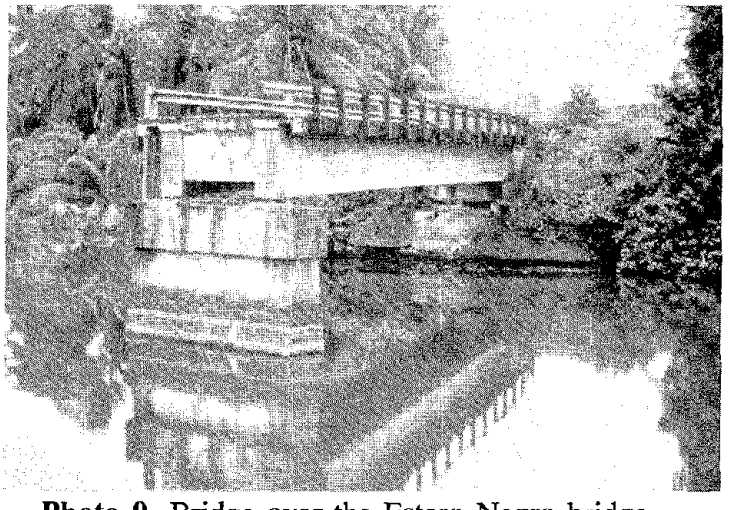

Photo 9 Bridge over the Estero Negro bridge

It is worth to mention that there is another bridge crossing a small creek about 3 km south from the Rio Estero Negro bridge. The approach roadway subsided but the bridge was not damaged.

The southern bound of the reconnaissance was the Estrella river. The two 75 m steel truss spans bridge, with 25 m prestressed concrete I-beam completely collapsed (Photo 10); both truss spans fell down from the center pier. The damage is supposed not to be directly related to the liquefaction.

Photo 10 Bridge over the Estrella river

LIQUEFACTION AT COLLAPSED BRIDGE

The liquefaction potential is computed based on the boring investigation performed preceding the construction of the bridges, in the year from 1969 to 1971. Based on the Specifications of Highway Bridge by Japanese Road Association, the resistance factor against liquefaction, F_L, is computed from the liquefaction strength R and shear stress induced by the earthquake L,

$$F_L = \frac{R}{L}$$

where

$$R = R_1 + R_2 + R_3$$

$$R_1 = 0.0882\sqrt{\frac{N}{\sigma'_{vo} + 0.7}}$$

$$R_2 = \begin{cases} 0.19 & (0.02mm \le D_{50} \le 0.05mm) \\ 0.225\log_{10}(0.35/D_{50}) & (0.05mm < D_{50} \le 0.60mm) \\ -0.05 & (0.60mm < D_{50} \le 2.00mm) \end{cases}$$

$$R_3 = \begin{cases} 0.0 & (0\% \le F_c \le 40\%) \\ 0.004F_c - 0.16 & (40\% < F_c \le 100\%) \end{cases}$$

$$L = \frac{\alpha_{max}}{g}(1 - 0.015z)\frac{\sigma_{vo}}{\sigma'_{vo}}$$

in which N denotes SPT N-value, α_{max} denotes peak acceleration at the ground surface, g is the acceleration of gravity, z is depth in m, and σ_{vo} and σ'_{vo} denote total and effective overburden pressures in kgf/cm^2, respectively.

The following assumptions are employed:

1) Referring Figure 3, peak accelerations of 250 and 400 Gals are investigated for α_{max}.
2) The height of the ground surface may be changed during the construction of the bridge, but it is not taken into account.
3) Mean diameter of soil particle and fine content of the fine sand are assumed to be 0.22 mm and 11 %, respectively, based on the sand sampled at the Bananito river. Those for the other layers and other quantities such as unit weight are estimated from the soil classification following the specification.
4) Energy delivery ratio from the hammer to the rod when counting the SPT N-value in Costa Rica is the same than that in Japan.

The results of the analysis are shown in Figures 9, 10, 11, and 13 for the Vizcaya, Bananito, Estero Negro, and Estrella bridges, in which the range shown as L_q is the one liquefied under the peak acceleration of 250 Gals. The lengths of the piles are 15.5 m at the Rio Vizcaya bridge, about 13 m for abutment and 16.2 m for center pier at the Rio Bananito bridge, 12.75 m for abutment and 18 m for pier at the Rio Estero Negro bridge, and 20.7 m for left abutment and pier and 8.7 m for right abutment at the Rio Estrella bridge, respectively. The length of the test pile is 2 m longer than the ordinary piles.

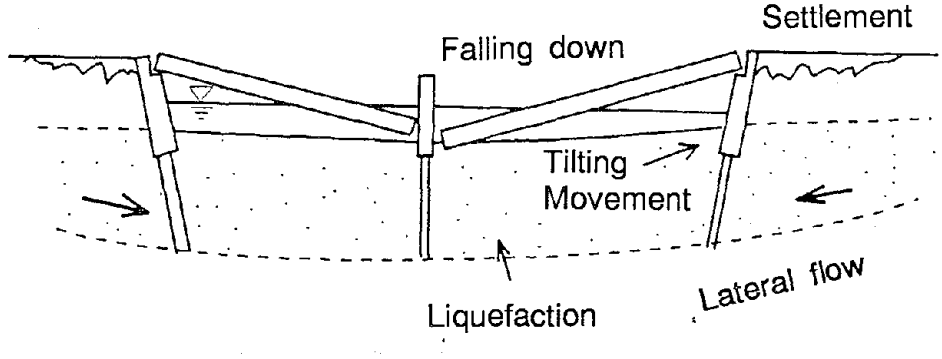

Figure 12 Mechanism of the damage of bridge due to lateral flow of the river bank

Liquefaction is supposed to occur down to the depth of the pile tip for 3 bridges, the Vizcaya, Bananito and Estero Negro bridges, under α_{max}=400 Gals, and more than a half pile length liquefied even under α_{max}=250 Gals. Consequently, the mechanism of the collapse of the bridges is supposed to be as follows (Figure 12). The ground at one river bank or both river banks liquefied down to the depth of the pile tip or more, and the ground flowed laterally towards the river center, pushing and/or sweeping off the abutment and causing the falling down of the span. Since the ground liquefied at the pile tip, settlement of the abutment and pier may occur due to loss of the sustaining capacity, but it is not supposed to be the predominant reason of the collapse.

Liquefaction was supposed not to occur at the Rio Estrella bridge because F_L>1 even under α_{max}=400 Gal as shown in Figure 13.

In addition to the liquefaction-induced ground movement, some factors aggravated the damage of the bridge. Girders were simply supported by the abutment and pier, hence redundancy was small. Moreover, the width of the inner pier was too small and a small amount of lateral movement caused falling down of girders.

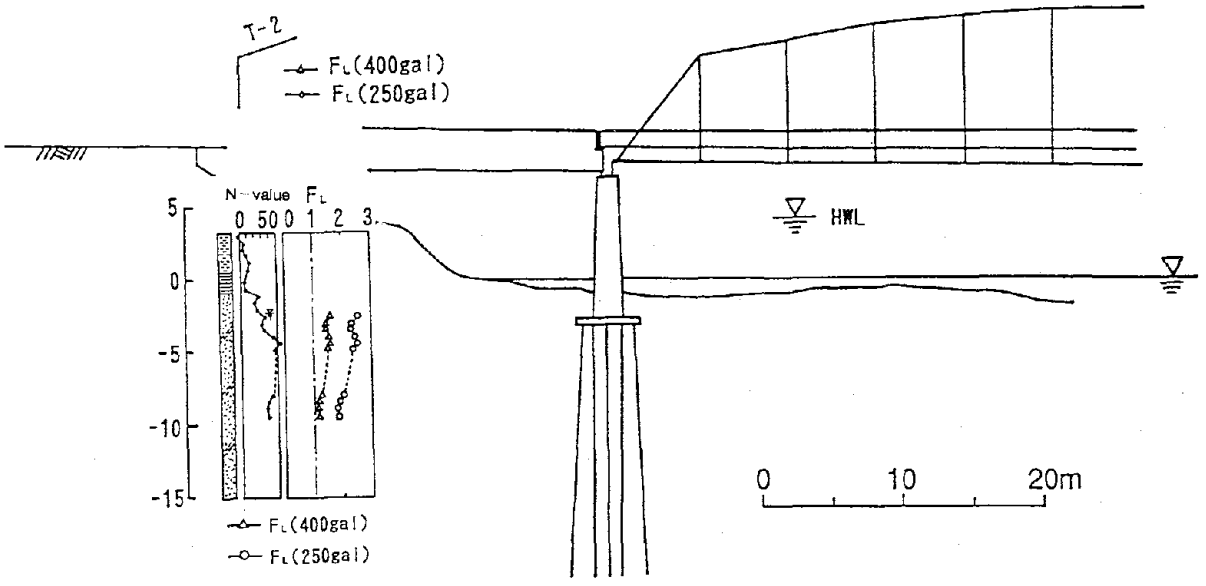

Figure 13 F_L value at the Rio Estrella bridge

CONCLUDING REMARKS

Damage during the 1991 Telire-Limón earthquake is described focusing on the liquefaction-induced ground failure and related damage to structures. Liquefaction occurred in the widespread area: inland alluvial plain developed by the rivers, sand bar and marsh along the Caribbean sea shoreline, and coastal areas along the rivers. It caused significant damage to road and bridges.

The road embankment was damaged due to the liquefaction occurred under the embankment. The road on the sand bar was damaged because of the ground spread laterally toward the marsh or channel in the inland side due to liquefaction.

The bridges were damaged because of lateral flow in the ground pushed and/or swept off the abutment and girder causing the collapse. Previous countermeasures against lateral spreading were not applied. Insufficient design of the bridge, small redundant support of girders and short width of inner pier, aggravate the damage. Approach fill to the bridge were also slumped because of the liquefaction under the foundation ground.

ACKNOWLEDGEMENT

We express our great appreciation to prof. K. Ishihara, the University of Tokyo, who arranged the reconnaissance. Thanks are extended to H.L.P. Acuna and other engineers at Ministerio de Obras Publicas y Transportes for data of the collapsed bridges.

REFERENCES

1) EQE International (1991), The April 22, 1991, Valle de la Estrella, Costa Rica Earthquake, A Quick Look Report
2) Allan Astorge Gattgens (1991), Informe técnico sobre el levantamiento de la Costa Caribe de Costa Rica, Como consecuencia del terremoto del 22 de Abril de 1991, ICE]
3) G. Santana B. (1991) Registros de Aceleraciones del Terremoto de Limón, 22 de Abril de 1991, Laboratorio de Ingeniería Sísmica, Institute de Investigaciones en Ingenieria, Universidad de Costa Rica
4) A. Climent M. (1991), Sismo del 22 de Abril, reporte preliminar de aceleraciones, ICE
5) Kuribayashi,E. and Tatsuoka,F., Brief review of soil liquefaction during earthquakes in Japan, Soils and Foundations, Vol.15, No.4, pp.81-92, 1975
6) Youd,Y.L., Discussion of "Brief review of soil liquefaction during earthquakes in Japan," Soils and Foundations, Vol.17, No.1, pp/83-85, 1977
7) Wakamatsu,K., Maps for historic liquefaction sites in Japan, Tokai University Press, Japan, p.341, 1991 (in Japanese)

Site Response and Soil Liquefaction in San Francisco During the Loma Prieta Earthquake

T.D. O'Rourke[1], W.D. Meyersohn[2], H.E. Stewart[3], J.W. Pease[2], and M. Miyajima[5]

ABSTRACT

During the 1989 Loma Prieta earthquake, liquefaction in San Francisco occurred at four principal locations: the Marina, Foot of Market, South of Market, and Mission Creek areas. The result of soil investigations in these areas are presented, and used to characterize the subsurface conditions. Digitized strong motion records at several rock sites in the vicinity of these areas are used in conjunction with response analyses, using equivalent linear procedures, to evaluate site amplification at each location and its relationship with soil liquefaction. The role of Holocene bay mud is explored with respect to its influence on peak acceleration and predominant period of ground motion. Special attention is directed to the Mission Creek area where liquefaction in 1906 and 1989 occurred at the same locations in the eastern portions of the old creek bed, but not in its western part. Since liquefaction in the western part during the 1906 earthquake was responsible for catastrophic water main rupture and building collapse, the absence here of liquefaction in 1989 is of considerable interest. Explanations are given for this intriguing behavior.

1, 2, 3, 2 - Professor, Graduate Research Assistant, Associate Professor, respectively, Cornell University, Ithaca, NY
5 - Assistant Professor, Kanazawa University, Japan

INTRODUCTION

In this paper, emphasis is placed on the four areas of San Francisco illustrated in Figure 1. These areas were investigated after the 1989 Loma Prieta earthquake within the approximate boundaries shown by the solid lines. A description, with maps and photos of the observed ground deformations in these areas, has been given by O'Rourke and Pease (1992). It should be recognized that soil liquefaction effects were observed at locations in San Francisco other than those highlighted in Figure 1. Descriptions of liquefaction effects along the Embarcadero and Hunter's Point are provided by Seed, et al. (1990) and Chameau, et al. (1991). In general, the influence of liquefaction outside the areas shown in Figure 1 was minor, with the exception of Pier 45 and Hunters's Point.

The areas of prominent soil liquefaction in Figure 1 were also areas of liquefaction and large ground deformation during the 1906 earthquake (e.g., O'Rourke, et al, 1990; 1991). These areas are soft soil sites, situated mostly on loose saturated fills and soft Holocene bay mud. They include the Marina, Foot of Market, South of Market, and Mission Creek areas.

In this paper, the results of soil investigations in each area are presented, and used to characterize the subsurface conditions. Digitized strong motion records at several rock sites in the vicinity of these areas are used in conjunction with response analyses, using equivalent linear procedures, to evaluate site amplification at each location and its relationship with soil liquefaction. The role of Holocene bay mud is explored with respect to its influence on peak acceleration and predominant period of ground motion. Special attention is directed to the Mission Creek area where liquefaction in 1906 and 1989 occurred at the same locations in the eastern portions of the old creek bed, but not in the western part. Since liquefaction in the western part during the 1906 earthquake was responsible for catastrophic water main ruptures and building collapse, the absence here of liquefaction in 1989 is of considerable interest. Explanations are given for this intriguing behavior.

REPRESENTATIVE SOIL PROFILES

The general stratigraphy at the four soft soil sites consists, essentially, of loose saturated sands and silty sands overlying soft Holocene bay mud which, in turn, rests on a series of Pleistocene deposits of dense sands and stiff to hard clays. Although the same general layering sequence persists across most of these sites, thickness and depth of the different units will vary from place to place.

Over 400 conventional boring logs and over 20 Cone Penetration Test (CPT) soundings, obtained from engineering projects performed both before and after the earthquake, were reviewed, and representative cross-sections for these areas were developed. A representative soil profile for each site was developed on the basis of borehole information and shear wave velocity measurements which were performed in each of the areas. Five representative soil profiles were developed, which are shown in Figures 2 and 3.

The Marina soil profile corresponds approximately to the intersection of Marina Blvd. and Scott St. Holocene bay mud and bedrock extend to substantial depths at this location. The upper 8 m of the profile consists of land-tipped fill composed chiefly of loose to medium dense fine sand and silt with inclusions of gravel and rubble. The water table is about 2.5 m deep. The thickness of the Holocene bay mud is 23 m. Beneath the bay mud, interbedded dense sands and stiff clays and sandy clays, often referred to as old bay sediments, extend to bedrock at a depth of about 75 m (O'Rourke et al. 1991). Shear wave velocity values assigned to the different deposits were based on measurements performed by Kayen, et al. (1990), and Bardet, et al. (1991) in the Marina.

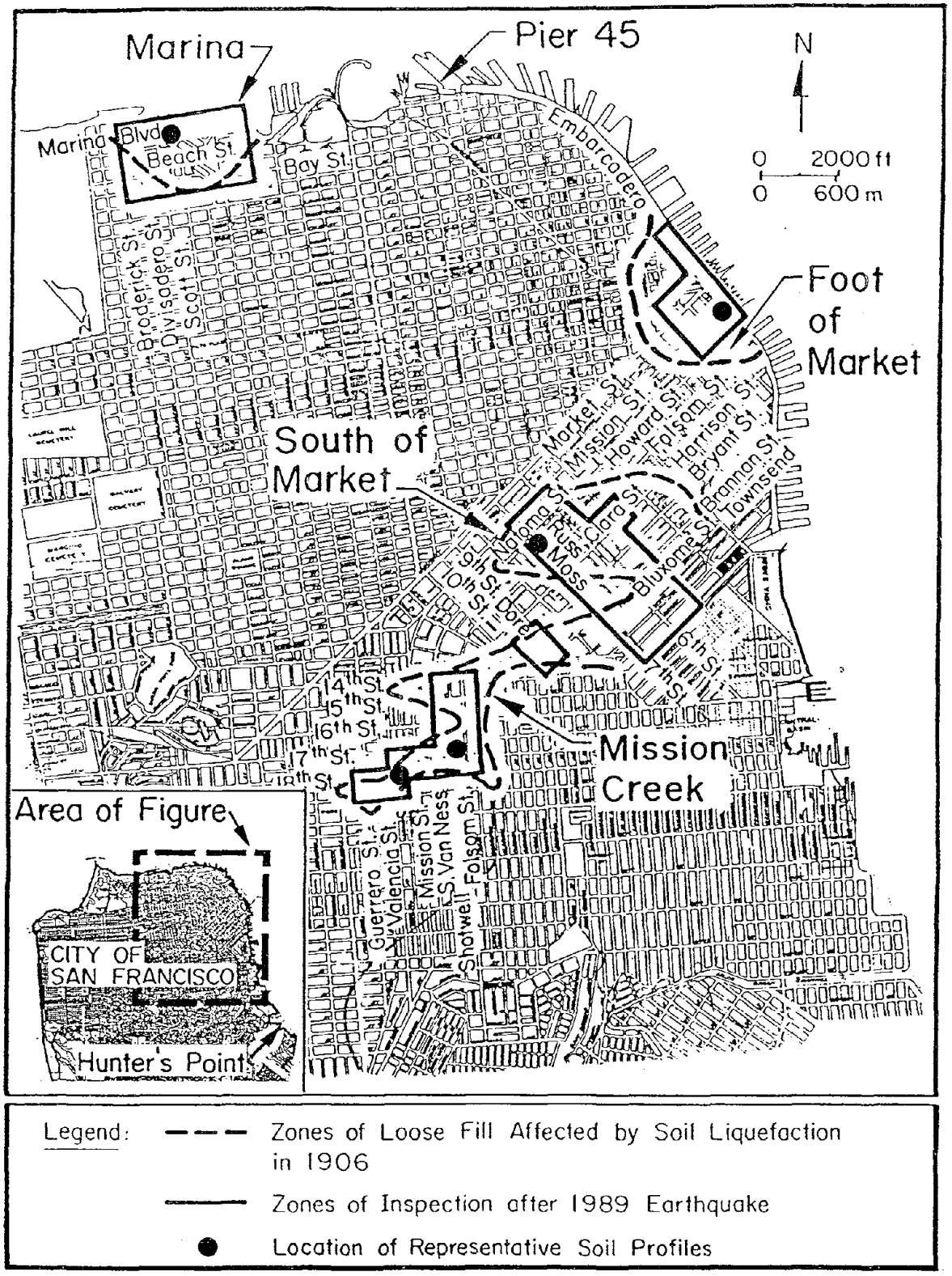

Figure 1. Plan View of San Francisco Showing Zones Investigated after the 1989 Earthquake and Locations of Representative Soil Profiles

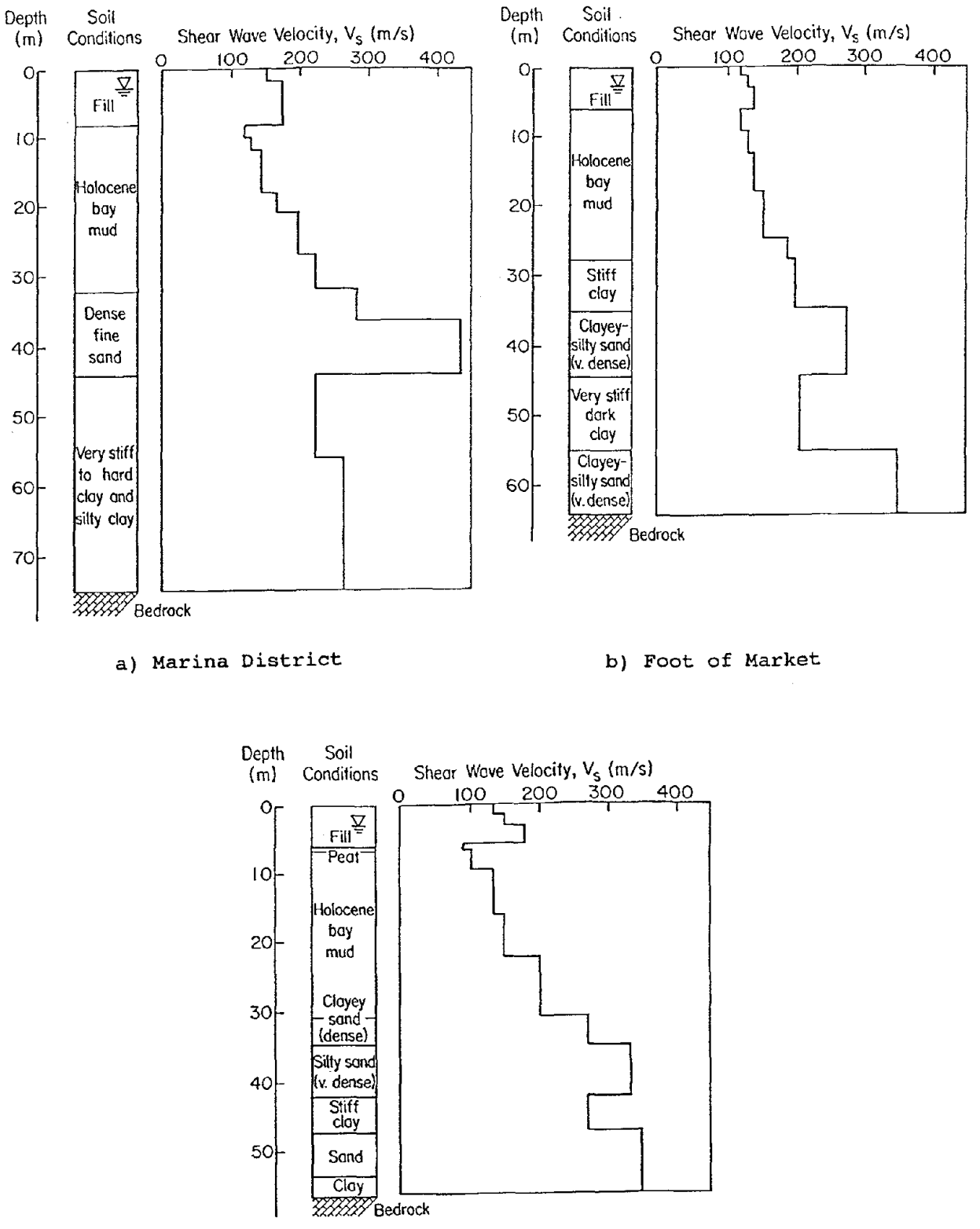

Figure 2. Representative Soil Profiles and Shear Wave Velocity Values for The Marina, Foot of Market, and South of Market Areas

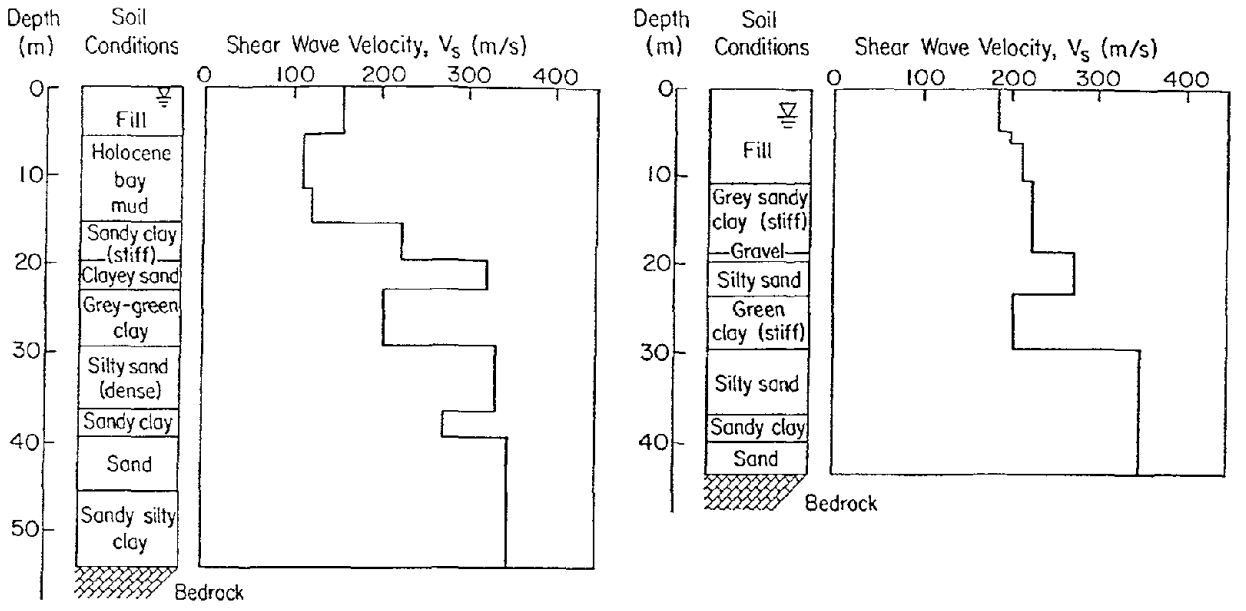

a) Shotwell St.

b) Valencia St.

Figure 3. Representative Soil Profiles and Shear Wave Velocity Values for The Mission Creek Area

Along the shoreline of the Foot of Market area, soil deposits vary in thickness, with a depth to bedrock from 55 m to about 90 m. The thickness of Holocene bay mud increases towards the bay, from 20 m at Spear St. to 30 m at the Embarcadero. Artificial deposits of loose and medium sandy fill, approximately 6 to 9 m deep, overly the bay mud. The water table varies from 2 to 3 m in depth. The soil profile in Figure 2b corresponds to the intersection of Mission St. and the Embarcadero. The bedrock at this location is 62 m deep and the bay mud is about 22 m thick. This figure also shows shear wave velocities, which were obtained from downhole and Oyo suspension log tests conducted at this location (Redpath, 1990).

The South of Market area is located over the old Sullivan Marsh, a tidal marsh that once existed immediately northwest of Mission Bay. Figure 2c shows a representative soil profile of the South of Market area. The profile corresponds to the intersection of Howard and 7th Sts. Near this location, severe ground deformation was observed during both the 1906 San Francisco and the 1989 Loma Prieta earthquakes. The total thickness of fill is about 6 m. The water table was found at a depth of 2.7 m. A peat layer, approximately 0.6 m thick, overlies Holocene Bay mud, whose thickness reaches 24 m. Shear wave velocity measurements for the upper 15 m of the profile were obtained as part of study undertaken by Cornell University for the U.S. Geological Survey (USGS). Shear wave velocity values for the lower portions of the bay mud and deeper sediments were extrapolated from measurements made in the Marina and the Foot of Market area by Kayen, et al. (1990) and Redpath (1990), respectively.

For the Mission Creek area, two locations were selected. The first one corresponds to a site on Shotwell St., where liquefaction and severe damage to timber framed structures were observed during the 1989 Loma Prieta earthquake. The soil profile, shown in Figure 3a, was obtained from exploratory borings and CPTs performed under USGS sponsorship. The water table was found at a depth of 1.0 m. The fill thickness is 5.5 m, and the thickness of bay mud is 9.5 m. The total thickness of the deposit is about

55 m. Shear wave velocities of the upper 17 m were determined from a seismic CPT survey conducted by Cornell University for USGS. The upper bay mud at this location is soft, with a shear wave velocity of only 115 m/s. Values of shear wave velocities at greater depths were, again, extrapolated from the measurements performed by Redpath (1990) at the Foot of Market area.

The second site in the Mission Creek area is Valencia St., between 18th and 19th Sts. Several CPTs and a conventional soil boring with standard penetration tests (SPT), were performed to determine the subsurface characteristics. Figure 3b presents the soil profile at the Valencia St. site. The fill, which is about 10.6 m thick, rests directly over deposits of dense sands and stiff clays. The depth to water table is approximately 3.0 m. Shear wave velocities for the upper 11 m were determined from seismic CPTs performed at nearby locations.

Because of time and logistic constraints, the Valencia St. borings and soundings were not able to reach bedrock. Nevertheless, on the basis of bedrock elevations from boreholes at different locations in the Mission Creek area, and rock outcrops of surrounding hilly areas, it was possible to develop a three dimensional view of the bedrock underlying the Mission Creek area. Based on this three-dimensional view, the depth to bedrock at the Valencia St. site is estimated as 45 m.

SITE RESPONSE ANALYSES

At each of the sites, ground response was determined using the equivalent linear model SHAKE (Schnabel et al., 1972). In SHAKE, the nonlinear degradation of soil as a function of increasing shear strain is taken into account by modifying the average soil shear modulus and damping ratio until they are compatible with the calculated average shear strains. SHAKE is a total stress analysis code, and thus, it precludes an assessment of porewater pressure and liquefaction. Because SHAKE is a one-dimensional dynamic analysis model, two and three dimensional effects can not be accounted for. Similar equivalent linear analyses were performed by Idriss (1990) and Seed, et al., (1992) for several soft sites affected by the Loma Prieta earthquake. Despite the assumptions and inherent restrictions of the model, their analyses have shown good agreement, both in shape and magnitude, between calculated and recorded surface response spectra. It appears that, for the Loma Prieta earthquake, SHAKE can be considered a useful tool in estimating surface ground motion.

Dynamic properties of Holocene bay mud, expressed as a degradation of shear modulus as a function of cyclic shear strain, were determined by torsional shear and resonant column tests performed at Cornell University (Stewart and Hussein, 1992). Strain dependent moduli for the deep, overconsolidated old bay sediments were modeled using the Plasticity Index correlation curves proposed by Vucetic and Dobry (1991). Values of modulus degradation for sands and damping ratios for both sands and clays were obtained from data published by Idriss (1990) and Seed and Sun (1989).

Rock motions used in the analyses were obtained from seismic stations located in the northeastern corner of San Francisco. These station are Pacific Heights (PACI), Rincon Hill (RINC), and Yerba Buena Island (YERB). Because these stations are located within 4 to 5 km of the soft soil sites shown in Figure 1, differences in rock motion due to attenuation effects would have been small and were ignored as a practical simplification. The accelerogram recorded at the station on Telegraph Hill (TELE) was not used in the analyses because its time record indicates that the station was triggered about 5 seconds after the arrival of the P-waves, and thus, a portion of the ground motion was not recorded (California Division of Mines and Geology, 1989).

ANALYTICAL RESULTS FOR MARINA, FOOT, AND SOUTH OF MARKET

Results for the Marina District, Foot of Market, and South of Market areas are shown in Figure 4. The figure shows the maximum acceleration profile and the surface spectral acceleration at each site. The acceleration response spectra for all cases was calculated using a damping ratio of 5%. The acceleration profile represents the envelope of maximum calculated acceleration values at each depth through the soil profile. At each site, analyses were performed with the input motions PACI, RINC, and YERB.

The calculated acceleration profiles at the Marina show a remarkably consistent pattern for the three input motions. Almost all the acceleration amplification takes place in the upper portion of the Holocene bay mud, with minor contributions in the fill. The same trend is observed, but with less uniformity, at the Foot and South of Market areas. Maximum computed surface acceleration for the three sites ranges from 0.14 to 0.18 g, with a mean value of 0.16 g.

Acceleration response spectra show also a good degree of consistency. Maximum spectral acceleration values are indicated at periods of 0.8 and 1.3 s for the three profiles. The magnitudes of peak spectral accelerations are in relatively close agreement for each of the input motions. The similarity in both acceleration profile and spectral response is most likely the result of similarities in geometry and properties among the three soil profiles. Depth to bedrock, thickness of fill and Holocene bay mud, and stratification sequence in the upper 10 to 15 m are similar at these sites.

ANALYTICAL RESULTS FOR MISSION CREEK

The acceleration profiles and response spectra are shown for the two Mission Creek sites in Figure 5. The acceleration response spectra for Shotwell St. shows, as for the previous three cases, peak values at periods of 0.8 and 1.3 s. However, the magnitude of the spectral acceleration at the period of 1.3 s is significantly lower than that at a period of 0.8 s. This difference most likely is the result of diminished bay mud thickness. The mud at this location is only 9.5 m thick. Accordingly, the soil deposit at the Shotwell St. site tends to be stiffer in relation to those at Marina, Foot, and South of Market, which results in a spectral response shift towards lower periods.

The surface spectral acceleration for the Valencia St. site presents higher spectral content at lower periods, especially the spectrum resulting from the rock motion RINC. The higher frequency content is the result of the stiffer character of the profile. The absence of bay mud and the reduced depth to bedrock tend to decrease the natural period of the deposit, relative to those of the other four sites.

The acceleration profiles for the Valencia St. site show significant differences. The profiles resulting from input motions RINC and YERB increase steadily to a level of about 20 m from the ground surface. Then, they increase at a faster rate with decreasing depth, with most of the contribution taking place in the sandy fill. At the ground surface the maximum acceleration is about 0.18 g. On the other hand, the acceleration profile resulting from the base motion PACI is quite different. No significant increase in acceleration at shallow depths is observed and the maximum surface acceleration reaches a value of only 0.10 g. In this paper, the ground surface response at the Valencia St. site from the PACI record is taken as a lower bound on surface motion. As a practical matter, the difference in response generated by the RINC and PACI inputs may be regarded as a range of uncertainty in the dynamic performance of this site.

The marked difference in calculated acceleration profile at Valencia St. is most likely the result of the frequency content of the input motion and its interaction with the predominant frequency of the soil deposit. Surface

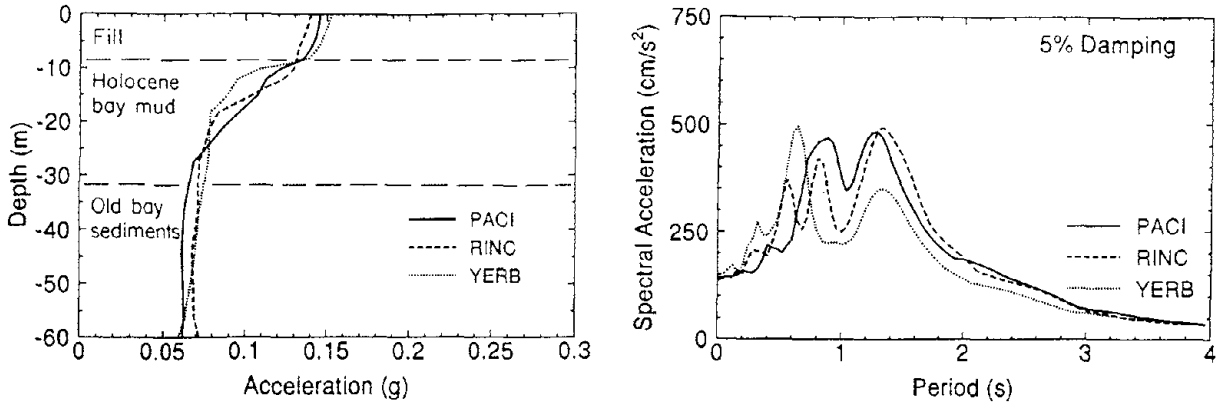

a) Marina District

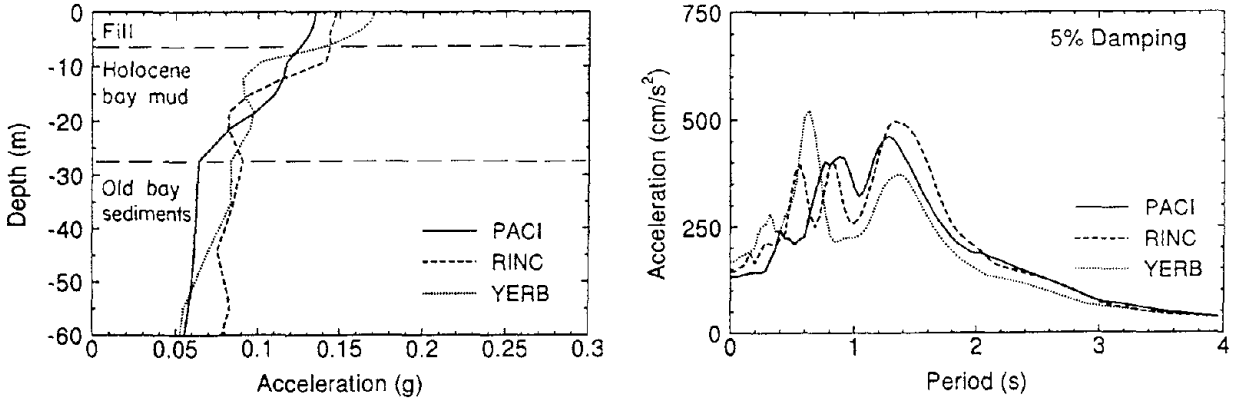

b) Foot of Market

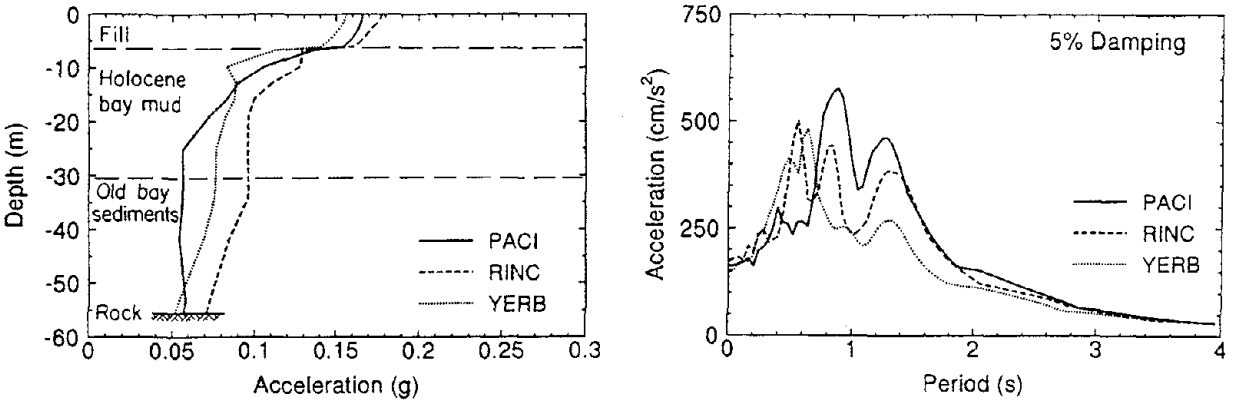

c) South of Market

Figure 4. Maximum Acceleration Profiles and Acceleration Response Spectra for the Marina, Foot of Market, and South of Market

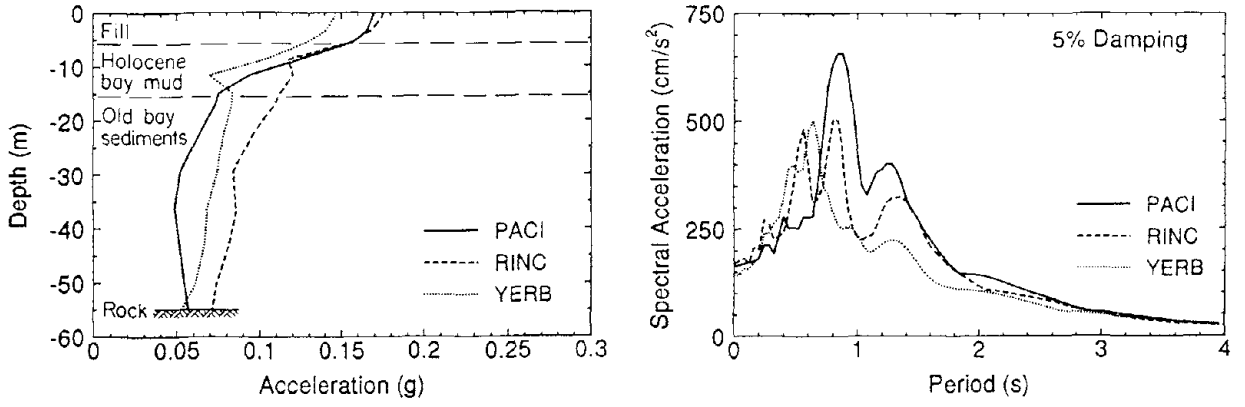

a) Shotwell St.

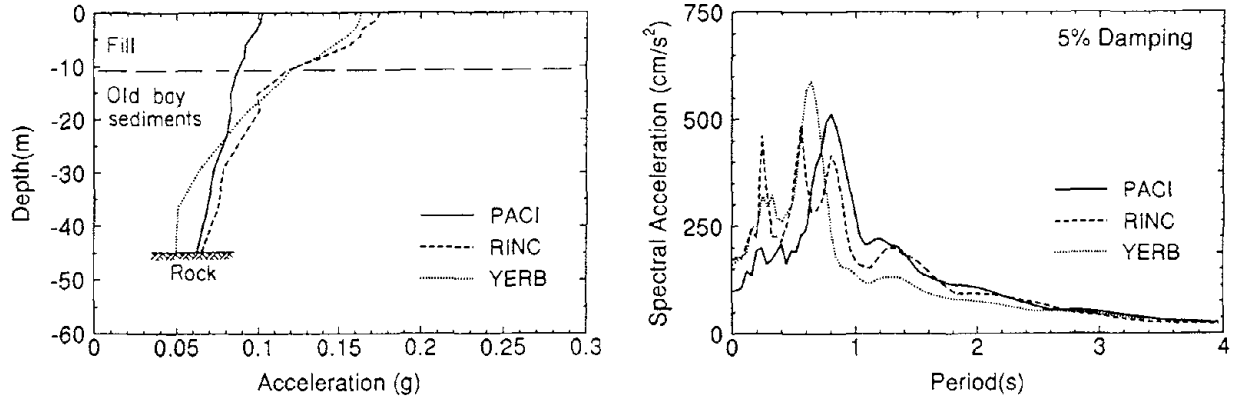

b) Valencia St.

Figure 5. Maximum Acceleration Profile and Acceleration Response Spectra for Shotwell and Valencia Sts. in the Mission Creek Area

motion tends to be amplified at frequencies close to the natural frequency of the deposit. Figure 6 shows the calculated Fourier Amplitude Spectrum (FAS) at Valencia St. for input motions RINC and PACI. As evidenced by the FAS of the input rock motion RINC, most of the energy is contained in a frequency window from about 0.6 Hz to 2.1 Hz. In addition, there is a secondary peak at a frequency of about 4.0 Hz. In contrast, the FAS of the PACI indicates that almost all amplification takes place in a narrow window from 1.0 to about 1.6 Hz; there is almost not significant energy being delivered at frequencies higher than about 1.8 Hz.

INFLUENCE OF HOLOCENE BAY MUD

It is of interest to evaluate the influence of Holocene bay mud thickness on ground surface motion. As indicated in the previous section, the effect of bay mud is to amplify spectral contents at larger periods as its thickness increases. To examine more closely its effects on ground surface motion, the soil profile at Shotwell St. was selected for a parametric study. The total thickness of the Holocene bay mud was varied from zero to 20.5 m, keeping the

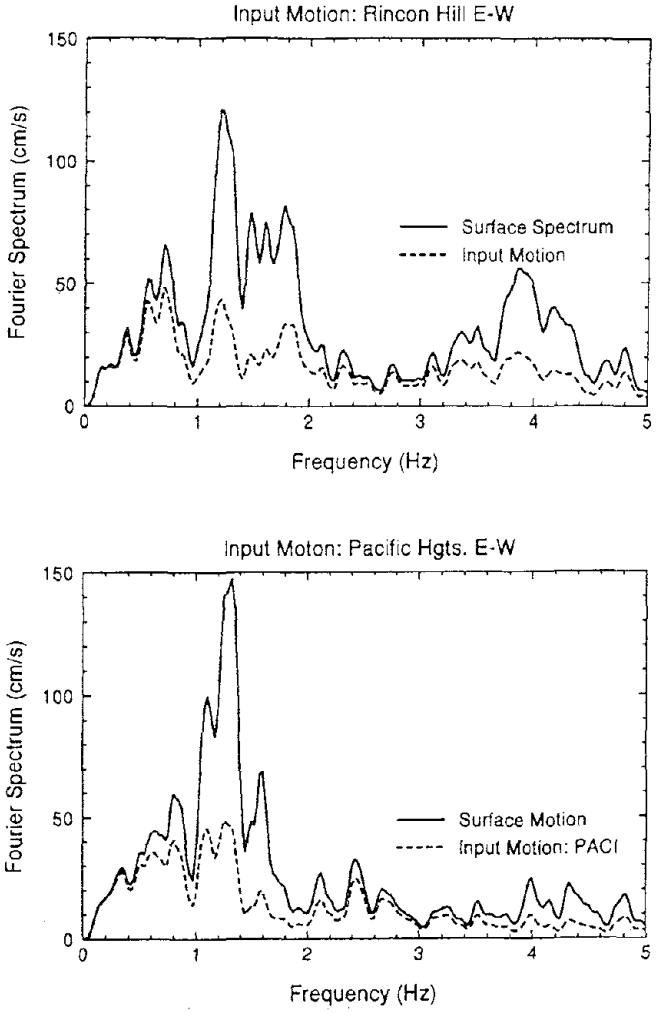

Figure 6. Fourier Amplitude Spectra of Calculated Surface Motion at Valencia St. from Input Motions RINC and PACI

total thickness of the deposit and all other parameters unchanged. Figure 7a shows the calculated surface spectral acceleration for three different thicknesses of Holocene bay mud. The mud thickness has a significant influence on both the maximum surface acceleration and spectral content. Spectral values for periods of 1.0 s and less are damped out as the thickness of mud increases. In contrast, spectral values at higher periods increase with increasing thickness. Figure 7b shows the predominant period and maximum surface acceleration as a function of normalized bay mud thickness. The predominant period is defined here as the period at which the highest spectral acceleration takes place. The normalized thickness is the thickness of the bay mud divided by the total thickness of the deposit. Rock motions RINC and PACI were used in the analysis. For both rock motions, the trends for predominant period and maximum surface acceleration are similar. It is apparent that the spectral shift starts to take place at thicknesses larger than 12.0 m. For thicknesses smaller than 12.0 m, the predominant period is 0.8 s and increases to 1.3 s when the thickness reaches the maximum value of 20.5 m.

The maximum surface acceleration decreases as the mud thickness increases. The lowest calculated value of 0.11 g occurs for a thickness of 20.5 m. This

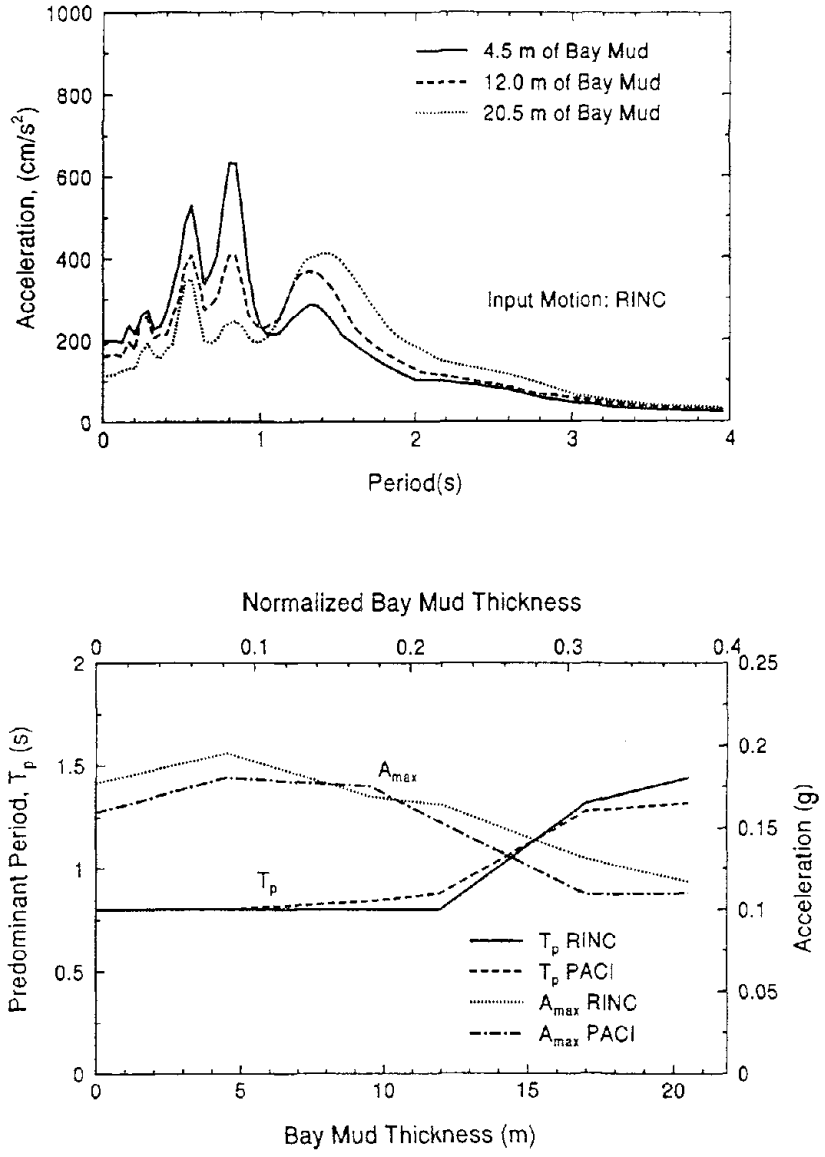

Figure 7. Influence of Bay Mud Thickness on Surface Acceleration and Acceleration Response Spectra

behavior is the result of both shear modulus degradation and increased damping in the clay. It should be kept in mind, however, that ground response is not only affected by mud thickness, but also by the total thickness of the soil deposit. The results in Figure 7 indicate that a thicker deposit of bay mud does not necessarily cause a higher surface acceleration. The most prominent effect of increased mud thickness is an increase in spectral acceleration at higher periods.

Additional analyses were performed in which the total thickness of the deposit was increased while maintaining the fill and Holocene bay mud thicknesses at 5.5 and 9.5 m, respectively. The results show that acceleration spectral values increased at periods between 0.7 and 1.0 s as the total thickness increased, although there was no significant change in the maximum surface acceleration.

SOIL LIQUEFACTION IN MISSION CREEK

During the 1906 earthquake, severe liquefaction effects were observed both east and west of Valencia St. Along Valencia St. between 18th and 19th Sts., a lateral spread with a maximum 2.4 m displacement was responsible for the collapse of the former Valencia Hotel and the rupture of critical water pipelines from the College Hill Reservoir (O'Rourke et al., 1992). Settlements as high as 1.8 m were observed in front of the hotel. In contrast, there was no sign of liquefaction or permanent ground deformation at Valencia St. after the 1989 Loma Prieta earthquake. Soil deformation and associated structural damage in 1989 were confined principally to an area bounded by South van Ness and Folsom Sts. between 17th and 18th Sts.

The liquefaction potential of the fill at Valencia St. was evaluated using the empirical relationships between cyclic stress ratio and CPT values developed by Seed and DeAlba (1986). The values of modified cone tip resistance, q_{c1}, were obtained from two CPT soundings performed at the site according to ASTM specifications (ASTM, 1991).

Figure 8a shows the variation of modified tip resistance, q_{c1}, with depth at Valencia St. The q_{c1} values are from two different CPT soundings separated by approximately 40 m. Superimposed are liquefaction potential lines for a median grain size, D_{50}, of 0.20 and 0.25 mm. These lines were determined according to the recommendations of Seed and DeAlba (1986) for a surface acceleration of 0.18 g and a 7.1 magnitude earthquake. The median grain size for the fill at the Valencia St. site is between 0.20 to 0.23 mm. There is considerable variation in the in situ density of the fill, as evidenced by the q_{c1} profiles, with most of the q_{c1} values plotting to the right of the liquefaction potential lines.

Figure 8b shows bands corresponding to cyclic stress ratios for the fill between 5.0 and 8.5 m. The cyclic stress ratios were determined for peak surface accelerations of 0.10 and 0.18 g, which were calculated at the Valencia St. site from PACI and RINC input motions, respectively. In addition, the empirical dividing lines for median grain size are also shown. The inset in Figure 8b presents a histogram of the distribution of q_{c1} values for the liquefiable layer. Normal and log-normal probability density functions, which were fitted to the data, are also shown. The statistical distribution of q_{c1} indicates that it follows approximately a normal trend, with a mean value of about 4.5 MPa. Values of cyclic stress ratio, in relation to the liquefaction lines and statistical distribution of cone penetration resistance, indicate that the Valencia St. site was just on the verge or in the initial stages of liquefaction. Approximately 15% and 35% of the q_{c1} values plot to the left of the 0.20 mm and 0.25 mm limiting lines, respectively, for a surface acceleration of 0.18 g. For an acceleration of 0.10 g, however, the cyclic stress ratio falls below and to the right of both liquefaction limiting lines.

Similar analyses were performed for the Shotwell St. site. Figure 9a shows the variation of q_{c1} with depth. A total of four CPT soundings where performed at this site. The q_{c1} values are from two different CPT soundings, approximately 21 m apart. These two soundings represent the highest and lowest CPT measurements which were obtained within the zone of liquefiable soil. This figure indicates the presence of a liquefiable layer extending from approximately 2.5 to 4.5 m. It should be noted that some shallow excavation (< 1 m deep), densification of near surface soil, and replacement of fill had been undertaken at this site before the CPT measurements. The liquefiable layer, therefore, could have been larger and shallower before the earthquake. Chameau, et al., (1991), have shown that post liquefaction consolidation generated by the Loma Prieta earthquake resulted in densification of fill along the Embarcadero. Such densification may have occurred at both the Valencia and Shotwell St. sites, thereby increasing the density or liquefaction resistence of the liquefiable soil relative to the conditions before the earthquake.

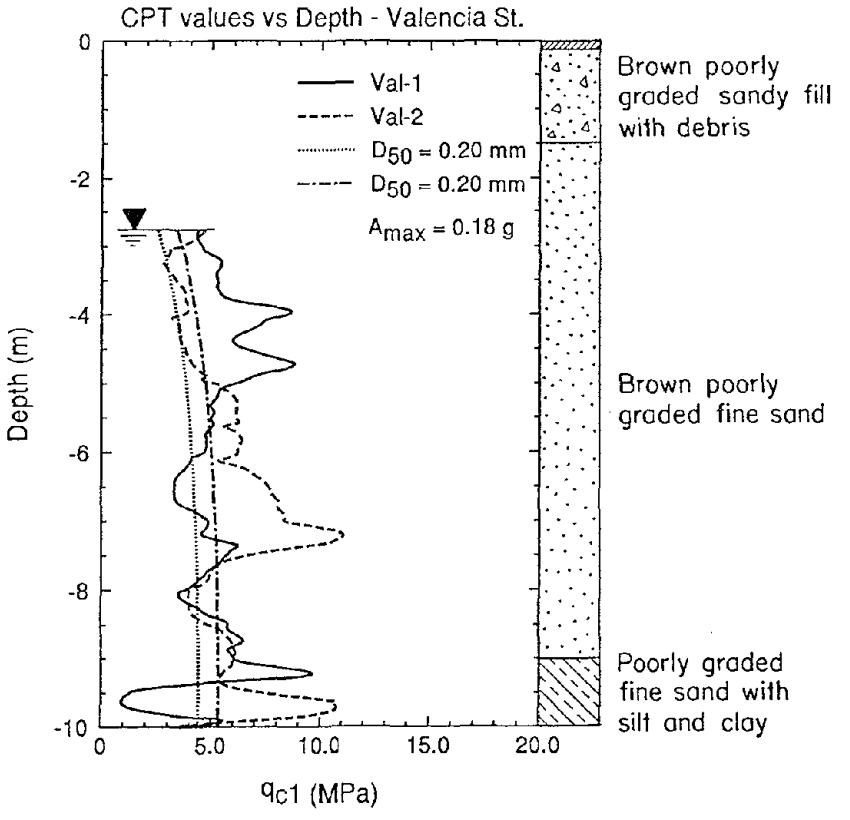

a) Cone Tip Resistance with Depth

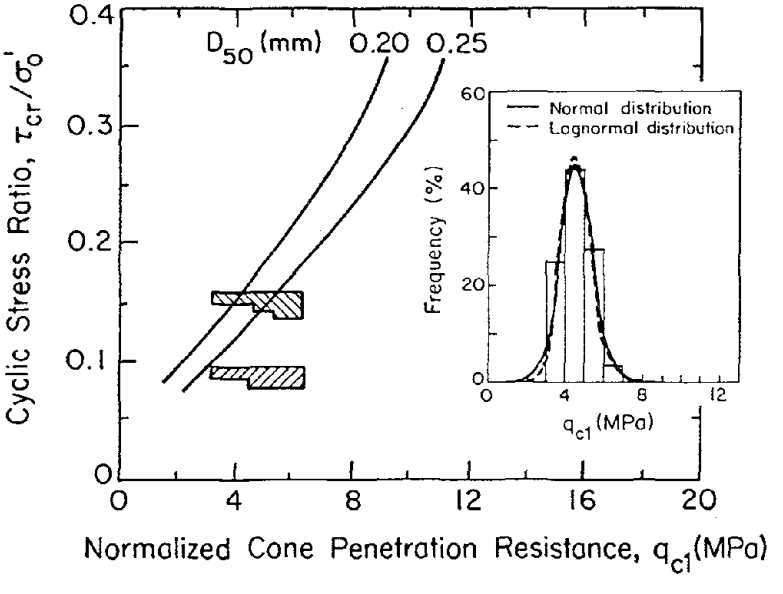

b) Cyclic Stress Ratio

Figure 8. Cyclic Stress Ratio Plot and Distribution of Cone Tip Resistance with Depth at Valencia St.

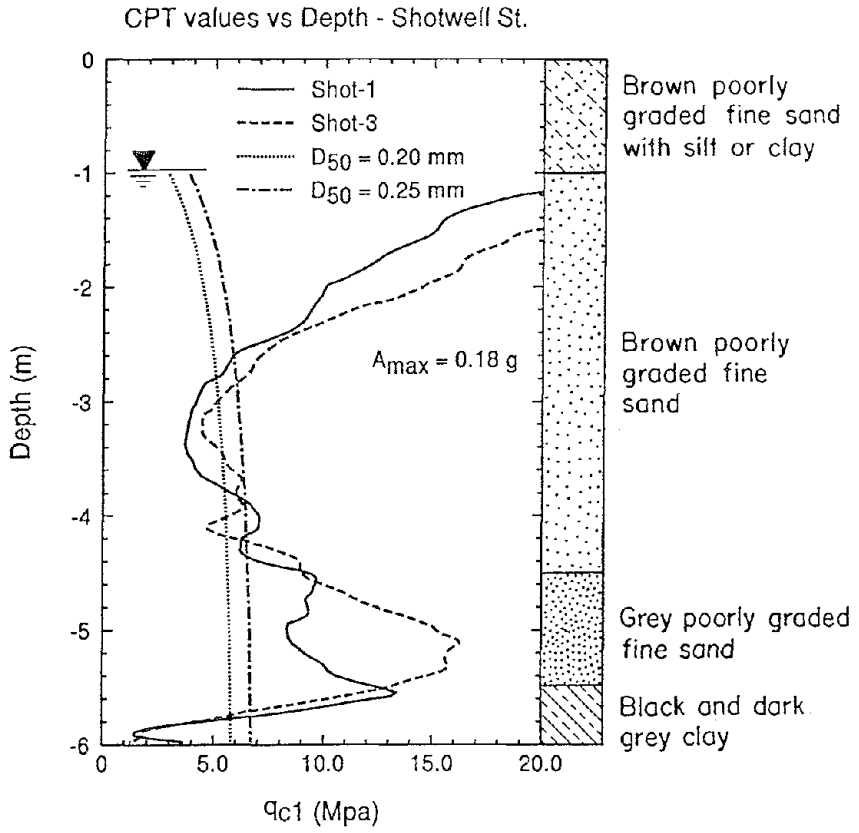

a) Cone Tip Resistance with Depth

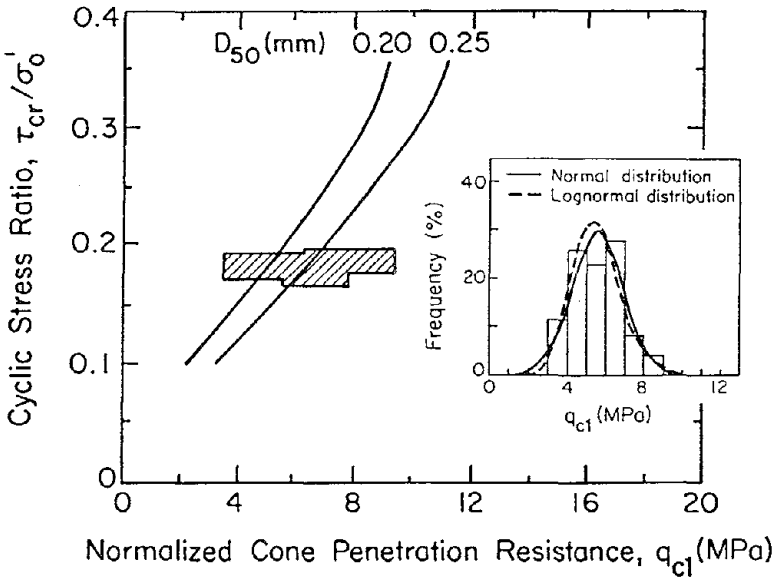

b) Cyclic Stress Ratio

Figure 9. Cyclic Stress Ratio Plot and Distribution of Cone Tip Resistance at Shotwell St.

Figure 9b shows bounds corresponding to cyclic stress ratios of the fill between 2.5 and 4.5 m and empirical dividing lines for D_{50} of 0.20 mm and 0.25 mm. The higher water table at Shotwell St. results in a larger cyclic stress ratio for most depths at a given peak acceleration because of reduced effective confining stress. In contrast to the two distinct bands in Figure 8b, only one band is shown in Figure 9b because the computed acceleration values for the fill at the Shotwell St. site (see Figure 5) plot within a narrow range. Approximately 30% and 50% of the q_{c1} values plot to the left of the 0.20 mm and 0.25 mm limiting lines.

By comparison of Figures 8 and 9, it can be seen that the fill at Shotwell St. is more vulnerable to soil liquefaction. In addition, liquefaction at each site appears to be sensitive to the way in which rock motions are amplified through the soil column. Analytical results indicate that some input rock motions at the Valencia St. site lead to relatively low levels of acceleration in the upper fill, whereas all input rock motions used in this study lead to acceleration levels in the fill at Shotwell St. consistent with liquefaction.

The presence of sand boils at Shotwell St. (O'Rourke and Pease, 1992) indicates that excess pore water pressure was enough to breach the surface layer. According to the case histories assembled by Ishihara (1985) regarding the influence of an overlying liquefaction-resistant stratum, sand boils often are not observed at the ground surface when the thickness of the nonliquefiable layer exceeds 3 m. Thus, the thickness of the nonliquefiable surface layer at Shotwell St., about 2.5 m, is consistent with observations elsewhere. On the other hand, there is considerably variability of in situ density in the near surface soils at Valencia St., with the top of the liquefiable layer as deep as 5.0 m in one of the soundings.

IMPLICATIONS OF GROUND RESPONSE ON STRUCTURAL PERFORMANCE

Analyses of surface shaking often focus on acceleration, and it is common to evaluate surface response by means of acceleration response spectra. In a recent study of timber frame buildings in the Marina District, Harris and Egan (1992) used displacement response spectra to assess the threshold and extent of damage to four-story, timber frame, corner apartment buildings. They simplified building response as a single degree-of-freedom system in which strength and stiffness was furnished by the first floor, while the upper floors behaved as a rigid body. Their calculated natural period of four-story buildings in the Marina was 0.8 to 1.25 s. Spectral displacements associated with these periods was 10 to 30 cm. It should be mentioned that the predominant period of these structures would be higher if one accounts for the additional flexibility provided by the upper floors. In addition, irreversible deterioration of joints and nailed connections during shaking would contribute to a further increase in natural period.

Figure 10 shows the spectral displacement for the Marina, Shotwell St., and Valencia St sites. The bands represent envelopes associated with the input motions used: RINC, PACI, and YERB. As shown in this figure, spectral displacements for the Marina plot above those associated with Shotwell St., which in turn plot above those of Valencia St., although some overlap is evident. Note how, at periods larger that about 1.0 s, spectral displacements at Marina and Shotwell St. increase steeply.

Maximum spectral values for the Marina occur at periods larger than about 1.4 s, which is slightly higher than the fundamental building periods estimated by Harris and Egan (1992). However, as noted above, the actual periods of four story corner buildings during shaking will be higher because of hysteritic effects and additional flexibility from upper stories. Maximum spectral values at Shotwell and Valencia St., for periods in the range of 0.8 to 1.4 s, vary from 8 to 16 cm and 5 to 9 cm, respectively.

Of the structures surveyed by Harris and Egan (1992), almost all with small

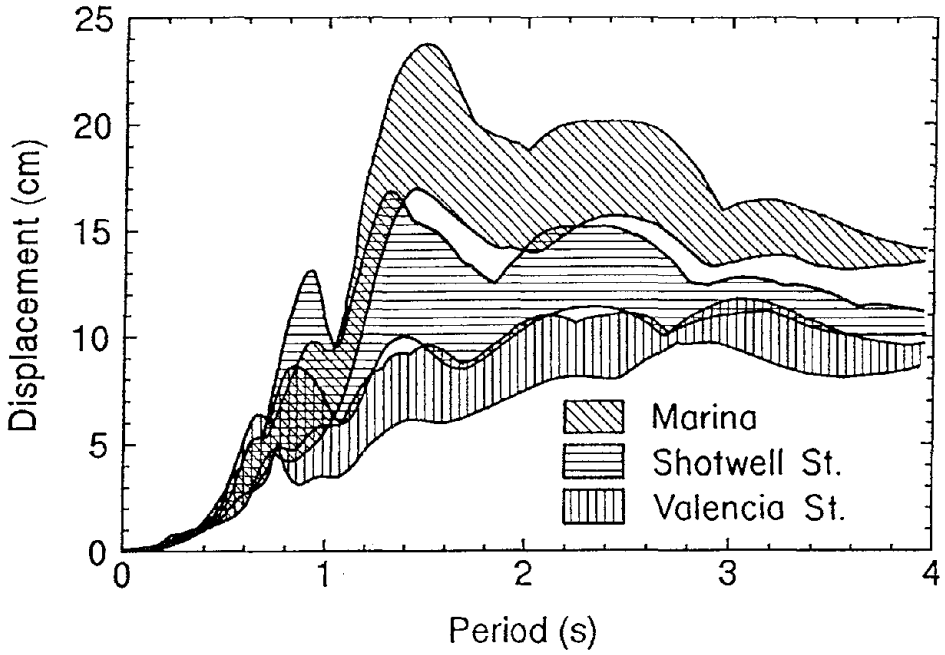

Figure 10. Envelopes of Spectral Displacement at Marina, Shotwell, and Valencia Sts.

to negligible damage were associated with a spectral displacement of 17 cm or lower. The low values of calculated spectral displacement at Valencia St. would have been too small to damage similar structures in this section of San Francisco. Spectral displacements at Shotwell St. are also below the threshold of 17 cm. Structural damage observed at Shotwell St. was associated principally with soil liquefaction and building settlement.

CONCLUDING REMARKS

In this paper, a study of ground response during the Loma Prieta earthquake is presented for the Marina, Foot of Market, South of Market, and the Mission Creek areas. One-dimensional site response analyses, using equivalent linear procedures, show maximum surface acceleration between 0.14 and 0.18 g, with the exception of the Valencia St. site. Values of maximum acceleration at different depths are remarkably consistent at the Marina, as well as at the Foot and South of Market areas. Spectral surface acceleration values are also quite consistent in magnitude at different periods and indicate that amplification occurs primarily at periods of about 0.8 and 1.3 s at the Marina, Foot, and South of Market areas.

The influence of the thickness of the Holocene bay mud was studied by varying the thickness of bay mud at the Shotwell St. site. Its main effect on surface motion is to increase the predominant period of motion from 0.8 to 1.5 as the thickness increases from about 5 to 20 m. The maximum surface acceleration decreases as the thickness of bay mud increases. It drops from 0.18 g for no bay mud to about 0.11 g for a thickness of 20 m. This reduction is caused by shear modulus degradation and increased damping in the clay.

Liquefaction potential analysis using CPT data performed at Valencia St., in the Mission Creek area, suggests that the site was on the verge or in the initial stages of liquefaction. Liquefaction potential analysis performed at the Shotwell St. site indicates the presence of a liquefiable layer between the approximate depths of 2.5 and 4.5 m. Liquefaction of this layer is

believed to be responsible for the sand boils and building settlement observed at Shotwell St. after the Loma Prieta earthquake.

ACKNOWLEDGEMENTS

The research reported in this paper was supported by the U.S. Geological Survey under Grant No. 14-08-0001-62128 and by the National Center for Earthquake Engineering Research under Project No. 912331.

LIST OF REFERENCES

American Society for Testing and Materials, "Standard Test Method for Deep, Quasi-Static, Cone and Friction-Cone Penetration Tests of Soils," Annual Book of Standards (D-3441-86), Vol. 4.08, ASTM, Philadelphia, PA, 1991, pp. 439-444.

Bardet, J.P., M. Kapuskar, G.R Martin, and J. Proubet, "Preliminary Results on the Dynamic Response of the Marina District of San Francisco During the Loma Prieta Earthquake," 3rd Japan-US Workshop on Earthquake Resistant Design of Lifeline Facilities and Countermeasures for Soil Liquefaction," Technical Report NCEER 91-0001, Buffalo, NY, Feb., 1991, pp. 109-128.

California Division of Mines and Geology, "Plots of the Processed Data for the Interim Set of 14 Records from the Santa Cruz Mountains (Loma Prieta) Earthquake of October 17, 1998," California Strong Motion Instrumentation Program, Report No. OSMS 89-08, Sacramento, CA, 1989.

Chameau, J.L., G.W. Clough, F. Reyna, and J.D. Frost, "Liquefaction Response of San Francisco Bayshore Fills," Bulletin of the Seismological Society of America, Vol. 81, No.5, Oct. 1991, pp. 1998-2018.

Harris, S.K., and J.A. Egan, "Effects of Ground Conditions on the Damage to Four-Story Corner Apartment Buildings," USGS Professional Paper 1551-F, Marina District, T.D. O'Rourke, Ed., Washington, D.C. in press.

Hryciw, R.D., K.M. Rolling, M. Homolka, S.E. Shewbridge, and M. McHood, "Soil Amplification at Treasure Island During the Loma Prieta Earthquake," Proceedings, 2nd International Conference on Recent Advances in Geotechnical Earthquake Engineering and Soil Dynamics, Vol II, St. Louis, MO, Mar., 1991, pp. 1679-1685.

Idriss, I.M., "Response of Soft Soil Sites During Earthquakes," Proceedings, H. Bolton Seed Memorial Symposium, Berkeley, CA, May, 1990, pp. 273-290.

Ishihara, K., "Stability of Natural Deposits During Earthquakes," Proceedings, 11th International Conference on Soil Mechanics and Foundation Engineering, A.A. Balkema Publishers, Rotterdam, Netherlands, 1985, pp. 321-376.

Kayen, R.E., H.-P. Liu, T.E. Fumal, R.E. Westerlund, R.E., Warrick, J.F. Gibbs, and H.J. Lee, "Engineering and Seismic Properties of the Soil Column at Winfield Scott School, San Francisco," U.S. Geological Survey Open File Report 90-253, Apr., 1990, pp. G-1 to G-18.

O'Rourke, T.D., P.A. Beaujon, and C.R. Scawthorn, "Large Ground Deformations and Their Effects on Lifeline Facilities: 1906 San Francisco Earthquake," Technical Report NCEER 92-0002, Case Studies of Liquefaction and Lifeline Performance During Previous Earthquakes, T.D. O'Rourke and M. Hamada, Eds., NCEER, Buffalo, NY, May, 1992, pp. 1-1 to 1-134.

O'Rourke, T.D., and J.W. Pease, "Large Ground Deformations and Their Effects on Lifeline Facilities: 1989 Loma Prieta Earthquake, Technical Report NCEER 92-0002, Case Studies of Liquefaction and Lifeline Performance During Previous

Earthquakes, T.D. O'Rourke and M. Hamada, Eds., NCEER, Buffalo, NY, May, 1992, pp. 5-1 to 5-85.

O'Rourke, T.D., T.E. Goudy, H.E. Stewart, and J.W. Pease, "Lifeline and Geotechnical Aspects of the 1989 Loma Prieta Earthquake," Proceedings, 2nd International Conference on Recent Advances in Geotechnical Earthquake Engineering and Soil Dynamics, St. Louis, MO, Mar. 1991, Vol II, pp. 1601-1612.

O'Rourke, T.D., H.E. Stewart, F.T. Blackburn, and T.S. Dickerman, "Geotechnical and Lifeline Aspects of the October 17, 1989 Loma Prieta Earthquake in San Francisco," Technical Report NCEER 90-001, National Center for Earthquake Engineering Research, Buffalo, NY, Jan., 1990.

Redpath, B.B., "Borehole Velocity Surveys at the Embarcadero in San Francisco and the Cypress Structure in Oakland," Report for the California Department of Transportation, Contract No. 65M598, 1990.

Schnabel, P.B., J. Lysmer, and H.B. Seed, "SHAKE A Computer Program for Earthquake Response Analysis of Horizontally Layered Sites," Report No. EERC 72-12, University of California, Berkeley, CA, Dec., 1972.

Seed, H.B., and P. De Alba, "Use of SPT and CPT Tests for Evaluating the Liquefaction Resistance of Sands," Proceedings, In Situ '86 Specialty Conference, ASCE, New York, NY, 1986, pp. 281-302.

Seed, H.B., and J.I. Sun, "Implication of Site Effects in the Mexico City Earthquake of Sept. 19, 1985 for Earthquake Resistant Design Criteria in the San Francisco Bay Area of California," Report No. UCB/EERC-98/03, University of California, Berkeley, CA, Mar., 1989.

Seed, R.B., et al. "Preliminary Report on Principal Geotechnical Aspects of the October 17, 1989 Loma Prieta Earthquake," Report UCB/EERC-90/05, University of California, Berkeley, CA, Apr. 1990.

Seed, R.B., S.E. Dickenson, and C.M. Mok, "Seismic Response Analyses of Soft and Deep Cohesive Sites: A Brief Summary of Recent Lessons," paper presented at Workshop on Site Amplification of Earthquake Ground Motion, National Institute of Standards and Technology, Jan., 1992.

Stewart, H.E., and A.K. Hussein, "Determination of the Dynamic Shear Modulus of Holocene Bay Mud for Site Response Analysis," USGS Professional Paper 1551-F, Marina District, T.D. O'Rourke, Ed., Washington, D.C. in press.

Vucetic, M, and R. Dobry, "Effect of Soil Plasticity on Cyclic Response," Journal of Geotechnical Engineering, ASCE, Vol. 117, No. 1, Jan. 1991, pp. 89-107.

Liquefaction Hazard Mapping, Deposional Faces, and Lateral Spreading Ground Failure in the Monterey Bay Area, Central California, during the 10/17/89 Loma Prieta Earthquake

John C. Tinsley, Ph. D.
Research Geologist
U.S. Geological Survey
345 Middlefield Road, MS-975
Menlo Park, California, 94025

William R. Dupré, Ph. D.
Professor of Geology
Department of Geology
University of Houston
Houston, Texas 77004-4231

ABSTRACT

The 1989 Loma Prieta Earthquake provided opportunities to (1) evaluate the accuracy of geologic and liquefaction susceptibility maps of Quaternary deposits in the central Monterey Bay region (Dupré, 1975a; Dupré and Tinsley, 1980) and (2) gain insight into the types of deposits most susceptible to lateral spreading ground failure. The relative susceptibility for liquefaction was determined by combining detailed geologic mapping of Quaternary deposits with information on geotechnical properties of the deposits, depth to water table, and the response of these and similar units in previous earthquakes. The geologic maps were compiled from regional Quaternary geologic mapping prepared by Dupré (1975b) and Tinsley (1975), augmented by additional field mapping during 1976-1979 by Dupré and Tinsley in selected areas. The liquefaction susceptibility map was produced according to the methods of Youd and Perkins (1978). Occurrences of lateral spreading were then compared to the geologic maps as well as the geomorphic setting and the presence of accretionary topography to ascertain the types of sedimentary deposits involved in the lateral spreads.

Liquefaction-induced ground failure manifested as vented sand (sand boils), differential settling, and lateral spreading was widespread in the Monterey Bay region during the the 1989 Loma Prieta earthquake (M_S=7.1). The areal extent of the liquefaction was much less than that caused by the 1906 San Francisco earthquake (M_S=8+), as would be expected given the smaller magnitude of the 1989 earthquake. Nonetheless, within the area affected by the Loma Prieta earthquake, almost all of the 1906 failures compiled and identified by Lawson (1908) and Youd and Hoose (1978) were reactivated, clearly demonstrating that the phenomenon of recurrent liquefaction is a potentially significant engineering issue and cannot be ignored on the basis of a prior history of liquefaction.

Liquefaction caused ground failure mainly in areas underlain by water-saturated, late Holocene alluvial and estuarine deposits along the San Lorenzo, Pajaro, and Salinas Rivers, and along estuaries and spits near Moss Landing. All major occurrences of liquefaction were in areas previously mapped as having a high to very high susceptibility to liquefaction (Dupré, 1975a; Dupré and Tinsley, 1980). It was noted, however, that large areas zoned as having high to very high susceptibility did not fail, even though similar units in adjacent areas did liquefy. The absence of failure apparently reflects the lack of sand-rich facies within those geologic units (e.g. younger fluvial deposits and basin deposits), which had not been recognized on the basis of surficial materials mapping and geomorphic mapping. Future mapping showing liquefaction susceptibility should distinguish sand-poor basinal facies from sand-rich basinal facies where ever possible. In addition, lowered water tables owing to the recent drought might have prevented liquefaction in some areas within some younger fluvial deposits.

The strong correlation between observed liquefaction and areas mapped as having high to very high susceptibility for liquefaction demonstrates that regional geologic mapping is a powerful asset in helping the public and private sector to minimize losses caused by liquefaction in future earthquakes. Fluvial deposits, especially point bar and channel deposits of meandering streams, are the facies of

most susceptible to lateral-spreading ground failure near Monterey Bay. Estuarine deposits occur along the coast and are also highly susceptible to liquefaction. These deposits formed in a littoral setting and include tidal inlet deposits, washover deposits, estuarine channel deposits (Dupré and Tinsley, in press; Tinsley and others, in press). Of 47 lateral-spread ground failures, 95% were distributed among the fluvial channel, fluvial point bar, and estuarine depositional environments.

INTRODUCTION

In 1973, the U.S. Geological Survey began a cooperative program with Santa Cruz County to provide a series of maps to aid regional planners in evaluating the County's potential geologic hazards. These maps included active and potentially active faults (Hall and others, 1974), landslide deposits (Cooper, Clark and Associates, 1975), and Quaternary deposits and their liquefaction susceptibility (Dupré, 1975a). The maps were incorporated within Santa Cruz County's Seismic Safety Element. The mapping of Quaternary deposits and their liquefaction susceptibility was extended into the central Monterey Bay region by Dupré and Tinsley (1980), funded in part by Monterey County, and into the southern Monterey Bay region more recently by Dupré (1990). The 1989 Loma Prieta Earthquake (M_S=7.1) provided an opportunity to test the validity of the maps and to learn about geologic controls on the occurrence of lateral spreading. This paper briefly describes the methods by which the maps were prepared, gives an example of the manner in which the mapping predicted the occurrence of liquefaction near Watsonville, and documents the degree to which selected depositional environments were associated with the occurrence of lateral-spread ground failure in the Monterey Bay region. The discussion of map preparation is condensed largely from Dupré and Tinsley (in press) and Tinsley and Dupré (in press) and emphasizes the fluvial deposits of the region; coastal deposits are not fully discussed in this paper for reasons of brevity.

MAP PREPARATION

Liquefaction is the transformation of a granular material from a solid to a liquefied state owing to an increase in pore-fluid pressure. This transformation typically is induced by cyclic loading owing to earthquake shaking (Youd, 1973). The phenomenon is largely restricted to water-saturated, relatively unconsolidated well-sorted deposits of sand and silt in regions of high seismicity. Predicting the susceptibility of sedimentary deposits to earthquake-induced liquefaction requires knowledge of their age and mode of deposition, their physical properties including relative density and degree of water saturation, and the distribution of cohesionless sand and silt within the deposits. Detailed mapping of Quaternary deposits, combined with information on depth to water table, geotechnical properties of the geologic units, and evidence of previous liquefaction provide the data necessary for such mapping (Youd, 1973; Youd and others, 1975; Youd and Perkins, 1978). The method of Youd and Perkins (1978) was the basis for making our maps (Dupré, 1975a, Dupré and Tinsley, 1980; Dupré, 1990; Dupré and Tinsley, 1992). Other studies of liquefaction using the methods of Youd and Perkins (1978), sometimes with slight modifications, include Roth and Kavazanjian (1984), Tinsley and others (1985), and Youd and Perkins (1987b).

Preparation of a Geologic Map

A geologic map of Quaternary deposits delineates geologic units on the basis of relative age and lithology. In California, the most significant age distinctions that correspond to decreasing liquefaction susceptibility are among Latest Holocene, Pre-latest Holocene, Late Pleistocene, and Pre-late Pleistocene deposits (see Table 1). In the Monterey Bay area these four groups of deposits could generally be recognized on the basis of pedogenic soil development (Dupré, 1975b; Tinsley, 1975). See Janda and Croft (1967), Tinsley (1975), and/or Birkeland (1984) for a description of the key characteristics of the soil profile used in making these age discriminations. These first-order age distinctions can commonly be made using soils maps from the U. S. Department of Agriculture, Soil

Conservation Service. In the Monterey Bay region, for example, the mapping by Carpenter and Cosby (1925) and Storie (1944), was especially useful,. The value of these old soil maps is discussed by Hathaway (1991).

Aerial photography flown by various agencies from the late 1920's through 1975 provided much useful information; the earlier photography allows more accurate identification and delineation of Holocene depositional environments because they pre-date much of the urbanization and intensive agricultural development in the region. The resulting geologic map of the Quaternary deposits delineates 23 Pleistocene and 12 Holocene units; a portion of the geologic map is shown in figure 2A. The recognition and delineation of genetically related Quaternary depositional environments and associated deposits provided by such mapping is essential in determining the age and distribution of potentially liquefiable deposits, and is the cornerstone for the preparation of liquefaction susceptibility maps.

Preparation of a Liquefaction Susceptibility Map

Information on geotechnical properties of sediments was limited to a small number of unpublished engineering reports. Correlation of the properties of the geologic units that were explored and tested in these reports with similar deposits in nearby areas greatly expanded the data base on which our work rests. Similarly, information on the depth to the free water surface (the unconfined water table) was largely limited to a small number of engineering test borings and water-well logs. The occurrence of unconfined near-surface water is locally complicated by perched water tables, the presence and seasonal persistence of which is difficult to predict because shallow ground water is seldom monitored.

Index properties of sediment such as grain size, clay content, standard penetrometer tests, and depth to free ground water were used to estimate the relative susceptibility of the sediments to liquefaction in the event of an earthquake of magnitude (M) 8.3 on the San Andreas fault, using criteria developed by Youd (1973), Youd and others (1975; Youd and Perkins, (1978). These estimates, combined with the historical evidence of liquefaction-induced ground failure caused by the 1906 San Francisco earthquake (Lawson, 1908; Youd and Hoose, 1978), demonstrated a clear correlation among the mapped geologic units and their relative susceptibility for liquefaction (Table 1). These relations, combined with the geologic maps of Quaternary deposits, are the foundations for the liquefaction susceptibility maps (fig. 2B).

Table 2 describes the hazard zonation corresponding to the relative susceptibility to liquefaction in the event of an earthquake similar in magnitude to the 1906 San Francisco earthquake. Given the large magnitude of that event, the relatively long duration of the ground motion and the nearby proximity of the San Andreas fault, this zonation may be considered to represent the maximum likelihood for liquefaction under present-day water-table conditions. Sediments that had an estimated high susceptibility for liquefaction on the basis of regional geologic mapping but which showed little or no historical evidence of ground failure, such as the older flood-plain deposits (unit Qof, figure 2), were zoned in a lower hazard category than sediments that experienced widespread failure in the 1906 earthquake, for example, the younger flood-plain deposits (unit Qyf, figure 2).

Analyses of historical occurrences of liquefaction indicate that the more recently a sediment has been deposited, the more likely it is to be susceptible to liquefaction and that certain types of deposits, such as river-channel and other non-cohesive floodplain deposits, are more susceptible to liquefaction than other deposits such as beach or alluvial fan deposits (Youd and Perkins, 1978). Tinsley and others (1985, Table 40B, p. 269) discuss erosional processes affecting grain-size, sorting, and bedding characteristics of sedimentary deposits with respect to liquefaction hazard and confirm that a sedimentary deposit develops an increased resistance to liquefaction as its geologic age substantially increases. The decrease in liquefaction susceptibility with time is most notable during the early stages of compaction and lithogenesis during the Holocene and late Pleistocene in this region. Assuming the

presence of well-sorted sands and silts (a function of depositional environment), this trend is used to assign a level of risk to a deposit chiefly on the basis of age. For example, distinguishing Holocene deposits from Pleistocene deposits works well in basins where incisional and depositional cycles reflect glacio-eustatically controlled changes in sea level and the difference in the ages of the respective deposits is on the order of tens of thousands of years. However, when deposits are hundreds of years apart in age as is the case for deposits mapped as units Qyf and Qof in the Pajaro and Salinas valleys, attributes of the deposit other than age, such as bedding thickness and clay content, also control the susceptibility to liquefaction. A study of the effects of numerous earthquakes worldwide by Youd (1984) showed that sediments which liquefied in the past are more likely to subsequently liquefy than those which had no historic evidence of liquefaction.

Dupré and Tinsley (1980) distinguish degrees of liquefaction susceptibility on their map as follows: a query (?) indicates that the identification of the geologic unit is in doubt. A combination of two susceptibility categories, such as MODERATE-LOW (M-L), indicates that the geologic unit varies areally in its susceptibility; a single geologic unit may underlie the entire area, for example, but factors such as sand thickness or continuity of sand layers may vary, so that susceptibility may be LOW in one part and MODERATE in another. In such instances we often lack data to show which characterization to apply to subdivisions of the area, so we must combine categories. A geologic unit which has a lowered susceptibility to liquefaction due to a water table depressed artificially as by pumping is indicated by a subscript '$_W$' (for example, L_W). The location of shallow ground water is commonly the most difficult parameter to estimate with precision, as it may vary in space and time and it rarely is monitored (Tinsley and others, 1985).

The maps prepared by Dupré (1975a) and Dupré and Tinsley (1980) are at a scale of 1:62500 and are intended for regional land-use planning, thus are not suitable for determining the actual hazard at any specific site. The local absence of sandy or silty layers in high-susceptibility zones would inhibit liquefaction, as would locally deep water tables. Similarly, we have not made any effort to estimate the relative amount of ground displacement that may accompany ground failure owing to liquefaction. The proximity of a free face or scarp is likely to increase the probable severity of a failure in a zone classified as high or as moderate. Lastly, some units (e.g. artificial fill), may be too small to be delineated on the scale of the map as published. Thus the hazard at a particular site owing to liquefaction should be determined only after field investigations by qualified engineering geologists or engineers. Nonetheless, comparing the distribution of liquefaction-induced ground failures following the Loma Prieta earthquake with the geology and hazard zones of Dupré and Tinsley (1980) clearly demonstrates the utility of regional mapping for appraising liquefaction hazard, as discussed in the following section.

LIQUEFACTION DURING THE LOMA PRIETA EARTHQUAKE

Liquefaction and associated ground failure in the Monterey Bay region during the Loma Prieta Earthquake was widespread (fig. 3; see also Tinsley and others, in press). Mappable effects of liquefaction were manifested as ejected sand (sand boils) issuing from isolated vents or from extensional fissures, differential settling of buildings, levees, or other overburden into a liquefied substrate, loss of bearing capacity indicated by tilted structures, and lateral spreading indicated by systematic extensional ground cracking typically involving displacement towards a free-face. Liquefaction-induced ground failure caused extensive damage to flood-control levees, pipelines and sewers, buildings, utilities, irrigation facilities (including water wells), bridges, and precisely graded agricultural tracts. Liquefaction occurred almost exclusively within areas underlain by water-saturated, late Holocene alluvial and estuarine deposits. It was especially conspicuous along the lower (tidewater) reaches of the San Lorenzo, Pajaro, and Salinas Rivers where ground water is perpetually near-surface, as well as along estuaries, abandoned channels, and adjacent fluvial tributaries in the Moss Landing area. All major occurrences of liquefaction, especially lateral spreads, were in areas previously mapped by Dupré

and Tinsley (1980) as having high to very high susceptibility to liquefaction; a map showing the distribution of ground failures in the lower Pajaro Valley is show in figure 3.

Lateral spreading occurred along approximately 60% of the lower 15 km of the Pajaro River, and was also common along the lower 15 km of the Salinas River and the lower 2 km of the San Lorenzo River at Santa Cruz, California. Failures also occurred along the margins of estuaries and the tidal inlet in the vicinity of Moss Landing. In all instances but one, the lateral spreading was restricted to late Holocene fluvial, basin, estuarine, or channel fill deposits (most mapped as units Qyf, Qb, and Qcf by Dupré, 1975a; Dupré and Tinsley, 1980).

The lateral-spread failures typically occurred within 150 m of the margins of active stream channels characterized by a free-face or gently sloping point bar 3-5 m high. Often, the failure headed along the contact of a highly susceptible unit with a less susceptible geologic unit. Some failures occurred along the margins of abandoned channels filled with organic-rich sediment, however, where the free face was less than 2 m high; however, in this setting, the compressible material filling the channel readily accomodated the laterally-displaced mass. Lateral displacements ranged from a few millimeters to as much as 2 m, measured cumulatively across a given failure from its head to its toe; vertical displacements were of a similar range, but usually were less than 0.3 m. Failure commonly occurred on both sides of the modern channel, and zones of failure were mappable for distances ranging from tens of meters up to 2 km along the channel margins. In fluvial deposits, the head of the lateral spreads was localized at the contact of young channel deposits with either overbank deposits of equivalent age or overbank deposits of older Holocene stratigraphic units. This trend appears to be a stratigraphically controlled pattern and is and mappable; it is not a simple function of distance from or height of the free face as represented by the channel of the nearby stream.

Comparison with published liquefaction susceptibility mapping:

Of the more than seventy liquefaction sites identified in the map area by Tinsley and others (in press), only four were not zoned by Dupré and Tinsley (1980) as having a high or very high susceptibility to liquefaction. Minor sand boils and ground settlements occurred at two localities zoned as moderate in basin deposits along the lower part of the Pajaro Valley. These sites appear to be associated with remnants of buried channels within the floodbasin. Minor lateral spreading occurred along Carlton Road at Site 1 (figure 4) which was zoned moderate. This failure developed in a thin wedge of Holocene alluvial fan deposits and also included irrigation-saturated artificial (road) fill too small to be mapped at the publication scale of 1:62,500. Differential settlement without vented sand occurred in road fill at a culvert along Carlton Road, about 1 km east of Site 1 (figure 4), which was zoned as low. In summary, the high correlation of liquefaction during the Loma Prieta earthquake and areas mapped as high to very high susceptibility to liquefaction demonstrates the utility of the methodology proposed by Youd and Perkins (1978).

The question remains as to why large areas zoned as having a high or very high susceptibility did not fail, even when adjacent areas within the same category did. A more careful examination of the geology of these sites reveals some important differences not noted during the original mapping.

Most of the 1989 liquefaction occurred within fluvial deposits in areas mapped as **abandoned channel fill** and **younger fluvial deposits** (units Qcf and Qyf of Dupré and Tinsley, 1980). Liquefaction within the younger fluvial deposits appears to be largely restricted to the sandy point-bar facies of this unit. The areas of younger fluvial deposits that showed no evidence of liquefaction probably consist of locally undifferentiated floodbasin deposits. These sediments are water saturated and most are of late Holocene age, but they tend to lack beds of liquefiable sand and silt of any significant thickness; it is only where such beds are locally present (e.g. near small tributaries), that minor liquefaction occurred . Wherever possible, floodbasin deposits were mapped as **basin deposits** (unit Qb of Dupré and Tinsley,

1980). Unfortunately, basin deposits as mapped included a variety of relatively clay-rich depositional environments that differ in sand content, hence in susceptibility to liquefaction. Most of the floodbasin deposits within this map unit did not fail, but large areas of estuarine, tidal flat, and abandoned tidal channel deposits (also mapped as unit Qb) did fail, especially where they were located within a few hundred meters of the coast. Future mapping needs to distinguish between these different types of "basin" deposits. In addition, dune deposits (unit Qd of Dupré and Tinsley, 1980) exhibited ground failure only where underlain by young estuarine or tidal channel deposits; failure actually occurred within the underlying estuarine or tidal channel deposits.

A puzzling question is why conclusive evidence of liquefaction was lacking upstream of State Highway 152 in younger fluvial deposits along Corralitos Creek, a major tributary to the Pajaro River, even though these deposits are similar in age to those that failed extensively along the Pajaro River, and were much closer to the earthquake's source. Corralitos Creek is smaller and shorter, has a steeper gradient, and consists of slightly coarser and more poorly sorted sediment than the Pajaro River. We speculate that the Corralitos sediments may not fall within the optimum size distribution for liquefaction (median particle diameter, D_{50}, range is from 0.08mm-0.7mm; see Housner and others, 1985). Grain size distributions currently being analyzed may help explain the observed anomaly. Possibly the water table was sufficiently deep along Corralitos Creek at the time of the earthquake that potentially liquefiable sediment was dry. Information about the location of perched or shallow ground water for the critical period in question is unavailable for Corralitos valley.

Evidence of recurrent liquefaction:

Within the area affected by the 1989 Loma Prieta earthquake, most of the failures that occurred during the 1906 San Francisco earthquake (as compiled by Youd and Hoose, 1978) were reactivated, clearly demonstrating recurrent liquefaction (see also Youd, 1984). The horizontal component of displacement and the differential vertical component of settlement noted in ground failures in 1989 were, however, generally of a significantly lesser magnitude than the displacements occurring in 1906, apparently owing to the Loma Prieta Earthquake (M_S=7.1) being significantly smaller and of shorter duration, releasing energy amounting to about 1/60 of that released by the 1906 San Francisco earthquake.

Lateral spreading and associated depositional facies

We mapped 47 lateral spreads formed during the October 17, 1989 earthquake in 5 sedimentary environments to determine which sedimentary environments would be especially susceptible to lateral-spread ground failure. Sedimentary environments included the fluvial channel deposits and fluvial point-bar deposits comprising the principal laterally-accreted facies of meandering streams, plus estuarine/tidal channel deposits, beach deposits, and alluvial fan deposits.

The depositional facies of the deposits in which the ground failure likely nucleated was assigned on the basis of field evidence and geomorphic setting. For example, vented sand found by visual inspection to be noticeably finer-grained than modern channel deposits and which was associated geomorphically with the insides of meanders or with meander scrolls visible in aerial photographs was assigned to the point bar facies as a subset of the laterally-accreted channel assemblage as generally recognized by fluvial sedimentologists (see Visher, 1972, p. 95; Allen, 1970; Schumm, 1981;). Failures associated with the modern or abandoned fluvial channels were assigned to the channel facies. Ground failures judged to involve estuarine deposits, tidal inlet deposits, and/or washover deposits were assigned to the estuarine facies. It should be apparent that distinguishing fluvial channel deposits from estuarine channel deposits can be somewhat arbitrary near the coast. Alluvial fan and beach facies were recognized on the basis of their geomorphologic and sedimentologic associations. The sole failure attributed to beach deposits may in fact have been initiated in underlying fluvial channel deposits. The location of each ground failure and its apparent facies association is shown in figure 4.

The distribution of lateral spreads among the 5 facies identified in this study indicates that about 9 of 10 ground failures occurred in fluvial or estuarine deposits. Most likely to sustain lateral-spread ground failure are fluvial point-bar deposits (55%), fluvial channel deposits (23%), and estuarine deposits (17%). Alluvial fan deposits and beach deposits rarely failed. These data are summarized in figure 5.

Jackson (1978) points out that the classical model of a fining-upward sequence including a decrease in grain size and thickness or amplitude of cross stratification is not always expressed in deposits of meandering streams, thus may limit the utility of this field association for identifying sediments susceptible to liquefaction in some basins. However, the classical point-bar model seems to work well for the Pajaro and Salinas rivers.

CONCLUSIONS

• Detailed geologic mapping of Quaternary deposits in the Monterey Bay region, combined with concepts devised by Youd and Perkins (1978), resulted in a regional map of relative susceptibility to liquefaction (Dupré and Tinsley, 1980).

• The strong correlation of areas of liquefaction in 1989 and areas mapped as having high to very high susceptibility to liquefaction clearly demonstrates the utility of regional mapping for minimizing losses due to liquefaction in future earthquakes.

• All major liquefaction-induced ground failures including all but one lateral spread during the October 19, 1989 Loma Prieta earthquake were in sediments mapped by Dupré and Tinsley (1980) as having a high to very high susceptibility for liquefaction. These sediments were mainly youngest Holocene fluvial deposits, abandoned channel fill and point bar deposits, and estuarine sediments. Areas that did not appear to liquefy, yet were zoned as having a high to very high susceptibility for liquefaction, mainly consisted of young, water-saturated deposits where a sandy facies was apparently lacking in the subsurface. One exception may be the younger fluvial deposits along Corralitos Creek west of Highway 152, where the lack of liquefaction might have been related to a low water table.

• Future mapping should attempt to differentiate sand-poor and sand-rich facies within basin and fluvial deposits in order to more accurately delineate zones of liquefaction susceptibility. In addition, relatively young estuarine deposits should be differentiated from other types of basin deposits, as they are particularly prone to failure.

• About 95% of the lateral spreads occurred in fluvial channel, point bar, and estuarine settings. The point bar facies where well expressed in result of deposition by certain meandering streams may be of significant value in anticipating the occurrence of lateral spreading ground failure.

ACKNOWLEDGMENTS

The original mapping by Dupré (1975a) and Dupré and Tinsley (1980) was initiated as part of the National Program for Earthquake Hazard Reduction of the U.S. Geological Survey. Earl E. Brabb of the U.S. Geological Survey established this project, provided base maps, funded field work, edited the maps and facilitated their publication. Additional support of field work was provided by Monterey County. Our 1989-1992 post-earthquake study was funded by the Office of Earthquake Studies, Branch of Engineering Seismology and Geology; supplemental support was provided by the University of Houston Coastal Center. We are grateful to Thomas L. Holzer and Michael J. Bennett for their thoughtful and constructive reviews of the manuscript, and to the many geologists and engineers who have shared freely of their expertise as well as giving us access to historical maps and aerial photographs, unpublished engineering reports, and well logs. Lastly, we thank the many landowners and lessees who graciously granted access to their property; without such access, we have no study.

REFERENCES CITED

Allen, J. R. L., 1970, Physical processes of sedimentation: American Elsevier, Earth Science Series No. 1, 248 p.

Birkeland, P. W., 1984, Soils and geomorphology: Oxford University Press, New York, 372 p.

Carpenter, E.J., and Cosby, S.W., 1925, Soil survey of the Salinas area, California: U.S. Dept Agriculture, Bur. Chem. and Soils, Series 1925, no. 11, 80 p.

Cooper, Clark, and Associates, 1975, Preliminary map of landslide deposits in Santa Cruz County, California, in Seismic Safety Element, Santa Cruz County, California, 132 p.

Dupré, W.R., 1975a, Maps showing geology and liquefaction potential of Quaternary deposits in Santa Cruz County, California: U.S. Geological Survey Miscellaneous Field Studies Map MF-648, scale 1:62,500.

_____, 1975b, Quaternary History of the Watsonville Lowlands, North-Central Monterey Bay Region, California: unpublished Ph. D. dissertation, Stanford University, 145 p.

_____, 1990, Maps showing geology and liquefaction susceptibility of Quaternary deposits in the Monterey, Seaside, Spreckles, and Carmel Valley quadrangles, Monterey County, California: U.S. Geological Survey Miscellaneous Field Studies Map MF-2096, scale 1:24,000.

Dupré, W.R., and Tinsley, J.C. III, 1980, Maps showing geology and liquefaction potential of Northern Monterey and Southern Santa Cruz counties, California: U.S. Geological Survey Miscellaneous Field Studies Map MF-1199 (2 sheets), scale 1:62,500.

Dupré, W.R., and Tinsley, J.C. III, IN PRESS, Evaluation of liquefaction-hazard mapping in the Monterey Bay area, Central California, in Holzer, T. H., ed., Liquefaction, Chapter B *of* Strong ground motion and ground failure, v. 2 *of* The Loma Prieta earthquake of October 17, 1989: USGS Professional Paper 1551-B.

Greene, H.G., Gardner-Taggart, J., Ledbetter, M.T., Barminski, R., Chase, T.E., Hicks, K.R., and Baxter, C., 1991, Offshore and onshore liquefaction at Moss Landing spit, central California-Result of the October 17, 1989, Loma Prieta earthquake: Geology, v. 19, p. 945-949.

Hall, N.T., Sarna-Wojcicki, A.M., and Dupré, W.R., 1974, Faults and their potential hazards in Santa Cruz County, California; U.S. Geological Survey Miscellaneous Field Studies Map MF-626, (two sheets), scale 1:62,500.

Hathaway, A.W., 1991, The value of historical American soil survey reports and maps: Association of Engineering Geologists News, July 1991, p. 21-23.

Housner, G.W., and the Committee on earthquake Engineering, 1985, Liquefaction of Soils During Earthquakes: National Research Council, National Academy Press, Washington, D.C., 240 p.

Janda, R. J., and Croft, Mac G., 1967, The stratigraphic significance of a sequence of non-calcic brown soils formed on the Quaternary alluvium of the northeastern San Joaquin Valley, California, in Quaternary Soils: International Assoc. Quaternary Research (INQUA), 7th Congress Proceedings, v. 9, Reno, Univ. Nevada, p. 158-190.

Jackson, R. G., II, 1978, Preliminary evaluation of lithofacies models for meandering alluvial streams *in* Miall, A. D., ed., Fluvial Sedimentology: Canadian Society of Petroleum Geologists, Memoir 5, p. 543-576.

Lawson, A.C., (ed), 1908, The California earthquake of April 18, 1906-Report of the State Earthquake Investigation Commission: Carnegie Institute of Washington Publication 87, v. 1 and atlas.

Rogers, J.D., Wills, C.J., and Manson, M.W., 1991, Two sequences of fine grained soil liquefaction at Soda Lake, Pajaro River Valley, Santa Cruz County, California: Paper of Second International Conference on Recent Advances in Geotechnical Earthquake Engineering and Soil Dynamics, St. Louis, MO, 14 p.

Roth, R.A., and Kavazanjian, E. Jr., 1984, Liquefaction susceptibility mapping for San Francisco, California: Bull. Assoc. Engineering Geologists, v. 21, p. 459-478.

Shumm, S. A., 1981, Evolution and response of the fluvial system, sedimentologic implications *in* Etheridge, F. G. and Flores, R. M. eds., Recent and ancient non-marine depositional environments:

models for exploration: Society of Economic Paleontologists and Mineralogists, Special Publication No. 31, p. 19-29.

Storie, R.E., 1944, Soil Survey: The Santa Cruz Area, California: U.S. Dept. Agriculture, Soil Conservation Service Soils Report, Series 1935, No. 25.

Tinsley, J.C. III, 1975, Quaternary Geology of Northern Salinas Valley, Monterey County, California: unpublished Ph. D. dissertation, Stanford University, 195 p.

Tinsley, J.C. III, Youd, T.L., Perkins, D.M., and Chen, A.T.F., 1985, Evaluating liquefaction potential, in Ziony, J.I. (ed.) Evaluating Earthquake Hazards in the Los Angeles Region - an Earth-Science Perspective: U.S. Geological Survey Professional Paper 1360, p. 263-316.

Tinsley, J. C., Bennett, M. J., Dupré, W. R., and others, IN PRESS, Liquefaction-related ground failure in the Monterey Bay area during the Loma Prieta earthquake *in* Holzer, T. H., ed., Liquefaction, Chapter B *of* Strong ground motion and ground failure, v. 2 *of* The Loma Prieta earthquake of October 17, 1989: USGS Professional Paper 1551-B.

Tuttle, M., Cowie, P., Tinsley, J., Bennett, M., and Berrill, J., 1990, Liquefaction and foundation failure of Chevron oil and gasoline tanks at Moss Landing, California: Geophysical Research Letters, v. 17, p. 1797-1800.

Visher, G. S., 1972, Physical characteristics of fluvial deposits *in* Rigby, J. K. and Hamblin, W. K., eds., Recognition of ancient sedimentary environments: Society of Economic Paleontologists and Mineralogists, Special Publication No. 16, p. 84-97.

Wills, C.J., and Manson, M.W., 1990, Liquefaction at Soda Lake: Effects of the Chittenden earthquake swarm of April 18, 1990, Santa Cruz County, California: California Geology, v. 43, no. 10, p.225-232.

Youd, T.L., 1973, Liquefaction, flow, and associated ground failure: U.S. Geological Survey Circular 688, 12 p.

_____, 1984, Recurrence of liquefaction at the same site, in Proc. 8th World Conf. on Earthquake Engineering, v.3: Prentice Hall, Inc., Englewood Cliff, N.J., p. 231-238.

Youd, T.L., Nichols, D.R., Helley, E.J., and Lajoie, K.R., 1975, Liquefaction potential, in Studies for seismic zonation of the San Francisco Bay region: U.S. Geological Survey Professional Paper 941-A, p. A68-A74.

Youd, T.L., and Hoose, S.N., 1977, Liquefaction susceptibility and geologic setting: Proc. 6th World Conf. on Earthquake Engineering., v. 3: New Dehli, p. 2189-2194.

_____,1978, Historical ground failures in northern California triggered by earthquakes: U.S. Geological Survey Professional Paper 993, 177 p.

Youd, T.L., and Perkins, D.M., 1978, Mapping liquefaction-induced ground failure potential: Journal of the Geotechnical Engineering Division, American Society of Civil Engineers, v. 104, no. GT4, Proceedings Paper 13659, p. 433-446.

_____, 1987a, Mapping of liquefaction severity index: Journal of Geotechnical Engineering, v. 113, p.1374-1393.

Youd, T.L., and Perkins, J.B., 1987b, Map showing liquefaction susceptibility of San Mateo County, California: U.S. Geological Survey Miscellaneous Investigations Series Map I-1257-G.

Table 1

Probable susceptibility to liquefaction of cohesionless, granular, non-gravelly deposits, used to compile liquefaction susceptibility map (modified after Tinsley and others, 1985).

AGE	DEPTH TO WATER TABLE			
	0-10 ft	10-30 ft	30-50 ft	50+ ft
Holocene:				
Latest.....	Very High-High	Moderate	Low	Very Low
Pre-latest.....	High	Moderate	Low	Very Low
Late Pleistocene	Low	Low	Very Low	Very Low
Pre-late Pleistocene	Very Low	Very Low	Very Low	Very Low

Table 2

Description of zones of relative liquefaction susceptibility, modified after Dupré and Tinsley, (1980), and Dupré (1990)

VERY HIGH	Very likely to liquefy in the event of even a moderate earthquake. Sediments characterized by high susceptibility to liquefaction (on the basis of engineering tests and high water table) and for which there is evidence of extensive liquefaction-induced ground failure in the 1906 earthquake. Chiefly restricted to younger flood-plain deposits,but also includes some basin deposits, and estuarine, beach, and some dune sands in the vicinity of the coast.
HIGH	Likely to liquefy in the event of a nearby major earthquake. Includes sediments for which engineering tests, shallow water tables, and nearby free faces indicate high susceptibility for liquefaction and resultant ground failure, but for which no historical evidence for liquefaction has been reported. Includes some basin deposits and younger flood-plain deposits, as well as most undifferentiated alluvial deposits and abandoned channel-fill deposits.
MODERATE	May liquefy in the event of a nearby major earthquake. Includes sediments for which moderate susceptibilities were calculated but which lack historical evidence of liquefaction, as well as sediments with high susceptibilities but where water table is between 10 and 30 ft below the ground surface. Includes beach and older flood-plain deposits, most basin and colluvium deposits, most undifferentiated alluvial deposits, and some Holocene aeolian deposits.
LOW	Unlikely to liquefy, even in the event of a nearby major earthquake. Includes younger Pleistocene deposits (older dunes and landslide deposits), as well as Holocene deposits where the water table is more than 30 ft deep (for example, most of the alluvial fan deposits and some older flood-plain deposits in areas where groundwater pumping has lowered the water table).
VERY LOW	Very unlikely to liquefy, even in the event of a nearby major earthquake. Includes all pre-late Quaternary deposits.
VARIABLE	Restricted to areas of artificial fill. Susceptibility to liquefaction may range from very high to low depending on the type of fill and method of emplacement. Much liquefaction-induced ground failure associated with the 1906 earthquake occurred in hydraulically emplaced fill over bay and estuarine muds.

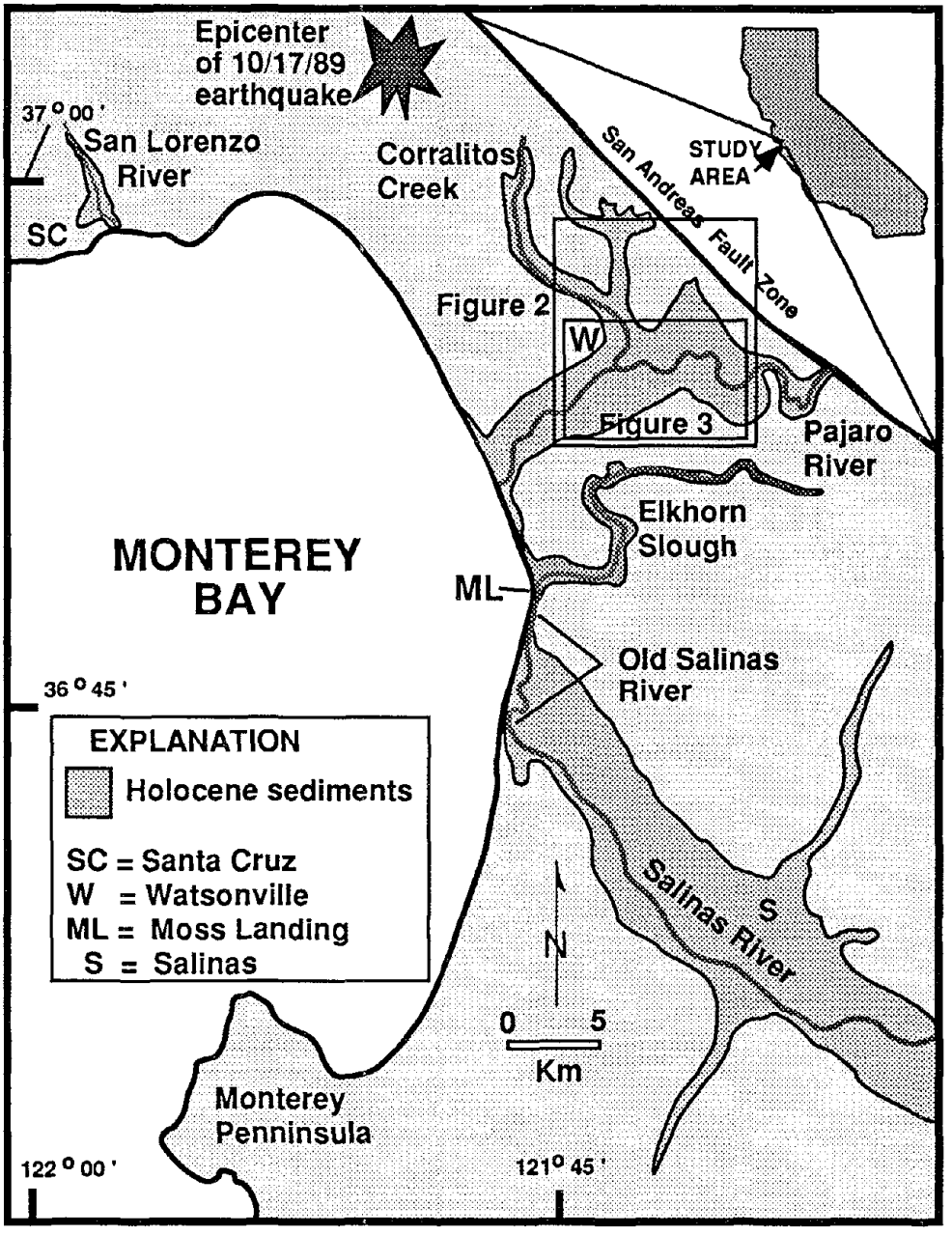

Figure 1
Location map of study area.
Insets indicate location of figures 2-3.

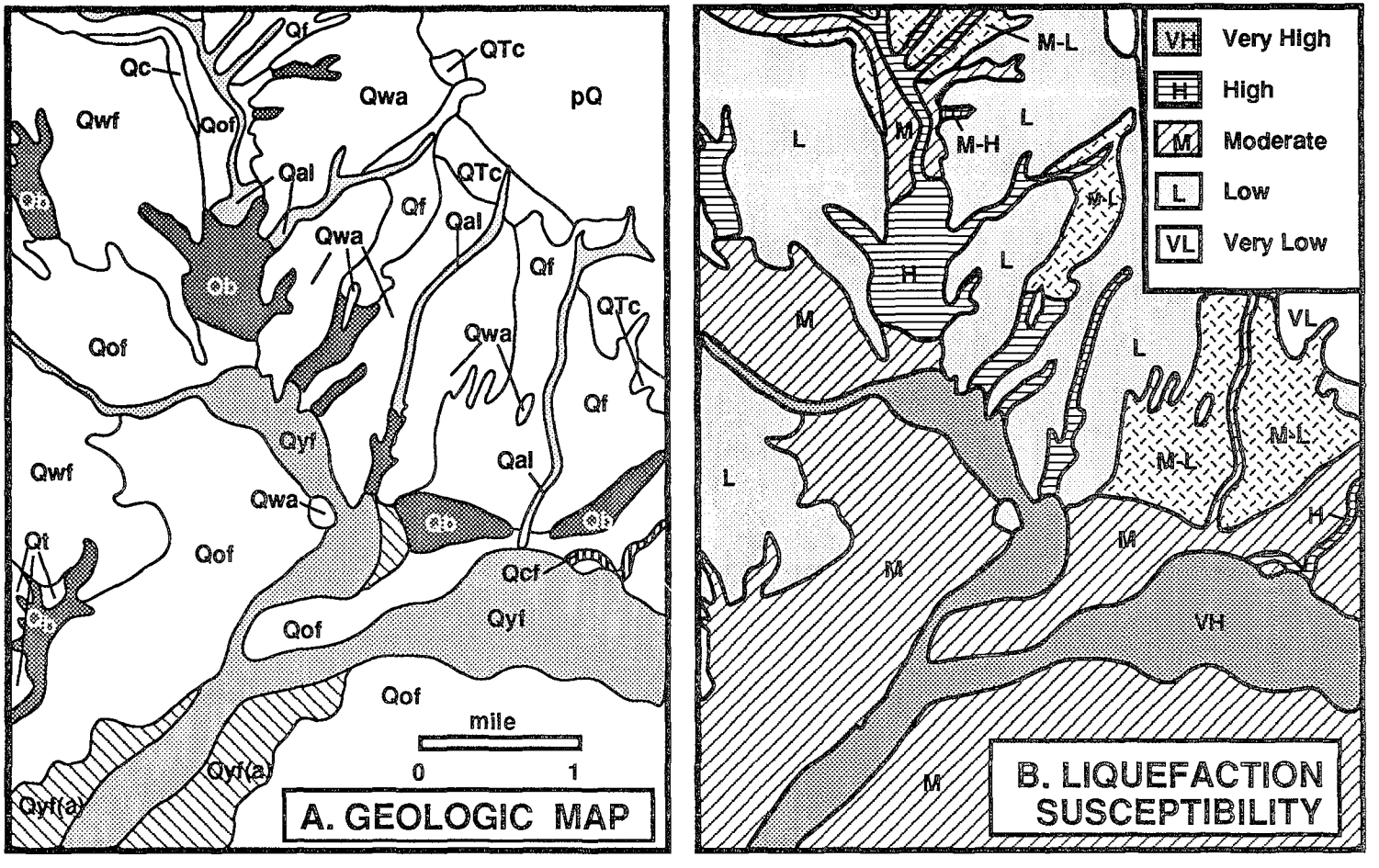

FIGURE 2A: Map showing Quaternary deposits in the Watsonville area (modified after Dupré and Tinsley, 1980), from which a derivative map showing liquefaction susceptibility (fig. 2B) was made. Map-unit symbols: Qb, Quaternary basin deposits (Holocene); Qal, Quaternary alluvial deposits, undivided (Holocene); Qf, Quaternary alluvial fan deposits (Holocene); Qyf, Quaternary younger flood-plain deposits (Holocene); Qyf(a), Quaternary younger floodplain deposits as a veneer overlying older flood-plain deposits (Holocene); Qc, Quaternary colluvium (Holocene); Qcf, Quaternary channel-fill deposits (Holocene); Qt, Quaternary terrace deposits, undivided (Pleistocene); Qwf, Quaternary terrace deposits of Watsonville, fluvial facies (Pleistocene); Qwa, Quaternary terrace deposits of Watsonville, alluvial fan facies (Pleistocene); QTc, Pliocene and Pleistocene continental deposits, undivided; pQ, pre-Quaternary sedimentary, igneous, and metamorphic rocks. FIGURE 2B: Map showing liquefaction susceptibility of sediments in the Watsonville area (modified after Dupré and Tinsley, 1980).

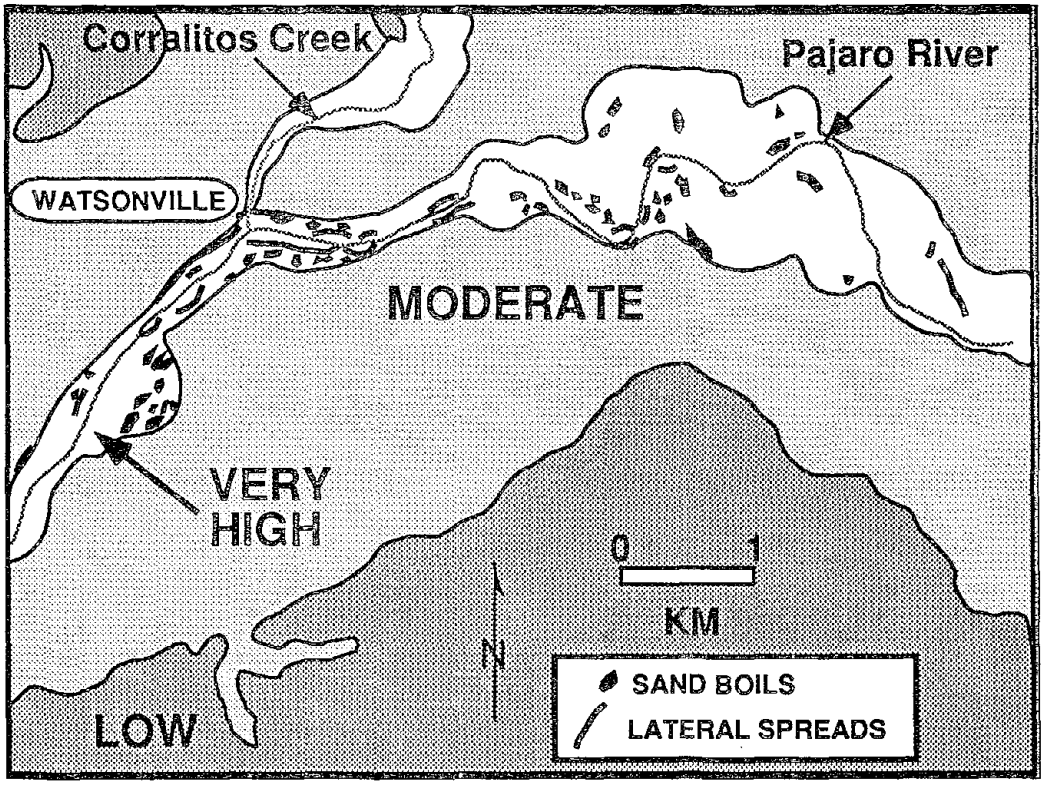

Figure 3: Map showing distribution of liquefaction effects in the Watsonville area, in relation to the predicted susceptibility to liquefaction (Dupre´and Tinsley, 1980). See Figure 1 for location of map area.

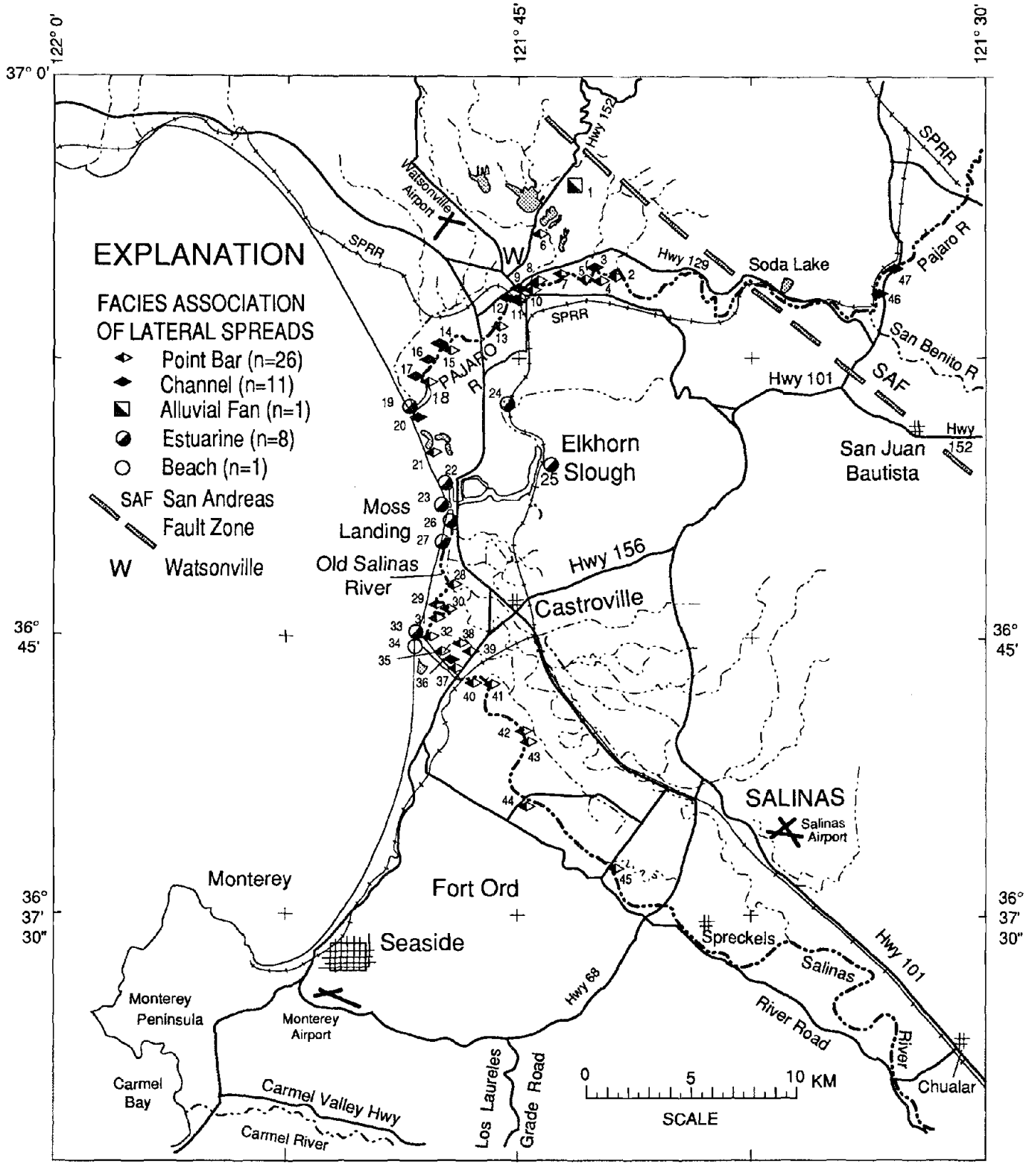

Figure 4

Lateral spread ground failures grouped by facies.

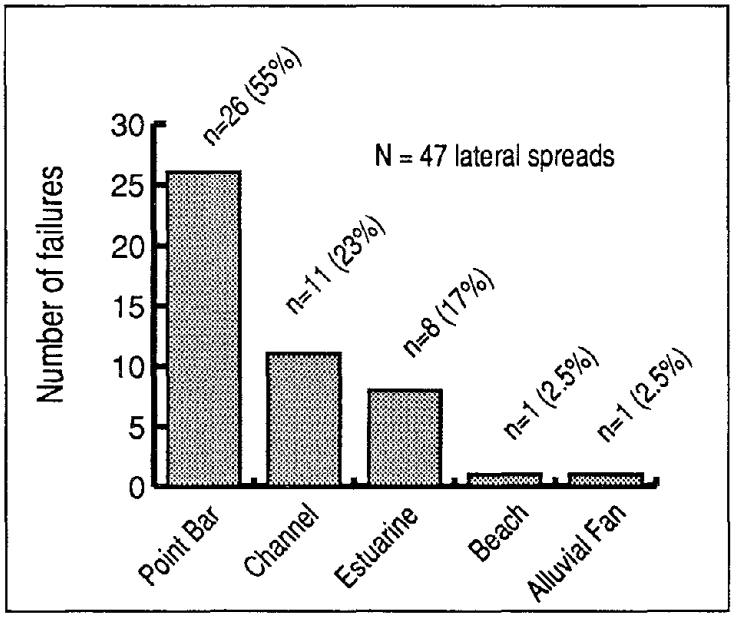

Figure 5

Histogram showing distribution of lateral-spread ground failures according to sedimentary facies for the Loma Prieta earthquake.

Analysis of Wildlife Site Liquefaction during the 1987 Superstition Hills Earthquake

Ahmed-W. Elgamal and Mourad Zeghal
Department of Civil and Environmental Engineering
Rensselaer Polytechnic Institute
Troy, New York 12180

ABSTRACT

The recorded surface and downhole accelerations of Wildlife site during the 1987 Superstition Hills earthquake were utilized to estimate the site average shear stress-strain time history. This history provided valuable insight into the site constitutive behavior during liquefaction and associated loss of soil stiffness and strength. It clearly showed that the effect of excess pore pressure buildup on soil behavior started at about 14 sec. Thereafter, as the pore pressure steadily increased, the site stiffness and strength gradually decreased. After the strong shaking phase (21 sec), the site behavior was characterized by cycles of large shear strains and minimal stresses. At these large strains, evidence of hardening behavior was observed.

INTRODUCTION

Recent major shaking events, such as the Loma Prieta (1989) earthquake, demonstrated the spectacular effects of site failure due to liquefaction and loss of strength. Laboratory experimentation has provided valuable insight into the mechanisms associated with excess pore-pressure buildup, but there still remains a need to understand and to identify the characteristics of in-situ soil strength and stiffness degradation during strong motion earthquakes. Advances toward our comprehension of site liquefaction are yet to be confirmed by actual recorded acceleration and pore-pressure buildup data. In this regard, the Wildlife site records during the Superstition Hills earthquake (05:15 PST, November 24, 1987) are, to this date, unique in the United States. During this earthquake, the site was monitored with surface and downhole strong motion instruments and with pore-water pressure sensors. Field investigations after the earthquake provided strong evidence of site failure due to liquefaction [3].

The records of the Superstition Hills earthquake have been used in numerical modeling by several researchers [2,6,7]. In this paper, the recorded accelerations were directly used to evaluate estimates of the average shear stress-strain history during the 1987 Superstition Hills earthquake (in the north-south direction), and to identify the nature of the site constitutive behavior. Using the same analysis technique, a complete investigation of the site response is currently being finalized [9].

THE WILDLIFE SITE

The Wildlife site is located on the west side of the Alamo river in Imperial County California. During the Westmoreland earthquake (April 26, 1981, $M_L = 5.9$), evidence of liquefaction was observed at the site [8]. This earthquake triggered an interest in Wildlife which was instrumented in 1982 with accelerometers and pore water pressure transducers [3]. A number of in-situ and laboratory soil investigations were also conducted [1].

Geological material at the site consisted of a surface silt layer down to 2.5 m depth, a silty sand layer between 2.5 and 6.8 m depth, and a silty clay layer from 6.8 m to about 11.5 m depth. The ground water level was at about 1.5 m depth. Site instrumentation consisted of two 3-component accelerometers, one at the surface and the second at 7.5 m depth, and six piezometers. The site was also equipped with an inclinometer casing to detect permanent lateral subsurface deformation (to a depth of 8.8 m). Fig. 1 depicts a cross-section of the site with locations of the two accelerometers, SM2 at the ground surface and SM1 at the base of the liquefiable silty sand layer. Five of the piezometers (P1 to P5) were located in this liquefiable silty sand layer. The sixth piezometer (P6) was located at about 12 m depth separated from the liquefiable layer by a thick silty clay stratum. A recent in-situ effort to calibrate the piezometers showed that the P5 transducer responded consistently similar to the employed reference transducer [4].

THE NOVEMBER 24, 1987 SUPERSTITION HILLS EARTHQUAKE

On November 23-24, 1987 the Wildlife site was shaken by two earthquakes [3]. No pore pressure increase was recorded during the first event (Elmore Ranch earthquake, 17:54 PST, November 23, 1987, $M_L = 6.2$). The second event, the Superstition Hills earthquake ($M_L = 6.6$), produced increase in pore water pressure, and field investigations showed evidence of site liquefaction [3] in the form of sand boils with eruption of water and muddy sediment. Ground cracking, indicative of lateral spreading was also observed. Cumulative opening across ground cracks at the array was 125 mm. The top of the inclinometer was deflected approximately by 180 mm in a N15°E direction relative to its base beneath the liquefied layer [3].

Figs. 2 and 3 display the strongest North-South (NS) component of the recorded accelerations at the ground surface and downhole (at 7.5 m depth), and Fig. 4 shows the excess pore water pressure measured by the P5 piezometer.

The recorded accelerations and pore water pressure (Figs. 2-4) may be divided into three stages:

Stage 1: (0 sec to 14 sec). The ground acceleration had a relatively low amplitude (maximum ground accelerations were of the order of 0.13 g and 0.10 g at the surface and downhole, respectively), and pore water pressure buildup was small.

Stage 2: (14 sec to 21 sec). This stage corresponds to the strongest shaking (with peak accelerations of 0.21 g and 0.17 g at the surface and downhole, respectively). The pore water pressure increased quickly with very small instantaneous dips that coincided with negative peaks [3] in the surface acceleration record (Figs. 2 and 4).

Stage 3: (21 sec to 97 sec). The recorded accelerations did not exceed 0.06 g, and had a longer period (at the surface) than in Stages 1 and 2. The surface acceleration exhibited several spikes predominantly in the negative direction (Fig. 2), which coincided with instantaneous drops in the pore water pressure record (Fig. 4).

ANALYSIS AND DISCUSSION

The recorded NS accelerations at the surface and downhole stations were utilized to evaluate the site average shear stress-strain time history (representative of the 0-7.5 m top layer) during the 1987 Superstition Hills earthquake. A one-dimensional stress-strain history due to upward shear wave propagation was estimated. The main elements of the procedure are:

1. The site average shear-strain history was evaluated using the recorded accelerations:

$$\gamma = (d_1 - d_2)/h \tag{1}$$

in which γ is shear strain, d_1 and d_2 are horizontal displacements histories of the accelerometers SM1 and SM2, respectively (obtained by integration of the corresponding acceleration records), and h is the vertical distance between SM1 and SM2 (7.5 m).

2. The site average shear-stress history was evaluated as:

$$\tau = \frac{1}{2}\rho h a_1 \tag{2}$$

in which τ is average shear stress, ρ is mass density (2100 kg/m^3), and a_1 is recorded absolute acceleration history at SM1.

3. The nature of the site shear stress-strain history was investigated by displaying the estimated stresses as a function of the estimated strains.

Following the above-mentioned steps, Fig 5 displays the NS component of the shear stress-strain history during the November 24, 1987 earthquake. This figure exhibits the following site response features:

1. During Stage 1 of excitation (0 sec to 14 sec), the site stiffness showed strain dependency but no evidence of site weakening was observed. Note that, during this stage, no appreciable rize in pore pressure was detected by piezometer P5 (Fig 4).

2. During the strong shaking phase (14 sec to 21 sec) the site exhibited a clear and gradual reduction in stiffness associated with the sharp increase in pore water pressure (Fig. 4),

3. Following this strong saking phase, the site stiffness was reduced considerably, and the site behavior was characterized by large strains and relatively minimal stresses (Figs. 5),

4. The site response during and after the strong shaking phase displayed evidence of hardening behavior (Fig. 5) similar to the laboratory documented soil behavior shown schematically in Fig. 6 (after Ref.[5]). The hardening phase of the stress-strain history (on the negative side) coincided with the transient dips in the pore water pressure record of Fig. 4.

CONCLUSIONS

The average shear stress-strain history of the top 0-7.5 m layer of Wildlife site during the 1987 Superstition Hills earthquake revealed salient features of the site response. It was observed that: (*i*) during the strong shaking phase, the site stiffness and strength steadily decreased with the increase in site pore pressure, (*ii*) after the strong-shaking phase, the site behavior was characterized by large strains and minimal restoring stresses, and (*iii*) at large strains, the site displayed evidence of hardening behavior.

ACKNOWLEDGMENT

This research was partially supported by NCEER grant No. 90-1503 under NSF master agreement ECE-89 23222 and by KAJIMA Corporation, Japan. This support is gratefully acknowledged.

REFERENCES

1. Benett, M. J., McLaughlin, P. V., Sarmiento, J. S., and Youd, T. L., "Geotechnical Investigation of Liquefaction Sites, Imperial Valley, California," *U.S. Geological Survey Open-File Report* 84-15, 1984.

2. Dobry, R., Elgamal, A.-W., Baziar, M. and Vucetic M., "Pore Pressure and Acceleration Response of Wildlife Site During the 1987 Earthquake," *2nd US-Japan workshop on Soil Liquefaction*, O'Rourke, T. D. and Hamada, M., eds. 145-160, Sept. 1989.

3. Holzer, T. L., Youd T. L. and Hanks T. C., "Dynamics of Liquefaction During the 1987 Superstition Hills, California Earthquake," Science, Vol 244, 56-59, 1989.

4. Hushmand, B., Scott, R. F. and Crouse, C. B., "In situ Calibration of USGS Piezometer Installations" in Recent Advances in Instrumentation, Data Acquisition and Testing in Soil Dynamics, edited by Bhatia, S. K. and Blaney, G. W., ASCE, Geotechnical Special Publication No. 29, 1991.

5. Ishihara, K., "Stability of Natural Deposits During earthquakes," *Proceedings of the Eleventh International Conference on Soil Mechanics and Foundation Engineering*, San Francisco, 1985.

6. Keane, C. M. and Prevost, J. H. "An Analysis of Earthquake Data Observed at the Wildlife Liquefaction Array Site, Imperial County, California," *2nd US-Japan workshop on Soil Liquefaction*, O'Rourke, T. D. and Hamada, M., eds.176-192, Sept. 1989.

7. Vucetic, M., and V. Thilakarantne, "Liquefaction at the Wildlife Site - Effect of Soil Stiffness on Seismic Response," *Proc. 4th Int. Conf. Soil Dyn. and Earthq. Eng., 1989.*

8. Youd, T. L., and Wieczorek, G. F., "Liquefaction During 1981 and Previous Earthquakes Near Westmoreland California," *U.S. Geological Survey Open-File Report 84-680.*

9. Zeghal, M. and Elgamal, A.-W., "Analysis of Wildlife Site Liquefaction Using Earthquake Records," in preparation for journal publication.

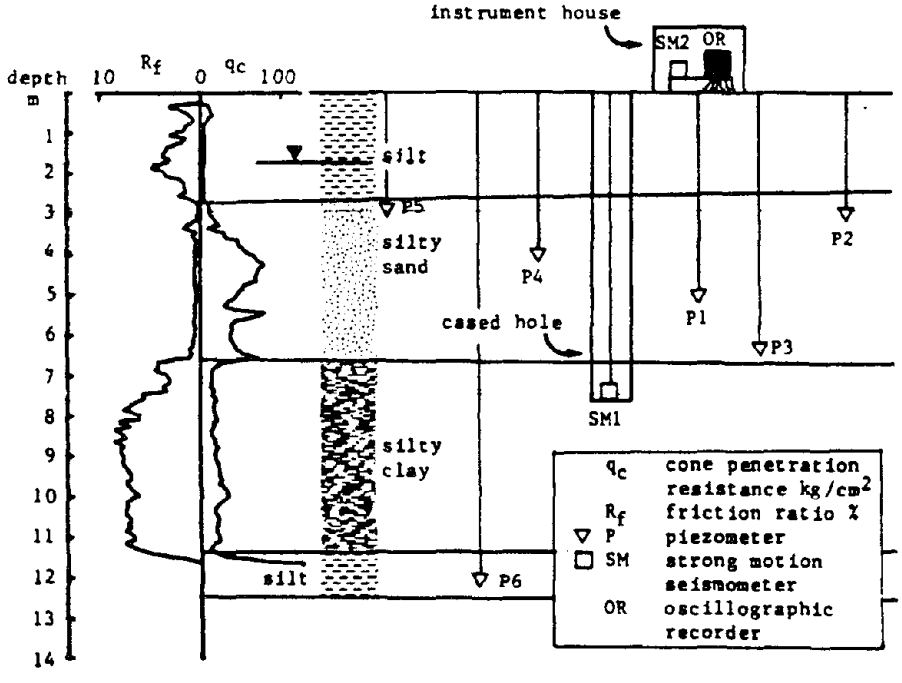

Figure 1: Cross-section and instrumentation at the Wildlife site.

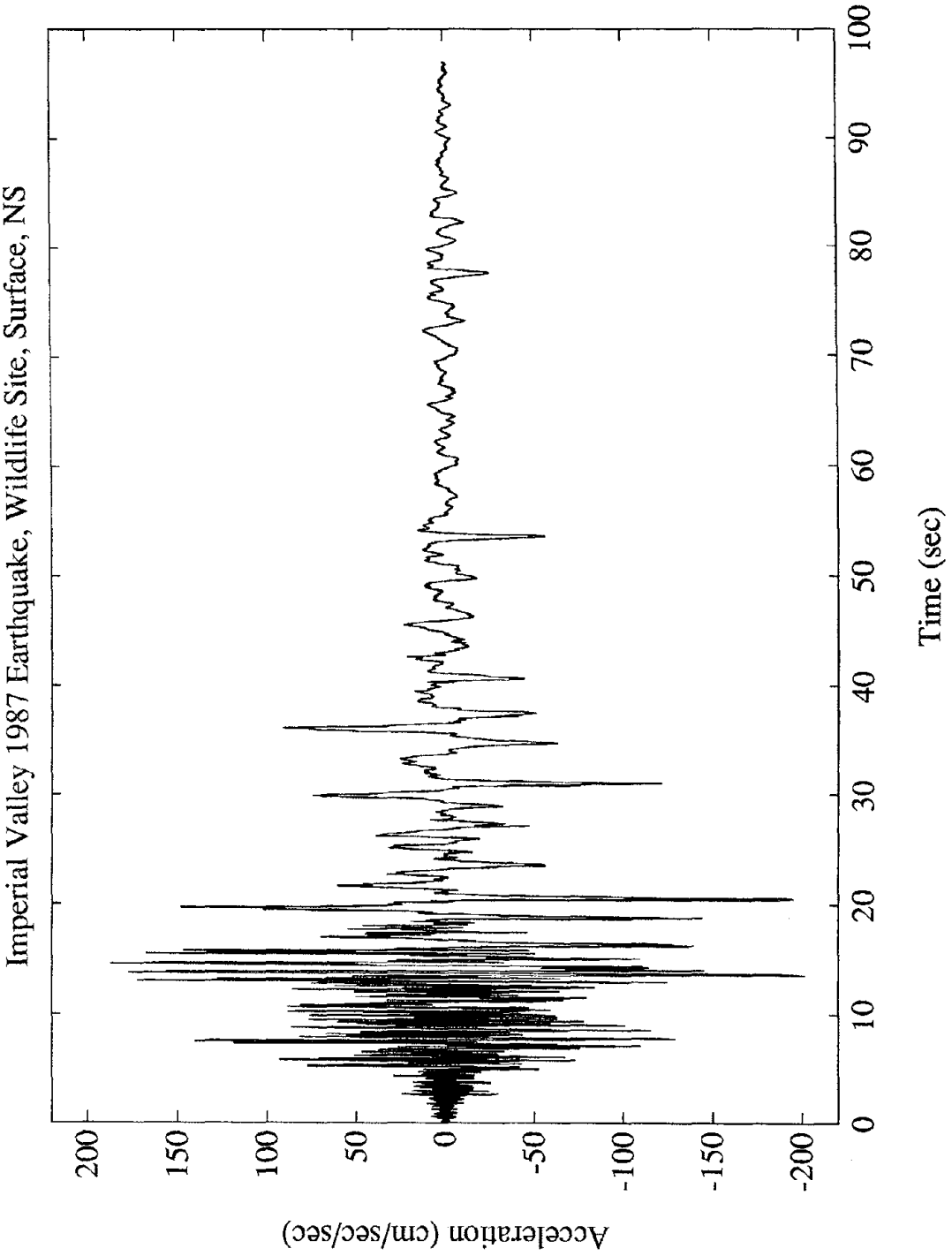

Figure 2: Recorded acceleration at the ground surface, NS component, during the November 24, 1987 Earthquake.

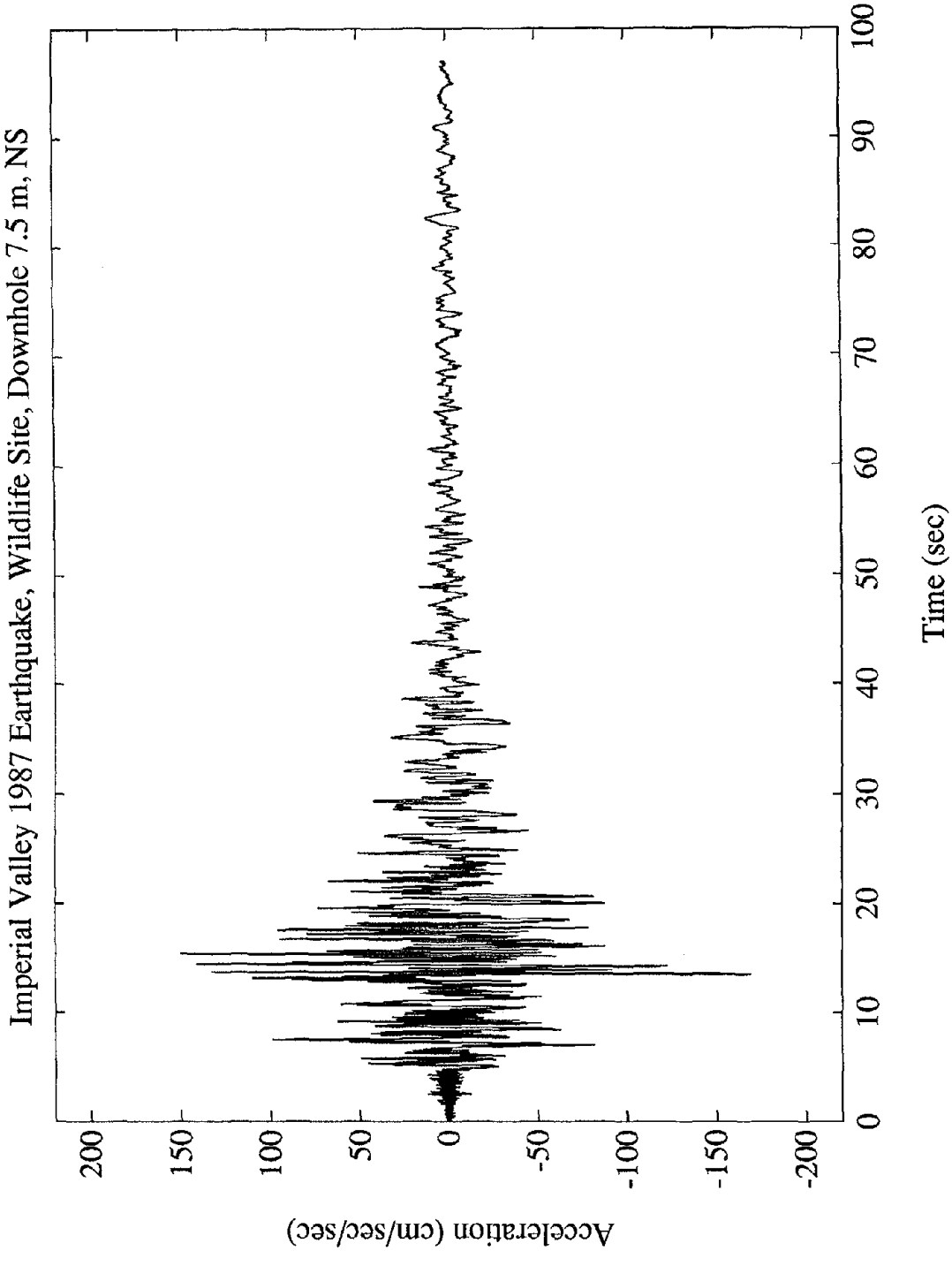

Figure 3: Recorded acceleration at downhole, NS component, during the November 24, 1987 Earthquake.

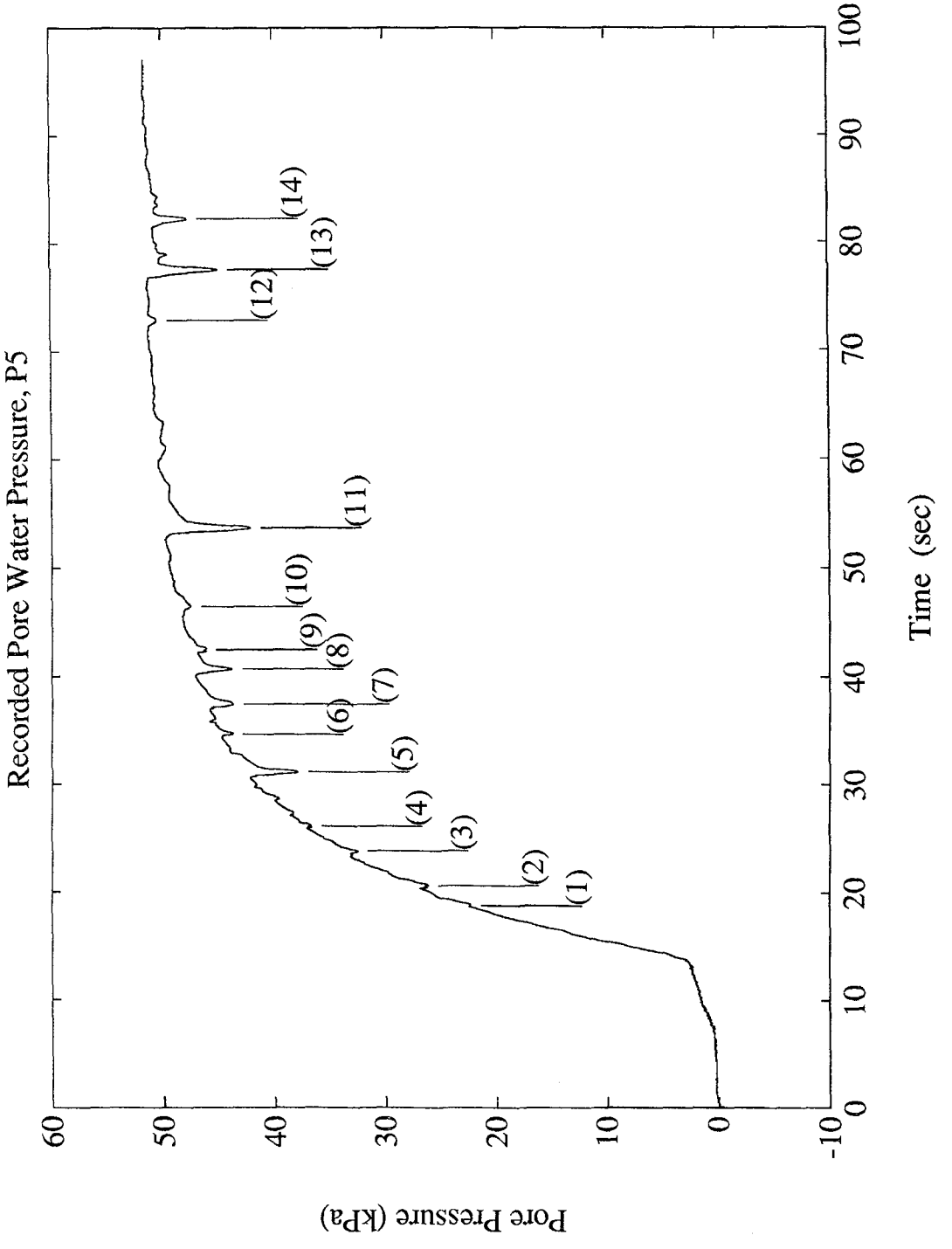

Figure 4: Pore water pressure measured by P5, during the November 24, 1987 Earthquake.

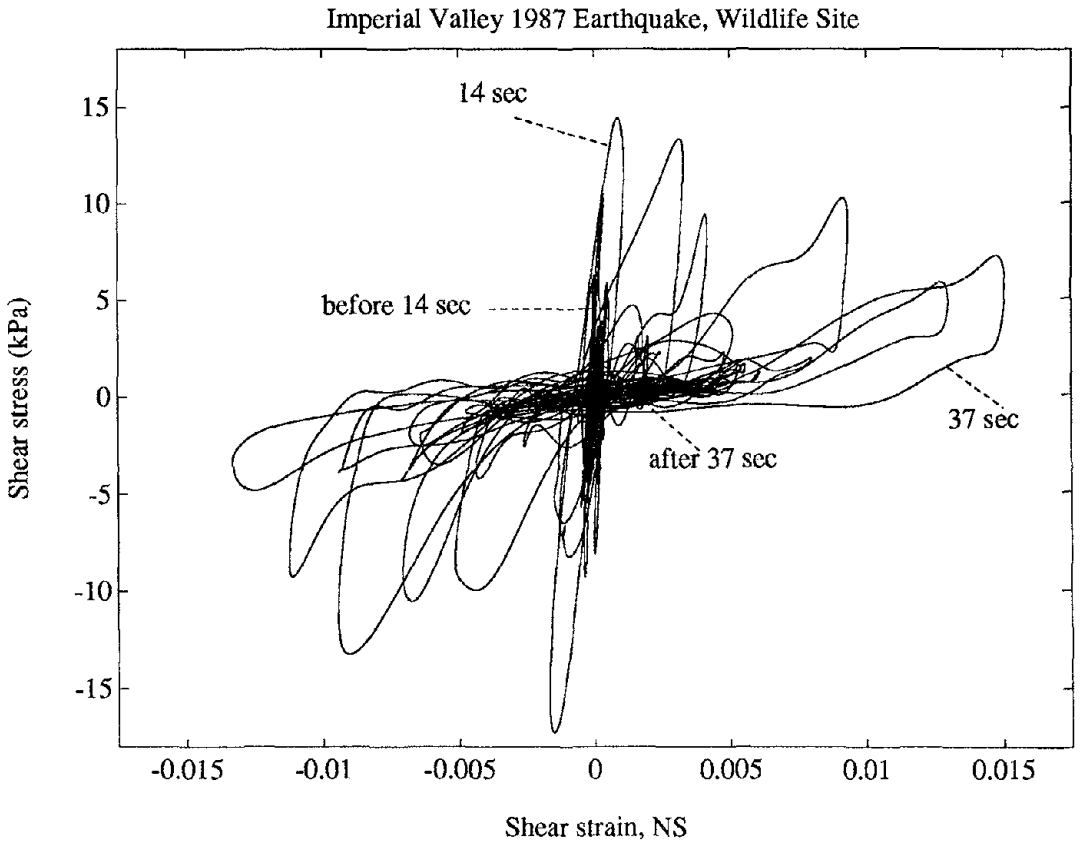

Figure 5: Average stress-strain time history during the November 24, 1987 Earthquake.

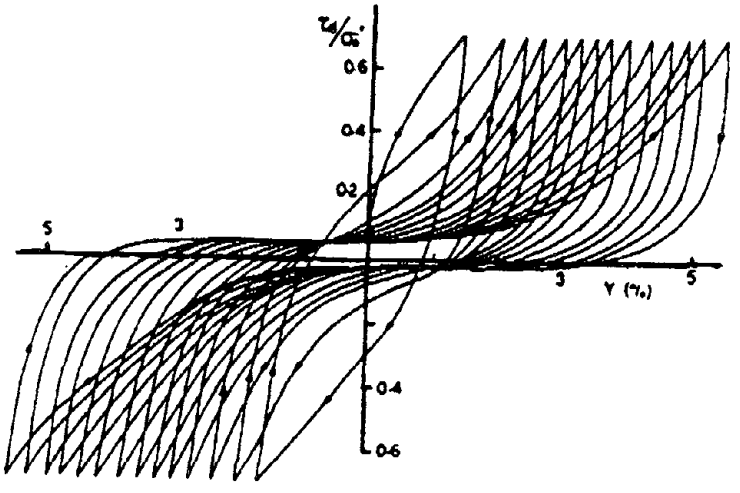

Figure 6: Schematic shear stress-strain hardening behavior (after Ref. [5]).

Liquefaction History, 416–1990, in Japan

K.Wakamatsu

Research Associate
Waseda University at Tokyo

ABSTRACT

Liquefaction has been known to recur at the same site during successive earthquakes. Maps showing locations of past liquefaction occurrences are very useful to delineate and characterize areas of liquefaction susceptibility for future earthquakes. This paper summarizes historical occurrences of liquefaction during the period 416–1990 in Japan. Maps showing distribution of liquefied sites in these earthquakes are compiled based on documentary study, post–earthquake reconnaissance investigations, and interviews to local residents. Totally 123 earthquakes which induced liquefaction are listed. More than 100 locations where liquefaction recurred at the same site during successive earthquakes are presented. Furthermore, seismic intensities which generated the liquefaction effects are examined and relationships between the distance from epicenter and energy source to the farthest liquefied sites and an earthquake magnitude are studied, respectively based on data from the earthquakes.

---

[1]This material is part of "Maps for Historic Liquefaction Sites in Japan" and "Regional Maps for Liquefaction Sites in Japan" Tokai Univ. Press, Tokyo, Japan, 1991.

INTRODUCTION

Liquefaction is known to occur at the same site during more than one earthquake as shown by examples from Japan and United States[2-4]. The maps and records of sites of past liquefaction provide important data for earthquake hazards assessments. The author have been collected records on occurrences of liquefaction during the past twenty years and recently compiled these data into a book entitled "Maps for historic liquefaction sites in Japan"[1]. The data of liquefaction consists of three parts; 284 sheet of maps for liquefied sites on a scale of 1:50,000, regional maps on a scale of 1:200,000 for twelve areas in which liquefied sites were densely distributed, and catalogue for mapped sites. This paper summarizes case histories of liquefaction in Japan based on this liquefaction data.

EARTHQUAKE INVESTIGATED

Up to the present, approximate 850 destructive earthquakes have been recorded in various kind of historical materials and seismic data in Japan[5]. The oldest one among the earthquakes is the September 23, 416 earthquake, which was documented in the "Nihon Shoki", authorized historical document of Japan. These 850 earthquakes of the period 416 through 1990 in Japan were investigated in this study. They include about 450 earthquakes of the period until 1884 which documented in nonscientific materials, and about 400 recent earthquakes after 1884 when a nationwide earthquake observation was started in Japan. No instances of prehistoric liquefaction which were revealed by excavation are included in the liquefaction sites in this study, since date of the earthquake generated liquefaction can be hardly identified.

METHODS OF INVESTIGATIONS AND RECOGNITION OF LIQUEFACTION SITES

To search for records of liquefaction effects, various kind of materials on earthquake damage were collected. They include several compilations of historic materials on the earthquakes prior to 1884. In addition, post-earthquake reconnaissance investigations and interviews to local residents were performed by authors after the several earthquakes. In the investigations, occurrences of liquefaction were recognized from sand and/or water boiling or floating up of buried structures, excluding fissures and/or cracks, flowslides, ground subsidence and settlement of structures leading to no eruption of sand and/or water boils.

EARTHQUAKES WHICH CAUSED LIQUEFACTION

The investigation revealed that totally 123 events induced liquefaction at several thousand sites during the period, 416-1990. The descriptions of liquefaction effects due to these earthquakes

were documented in approximate 300 materials on the earthquake damage. The earthquakes are summarized in Tables 1 and 2 and locations of their epicenters are plotted in Fig. 1. Minimum value of earthquake magnitude is 5.2, for the earthquakes, Nos. 67 and 86 in Table 2 and maximum value is 8.4 for the shocks, Nos. 17, 46 and 47 in Table 1.

The oldest event which was identified to induce liquefaction is the 863 earthquake occurred in Niigata region located northwestern part of Honsyu Island, whereas the latest one is the 1987 Chibaken-toho-oki earthquake which attacked the Boso region east of Tokyo. Concerning the period after 1884, 69 earthquakes have generated liquefaction. Thus liquefaction has occurred twice in every three years at somewhere in Japan during the last 105 years.

LOCATION OF HISTORIC OCCURRENCES OF LIQUEFACTION

Figures 2 and 3 show distribution of occurrences of liquefaction due to the earthquakes of the periods before and after 1884, respectively, in which locations of liquefaction could be identified. Excepting a few cases, the liquefied sites located on low-lying areas whose subsurface ground is consist of Holocene alluvial-fan, fluvial, deltaic, beach and aeolian deposits and artificial fills. In some areas such as the plains of Nohbi, Akita, Niigata, Kanto, Osaka, Kanazawa, Tsugaru, Sendai, Takada, Shizuoka and Tenryu, and Kyoto Basin, liquefaction observed in more than five successive earthquakes for the last fifteen centuries (See Fig.4 for locations of the plains and basin).

Some liquefied sites due to Nos. 46 and 47 earthquakes could hardly distinguished whether the liquefaction was generated by Nos. 46 or 47 earthquakes since these earthquakes occurred on December 23 and 24 in the same year, successively. Therefore locations of liquefaction during the two earthquakes were plotted by same symbol and enclosed them with a single break line in Fig. 2.

The sites of liquefaction extend over the area of several hundreds kilometers in diameter due to the large earthquakes with the magnitude of the order of eight or more such as the 1707 Oct.28 (Hoh-ei) earthquake in Fig. 2 and the 1891 Oct.28 (Nohbi), the 1946 Dec.21 (Nankai) earthquakes in Fig. 3 . In contrast, the liquefaction effects developed within the source area during the small earthquakes with the magnitude less than six such as the earthquakes of 1892 Jan.3,1893 Sep.7, 1897 Jan.17, 1925 July 4, 1927 Oct.27, 1955 Oct.19, and 1961 Feb.27 in Fig.3.

RECURRENCE OF LIQUEFACTION AT SAME SITE

Several examples of recurrence of liquefaction have been reported in Japan and United States[2-4]. Figure 4 shows locations at which liquefaction recurred during the last fifteen centuries in Japan. The site which experienced liquefaction in two or three successive earthquakes are 124 in total. They are, geomorphologically, located on natural levees, marginal part of sand dunes, former river courses, lower edge of alluvial-fans and reclaimed lands. At the localities plotted in Fig.4, liquefaction might recur during future successive earthquakes if water table and sediment conditions remain unchange.

SEISMIC INTENSITY AT LIQUEFIED SITE

To clarify the intensity of earthquake ground motion which caused liquefaction, seismic intensity on the Japan Meteorological Agency (JMA) Scale at the liquefied sites were examined. Figure 5 shows distributions of liquefied sites and seismic intensities on the JMA Scale in the recent earthquakes. The most of the liquefied sites in each earthquake located within the zones of intensity in excess of V which is almost equivalent to VIII on the Modified Mercalli (MM) Scale (See Appendix I).

Widespread liquefaction was induced in case low-lying areas are widely developed in the zone of the intensity V and over (e.g. the 1964 Niigata earthquake), whereas liquefaction occurred locally in case they are confined narrow areas (e.g. the 1968 Tokachi-oki earthquake). Thus the distribution of liquefied sites in the zones of intensity in excess of V in each earthquake was affected by geologic and geomorphologic settings.

Figure 6 shows seismic intensity at liquefied sites on the JMA Scale for earthquake magnitude M in the earthquakes of the period after 1936 when current JMA Intensity Scale has been applied. The plots show that the liquefaction is generally induced by seismic shaking with an intensity in excess of V on the JMA Scale as pointed out by Kuribayashi and Tatsuoka[2]. But, sometimes, it occurred even at intensity IV or lower. The minimum seismic intensity which induced liquefaction decreases gradually as earthquake magnitude increases. This reflects the significant effect that longer duration and period characteristics of ground motion associated with large-magnitude events may have on liquefaction potential.

MAXIMUM EPICENTRAL AND SOURCE DISTANCES TO A LIQUEFIED SITE

The maximum extent of the area of liquefaction susceptibility also can be estimated based on relationship between an earthquake magnitude and epicentral distance to farthest liquefied sites. Kuribayashi and Tatsuoka[2] have shown, for 44 historic Japanese earthquakes, that the farthest

epicentral distance to the liquefied sites, R, is bounded by a straight line on a magnitude, M, versus logarithm of distance plot, which expressed as follows:

$$\log R = 0.77\ M - 3.6 \qquad (1)$$

where, R is in km.

Ambraseys[8] also proposed a similar bound for shallow focus earthquakes based on more extensive study of epicentaral distances at which liquefaction has occurred for 137 earthquakes including 44 and 27 events from Kuribayashi and Tastuoka[2] and from other previous investigations[9–12], respectively.

Figure 7 shows the plots of the maximum distance, R, from the epicenter to the liquefaction sites for an earthquake magnitude, M on the JMA Scale (see Appendix II), for 67 Japanese earthquakes listed in Table 2, in which bounds by Kuribayashi and Tastuoka[2] and by Ambraseys[8] were also plotted. In analyzing the data in Fig. 7, magnitude and epicenter of the earthquakes were adapted the most recent version reestimated by Utsu[6] and JMA[7]. The plots include the data from the 44 Japanese earthquakes studied by Kuribayashi and Tatsuoka and by Ambraseys, but some of their farthest sites were renewed by the author. The plots are summarized in a form of an upper bound relationship between M and R, for the events with $M > 5.0$ as follows:

$$\log R = 2.22 \log (4.22\ M - 19.0) \qquad (2)$$

Where, R in km. The bound suggested by the author seems to account more distant bound than that by Kuribayashi and Tatsuoka and by Ambraseys. This is not only the effect of the difference in scale between the magnitudes assigned in terms of the JMA scale and moment magnitude scale which was adopted by Ambraseys' bound (see Appendix III), but is also due to the fact that more new data were found after the previous investigations.

For near-field conditions or for the larger magnitude earthquakes, the distance to the seismic source may be more appropriate if fault rupture model of the earthquakes are available. To define the source-distance bound, Youd and Perkins[13], Ambraseys[8], and Midorikawa and Wakamatsu[14] plotted the distance based on such a measure.

Figure 8 shows a plot of D, that is of the closest distance from a seismic source to the farthest Japanese earthquakes studied by Midorikawa and Wakamatsu[14] and for the 1987 Chibaken-toho-oki earthquake supplemented by author, along with the bounds by Youd and Perkins and by Ambraseys for comparison. Excepting a few cases, upper bound line for the distance where liquefaction effects has been observed is represented by

$$\log D=0.6M-2.4 \qquad (3)$$

as has been suggested by Midorikawa and Wakamatsu. This bound yields almost same distance for events with magnitude ranging from 6.0 to 7.5 as that suggested by Ambraseys. Whereas the bound suggested by Youd and Perkins yields lesser distance for magnitude less than 7 events. This is probably for the reason that their distance bound is defined as distances to localities where liquefaction effects were associated with ground displacements of 100 mm or greater, while the bounds given by Midorikawa and Wakamatsu and by Ambraseys are defined as distance to all effects of liquefaction.

CONCLUSIONS

The following characteristics can be summarized from the case histories of liquefaction due to the earthquakes occurred in Japan from 416 to 1990.

(1) Totally 123 events with magnitudes ranging from 5.2 to 8.4 have induced liquefaction during the period, 416–1990.

(2) Several thousand sites of liquefaction appeared in most part of Japan due to the 123 earthquakes. They are located on low-lying areas whose subsurface ground is consists of Holocene alluvial-fan, fluvial, deltaic, beach and acolian deposits and artificial fills.

(3) Liquefaction was observed in more than five successive earthquakes in the last fifteen centuries, respectively, in such areas as the plains of Nohbi, Akita, Niigata, Kanto, Osaka, Kanazawa, Tsugaru, Sendai, Takada, Shizuoka and Tenryu and Kyoto Basin.

(4) The sites which recurred liquefaction in two or three successive earthquakes are as many as 124. They are, geomorphologically, located on natural levees, marginal part of sand dunes, former river courses, lower edge of alluvial-fans, reclaimed lands in that order.

(5) The liquefaction was generally triggered by the ground motion of intensity in excess of V on the JMA Scale, but sometimes, it occurred even at less than V.

(6) Minimum seismic intensity which induced liquefaction decreases gradually as an earthquake magnitude increases.

(7) The upper bound relationship between M and R, for events with $M > 5.0$ can be expressed by

$$\log R = 2.22 \log (4.22 M - 19.0)$$

where, R is distance from epicenter to farthest liquefied sites, in km and M is earthquake magnitude on the JMA Scale.

(8) The upper bound relationship between M and D, for events with M > 6.5 may be approximated by

$$\log D = 0.6M - 2.4$$

where, D is distance from seismic source to farthest liquefied site, in km and M is earthquake magnitude on the JMA Scale.

ACKNOWLEDGEMENTS

The author would like to express her appreciation to Professors K. Kubo and M. Hamada at Tokai University for their strong support to the research. She also wishes to express her thanks to Prof. S. Yasuda at Kyushu Institute of Technology and Dr. N. Yoshida at Sato Kogyo Co., Ltd., for their helpful discussions. The author extend her sincere thanks to many researchers of liquefaction case histories who provides her detailed data of their investigations.

REFERENCES

1) Wakamatsu, K., "Maps for Historic Liquefaction Sites in Japan" and "Reagional Maps for Liquefaction Sites in Japan (attached maps)" Tokai Univ. Press, Tokyo, Japan, 352pp.,1991 (in Japanese with English abstract).
2) Kuribayashi, E. and Tatsuoka, F., "Brief Review of Soil Liquefaction during Earthquakes in Japan," Soils and Foundations, Vol.15, No.4, pp.81-92, 1975.
3) Youd, T.L., "Recurrences of Liquefaction at Same Site, "Proc., 8th World Conf. on Earthquake Engineering, San Francisco, Cal., Vol.3, pp.231-238, 1984.
4) Yasuda, S. and Thono, I., "Sites of Reliquefaction Caused by the Nihonkai-Chubu Earthquake," Soils and Foundations, Vol.28, No.2, pp.61-72, 1988.
5) Usami, T., "Materials for Comprehensive List of Destructive Earthquakes in Japan," Univ. of Tokyo Press., Tokyo, 434 pp., 1988 (in Japanese).
6) Utsu, T., "Catalogue of Large Earthquakes in the Region of Japan from 1885 through 1980," Bull. of the Earthquake Res. Instit., Univ. of Tokyo, Vol.57, pp.401-463, 1982 (in Japanese with English abstract).
7) Japan Meteorological Agency (JMA), "Catalogue of Relocated Major Earthquakes in and near Japan (1926-1960)," The Seism. Bull. of The Japan Meteorological Agency, Supplementary Volume No.6, 1982.
8) Ambraseys, N.N., "Engineering Seismology," Earthquake Engr. and Soil Dynamics, No.17,

pp.1–15, 1988.
9) Youd, T.L., "Discussion of Brief Review of Liquefaction during Earthquakes in Japan by E.Kuribayashi and F.Tatsuoka," Soils and Foundations, Vol.17, No.1, pp.82–85, 1977.
10) Davis, R.O. and Berrill, J.B., "Comparison of a Liquefaction Theory with Field Observations," Geotechnique, Vol.33, No.4, pp.355–460, 1983.
11) Davis, R.O. and Berrill, J.B., "Discussion of Comparison of a Liquefaction Theory with Field Observations," Geotechnique, Vol.34, No.4, pp.627–629, 1984.
12) Fairless, G. and Berrill, J., "Liquefaction during Historic Earthquakes in New Zealand," Bull. of New Zealand National Soc. of Earthquake Eng., Vol.17, pp.290–291, 1984.
13) Youd, T.L. and Perkins,D.M., "Mapping Liquefaction Induced Ground Failure Potential," Journal of the Geotechnical Engr Div., ASCE 104 (GT4), pp.433–446, 1978.
14) Midorikawa, S. and Wakamatsu,K., "Intensity of Earthquake Ground Motion at Liquefied Sites," Soils and Foundations, Vol.23, No.2, pp.73–84, 1988.
15) Seismological Division, J.M.A., "The Records of Seismic Intensity Observed in Japan," Technical Report of Japan meteorological Agency, No.76, 222 pp.,1971 (in Japanese).
16) Japan Meteorological Agency, "The Seismological Bulletin of the Japan Meteorological Agency for January 1992." pp.i–ii, 1992.
17) Katsumata, M., " A Method to Determine the magnitude of Deepfocus Earthquake In and Near Japan," Zishin, II, Vol.17, pp.158–165, 1964 (in Japanese).
18) Utsu, T., "Relationships between Earthquake Magnitude Scales." Bull. of the Earthquake Res. Instit., Univ. of Tokyo, Vol.57, pp.465–497, 1982 (in Japanese with English abstract).

Table 1 Earthquakes which Induced Liquefaction in Japan during the Period, 416–1884

No.	Date	Earthquake	Epicenter	M
1	863 Jul.10		–	–
2	1185 Aug.13		35.0N –135.8E	≈7.4
3	1257 Oct.9		35.2N –139.5E	7.0–7.5
4	1449 May 13		35.0N –135.75E	5 3/4–6.5
5	1596 Sep.4		33.3N –131.6E	7.0±1/4
6	1596 Sep.5		34.65N–135.6E	7 1/2±1/4
7	1605 Feb.3	Keicho	33.5N –138.5E	7.9
8	1633 Mar.1		35.2N –139.2E	7.0±1/4
9	1644 Oct.18		39.4N –140.0E	6.5±1/4
10	1662 Jun.16		35.2N –135.95E	7 1/4–7.6
11	1666 Feb.1		37.1N –138.2E	≈6 3/4
12	1685 Oct.7		–	–
13	1694 Jun.19		40.2N –140.1E	7.0
14	1694 Dec.12		–	–
15	1703 Dec.31	Genroku	34.7N –139.8E	7.9–8.2
16	1704 May 27		40.4N –140.0E	7.0±1/4
17	1707 Oct.28	Hoh–ei	33.2N –135.9E	8.4
18	1717 May 13		38.5N –142.5E	≈7.5
19	1717 –		36.5N –136.5E	≈6 1/4
20	1723 Dec.19		32.9N –130.6E	6.5±1/4
21	1729 Mar.8		–	–
22	1734 –		–	–
23	1751 Mar.26		35.0N –135.8E	5.5–6.0
24	1751 May 21		37.1N –138.2E	7.0–7.4
25	1762 Oct.31		38.1N –138.7E	≈7.0
26	1766 Mar.8		40.7N –140.5E	7 1/4±1/4
27	1769 Aug.29		33.0N –132.1E	7 3/4±1/4
28	1774 Jun.[illegible]		–	–
29	1782 Aug. 23		35.4N –139.1E	≈7.0
30	1792 May 21		32.8N –130.3E	6.4±0.2
31	1793 Feb.8		40/85N–139.5E	6.9–7.1
32	1799 Jun.29		36.6N –136.6E	6.0±1/4
33	1802 Nov.18		35.2N –136.5E	6.5–7.0
34	1804 Jul.10	Kisagata	39.05N–139.95E	7.0±0.1
35	1810 Sep.25		39.9N –139.9E	6.5±1/4
36	1819 Aug.2		35.2N –136.3E	7 1/4±1/4
37	1828 Dec.18		37.6N –138.9E	6.9
38	1830 Aug.19		35.1N –135.9E	6.5±0.2
39	1833 Dec.7		38.9N –139.25E	7 1/2±1/4
40	1834 Feb.9		43.4N –141.4E	≈6.4
41	1841 Apr.22		35.0N –138.5E	≈6 1/4
42	1843 Apr.25		42.0N –146.0E	≈7.5
43	1847 May 8	Zenkohji	36.7N –138.2E	7.4
44	1847 May 13		37.2N –138.3E	6 1/2±1/4
45	1854 Jul.9		34.75N–136.5E	7 1/4±1/4
46	1854 Dec.23	Ansei–Tokai	34.0 –137.8E	8.4
47	1854 Dec.24	Ansei–Nankai	33.0N –135.0E	8.4
48	1855 Mar.15		–	–
49	1855 Nov.7		34.5N –137.75E	7.0–7.5
50	1855 Nov.11	Edo	35.65N–139.8E	6.9±0.1
51	1856 Aug.23		41.0N –142.25E	≈7.5
52	1858 Apr.9		36.4N –137.2E	7.0–7.1
53	1859 Jan.5		34.8N –131.9E	6.2±0.2
54	1872 Mar.14	Hamada	35.15N–132.1E	7.1±0.2

M : Earthquake magnitude assigned in terms of JMA (Japan Meteorological Agency) Scale, which was estimated by Usami[5] (See Appendixs II and III)

– : Unknwon

Table 2 Earthquakes which Induced Liquefaction in Japan during the Period, 1885–1990

No.	Date	Earthquake	Epicenter	h	M
55	1887 Jul.22	Koshigun	35.7N –138.9E	–	5.7
56	1889 Jul.28	Kumamoto	32.8N –130.65E	–	6.3
57	1890 Jan.7	Saigawa-ryuiki	36.45N–137.95E	–	6.2
58	1891 Oct.28	Nohbi	35.6N –136.6E	–	8.0
59	1892 Jan.3	Aftershock, Nohbi	35.3N –137.1E	–	5.5
60	1892 Sep.7	Aftershock, Nohbi	35.7N –137.0E	–	6.1
61	1893 Sep.7	Chiran	31.4N –130.5E	–	5.3
62	1894 Jan.10	Aftershock, Nohbi	35.4N –136.7E	–	6.3
63	1894 Jun.20	Tokyo-wan-hokubu	35.6N –139.8E	–	7.0
64	1894 Oct.22	Shonai	38.9N –139.9E	–	7.0
65	1895 Jan.18	Kasumigaura-fukin	36.1N –140.4E	–	7.2
66	1896 Aug.31	Riku-u	39.5N –140.7E	–	7.2±0.2
67	1897 Jan.17	Naganoken-hokubu	36.65N–138.25E	–	5.2
68	1897 Feb.20	Sendai-oki	38.1N –141.9E	–	7.4
69	1898 Apr.3	Mishima	34.6N –131.2E	–	6.2
70	1898 Apr.23	Miyagiken-oki	38.6N –142.0E	–	7.2
71	1898 May 26	Muikamachi	37.0N –138.9E	–	6.1
72	1898 Aug.10	Fukuoka	33.6N –130.2E	–	6.0
73	1898 Sep.1	Yaeyama-gunto	24.5N –124.75E	–	7
74	1899 Mar.7	Kiihanto-nanseibu	34.1N –136.1E	–	7.0
75	1901 Aug.9	Aomoriken-toho-oki	40.5N –142.5E	–	7.2
76	1904 May 8	Muikamachi	37.1N –138.9E	–	6.1
77	1905 Jun.2	Geiyo	34.1N –132.5E	–	6.7
78	1909 Aug.14	Gohno (Anegawa)	35.4N –136.3E	–	6.8
79	1914 Mar.15	Akita-senpoku	39.5N –140.4E	–	7.1
80	1922 Dec.8	Chijiwa-wan	32.7N –130.1E	–	6.9
81	1923 Sep.1	Kanto	35.2N –139.3E	–	7.9
82	1925 May 23	Kita-Tajima	35.6N –134.8E	–	6.8
83	1925 Jul.4	Miho-wan	35.3N –133.3E	–	5.8
84	1927 Mar.7	Kita-Tango	35.53N–135.15E	0	7.3
85	1927 Aug.6	Miyagiken-oki	37.93N–142.12E	10	6.7
86	1927 Oct.27	Sekihara	37.5N –138.8E	10	5.2
87	1930 Oct.17	Daishoji	36.30N–136.28E	0	6.3
88	1930 Nov.26	Kita-Izu	35.1N –139.0E	0	7.3
89	1931 Sep.21	Nishi-Saitama	36.15N–139.23E	0	6.9
90	1933 Sep.21	Noto-hanto	37.1N –137.0E	15	6.0
91	1935 Jul.11	Shizuoka	34.97N–138.42E	10	6.4
92	1936 Feb.21	Kawachi-Yamato	34.58N–135.72E	0	6.4
93	1936 Nov.3	Kinakazan-oki	38.15N–142.13E	40	7.5
94	1939 May 1	Oga	40.13N–139.52E	0	6.8
95	1941 Jul.15	Nagano	36.72 –138.23E	0	6.1
96	1943 Mar.4	Tottori-oki	35.43N–134.22E	0	6.2
	1943 Mar.5	"	35.50N–134.22E	0	6.2
97	1943 Sep.10	Tottori	35.52N–134.08E	0	7.2
98	1944 Dec.7	Tohnankai	33.8N –136.62E	30	7.9
99	1945 Jan.13	Mikawa	34.7N –137.0E	0	6.8
100	1946 Dec.21	Nankai	33.03N–135.62E	20	8.0
101	1947 Sep.27	Ishigakijima	24.7N –123.3E	95	7.4
102	1948 Jun.28	Fukui	36.17N–136.2E	0	7.1
103	1952 Mar.4	Tokachi-oki	41.80N–144.13E	0	8.2
104	1952 Mar.7	Daishoji-oki	36.48N–136.20E	0	6.5
105	1955 Jul.27	Tokushimaken-nanbu	33.73N–134.32E	10	6.4
106	1955 Oct.19	Futatsu-i	40.27N–140.18E	0	5.9
107	1961 Feb.2	Nagaoka	37.45N–138.83E	20	5.2
108	1961 Feb.27	Hyuganada	31.60N–131.85E	40	7.0
109	1962 Apr.23	Hiro-o-oki	42.23N–143.92E	60	7.0
110	1962 Apr.30	Miyagiken-hokubu	38.73N–141.13E	0	6.5
111	1964 May 7	Ogahanto-oki	40.33N–139.0E	0	6.9
112	1964 Jun.16	Niigata	38.35N–139.18E	40	7.5
113	1968 Feb.21	Ebino	32.02N–130.72E	0	6.1
114	1968 Apr.1	Hyuganada	32.28N–132.53E	30	7.5
115	1968 May 16	Tokachi-oki	40.73N–143.58E	0	7.9
116	1973 Jun.17	Nemurohanto-oki	42.97N–145.95E	40	7.4
117	1978 Jan.14	Izu-Ohshima-kinkai	34.77N–139.25E	0	7.0
118	1978 Feb.20	Miyagiken-oki	38.75N–142.20E	50	6.7
119	1978 Jun.12	Miyagiken-oki	38.15N–142.17E	40	7.4
120	1982 Mar.21	Urakawa-oki	42.07N–142.48E	40	7.1
121	1983 May 26	Nihonkai-chubu	40.35N–139.08E	14	7.7
122	1983 Jun.21	Aftershock, Nihonkai-chubu	41.26N–139.00E	6	7.1
123	1987 Dec.17	ChibakEn-toho-oki	35.35N–140.48E	58	6.7

h : Focal depth in km

M : Earthquake magnitude assigned in terms of JMA (Japan Meteorological Agency) Scale which was estimated by Utsu[6] for the earthquakes before 1922 and by JMA[7] for that after 1922. (See Appendixs II and III)

– : Unknown

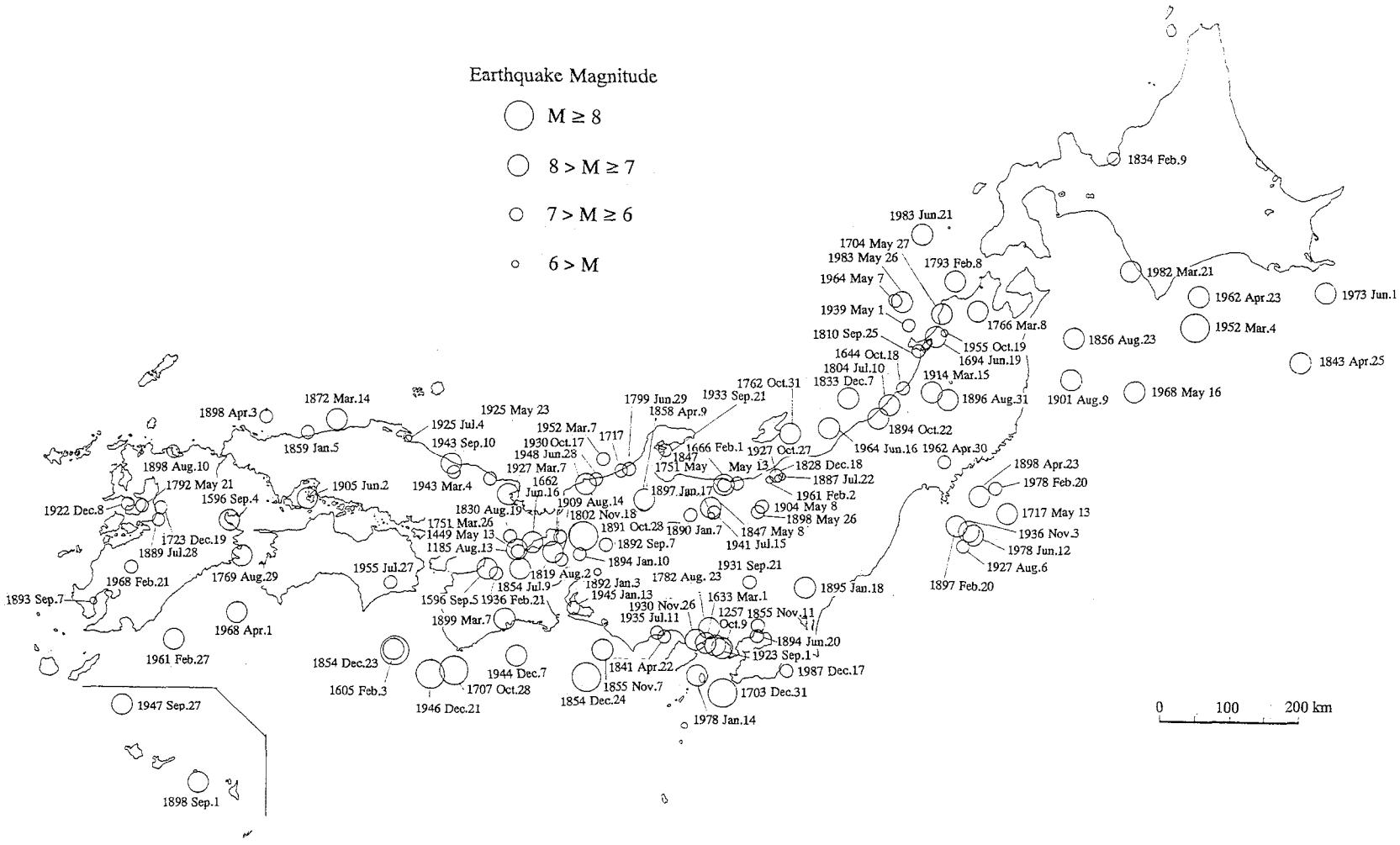

Fig.1 Map Showing Epicenters and Magnitudes of the Earthquakes which Caused Lique·faction in Japan

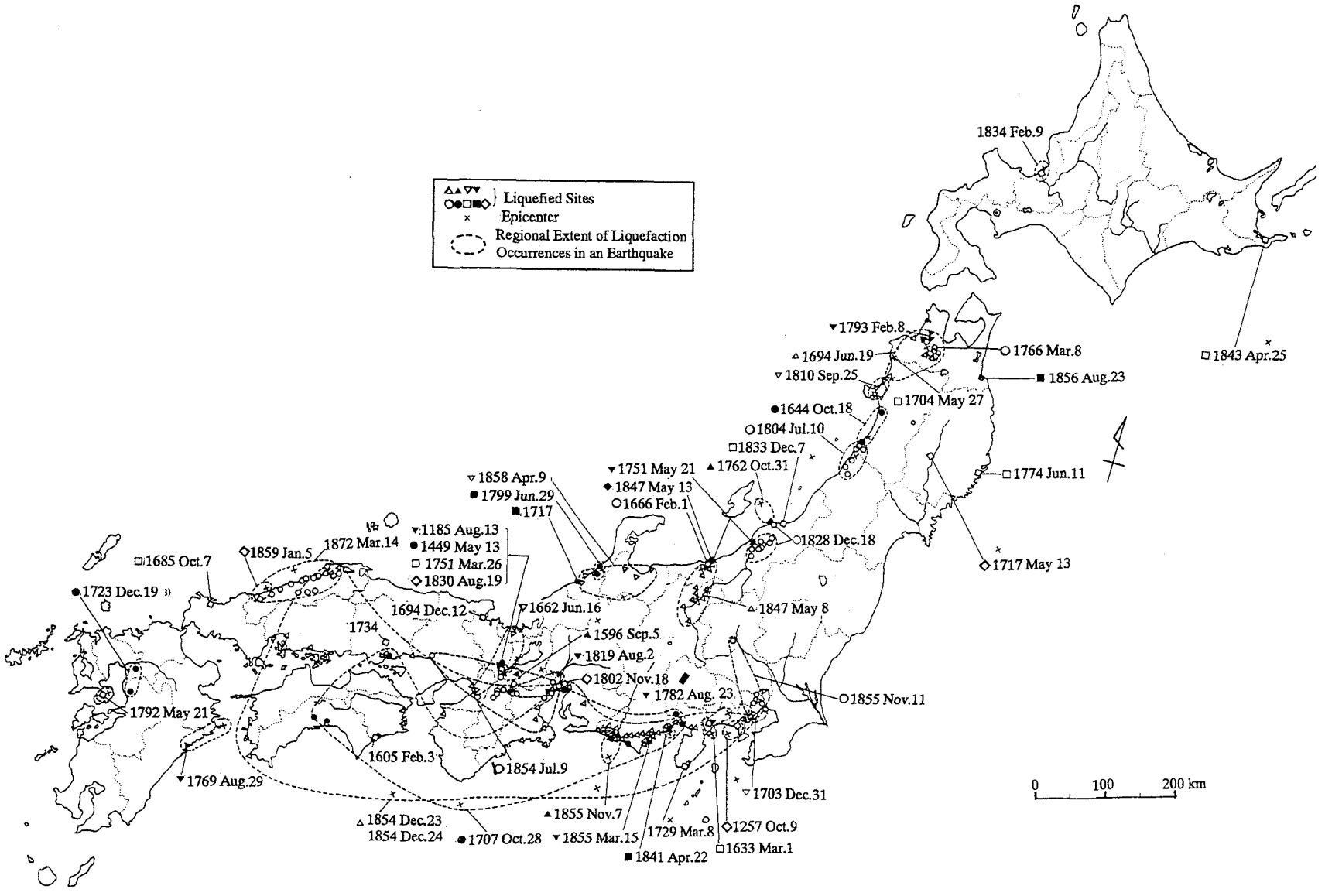

Fig.2 Map Showing Distribution of Historic Occurrences of Liquefaction during the Period, 416–1884

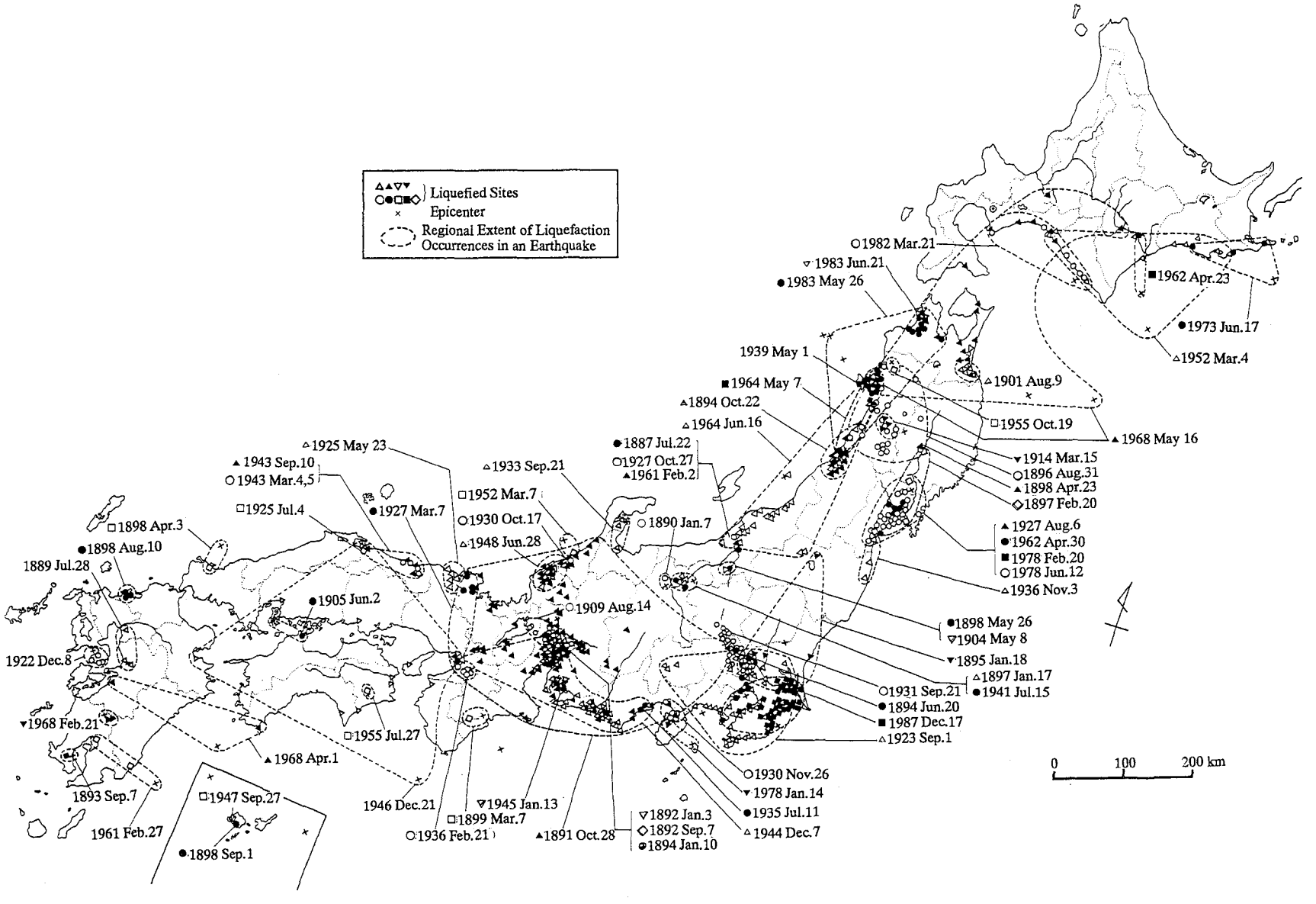

Fig.3 Map Showing Distribution of Historic Occurrences of Liquefaction during the Period, 1885–1990

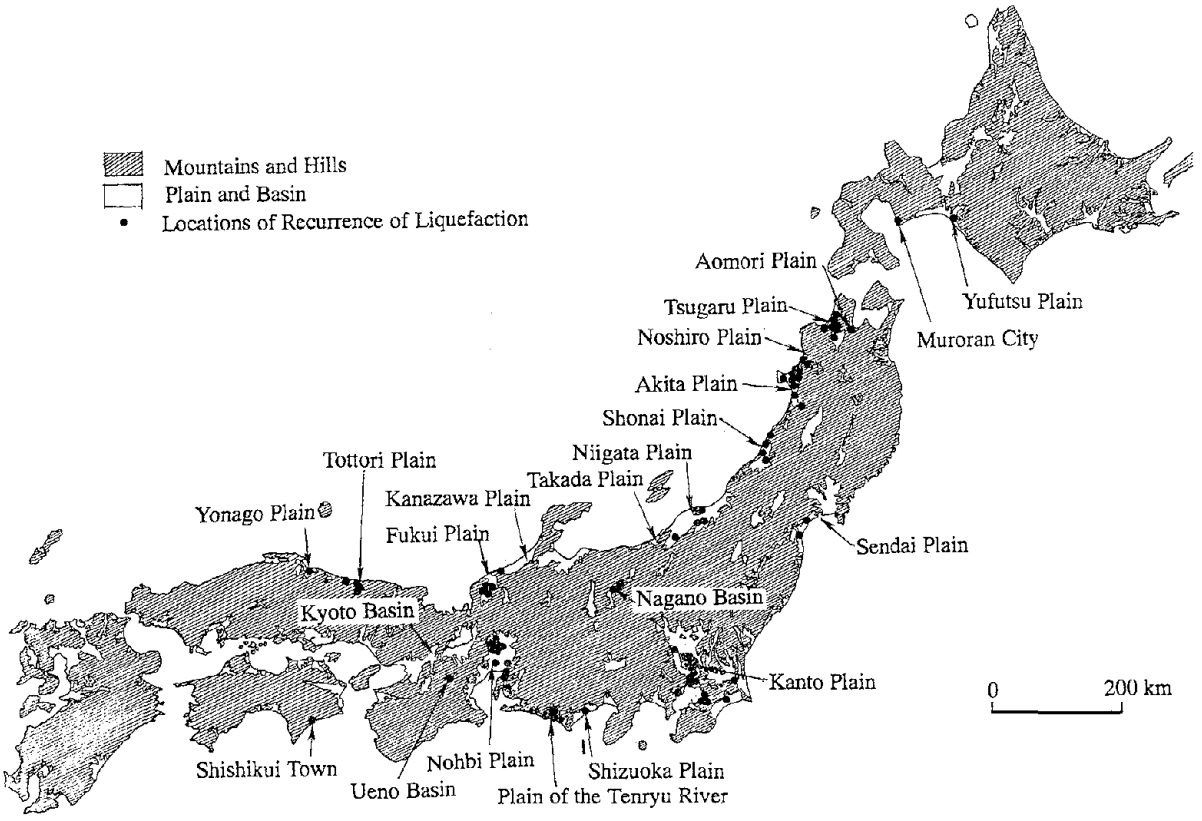

Fig.4 Map Showing Locations at which Liquefaction Recurred during Successive Earthquakes

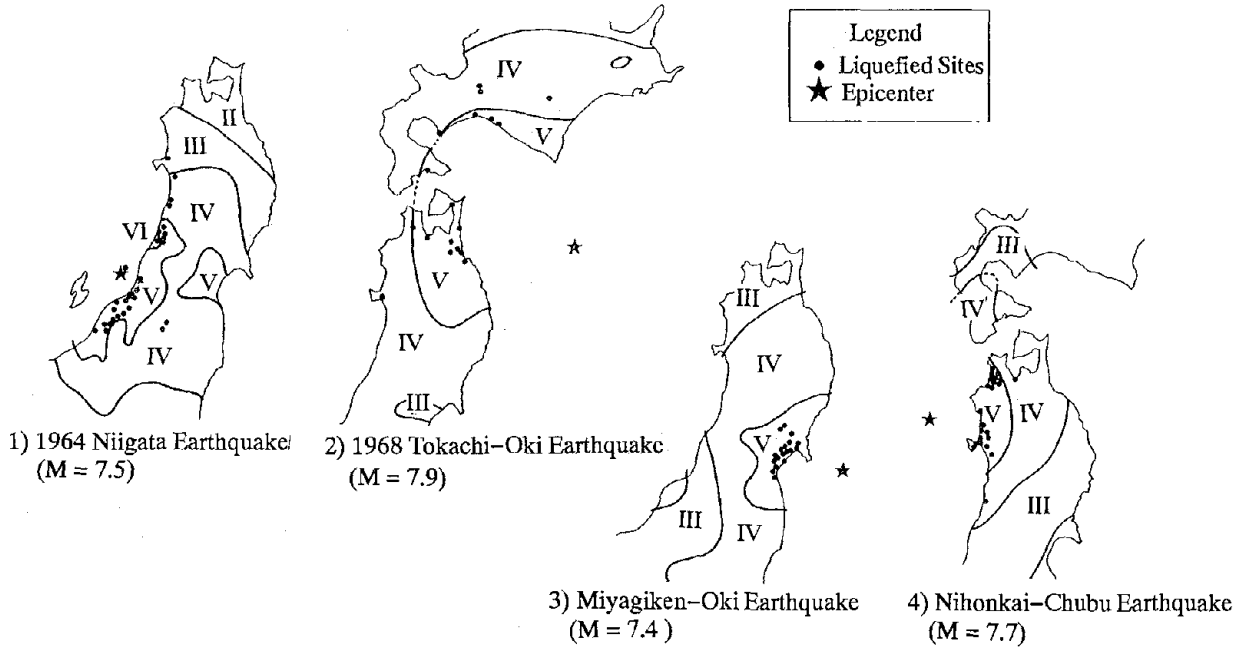

Fig.5 Maps Showing Distributions of Liquefied Sites and Seismic Intensities on the JMA Scale in the Recent Earthquakes.

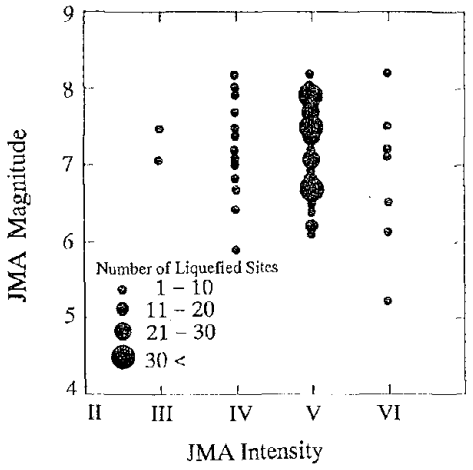

Fig.6 Seismic Intensity at Liquefied Sites on the JMA Scale for an Earthquake Magnitude, M, during the Period, 1936–1990

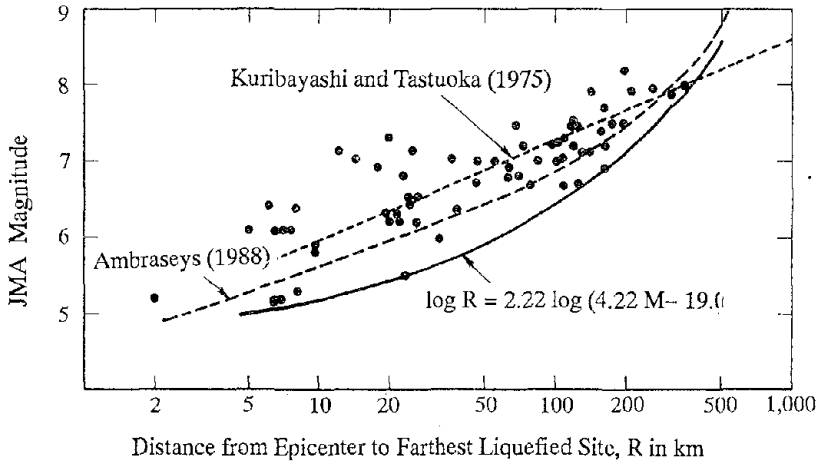

Fig.7 Epicentaral Distance to Farthest Liquefied Sites, R in km, for an Earthquake Magnitude, M, for 67 Earthquakes after 1884

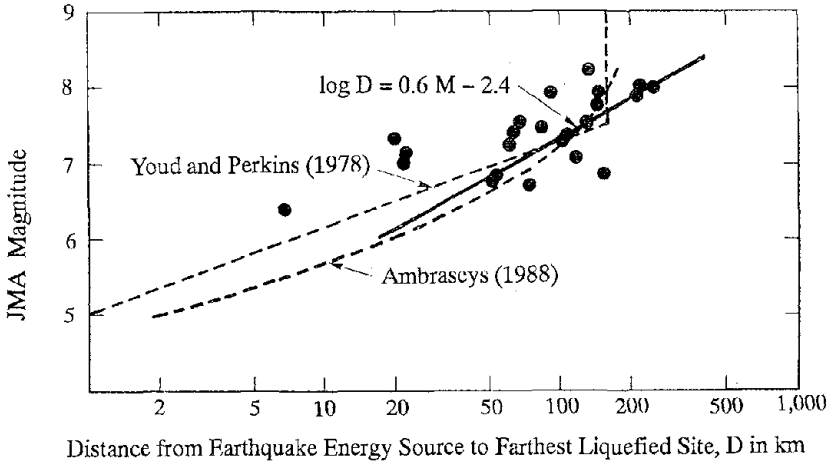

Fig.8 Source Distance to Farthest Liquefied Sites, D in km, for an Earthquake Magnitude, M, for 23 Earthquakes after 1884 (Modified from Midorikawa and Wakamatsu,1988)

APPENDIX I: Approximate correspondence among the JMA (Japan Metcorological Agency), MM (Modified Mercalli), and MSK (Medvedev Sponheuer Karnick) scales and peak ground acceleration[15]

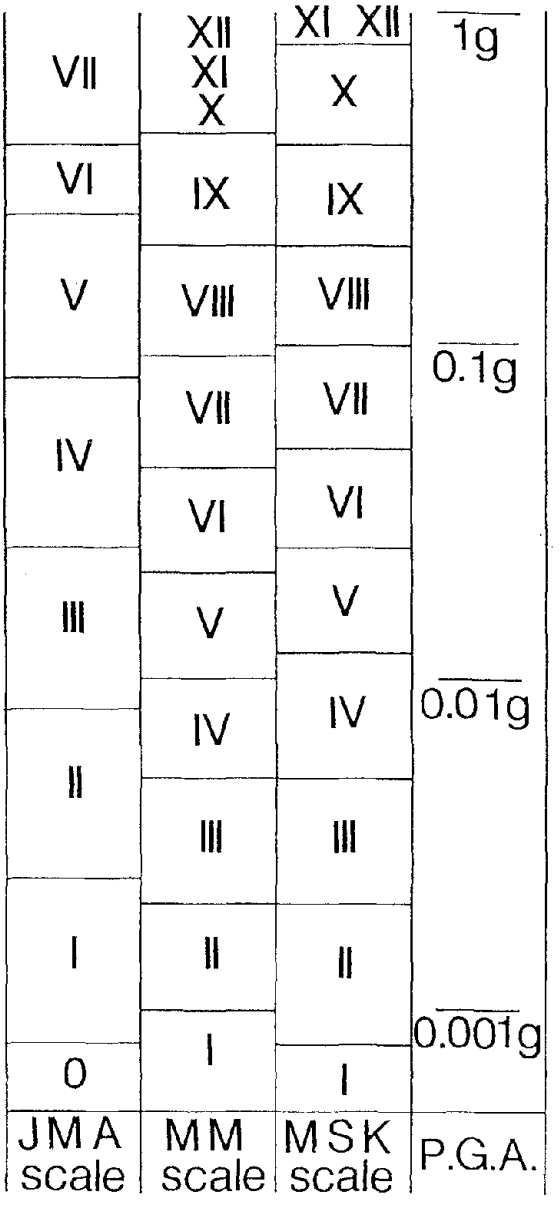

APPENDIX II: JMA magnitude[16]

Magnitudes are calculated by the following methods for the earthquake with the focal depth, $H \leq 60$ km and $H > 60$ km, respectively.

(i) Magnitude for the shallow earthquake, $H \leq 60$ km

a) Station magnitudes are calculated according to the following formulas using the data of maximum displacement and maximum velocity amplitudes respectively.

$$M = \tfrac{1}{2}\log(A_N^2 + A_E^2) + 1.73\log \quad - 0.83 \qquad (H \leq 60 \text{ km})$$

$$M = \log A_z + 1.64 \log \triangle + \alpha \qquad (H \leq 60 \text{ km}, \triangle \leq 700 \text{ km})$$

where, H is focal depth in km, $\triangle$ is epicentral distance in km, α is 0.22 for seismograph EMT and 0.44 for seismographs EMT 76 or OBS, A_N and A_E are maximum ground amplitude of N and E components in micrometer (10^{-6} m), and A_Z is maximum velocity amplitude of Z component in millikine (10^{-5} m/s) obtained with seismographs EMT, EMT76 or OBS.

b) For the earthquake with maximum displacement amplitudes available from 3 or more stations, the mean values for the displacement and velocity data are computed independently.

c) If the difference between above two mean values are greater than or equal to 0.5 or the mean value of the magnitudes from the displacement data are greater than or equal to 5.5, only the displacement data are used for the magnitude determination.

d) For the earthquake not satisfying the above criterion, the magnitude is obtained by averaging both displacement and velocity data.

e) In the calculation of mean value, the station data deviated more than 0.5 in magnitude are eliminated. The magnitude is determined in case the standard deviation of mean value is less than 0.35.

(ii) Magnitude for the deep earthquake, $H > 60$ km

Station magnitudes are calculated according to the following formula (The magnitude are calculated in a same way as above e)). The velocity data are not in use. Column of magnitude is left bank if amplitude data are insufficient.

$$M = \tfrac{1}{2}\log(A_N^2 + A_E^2) + K(\triangle, H) \qquad (H > 60 \text{ km})$$

where, H is focal depth in km, $\triangle$ is epicentral distance in km, K is depth–distance factor given by Katsumata[17], and A_N and A_E are maximum ground amplitude of N and E components in micrometer (10^{-6} m).

APPENDIX III: Curves showing the variation of the average magnitude difference[18]

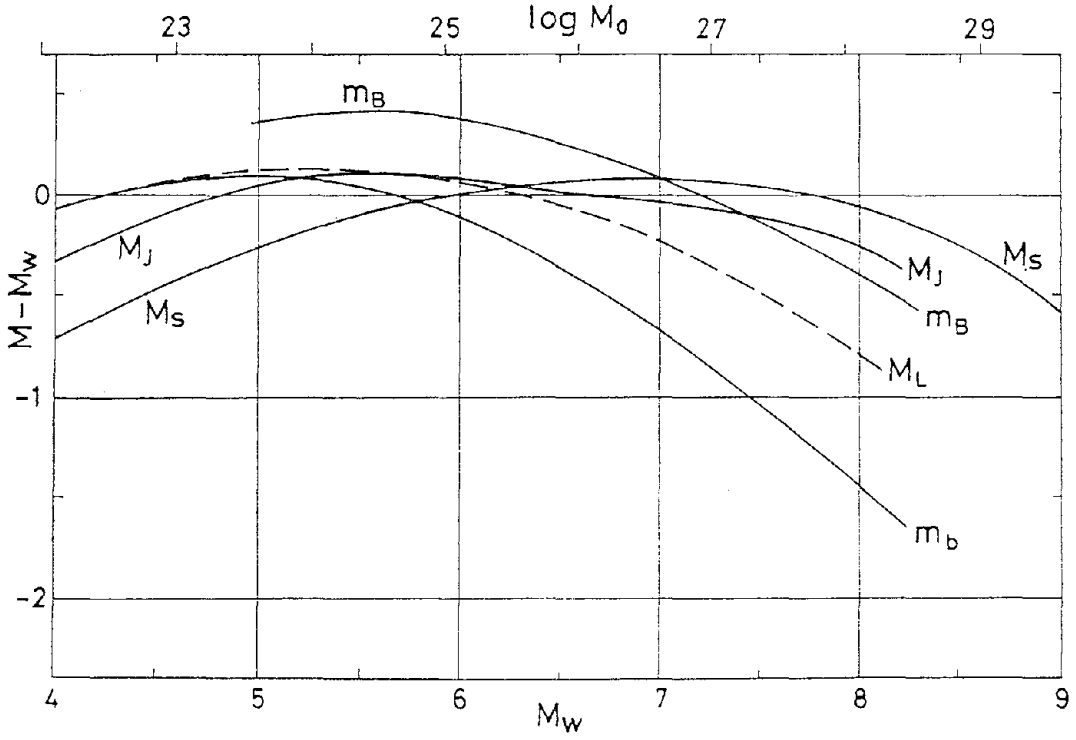

M_w:Moment magnitude defined by Kanamori
M_s:Surfacc wave magnitude
M_j:JMA magnitude
M_L:Richter's local magnitude
m_B:Body wave magnitude from medium– to long– period seismometer records
m_b:Body wave magnitude from short–period seismometer records

A Summary of Case Studies on Liquefaction-Induced Ground Displacements

Masahiko Doi[1] and Masanori Hamada[2]

(1)Research Engineer,Engineering Research Center, Tokyo Electric Power Co., Inc. Tokyo,Japan.
(2)Professor, School of Marine Science and Technology, Tokai University, Shimizu,Japan.

ABSTRACT

The purpose of this paper is to investigate the following two topics on the case studies on the liquefaction-induced ground displacements during Japanese past four earthquakes namely, the 1923 Kanto, the 1948 Fukui, the 1964 Niigata, the 1983 Nihonkai-Chubu earthquakes.

(1) The mechanism of the occurrence of liquefaction-induced ground displacements,
(2) Influences of liquefaction-induced ground displacements on underground structures,

From the present investigation, it is concluded that the ground displacements were caused as a result of flow-type of behavior of the liquefied ground, and the effects of the ground displacements on underground structures such as foundation piles and buried pipes could be represented by a drag force from the liquefied soil.

INTRODUCTION

A large number of case histories on liquefaction-induced ground displacements, its related damage to structures and geological and soil conditions was collected and analyzed by the Japan-U.S. cooperated research work[1)2)]. The purpose of this paper is to investigate the following two topics from the collected data on four Japanese earthquakes.

(1) The mechanism of the occurrence of liquefaction-induced ground displacements.
(2) Influences of liquefaction-induced ground displacements on underground structures.

GROUND DISPLACEMENTS, AND GEOLOGICAL AND SOIL CONDITIONS

In order to show the relationship between the occurrence of the liquefaction-induced ground displacements and the geological and soil conditions, the case histories at Ohgata area in Niigata city during 1964 Niigata earthquake and at Morita area in Fukui city during 1948 Fukui earthquake were summarized as follows:

Ohgata Area during the 1964 Niigata earthquake

The vectors in Figures 1 show the horizontal ground displacements and the numerals in the

parentheses are the vertical displacements at Ohgata area, which were caused by the 1964 Niigata earthquake. The shadowed area of Figure 1 represents the natural levee, and the other area the old river bed. Figure 1 also shows the locations of the ground failure such as sand boils and ground fissures. Figure 2 shows the vectors of the horizontal ground displacements at measurement points.

The ground mostly moved in a radial direction from the Ohgata Primary School which was located on the top of the natural levee. Displacements to the north-west direction that began in the vicinity of the primary school, were particularly dominant. The length of the fissure was measured as 300 m long, and the fissure was terminated in the vicinity of the Tsusen River. The maximum displacement in this area reached over 8 m. The displacements suddenly decreased on the south bank of Tsusen River and ceased on the north bank of the river. As shown in Figure 1, the ground displacements occurred from the natural levee with a higher elevation toward the Tsusen River with a lower elevation. These ground displacements from a higher ground to a lower one are much clearly seen in Figure 2.

In the vicinity of the primary school, where the ground displacements originated, numerous ground fissures were caused due to the tensile strain in the ground. On the contrary, in the area of the Tsusen River, where the ground displacements terminated, a large number of sand and water boils were observed. Photo 1 shows one example of the ground fissures in the ground, the width of which was 2 to 3 m.

According to the result of measurements of vertical displacements, the primary school and its neighborhood, where the ground displacements initiated, largely subsided with a maximum drop of about 2.0 m. On the other hand, in the area of the Tsusen River where the ground displacements terminated, the ground surface rose up at many measuring points.

Figure 3 shows the soil condition along section A-A' in Figure 1. The estimated liquefied soil[3)]with a thickness of about 5 m was distributed from the Ohgata Primary School to the Tsusen River, but its thickness was abruptly decreased on the south bank of the river. No liquefiable layer was detected on the north bank of the river. The boundary between the estimated liquefied layer and non-liquefied layer above it inclines toward the Tsusen River with a gradient of about 1%. The ground surface also inclines toward the river with a gradient of about 0.5%.

Morita Area during the 1948 Fukui earthquake

Figure 4 shows the horizontal ground displacements measured at Morita area, which was caused by the 1948 Fukui earthquake. The shadowed area represents the natural levee, and the other area is the old river bed of the Kuzuryu River. Figure 4 also shows the locations of the ground failure. The ground displacements started from the natural levee and ended at the Yoshino River which had been one of the old river bed of the Kuzuryu River. The ground displacements toward the Yoshino River are dominant and much larger than those toward the Kuzuryu River. The maximum ground displacement in this area was greater than 4 m. On the upper part of the natural levee, where the ground displacements began, many ground fissures appeared. On the other hand, in the vicinity of the Yoshino River, where the ground

displacements terminated, a large number of sand boils were observed as seen on the photograph.

The ground displacements in the vertical direction are not available in the case of the Fukui earthquake because of the poor accuracy of the measurements. However, according to the witnesses and the existing damage reports[4], the natural levee and its surrounding area subsided with a magnitude of 1 to 2 m, but the bed of the Yoshino River rose up. The river was greatly reduced in width and partially filled. The river was re-excavated after the earthquake.

Figure 5 and 6 show the correlation of thickness of the liquefied layer and the gradient of the ground surface with the magnitude of permanent ground displacements in the horizontal direction. A comparatively good correlation can be found between the magnitude of the ground displacements and the thickness of the liquefied layer as shown in Figure 5. However, no correlation can be found between the magnitude of ground displacements and the gradient of the ground surface, as shown in Figure 6. The horizontal distances over which the gradients were estimated varied from 5 times to 30 times the thickness of the liquefied layer in Figures 6(a) and 6(b), but the correlation could not be improved.

The above result appears to contradict with the fact that the ground was displaced from the higher ground toward the lower ground. However, this contradiction can be solved if it is assumed that the ground displacements were caused by fluid behavior of the liquefied soil. The gradient of the liquid surface has little influence on the magnitude of the liquid, but does affect its velocity.

Similar results were obtained from the case studies of the 1923 Kanto and the 1983 Nihonkai-Chubu earthquakes. During the Kanto earthquake, it is observed that the ground moved from a natural levee of a higher elevation toward the Furu-Tone River in a lower elevation. Furthermore, a large displacement of more than 5 m was observed from the top of a sand dune toward the downward in Noshiro City during the Nihonkai-Chubu earthquake.

From the case studies on Japanese four earthquakes, the following conclusions can be drawn about the relationship of the occurrence of the ground displacements, the ground failures caused by the occurrence and their geological and soil conditions.
(1)The ground displacements occurred from the natural levee or sand dune with a higher elevation toward the old river bed or low lands between dunes with lower elevation.
(2)In the areas with a higher elevation, where the ground displacements began, the numerous ground fissures were caused due to the tensile strain in the ground, and the ground surface largely subsided. In the areas with a lower elevation, where the ground displacements terminated, a large number of sand and water boils were observed, and the ground surface rose up. This fact suggests that the ground displacements were caused by a voluminal transfer of the liquefied soil.
(3)The magnitude of ground displacements has a comparatively close correlation with thickness of liquefied layer, but no correlation can be found with the gradient of the ground surface.

EFFECTS OF THE GROUND DISPLACEMENTS ON UNDERGROUND STRUCTURES

In order to investigate the effects of the ground displacements on the underground structures, two examples of damage to foundation piles during the 1964 Niigata earthquake and one example of the damage to a sewage pipe during the 1983 Nihonkai-Chubu earthquake are examined.

Damage to Foundation Piles during the Niigata Earthquake

Figures 7(a) and (b) show damages to foundation piles with soil conditions at the Court House and the old NHK Building, respectively, and Photo 2 shows the broken piles of the two buildings. The Court House was a four-story reinforced concrete building. It was constructed on the concrete pile foundations, each with a diameter of 35 cm and a length of 6 to 9 m. After the earthquake, the building inclined due to differential settlement of ground, and it was conjectured that the foundation piles were damaged. However, after minor repairs, made to the inclined floors, the building could be used for 25 years. When the building was reconstructed, foundation piles were excavated. The ground in the vicinity of Court House consists of a loose sandy layer with the N-values of less than 10 down to -8.0 m. It can be assumed that the liquefied sandy layer is below the ground water level of -1.7 m and above - 8.0 m during the earthquake.

The damaged piles in the Court House were observed at two locations. It is noteworthy that the two locations roughly coincide with the boundaries between the estimated liquefied layer and non-liquefied layers. At the lower location, there were several horizontal cracks caused by large bending moments as shown in Photo 2(b). While at the upper location the concrete was crushed and the steel bars were severely bent as shown in Photo 2(a). At the upper damaged location, there was a slight shear displacement of the lower part of the pile relative to the upper part. This suggests that the lower liquefied ground layer moved more than the upper non-liquefied ground. It appears, that slippage occurred between liquefied soil and non-liquefied soil beneath the building.

The old NHK Building was a four-story reinforced concrete building with reinforced concrete pile foundations with a diameter of 35 cm and a length of 11 to 12 m. When the foundations of the building were excavated for reconstruction, about 20 years after the earthquake, the piles were found to be completely fractured as shown in Figure 7(b). The breakage was also discovered at two locations, 2.5 to 3.5 m from the upper end of the pile and 2.0 to 3.0 m from the bottom. As shown in Figure 7(b), the piles were fractured in a similar way to those of the Court House shown in Figure 7(a) and Photo 2(a) and 2(b). The subsurface soils at the old NHK Building site consist of a loose sandy layer with N-value of 5 to 10 down to -10.0 m, as shown in Figure 7(b). The loose sandy layer is thought to have been liquefied during the earthquake.

The followings can be pointed out about the characteristics of the damage to foundation piles from the above-mentioned two examples.

(1)The breakages were located at two locations. The upper breakage was located at the

boundary between estimated liquefied layer and non-liquefied layer above it. The lower breakage was located around the lower boundary of the estimated liquefied layer. The occurrence of the breakage at the lower location suggests that the displacement on the ground surface was not caused by a slippage between the liquefied layer and upper non-liquefied layer, but by the movement of whole mass of the liquefied soil.
(2)The direction of the bending moment at the upper location is opposite to that at the lower location.

Damage to the Sewage Pipe during the Nihonkai-Chubu Earthquake

Figure 8 shows the horizontal displacements on the ground surface and the movement of asbestine cement sewage pipe with a diameter of 30 cm in Noshiro City at the time of the Nihonkai-chubu earthquake. The ground displacements were measured by using pre- and post-earthquake aerial photographs. The movement of the sewage pipe was measured as the relative displacement between the pipe axis after the earthquake and the line between two neighboring manholes. The sewage pipe was buried on the straight line before the earthquake. The maximum relative displacement of the pipe was more than 160 cm, but the maximum displacement of the ground surface was about 80 cm.

Figure 9 shows the movement in cross section A-A' in comparison with the displacement of the ground surface. The total displacement of the pipe is estimated to be 255 cm, and this value obtained by adding the relative displacement between the manholes and the pipe, 160 cm, to the mean displacement of the manholes, 95 cm. Figure 9 also shows the soil profile with N-values at a site about 50 m north of the sewage pipe. The subsurface consists of sandy fill and the sand dune. The surface of the ground water is located at -1.7 m below the ground surface, and the soil layer between -1.7 m and around 4.2 m can be regarded as liquefied during the earthquake. The sewage pipe was located in this liquefiable layer. The above-mentioned result suggests that the liquefied layer was displaced more than the upper non-liquefied layer.

AN EXAMPLE OF A NON-DAMAGED STRUCTURE IN A LIQUEFIED AREA

Figure 10 shows the ground displacements in the vicinity of the Hokuriku-Building which was not damaged even though it was located in the area where the large permanent ground displacements occurred. This building has ten stories and is adjacent to the old NHK Building, the concrete foundation piles of which were severely damaged as mentioned previously. The Hokuriku-Building also founded on reinforced concrete piles with a diameter of 40 cm and a length of 12 m, but no damage was reported to the superstructure after the earthquake.

The following characteristics of the foundation, shown in Figure 11, may be considered as probable reasons why the building suffered no damage.
(1)The building has a one-story basement, which goes 6 to 7 m below the ground surface as shown in Figure 11.
(2)The foundation piles were driven from the basement floor level into the non-liquefied layer at a depth of about 12 m. The arrangement of foundation piles is shown in Figure 11. The

total number of foundation piles of the ten-story Hokuriku-Building was more than that in the four-story the old NHK Building. It is conjectured that a large number of piles had a great effect on densification of the soil as well as the prevention of ground displacements in the horizontal direction.
(3)For the excavation of the basement, in-ground walls were constructed using steel sheet piles and cast-in-place concrete piles which were driven in a continuous line at the perimeter of the excavation. It is reported that, after completion of the building, the in-ground walls made of steel sheet piles were removed, but the cast-in-place concrete piles remained.

As shown in Figure 10, the following characteristics can be pointed out. To the north of the building, the ground moved in a south direction mainly toward the building, but the displacements were much smaller at the south of the building, than the at its rear side. Moreover, along the north side of the building, the ground surface rose up 0.6 to 1.0 m, while in the area away from the building, it was mostly subsided. No decisive conclusion can be drawn because there is a lack of measuring points for the ground displacement behind the building, but it maybe conjectured that the existence of the basement and the in-ground walls as well as the large number of foundation piles, obstructed the flow of liquefied soil.

CONCLUSIONS

From the case studies of four Japanese earthquakes, the following instructive information was obtained in order to clarify the mechanism of the occurrence of liquefaction-induced ground displacements and their effect on underground structures.
(1)The ground displacements started from the natural levees or the sand dunes with a higher elevation and ended in old river beds with a lower elevation. In the area where the ground displacement started, numerous ground fissures were observed and the ground surface was largely subsided. On the other hand, in the area where the ground displacements terminated, a large number of sand and water boils was seen and the ground surface rose up.
(2)The magnitude of the ground displacements in the horizontal direction had a comparatively good correlation with the thickness of the estimated liquefied layer, but no clear correlation exist with the gradient of the ground surface. A comparatively good correlation between the magnitude of the ground displacements and the thickness of the liquefied layer was found. This obscure of correlation appears to contradict the fact that the ground moved from higher to lower elevations, as mentioned in (1). This contradiction can be solved if it is assumed that the ground displacements were caused by the fluid behavior of the liquefied soil. The gradient of the liquid surface has little influence on the magnitude of the movement of the liquid, but does affect its velocity.
(3)The reinforced concrete piles were severely broken at two locations. These locations roughly coincide with the boundaries between the estimated liquefied layer and non-liquefied layer. This suggests that the displacement on the ground surface was not caused by a slippage between the liquefied layer and the upper non-liquefied layer, but by the movement of whole mass of the liquefied soil.
(4)The sewage pipes which were laid in the liquefied layer were moved more than that located the non-liquefied layer above it. This suggests that the liquefied layer moved much more than

the upper non-liquefied layer.
(5)No damage was reported at the Hokuriku-Building, while the neighboring the old NHK Building suffered sever damage to its foundation piles. The Hokuriku-Building has one story basement together with a large number of foundation piles and temporary in-ground walls for excavation of the basement.

From the present investigation, it is concluded that the ground displacements were caused as a result of flow-type of behavior of the liquefied ground, and the effects of the ground displacements on underground structures such as foundation piles and buried pipes could be represented by a drag force from the liquefied soil.

REFERENCES

(1)Hamada, M., and O'Rourke, T.D., "Case Studies of Liquefaction and Lifeline Performance During Past Earthquakes," Volume 1, Japanese Case Studies, Tech. Rept. NCEER-92-0001, Nat. Center for Earthquake Engineering Research, Buffalo, N.Y.

(2)O'Rourke, T.D., and Hamada, M., "Case Studies of Liquefaction and Lifeline Performance During Past Earthquakes," Volume 2, U.S Case Studies, Tech. Rept. NCEER-92-0002, Nat. Center for Earthquake Engineering Research, Buffalo, N.Y.

(3)Iwasaki, T., Tatsuoka, F., Tokida, K., and Yasuda, S., "A Practical Method for Assessing Soil Liquefaction Potential Based on Case Studies at Various Sites in Japan," Proceedings, Fifth Japan Earthquake Symposium, Tokyo, Japan, 1978.

(4)Fukui Prefectural Government, "Report on the 1948 Fukui Earthquake," Fukui, Japan.

(5)Yoshimi, Y., "Liquefaction of Sandy Ground, Second Version," Gihodo, Tokyo, Japan, 1990.

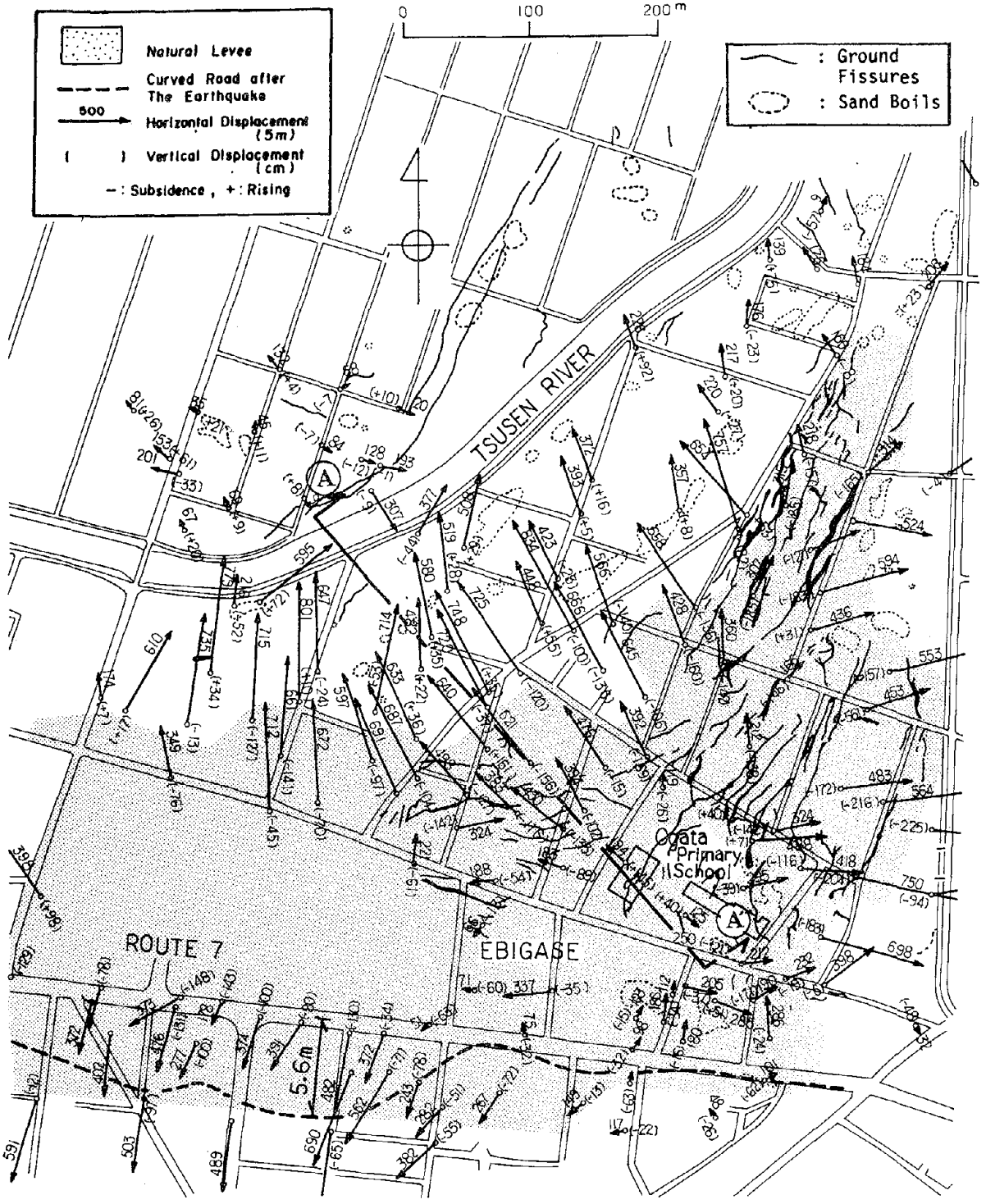

Figure 1. Permanent Ground Displacements and Ground Failures in the Vicinity of the Ohgata Primary School during the 1964 Niigata earthquake

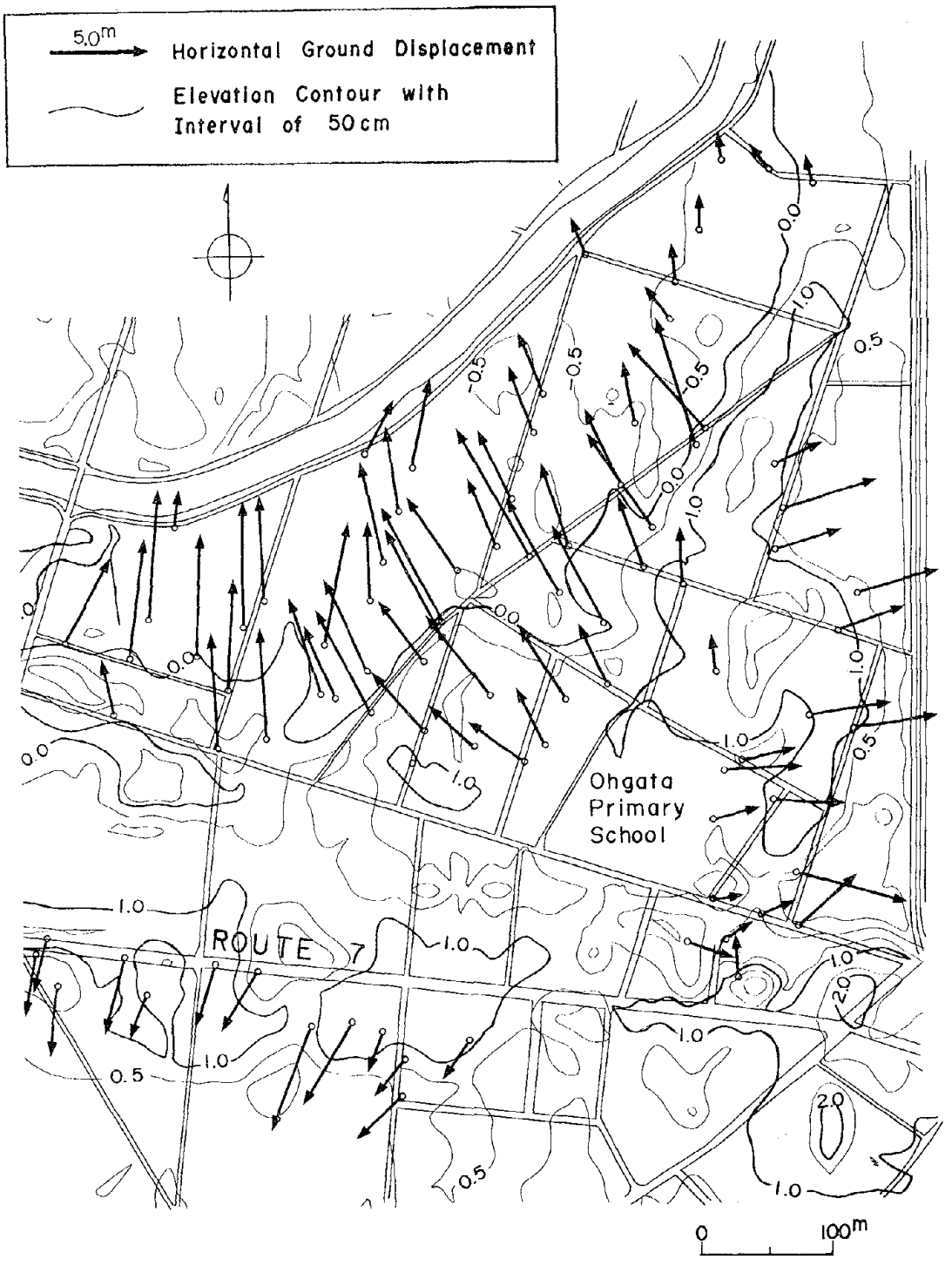

Figure 2. Permanent Ground Displacement in the Horizontal Direction on a Contour Map (Numbers on the contours denote elevations above the mean sea level, Unit:m)

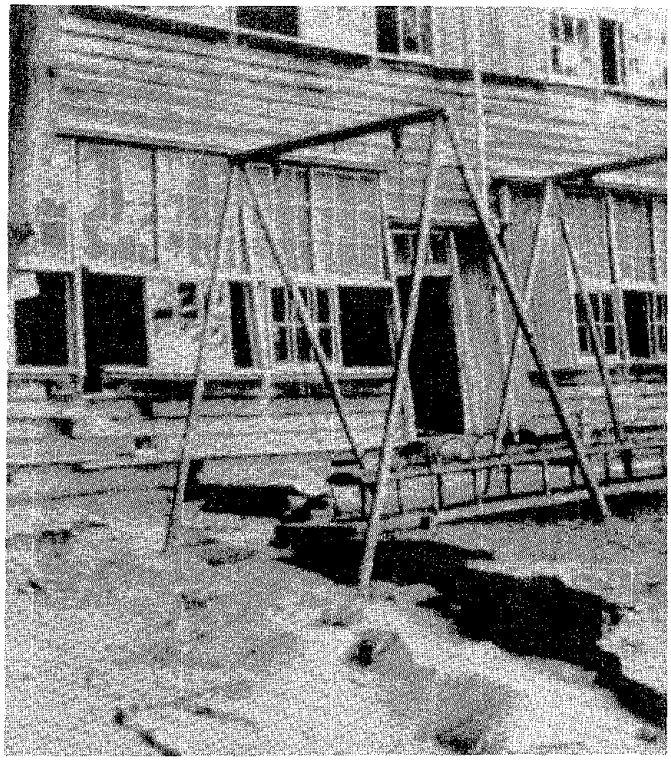

Photo 1. A Ground Fissure underneath a Wooden School Building

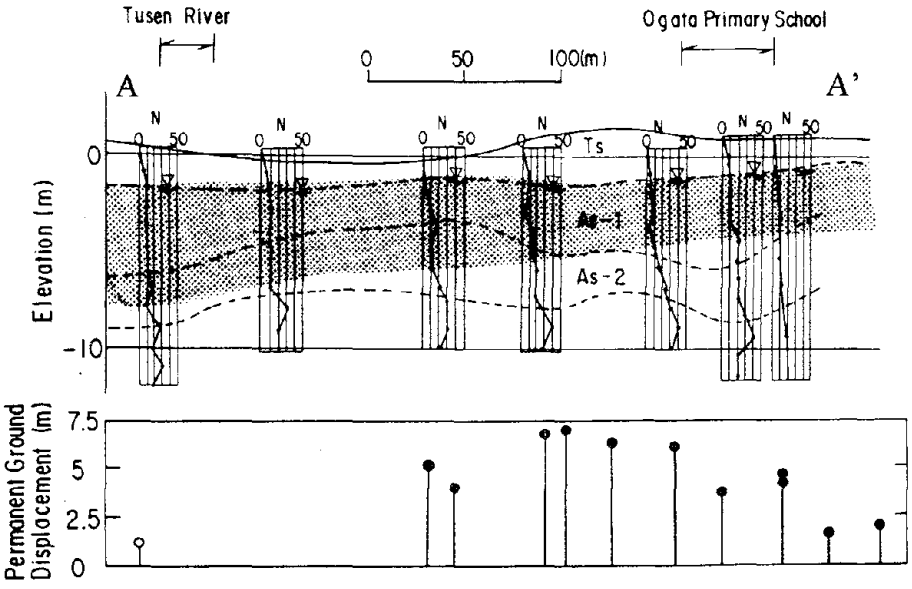

Section A-A'

Figure 3. Soil Condition and Estimated Liquefied Layer

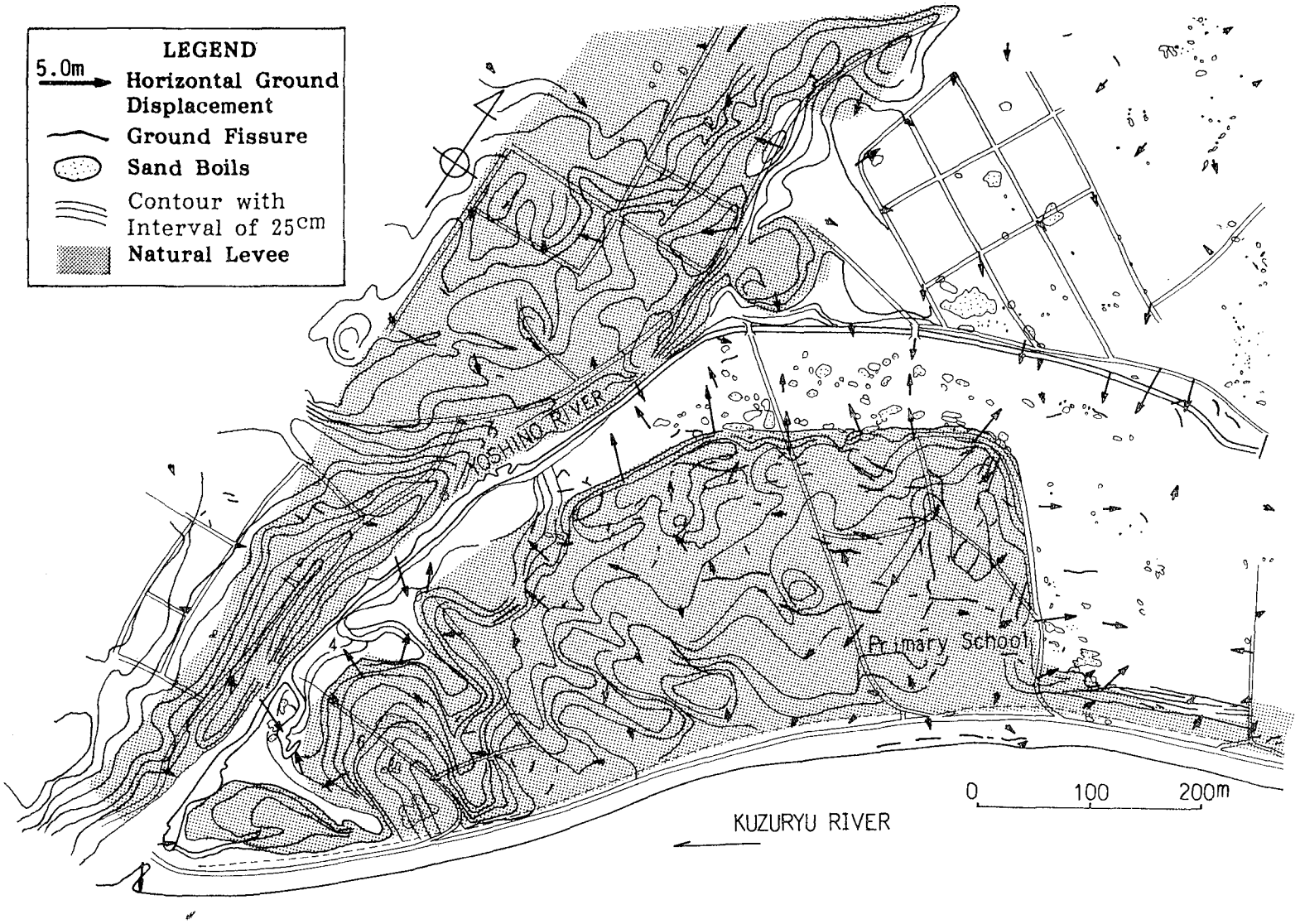

Figure 4. Permanent Ground Displacements and Ground Failures in Morita area during the 1948 Fukui earthquake

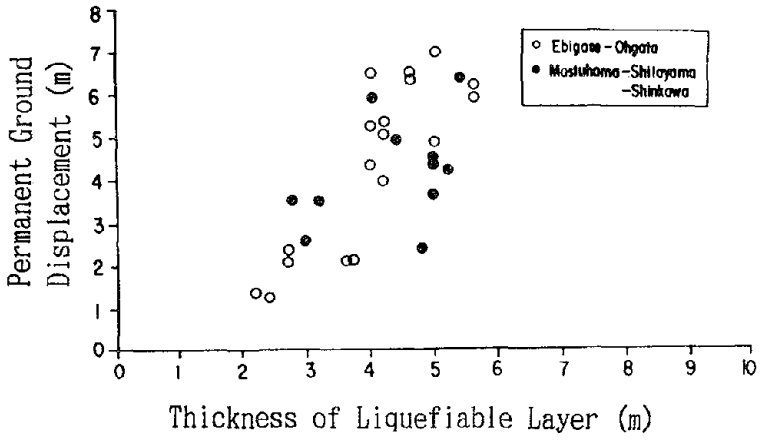

Figure 5. Correlation between Magnitude of Ground Displacement and Thickness of Estimated Liquefied Layer

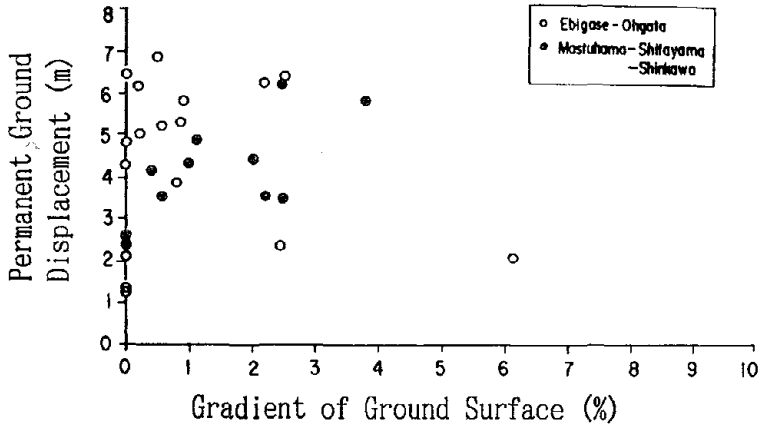

(a)Horizontal distance is 5 times thickness of estimated liquefied layer

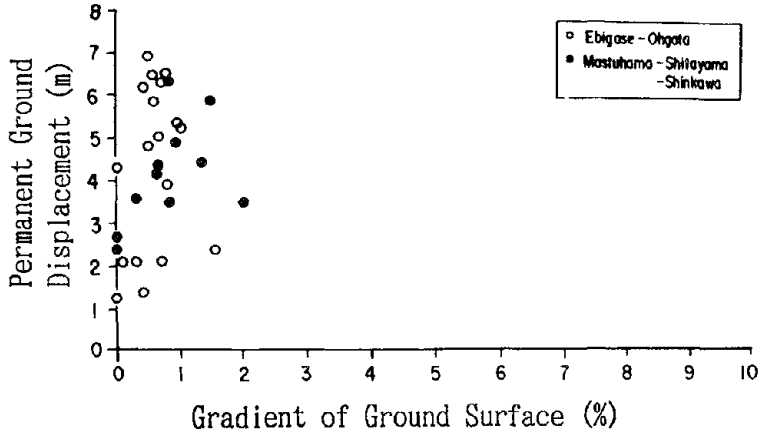

(b)Horizontal distance is 30 times thickness of estimated liquefied layer

Figure 6. Correlation Between Magnitude of Ground Displacement and Gradient of Ground Surface

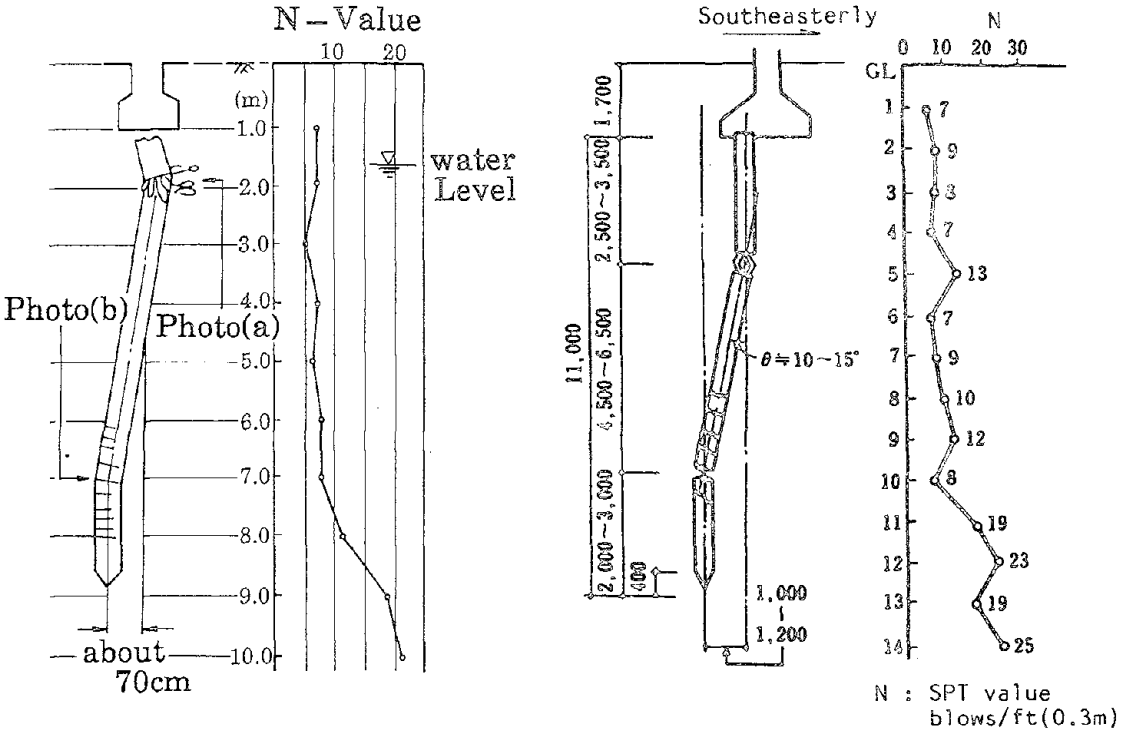

(a)Court House (b)NHK Building

Figure 7. Damage to Foundation Piles and N-values of the Ground

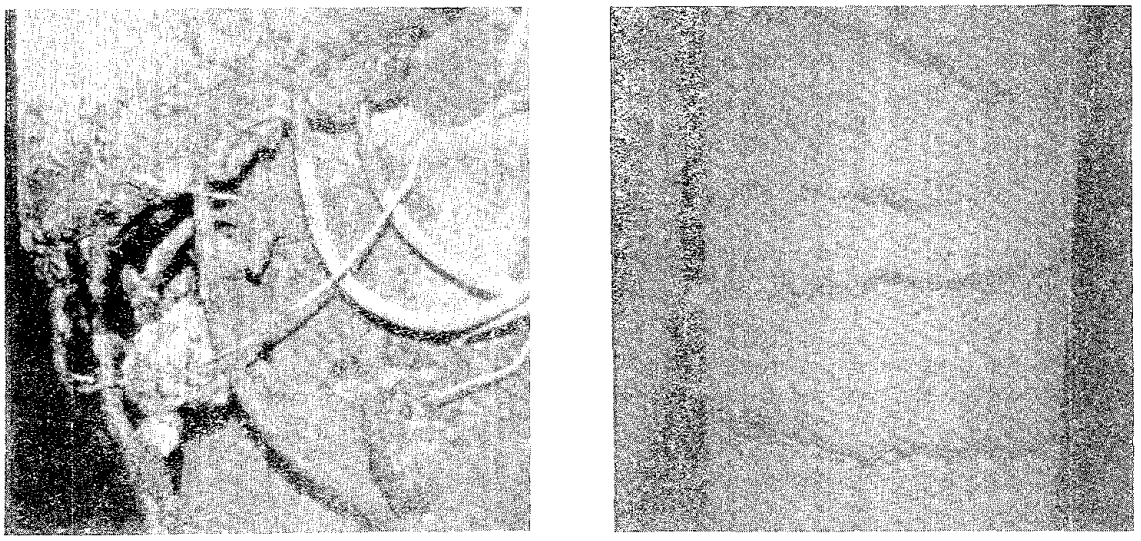

(a)Upper Part of Pile of Court House (b)Lower Part of Pile of Court House (Bending Cracks)

Photo 2. Damage to the Foundation Piles

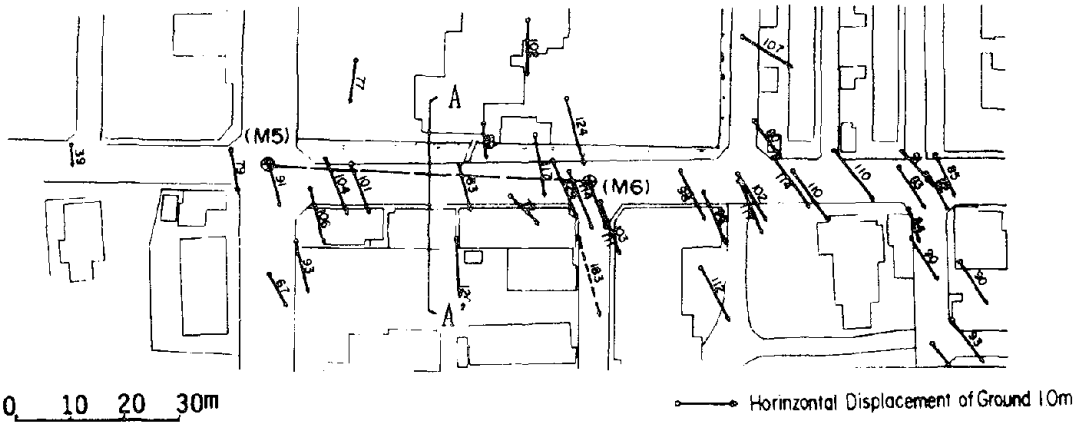

(a)Ground Displacements

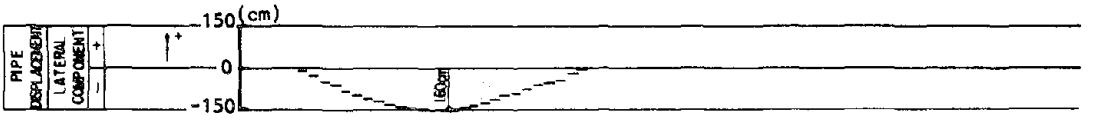

(b)Movement of Sewage Pipe

Figure 8. Movement of Sewage Pipe and Ground Displacement

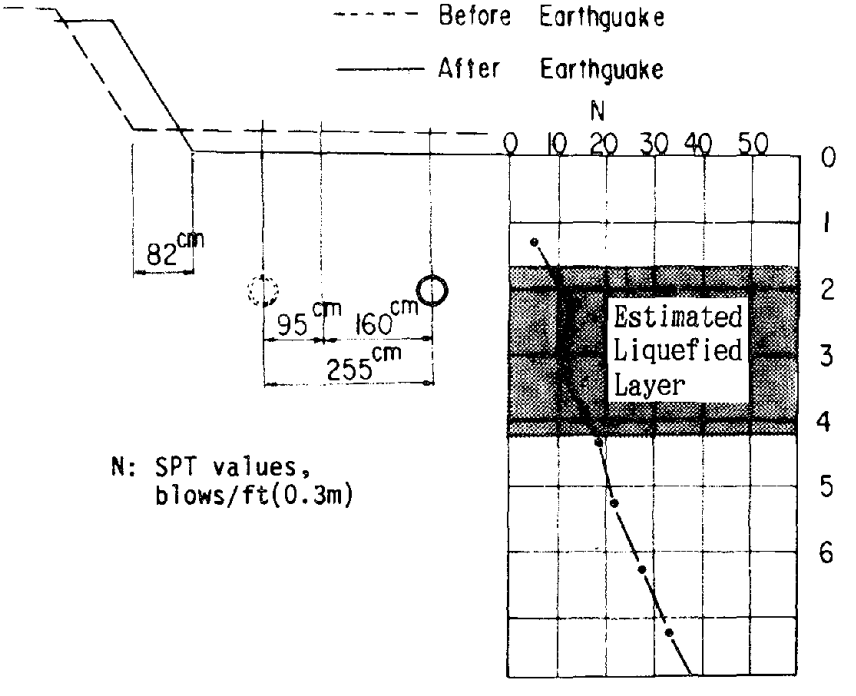

Figure 9. Movement of Sewage Pipe and Ground Displacements in Cross-Section A-A'

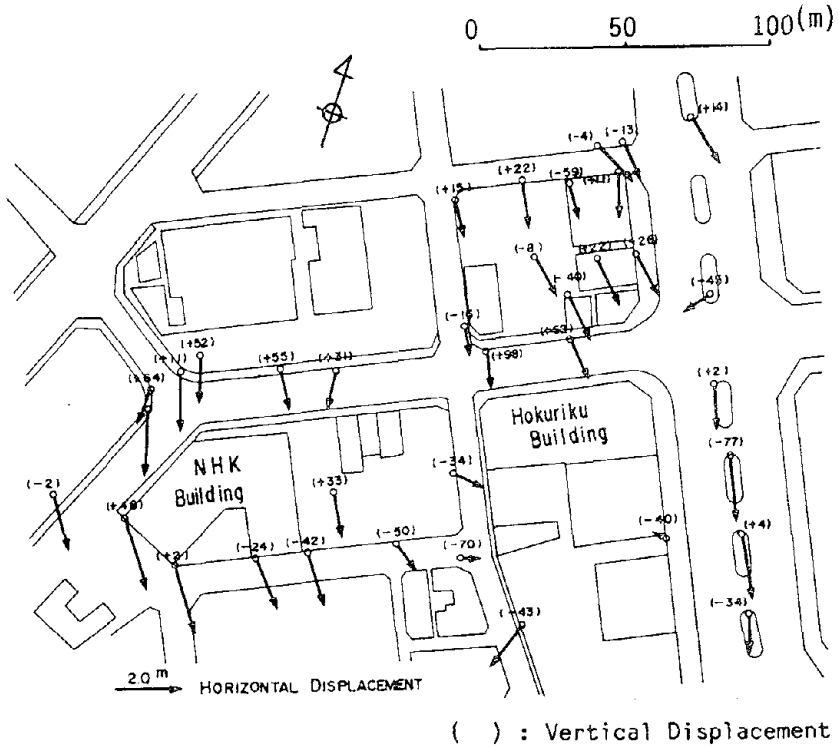

Figure 10. Permanent Ground Displacement in the Horizontal Direction in the Vicinity of the Hokuriku-Building

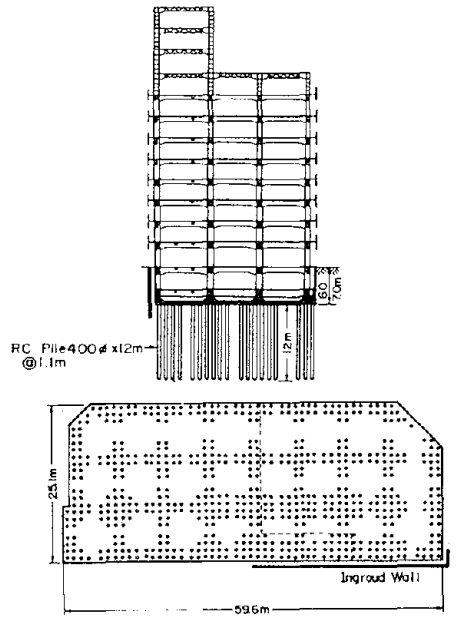

Figure 11. Outline of the Hokuriku-Building and Arrangement of Foundation Piles (Y.Yoshimi)[5]

Recent Lessons Regarding Seismic Response Analysis of Soft and Deep Clay Sites

by

R. B. Seed, S. E. Dickenson and C. M. Mok

Department of Civil Engineering
University of California at Berkeley

ABSTRACT

The strong motion data obtained during the 1989 Loma Prieta Earthquake provides an unprecedented opportunity for study of the seismic response of "soft" and deep clay sites. The first phase of the studies described herein investigated the ability of contemporary response analysis techniques using both "equivalent linear" and fully nonlinear modelling to accurately predict observed response of soft clay sites at the moderate levels of shaking experienced during the Loma Prieta event. The "predictive" capability of both types of analysis was found to be very good, but only when coupled with thorough characterization of soil behavior and parameter evaluation, and suitable consideration of nonlinearity and potential soil "failure". As a second phase of these studies, additional analyses were performed at higher (and more typical "design") levels of shaking, and some of the important findings are noted. The results of these studies indicate a potential need to reconsider the fundamental basis and principles of current practice in this field, as well as an obvious need to re-assess widely-used current seismic building codes.

INTRODUCTION

Due to the absence of strong motion records obtained at "soft" and deep cohesive sites during large, near-field earthquakes, much of current design for such sites is based on theoretical response analyses. Strong motion records obtained at ten "soft" and/or "deep" cohesive soil sites throughout the San Francisco Bay Region during the 1989 Loma Prieta Earthquake provide a unique opportunity to test the accuracy and reliability of current seismic site response analysis techniques using field response data for moderate levels of seismic shaking ($a_{max} \approx 0.15g$ - $0.35g$). Coupled with previous studies using response data from prior seismic events (e.g., the 1985 Mexico City Earthquake) in which response recordings for smaller levels of shaking were obtained, these studies provide a basis for: (a) evaluation of the accuracy and reliability of response analysis methods at low and moderate levels of shaking, and (b) calibration of analytical methods as well as soil behavior models and related modelling parameters. These calibrated analytical methods and soil property models then provide the best currently available basis for prediction of likely response of soft and deep cohesive sites to stronger levels of shaking (levels more typically used for "design" in regions of significant seismicity.)

The first phase of these studies consisted of collection and processing of data regarding seismic soil properties for the principal geologic materials affecting the seismic response characteristics of ten strong motion recording stations situated on soft and/or deep cohesive sites in the San Francisco Bayshore region whose recordings from the 1989 Loma Prieta Earthquake were used as a basis for evaluation and calibration of modelling and analysis techniques. Response analyses for the ten strong motion recording sites were then performed using both (a) simplified "equivalent linear" and (b) fully nonlinear (time domain) response analysis methods, and the results were compared with the strong motion recordings obtained at these sites. A number of interesting lessons resulted, and the most important of these will be briefly discussed.

The final phase of these studies involved using the lessons learned, as well as the now calibrated soil models and analytical methods, to perform similar response analyses for soft and deep cohesive sites subjected to stronger levels of shaking ($a_{max} \approx 0.3$ to $0.6g$) more typical of "design" conditions in seismically active regions. The results suggest a need to reconsider much of current practice in this field, as well as an obvious need to re-assess current seismic codes and their treatment of response of "soft" cohesive sites.

SEISMIC RESPONSE ANALYSES: LOMA PRIETA MOTIONS

Requisite input for the analyses of seismic soil response described herein include suitable input ("bedrock") strong motion records (acceleration time histories), and representative dynamic properties for soils at the site. In addition to unit weight, which can be readily estimated, the two principal dynamic soil properties of interest in response analyses are: (a) some measure of stiffness (e.g., the dynamic shear modulus; G), and (b) some measure of dynamic material damping (e.g. damping ratio-%). The shear wave

velocity (V_s) and the "small strain" ($\gamma \leq 1.0 \times 10^{-4}\%$) dynamic shear modulus are related as: $G_{max} = V_s^2 \gamma_t / g$, where G_{max} is the small strain dynamic shear modulus, V_s the shear wave velocity, γ_t the total unit weight of the soil, and g is the acceleration of gravity.

Regional correlation studies of in-situ seismic wave velocities with other index tests or engineering properties of the soils have been shown to be useful for estimating shear wave velocity (V_s) profiles at sites lacking geophysical data. As an initial portion of these current studies, a data base was established for the evaluation and modelling of shear wave velocities of soft soil units in the San Francisco Bay area. Data involving in-situ V_s measurements for more than 50 sites in the Bay region was collected from the geotechnical literature, state and federal agencies, local geotechnical consulting firms, and practicing geotechnical consultants and geophysicists, and was used as a basis for developing correlations between V_s and other geotechnical index properties (Dickenson & Seed, 1992). As an example, the relationship between the (static) undrained shear strength (S_u corresponding to that obtained in a TXCU test) and shear wave velocity for Bay Mud (a silty clay Holocene alluvium that represents the predominant "soft" clay deposit in the San Francisco Bay basin) is shown in Figure 1. The undrained (static; not seismic) shear strength of normally consolidated Bay Mud is readily estimated using $Su/p' \approx 0.32$. Similar relationships were developed for the stiffer, overconsolidated "Older Bay Clays" underlying the young Bay Mud deposits. (The total depths can be up to 800 feet in the deepest portions of the bay basin.) V_s values in sandy units were estimated using correlations with SPT data proposed by Seed et al. (1984). Response analyses performed to date for the strong motion recording sites situated on soft soil deposits around the edges of San Francisco Bay provide excellent agreement with strong motion recordings from the Loma Prieta earthquake, and suggest that these simple,empirical correlations and relationships provide a reliable basis for evaluation and modelling of dynamic soil properties for many engineering applications.

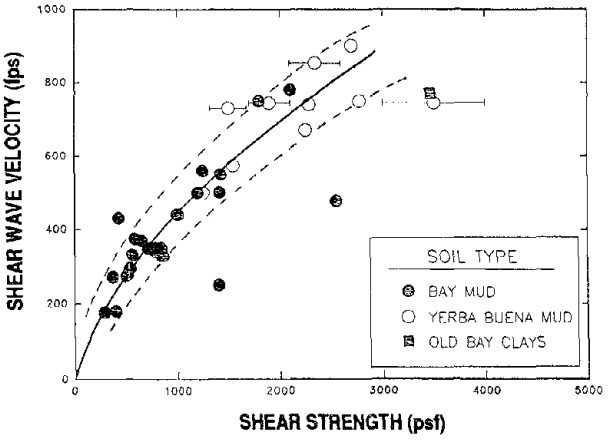

Figure 1: V_s vs. Undrained Shear Strength for Cohesive Deposits in the San Francisco Bay

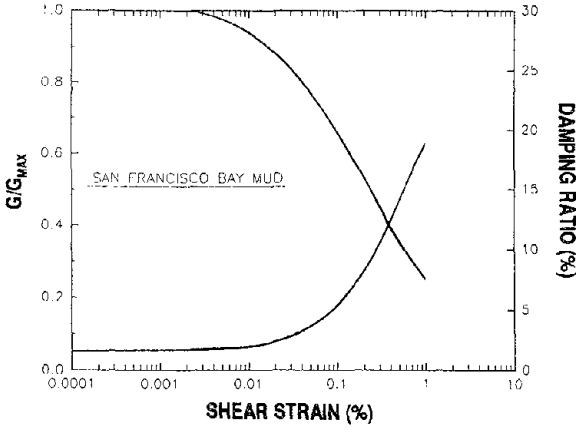

Figure 2: Variation of Dynamic Shear Modulus and Damping Ratio vs. Shear Strain for San Francisco Bay Mud

The first set of dynamic ground response analyses performed in the first phase of this study were performed using the program SHAKE90, a one-dimensional dynamic site response analysis based on vertical propagation of shear waves. The program SHAKE90 is a slightly modified version of the well-known program SHAKE (Schnabel, et al., 1972), and uses the equivalent linear method to model nonlinear dynamic soil moduli and damping as a function of shear strain. Nonlinear dynamic properties of Bay Mud were modelled with the modulus reduction and damping curves shown in Figure 2. Nonlinear, strain-dependent moduli and damping for deeper, stiffer, overconsolidated, Older Bay Clays were modelled using the Plasticity Index - dependent (and shear strain-dependent) modulus degradation and damping curves proposed by Vucetic and Dobry (1991), and nonlinear dynamic moduli and damping (again as a function of shear strain) for cohesionless soils were modelled using the relationships proposed by Seed, et al. (1984).

Additional ground response analyses were next performed with a slightly modified version of the fully nonlinear code DESRA-2 (Lee & Finn, 1978). The modified program, currently called MAR-DESRA, incorporates the Martin-Davidenkov model for nonlinear soil behavior, allowing for a slightly more accurate representation of the fully nonlinear (strain-dependent) dynamic moduli and damping than is possible with the originally coded hyperbolic stress-strain relationship.

One of the principal aims of the current study was to perform both simplified equivalent linear and fully nonlinear ground response studies for the soft soil sites affected by the Loma Prieta earthquake to assess the strengths and limitations of these two widely-used response analysis methods. The specification of input for the dynamic analyses was very simple and straightforward, and involved only; (1) generation of the V_s profile using the correlations described previously, and (2) incorporation of the strain-dependent shear modulus and damping curves described previously.

The only additional parameters subject to modification were: (a) input motions ("rock" motions), and (b) the level of "effective" strain (n) used as a basis for modelling strain-dependent moduli and damping in the simplified equivalent linear analyses. The equivalent linear method incorporated in SHAKE90 approximates nonlinear soil behavior with an iterative method that uses a linear wave propagation formulation with soil properties that are compatible with representative or "effective" shear strain levels within each of the soil sublayers comprising the soil column. At each iteration, n% of the peak strains computed at the mid-point of each soil sub-layer from the previous iteration are used to obtain new values of strain-dependent modulus and damping ratio. The program iterates until the modelled strain-dependant soil properties are compatible with the strain levels associated with the calculated response of the system. The commonly used value of $n = 0.65$ (or 65%) is generally too high for most such analyses. Selection of better values of n is too complex an issue to describe within the length restrictions of this paper, but it may be noted that significant improvement over the widely-used value of $n=0.65$ can generally be achieved using $n \approx 0.30$ to 0.55 for $M_s = 6$ to 7 events, and $n \approx 0.50$ to 0.65 for $M_s = 7$ to 8 events. All analyses of Loma Prieta recordings described herein were performed using $n = 0.40$, and

the analyses of stronger levels of shaking performed in the later phases of these studies (for M = 7½ and larger events) were performed using n = 0.65.

A total of ten soft/deep cohesive strong motion recording sites have been analyzed using both the equivalent linear and fully nonlinear methods. Figure 3 shows the locations of these ten "clay" sites (solid "dots"), as well as the locations of "rock" or "near rock" sites whose strong motion recordings provided "input" motions for the various response analyses performed. (The northernmost end of the Loma Prieta Earthquake fault rupture segment [M_s = 7.1] occurred approximately 40 km to the south of the bottom edge of Figure 3.) Owing to length constraints on this paper, the results of response analyses for only four sites will be discussed herein. These four sites span essentially the full range of "soft clay" site conditions present among the ten soft clay recording sites, having (a) "soft" clay (San Francisco Bay Mud) thicknesses ranging from about 25 feet to 90 feet, and (b) ranging from the northernmost to southernmost sites, on both the east and west sides of the bay, and including the centrally located Treasure Island site.

All strong motion records used in these studies have been processed to develop horizontal acceleration time histories in two orthogonal directions: (a) in the "radial" direction of propagation from the fault rupture zone, and (b) in the orthogonal "transverse" direction. All "input" motions were scaled to the average regional peak horizontal ground surface acceleration on "rock" based on their distance from the fault rupture (using separate attenuation plots for "radial" and "transverse" strong motions.)

TREASURE ISLAND

An excellent example of the influence of local soil conditions on ground shaking characteristics is provided by the sets of strong motion recordings obtained at two stations: (1) on Yerba Buena Island, and (2) on Treasure Island approximately 2 km to the north. Both islands are located at the center of the San Francisco Bay, approximately 70 to 75 km northwest of the 1989 Loma Prieta Earthquake fault rupture surface, and the strong motions recorded at these two stations differ significantly as a result of different foundation conditions. Yerba Buena Island is a large, rocky outcrop near the center of the bay, and anchors the center of the San Francisco Bay Bridge. Treasure Island is a man-made island comprised primarily of loose, dredged hydraulic fill underlain by soft to medium stiff Bay Mud and other dense and stiffer (and much older) natural bay sediments. The strong motion recordings at the Treasure Island and Yerba Buena Island stations thus represent a pair of recordings at nearly the same location (and distance from the fault rupture), but for a "rock" and a "deep, soft soil" site.

Figure 4(a) presents a schematic illustration of the soil column underlying the Treasure Island recording station. Included in this figure are the measured shear wave velocity profile, and the "estimated" V_s profile (based on the correlation studies discussed previously). As shown in this figure (as well as in Figure 4(c)), agreement between "estimated" and measured V_s values was generally very good. All response analyses

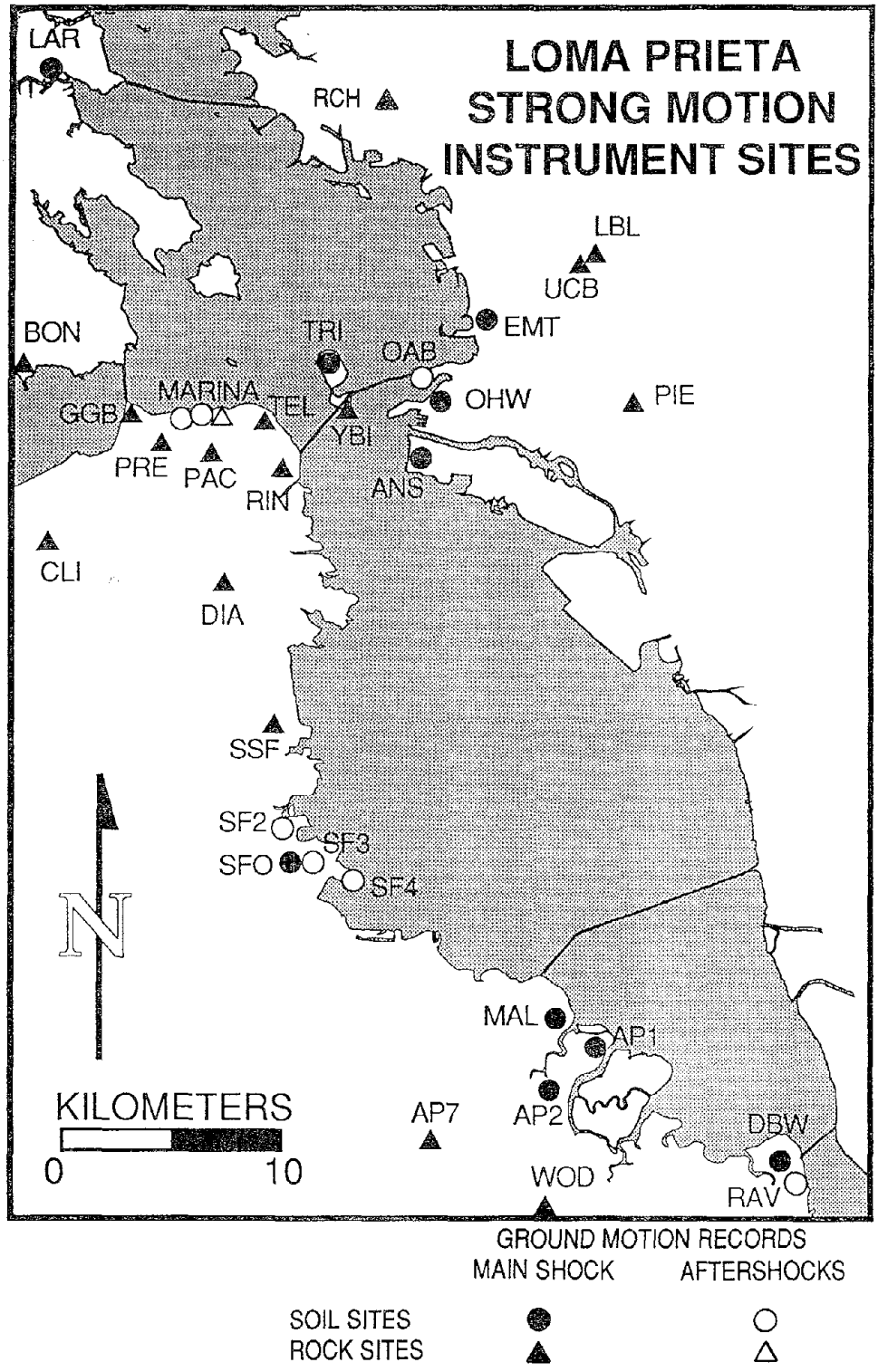

Figure 3: Map of the Central San Francisco Bay Region Showing Locations of Soft/Deep Clay Sites Studied and Locations of Strong Motion Recordings Used in These Studies

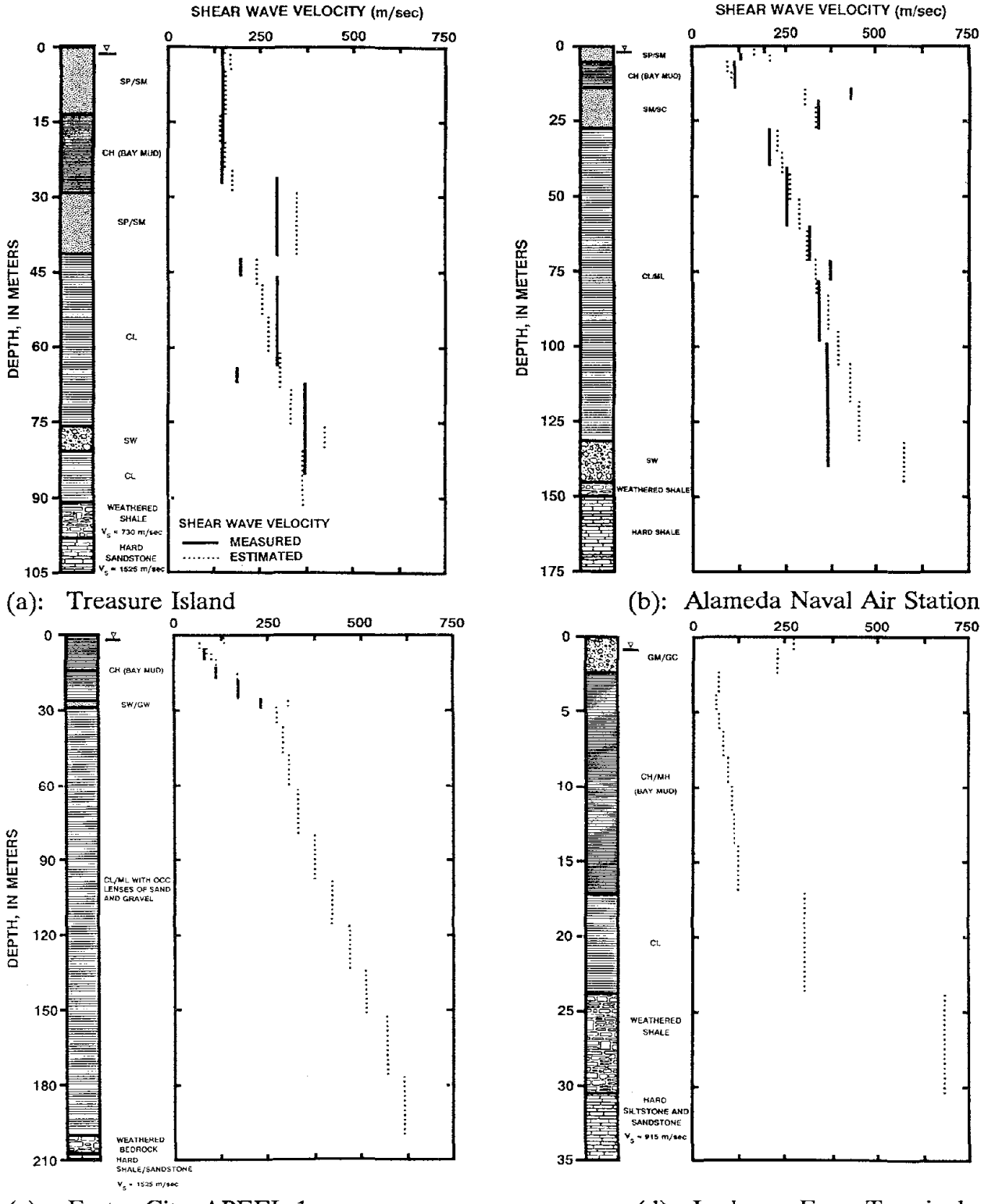

(a): Treasure Island

(b): Alameda Naval Air Station

(c): Foster City, APEEL 1

(d): Larkspur Ferry Terminal

Figure 4: Schematic Soil Profiles and Shear Wave Velocity Profiles for Selected Soft and Deep Cohesive Soil Sites

discussed herein were performed using the "estimated" V_s profiles, though it may be noted that analyses have also been performed using measured V_s-values for those 5 (of the 10) sites where such measurements are available, and the resulting calculated surface responses are in excellent agreement with those calculated based on "estimated" V_s values.

Figures 5(a) and 6(a) show the results of these one-dimensional ("columnar") dynamic response analyses using both SHAKE90 and MAR-DESRA. In each of these figures, the lower solid line represents the response spectrum of the input "rock" motion, and the two upper dashed lines represent the spectra for the ground surface motions calculated using the equivalent linear and fully nonlinear methods. Also shown for comparison, with solid lines, are the actual recorded ground surface motions at the Treasure Island site. The two "input" motions used were: (a) the "radial" component of the Yerba Buena Island record, scaled to a_{max} = 0.07g, and (b) the "transverse" Yerba Buena Island record, scaled to a_{max} = 0.04g. As shown in these figures, the responses determined using both the equivalent linear (SHAKE90) and fully nonlinear (MAR-DESRA) analyses are in good agreement with the recorded surface responses. The calculated maximum horizontal ground surface accelerations agree reasonably well with the recorded values, and the calculated motions also provide a good "fit" for the response spectra of the transverse and radial recorded motions.

THREE ADDITIONAL SOFT CLAY STRONG MOTION RECORDING SITES

Figures 4(b) through (d) show schematic soil columns and V_s-profiles for three additional "soft clay" strong motion recording sites. The Alameda Naval Air Station site is located in the east bayshore area; a region in which widespread liquefaction, structural damage, and damage to harbor facilities occurred during the Loma Prieta Earthquake. The other two sites, Foster City (APEEL1) and Larkspur Ferry Terminal are both on the west Bay shoreline, and represent the northernmost and nearly the southernmost "soft clay" recording sites. Figures 5 (b-d) and 6 (b-d) show comparisons between recorded and calculated transverse and radial motions at these three additional stations. Input motions were again scaled slightly to the regional average $a_{max,rock}$ values (radial & transverse). There is no single suitable nearby "rock" or "near rock" recording for use as input at the Larkspur Ferry Terminal site, so three different motions (BON, RCH and YBI) were each scaled for use as input motions; the results shown in Figures 5(d) and 6(d) are average results from these three sets of analyses. As shown in Figures 5 and 6, both the equivalent nonlinear and fully nonlinear analyses appear well-able to "predict" the actual recorded motions with good accuracy. It should not pass unnoticed, however, that accomplishing this required considerable effort with regard to evaluation and modelling of both dynamic soil properties as well as shear velocities of underlying "rock" units.

HIGHER (DESIGN) LEVELS OF SHAKING

The foregoing leads to the apparently satisfying conclusion that simple (oversimplified?) one-dimensional site response analyses, using the iterative "equivalent"

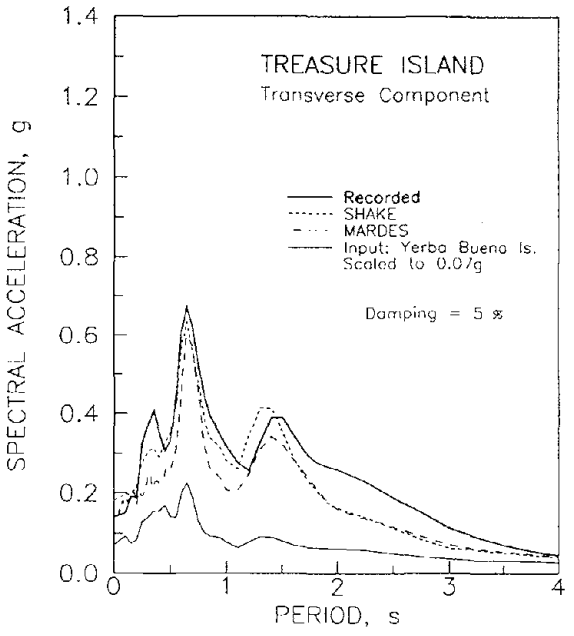

(a): Treasure Island

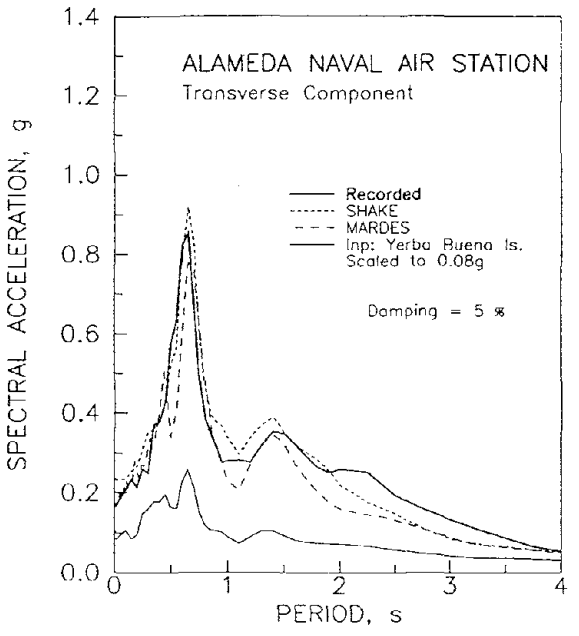

(b): Alameda Naval Air Station

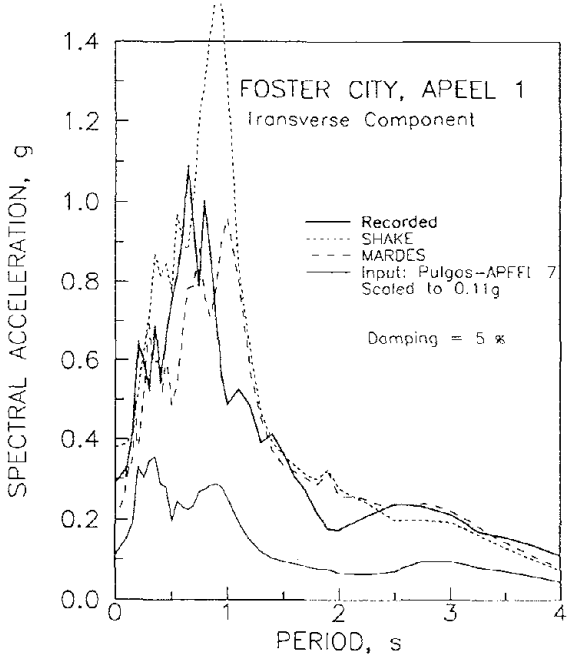

(c): Foster City, APEEL 1

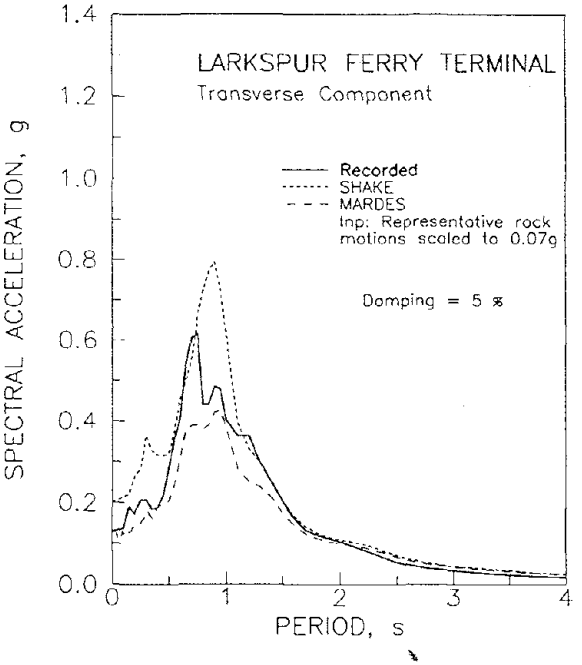

(d): Larkspur Ferry Terminal

Figure 5: Comparison Between Recorded Ground Surface Acceleration Response Spectra (Transverse Components) and Spectra Calculated by (a) Equivalent Linear and (b) Fully Nonlinear Methods at Four Recording Sites

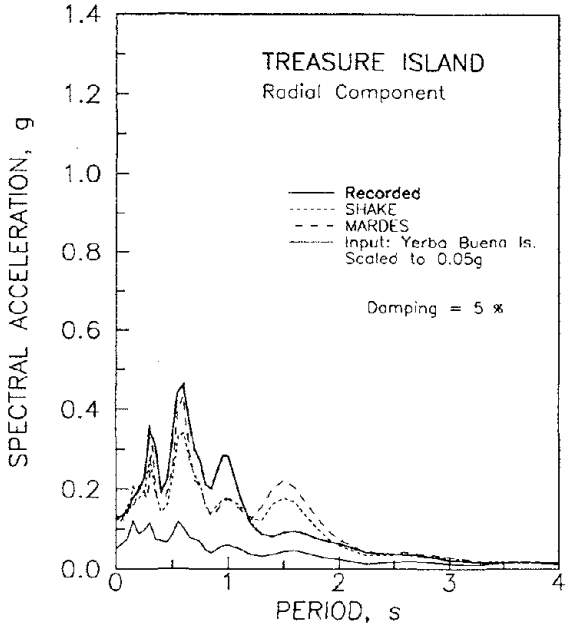

(a): Treasure Island

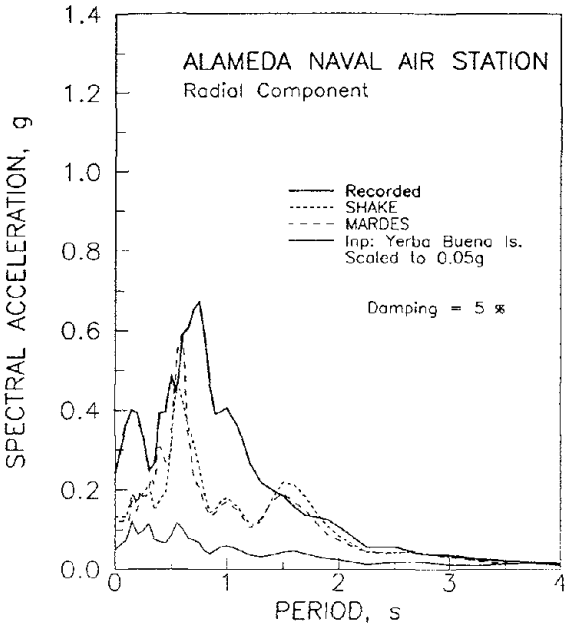

(b): Alameda Naval Air Station

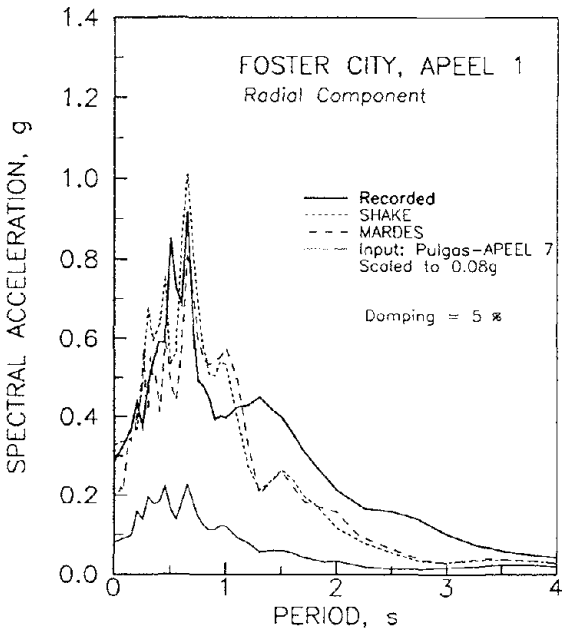

(c): Foster City, APEEL 1

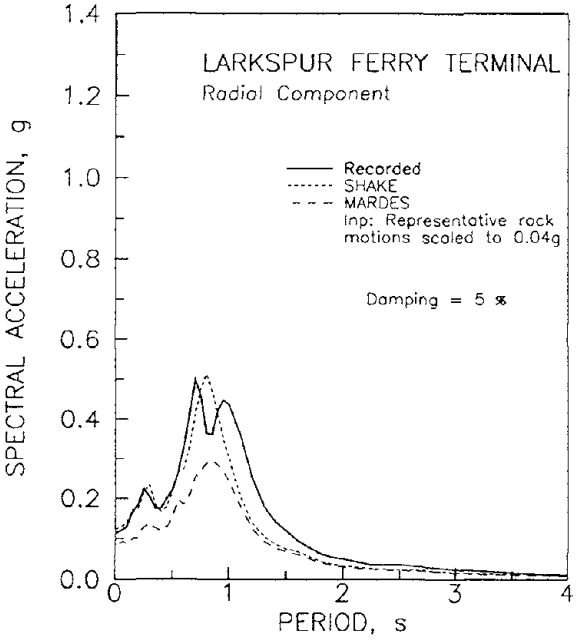

(d): Larkspur Ferry Terminal

Figure 6: Comparison Between Recorded Ground Surface Acceleration Response Spectra (Radial Components) and Spectra Calculated by (a) Equivalent Linear and (b) Fully Nonlinear Methods at Four Recording Sites

linear approach to modelling strain-dependent nonlinearity, and incapable of correctly accounting for two- and three-dimensional effects, surface waves, basin response, ray path focussing, etc., are well able to accurately and reliably reproduce (or "predict") the observed response behavior of soft and deep cohesive sites during the Loma Prieta Earthquake, and that these analytical methods thus provide a robust basis for engineering analysis and design. Unfortunately, this is not quite the case.

The Loma Prieta event produced only moderate levels of ground shaking, and these levels are considerably lower than those typically used for design studies in the Bay Area. At higher (design) levels of acceleration, nonlinearity of soil response becomes an increasingly important factor. At these higher levels of shaking, the ability of the fully nonlinear analysis techniques and soil parameters (the MAR-DESRA analyses) take on additional importance, as they are theoretically better able to model the increasingly important nonlinearity. Fortunately, these fully nonlinear analyses also performed well in "predicting" the observed Loma Prieta Earthquake soft clay site response behavior at moderate levels of shaking. Accordingly, the second phase of these studies has consisted of using the verified soil properties and lessons learned from Phase I (back-analysis of Loma Prieta response), and performing analyses of higher levels of shaking for forward projection of response at (higher) "design" levels of seismic excitation. These analyses were performed using both the equivalent linear and fully nonlinear approaches.

It is not possible to begin to properly discuss all of the important details of such analyses, nor the lessons learned, within the length constraints of this short summary paper. The following are brief summaries of a few of the more important findings:

1. Fully nonlinear (time domain) response analyses can, as accurately and reliably as the simpler "SHAKE" analyses previously described, reproduce the observed Loma Prieta response records. Unfortunately, such analyses are often performed in "practice" in a manner such that ground surface response is often underpredicted either due to (a) overdamping produced by the numerical algorithm employed, or (b) poor modelling of soil behavior due to difficulties in soil parameter evaluation, and corresponding failure to verify the validity of the behavior modelled by the soil parameters used.

2. At significant levels of "input" acceleration, soft soils may plastify, or soften and fail; the results include (a) de-amplification of the peak ground surface acceleration, (b) a partial shift in spectral response energy to longer period motions, and (c) large ground surface displacements. The equivalent linear analyses, performed in a "conventional" manner, do not do a good job of modelling this softening or "failure"; peak shear stresses within critical soil zones may greatly exceed the actual dynamic strengths of the soils, and the result is overprediction of peak ground accelerations and high frequency motions. These analyses can be iteratively modified, however, progressively "softening" the soils in critical (overstressed) layers by using lowered G/G_{max} values at shear strains of greater than 0.1% (or so); such "modified" analyses

can produce accelerations and acceleration response spectra in good agreement with those calculated using the fully nonlinear approach (MAR-DESRA).

3. Nonlinearity (or "softening") can limit the peak accelerations transmitted to the ground surface. An example is shown in Figure 7. In this figure, peak ground surface accelerations (a_{max}) for the APEEL1 soft clay site have been calculated using both SHAKE90 (with softening to limit dynamic shear stresses) and MAR-DESRA (fully nonlinear) for input motions representative of M=7½ to 8 events, and with "input" $a_{max,rock}$ values scaled to 0.15g, 0.30g and 0.60g. As the site "fails" to be able to carry high shear stresses, the ground surface a_{max} values reach a limiting value of approximately 0.4 to 0.45g.

4. The large ground surface displacements associated with strong levels of shaking are due in large part to large shear distortions within the "soft" clay strata. These are typically localized within a "softened" or plastified shear zone of finite width. This has potentially serious ramifications with regard to: (a) pile performance, and (b) edge (or shoreline) slope stability in sensitive marine clays (e.g. San Francisco Bay Mud) which may suffer significantly post-peak strength loss with "remoulding/disturbance" or accretion of large shear

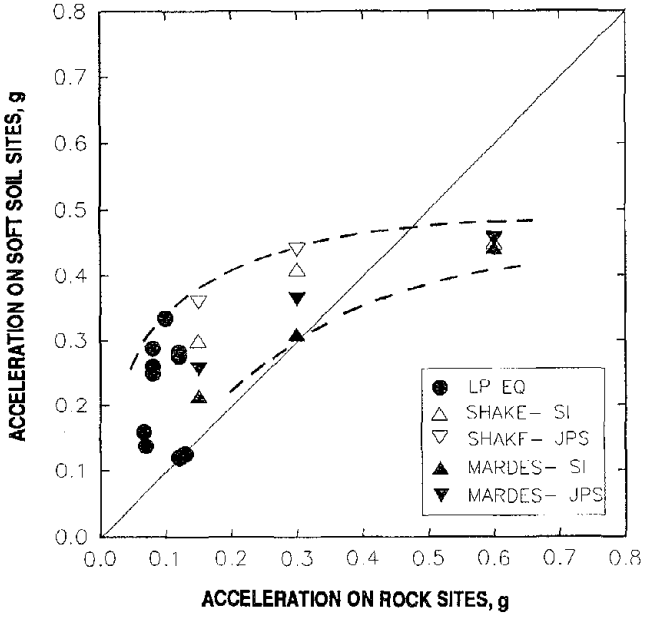

Figure 7: Peak Ground Surface Accelerations on Soft Clay Sites vs. "Input" (Rock) Peak Accelerations for Both the Loma Prieta Earthquake and Hypothetical Stronger Shaking Levels

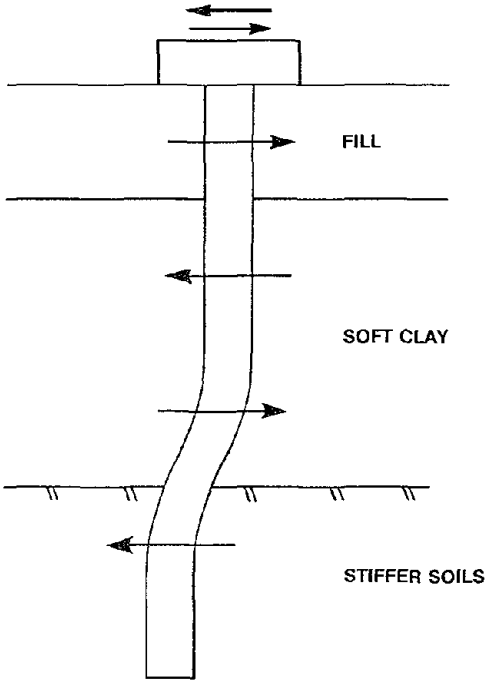

Figure 8: Schematic Illustration of Large Shear Displacements Within a Softened Shear Zone

displacements. Although "softening" of soil strata to reduce shear stresses calculated using "equivalent linear" analyses to values not exceeding the dynamic shear strengths of the strata can generate acceleration response behavior pleasingly similar to that calculated using fully nonlinear (time domain) analyses, the fully nonlinear analyses appear to provide a better basis for calculation of likely displacements.

5. The large shear displacements over a finite layer within the soft clay (Bay Mud) can have potentially serious ramifications with regard to potential overstressing of piles passing through this shear zone, as illustrated schematically in Figure 8. It has not previously been customary practice in most U.S. projects to study pile survivability in such cases.

6. Similarly, in most previous design studies, site response analyses have been performed for "virgin" site conditions (with no piles present). As piles are often used for structures founded on "soft" (and thus compressible) clays, the potential impact of the piles on site response should also be considered. If sufficient piles are installed to "reinforce" or strengthen the soft clay strata and thus preclude pile failure, then the piles can have a significant impact on site response. Failure to account for this can result in an unconservative underestimation of strong surface motions for use in structural analysis and design.

7. The increased complexity and sensitivity of fully nonlinear analyses places much increased importance on many details of the analysis process. Issues which merit increased attention include the following:

   - Peak dynamic shear strength evaluation for cohesive soils,
   - "Input" motions, their selection and characteristics,
   - Characteristics of near-source motions, including fling, vertical accelerations, incoherence, etc.
   - Parameter sensitivity; fully nonlinear soil models often employ parameters which can be difficult to evaluate, but which can have a significant impact on resulting calculations,
   - Soil/pile interaction, and nonlinearity of the response of composite soil/pile systems, and
   - Survivability of piles and pile groups at very high levels of shaking.

CONCLUSIONS

The set of strong motion records obtained during the Loma Prieta earthquake constitute a valuable data base of time histories for a wide variety of soil and rock conditions. These records will certainly foster a greater understanding of the response characteristics of soft and deep cohesive soil sites. This initial study has identified a number

of potentially serious shortcomings both in the current applicable design codes, as well as in current practice, and ongoing research is underway to develop improved analysis methods as well as improved structural seismic code specifications for soft and deep cohesive soil sites. Some of the primary conclusions of these studies to date include:

1. Relatively "simple" one-dimensional, equivalent linear and also fully nonlinear response analyses, performed using simple empirical correlations and simple modelling of nonlinear dynamic soil properties, are well-able to accurately and reliably "predict" the observed response of soft and deep cohesive bayshore sites to the relatively moderate levels of shaking which occurred during the 1989 Loma Prieta Earthquake. As these analyses are relatively easy to perform, the observed response of such sites during the Loma Prieta Earthquake should not be construed as representing a "surprise" to the earthquake engineering profession.

2. "Soft" clay sites (as well as other types of sites with "soft" and/or liquefiable soil layers) can require response analyses which consider interaction of the foundation soils and piles within these soils. Specifically, either: (a) the soil may potentially threaten to overstress (or overly deform) the piles, or (b) the piles may strengthen and stiffen the soils sufficiently as to significantly alter the overall site response characteristics. Neglecting these interactions can be dangerous with regard to: (a) potential pile breakage or failure, and/or (b) potential underestimation of shaking levels which must be dealt with in structural analysis and design.

3. Current code criteria for defining (and differentiating between) S_3 and S_4 sites, though representing a good initial effort, merit reconsideration in light of lessons learned over the past few years. Both the definition of cohesive sites, and the effects of nonlinearity on site specific amplification (and de-amplification) and spectral response should be revisited.

4. Fully nonlinear analyses of higher levels of shaking (more typical of "design" levels in the San Francisco Bay Area) give rise to a series of relatively "new" or under-examined issues. These are likely to have a significant impact on design practice in the years ahead.

ACKNOWLEDGEMENTS

The studies reported herein were based in large part on the collection of data contained in numerous personal and proprietary files; this paper would certainly not have been possible without the generous contributions of many individuals and organizations. The authors also wish to express their appreciation and gratitude to a number of people who provided special assistance with these studies. Special thanks are extended to: Adlai Goldschmidt and Ken Jackura of the California Department of Transportation

(CALTRANS), Dr. I.M. Idriss of the University of California at Davis, Dr. Liam Finn of the University of British Columbia, Dr. Lelio Mejia and Dr. Joseph Sun of Woodward-Clyde Consultants, Bruce Redpath of Redpath Geophysics, Dr. John Schnieder of the Electric Power Research Institute, Frank Rollo of Treadwell and Rollo, Inc., Tom Fumal and Dr. Roger Borcherdt of the U.S. Geological Survey, Dr. J. David Rogers of Rogers Pacific, and Dr. C.Y. Chang of Geomatrix Consultants. Support for these studies was provided by the California Department of Transportation (CALTRANS) under Contract No. RTA-59N224, and by the U.S. National Science Foundation under Research Grant No. MSM-8847137, and this support is gratefully acknowledged.

REFERENCES

1. Applied Technology Council (1978). "Tentative Provisions for the Development of Seismic Regulations for Buildings," ATC-3, Palo Alto, California.

2. Building Seismic Safety Council (1988). "NEHRP Recommended Provisions for the Development of Seismic Regulations for New Buildings," Part 2, Commentary; Washington, D.C.

3. Dickenson, S.E., and Seed R.B. (1992). "Correlations of Shear Wave Velocity and Engineering Properties for Soft Soil Deposits in the San Francisco Bay Region," Report No. UCB/EERC-92/XX, Univ. of California, Berkeley, Earthquake Engineering Research Center, in press.

4. Lee, M.K.W., and Finn, W.D.L. (1978). "DESRA-2, Dynamic Effective Stress Response Analysis of Soil Deposits with Energy Transmitting Boundary Including Assessment of Liquefaction Potential," Univ. of British Columbia, Vancouver.

5. Schanbel, P.B., Lysmer, J., and Seed, H.B. (1972). "SHAKE: A Computer Program for Earthquake Response Analyses of Horizontally Layered Sites," Univ. of California, Berkeley, Earthquake Engineering Research Center, Report No. EERC 72-12.

6. Seed, H.B., (1984). "Moduli and Damping Factors for Dynamic Analyses of Cohesionless Soils," Univ. of California, Berkeley, Earthquake Engineering Research Center, Report No. UCB/EERC-84/14.

7. Seed, H.B., and Sun, J.I. (1988). "Implications of Site Effects in the Mexico City Earthquake of Sept. 19, 1985 for Earthquake-Resistant Design Criteria in the San Francisco Bay Area of California," Univ. of California, Berkeley, Earthquake Engineering Research Center, Report No. UCB/EERC-89/03.

8. Vucetic, M., and Dobry, R. (1991). "Effect of Soil Plasticity on Cyclic Response," Jrnl. of Geotechnical Engineering, ASCE 117(1): 89-107.

III Assessment of Liquefaction Potential and Modeling of Liquefaction Mechanisms

Liquefaction Potential of the Ground Underlying the City of Honolulu, Hawaii

A. S. Furumoto[1], G. T. Taoka[1], G. Hao[2], N. Kobayashi[3], M. Nakamura[4], T. Maiguma[5], N. Nakajima[6], M. Abe[7], and T. Saito[8]

1. University of Hawaii, Honolulu, Hawaii
2. Harding Lawson Associates, Honolulu, Hawaii
3. Chuo University, Tokyo, Japan
4. Nippon Geophysical Prospecting Inc., Tokyo, Japan
5. Saitama University, Urawa, Japan
6. Tokyo Soil Research, Inc., Tsukuba, Japan
7. Tohoku University, Sendai, Japan
8. Iwate University, Morioka, Japan

ABSTRACT

The city of Honolulu sits on a wedge-shaped sedimentary layer that varies from a thin deposit at the foot of the mountains to a thickness of 330 meters at the seashore. As earthquakes in the magnitude range of 7 have occurred in the Molokai Fracture Zone nearby, liquefaction potential of the ground under Honolulu is being studied by several groups of investigators. General coordination is done by the Office of Civil Defense of the State of Hawaii.

From analyses of a voluminous data set of available bore-hole logs and impact measurements, for a design earthquake of magnitude 7.0, the heavily populated area of Honolulu has been zoned into four categories: Zone 1, very low liquefaction potential; Zone 2, low potential; Zone 3, moderate potential; and Zone 4, high potential.

Micro-tremor observations in three components were carried out at widely separated points in the city. Spectra from these observations had common characteristics. A very prominent peak centered around 0.3 hertz was found in all measurements. The amplitudes in the frequency range of 1 to 10 hertz were usually low, except at the Central Post office site which had spikes at 4 hz and 6 hz. The Central Post Office site falls under Zone 4 in the bore-hole data classification.

The sedimentary column can be characterized as interbedding of calcareous shallow marine deposits and detrital wash from basaltic mountains. Although firm conclusions are premature, data up to the present indicate that such structure has lower liquefaction potential than other places, such as Sakura City of Chiba Prefecture, Japan.

INTRODUCTION

In the Hawaiian Islands, because 90% of the earthquakes with local magnitude greater than 3 are associated with volcanic activity, an erroneous belief persists that all Hawaiian earthquakes are volcanic. However, destructive earthquakes have occurred near islands where the volcanoes have been extinct for millennia. In particular the 1871 Lanai earthquake with magnitude 7.1 and the 1938 Maui earthquake with magnitude 6.9 have caused notable damage (Figure 1). These earthquakes are considered to be associated with the Molokai Fracture Zone, which is the extension of a transform fault (Furumoto et al. 1990). The city of Honolulu, which is only 70 km from the Molokai Fracture Zone, with a de facto population of over 800,000, sits on a wedge-shaped sedimentary plain which is thin on the mountainside but thickens to 1000 feet (305 m) at the seashore (Figure 2). In the tourist district of Waikiki, which has a very dense year-round transient population, the sedimentary layer is 240 to 300 m thick.

The combination of proximity to a fault and of sedimentary layer led to a concern of potential earthquake hazard to Honolulu. As earthquake hazard can take many different forms, it is wise to investigate thoroughly one type of hazard at a time. The hazard of potential liquefaction of the ground was selected for the first round of serious investigation.

The liquefaction study has been proceeding along three avenues by separate groups of investigators. The avenues are:

1. collation and analysis of all available and useable bore-hole data to evaluate liquefaction potential of the ground;
2. ground vibration survey;
3. laboratory testing of soil samples;

This paper will describe the results to date from the first two lines of investigation.

BORE-HOLE DATA COLLATION, ANALYSES AND EVALUATION

The Office of Civil Defense of the State of Hawaii commissioned the firm of Harding Lawson Associates (HLA) to evaluate the liquefaction potential of the ground under Honolulu. HLA proceeded to collect information on subsurface conditions from its own archives, from reports field with the various state and county government departments, such as the Building Department, Department of Public Works, Department of Housing and Community Development, Board of Water Supply, Department of Transportation, and from other sources such as the Bishop Museum and the U.S. Geological Survey (Koh et al., 1992).

The most useful data came from bore-hole logs. In Figure 3 an example is shown how data from several bore-holes within a neighborhood of 500 feet were assembled to compile a composite profile. The particular profile is adjacent to the Ala Moana Canal which forms the northern boundary of Waikiki District. The ground surface is only 3 feet (1 m) above mean sea level. The first layer below the surface is a mixture of sand (circles in Figure), gravel (triangles) and silt (squares). The numbers indicate the N value in blows for standard penetration test (SPT). At a depth of 40 feet (12 m) a coral layer was encountered. This coral layer is considered to be firm enough that piles in building construction are anchored into it.

The analysis by HLA assumed a design earthquake of magnitude 7.0 which will produce a peak ground acceleration of 0.15 g. Using this assumption the behavior of the ground was classified into four zones, as shown in Figure 4. The characteristic of each zone is expressed in terms of probability P of liquefaction.

Zone I.	Very low liquefaction potential	0%	$< P < 16\%$
Zone II.	Low liquefaction potential	16%	$< P < 32\%$
Zone III.	Moderate liquefaction potential	32%	$< P < 48\%$
Zone IV.	High liquefaction potential		$P > 48\%$

HLA suggested that site specific liquefaction analyses should be done for Zone II and higher. In Zone IV liquefaction should be expected to occur under the design earthquake.

GROUND VIBRATION SURVEY

The Study Group of Long and Short Period Microtremors, a group composed of academic and industry investigators from the vicinity of metropolitan Tokyo, offered to come to Honolulu to conduct ambient ground vibration survey in connection with the liquefaction study. The offer was accepted and the group came in August 1991 to carry out the survey. The Civil Defense Office supplied logistic support and the School of Ocean and Earth Science and Technology provided necessary assistance. The instrument package used by the group consisted of three component sensors, digital recorders and a computer system that could provide in the field hard copy seismograms and amplitude spectra for the frequency of 0.1 to 10 hz ten minutes after recording.

The observations were done in the wee hours of the morning to avoid contamination by traffic noise. Although the results of HLA were not available to plan the site selection for the survey, as the sites were selected on the basis of known geology (Farrell, 1976), the sites turned out to include Zones I, III, and IV. The missing of Zone II does not detract from the usefulness of the survey because Zone II occur only in small patches (Figure 4).

The spectra of Figure 5 were obtained from observations done in the parking lot of the Hawaii Institute of Geophysics, University of Hawaii. The parking lot sits on a massive lava flow of nephelinite, 25 meters thick. The spectra may be taken as standard for basement rock for the island of Oahu. The peak at 0.2 hz is considered to be resonant vibration of the island mass. The amplitude spectra roll off exponentially from this peak on both sides.

The spectra of Figure 6 resulted from recording on a coral layer within the university campus. Notice that the peak at 0.2 to 0.3 hz is prevalent. Although the coral layer is on the whole rather solid, there are pockets or sink holes in the layer. The spike at 9 hz is probably due to a sinkhole. The spectra may be considered to be representative of Zone I or II. Even in these zones there is a possibility that a structure was built over a fill in a sink hole.

The spectra of Figure 7 resulted from recording at Kapiolani Park on the eastern edge of Waikiki District. The island mass resonance shows up at 0.2 to 0.3 hz. The higher frequencies of 5 to 10 hz have low amplitudes. This figure is representative of Zone III.

The spectra of Figure 9 resulted from recordings in downtown Honolulu in the parking lot of the Central Post Office. The amplitude level at the high frequency end is about that of the other Zone IV spectra. At this site we notice a few spikes in the range of 2 to 10 hz.

DISCUSSIONS

As comparison, spectra resulting from recordings at Inpa Swamp near Sakura City in Chiba Prefecture, Japan, are shown in Figure 10. The swamp area has soft ground and is considered to be a good candidate for liquefaction during an earthquake. There is a peak at 3 hz as well as a crustal resonance peak at 0.2 hz. The difference in peak levels is less than an order of magnitude. For areas with soft layers, peaks are noticeable in the frequency range from 1 to 10 hz. The significance of the results obtained at Honolulu is that peaks in the range of 1 to 10 hz are missing, although there are isolated spikes in the frequency range. Absence of peaks indicate that the ground under Honolulu is less prone to failure than at Sakura City. However the presence of spikes in two of the observations done is disturbing. We do not have a firm explanation for phenomena. A tentative suggestion was made that these spikes may be connected with sink holes, because in the university campus coral layer there are sink holes.

Liquefaction study for the city of Honolulu is still underway. From the literature survey completed by Harding Lawson Associates, the next step is the specific studies in areas designated as Zone III or IV. Filled land areas in Zone IV should be targeted for intensive study. Unfortunately ground vibration recording was not done in any filled land areas.

Engineering property studies of soil samples are being done by a few faculty members in the Department of Civil Engineering, independent of the ongoing liquefaction program. Liaison with these faculty members should be established in the near future.

The first layer of the sedimentary column under Honolulu has been called the "lagoonal mud" layer (Farrell, 1976). However a good portion of the layer are calcareous debris. It is better to consider the layer as a mixture of calcareous fragments and siliceous detritus. Calcareous fragments are sand and bits of coral due to break up of reef material by wave action. Siliceous detritus are wash from basaltic mountains. In the not too distant geological past, erosive action on the volcanic edifice must have been much more vigorous than the present one. Products of these two dynamic processes make up the shallow layer under Honolulu. As this type of mixed layer is found in other Pacific Islands, it should be the object of deliberate study.

REFERENCES

Ferrall, C. C., 1976. Subsurface geology of Waikiki, Moiliili and Kakaako with engineering application. M. A. Thesis, Univ. Hawaii.

Furumoto, A. S., E. Herrero-Bervera and W. M. Adams, 1990. Earthquake risk and hazard potential of the Hawaiian Islands. Haw. Inst. Geophys. Univ. Hawaii.

Koh, B. H., S. Vahdani, and C. P. Muller, 1992. Liquefaction study: Waikiki, downtown Honolulu and elevated sections of the H-1 Freeway, Oahu, Hawaii, Harding Lawson Associates.

Palmer, H. S., 1946. The geology of Honolulu ground water supply. Board of Water Supply City and County of Honolulu. 55 pp.

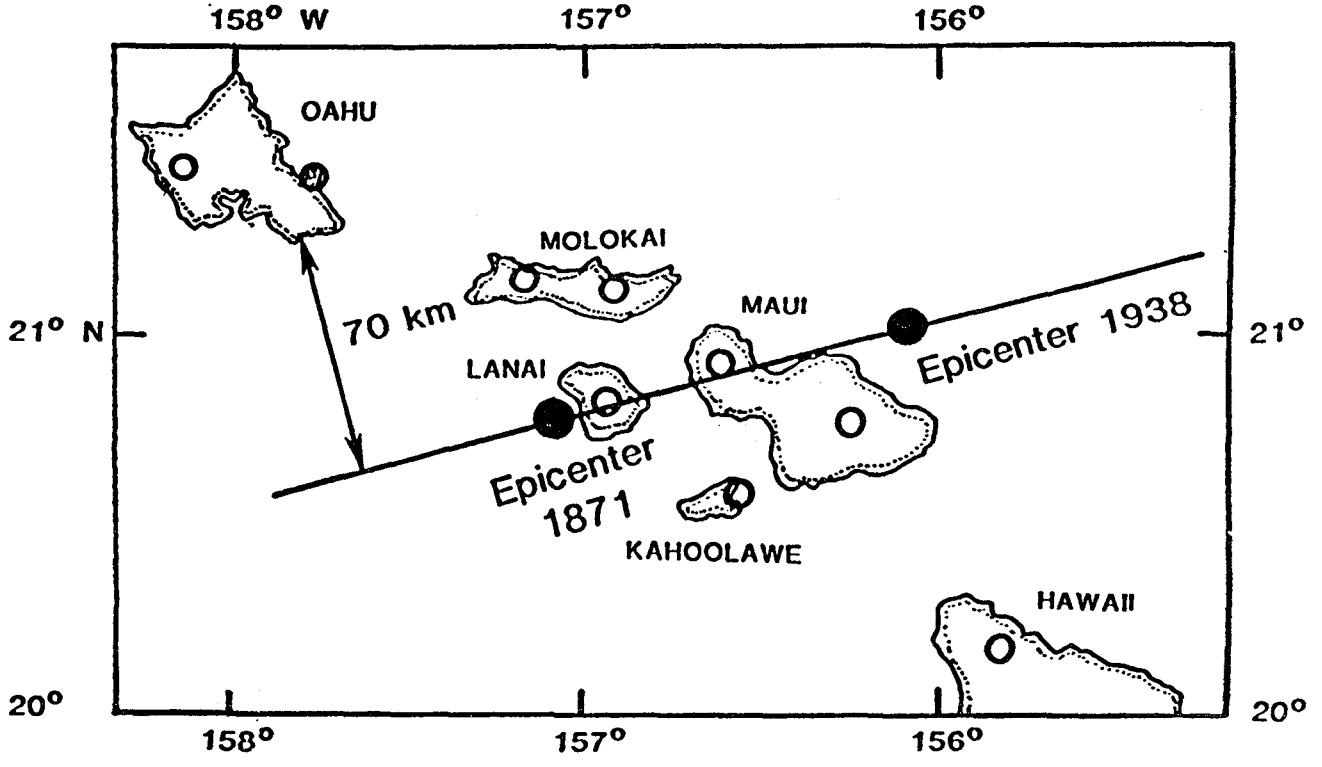

Figure 1. Collinearity of the epicenters of the 1871 and 1938 earthquakes and the centers of West Maui and Lanai Volcanoes. Empty circles indicate various volcanic centers.

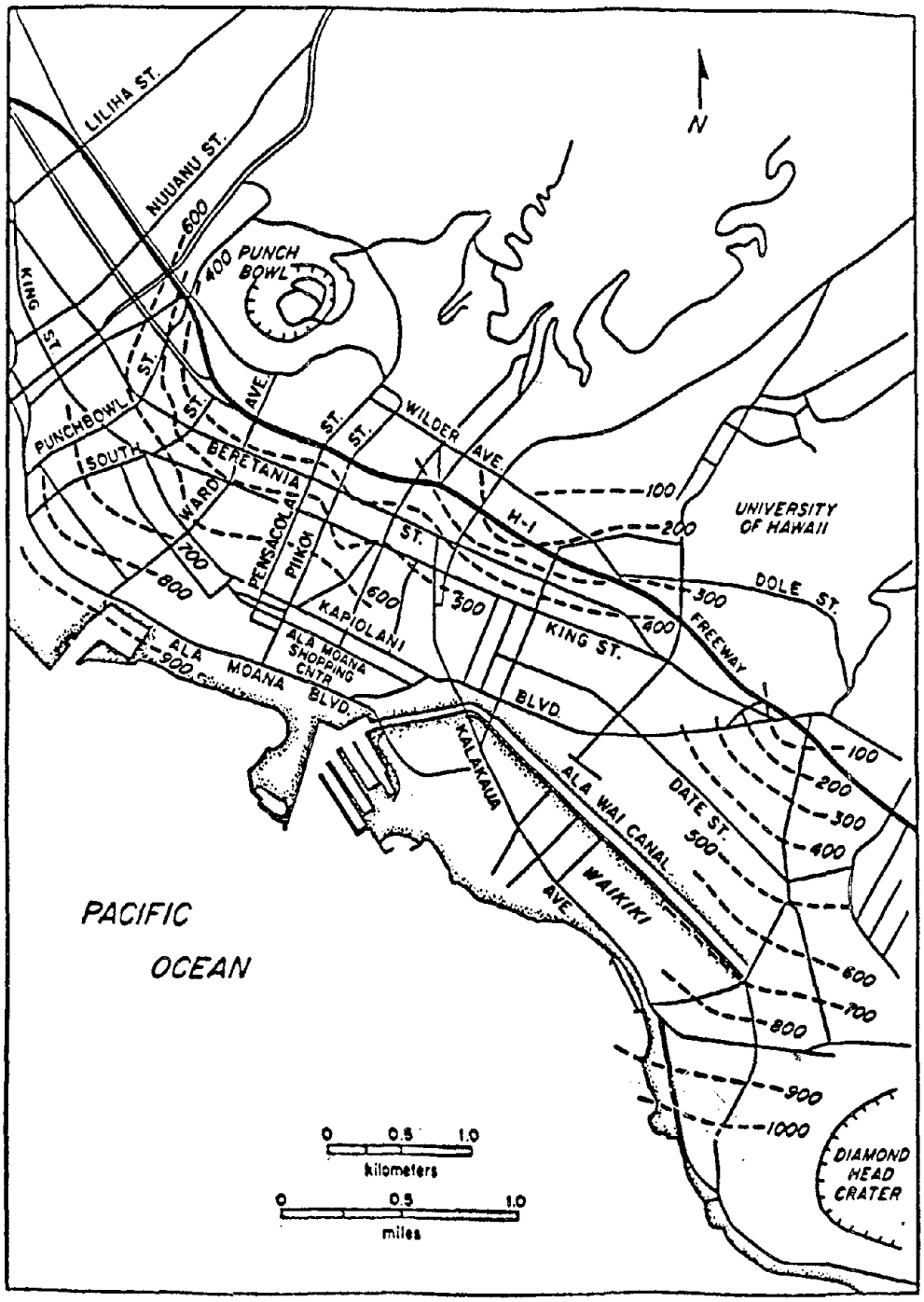

Figure 2. Thickness of sedimentary layer under Honolulu. Data provided by Palmer (1946) and base map redrawn from road map by California Drafting Service, Inc. (1988).

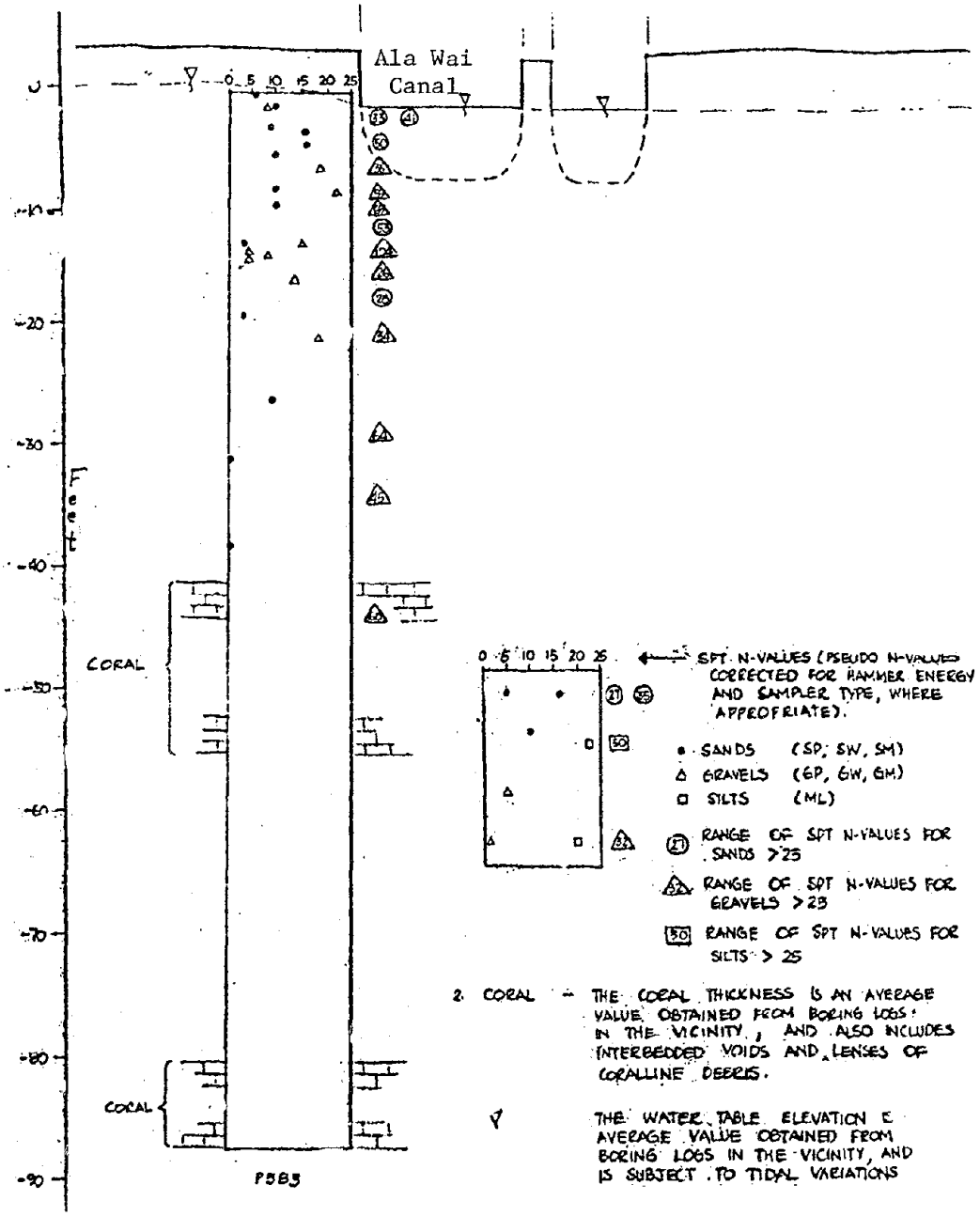

Figure 3. Composite bore-hole data for site near Ala Wai Canal.

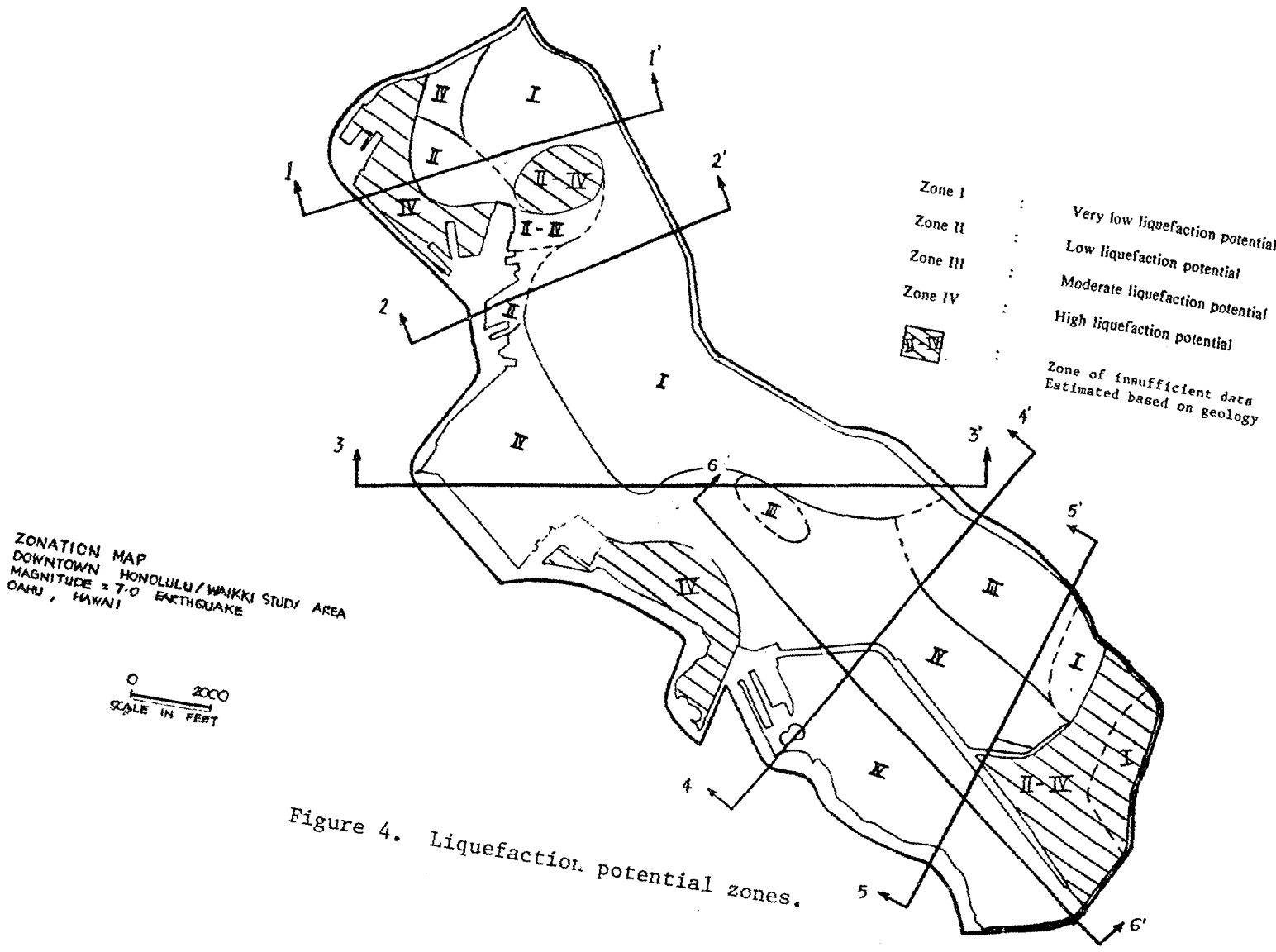

Figure 4. Liquefaction potential zones.

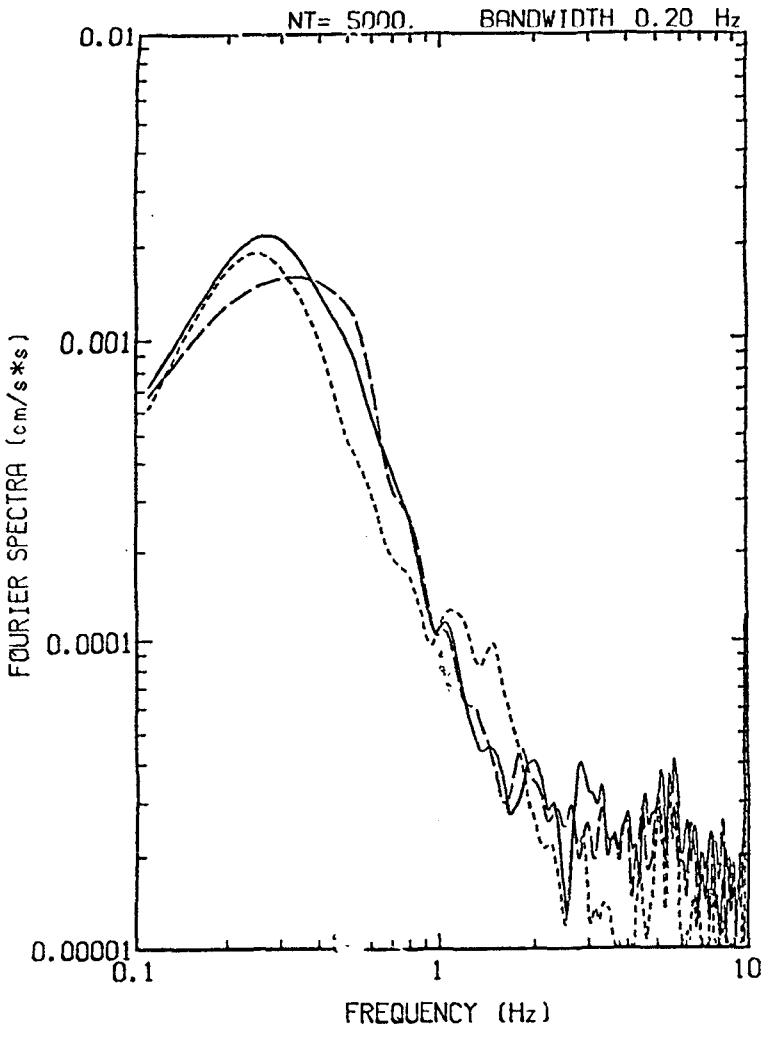

HAWAII UNIV. HIG 1991/08/24 04:12

NS:Solied Line EW:Broken Line UD:Dotted Line

Figure 5. Ground vibration spectra on nephelinite lava flow.

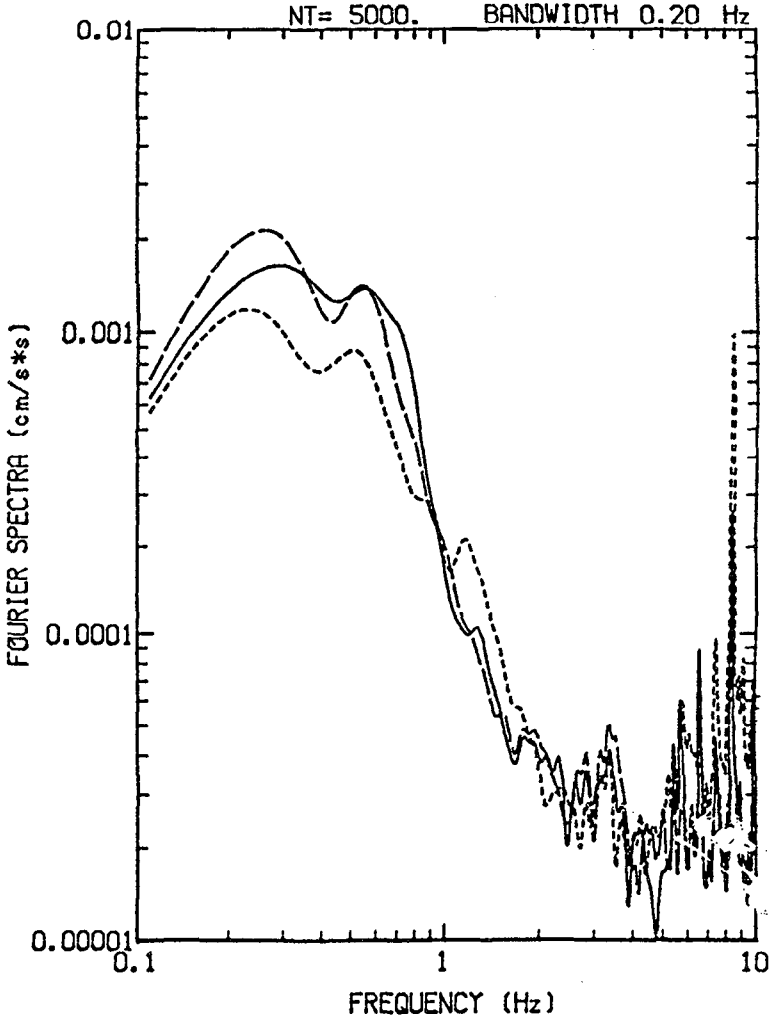

HAWAII UNIVERSITY 2 1991/08/24 04:50

NS:Solied Line EW:Broken Line UD:Dotted Line

Figure 6. Ground vibration spectra on coral layer.

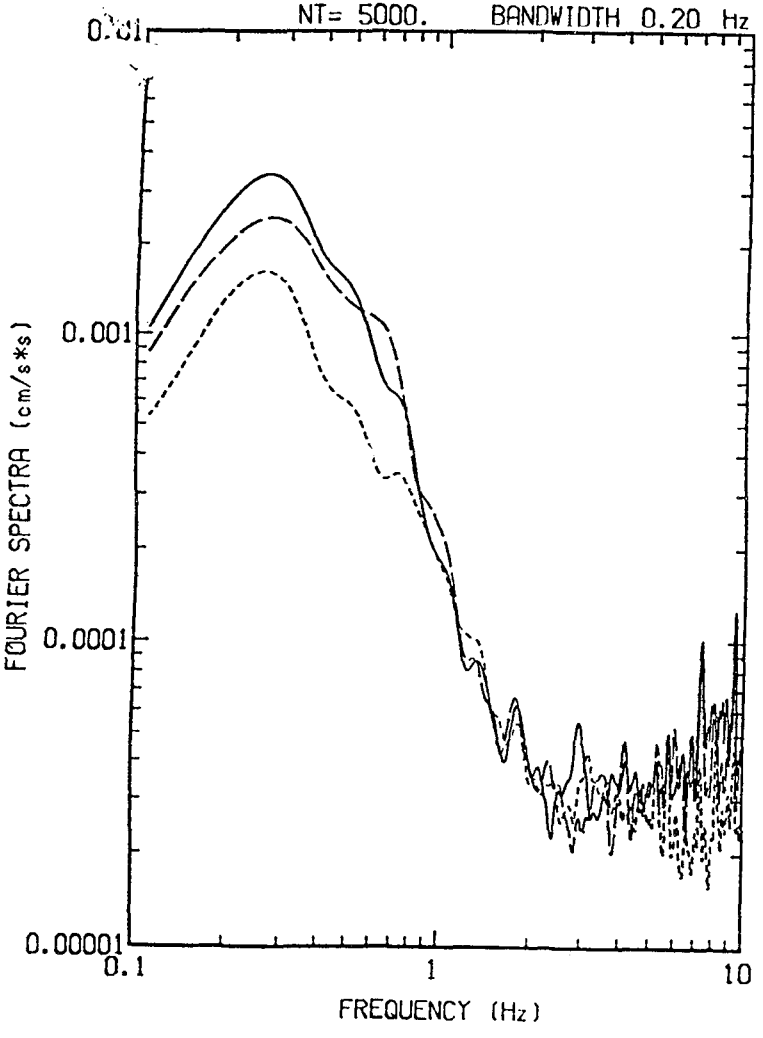

ALAWAI PARK 1991/08/25 04:08

NS:Solied Line EW:Broken Line UD:Dotted Line

Figure 7. Spectra in Zone IV.

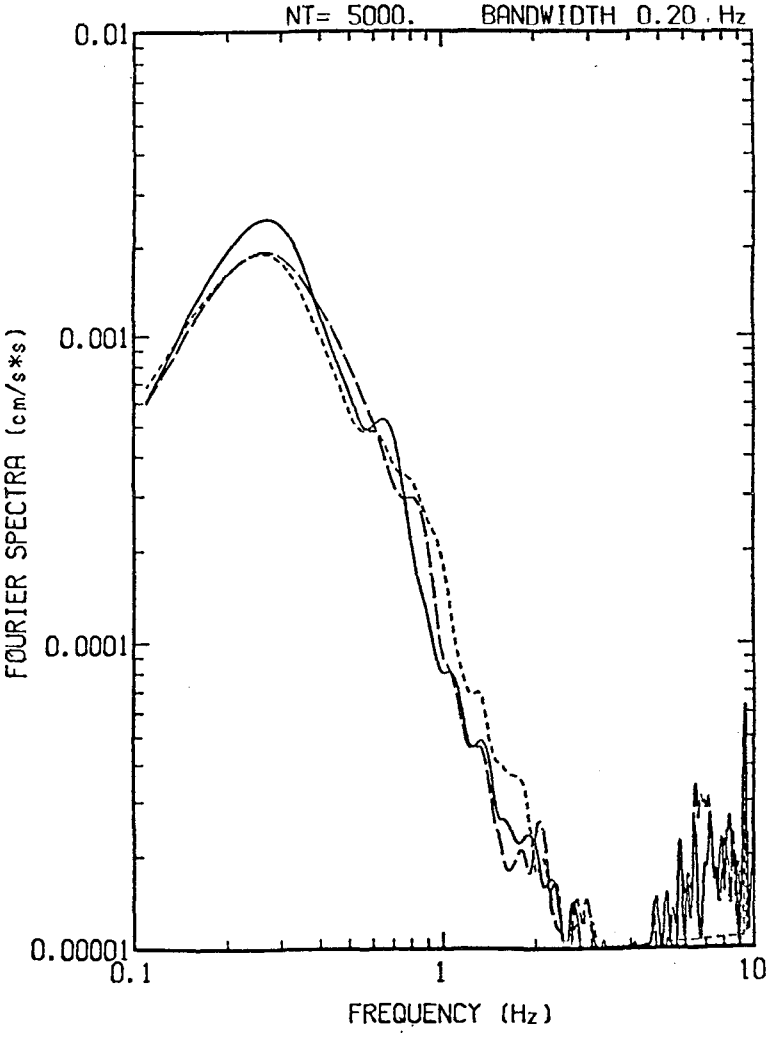

KAPIØRANI PARK 1991/08/25 03:34

NS:Solied Line EW:Broken Line UD:Dotted Line

Figure 8. Spectra in Zone III.

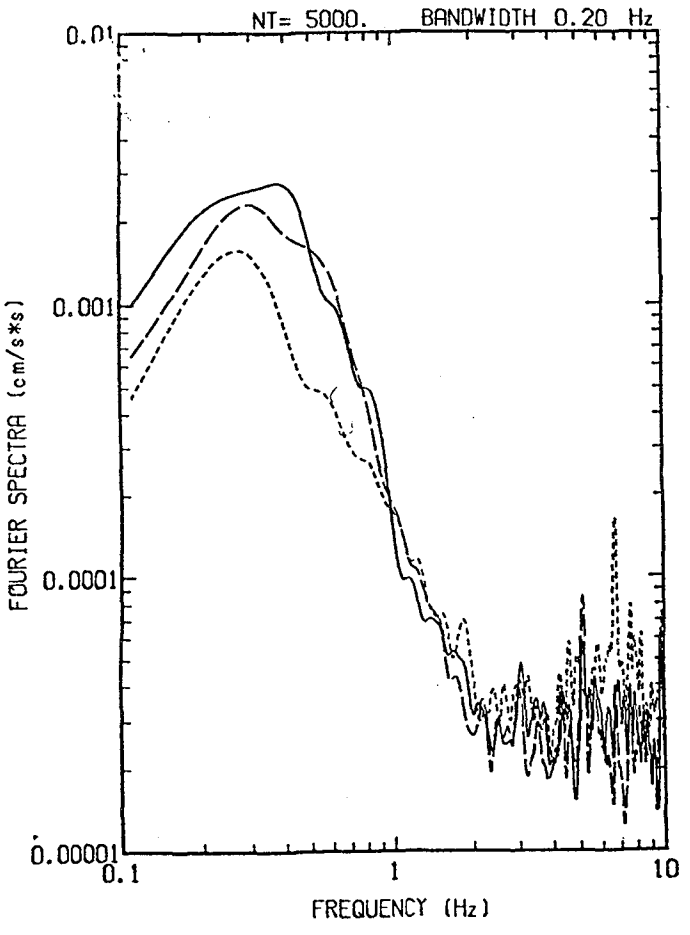

CENTRAL POST OFFICE 1991/08/25 05:21
NS:Solied Line EW:Broken Line UD:Dotted Line

Figure 9. Spectra on Zone IV.

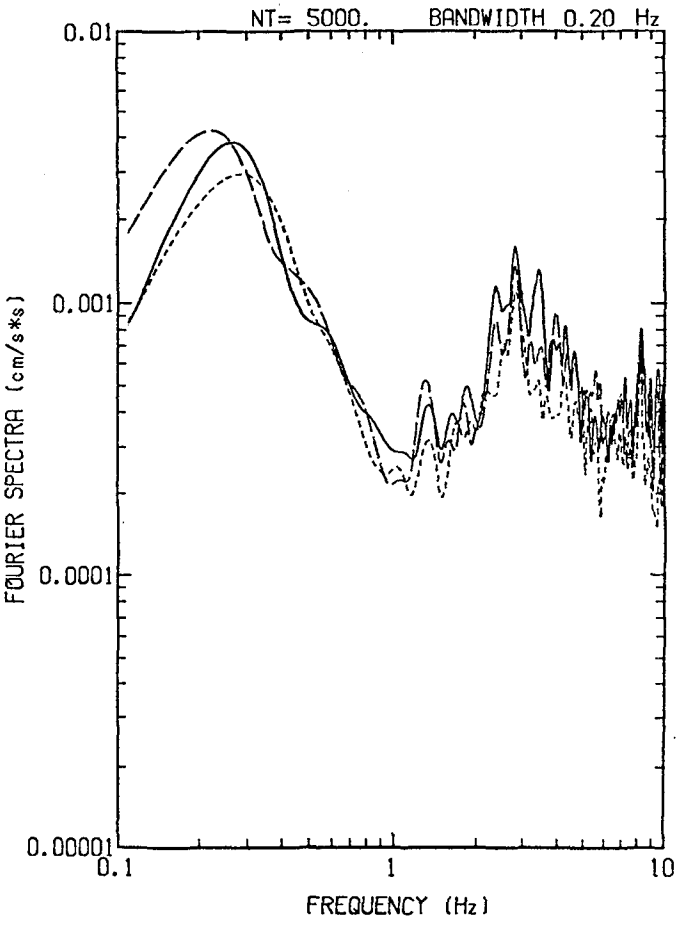

SAKURA C. MICROTREMOR
1991/08/10 5S. VEL. REKIHAKU

Figure 10. Ground vibration spectra at Sakura City, Japan.

Probabilistic Evaluation of Liquefaction Potential at President Island, Memphis

Howard H. M. Hwang and Chen Sam Lee

Center for Earthquake Research and Information
Memphis State University
Memphis, TN 38152

ABSTRACT

By using a site at President Island, Memphis, Tennessee, we present a probabilistic method for evaluating the liquefaction potential of a site. In this method, the liquefaction potential of a soil layer is estimated by using the factor of safety $F_L = R/L$. The earthquake-induced shear stress ratio L is determined from nonlinear site response analysis. On the other hand, the resistance shear stress ratio R is determined from cyclic test data based on the equivalent uniform cycles N_{eq} and relative density D_r. The F_L value together with the depth and thickness of each liquefied layer is used to calculate the liquefaction potential index P_L as proposed by Iwasaki et al. The P_L value indicates the liquefaction severity of a site: no or little liquefaction ($P_L = 0$), minor liquefaction ($0 < P_L \leq 5$), moderate liquefaction ($5 < P_L \leq 15$), and major liquefaction ($P_L > 15$). Uncertainties in site parameters (relative density and shear modulus) and seismic parameters (stress parameter, strong-motion duration, and random phase angles), are quantified to establish 81 earthquake-site models. Given a moment magnitude, the probabilities of no, minor, moderate, and major liquefaction can be determined from analyses of these earthquake-site samples. By repeating the same procedure for various moment magnitudes, the liquefaction potential probability matrix and the fragility curves can be constructed. The proposed method incorporates local site condition and regional seismicity in the evaluation of liquefaction potential of a site. In addition, uncertainties in seismic and site parameters can be easily included in the analysis.

INTRODUCTION

The liquefaction potential of a saturated sand site is affected by site parameters such as relative density, percentage of clay, and effective confining pressure and by seismic parameters such as the magnitude, frequency content, and duration of an earthquake. By using an analytical approach that incorporates local site condition and regional seismicity, uncertainties in seismic and site parameters can be easily included in the analysis. In this paper, we present a probabilistic method for evaluating liquefaction potential of a site and apply it to a selected site at President Island, Memphis, Tennessee.

NONLINEAR SITE RESPONSE ANALYSIS

The soil liquefaction is caused by the buildup of excess pore pressure induced by the cyclic shear stress in the event of an earthquake [1]. In this study, we perform the nonlinear site response analysis by using the MASH computer program [2] to determine the cyclic shear stress in a soil deposit. The dynamic soil model in the MASH program consists of a horizontally multi-layered soil profile with a fixed base. The soil profile of the selected site is shown in Figure 1. Soil exhibits a pronounced nonlinear behavior under cyclic loading. The secant shear modulus G is strain-dependent and decreases with increasing shear strain γ. In the MASH program, the secant shear modulus is expressed as

$$\frac{G}{G_o} = 1 - \left[\frac{[\gamma/\gamma_o]^{2B}}{1 + [\gamma/\gamma_o]^{2B}}\right]^A \qquad (1)$$

where G_o is the low-strain shear modulus; γ_o is the reference strain; and parameters A and B define the shape of the shear modulus reduction curve. These four parameters for sand and clay have been determined [3].

A seismological model is used to generate the horizontal acceleration time histories at the base of the soil column. In this study, the seismic source is assumed at Marked Tree, Arkansas, which is near the southern end of the New Madrid seismic zone (NMSZ). The epicentral distance from the seismic source to the site is about 57 km (Figure 2). Considering the source mechanism, path attenuation, and soft-rock effects, the Fourier acceleration amplitude spectrum at the base of a soil profile can be determined as [4, 5]

$$A(f) = C \times S(f) \times D(f) \times AF(f) \quad (2)$$

where C is a scaling factor; $S(f)$ is a source spectral function for acceleration; $D(f)$ is a diminution function; and $AF(f)$ is an amplification factor for the soft-rock effect. From the Fourier amplitude spectrum, the one-sided power spectrum $S_a(f)$ can be derived as

$$S_a(f) = \frac{2}{T_e} |A(f)|^2 \quad (3)$$

where T_e is the strong-motion duration. Given the power spectrum, we can generate the synthetic time histories by using the method proposed by Shinozuka [6]. The seismic parameters used to generate synthetic earthquakes are summarized in Table 1.

EARTHQUAKE-SITE SAMPLES

From reviewing existing boring logs of the selected site, the clayey silts and silty clays are found to have a high clay content (>15%). These types of soils are not likely to liquefy in the event of an earthquake [1]. Thus, only sandy soils are considered potentially liquefiable in this study. For each liquefiable soil layer, uncertainties in two site parameters (relative density D_r and shear modulus G) are included in the probabilistic analysis. The relative density D_r of a soil layer is estimated on the basis of the corrected standard penetration test blowcount $(N_1)_{60}$, which in turn is computed from the N_{SPT} value. The three representative D_r values are determined from the range of N_{SPT} values (Figure 1). The low-strain shear Modulus for a sand layer G_o is affected mainly by the confining pressure and relative density [1]. The confining pressure varying with depth is taken as deterministic; thus, the variation of G_o representing by three typical values is determined from three selected D_r values. From the experimental data available in the literature, the shear modulus reduction curves for sand are determined as shown in Figure 3. The values of parameters A and B corresponding to mean, mean plus one standard deviation (SD), and mean minus one SD curves are shown in Table 2 [7]. Thus, three D_r and corresponding G_o values and three pairs of parameters A and B are used to establish nine dynamic soil models.

The seismological model for generating horizontal accelerations at the base of a soil column is defined by seismic parameters listed in Table 1. Some

parameters such as the crustal density ρ, shear-wave velocity β, and cut-off frequency f_m appear to have less influence on the resulting horizontal accelerations. On the other hand, the stress parameter $\Delta\sigma$ and strong-motion duration T_e have significant effects on the accelerations. Thus, uncertainties in these two parameters, $\Delta\sigma$ and T_e, are included in the analysis. For central and eastern North America, three representative values of the stress parameter are selected as 100, 150, and 200 bars. In this study, the mean value of the strong-motion duration T_e is set as the source duration, which is the reciprocal of the corner frequency f_0 [8]. The strong-motion duration has significant variation. Thus, the coefficient of variation of 50% is used to determine three representative values. From the combination of three representative values of two seismic parameters, $\Delta\sigma$ and T_e, nine earthquake models are established. From each model, nine earthquake time histories are generated by using different random phase angles. Thus, a total of 81 earthquake time histories is generated for a specified moment magnitude. Finally, nine site models and 81 time histories are combined by using the Latin hypercube sampling technique to establish 81 earthquake-site samples [7].

EVALUATION OF LIQUEFACTION POTENTIAL

In this study, the liquefaction potential of a soil layer is estimated by using the factor of safety $F_L = R/L$ [1]. The earthquake-induced shear stress ratio L is the average shear stress ratio determined from the nonlinear site response analysis. The irregular shear stress time history of each liquefiable layer is converted into the equivalent uniform cycles N_{eq} at the average shear stress ratio based on the procedure proposed by Seed et al. [9]. By using the equivalent uniform cycles N_{eq} and relative density D_r, the resistance shear stress ratio R is determined from the cyclic test data for sand (SP), silty sand (SM), and clayey sand (SC). Figure 4 shows the cyclic test data for sand [10].

The F_L value only indicates the occurrence of liquefaction in a soil layer on a yes or no basis and does not reflect the liquefaction severity of a site. The liquefaction potential of a site is affected by the F_L value, and the thickness and depth of liquefied layers in a soil profile. In this study, the liquefaction potential index P_L proposed by Iwasaki et al. [11] is used to quantify the liquefaction severity of a site.

$$P_L = \sum_{i=1}^{n} Q_i \times W_i \times H_i \qquad (4)$$

where H_i is the thickness of the i-th layer in meters and Q_i accounts for the severity of the i-th liquefied layer.

$$Q_i = 1 - F_{Li} \qquad \text{for } F_{Li} \leq 1.0 \text{ (liquefied)} \tag{5}$$

$$Q_i = 0 \qquad \text{for } F_{Li} > 1.0 \text{ (non-liquefied)}$$

W_i accounts for the influence of the depth of i-th liquefied layer on the liquefaction severity of a site.

$$W_i = 10 - 0.5\, z \tag{6}$$

where z is the depth measured from the ground level in meters. The maximum depth considered in this study is 20 m. The P_L value indicates the liquefaction severity of a site: no or little liquefaction ($P_L = 0$), minor liquefaction ($0 < P_L \leq 5$), moderate liquefaction ($5 < P_L \leq 15$), and major liquefaction ($P_L > 15$).

PROBABILISTIC LIQUEFACTION ANALYSIS

For a specified moment magnitude M_i, 81 P_L values are obtained from the analyses of the earthquake-site samples. According to the P_L value, each sample can be classified as having no, minor, moderate, or major liquefaction. Then, the probabilities of no, minor, moderate, and major liquefaction can be calculated as follows:

$$\begin{aligned} P(no|M_i) &= (N_{no}|M_i)/N \\ P(min|M_i) &= (N_{min}|M_i)/N \\ P(mod|M_i) &= (N_{mod}|M_i)/N \\ P(maj|M_i) &= (N_{maj}|M_i)/N \end{aligned} \tag{7}$$

where $P(no|M_i)$, $P(min|M_i)$, $P(mod|M_i)$, and $P(maj|M_i)$ denote the conditional probability of no, minor, moderate, and major liquefaction, respectively, if an M_i magnitude earthquake occurs. $(N_{no}|M_i)$, $(N_{min}|M_i)$, $(N_{mod}|M_i)$, and $(N_{maj}|M_i)$, are the number of samples with no, minor, moderate, and major liquefaction caused by an M_i earthquake, and N is the sample size (81 in this study). By repeating the same process for various

moment magnitudes, the liquefaction potential probability matrix for the selected site can be constructed as shown in Table 3.

The fragility curves express the probabilities that a site will experience at least minor, moderate, or major liquefaction, if an earthquake occurs. For an earthquake of moment magnitude M_i, these probabilities can be determined as follows:

$$\begin{aligned} F_r(\text{min}|M_i) &= P(\text{min}|M_i) + P(\text{mod}|M_i) + P(\text{maj}|M_i) \\ F_r(\text{mod}|M_i) &= P(\text{mod}|M_i) + P(\text{maj}|M_i) \\ F_r(\text{maj}|M_i) &= P(\text{maj}|M_i) \end{aligned} \tag{8}$$

where $F_r(\text{min}|M_i)$, $F_r(\text{mod}|M_i)$, and $F_r(\text{maj}|M_i)$ denote the probability that the site will experience at least minor, moderate, or major liquefaction, respectively, if an earthquake of moment magnitude M_i occurs. From the liquefaction potential probability matrix (Table 3), the fragility curves can be constructed as shown in Figure 5.

COMPARISON OF RESULTS

The factor of safety against liquefaction F_L can also be computed by using the simplified procedure developed by Seed and Idriss [12]. Then, the liquefaction potential index, liquefaction potential probability matrix, and fragility curves can be determined by using the same approach as the proposed method. For the selected site, the fragility curves determined by using the simplified procedure are also shown in Figure 5 [7]. For an $M = 7.0$ earthquake, the results predicted by both methods are comparable. For an $M \geq 7.5$ earthquake, the chance of liquefaction estimated by the proposed method is much larger than that obtained by the simplified method. However, the reverse is true for an $M = 6.5$ earthquake.

The earthquake-induced shear stress ratios L obtained from the simplified method are close to those obtained from site response analysis in the proposed method. It is noted that the peak ground acceleration used in the simplified formula is also from the results of nonlinear site response analysis. Thus, the L values computed by both methods are expected to be close. The resistance shear stress ratios R evaluated by both methods are quite different. In the proposed method, the R is computed based on the equivalent uniform cycles N_{eq}, relative density D_r, and the laboratory test data, while the R value obtained by using the simplified procedure is based

on the field data and corrected blowcount $(N_1)_{60}$. The equivalent uniform cycles N_{eq} used in the simplified method suggested by Seed and Idriss [12] are quite different from those obtained from New Madrid earthquakes. The difference in the equivalent uniform cycles contributes significantly to the difference in the R value.

CONCLUSIONS

In this paper, we present a probabilistic approach for evaluating liquefaction potential of a site and illustrate it by using a site at President Island, Memphis, Tennessee. The results are presented in terms of the liquefaction potential probability matrix and fragility curves. The major conclusions are as follows:

1. The proposed method incorporates local site conditions and regional seismicity in evaluating the liquefaction potential of a site. In addition, uncertainties in seismic and site parameters can be easily included in the analysis. Thus, the proposed probabilistic method is appropriate for evaluating the liquefaction potential of a specific site.

2. The site at President Island, Memphis, probably will not be liquefied if a moderate New Madrid earthquake (e.g., **M** = 6.5) occurs. On the other hand, when the site is subject to a large earthquake, for example, a 7.5 moment magnitude earthquake, the site has 43% chance to experience a major liquefaction, 80% chance to suffer at least moderate liquefaction; and the site is almost certain to have at least minor liquefaction. Thus, the liquefaction potential of President Island should be carefully evaluated if a critical facility is to be constructed there.

ACKNOWLEDGMENTS

This paper is based on the research sponsored by the National Center for Earthquake Engineering Research (NCEER) under contract number NCEER-90-3009. (NSF Grant No. ECE-86-07591). Any opinions, findings, and conclusions expressed in the paper are those of the authors and do not necessarily reflect the views of NCEER or NSF of the United States.

REFERENCES

1. Seed, H.B., and Idriss, I.M., "Ground Motions and Soil Liquefaction During Earthquakes," Earthquake Engineering Research Institute (EERI), Pasadena, California, December, 1982.

2. Martin, P.P., and Seed, H.B., "MASH, A Computer Program for the Non-linear Analysis of Vertically Propagating Shear Waves in Horizontally Layered Deposits," Report No. UCB/EERC-78/23, Earthquake Engineering Research Center, University of California, Berkeley, California, October, 1978.

3. Hwang, H., and Lee, C.S., "Parametric Study of Site Response Analysis," International Journal of Soil Dynamics and Earthquake Engineering, Vol. 10, No. 6, August, 1991, pp. 282-290.

4. Hanks, T.C., and McGuire, R.K., "The Character of High Frequency Strong Ground Motion," Bulletin of Seismic Society of America, Vol. 71, 1981, pp. 2071-2095.

5. Boore, D.M., and Atkinson, G.M., "Stochastic Prediction of Ground Motion and Spectral Response Parameters at Hard-Rock Sites in Eastern North America," Bulletin of the Seismological Society of America, Vol. 77, No. 2, April, 1987, pp. 440-467.

6. Shinozuka, M., "Digital Simulation of Random Processes in Engineering Mechanics with the Aid of FFT Technique," in Ariaratnam, S.T., and Leipholz, H.H.E., eds., Stochastic Problems in Mechanics, University of Waterloo Press, Waterloo, 1974, pp. 277-286.

7. Hwang, H., and Lee, C.S., "Probabilistic Evaluation of Liquefaction Potential," Technical Report NCEER-91-0025, National Center for Earthquake Engineering Research, State University of New York at Buffalo, Buffalo, NY, November, 1991.

8. Hanks, T.C., "b-values and $\omega^{-\gamma}$ Seismic Source Models: Implications for Tectonic Stress Variations Along Active Crustal Fault Zones and the Estimation of High-Frequency Strong Ground Motion," Journal of Geophysical Research, Vol. 84, 1979, pp. 2235-2242.

9. Seed, H.B., Idriss, I.M., Makdisi, F., and Banerjee, N., "Representation of Irregular Stress Time Histories by Equivalent Uniform Stress

Series in Liquefaction Analyses," EERC 75-29, Earthquake Engineering Research Center, University of California, Berkeley, October, 1975.

10. Seed, H.B., and Peacock, W.H., "Test Procedures for Measuring Soil Liquefaction Characteristics," Journal of the Soil Mechanics and Foundations Division, ASCE, Vol. 97, No. SM8, August, 1971, pp. 1099-1119.

11. Iwasaki, T., Tokida, K., Tatsuoka, F., Watanabe, S., Yasuda, S., Sato, H., "Microzonation for Soil Liquefaction Potential Using Simplified Methods," Proceedings of the 3rd International Earthquake Microzonation Conference, Seattle, 1982.

12. Seed, H.B., and Idriss, I.M., "Simplified Procedure for Evaluating Soil Liquefaction Potential," Journal of the Soil Mechanics and Foundations Division, ASCE, Vol. 97, No. SM9, September, 1971, pp. 1249-1273.

Table 1 Seismic Parameters

Item	Symbol	Value
Moment magnitude	M	varied
Epicentral distance	R	57 km
Focal depth	h	10 km
Radiation pattern	$<R_{\theta\phi}>$	0.55
Horizontal component	V	0.71
Shear-wave velocity	β	3.5 km/sec
Source-rock density	ρ	2.7 gm/cm^3
Quality factor	$Q(f)$	$1500f^{0.4}$
Stress parameter	$\Delta\sigma$	varied
Cutoff frequency	f_m	30 Hz
Strong-motion duration	T_e	varied

Table 2 Parameter Values of A and B for Sand

Curves	A	B
Mean - SD	0.705	0.445
Mean	0.941	0.441
Mean + SD	1.268	0.446

Table 3 Liquefaction Potential Probability Matrix

M	Mean PGA (g)	Probability of Liquefaction (%)			
		No	Minor	Moderate	Major
6.5	0.13	90.12	8.64	1.23	0.00
7.0	0.16	45.68	27.16	18.52	8.64
7.5	0.20	3.70	14.81	38.27	43.21
8.0	0.24	0.00	0.00	12.35	87.65

Depth (m)				
0				
		MEDIUM DENSE SM-SP		
	γ_S = 19.6 kN/m^3	D_r = 0.502, 0.668, 0.761		N_{SPT} = 7-16
2.9				
		STIFF ML-CL		
	γ_S = 19.6 kN/m^3	PI = 10-20	S_u = 89.7 kN/m^2	N_{SPT} =15
5.5				
		MEDIUM DENSE SM-SC		
	γ_S = 18.9 kN/m^3	D_r = 0.423, 0.511, 0.588		N_{SPT} = 9-17
11.6				
		MEDIUM DENSE SP		
	γ_S = 19.6 kN/m^3	D_r = 0.405, 0.521, 0.618		N_{SPT} = 11-25
17.7				
		DENSE SP-GP		
	γ_S = 21.2 kN/m^3	D_r = 0.713, 0.757, 0.786		N_{SPT} = 40-49
19.2				
		STIFF CL		
	γ_S = 20.4 kN/m^3	PI = 20-40	S_u = 95.8 kN/m^2	N_{SPT} =16
23.2				
		DENSE SP		
	γ_S = 21.2 kN/m^3	D_r = 0.90		
27.5				
		VERY STIFF CL		
	γ_S = 20.4 kN/m^3	PI = 20-40	S_u = 119.7 kN/m^2	
29.3				
		DENSE SC		
	γ_S = 21.2 kN/m^3	D_r = 0.84		
36.9				
		VERY DENSE SP		
	γ_S = 22.0 kN/m^3	D_r = 0.925		
46.4				
		VERY STIFF CL		
	γ_S = 20.4 kN/m^3	PI = 20-40	S_u = 192.0 kN/m^2	
53.4				
		VERY STIFF CL		
	γ_S = 20.4 kN/m^3	PI = 20-40	S_u = 215.4 kN/m^2	
60.0				

Figure 1 Soil Profile of a Site at President Island, Memphis

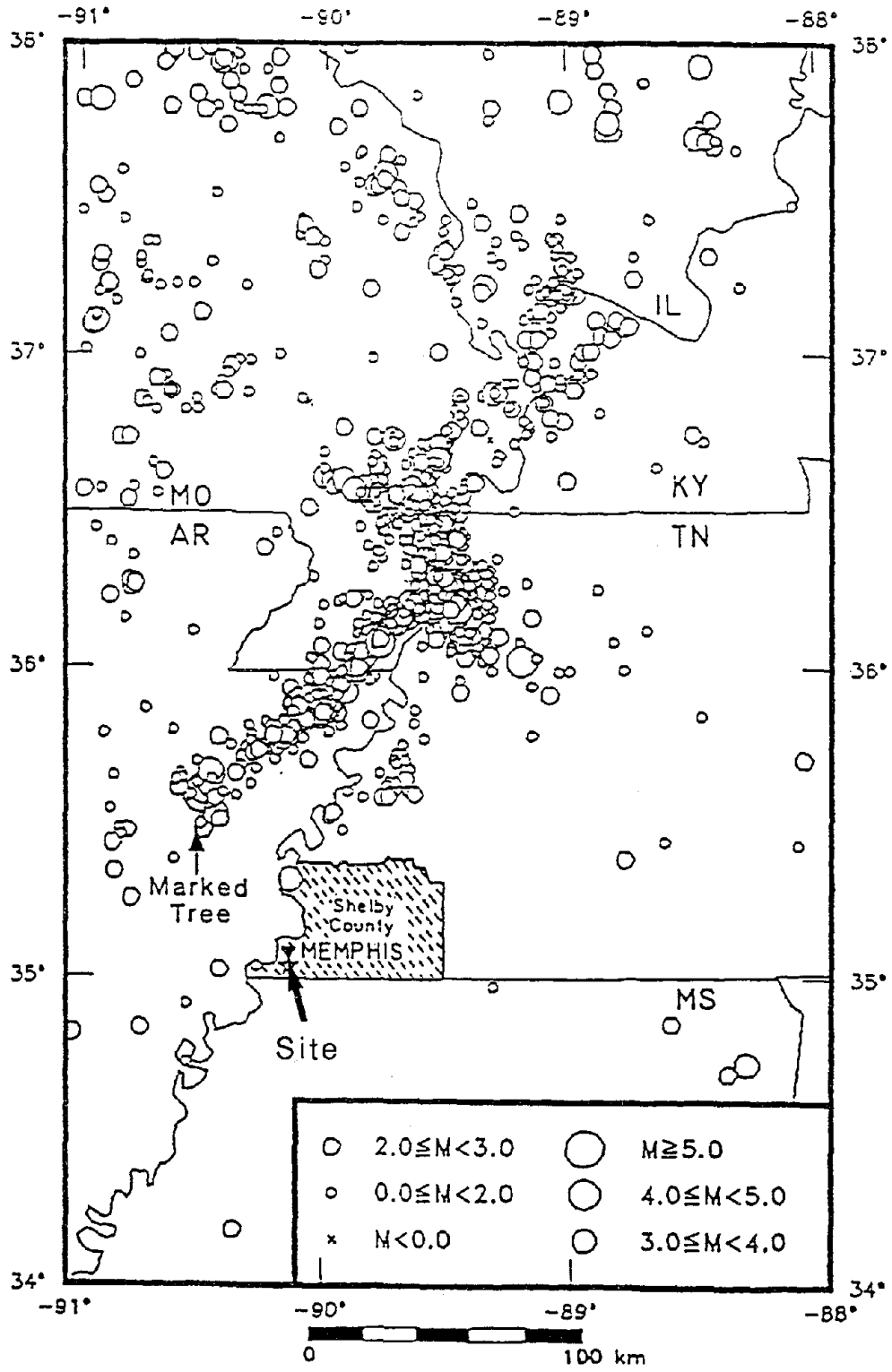

Figure 2 Locations of Seismic Source and Site

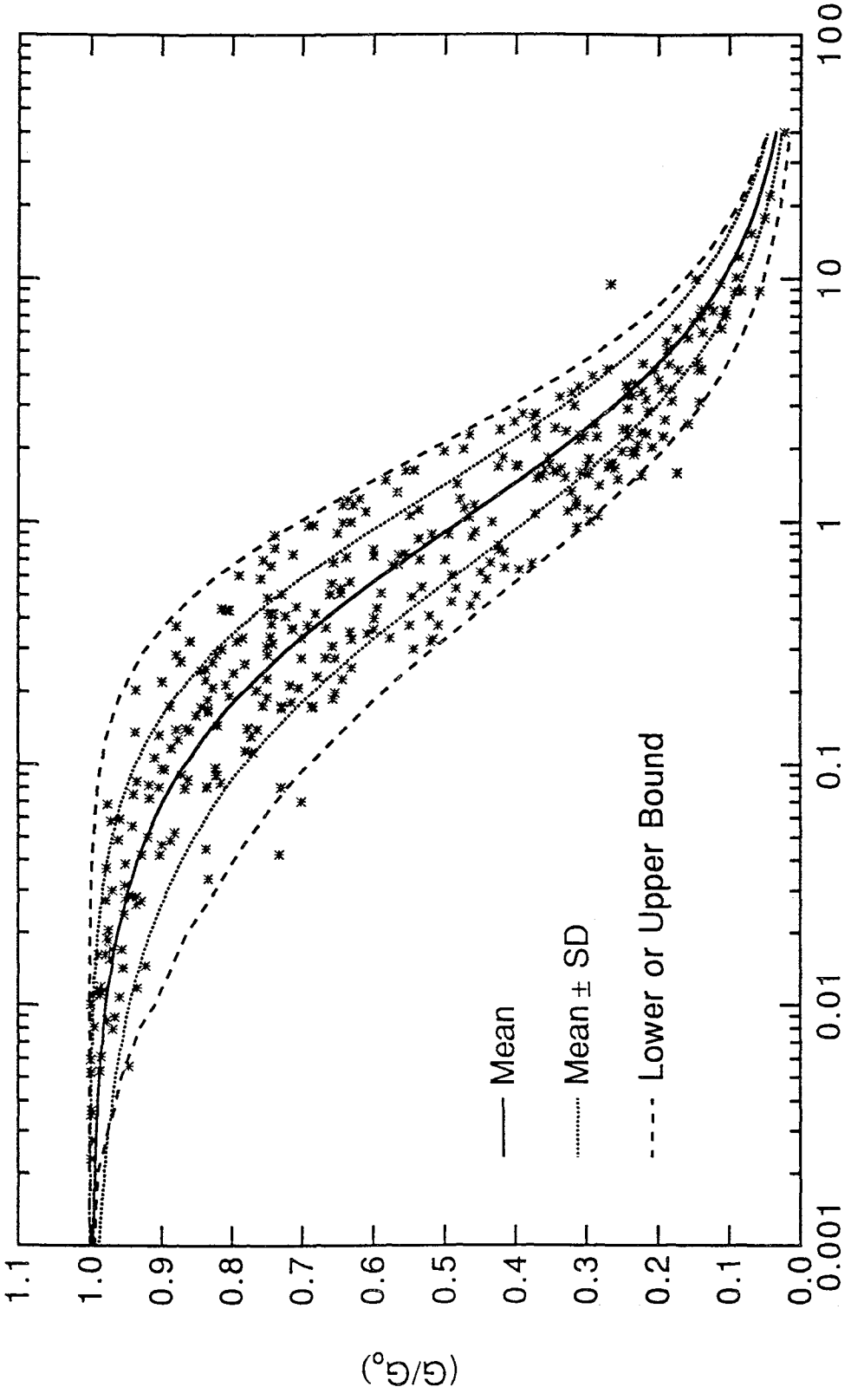

Figure 3 Shear Modulus Reduction Curves for Sand

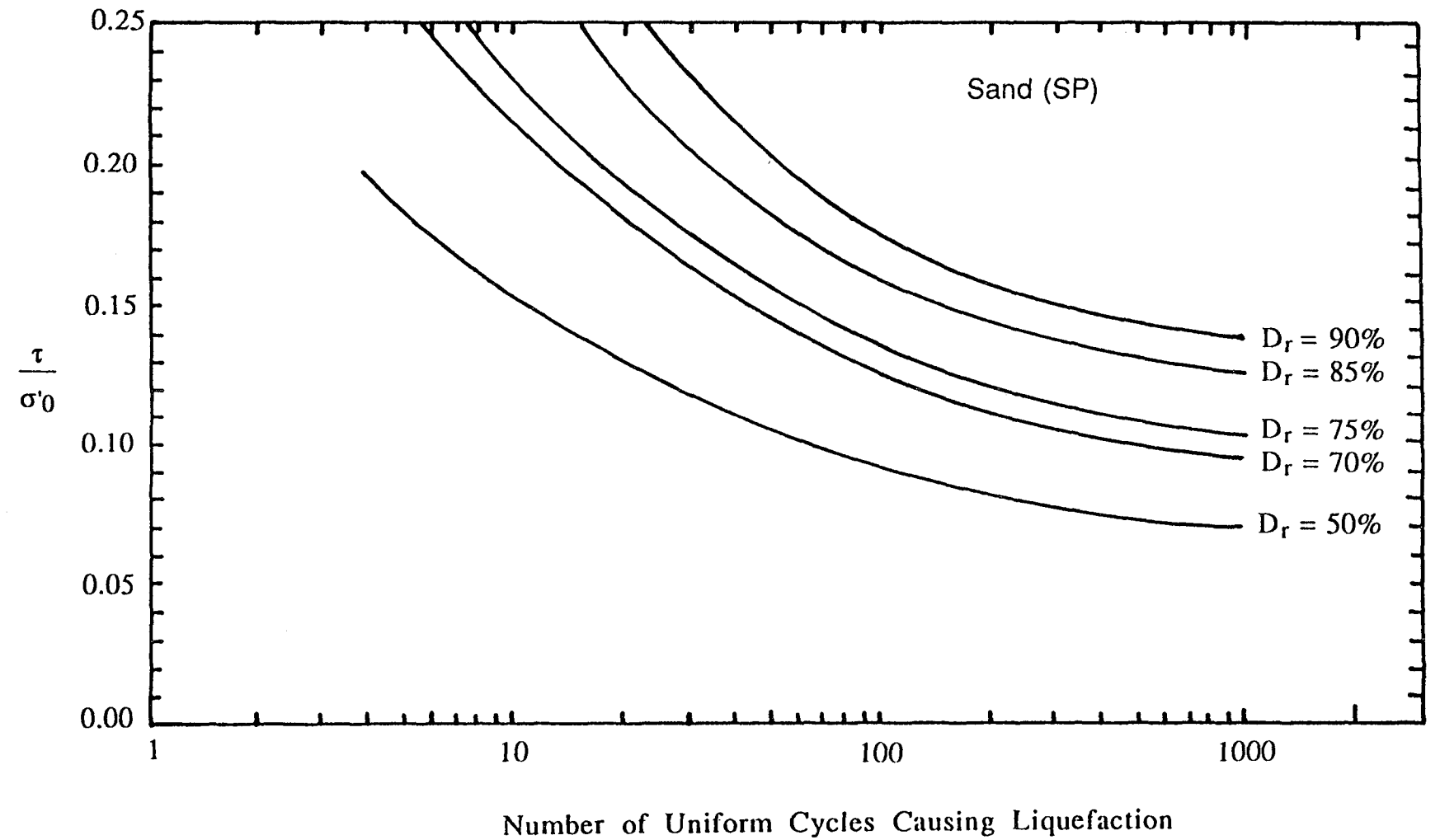

Figure 4 Cyclic Test Data for Sand (after Seed and Peacock 1971)

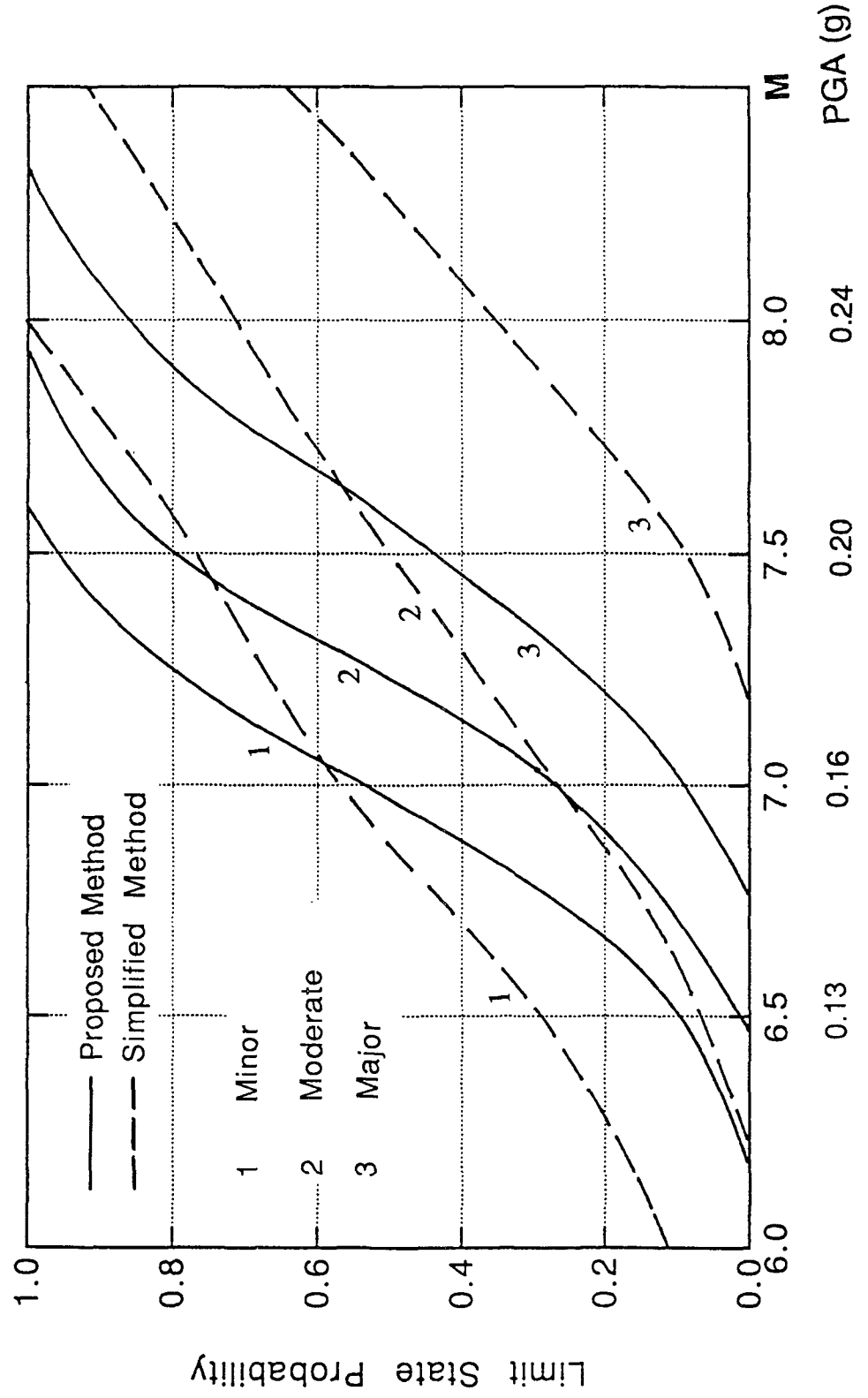

Figure 5 Liquefaction Fragility Curves of President Island Site

Evaluation of SPT-, CPT-, and Shear Wave-Based Methods for Liquefaction Potential Assessment Using Loma Prieta Data

Kayen, R.E.[1], Mitchell, J.K.[2], Seed, R.B.[3], Lodge, A.[4],
Nishio, S.[5], and Coutinho, R.[6]

[1] Research Civil Engineer, United States Geological Survey, Menlo Park, CA
[2] Edward G. and John R. Cahill Professor of Civil Engineering,
University of California, Berkeley.
[3] Professor of Civil Engineering, University of California, Berkeley, CA
[4] Graduate Research Assistant, University of California, Berkeley.
[5] Research Engineer, Shimizu Corporation, Tokyo, Japan
[6] Associate Professor, Federal University of Pernambuco, Recifie, Brazil

ABSTRACT

Soil liquefaction during the Loma Prieta Earthquake was observed in unimproved artificial fill deposits along the eastern shoreline areas of San Francisco Bay. Sites of significant damage extend from the Oakland International Airport, 65 Km from the northern end of the fault rupture, to the Port of Richmond, 85 Km to the north. Typical of all of these sites are low values of penetration resistance in zones of cohesionless hydraulic fill overlying deep cohesive soil profiles which amplified bedrock motions.

Post-earthquake investigations using Standard Penetration Testing (SPT) and Seismic-Cone Penetration Testing (SV-CPT) provide a basis for evaluation of the ability of each of these in-situ testing methods to correctly predict liquefaction resistance in loose hydraulic fill. A comparison between observed and predicted behavior suggests that SPT and CPT testing methods provide a good means of assessing soil liquefaction. A liquefaction boundary in cyclic stress ratio - overburden-normalized shear wave velocity space is proposed which segregates liquefiable from non-liquefiable soils at our east bay sites.

INTRODUCTION

During the Loma Prieta earthquake, soil liquefaction and associated ground deformations were observed in uncompacted artificial fill deposits along the east side of San Francisco Bay from Oakland Airport to the Port of Richmond at distances of between 65 to 85 Km from the northern end of the fault rupture (Figure 1). Considerable damage occurred at transportation, military, and shipping facilities near the shoreline area. This study describes liquefaction-related damages near the East Bay shoreline, and provides an assessment of methods for prediction of liquefaction resistance based on SPT, CPT, and shear wave velocity measurements for five sites: (1) the Port of Richmond; (2) San Francisco-Oakland Bay Bridge Toll Plaza; (3) Port of Oakland, 7th St. Marine Container Facility; (4) Bay Farm Island; and (5) Oakland International Airport (Figure 2).

Peak horizontal accelerations on rock and stiff, shallow soil sites in the east bayshore region generally ranged from about a_{max} = 0.08 to 0.12g, but amplification due to the presence of soft and/or deep cohesive soil deposits underlying the east bayshore fills produced peak accelerations of between about 0.11 to 0.29g at strong motion recording stations sited on bayshore fills in this region. It appears that peak horizontal ground accelerations on the bayshore fills in the vicinity of Oakland International Airport, and Bay Farm Island were about 0.27 to 0.29g, and the peak accelerations at the Toll Plaza of the San Francisco-Oakland Bay Bridge and 7th Street Marine Terminal sites were probably about 0.28 to 0.29g.

At the most northerly site, the Port of Richmond, there were no strong motion recordings nearby on similar soil conditions. Site response analyses were performed using the program SHAKE90 (a modified version of the site response computer program SHAKE: Schnabel, Lysmer, and Seed, 1972). The analyses were based on regionally averaged rock motions, modified to account for the effects of soft and deep underlying cohesive soil deposits. These studies suggest that peak horizontal accelerations at the Port of Richmond were probably about 0.13 to 0.18g.

IN-SITU TESTING METHODS

Standard Penetration testing (SPT) was performed in shallow 4 inch diameter uncased rotary wash borings following the guidelines specified by the American Society for Testing and Materials (1984). Liquefaction evaluations using SPT data were made using the procedures specified by Seed et al. (1984). SPT-energy calibrations using the stress wave method (Farrar, 1991) were made on the CME-450 drilling system used for the study to adjust field measured N-values to the standardized sixty-percent energy efficiency, $(N_1)_{60}$, required for the liquefaction analyses (Seed et al., 1984).

The electronic cone penetration test method followed the procedures specified by the American Society for Testing and Materials (1986). Liquefaction analyses were done using the methods of Robertson (1986), Robertson and Campanella (1985), Shibata and Teparaksa (1988), Robertson (1990), and Mitchell and Tseng (1990). The cone apparatus used has a standard cross-sectional area of 10cm^2, and a standard 60° apex tip. A single pore pressure transducer and porous stone were mounted directly behind the cone followed by a standard 150cm^2 friction sleeve. Mounted above the sleeve is a single component accelerometer which was used to measure vertically propagating shear wave travel-times for shear waves propagating from the ground surface down to the cone tip. Shear wave travel-time measurements and velocity calculations were made using the seismic-CPT method of Robertson et al., (1986).

PORT OF RICHMOND

Soil liquefaction occurred at a site at the western portion of Richmond Inner Harbor, as shown in Figure 3. The area which liquefied on October 17, 1989 is a zone approximately 250 ft wide and 1,000 ft long at the foot of Harbor Way Rd. (10th Street). At approximately 85 kilometers north of the fault rupture, this site represents the most distant point from the zone of energy release to suffer soil

liquefaction sufficient to damage structures during the Loma Prieta Earthquake. Much of the land at the edges of Richmond Inner Harbor was created by placement of uncompacted sandy hydraulic fill. The site where liquefaction occurred overlies deposits of soft to medium stiff, normally consolidated San Francisco Bay Mud, which are underlain, in turn, by deeper deposits of stiffer, overconsolidated non-cohesive and cohesive soils.

The site overlies Bay Mud and older cohesionless soils that naturally filled in a deep fluvial channel that exists at the western end of Richmond Inner Harbor. Thus, this site has thicker deposits than those of the Inner Harbor to the east, and it is likely that these thicker deposits amplified the level of ground motion at this site and so contributed to the observed soil liquefaction (Seed and others, 1990). The test site studied runs along the western wall of a factory structure and westward across an undeveloped field. Four large sand boils and a dozen smaller boils vented fine sand and silty sand from the underlying fill. In addition, minor settlements of approximately 2 to 8 cm and lateral movements of similar magnitude occurred at the edge of the harbor adjacent to a small pile-supported dock.

Figure 3 shows the locations of SPT borings and adjacent CPT soundings (POR-2,3,4) taken at three locations in the open space north of the Tweed Towing/Maas Boats facility. A representative soil log is shown in Figure 4. The first three columns present plots of (a) cone tip resistance (q_c), expressed in mega-Pascals; (b) friction ratio, F_r, calculated as the measured sleeve friction, *fs*, normalized by the total overburden stress corrected cone tip resitance q_c-σ'_{vo} (presented as a percent)

$$F_r = \frac{fs}{q_c - \sigma_{vo}} \times 100 \qquad (1)$$

and (c) the normalized pore pressure ratio, B_q, calculated as the measured deviation of pore pressure from hydrostatic pressure during CPT penetration, normalized by the total overburden stress corrected cone tip resistance.

$$B_q = \frac{u - u_o}{q_c - \sigma_{vo}} \qquad (2)$$

Equations 1 and 2 were proposed by Wroth (1984), where σ_{vo} is the total overburden stress, u is the measured cone penetration pore water pressure, and u_o is the equilibrium pressure at the same depth (assumed to be hydrostatic). The Standard Penetration Test blow counts, N - blows/foot, measured in the adjacent SPT borings are presented in the fourth column. Shear wave velocity, V_s (m/sec), measured by the seismic-cone penetration method (SV-CPT) is presented in the fifth column. Finally, a soil profile determined through the borings and SPT sampling is presented in the sixth column of these figures.

The attributes of the SPT boring and CPT probe logs from the Port of Richmond are similar to each other with depth and are characterized in the upper section by the following: An oxidized tan-brown crust layer of silty sand to 0.8 m; oxidized tan-brown silty sand to 1.8 m; and an oxidized tan-brown sandy clay that transitions to a reduced sandy-clay at 4.1 m. The water table was at a depth of approximately 2.5 meters during sampling.

Below the upper-most layers, at depths of between 4.1 m and 7.8 m, is a reduced olive gray fine silty sand with shell fragments. This layer almost certainly was responsible for the observed liquefaction at the surface, and surface sand boil material is virtually identical to SPT samples of this

layer of fill. This layer has an extremely low cone penetration resistance of approximately q_c=1 to 3 MPa, friction ratios of f_r = 0.3 to 1.0% on average, and minor levels of pore pressure generation during cone penetration with the exception of one spike at 5 m. SPT values in this layer vary between N= 2 to 11 blows-per-foot, but are typically in the range of N=2 to 5 blows-per-foot. Below this loose, fine sandy and silty sand hydraulic fill is a thin deposit of soft bay mud to 9.5 m, below which are dense sand deposits. Shear wave velocity in the liquefied layer typically ranged between V_s = 140 m/s to 170 m/s.

SAN FRANCISCO-OAKLAND BAY BRIDGE MOLE

The San Francisco-Oakland Bay Bridge mole (peninsula approach fill) immediately south of Emeryville, was extensively damaged by soil liquefaction. Appreciable settlements occurred over most of the approach fill, with magnitudes of up to 16 inches in several locations. In some cases, differential settlements produced an uneven hummocky pavement surface with permanent "waves" of up to 6 inches in amplitude. Lateral spreading was also significant along most of the fill, and produced numerous longitudinal fissures in the road pavement parallel to the fill edges. Many of these fissures exuded fine sands and silty sands, and numerous additional sand boils occurred along the median strip of the roadway, as well as off the shoulders of the roadway in open undeveloped land at the Bay's edge.

Penetration Test Logs:

Five sets of logs were taken at locations along the median parking lot and open space between the east- and west-bound lanes of Interstate Highway 80, as shown in Figure 5. Sand boils, lateral spreading, and/or settlement was observed at each of the investigated sites, as discussed below.

Cone penetration log SFOBB-5, Figure 6, was taken at the western end of the median strip in a wooded area. The water table was measured at 2 meters at this site. The log shows a gravelly-sand deposit to 6 meters depth beneath a dense crust. Below 6 meters is a zone of silty and sandy soil of low cone penetration resistance, q_c=5 to 10 MPa, to a depth of 8.5 meters. Standard Penetration values of N=7 to 19 blows-per-foot were recorded in this layer, which appears to be the layer within which liquefaction occurred. Shear wave velocities in this layer were typically within the range of 130 and 170 m/sec.

THE PORT OF OAKLAND

Immediately south of the Bay Bridge, soil liquefaction caused considerable damage to marine container facilities at several locations in the Port of Oakland, adjacent to the Oakland Outer Harbor, as shown previously in Figure 1. Much of the extreme western region near the shoreline of Oakland, south of the Bay Bridge approach fill, is artificially filled land underlain by a relatively thin layer of soft, normally consolidated marine clay (Bay Mud). These shallow surface units are, in turn, underlain by upwards of 150 meters of older, stiffer, sedimentary deposits below. Most of the surface fills at the Port of Oakland were hydraullically placed to sea level, above which a combination of hydraulic and

dumped fill was placed. Following placement of the un-compacted hydraulic fill, a relatively thick asphalt-cement pavement was lain in many of the terminal areas to support heavy vehicles and shipping containers. The hydraulic fills consist primarily of fine dredged sands and silty sands.

The most severe damage to Port facilities occurred at the 7th Street Terminal, our test site (Figure 5). Liquefaction of the hydraulic fill resulted in settlement, lateral spreading, and cracking of the pavement over large areas of the terminal. Maximum settlements of the paved container yards inboard of the wharves were on the order of 0.3 m. Differential settlements along the wharves of the ground beneath the inboard crane rail rendered a number of the loading cranes, and thus the dock facility, inoperable following the earthquake.

Penetration Test Logs:

Three SPT borings and six SV-CPT soundings were performed at six sites at the Port of Oakland, 7th Street Terminal Site, as shown in Figure 5. All six sites show somewhat similar stratigraphy indicating the broad lateral extent of the fill sand layers as the site was constructed. These sites typically have a surface layer of high penetration resistance in the upper 3 to 4 meters with cone resistance values of typically between q_c=25 and 35 MPa, and SPT values between N=25 and 36 blows-per-foot (Figure 7). The water table is located at approximately 3 meters in this layer. Below this zone the fill consists of looser deposits of fine marine sands with cone penetration values between q_c=8 and 15 MPa, and SPT values that typically range between N=10 and 25 blows-per-foot. These lower sands exhibited low friction ratios and essentially no excess pore pressure generation during penetration. Liquefaction appears to have occurred in the materials occurring in the 4 to 8 meter depth range, based on correlations of SPT samples with samples of surface boil material recovered. Shear wave velocities in the liquefied layer typically ranged from 150 to 190 m/sec.

BAY FARM ISLAND

Bay Farm Island, immediately north of the Oakland International Airport, suffered considerable liquefaction damage along the northwest corner of the island and at points along the western edge of the fill. Most of the western portion of Bay Farm Island consists of sandy hydraulic fill, underlain by Bay Mud and deeper, stiffer alluvium. Fill in the perimeter dike was densified by dynamic-compaction. Densification appears to have successfully prevented soil liquefaction of the western-perimeter dike during the earthquake. In contrast, in an area of un-compacted fill, damage to roadway and parking lot pavements occurred at the South Loop Road business park.

Penetration Test Logs:

Cone Penetration and Standard Penetration Test logs taken along the improved perimeter dike are shown in Figure 8. The dike serves as a good 'non-liquefaction' site. The elevated dike structure had a water table at approximately 3 meters depth within the soil. Sandy deposits at depths of between 2.5 to 7 meters had penetration resistance values within a range of q_c=10 to 35 MPA and N=29 to 58 blows-per-foot (Figure 9). Shear wave velocity measurements were note made at this site.

At the Harbor Bay Island Business Park, testing was performed in a parking area on South Loop Road. As shown in Figure 10, the soil at this site consists of fine hydraulic fill sands of low penetration resistance to a depth of 4 meters, below which are interbedded Bay Muds. Liquefaction occurred in the 2

to 4 meter depth portion of this profile. Penetration resistance values in this layer were measured at 5 to 8 Mpa for the CPT and 11 to 19 blows-per-foot for the SPT. The average corresponding shear wave velocity for this layer was 139 m/sec. At this site the water table was recorded at 2 meters during sampling.

OAKLAND INTERNATIONAL AIRPORT

Immediately south of Bay Farm Island, soil liquefaction caused considerable damage to the main jet runway (Runway No. 11-29) at Oakland International Airport. Additional evidence of liquefaction, including sand boils, settlement and lateral spreading, occurred over wide areas of the airport fill to the north and south and east of the damaged runway section. As shown in Figure 8, the main runway is located at the southwestern edge of the Airport. The subgrade beneath much of the runway and inboard taxiway area is loose, sandy fill underlain at shallow depths by soft clay (Bay Mud), and at greater depths by older and much stiffer sedimentary deposits. The perimeters of the airport fill have dikes to prevent inundation during unusually high tides and storms.

Extensive soil liquefaction occurred at the western section of the airport fill, and damaged the northwestern 900 meters of the 3000 meter long main runway. Cracks in the main runway and the adjacent taxiway had widths of up to 0.3 meters and vertical offsets of up to 0.15 meters. Most of the runway damage was repaired within 4 weeks, and as a result, the airport was able to resume essentially full operations with a shortened operational runway 2700 m in length on November 20. The surrounding perimeter dikes at the west end of the runway fill also suffered from settlement and lateral spreading in several places. The maximum observed levee settlement was on the order of 0.5 to 0.7 m, and lateral deformations were similar in magnitude. Liquefaction-induced ground deformations also damaged an undeveloped area of fill to the north and northeast of the main runway. Liquefaction was also observed at the location of the main terminal buildings. The buildings themselves are supported on deeper foundations and did not suffer any significant damage, but settlements of up to 3 inches were observed in the surrounding soils. In addition, a below ground tramway, which allows service vehicles carrying passengers' luggage to pass under a portion of one of the main terminal buildings, filled to a depth of approximately six feet with exuded sands and water.

Penetration Test Logs:

The results from SPT boring and SV-CPT soundings taken at three locations along the northern end of Runway No. 11-29 are included in this report. A representative log is presented in Figure 11. There is little or no surficial crust between 0 and 2 meters depth where the water table was encountered. Below this zone, from 2 m to between 4.5 and 5.8 m depth, is an extremely loose deposit of fine sand hydraulic fill that almost certainly was responsible for the observed liquefaction and lateral spreading. Cone penetration resistance values within this zone range between q_c=2 and 14 MPa, and material from this layer correlates well with surface boil material. Standard penetration values of between N=1 and 4 blows-per-foot were measured in this layer. Below this layer, young Bay Mud deposits of low penetration resistance defines the remainder of the logged soil column.

DISCUSSION

The observed liquefaction behavior of the East Bay fills, along with the measured SPT and CPT penetration values and shear wave velocity values can be compared with that predicted by pre-existing correlations based on Standard Penetration resistance (N-blows-per-foot), cone penetration tip resistance (q_c - MPa), and shear wave velocity (V_S meters-per-second). In order to compare penetration resistance and shear wave velocity values from various depths in an equivalent manner, values must be normalized to those corresponding to a reference effective overburden stress (e.g., 1 atm). For example, SPT N-values can be normalized to a uniform effective overburden stress of 1 Atmosphere (σ'_{vo} = 0.096 MPa) by correcting for overburden effects on penetration resistance using the equation of Seed and Idriss (1971):

$$N_1 = C_n N \tag{3}$$

in which the overburden stress correction factor C_n can be reasonably expressed as:

$$C_n = \frac{2.2}{1.2 + \left(\frac{\sigma'_{vo}}{\sigma'_{ref}}\right)} \tag{4}.$$

In the above equations, N is the measured penetration resistance value (blows-per-foot), N_1 is the overburden corrected blowcount, σ'_{vo} is the effective overburden stress, in atm, and σ'_{ref} is a reference stress which equals 1 atm.

The "Simplified" method of Seed and Idriss was more recently modified by Seed, et al. (1984) to account for the effects of equipement and procedural variations. The principal factors considered are sampler configurations and the efficiency of the SPT hammer system. A SPT hammer efficiency standard of 60% energy transmission to the drill rod and sampler was adopted by Seed, et al. (1984), and the overburden corrected blowcount, N_1, is further corrected to an equivalent and procedurally "standardized" blowcount of $(N_1)_{60}$. The actual SPT hammer efficiency of the drill system (a CME-450) used during most of the testing at the East Bay sites was less than 60%. A Binary Instruments 102 SPT calibrator was used to determine the actual efficiency by stress-wave energy measurement, following the guidelines and recommendations of Mr. Jeffrey Farrar (Farrar, 1991; Farrar, Pers. Comm.). An average hammer efficiency of 48 to 50 percent was measured for the CME-450 using a standard safety hammer and NW drill rod. Penetration resistance values were corrected to an equivalent number of blows at 60 percent efficiency as specified by Seed et al. (1984), as:

$$(N_1)_{60} = N_1 \left(\frac{\text{measured energy efficiency \%}}{60\%}\right) \tag{5}$$

The efficiency of the CME-750 drill system used for the Port of Oakland measurements has not yet been measured. Its efficiency was assumed to be the same as the CME-450 for purposes of the analyses herein. Additional corrections are required if the sampler does not have a constant inside diameter of 1.38 inches. This occurs when the split spoon sampler is configured to permit the use of internal sampler liners, and the liners are omitted. This was the case during these studies, so the recorded blow counts

were increased by between 10% and 20% for low and high N-values respectively (Seed et al., 1984).

The sensitivity of penetration test values to fine-particle content is well documented (Seed, et al.,1984) and effects the position of the liquefaction correlation curve in Cyclic Stress Ratio-penetration resistance space. Grain size distributions were determined for critical soil layers and are presented in Figure 12. Liquefiable layers at the Toll Plaza area, Port of Oakland, Bay Farm Island, and the Oakland International Airport can be characterized as clean sand with a mean-grain-diameter (D_{50}) of 0.25mm or greater. The Port of Richmond site has a significantly higher fines content, with D_{50} of approximately 0.06mm-0.07mm.

An overburden stress correction factor can be used to evaluate Cone Penetration resistance values at different depth in a manner similar to that used for the SPT-values:

$$q_{c1} = C_q q_c \tag{6}$$

A CPT-based depth correction curve for the determination of C_n (later termed C_q) was presented by Seed, Idriss, and Arango, (1983). Recent work by Mitchell and Tseng (1990) used cavity expansion theory and laboratory tests to determine C_q curves for medium-to-loose and dense soils: The depth correction factor C_q proposed by Seed, et al. (1983), and Mitchell and Tseng (1990) can be reasonably expressed as:

$$C_q = \frac{1.8}{0.8 + \left(\frac{\sigma'_{vo}}{\sigma'_{ref}}\right)} \tag{7}$$

Shear wave velocity profiles can be normalized to a common reference effective overburden stress (e.g., 1ATM) using a modified version of the Hardin and Drnevich (1972) equation for small-strain dynamic shear modulus:

$$V_{s1} = V_s \left(\frac{\sigma'_{ref}}{\sigma'_{vo}}\right)^{0.25} \tag{8}$$

where V_S is the measured shear wave velocity and σ'_{ref} is the reference stress (1 atm, 0.096 MPa) expressed in the same units as the the effective overburden stress.

The equivalent uniform cyclic shear stress ratio induced by the earthquake at any point in the ground can be estimated as (Seed and Idriss, 1982):

$$CSR = 0.65 \frac{a_{max}}{g} \frac{\sigma_{vo}}{\sigma'_{vo}} r_d. \tag{9}$$

The cyclic stress ratio parameter CSR represents a simplified approximation of the complex and irregular earthquake-induced stress time history as an equivalent series of cyclic loads of uniform amplitude. The parameter a_{max} is the peak acceleration measured or estimated for the ground surface at the site, g is the gravitational acceleration (981 cm/sec^2), σ_{vo} is the total overburden stress, σ'_{vo} is the effective overburden stress, and r_d is a depth reduction factor. The depth reduction factor r_d can be estimated in the upper 10 meters of the soil column by the following equation:

$$r_d = 1\text{-}.012z \quad (10)$$

where z is the depth in meters.

The "Simplified" empirical stress analysis approach for liquefaction assessment can be performed using the above parameters, $(N_1)_{60}$, q_{c1}, and V_{s1} as a measure of the soil liquefaction resistance, and then comparing these with CSR, taken as a representative measure of the severity of earthquake loading. Values used in the analyses of critical soil strata at the East Bay sites studied are summarized in Table 1.

The representative corrected SPT $(N_1)_{60}$ values measured at the five sites are plotted versus CSR in Figure 13. The boundary curve presented is the curve proposed by Seed, et al. (1984) for soils with little or no fines content (< 5% fines). It can be seen that the soil layers observed to have liquefied generally lie to the left of the boundary, whereas those layers that did not liquefy fall to the right. The SPT-based liquefaction analysis appears to have performed well on the East Bay hydraulic fill soils.

One point denoting the SPT measurement at POO7-3, 4-5 meters depth, plots just to the right of the boundary curve proposed by Seed et al. (1984). This layer, adjacent to the PortView Park observation tower is believed to have liquefied during the earthquke, as evidenced by nearby sand boils, lateral spreading and severe pavement distress. The drill rig used to perform SPT sampling at this site, a CME 750, was not calibrated for blow-count energy efficiency. Calibration of the system may result in subsequent adjustment of the blow counts to a better estimate of 60% hammer efficiency and improve the correlation about the boundary curve.

Cone penetration resistance data can be presented in a similar fashion to the SPT data. In Figure 14, the overburden-normalized cone resistances, q_{c1}, are plotted against CSR. Due to the previous sparseness of cone penetration data at sites that had either liquefied or not liquefied under known levels of seismic loading in previous earthquakes, early correlations between q_{c1} and CSR were made indirectly through SPT-CPT correlations (e.g., Seed and DeAlba, 1986, Robertson and Campanella, 1985). More recently, Shibata and Teparaksa, (1988) and Mitchell and Tseng (1990) have presented more direct relationships between q_c and CSR. The Shiibata and Teparaksa (1988) method is based on a limited data set of direct measurements at liquefaction sites for earthquakes in Japan, China, and the United States. Mitchell and Tseng's (1991) method is based on curves developed directly through cone penetration resistance - density relationships at a given effective confining stress, and corresponding relationships between density and cyclic stress ratio required to cause liquefaction in the same soil at the same confining stress.

As shown in Figure 14, penetration resistance values for the East Bay sandy fill deposits observed to have liquefied plot on or to the left of the boundary curves of Robertson and Campanella (1985), Shibata and Teparaksa (1988), and Mitchell and Tseng (1990) for medium sands. With the slight exception of one soil layer at the Port of Oakland, these correlation curves appear to have performed well in segregating liquefiable soils from those non-liquefiable. The more deeply buried dense layers at POO7-3 and BFI-DIKE, that are not believed to have liquefied, plot to the right of all the boundary curves. The boundary curve of Seed and DeAlba (1986) did not fully capture the observed occurrences of liquefaction for a number of soil layers and apprears to be somewhat unconservative. The boundary curve for D_{50}= 0.05mm proposed by Shibata and Teparaksa (1988) falls to the left of the Port of Richmond values and may be slightly unconservative for silty-sand material.

Normalized shear wave velocity values, when plotted against cyclic stress ratio, do appear to

provide a clear segregation of liquefied and non-liquefied layers (Figure 15). The non-liquefaction point at the Port of Oakland marine container terminal at 7th Street plots far outside the field of points representing sites that clearly liquifed. A boundary curve for shear wave velocity presented on Figure 15 (based on Seed, Idriss, and Arango, 1983) was developed indirecly through N-value and shear modulus relationships. The curve was developed for shear wave velocity without overburden correction, and as such its position on Figure 15 is approximate. The proposed boundary curve performed reasonably well in capturing the liquefied points to the left of the curve, but the interspersion of the non-liquefaction point to the left of the curve suggests that this correlation may be somewhat overly conservative.

Robertson and Woeller (in press) presented a boundary curve for overburden-normalized shear wave velocity based on a limited field data set. It can be seen that values for liquefiable layers at the Port of Richmond and Port of Oakland plot to the right of this curve. A tentative boundary curve based on our data from the East Bayshore hydraulic fill deposits is plotted as a dashed line. This curve captures all of the East bay liquefaction points, as well as those evaluated by Robertson and Woeller.

CONCLUSIONS

Extensive soil liquefaction occurred during the Loma Prieta earthquake in uncompacted artificial fill deposits of the East Bay from Oakland Airport to the Port of Richmond, between 65 and 85 Km from the northern end of the fault rupture. The initial results of studies at five sites near the East Bay shoreline are presented in this paper: these sites are at the Port of Richmond, San Francisco-Oakland Bay Bridge Toll Plaza, Port of Oakland-7th St. Marine Container Facility, Bay Farm Island, and Oakland International Airport. Typical of all of these sites are low to extremely low penetration resistance values in zones of cohesionless hydraulic fill which overlie deep and primarily cohesive soil deposits. Two factors, low penetration resistance and amplification of seismic shaking by the underlying soils, combined to give the sites a relatively high susceptibility to liquefaction.

Cyclic stress-based analyses of liquefaction potential, based on the Standard Penetration Test and using the methods of Seed, et al. (1984), predicted the occurrence (or non-occurrence) of liquefaction in soils during the Loma Prieta Earthquake. Similarly, the cone penetration test performed well in predicting soil liquefaction potential. Boundary curves between liquefaction and non-liquefaction proposed by Mitchell and Tseng (1990), Robertson and Campanella (1985), and Shibata and Teparaksa (1988) did reasonably well in segregating soils, whereas, the boundary proposed by Seed and DeAlba (1986) appears to be somewhat unconservative.

Shear wave velocity also appeared to be a good basis for segregating soils of low and high liquefaction resistance for the hydraulic fills of the East Bay. However, the boundary curve proposed by Robertson and Woeller (1992, in press) did not capture a number of points for liquefiable layers at the Port of Richmond and Port of Oakland and may be slightly unconservative. A tentative liquefaction boundary curve in normalized shear wave velocity - cyclic stress ratio space is proposed, based on our data from the East Bayshore hydraulic fill deposits. Additional data from these sites for zones that did not liquefy during the Loma Prieta Earthquake would be helpful for further validation of the liquefaction potential curves.

ACKNOWLEDEMENTS

Funding for the field testing was provided by the United States Geological Survey and the Joint University of California, Berkeley - Shimizu Corporation Research Program on Cone Penetration and Shear Wave Velocity Methods for Assessment of Liquefaction Potential. This support is greatly appreciated.

REFERENCES

American Society for Testing and Materials, 1986, Standard Method for Quasi-Static, Cone and Friction Cone Penetration Test of Soil, ASTM D3441-86.

American Society for Testing and Materials, 1984, Standard Method for Penetration Test and Split-Barrel Sampling of Soils, ASTM D1586-84.

Campanella, R.G., and Robertson, P.K., 1982, State-of-the-Art in In-Situ Testing of Soils; Developments Since 1978, Proceedings, Engineering Foundation Conference on Updating Subsurface Sampling of Soils and Rocks and Their In-Situ Testing, Santa Barbara, 23 p.

Hardin, B.O., and Drnevich, V.P., 1972, Shear Modulus and Damping of Soils: Measurement and Parameter Effects, Journal of Soil Mechanics and Foundation Division, ASCE Vol. 98, No. SM6, Proc. Paper 8977.

Farrar, Jeffrey A., 1991, Field Energy Measurements of Standard Penetration Testing, unpublished Masters Thesis: University of Colorado at Denver.

Mitchell, J.K., and Tseng, D.-J., 1990, Assessment of Liquefaction Potential by Cone Penetration Resistance, James Duncan, ed., Proceedings, H. Bolton Seed Memorial Symposium, Vol. 2., p.

Robertson, P.K., 1986. In Situ Testing and its Application to Foundation Engineering, Can. Geotech. Jour., Vol.23, No.4, pp.573-594.

Robertson, P.K. and Campanella, R.G., 1985. Liquefaction of Sands Using the CPT, Jour. Geot Div., ASCE, Vol. 111, GT3, pp. 384-403.

Robertson, P.K., Campanella, R.G., Gillespie, D., and Rice, A., 1986. Seismic CPT In Situ Shear Wave Velocity, Jour. Geot Div., ASCE, Vol. 112, No. 8, pp. 781-803.

Robertson, P.K., 1990. Soil classification using the Cone Penetration Test, Can. Geotech. Jour., Vol.27, No.1, pp. 151-158.

Robertson, P.K. and Woeller, D.J., in press, Seismic Cone Penetration Testing for Evaluating Liquefaction Potential, Can Geotech. Jour.

Schnabel, P.B., Lysmer,J., and Seed, H.B.,1972, SHAKE:-A Computer Program for Earthquake Response Analysis of Horizontally Layered Sites, Earthquake Engineering Research Center, Report No. UCB/EERC-72/12, University of California, Berkeley, December 1972.

Seed, H.B., and deAlba, P., 1986, Use of SPT and CPT Tests for Evaluating the Liquefaction Resistance of Sands, Use of In-Situ Tests in Geotechnical Engineering (GSP 6), S.P. Clemence, ed., ASCE, New York, pp. 281-302.

Seed, H.B., and Idriss, I.M., 1971, Simplified Procedure for Evaluating Soil Liquefaction Potential, Journal of the Soil Mechanics and Foundations Division, ASCE, 97:SM9, pp.1249-1273.

Seed, H.B., and Idriss, 1982, Ground Motions and Soil Liquefaction During Earthquakes, Earthquake Engineering Research Institute, Berkeley California.

Seed, H.B., Idriss, I.M., and Arango, 1983, Evaluation of Liquefaction Potential Using Field Performance Data, Journal of Geotechnical Engineering, ASCE 109(3):458-482.

Seed, H.B., Tokimatsu, K., Harder, L.H., and Chung, R.M., 1984, The Influence of SPT Procedures in Soil Liquefaction Evaluations, Earthquake Engineering Research Center, Report No. UCB/EERC-84/15, University of California, Berkeley, October 1984.

Seed, R.B., Dickenson, R.B., Reimer,M.F., Bray, J.D., Sitar, N., Mitchell, J.K., Idriss, I.M., Kayen, R.E., Kropp, A., Harder, L.F., Jr., Power, M.S., 1990, Preliminary geotechnical aspects of the October 17, 1989 Loma Prieta earthquake., Earthquake Engineering Research Center, Report No. UCB/EERC-90/05, University of California, Berkeley, April 1990.

Shakal, A., Huang, M., Reichle, M., Ventura, C., Cao, T., Sherbourne, R., Savage, M., Darragh, R., and Petersen, C., 1989, CSMIP Strong-Motion Records from the Santa Cruz Mountains (Loma Prieta), California Earthquake of 17 October 1989, Calif. Div. Mines and Geol. Report OSMS 89-06.

U.S. Geological Survey, 1989, Lessons Learned from the Loma Prieta Earthquake of October 17, 1989, George Plafker and John P. Galloway, eds., U.S. Geological Survey Circular 1045.

Wroth, C.P., 1984, Interpretation of *In situ* soil test, 24th Rankine Lecture, Geotechnique, 34:449-489.

Table 1: Representative values of peak acceleration, q_{c1}, $(N_1)_{60}$, V_{s1}, and cyclic stress ratio (CSR) for critical soil layers at East Bay shoreline sites.

Liquefaction Resistance Data for Soils Tested at East Bay Shoreline Sites							
Boring ID	Depth (m)	a_{max} (g)	q_{c1} (MPa)	$(N_1)_{60}$	V_{s1}(m/sec)	CSR	Liquefaction
POR2	5-7	.13-.18	1.0	5	178	.11-.16	YES
POR3	5-7	.13-.18	1.3	3	170	.11-.16	YES
POR4	5-7	.13-.18	2	3	170	.11-.16	YES
SFOBB1	5-7.5	.28-.29	9	10	170	.28	YES
SFOBB2	6-9	.28-.29	11	12	168	.28	YES
SFOBB3	6-8	.28-.29	9		163	.28	YES
SFOBB4	6-8	.28-.29	5		186	.28	YES
SFOBB5	6-8	.28-.29	9.4	10	172	.28	YES
POO7-1	5-8	.28-.29	12.4		177	.24	YES
POO7-2	5-7	.28-.29	10	15	177	.24	YES
POO7-3	4-7	.28-.29	15	21	195	.23	YES
POO7-3	7-12	.28-.29	17	37	252	.27	NO
POO7-5	4-6	.28-.29	13		190	.21-22	YES
POO7-6	4-7	.28-.29	10			.23	YES
ACPT3	2-5	.27	10	3		.17-.25	YES
ACPT4	2-5	.27	5	14		.17-.25	YES
ACPT7	2-5	.27	10	15		.17-.25	YES
BFI-P6	2-5	.27	12	18	178	.17-25	YES
BFI-DIKE	3-5	.27	35	32		.17-.21	NO
BFI-CPT1	2-4	.27	10	18		.17-.21	YES

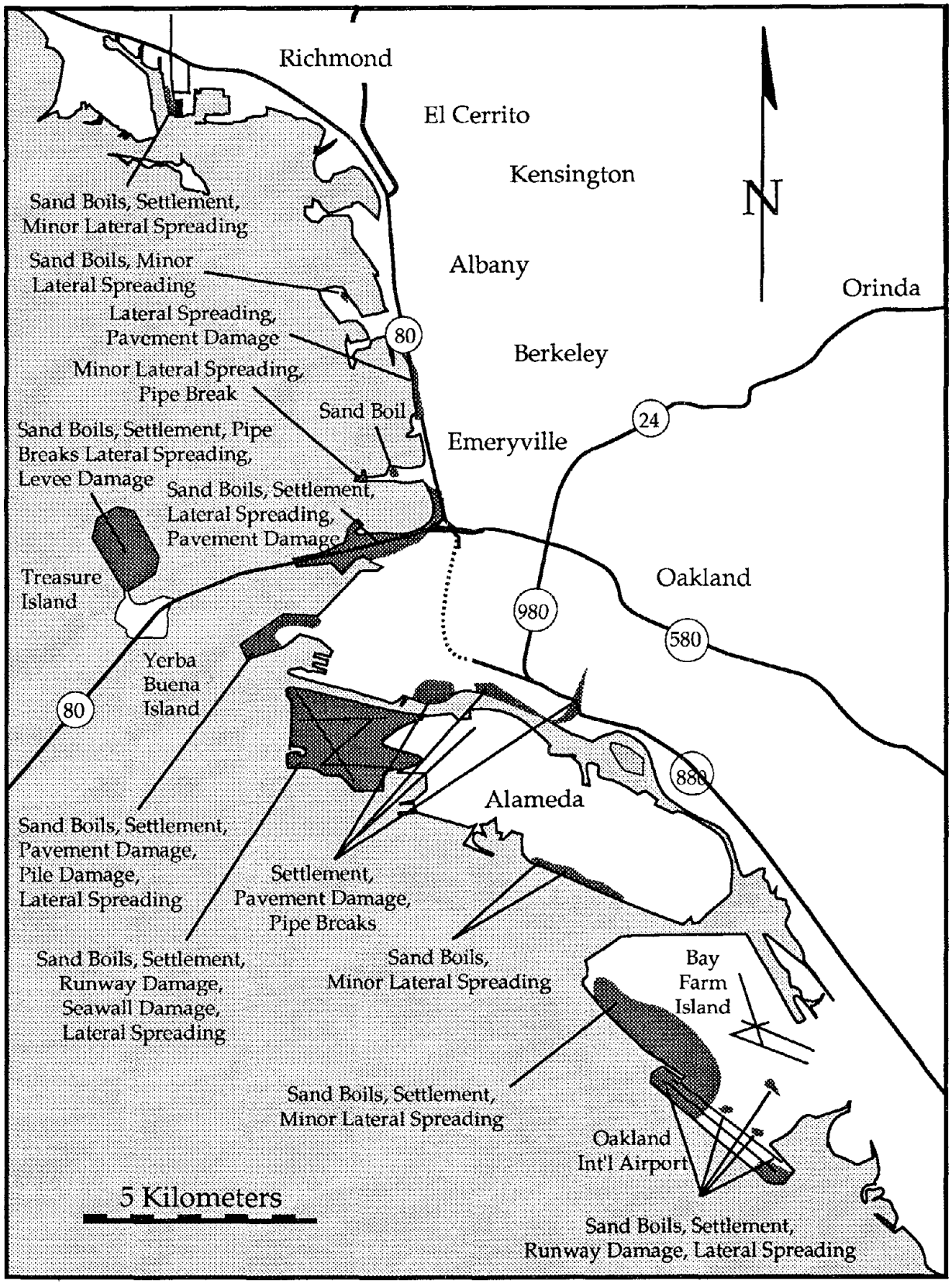

Figure 1. Map showing sites of liquefaction along the San Francisco Bayshore of Alameda and Contra Costa Counties during the Loma Prieta Earthquake.

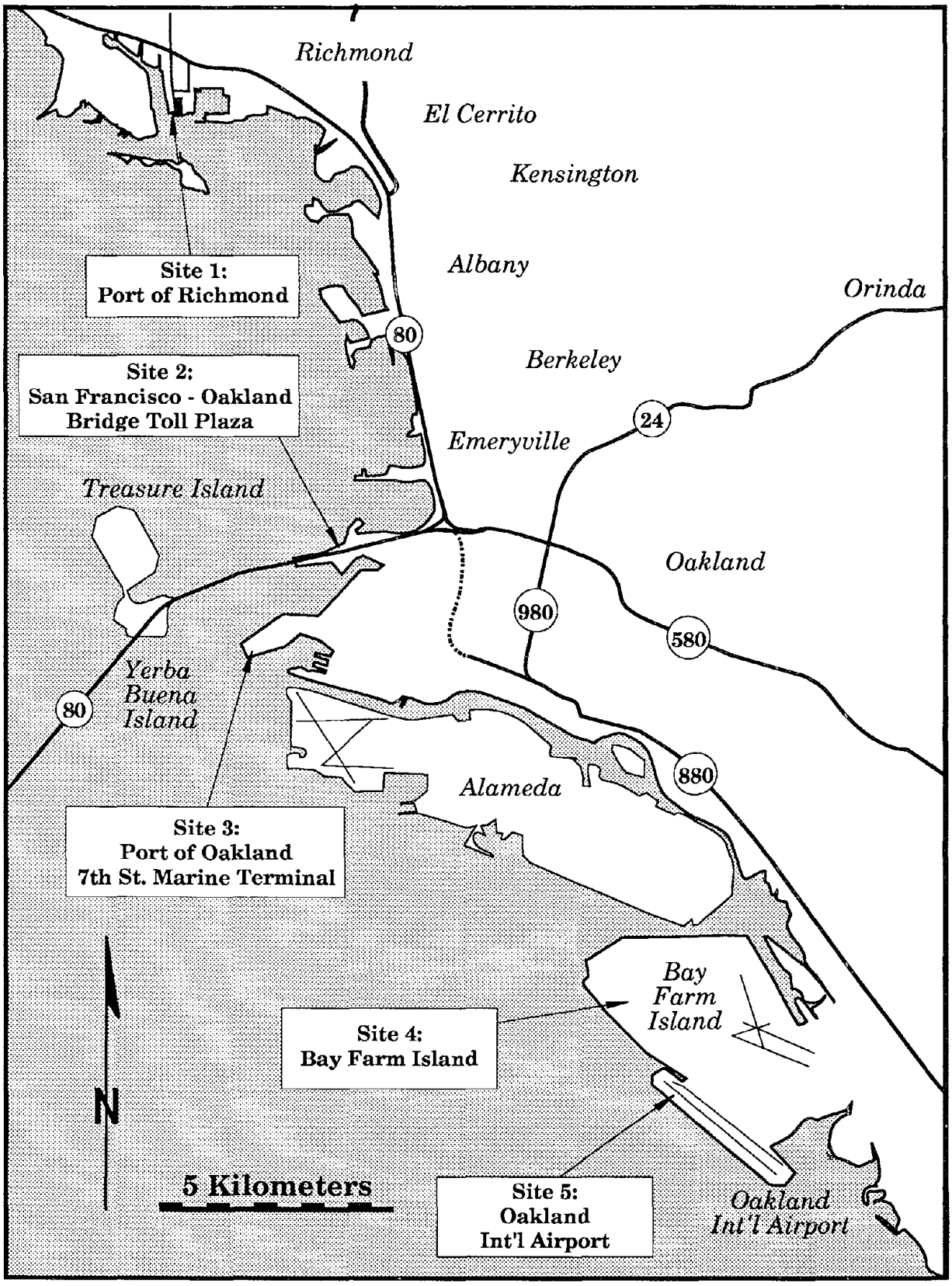

Figure 2. Sites near the East Bay shoreline where soil investigation were performed.

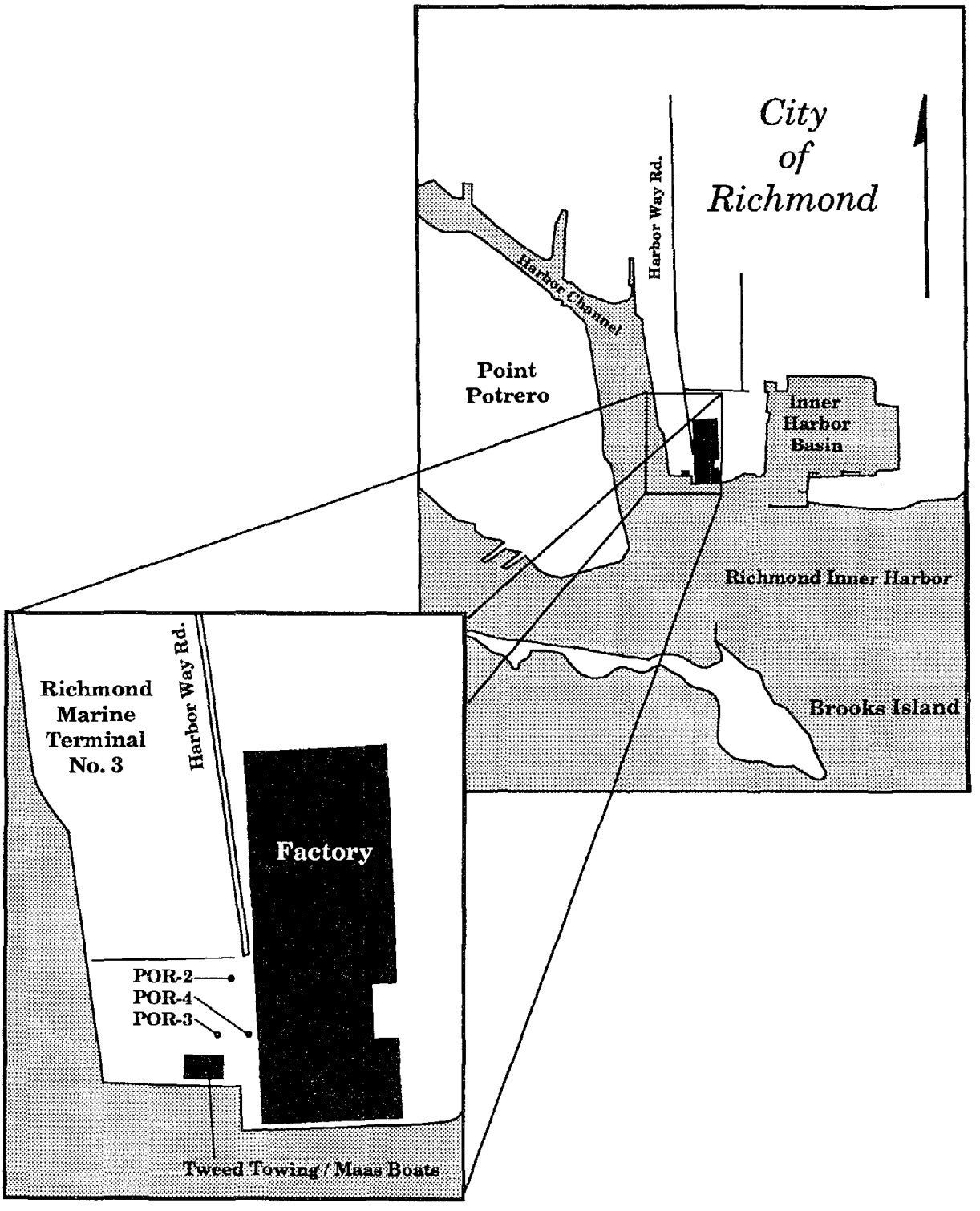

Figure 3. Map of the Port of Richmond, Inner Harbor Area.
Enlarged map shows SPT and CPT sites (black dots).

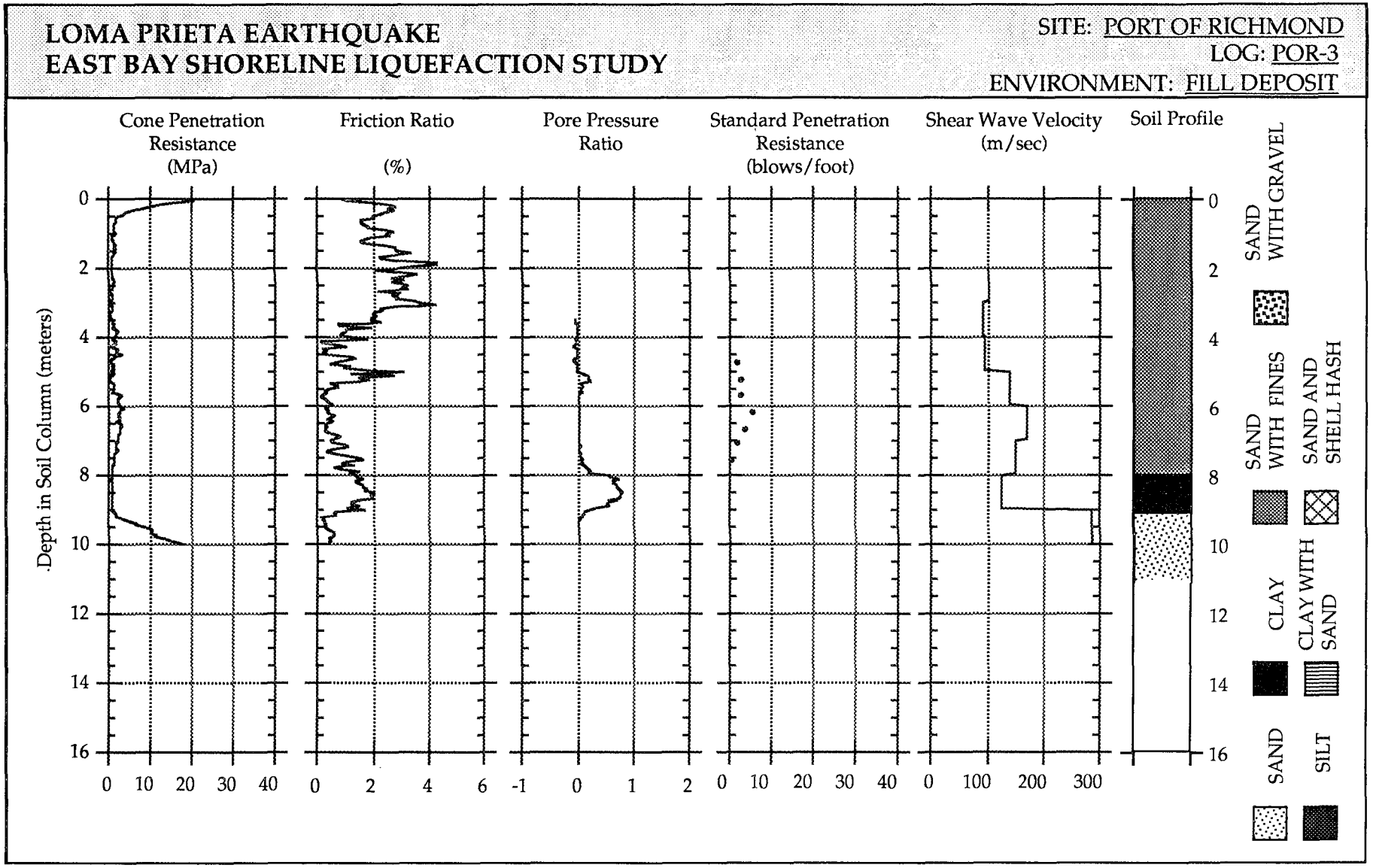

Figure 4. In-situ soil investigation log POR-3 at the Port of Richmond test site.

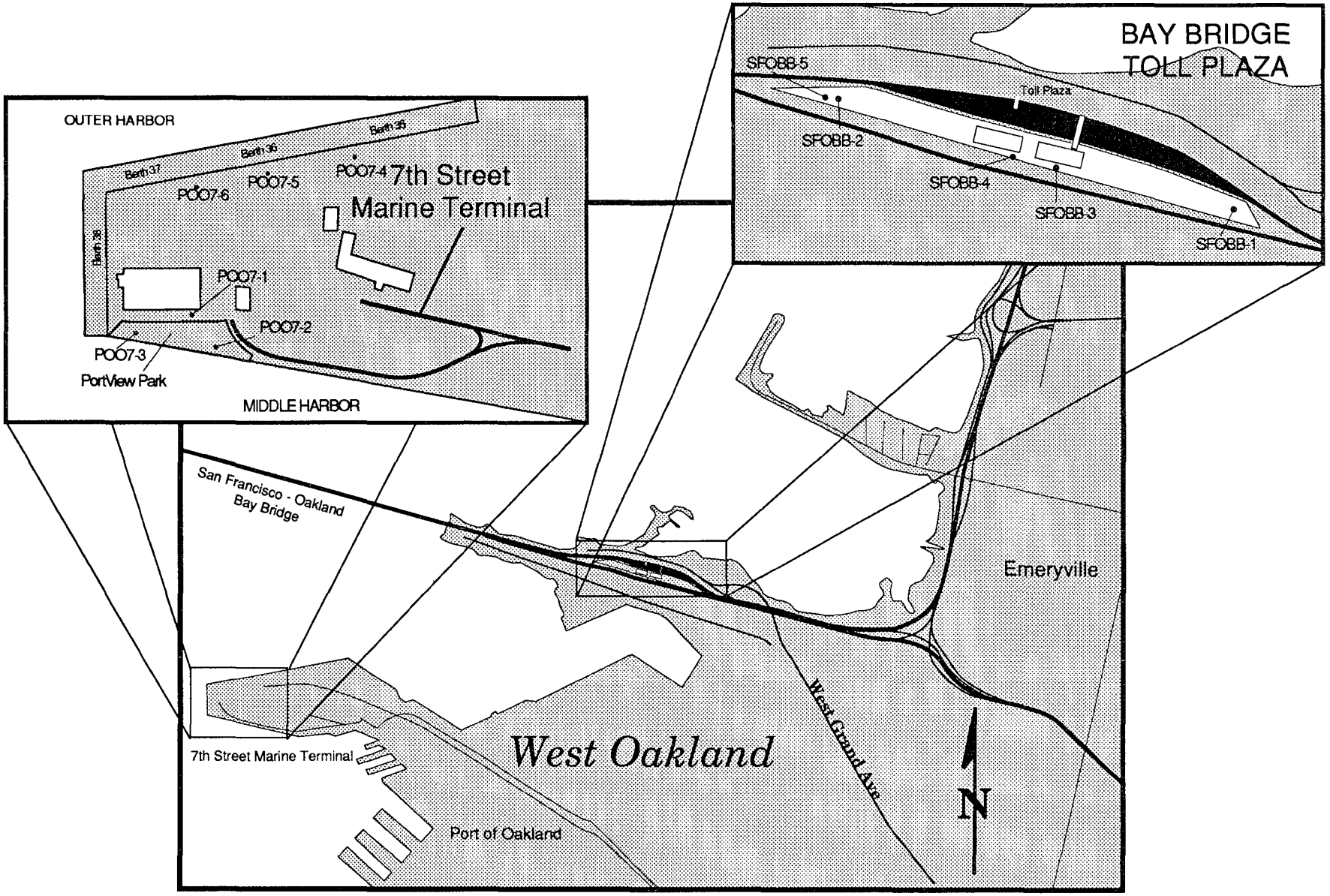

Figure 5. Map of the Emeryville and Oakland, Ca, shoreline region. Enlarged maps show SPT and/or CPT sites (black dots) near the Bay Bridge Toll Plaza and Port of Oakland.

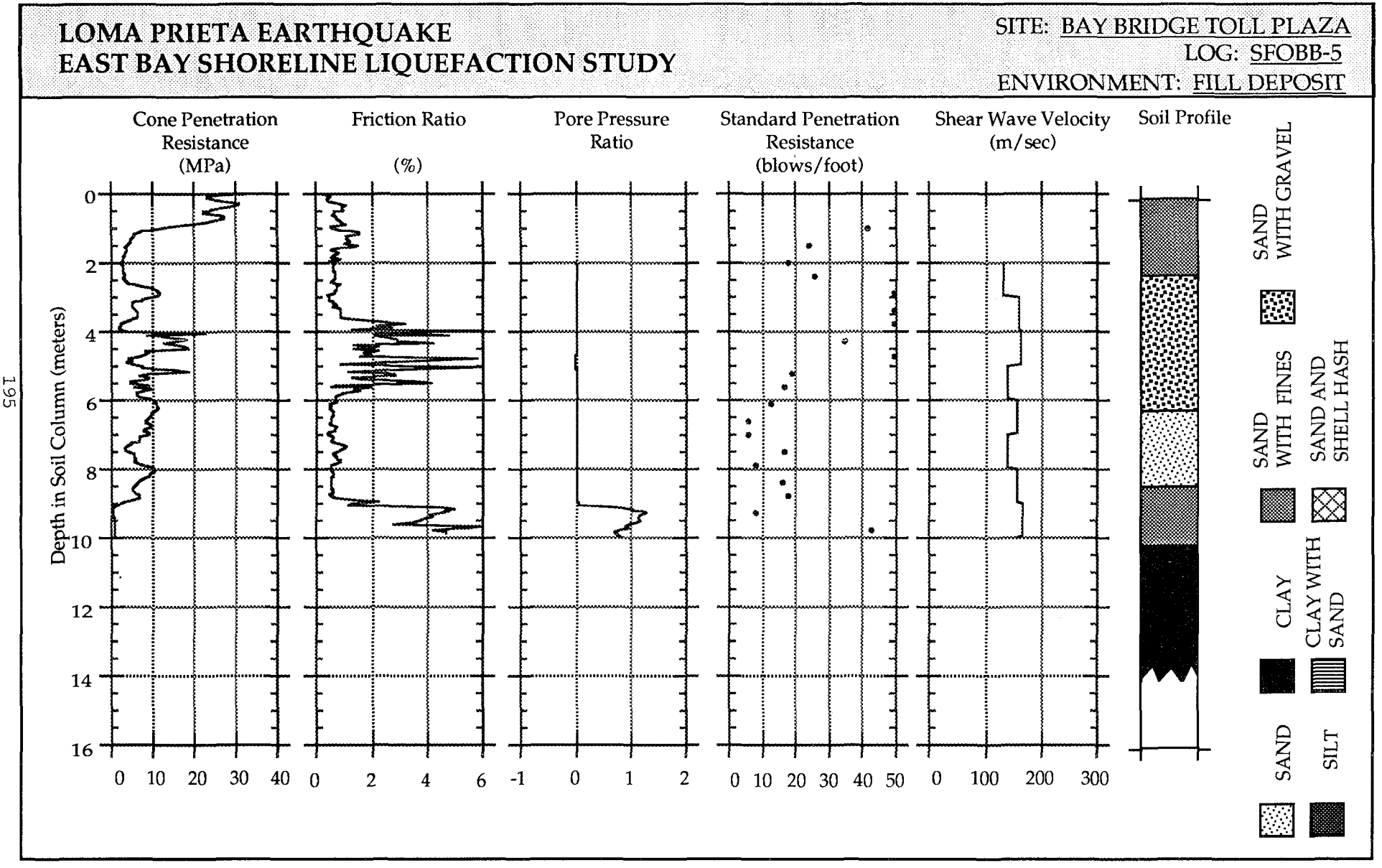

Figure 6: In-situ soil investigation log SFOBB-5 on the east shore Mole of the San Francisco - Oakland Bay Bridge.

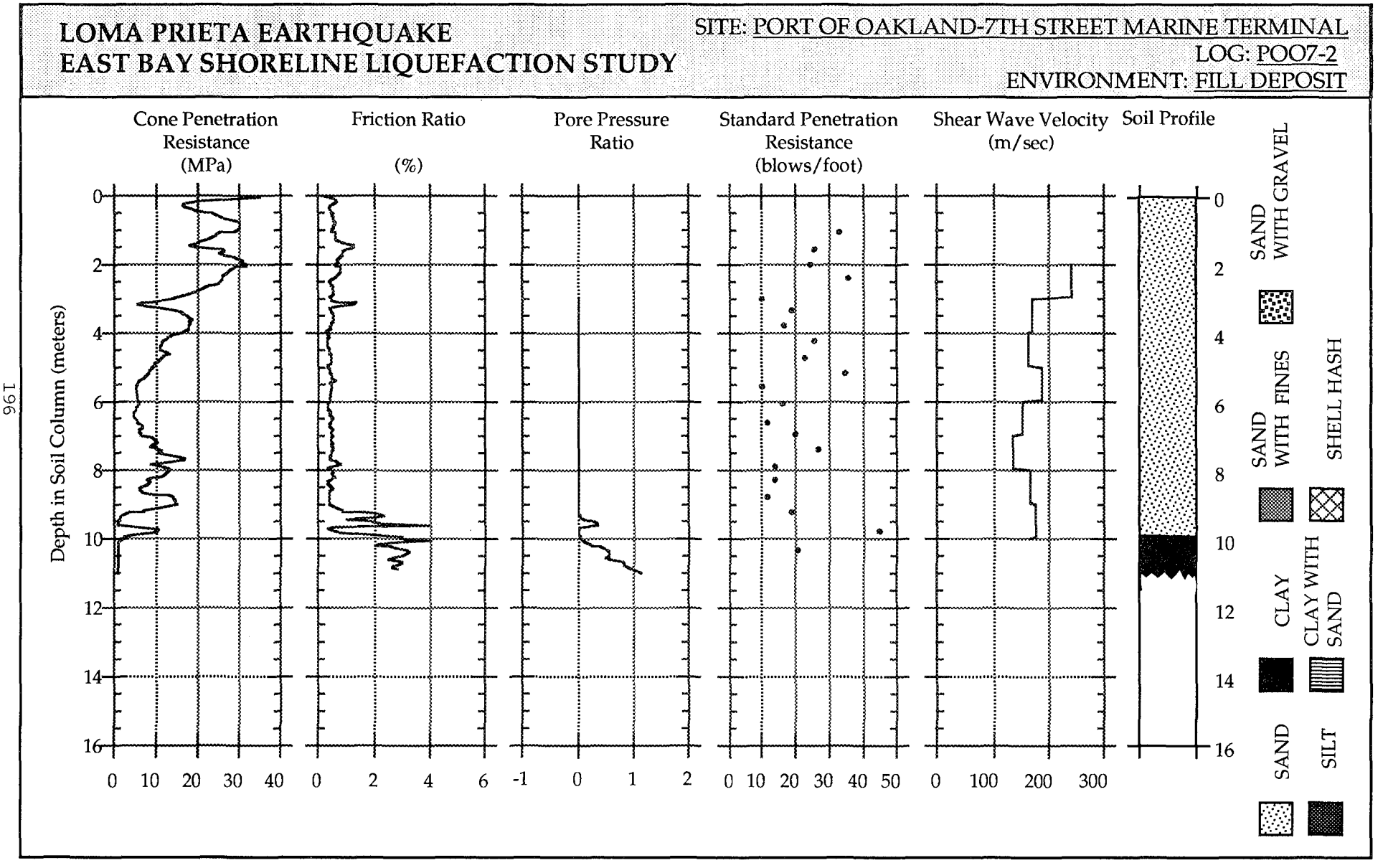

Figure 7: In-situ soil investigation log POO7-2 taken at the 7th Street Marine Container Terminal, Port of Oakland.

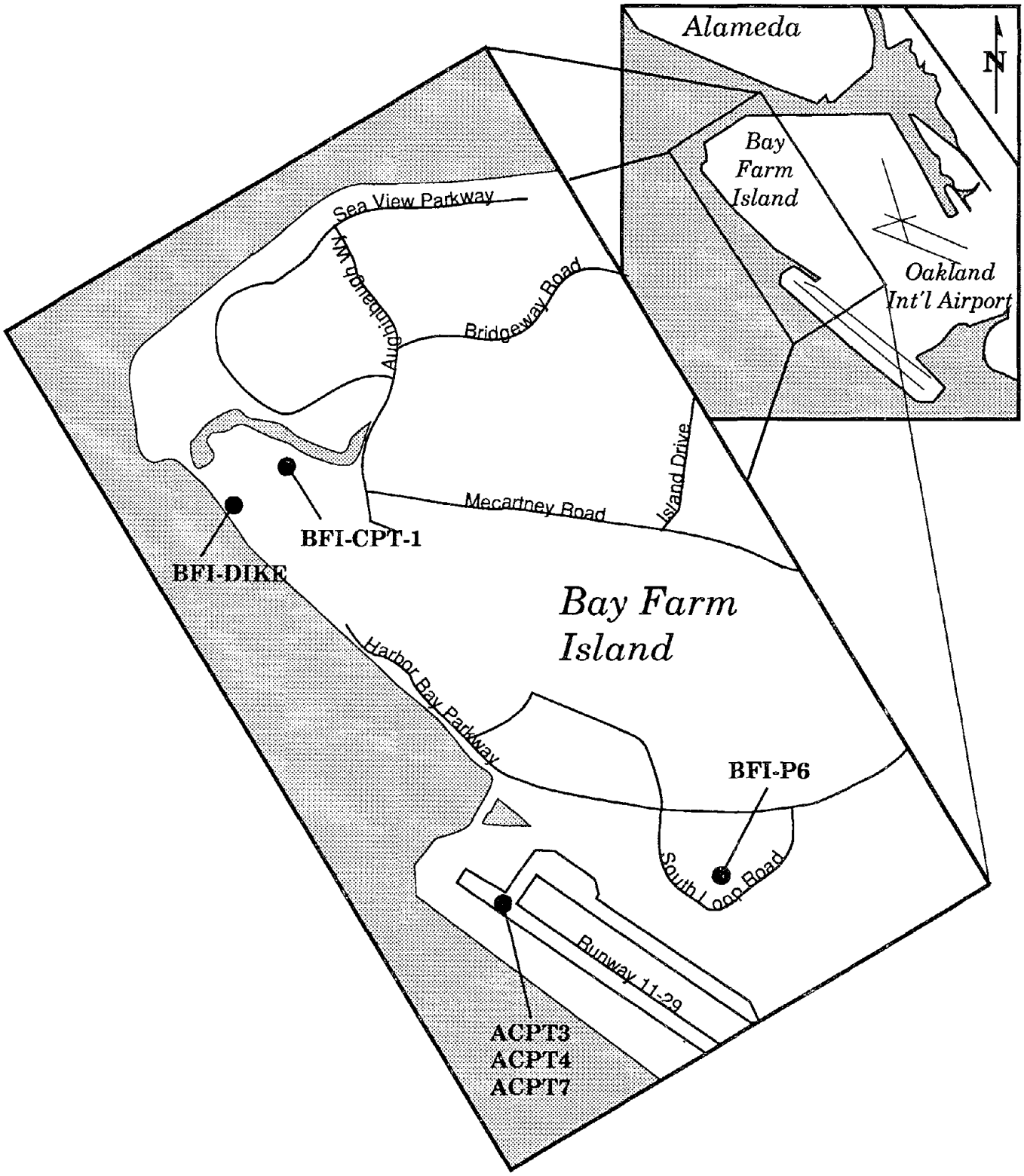

Figure 8: Map of study sites at Bay Farm Island and the northern portion of Oakland International Airport.

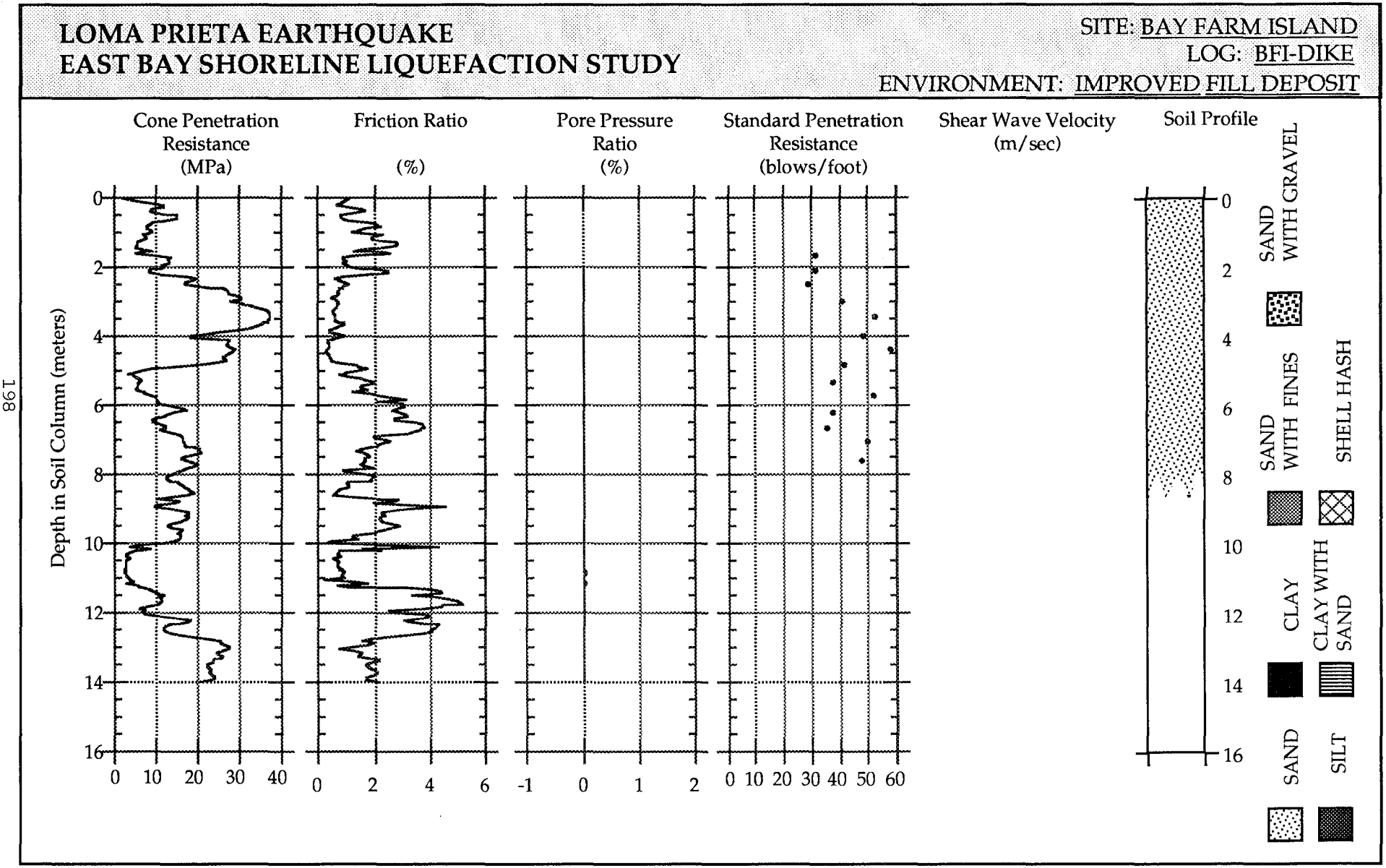

Figure 9: In-situ soil investigation log BFI-DIKE taken on the perimeter sand of Bay Farm Island near the Harbor Bay Ferry Terminal.

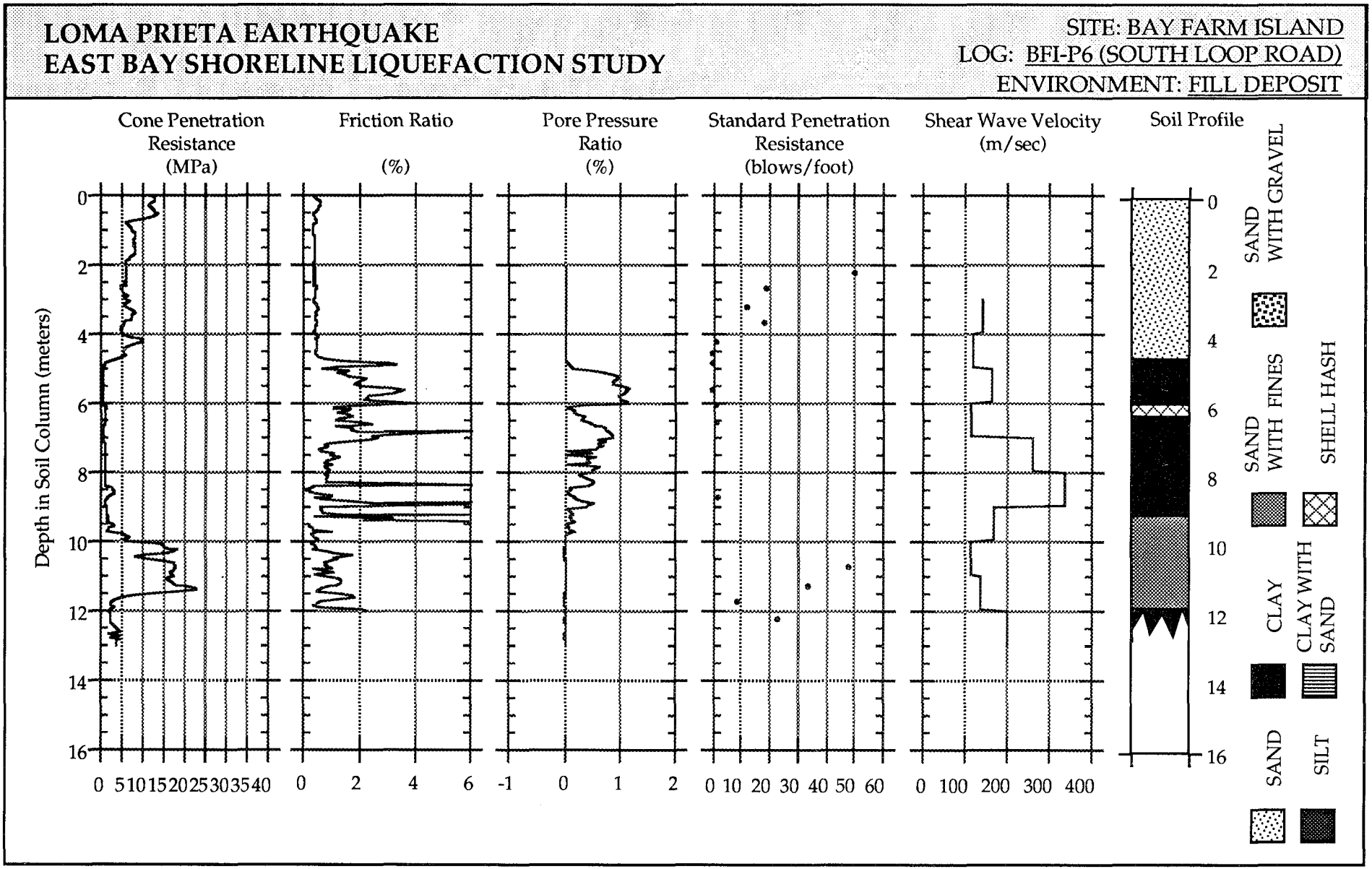

Figure 10: In-situ soil investigation log BFI-P6 taken near South Loop Road, Bay Farm Island.

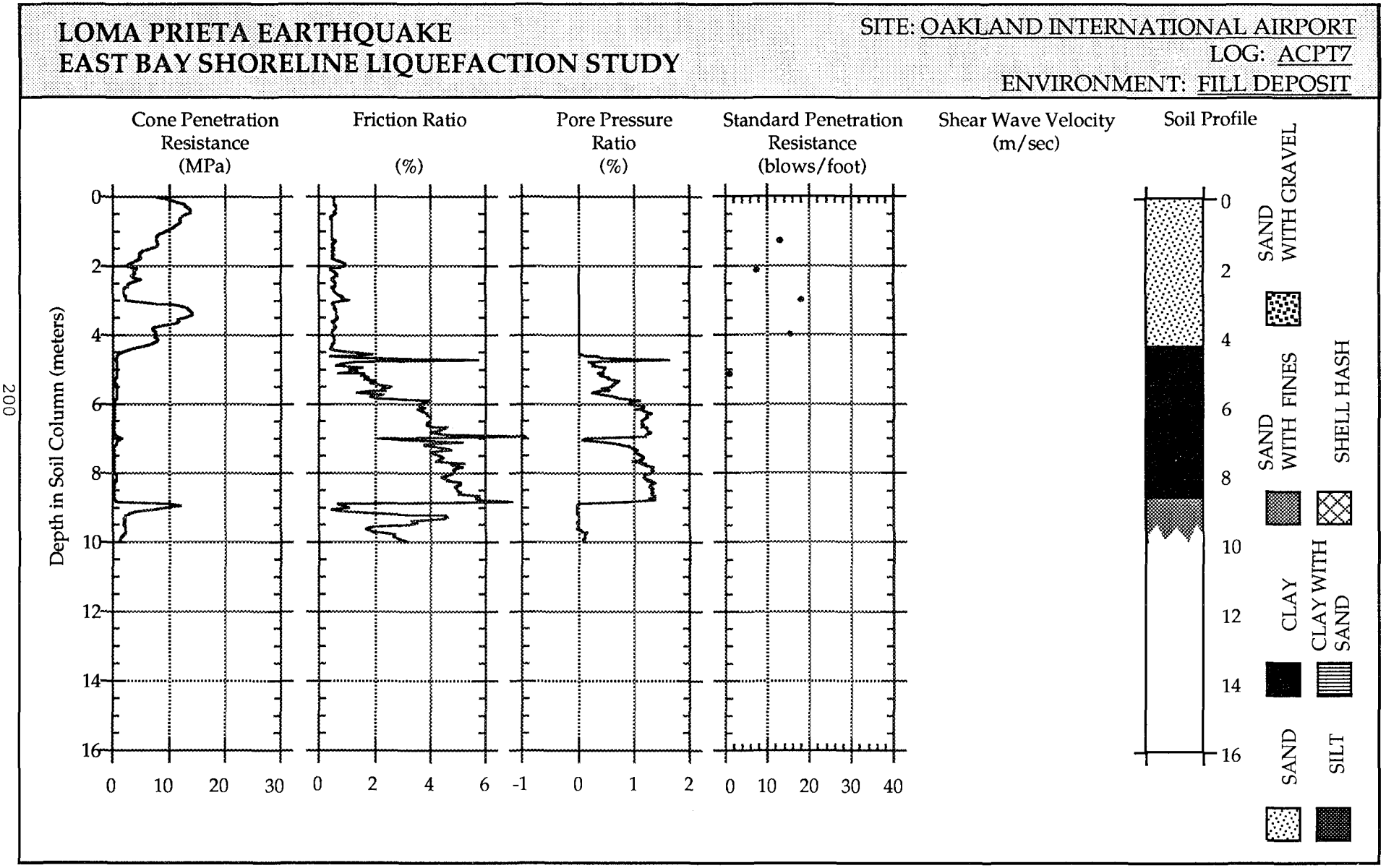

Figure 11: In-situ soil investigation log ACPT7 near the northern end of the main runway, Oakland International Airport.

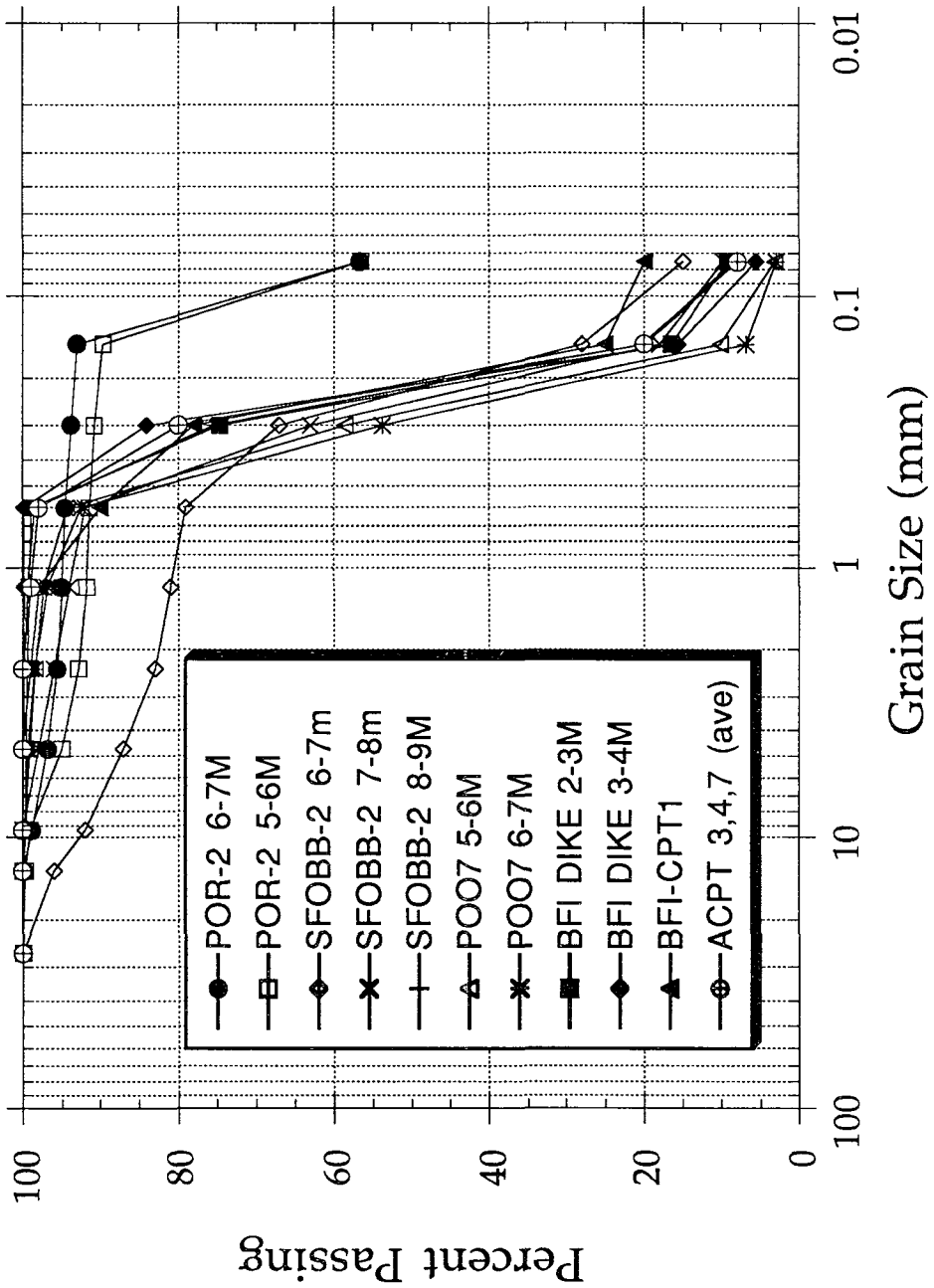

Figure 12: Grain size distribution curves for critical soil layers from the eastern shoreline area of San Francisco Bay.

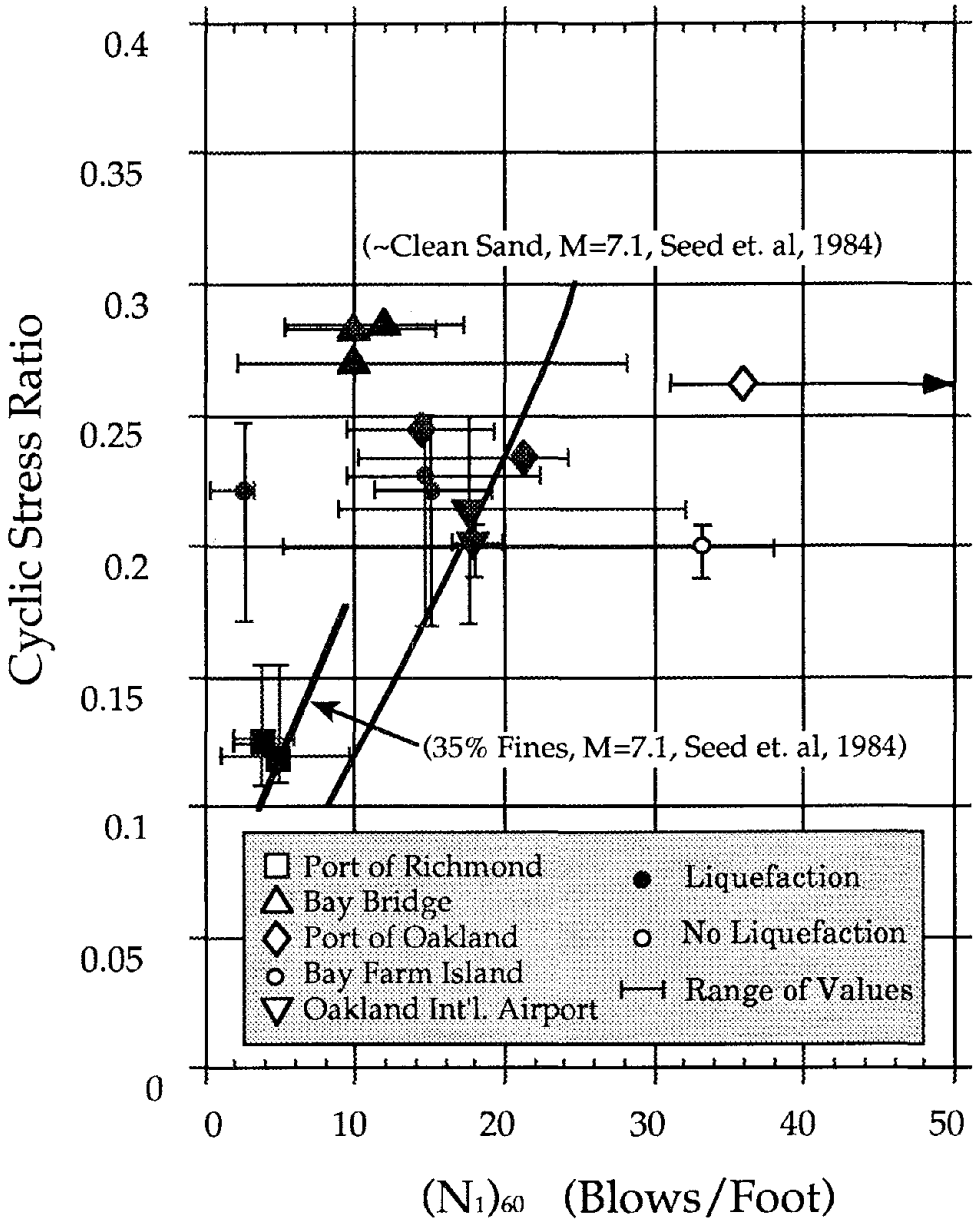

Figure 13: Standard Penetration Test Resistance, $(N_1)_{60}$, versus Cyclic Stress Ratio, CSR, estimated for the Loma Prieta Earthquake for critical soil layers along the East Bay shoreline. Filled and open symbols indicate observations regarding liquefaction.

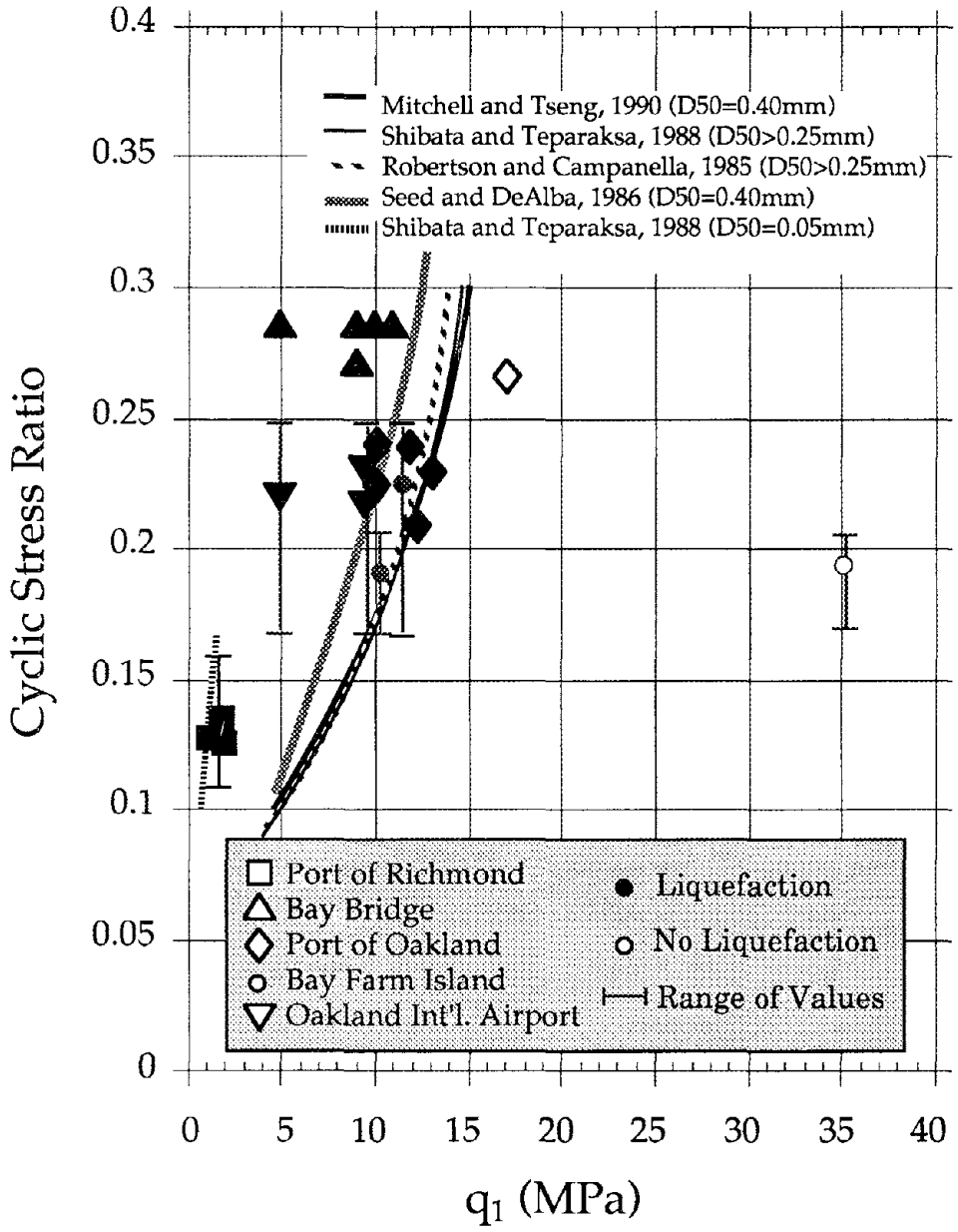

Figure 14: Cone Penetration Test Resistance, qc1, versus Cyclic Stress Ratio, CSR, estimated for the Loma Prieta Earthquake for critical soil layers along the East Bay shoreline. Filled and open symbols indicate observations regarding liquefaction.

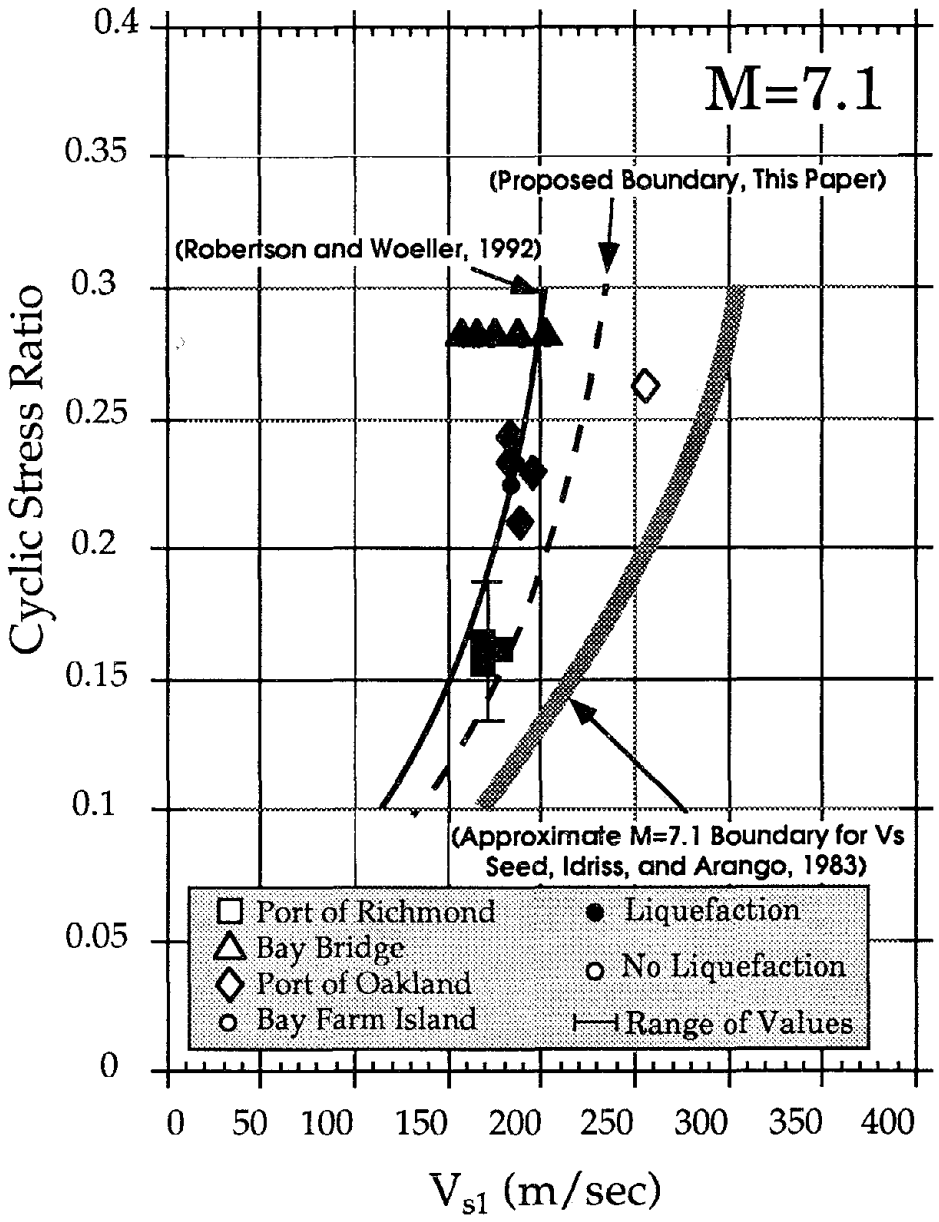

Figure 15: Overburden normalized shear wave velocity, V_{s1}, versus Cyclic Stress Ratio, CSR, estimated for the Loma Prieta Earthquake for critical soil layers along the East Bay shoreline. Filled and open symbols indicate observations regarding liquefaction.

Liquefaction Study, Sullivan Marsh and Mission Creek, San Francisco, California

Robert D. Darragh
Dames & Moore, San Francisco, California

Henry T. Taylor
Harding Lawson Associates, San Francisco, California

Charles Scawthorn
EQE International, San Francisco, California

Daniel Seidel
Kennedy/Jenks/Consultants, San Francisco, California

Charles Ng
Department of Public Works, City and County of San Francisco

ABSTRACT

The magnitude 8.3 1906 San Francisco earthquake and the magnitude 7.1 1989 Loma Prieta earthquake caused damage to lifeline facilities throughout the San Francisco Bay Area. This paper describes the geotechnical aspects of liquefaction failures in two areas of San Francisco. Utility performance during the two earthquakes is discussed in a companion paper appearing elsewhere in these proceedings. Both papers are based on the results of a liquefaction study performed for the City and County of San Francisco.

The study was based upon subsurface data from geotechnical investigations in the study areas. Widespread liquefaction and vertical and lateral ground movements occurred in the reclaimed land along the shoreline in the 1906 earthquake, and to a lesser degree, in the 1989 earthquake. The correlation between vertical settlements observed in these areas and calculated settlements where no lateral spreading displacement had occurred was poor for the 1906 earthquakes. In areas of significant lateral spreading, the strong influence of ground slope on both vertical and lateral deformation was established. The analytical studies and past empirical data provided a suitable basis for locating areas of liquefaction failures and for estimating locations of movements to be expected in a future magnitude 8.3 earthquake.

The deformation estimates were correlated with damage algorithms for expected damage to underground water and sewer utilities to estimate the extent and cost of utility repairs after a great earthquake. In addition, utility system upgrade schemes were developed to make the existing systems more resistant to future earthquake damage. Lastly, ground modification techniques were evaluated which would prevent liquefaction in selected street corridors that may be vital to system reliability.

INTRODUCTION

The liquefaction study discussed in this paper is an excerpt from a larger investigation of six shoreline areas of San Francisco damaged by earthquakes, from the Marina District on the north to Upper Mission Creek in the southern part of the city. This paper deals with only two of the six areas studied: the Sullivan Marsh Area south of Market Street, and the contiguous Mission Creek area. These were selected because they experienced the largest ground movements in 1906, and thus present useful case history data for comparison of the results of analytical and observed data. The Marina District liquefaction damage in 1989 has been reported very thoroughly in the previous papers and in this conference.

This paper compares calculations of the vertical and lateral deformations associated with liquefaction of predominantly loose dune sand fills with observed data from the 1906 earthquake. Vertical settlements were estimated using the procedure of Tokimatsu and Seed (1987). Lateral deformations were evaluated using the procedure of Towhata et al. (1990).

The studies described in this paper were performed by a team of geotechnical and civil engineering firms: Harding Lawson Associates, Dames & Moore, Kennedy/Jenks/Consultants, and EQE International, under contract to the City and County of San Francisco Public Works Department.

SITE CONDITIONS

The Sullivan Marsh and Mission Creek areas as they existed prior to filling are shown on Figure 1, a Coast Survey Map of 1856. The predominant fill materials in both of these areas are dune sands obtained from adjacent areas of San Francisco. In 1906, both areas were occupied primarily by light, wood-frame houses and commercial and industrial buildings.

For analyses of site response and liquefaction in Sullivan Marsh, 13 sites were selected within and bordering the former marshland where prior geotechnical investigations had been performed. The available subsurface information was used to characterize the earthquake response characteristics and the liquefaction potential of the fills in these areas. The 13 sites are shown on Figure 2. Subsurface conditions in the Sullivan Marsh area are as follows: at the surface is a layer of fill 10 to 25 feet thick consisting principally of uniform fine to medium sand with a trace of silt. The fill thickness can vary within short distances reflecting the effects of ground failures associated with reclamation processes. (Brown et al. (1932) reported that fill "settlements" of as much as 6 feet could occur the night after fill placement due to the displacement of the soft Bay Mud into the waves.) These dune sand fills are very loose to medium dense. Standard penetration resistances (N) varied from a low of 2 to a maximum of 24. The higher N values usually occurred in areas of greater fill thicknesses, sometimes partially due to the greater depth of groundwater. In most of the Sullivan Marsh area, the fill is underlain by soft Bay Mud. In the southern lobe, and near Mission Street in the northern lobe, up to 10 feet of peat was encountered in the borings. Bay Mud underlying the northern lobe of the Marsh has a maximum thickness of 50 to 70 feet near Howard Street. Beneath the Bay Mud are older Bay Clays and alluvial deposits. Depth to bedrock varies from about 50 feet

to more than 200 feet. Groundwater levels vary from 5 to 15 feet below existing ground surface. The steepest surface slope, in Sullivan Marsh near Mission Street, is about 2%. At the southerly end, near the Old Mission Bay, the surface slopes are less than 0.5%.

Thirteen additional study areas were selected to represent the variations in subsurface conditions and site response effects in the Mission Creek area, as shown on Figure 2. The subsurface conditions in the Mission Creek area are highly variable in all significant aspects: thickness of liquefiable sands, Bay Mud thickness and depth to rock. At the Mission Street crossing of the former creek border, the fill varies from 24 to 28 feet in thickness with N values as low as 2, and Bay Mud is thin or absent. The maximum ground surface slope in the steepest area of Upper Mission Creek normal to the section between Capp and Valencia Streets is about 1.3%. Between Capp and Folsom Streets, the slope flattens to about 0.8% along the northerly arm of old Mission Creek. Easterly of Folsom Street to the Old Mission Bay outlet of Mission Creek, the slopes are less than 0.2%.

Within the old watercourse area of Mission Creek the fill is underlain by soft Bay Mud, organic silts, and in some cases, peat. Outside the limits of the old watercourse, and particularly in the southern section of the area, the fill is underlain by a variety of recent sediments, ranging from loose to dense clayey sands, dense fine to medium sands, and dense silty sands, which are not considered susceptible to liquefaction. Below the Bay Mud, where it exists, there is a series of alluvial sediments in the upper reaches of the old creek, while at the mouth of the creek, both alluvial and old Bay Clay deposits were encountered. These older sediments are typically very dense to very stiff.

Depth to bedrock in Upper Mission Creek study area varies from 10 feet to 120 feet below ground in the borings; groundwater levels in vary between 6 feet and 12 feet below existing ground surface.

GROUND MOVEMENTS AND UTILITY BREAKS CAUSED BY 1906 AND 1989 EARTHQUAKES

O'Rourke et al. (1991) summarized the recorded ground deformations during the 1906 earthquake in the Sullivan Marsh area. Within the northern lobe of the marsh, lateral spreading failures occurred at several locations with movements of 5 to 8 feet horizontally near Mission Street where the ground surface slope is about 1.5 to 2%. In the Marsh northern lobe, vertical settlements ranged from 0.5 foot to 3 feet. There is no record either of ground settlements or lateral spreading in the southern lobe of the Sullivan Marsh, where the thickness of fill below the water level is limited.

At the time of the 1906 earthquake, the AWSS system did not exist and fire fighting was dependent upon supply of the municipal water supply system (MWSS). Over 23,000 service breaks and approximately 300 main breaks in the MWSS pipe were recorded in 1906 (Schussler, 1906). Approximately 50 of the 300 main breaks were located within the Sullivan Marsh area between Folsom and Mission Streets. There are no known reports of sewer damage following the 1906 earthquake in Sullivan Marsh. Duryea et al. (1907) report that where significant

ground deformations occurred south of Market Street, sewers were completely destroyed. In 1906, a 215-foot-long brick sewer on 7th Street near Mission Street was damaged in the earthquake, and a 30-foot-long brick sewer was damaged just outside the study area.

The Upper Mission Creek area suffered very severe damage during the 1906 earthquake. A large number of private residences and hotels collapsed, some of them sinking into the ground due to the loss of bearing after the loose fills had liquefied. There was significant damage to underground utilities, including failure of two water mains along Valencia Street near the western edge of the Mission Creek area. The water mains in the Upper Mission Creek area along Mission and Howard Streets suffered multiple breaks in the 1906 earthquake. Significant settlements and lateral deformations occurred, not only within the limits of the old marsh, but also in the adjacent areas. About 6 feet of lateral spreading occurred in Mission Creek in 1906, along Valencia Street between 18th to 19th Streets. Schussler (1906) reported 70 main breaks in the MWSS system within or very near the Mission Creek area.

The most notable ground movement in the 1989 earthquake was recorded at the corner of 7th and Natoma Streets, where 1 foot of vertical settlement was noted by O'Rourke (1990). In this area, a significant water main break occurred to the auxiliary water supply system (AWSS) in 1989. This break, combined with hydrant branch breaks in the South of Market area, drained the emergency firefighting water supply in the lower areas of San Francisco, including the Marina District, within 30 minutes. Full pressure was restored to the AWSS system within 4 hours after the earthquake. In 1989, less sewer damage was observed in Sullivan Marsh area than in the Marina District, due to the smaller inventory of vulnerable, rigid-joint vitrified clay pipe in Sullivan Marsh. Outside of the Marina in 1989, damage to the MWSS system was limited, with only 7 repairs being required in the Mission Creek area, compared to 123 in the Marina. The extent of damage to sewers in the 1906 earthquake in Mission Creek is unknown. In 1989, even in the area of the largest ground movements, little damage to sewers was noted.

DESIGN EARTHQUAKE GROUND MOTIONS

During the initial phase of this liquefaction study, site response analyses were performed so that the effect of variations in ground acceleration levels on liquefaction could be evaluated. For Sullivan Marsh, three soil profiles with depth to rock varying from 55 to 200 feet were selected for site response studies, using the 1989 version of U.C. Berkeley's computer program SHAKE.

The computed maximum accelerations of two of the sites, with depth to rock of 55 feet and 166 feet, ranged from 0.46 to 0.54 at the ground surface to about 0.34g at the bottom of the fill. The third site, which included a thin peat layer, had a computed ground acceleration that was significantly less at the ground surface, 0.38g. Similar reductions with depth have been reported by Kenai (1983) and Tsai (1990). Based primarily on engineering judgment and the recognition of the limitations of the SHAKE program in modeling high strain motions in soft Bay Mud and peat sediments, the peak ground accelerations used for liquefaction settlements in the Sullivan Marsh area were chosen as follows: 0.38g for areas where peat is present and 0.45g for all other areas.

In the liquefaction analysis, using Tokimatsu and Seed's procedures, the differences in computed peak ground accelerations for a 1906 earthquake were not significant, due to two factors:

1. Even for the densest fills (N = 25) the threshold ground motion accelerations causing liquefaction were about 0.25g, with minimum calculated accelerations of 0.38g at the ground surface and 0.34g at the base of the fills. Even the densest fills liquefied.
2. For the very loose to loose sands (N < 10) volumetric strain associated with post-liquefaction settlements varies dramatically, from 10% at N = 1 to 0.2% at N = 10. Unfortunately, variations in field procedures can result in inaccurate N values for these low relative density sands.

LIQUEFACTION ANALYSES

The evaluation of liquefaction effects involved two separate calculations: 1) the amount of vertical settlements that would be created by dissipation of excess pore water pressures in liquefied sand ignoring lateral spreading effects and the development of sand boils; and 2) the calculation of the downslope component of lateral deformation in areas of suspect lateral spreading.

Vertical Settlement

The vertical settlement component was calculated utilizing a procedure developed by Tokimatsu and Seed (1984). Table 1 presents a summary of the calculated vertical settlements in Sullivan Marsh for 11 of the 13 sites studied. Table 2 presents similar data for the 13 sites in the Upper Mission Creek area. Multiple entries for a given site represent the variation in liquefiable sand thickness and N values in the borings. The presence or absence of peat in the soil profile was also noted since it reduced the ground acceleration; however, the reduction was not enough to lessen settlements, as previously stated.

Calculated vertical settlements for an 8.3 magnitude event varied from 0.4 inch to 6.7 inches in Sullivan Marsh and less than 0.1 inch to 9.0 inches in Mission Creek. Unfortunately, for correlation with analytical results, there are few locations near the sites where vertical settlements alone were recorded in past earthquakes. Understandably, most of the reported data are for the more obvious and significant lateral spreading locations where both vertical and lateral deformations occurred. At 6th and Howard Streets, vertical ground settlement of 0.9 meter (36 inches) occurred at the edge of the marsh and may be related to unreported lateral spreading. The closest study site to this location is Site No. 3, with calculated settlements of 0.7 to 2.9 inches, hardly a good correlation. At 4th and Harrison 0.2m (8 inches) of settlement occurred in 1906, versus calculated values of 1.2 to 5.3 inches at Site No. 6 one-half block away and 7.3 inches at Site No. 12 on 4th Street north of Harrison. The 7.3 inches versus 8 inches correlation at Site 12 No. is excellent, but may be a coincidence, as there is only one boring nearby. The lower values calculated for Site No. 6 call attention to the likely significant variations over short distances.

For the 1989 earthquake, O'Rourke et al. (1990a) reported 0.3 meter (12 inches) of settlement at Natoma and 7th Streets near Site No. 2. This location is close to the site of a major rupture in the auxiliary water system in 1989. Calculated settlements for a 1906 earthquake at Site No. 2 were only 1.2 to 2.4 inches, again, a very poor correlation even with the less severe ground shaking conditions of 1989.

The poor correlation between observed and calculated settlements is primarily due to the limitation in the assumption in the Towhata and Seed method that the settlements are due only to pore pressure dissipation effects; sand boil effects or any vertical component of lateral spreading were ignored. Also, for this study there is considerable uncertainty in the knowledge of critical soil parameters, namely fill thickness and N values; both vary significantly over short distances due to non-engineered fills placed over mud flats where shear failures occurred during grading.

The southern lobe of Sullivan Marsh presents an interesting case history, in that adverse liquefaction effects could have been suspected in this dune sand filled marsh, but were not reported in either the 1989 or 1906 earthquakes. In this case, there is good correlation between calculations and observations. For Site No. 4, 0.4 inch to 0.9 inch of settlement was calculated for a magnitude 8.3 earthquake. Although somewhat lower ground motions may have occurred due to the presence of peat, that factor is not considered significant. Instead, the more plausible explanation is that the southern lobe of Sullivan Marsh has very limited thickness of liquefiable sands (3 feet) below the groundwater table in the Site No. 4 borings, where the calculated settlements were less than 1 inch. Earthquake-induced settlements of this small magnitude are not likely to be noticed in a former marshland where prior areal fill settlements occurred.

Lateral Deformation Analysis

Given the poor correlation between calculated and observed liquefaction effects for vertical settlements, it is optimistic to presume that greater accuracy can be obtained in calculating lateral deformations. Nevertheless, because of the adverse impact of lateral deformations on underground utility connections, an attempt was made to calculate lateral deformations for the 1906 earthquake using the procedure recently developed by Towhata et al. (1990).

This method was employed for the northern lobe of Sullivan Marsh's soil conditions and the ground surface profile shown on Figure 2. The groundwater and liquefiable soil conditions used for the Towhata analysis are shown on Figure 5 along with a plot of the results, i.e., the horizontal displacement of the ground surface for an 8.3 magnitude event. The results of two analyses are shown, one where the residual shear strength of the liquefied layer was taken at 10 pounds per square foot and the modulus of non-liquefied fill at 600 ksf (Case 2), and the other for a residual shear strength of 0 psf, such as Towhata used for his correlations, and a modulus value of 1,300 ksf (Case 1). The differences between these two cases are minor (less than 15%). The magnitude of the calculated horizontal displacement is primarily influenced by the street slopes. For the steeper slopes (2%) between Mission and Howard Streets, about 7 feet of horizontal displacement was calculated. Somewhat surprisingly, the correlation between observed and calculated lateral displacements is remarkably good. Lateral movements in 1906

at 7th and Mission from 1.5 to 2.4 meters (4.9 to 7.9 feet) were reported by O'Rourke et al. (1990b). The lateral spreading movements at this location were 4.9 feet.

For the flattest slopes (0.25%) between Folsom and Harrison Streets, the calculated horizontal displacements decreased from about 5 feet to 1 foot along the profile through the center of the marsh. No lateral ground movements were reported along the profile, possibly due to the fact that most of this sector is between streets where few observations of ground displacements were made. At the edge of the marsh, lateral spreads of 0.7 to 1.8 meters (2.9 to 5.9 feet) were observed at 5th and Folsom Streets in 1906 and 1.5m (4.9 feet) at 4th and Brannan.

O'Rourke et al. (1991) provide a comprehensive summary of the damage to utilities within the Upper Mission Creek area. Significant settlements and lateral deformations occurred not only within the limits of the old marsh, but also in adjacent areas, where original depressions were probably filled in at the same time as the marsh and water course areas.

The largest recorded movements in 1906 were in the Upper Mission Creek area. Lateral movements of 5 to 8 feet and settlements of 5 to 6 feet were recorded along Valencia Street between 18th and 19th Streets, where many buildings collapsed, including the four-story Valencia Hotel, resulting in numerous fatalities.

Along 19th Street, lateral movements up to 6 feet were recorded within what appeared to be an old (surface depression) ravine between Valencia and Guerrero Streets. Settlements of up to 2 feet were also recorded a short distance north of the area where the lateral deformations occurred. This location is south of the Upper Mission Creek area.

Somewhat smaller lateral deformations and settlements were recorded along Mission, Capp and Howard Streets, with essentially all recorded movements confined within the limits of the old marsh. Along Mission Street, lateral movements were less than 1 foot, while on Capp and Howard Streets, lateral movements up to 4 feet were recorded. Settlements up to 5 feet were also recorded in the area between Mission and Howard Streets (now South Van Ness).

In the area bounded by the limits of the old marsh between 11th Street and the James Lick Freeway, there was also a heavy concentration of pipeline breaks. Street settlements in this area are also indicated in Schussler's report (1906). O'Rourke et al. (1991) reported that large ground movements (from 0.5 to 6 feet) developed within a relatively small area bounded by Bryant, Brannan, and 9th and 10th Streets. Corresponding lateral displacements range from as little as 0.4 foot lateral offset to about 8 feet of lateral spreading. This is a relatively flat area, and the large lateral movements are surprising. O'Rourke et al. (1991) attribute these large movements to the presence of a small tributary of Mission Creek running along Dore Street between Brannan and Bryant. Assuming that this tributary was filled with liquefiable soil, the non-uniformity in subsurface conditions within a relatively short distance may be the cause of these otherwise unexplainable and surprisingly large ground movements. Similarly large and unexplainable movements were observed in the Sullivan Marsh area at the corner of 4th and Brannan Streets, and near 6th and Bluxome Streets. All of these areas seem to have the common characteristic of being along the border of either the old creek or old shoreline or both.

During the 1989 earthquake, there was a notable absence of ground movements and damage to buildings and utilities in the area west of Mission Street. The reasons for this are not clear but it is possible that it is in part due to the short duration of the earthquake, and also that the fills are underlain by a soil profile that did not amplify the bedrock motions sufficiently to cause liquefaction of the fills. However, there is no available soil information for areas west of Mission Street to verify this hypothesis.

East of Mission Street, liquefaction, ground movements and damage to buildings occurred principally in the area bounded by 17th and 18th Streets, and between South Van Ness and Folsom Streets. Sand boils were observed in this area. According to O'Rourke et al. (1990a), the most severe damage occurred at the middle-west side of Shotwell Street, where maximum building settlements on the order of 0.7 foot to 1.3 feet were observed. Differential settlements, tilting and racking of Victorian two- to four-story buildings occurred in the same areas and in a manner similar to those resulting from the 1906 earthquake.

Differential settlements and prominent street cracks were also observed by O'Rourke et al. (1990a) along 16th Street between Folsom and Harrison. This area is entirely within the limits of the old marsh. Differential settlements of two- to four-story timber buildings were reported on the north side of 15th Street about 100 feet west of Folsom Street, where sand boils were apparent along the curb line.

About 1 foot of subsidence was reported to have occurred in a parking lot off Dore Street, approximately 200 feet north of its intersection with Bryant Street. This area is outside the limits of the old marsh around Mission Creek, and in that respect, these movements are somewhat unexpected. In the area south of this location, however, large movements occurred during the 1906 earthquake, although the 1906 movements were entirely within the bounds of the old marsh. About 4 inches of settlement was observed on the sidewalks of the northeast corner of Dore and Bryant Streets, as well as differential movement of the building at this corner.

To evaluate lateral spreading effects in the Mission Creek area, lateral deformation analysis using the Makdisi and Seed (1978) method, as well as the method of Towhata et al. (1990) were performed. These were parametric in nature and supplement the analyses previously reported for the northern lobe of Sullivan Marsh. Their main objective was to provide a background for interpretation of observed movements during the 1906 and 1989 earthquakes.

O'Rourke et al. (1991) attempted to correlate lateral displacements resulting from lateral spreading to ground slope. Figure 4 presents the correlation developed by O'Rourke et al. (1991), based on well-documented occurrences of lateral spreading in the area south of Market (Sullivan Marsh) and Upper Mission Creek. There is a reasonable correlation between lateral spreading and ground slope. The correlation shows approximately 3 feet of lateral spreading for each 1% of slope inclination.

A series of parametric analyses were performed using the Makdisi and Seed method (1978), by varying the ground slope and residual shear strength of the liquefied zone of fill. The results

of the analyses are summarized on Figure 5. The upper figure shows yield accelerations as a function of residual shear strength for a range of ground slopes ranging from 0.5% to 2.0%. It is evident that ground slope has only a minor influence on yield acceleration, while the residual shear strength has a very significant effect. The calculated lateral displacements as a function of residual shear strength and ground slope indicate that extremely large movements would occur for residual shear strengths less than 100 psf.

Although the results obtained from the Makdisi and Seed method are instructive, but should be regarded with caution. First and foremost, the method was not intended to be applied to liquefaction-induced lateral spreading. Also, as the soil liquefies and loses strength, the shear forces cannot be transmitted upward to a non-liquefied layer. The heavy dashed line on the figure is a judgmental probable relationship between ground displacement and shear strength. For ground slopes greater than 1%, it recognizes that ground accelerations may be significantly less than 0.40g after liquefaction has occurred. The Makdisi and Seed method of analysis does not bear out the strong influence of ground slope on lateral movements shown on Figure 5. On that basis alone it would appear that for the very flat slopes involved, the method should be considered as providing only a qualitative guide to estimate lateral displacements due to liquefaction.

The results of parametric analyses performed by Towhata's method are considered to provide a better means of evaluating the effects of ground slope, residual shear strength, and thickness of liquefiable layer on lateral movements caused by liquefaction. The results of these analyses are shown on Figure 6. There is a strong correlation between lateral spreading and ground slope, although the residual strength of the fill, as well as the thickness of the liquefiable layer, also have an influence.

The empirical data shown on Figure 4, supplemented by the analytical results on Figure 6 provide the best guide for assessing the lateral movements due to liquefaction. Both the observations and analyses indicate that when lateral spreading occurs, the maximum lateral movements are roughly directly proportional to the surface gradient, or ground slope. This is considered to be the most important conclusion of the liquefaction analysis for this project.

It should be recognized that when a soil layer liquefies, its shear strength is reduced substantially, and the ground tends to deform and flow even under mild slopes. At small slopes, say less than 0.5%, very small residual shear strengths are required to arrest the movements. From analyses that we have performed based on Towhata's method, it appears that the required strength could be as low as 25 psf. Therefore, in areas with ground slopes less than 0.5%, lateral ground movements would be small, typically less than 1 foot. For steeper ground slopes greater shear strengths are required to arrest the ground movements; therefore, larger movements would tend to develop.

ESTIMATED REPAIR COSTS

The city's primary purposes for performing these studies were to obtain an order-of-magnitude cost of the damages to city utilities for a magnitude 8.3 earthquake and to assist city officials

in minimizing future earthquake damage to the city's utility systems. The estimated costs of repairs of broken water and sewer mains in the Sullivan Marsh and Mission Creek areas caused by a magnitude 8.3 earthquake are presented in Table 3. For comparison purposes, similar data for the Marina District are also presented.

The 1991 total estimated costs of repairs to water and sewer systems in Sullivan Marsh and Mission Creek are approximately the same, $35 million for Sullivan Marsh and $34 million for Mission Creek. The distribution of repairs between utility systems in these areas varies, however, due to variations in the length of services and the character and age of the piping systems. The priority for repairs or upgrade of the utility system considering life safety as the highest priority, followed by public health, results in logical conclusions. The auxiliary water supply system (AWSS), which is vital to fire protection, has been given highest priority, followed by the municipal water supply system (MWSS), and then the sewer system.

GROUND IMPROVEMENT SCHEMES

The liquefaction potential in the study areas can be reduced by a variety of special techniques for ground improvement. Because of the extensive urban development in the areas studied, it is not practical or economically feasible to prevent liquefaction everywhere, especially on private property. Nevertheless, ground improvement on selected streets could maintain utility service across a stabilized utility corridor. Of the alternative ground stabilization techniques studied, compaction grouting, stone columns, and deep soil mixing were considered to be the most effective ground improvement techniques within city streets. Stone columns and deep soil mixing method would require removal and replacement of utilities prior to stabilization. Compaction grouting would not require utility removal, but could damage the utilities. The estimated cost of stabilization of an area 40 feet wide, 1,000 feet long and 30 feet deep are as follows: Stone Columns — 0.8 million; Compaction Grouting — $1.2 to $2.8 million; and Deep Soil Mixing — $2.5 million.

These estimated costs are for the stabilization procedures only, and do not include the cost of utility replacement, pavement, engineering costs, inspection, etc. Areas of potential high benefit/cost ratios for ground stabilization include Howard Street in the Sullivan Marsh area between 6th and 7th Streets, and the following areas in Mission Creek: Shotwell Street, Bryant Street west of Florida Street, the Brannan Street crossing of the old marsh, and the 15th and 16th Street crossings of the old marsh.

CONCLUSIONS

Not surprisingly, there were several limitations to the correlations between observed deformations and calculated liquefaction-induced settlements for the strong ground shaking that occurred in 1906 for non-engineered fill sites underlain by soft soils. The currently available methods of analysis for vertical settlements consider only dissipation of pore pressure water effects. Lateral spreading displacements are even more difficult to estimate; using Towhata's methods, they are dependent upon parameters not well known for liquefied soils. Significant limitations on expected accuracy are also due to the inadequacy of the database, especially in the

areas of Upper Mission Creek. Further, standard penetration tests performed by various investigators over a 50-year time period are likely to be of variable reliability. Correlation between calculated and observed movements based on available geotechnical data was poor. Better correlation should be expected using more modern piezocone methods to characterize the in situ strength of the liquefiable sands.

Both observed and calculated lateral movements showed the strong effect of ground slope. The excellent empirical database for the 1906 earthquake coupled with the knowledge gained from the analytical studies permitted realistic identification of the probable locations and extent of liquefaction-induced ground motions for a future magnitude 8.3 earthquake. This study provided reasonable estimates of utility repair costs for a future magnitude 8.3 earthquake and will permit the City of San Francisco Public Works Department to plan systematic upgrading of utility systems to mitigate future earthquake damage. Cost estimates have also been prepared for ground modification techniques which could be used to stabilize critical utility corridors in areas of adverse ground movements associated with liquefaction.

Despite all the practical and theoretical limitations, the studies performed did provide valuable insight into the extent and location of probable future earthquake damage to the city's utilities, and did permit realistic evaluations of the maximum expected future movements. Confidence in predicted movements was primarily due to the records of observed movements in the 1906 earthquake. The most significant geotechnical factor corroborated by the studies is the great importance of the steepness of the slopes on the amount of lateral spreading.

ACKNOWLEDGMENTS

The studies described in this paper were performed for the City and County of San Francisco under the direction of Charles Ng, Chief Structural Engineer, and reviewed by Frank Moss, City Engineer, and Richard Evans, Director of Public Works. The work was performed by four San Francisco engineering firms: Harding-Lawson Associates, Dames & Moore, EQE International, and Kennedy/Jenks/Consultants. Henry Taylor, of Harding-Lawson Associates, was the project manager. Professor Thomas D. O'Rourke of Cornell University was a consultant to this team. Peer review was provided by a city-appointed Blue Ribbon committee: Professor James K. Mitchell, University of California, Berkeley, Chairman; Professor I.M. Idriss, University of California, Davis; Mr. Frank J. Rollo, Treadwell, Rollo and Associates; Mr. Maurice Power, Geomatrix Consultants; and Mr. Daniel Shapiro, SOH Associates.

REFERENCES

1. Brown, A.A., H. Forbes, L.H. Nishkian, James M. Owens and Frank G. White, 1932, Subsidence and the Foundation Problem in San Francisco, A Report of the Subsoil Committee of the San Francisco Section, American Society of Civil Engineers, September.
2. Duryea, E., O.D. Mark, F. Riffle, A. Adams and W. Harris, 1907, ASCE Transactions, "The Effects of the San Francisco Earthquake of April 18, 1906, on Engineering Construction," Paper No. 1056, Vol. LIX, December.

3. Harding Lawson Associates, Dames & Moore, Kennedy/Jenks/Chilton and EQE Engineering, 1992, Final Report, Liquefaction Study, North Beach, Embarcadero Waterfront, South Beach and Upper Mission Creek Area, San Francisco, California. HLA Job No. 17952,041.04. January 10.
4. Kenai, K., 1983, Engineering Seismology, University of Tokyo Press.
5. Makdisi, F.I., and H.B. Seed, 1978, "Simplified Procedure for Estimating Dam and Embankment Earthquake-Induced Deformations," Journal of Geotechnical Engineering Division, ASCE, Vol. 104, No. GT7, July, pp. 849-867.
6. NAVFAC DM 7.1 (1982), page 7.1-89.
7. O'Rourke, T.D., 1991, personal communication.
8. O'Rourke, T.D., P.A. Beaujon and C.R. Scawthorn, 1991. "Large Ground Deformations and Their Effects on Lifeline Facilities in 1906 San Francisco Earthquake," NCEER Report, February.
9. O'Rourke, T.D., H.E. Stewart, F.T. Blackburn and T.S. Dickerman, 1990a, "Geotechnical and Lifeline Aspects of the October 17, 1989 Loma Prieta Earthquake in San Francisco," Technical Report 90-001, National Center for Earthquake Engineering Research, Buffalo, New York.
10. O'Rourke, T.D., T.E. Gowdy, H.E. Stewart, and J.W. Peese, 1990b, "Lifeline Performance and Ground Deformation in the Marina During the 1989 Loma Prieta Earthquake," Proc. Third Japan-U.S. Workshop on Earthquake Resistant Design of Lifeline Facilities and Countermeasures for Soil Liquefaction, San Francisco, California, December.
11. Redpath Geophysics, 1990, "Borehole Velocity Surveys at the Embarcadero in San Francisco and the Cypress Structure in Oakland," For California Department of Transportation, Contract No. 65M598.
12. Schussler, H., 1906, The Water Supply of San Francisco, California, Martin B. Brown Press, New York.
13. Seed, H.B. and I.M. Idriss, 1970, "Analysis of Ground Motions at Union Bay Seattle during Earthquakes and Distant Nuclear Blasts," BSSA Vol. 60, No. 1, pp. 125-136.
14. Seed, H.B., R.T. Wong, I.M. Idriss, and K. Tokimatsu, 1984, "Moduli and Damping Factors for Dynamic Analyses of Cohesionless Soils," EERC Report No. 84/14.
15. Tokimatsu, K., and H.B. Seed, 1987, "Evaluation of Settlements in Sands Due to Earthquake Shaking," J. Geotech. Eng., ASCE, Vol. 113, No. 8, pp. 861-878.
16. Towhata, I., K. Tokida, Y. Tamari, H. Matsumoto, and K. Yamada, 1990, "Prediction of Permanent Lateral Displacement of Liquefied Ground by Means of Variational Principle," Proc. Third Japan-U.S. Workshop on Earthquake Resistant Design of Lifeline Facilities and Countermeasures for Soil Liquefaction, San Francisco, California, December.
17. Tsai, J.S., 1990, "Validation of Soil-Structure Interaction Analysis Methods," Ph.D. Dissertation presented to the Faculty of School of Engineering, University of California at Berkeley in partial fulfillment of the degree of Doctor of Philosophy.
18. Vucetic, M. and R. Dobry, 1991, "Effects of Soil Plasticity on Cyclic Response," Proceedings of ASCS, JGED, Vol. 117, No. 1, January, pp. 89-107.

TABLE 1 - CALCULATED VERSUS OBSERVED VERTICAL SETTLEMENT BY LIQUEFACTION - SULLIVAN MARSH

Site No.[1]	SPT (N) Used in Analysis	Thickness of Liquefiable Layer (feet)	Calculated Settlement (inches)	Observed Settlement (inches) 1906
1a	7	8	3.1	12
1b	24	8	1.4	
2a	6	6	2.3	59
	18	6	1.2	
	15	10	2.4	
2b	7	5	1.8	
3a	6	2	0.7	36
	4	6	2.9	36
	8	5	1.6	
3b	6	2	0.7	
4a	7	3	0.9	
4b	15	3	0.4	8 to 35
6a	7	5	1.7	
	6	13.5	5.3	
6b	7	3.5	1.2	
8a	7	15	5.1	
8b	13	8	1.5	
9	6	6	2.2	
10a	2	7	5.5	
10b	5	7	2.6	
11a	3	4	1.5	
	6	8	2.2	
11b	18	3	0.5	
12	5	13	7.3	8
13a	5	12	6.7	
13b	15	6.5	1.5	

[1]See Figure 2 for location. Lower case letters denote different investigations within the site.

TABLE 2 - CALCULATED VERSUS OBSERVED VERTICAL SETTLEMENT BY LIQUEFACTION - UPPER MISSION CREEK

Site No.[1]	SPT (N) Used in Analysis	Thickness of Liquefiable Layer (feet)	Calculated Settlement (inches)	Observed Settlement (inches) 1906
1a	4	15.5	9.0	24 to 35
	10	3	0.9	
1b	4	10.5	5.5	
2a	10	12	3.9	
	17	4	1.2	
2b	20	6	0.5	
	26	5	0.2	
3a	10	17.5	4.8	
3b	20	11.5	1.4	
4a	10	8	1.9	
	14	6.5	1.4	
4b	25	3	<0.1	
5a	10	6	1.4	
	14	6	1.3	
6a	10	8	2.1	
	25	10	2.3	
6b	11	9	2.2	
7a	5	12	5.4	
	20*	29	6.1	71
7b	15	4	1.3	
8a	10	6.5	1.6	6 to 35
	17	15	4.9	
8b	10	3	0.7	
9a	10	6	1.9	
	16	12	3.4	
	25	6	1.6	
9b	16	5	0.8	
10a	6	7	1.6	
	10	7	2.2	
	12	14	4.6	
10b	10	7	2.3	
11a	5	11	2.7	
11b	5	5.5	1.3	
12	10	9	2.3	
13	5	3	1.2	
	10	5	1.4	
	18	5	1.0	

[1] See Figure 2 for location. Lower case letters denote different investigations within the site.
[2] Calculation results are presented to 0.1 inch to help evaluate the differences in site conditions for the cases studied.
*Assumed no data.

TABLE 3 - ESTIMATED COST OF REPAIRS FOR BROKEN WATER AND SEWER MAINS CAUSED BY A MAGNITUDE 8.3 EARTHQUAKE

Study Area	AWSS SYSTEM		MWSS SYSTEM		SEWER MAINS	
	No. of Breaks	Repair Cost Millions	No. of Breaks	Repair Cost Millions	% Broken	Repair Cost Millions
Sullivan Marsh	84	$8.4	202	$15.0	65	$11.7
Mission Creek	25	$2.4	181	$17.5	64	$14.2
Marina Area	11	$1.1	82	$7.3	38	$5.3

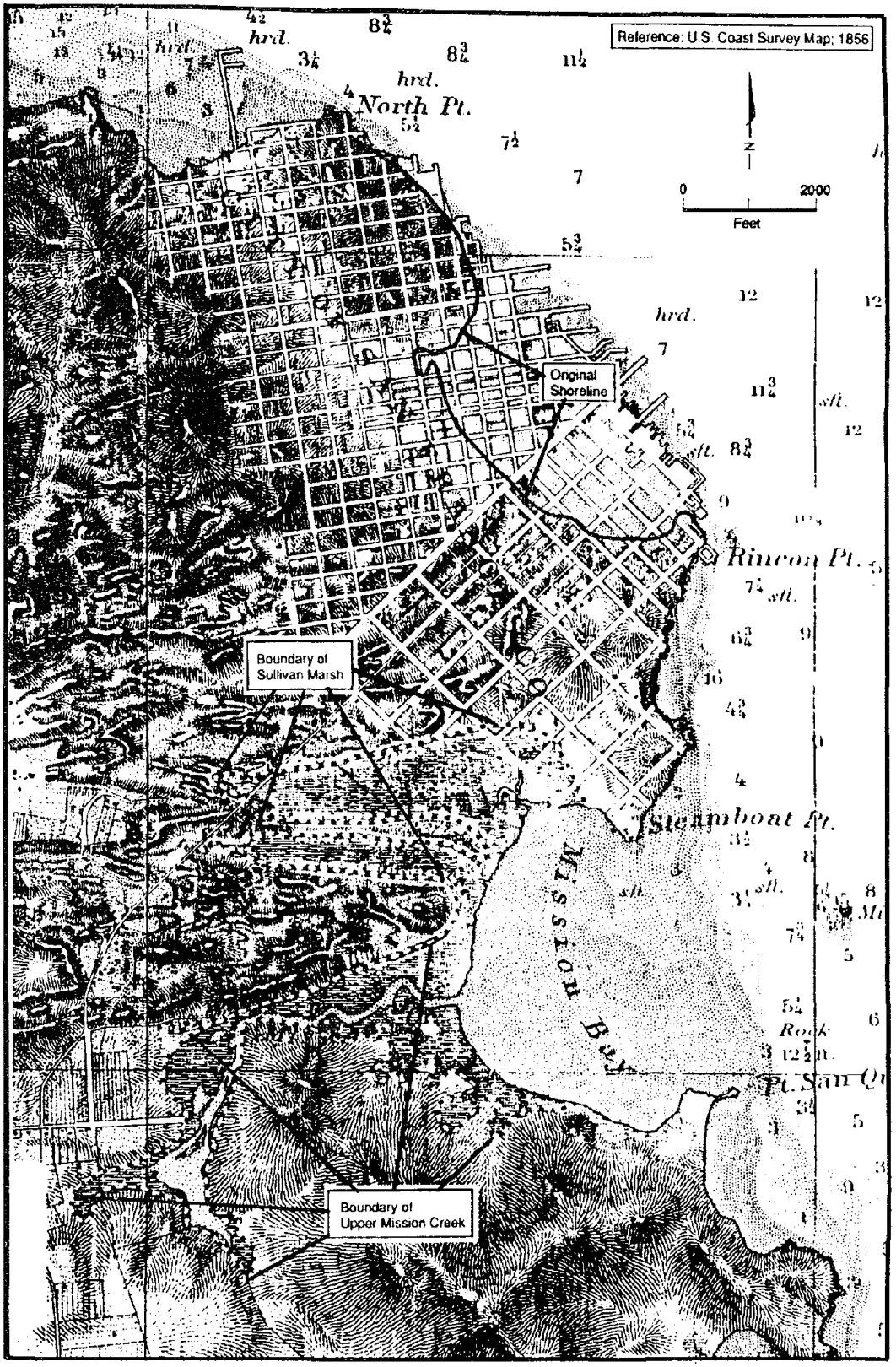

Figure 1. Map of Original Shoreline and Marsh Outline; U. S. Coast Survey Map, 1856

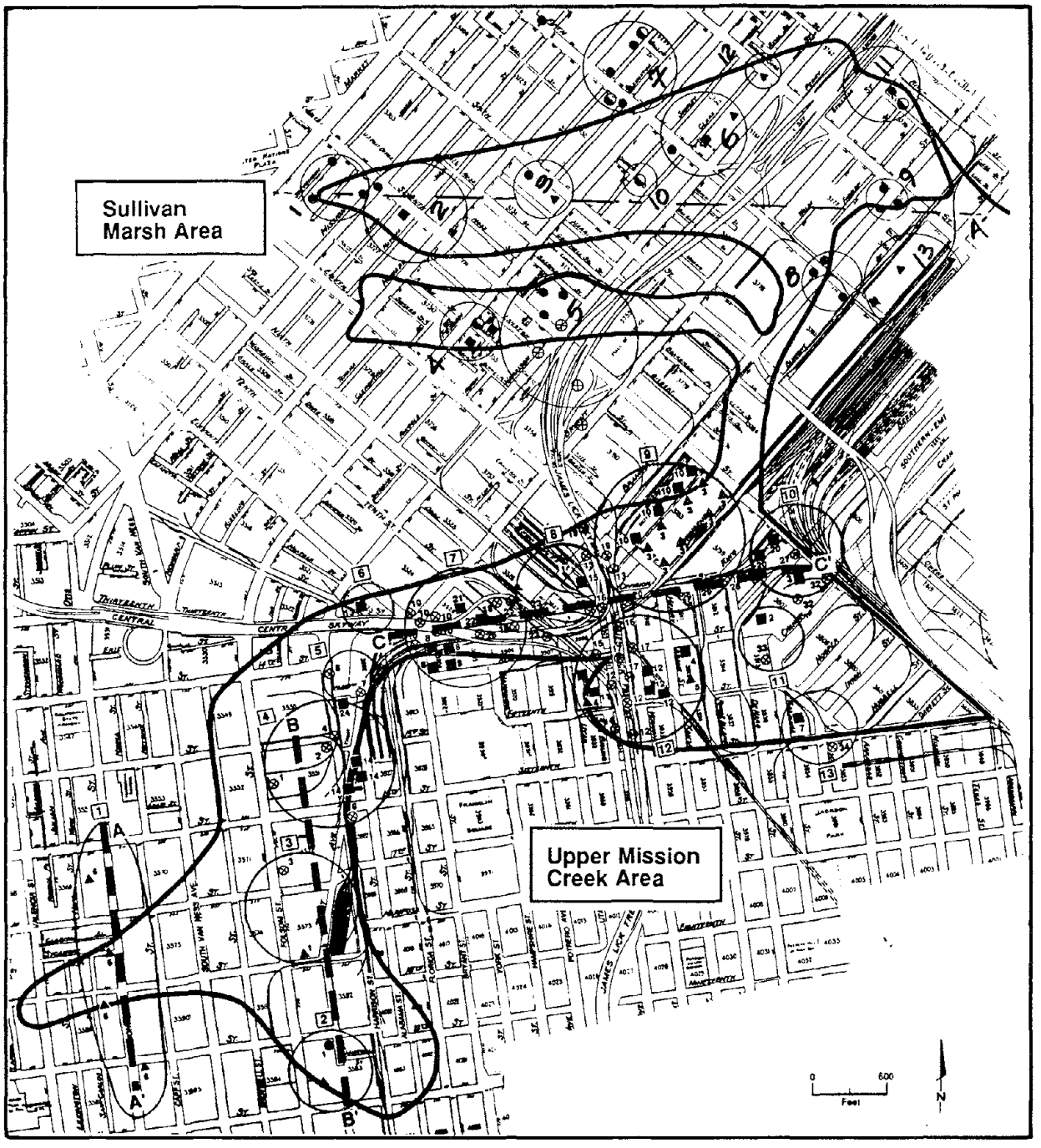

Figure 2. Limits of Study Area and Locations of Available Subsurface Data: Sullivan Marsh and Upper Mission Creek

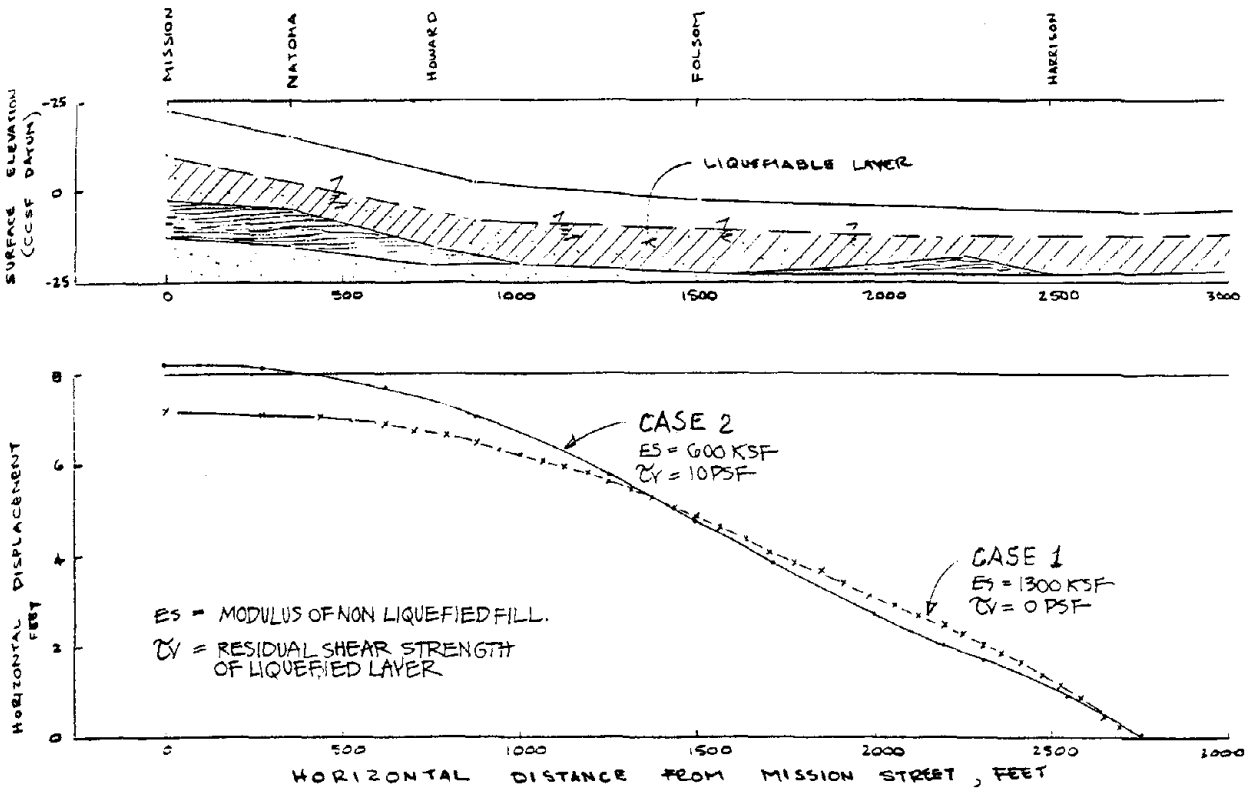

Figure 3. Profile of Calculated Lateral Deformations Due to Liquefaction

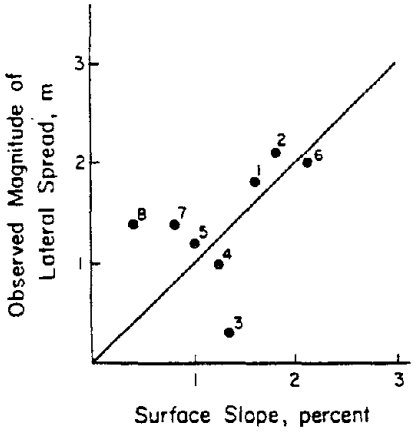

Summary of Lateral Spreads, Surface, and Subsurface Gradients of Locations of Documented Lateral Deformation During the 1906 Earthquake

Location	Number	Lateral Movement, m	Surface Slope, percent	Slope of Base of Liquefiable Deposit, percent
19th St. and Linda St.	1	1.8	1.60	4.40
Valencia St. between 18th - 19th Sts.	2	2.1	1.80	1.40
Mission St. between 17th - 18th Sts.	3	0.3	1.35	1.35
Capp St. between 17th - 18th Sts.	4	1.0	1.24	0.00
South Van Ness Ave. between 17th - 18th Sts.	5	1.2	1.02	0.00
Mission St. and 7th St.	6	2.0	2.10	2.10
Folsom St. between 5th - 6th Sts.	7	1.4	0.80	0.80
Harrison St. between 5th - 6th Sts.	8	1.4	0.40	0.00

Reference: From O'Rourke et al. (1991)

Figure 4. Correlation Between Lateral Spreading and Ground Slope

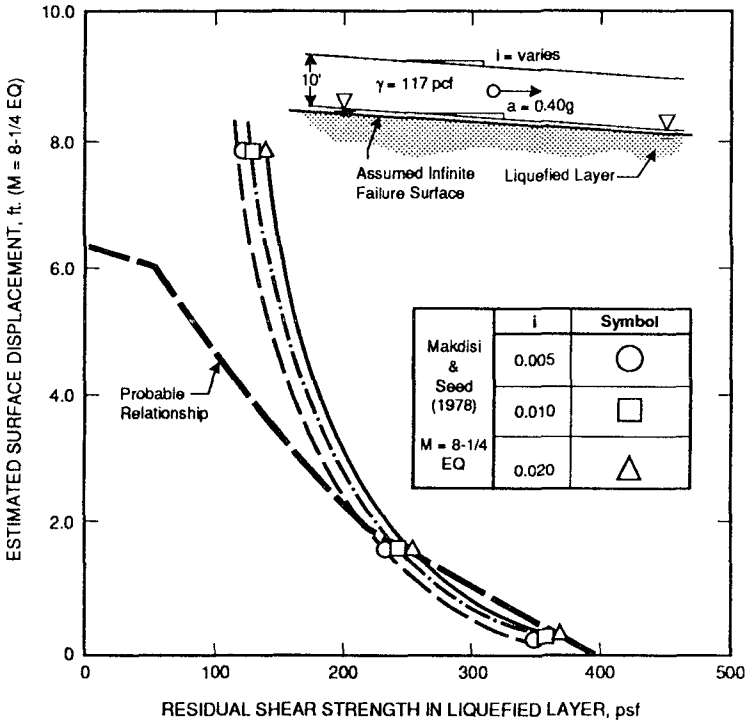

Figure 5. Variation in Lateral Displacements with Residual Shear Strength and Ground Slope

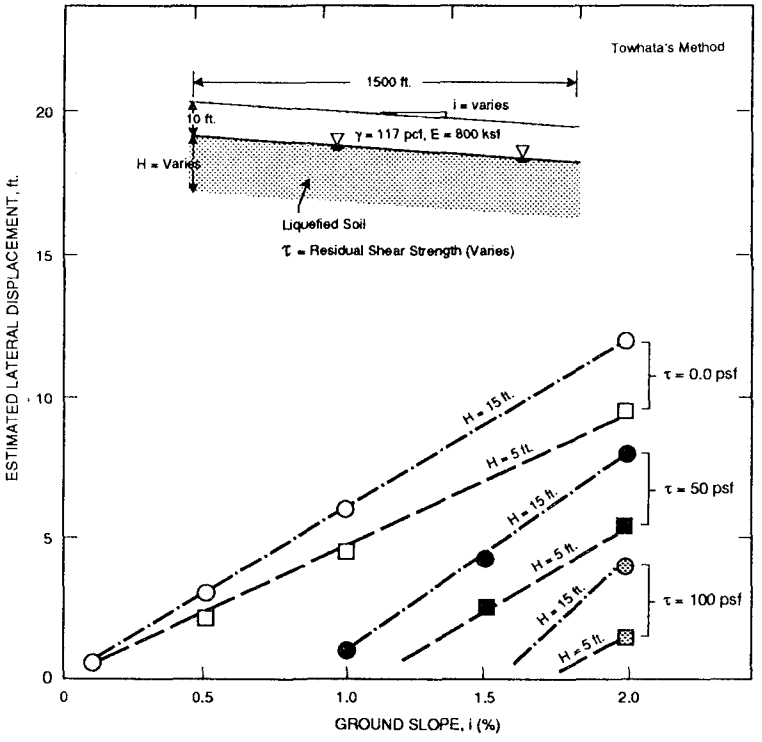

Figure 6. Estimated Lateral Displacements as a Function of Initial Ground Slope, Residual Shear Strength and Fill Thickness

Observed Effects of Testing Conditions on the Residual Strength of Loose, Saturated Sands at Large Strains

M.F. Riemer and R.B. Seed

Graduate Student and Professor, respectively
Dept. of Civil Engineering
University of California, Berkeley

ABSTRACT

Undrained residual strengths (or "steady state" strengths) are useful in assessing the potential for large ground deformations in deposits of loose, saturated sands due to the strain-softening behavior of these materials in undrained loading. Extensive research over the past decade has raised numerous issues regarding the effects of various testing conditions on these strengths when measured in the laboratory. In this paper, the authors present the results of a testing program which investigated the possible effects of consolidation stress level, the effective stress path during shearing, and the drainage conditions on the steady state strengths of Monterey #0 sand. The data suggests that the mode of deformation, or strain path during shearing, may be an important factor affecting the steady state strengths of cohesionless soils.

INTRODUCTION

Material Behavior

When tested under undrained conditions at sufficiently low densities, saturated sands exhibit a peak shear strength at relatively small strains, followed by a subsequent reduction in strength as deformations continue. This decline in strength results from the increasing pore pressures generated in response to the contractive tendency of the soil when sheared. During this period of strain softening the strength continues to decrease until, at large strains, the deforming sand reaches a state at which there is no further tendency for volume change. As a result, the pore pressure, effective stresses and shear strength remain constant as the sample continues to deform. This residual condition has been termed the "steady state of deformation" (Castro, 1975; Poulos, 1981), and is intimately related to Casagrande's concept of critical density. Early experimental research supported the concept that, for a given material, the stresses existing at the steady state are solely a function of the deforming soil's density. Since the steady state strength has been suggested to be the minimum undrained shear strength of a contractive deposit at its *in situ* density (Poulos et al., 1985), the steady state approach has potentially important implications for the analysis of seismic stability and deformations of deposits potentially subject to liquefaction.

Previous Research

Researchers have focused increased attention on the behavior of saturated, loose sands in recent years as a result of a number of developments, including the large-scale placement of such materials on the sea floor as foundations for offshore petroleum operations (Sladen et al., 1985), and the proposal of a method for the evaluation of liquefaction potential based on the steady state theory (Poulos et al., 1985). A partial list of those presenting important data on the behavior of these materials includes (alphabetically) --- Alarcon-Guzman et al. (1988), Been et al. (1991), Castro (1975), Hanzawa (1980), Ishihara et al. (1975), Jong (1988), Konrad (1990), Kramer and Seed (1988), Lade (1992), Lindenberg and Koning (1981), Mohamad and Dobry (1986), Sladen et al. (1985), Vaid et al. (1985, 1990) and many others. In addition to describing other aspects of the constitutive behavior of these materials, some of these studies directly describe the implications of their data regarding the assumption inherent to steady state theory that the effective stresses at the steady state are solely a function of density for a given soil.

By examining the conclusions of various researchers, certain testing conditions (such as the strain rate) can be conclusively identified as having little effect on the steady state relationship for cohesionless soils. Due to conflicting conclusions among different studies, however, a number of unresolved issues remain concerning the uniqueness of the steady state relationship for a given material. In particular, the effects of consolidation stress level (e.g. Konrad, 1990),

the stress path of loading (Vaid et al., 1990), and the drainage conditions (e.g. Alarcon-Guzman et al., 1988) have been identified by some researchers as additional factors which may significantly affect steady state conditions. Other researchers (Poulos et al., 1985, Been et al., 1991) have presented data supporting the position that these same factors do not affect the steady state relationship.

It is generally difficult to draw conclusions regarding these effects by comparing the results of two or more testing programs, since minor variations in material and procedure can have large impacts on the results of such tests. In light of these difficulties, this research was initiated to provide conclusive data on the effects of different testing conditions on the residual or steady state strength of a single material.

LABORATORY TESTING PROGRAM

Objectives

Among the objectives of the current testing program are the investigation of the effects of three factors on the shear strength of loose sands at large strains:

(1) the level of consolidation stress ($\sigma'_{3,c}$).
(2) the stress path to which the sand is subjected during shearing.
(3) the drainage conditions during shearing.

These effects were examined by performing an extensive laboratory testing program designed to isolate each of these factors in turn. The importance of the level of consolidation stress was investigated by performing several series of tests on samples carefully prepared to the same void ratio, but over a wide range of stresses. The second objective, the effect of the applied stress path, was investigated by subjecting similarly prepared samples to loading in (a) triaxial compression, (b) triaxial extension, and (c) a stress path referred to throughout this paper as "pore pressure injection". The steady state relationship was determined using each of these loading methods on samples of the same material. The effects of drainage conditions were evaluated by establishing the steady state relationship under both drained and undrained conditions for the same sand. This variation in drainage conditions is closely related to the stress path effect, since by altering the drainage conditions samples are subjected to entirely different effective stress paths, although in most cases such samples will deform in a similar manner.

In addition to isolating these various factors from each other, the testing procedures and material used for the study were selected to minimize the potential effects of other processes, such as grain breakage and density redistribution, which could take place during testing and complicate the comparison of test results.

Material

Monterey #0 sand was used throughout the testing program. It is a clean, fine beach sand consisting primarily of rounded to subrounded quartz grains, with a small fraction of grains of feldspar. Monterey #0 has a uniform gradation curve, as shown in Figure 1, and a specific gravity G_s = 2.65 (ASTM Test D854-58). The maximum void ratio, e_{max} = 0.86, was obtained by careful dry tipping of the sand in a large graduated cylinder, while the minimum void ratio, e_{min} = 0.53 was determined by the Modified Japanese method.

The primary advantage of testing such a material is that the relatively strong, rounded grains undergo very little breakage when tested under moderate stresses. In contrast, the gradation of an angular or weak material can change significantly during deformations under high confining stresses (Yapa, 1992; Jong and Seed, 1988). The resulting degradation of the material can complicate the comparison of tests performed at different stress levels by introducing additional differences in conditions, such as the angularity and fines content of the deforming material. By using a strong, rounded, fine sand such as Monterey #0, the grain

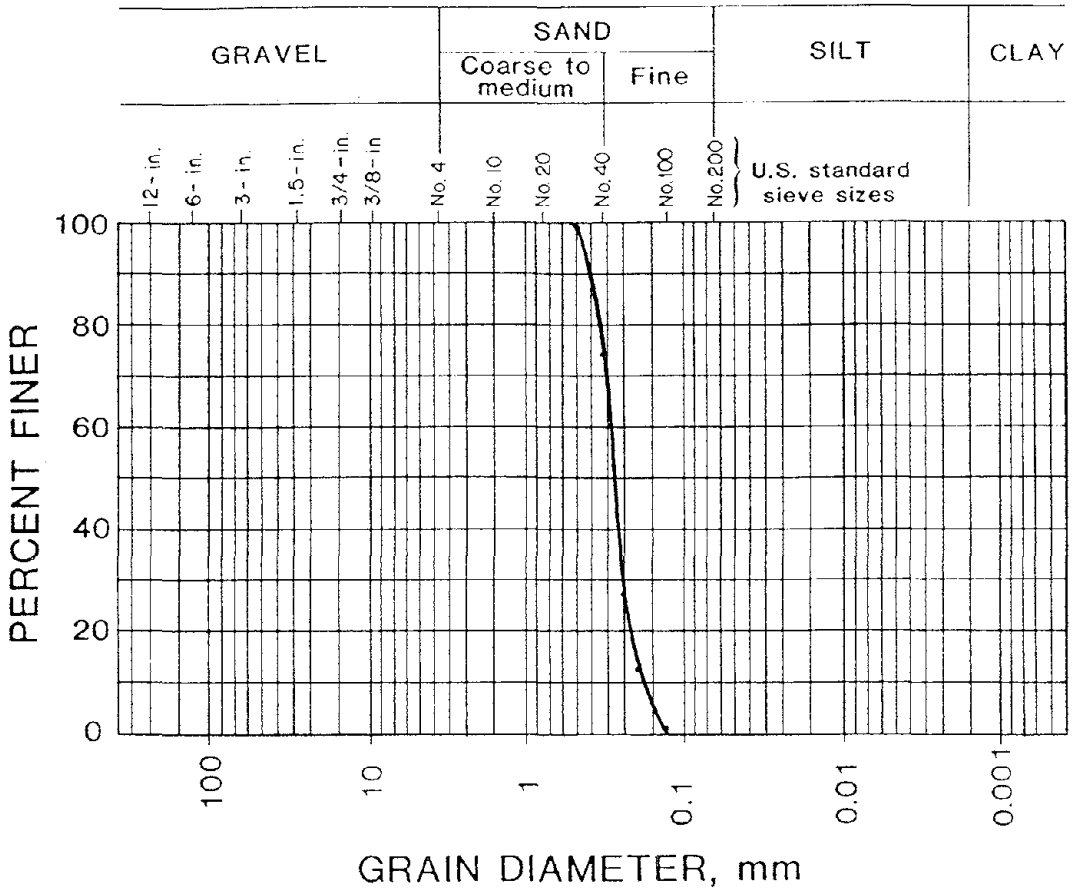

Figure 1: Gradation Curve for Monterey #0 Sand Used in this Research

properties can be assumed to be essentially constant over a large range of stresses. However, the properties of the sand had several important consequences for the scope of the testing program as well, since the characteristics of the grains have a strong influence on the nature of the steady state line (Poulos et al., 1985). The uniform grain size of Monterey #0 (C_u = 1.6) indicates that the sand will have a steady state line with relatively high strengths at high void ratios, and the rounded shape of the individual grains suggest the steady state line will have a flatter slope than a similarly graded sand with more angular particles. Taken together, these properties suggest that the steady state line will be confined to a region of relatively high void ratios for the range of effective stresses of practical interest, and this was indeed observed to be the case. As a result, the laboratory testing program required testing of extremely loose samples, while also requiring very careful monitoring of the sample volume throughout the testing process, since small volume changes would have large effects on the steady state strength.

The original intent of the study was to perform all the testing on a single sand, in order to limit the scope of the research to comparisons of varying testing conditions on the same material. Serendipity intervened, however, when some of the original Monterey #0 was inadvertently dried at high temperatures (225° C). Following the exposure to high temperatures overnight, the sand had acquired a distinctly rose-colored tint, though a re-examination of the index properties revealed no alteration of gradation or change in maximum or minimum density. Microscopic examination suggested that the color change resulted from oxidation of exposed surfaces of the feldspar grains. This material will be referred to as the "altered" sand throughout the remainder of this study. It was used in preparing the pore pressure injection samples, in addition to a number of subsequent triaxial compression samples tested for comparitive purposes.

Equipment and Procedure

All of the tests were performed using a modified form of the automated triaxial testing system developed and described by Li, Chan and Shen (1988). In addition to data acquisition, the current system utilizes the Georobot software for computer control of the chamber pressure and deviatoric load. Vertical stresses were applied by a dual pressure actuator, and for this study one chamber of the actuator was filled with oil and linked to an oil reservoir by a needle valve with adjustable aperture. This modification allows the researcher to limit the maximum rate at which the piston can descend, thereby limiting the strain rate of the sample during the strain softening portion of the test. In this way, reliable values of effective stress were obtained during softening by ensuring that the strain rate was slow enough so that the pore pressures measured at the ends of the sample were representative of the entire sample.

All of the samples in this study were prepared by moist tamping, since it proved to be the only reliable method of obtaining samples at the extremely low

densities required. The samples nominal dimensions of 7 cm in diameter and 15 cm in height. Since previous research has suggested that moist tamping can result in samples of non-uniform density (Mulilis et. al, 1975; Gilbert, 1984), a portion of the current study focused on the issue of sample non-uniformity and its effects on the observed behavior. While the procedures and results of these investigations lie beyond the scope of this paper and are described elsewhere (Riemer, 1992), the steady state results presented here represent values for uniform samples. Because of the extreme sensitivity of the behavior of the sand to its density, volume changes were very carefully monitored throughout the testing process. Following the preparation of a sample, wetting and saturation were performed largely outside the testing chamber, in order to minimize the occurrence of unintentional and undetectable volume changes associated with the testing of loose, cohesionless samples (Sladen and Handford, 1987). Final saturation was ensured by applying back pressures of 1 to 2 atmospheres until "B" values of 0.98 or higher were obtained. Despite the fine grain size of Monterey #0, the effects of membrane penetration on the effective sample volume were accounted for using the method developed by Anwar and Seed (1989) in order to obtain the best possible measure of density at the steady state. The slight changes in volume resulting from membrane compliance were estimated for the effective stress changes which occurred during both consolidation and testing.

TRIAXIAL COMPRESSION TESTING

Undrained Compression

The undrained triaxial compression test was selected as the "standard", or reference test against which to compare the results of other testing methods because it is the recommended method of determining the steady state relationship of a sand (Poulos et. al, 1985). In order to minimize any density redistribution which might result from dilative behavior, all of the samples were prepared at low densities and consolidated to states well to the right of the eventual steady state position (on a plot of void ratio vs. effective stress). By ensuring a strongly contractive response, the steady state was achieved at lower strains than would have been required for samples under lower initial confining stresses, as pointed out by Poulos, Castro and France (1985).

Figure 2 shows the results of more than 30 such tests, depicting the steady state relationship between the void ratio (corrected for membrane compliance) and the log of the bulk mean stress, p', as the samples deformed continuously at large strains. The point on the left axis (at e = 0.844) represents two nearly identical samples which collapsed away from the top cap during testing, and therefore indicate zero effective confining stress at large strains (Riemer et al., 1990). The line drawn through the data on Figure 2 is included to serve as a reference for the general position of the steady state line in undrained triaxial compression.

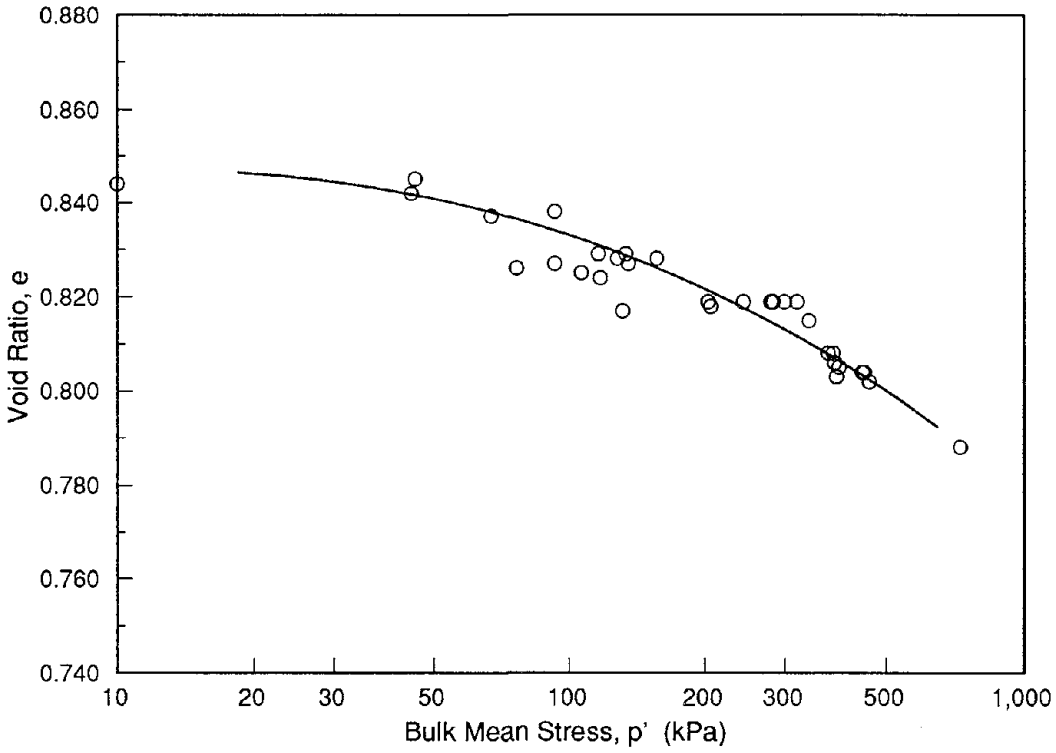

Figure 2: Steady state relationship as determined in undrained compression.

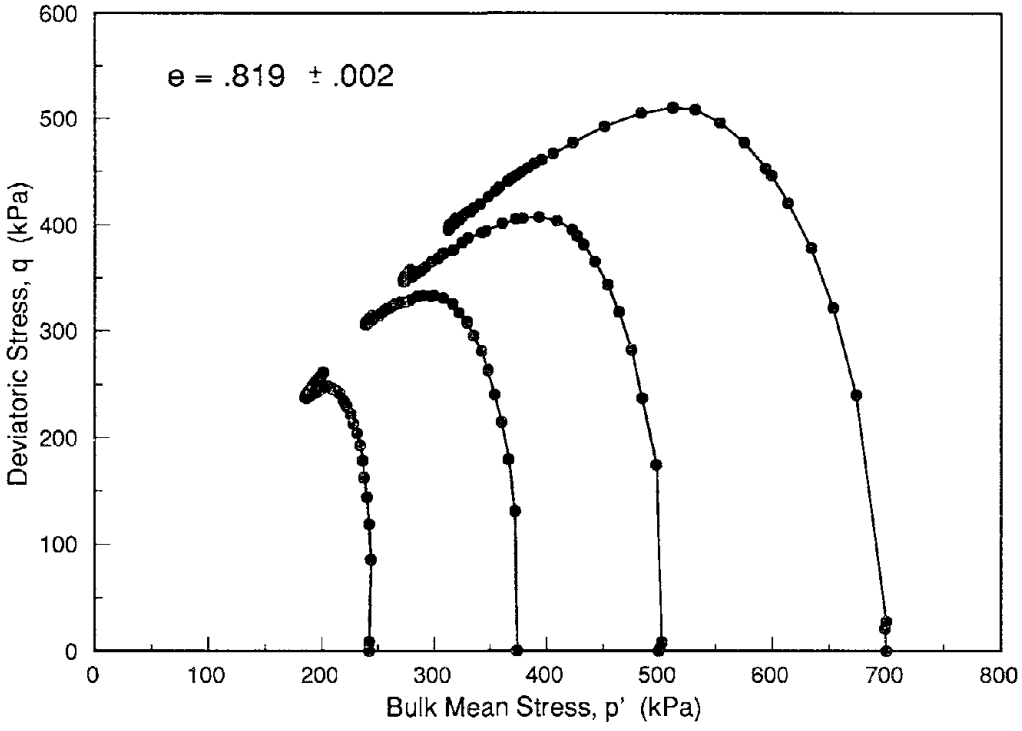

Figure 3: The effect of consolidation stress level in triaxial compression.

Effect of Stress Level

The apparent scatter of the data in Figure 2 around the line is not primarily due to material variation or random uncertainty in the measurement of the soil behavior; it is largely a consequence of the effect of the level of consolidation stress on the strength at large strains. Among the tests plotted in Figure 2 are several "suites" or series of samples which were carefully prepared and consolidated to a wide range of stress levels at essentially the same void ratio. Figure 3 illustrates the effective stress paths in terms of the bulk mean stress ($p' = [\sigma_1' + \sigma_2' + \sigma_3']/3$) and the deviatoric stress ($q = \sigma_1' - \sigma_3'$) measured for one such suite of tests in which four samples exhibited significantly different effective stresses at large strains, though all four had void ratios of e = 0.819. In comparison to the sample consolidated to very high stresses, the sample at the lowest stress (which is more realistic for such loose material) can sustain only 2/3 of the deviatoric stress at large strains.

Drained Compression

To investigate the effects of the drainage conditions on the strength at large strains, five samples prepared and consolidated in the same manner as the undrained samples were sheared in drained triaxial compression. The relationship between effective stress and void ratio for these five samples at large strains are plotted in Figure 4, along with the data from the undrained tests for comparison.

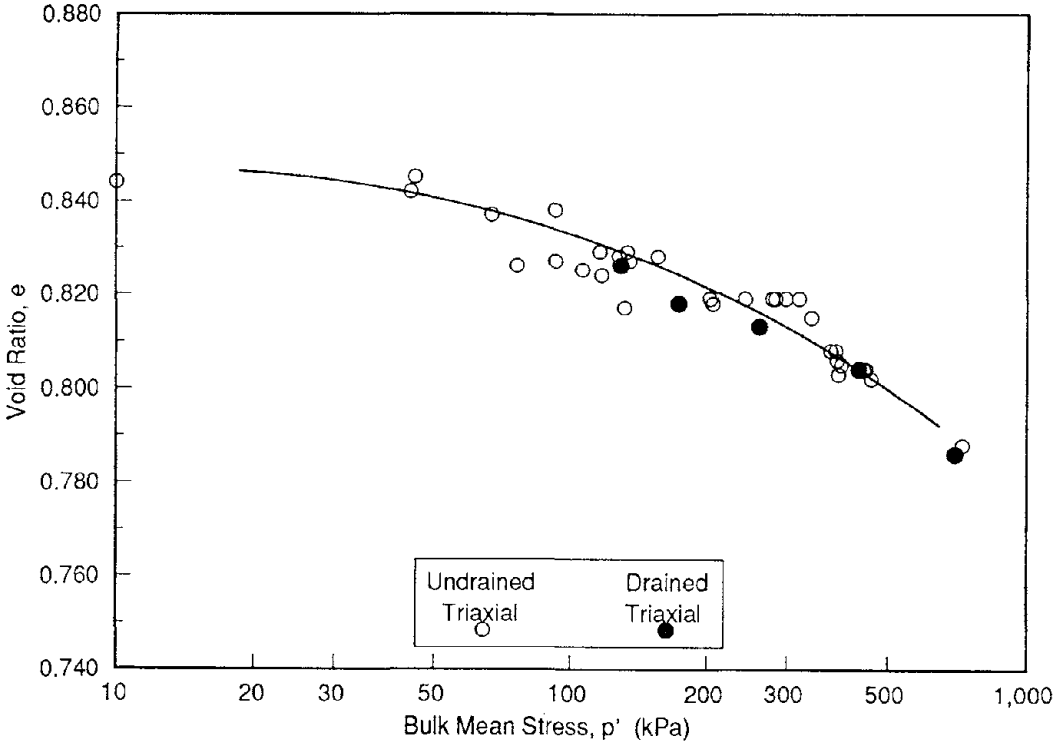

Figure 4: Results from Drained and Undrained Triaxial Compression

Like their undrained counterparts, these samples were isotropically consolidated to strongly contractive states (far to the right of the steady state line illustrated in Figure 2) to prevent dilation from occurring along preferential failure planes, which would lead to local variations in density. As a result, the samples exhibited relatively large volumetric strains during testing, which increased monotonically before stabilizing at essentially constant values at large strains. As shown in Figure 4, there is clearly no discernible effect of the drainage condition on the steady state relationship for Monterey #0 over the range of densities and stresses included in this research program.

ALTERNATE STRESS PATHS

Triaxial Extension

An additional series of triaxial tests were performed in undrained extension. These samples were prepared in the same manner as the triaxial compression samples, and were again isotropically consolidated to relatively high stress levels. Undrained shearing was performed by reducing the axial stress by applying tension to the loading rod, which was threaded into the sample top cap. In this method of loading, the axial stress becomes the minor principal stress, while the intermediate and major principal stresses are represented by the lateral effective stress. By performing the tests on highly contractive samples, the strain softening phase was completed prior to the appearance of significant "necking" of the sample. In a manner similar to those performed in undrained compression, a suite of undrained extension samples were prepared and consolidated to a wide range of stresses at a single void ratio in order to investigate the effects of stress level on the steady state behavior for this method of shearing. The results of this series of tests are plotted in Figure 5, which compares the effective stress paths of four extension tests with those of the four compression tests illustrated in Figure 3. The four extension samples were tested at essentially the same void ratio, e = .819, and should therefore exhibit the same steady state strength, yet again there is a distinct trend for the samples consolidated to higher stresses to yield higher shear strengths at large strains.

By comparing pairs of samples in Figure 5 that have been consolidated to the same stress level and void ratio but loaded by the two different methods, it consistently appears that the samples tested in extension are considerably weaker at large strains than those tested in compression. The steady state values of this suite of extension tests are plotted in Figure 6, in addition to five other extension tests performed over a range of densities. While the steady state line in extension has a similar slope to that in compression (which is included for comparison), it lies below (or to the left of) this "standard" relationship, suggesting that for a given void ratio the steady state strength would be lower in extension. This is consistent with similar results reported by Miura and Toki (1982), and Vaid et al. (1990).

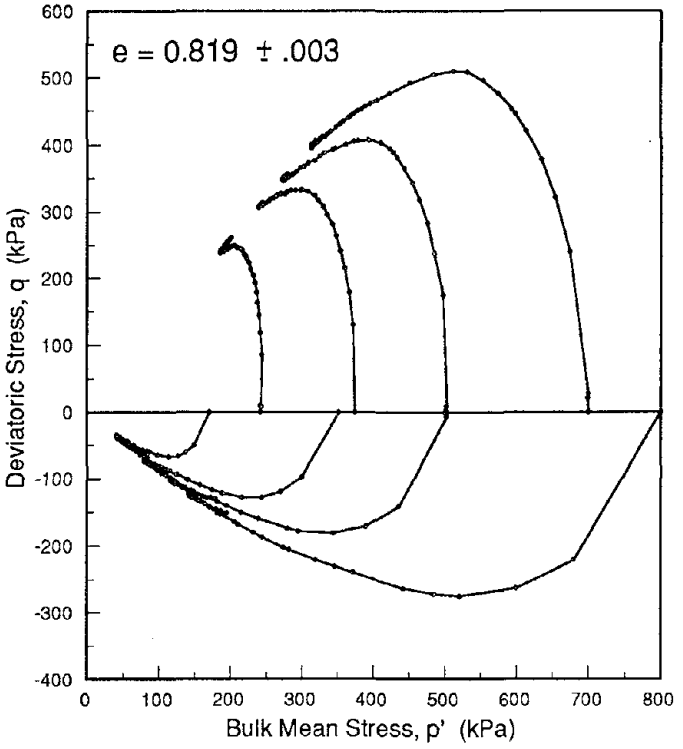

Figure 5: Comparison of stress level effect in compression and extension.

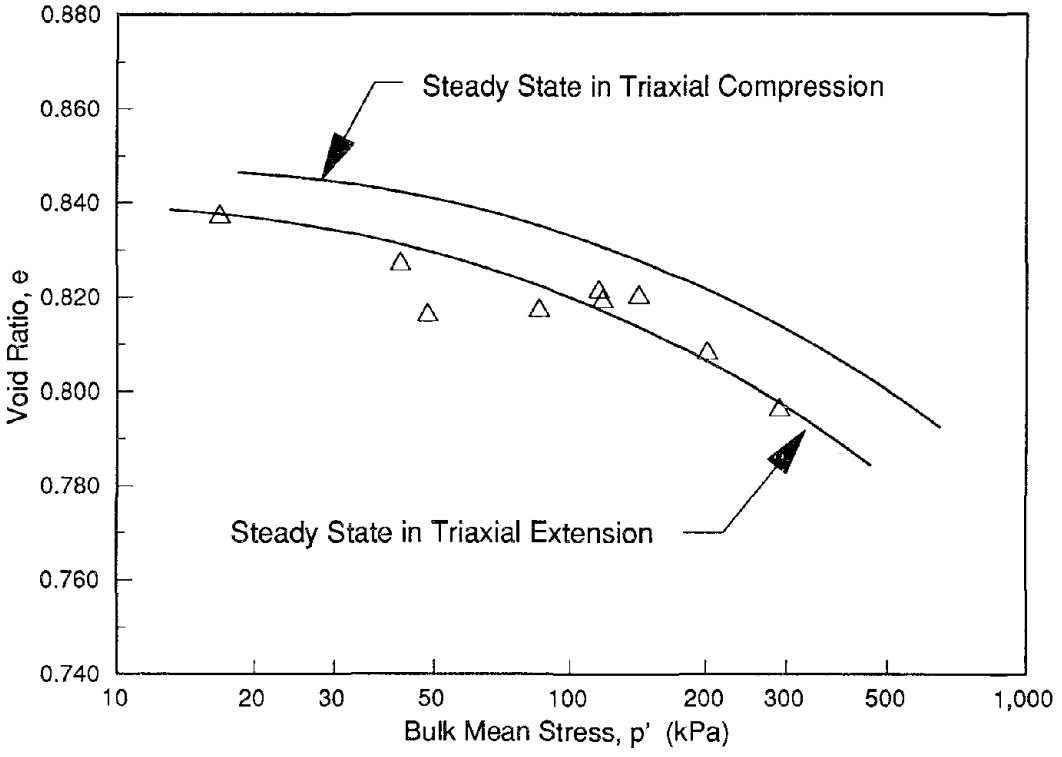

Figure 6: Results from Undrained Triaxial Compression and Extension.

Pore Pressure Injection

The final series of tests were performed using an effective stress path intended to simulate the response of soil on a slope subjected to a rise in the water table (Anderson, 1992). A schematic illustration of this "pore pressure injection" stress path is presented in Figure 7. After the sample is anisotropically consolidated to an initial level of shear and confining stresses, the confinement is reduced under drained conditions while the shear stress is maintained at its original magnitude. The tests in this study were performed on samples prepared in the triaxial apparatus following the same procedures described earlier for the standard steady state tests. Although samples tested by "injection" deform in a similar manner as those tested in triaxial compression, the effective stress paths are different for these two types of test, as shown in Figure 7.

The samples exhibited small increases in volume during the early stages of testing due to the unloading character of the test. As the samples approached the residual failure envelope, however, larger contractive volumetric strains were recorded as the samples collapsed, and a clearly defined relationship between void ratio and effective confinement at large strains became apparent. The results of five such "injection" tests are presented in Figure 8, and appear to form a line to the right of the one determined for the original Monterey #0 in triaxial compression tests (first presented in Figure 2). However, due to the alteration of the Monterey #0 used for these injection tests (as described in the *Material* section), it was not clear if the shift in the steady state relationship was the result of the change in stress path or the alteration of the material. To resolve this question, additional drained and undrained triaxial compression tests were performed on the altered material for purposes of comparison, and the results of these tests are also included in Figure 8. All three types of test performed on the altered material yield essentially the same steady state relationship, and thus it appears that this particular alternate stress path yields the same steady state relationship as determined by the "standard" method of undrained triaxial compression. In addition, the results presented in Figure 8 suggest that minor changes in the material being tested can exert a large influence on the position of the steady state line.

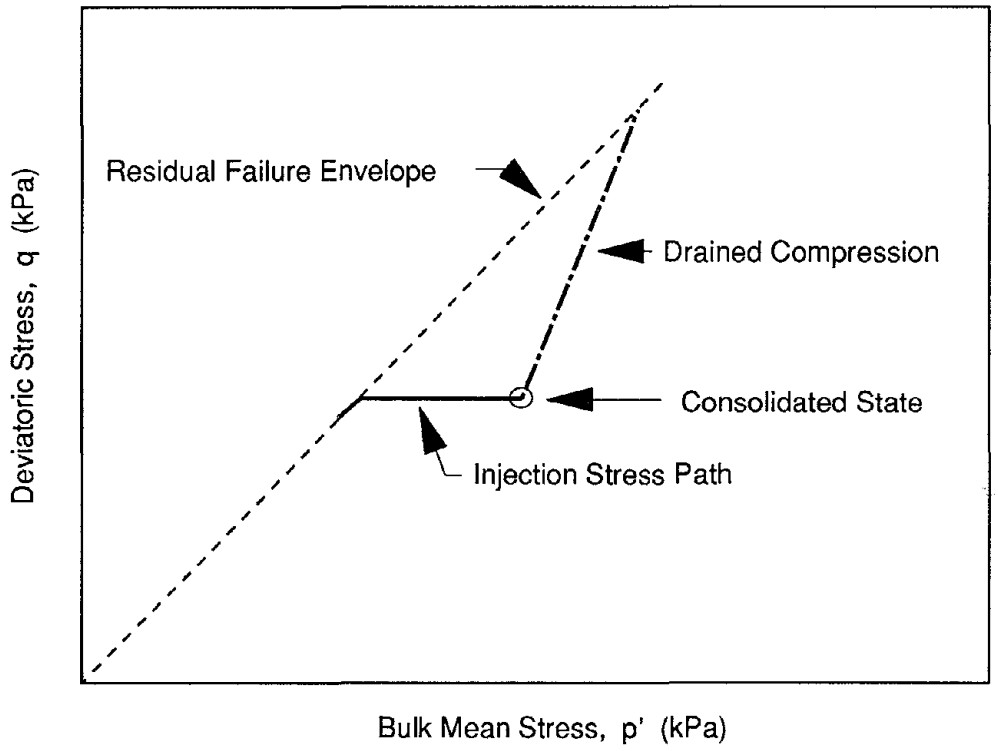

Figure 7: Pore Pressure Injection vs. Drained Compression Stress Path

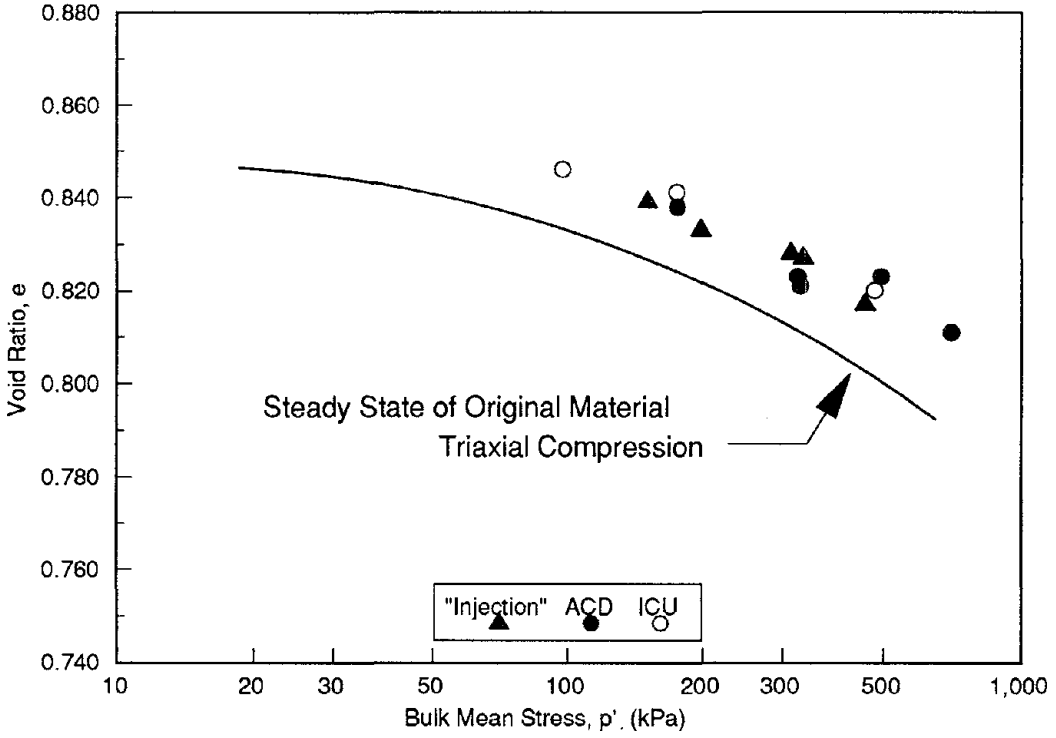

Figure 8: Various Stress Path Results for Steady State of "Altered" Sand.

CONCLUSIONS

From the results of the tests described in this paper, a number of conclusions can be reached regarding the effects of certain testing conditions on the observed shear strength of very loose, saturated Monterey #0 sand at large shear strains:

(1) The stress level to which samples are consolidated prior to shearing can significantly affect the measured residual or "steady state" strength in both triaxial compression and extension. Samples consolidated to higher stresses consistently exhibited higher strengths at large strains.

(2) Drainage conditions during shearing do not appear to significantly affect the steady state relationship in triaxial compression.

(3) Steady state strengths measured in triaxial extension are considerably lower than those measured in triaxial compression.

(4) Slight alteration of the sand can result in dramatic changes of the behavior at large strains.

Finally, the effects of stress path are not clear: the pore pressure injection and drained tests showed no effects on the position of the steady state line, while the extension tests yielded a significantly different line. On closer examination, however, the results are consistent within a different framework. The unifying factor in the test results appears to be the mode of deformation, or strain path of the samples. All of the tests which deformed in cylindrical axial compression yielded the same steady state relationship for a given material, regardless of the actual stress path, while samples which deformed in another mode (cylindrical axial extension) produced an alternate steady state line. It appears that the stress path itself is not an important factor, but that the mode of deformation (or strain path) can significantly impact the steady state conditions achieved at large strains.

Acknowledgement

The author's wish to acknowlege the invaluable advice and assistance of Clarence Chan in the design and performance of this testing program.

References

Alarcon-Guzman, A., Leonards, G.A., and Chameau, J.L., "Undrained Monotonic and Cyclic Strength of Sands," *J of Geotech Eng*, ASCE, 114(10), Oct. 1988, pp. 1089-1108.

Anderson, S.A., "The Role of Hydrologic Response and Soil Behavior in the Initiation of Rainfall-Induced Debris Flows," PhD. Thesis at UC Berkeley, Apr. 1992.

Anwar, H. "Membrane Compliance Effects in Undrained Testing of Saturated Cohesionless Soils," PhD. Thesis at Stanford University, Nov. 1989.

Been, K., Jefferies, M.G., and Hachey, J., "The Critical State of Sands," *Geotechnique*, 41(3), 1991, pp. 365-381.

Castro, G., "Liquefaction and Cyclic Mobility of Saturated Sands," *J. of the Geotech. Eng. Div.*, ASCE, 101(GT6), Jun. 1975, pp.551-569.

Gilbert, P. "Investigation of Density Variation in Triaxial Test Specimens of Cohesionless Soil Subjected to Cyclic and Monotonic Loading," Tech. Report GL-84-10, US Army Engineer Waterways Experiment Station, Vicksburg Miss., 1984.

Hanzawa, H., "Undrained Strength and Stability Analysis for a Quick Sand," *Soils and Foundations*, 20(2), Jun. 1980, pp.17-29.

Ishihara, K., Tatsuoka, F., and Yasuda, S., "Undrained Deformation and Liquefaction of Sand Under Cyclic Stresses," *Soils and Foundations*, 15(1), Mar. 1975, pp. 29-44.

Jong, H.L. and Seed, R.B., "A Critical Investigation of Factors Affecting Seismic Pore Pressure Generation and Post-Liquefaction Flow Behavior of Saturated Soils," Geotech. Res. Rept. No. SU/GT/88-01, Stanford Univ., Apr. 1988.

Konrad, J.M., "Minimum Undrained Strength of Two Sands," *J. of Geotech. Eng.*, ASCE, 116(6), Jun. 1990, pp. 932-947.

Konrad, J.M., "Minimum Undrained Strength Versus Steady-State Strength of Sands," *J. of Geotech. Eng.*, ASCE, 116(6), Jun. 1990, pp. 948-963.

Kramer, S. and Seed, H.B., "Initiation of Soil Liquefaction Under Static Loading Conditions," *J. of Geotech. Eng.*, ASCE, 114(4), Apr. 1988, pp. 412-430.

Lade, P., "Static Instability and Liquefaction of Loose, Fine Sandy Slopes," *J. of Geotech. Eng.*, ASCE, 118(1), Jan. 1992, pp. 51-71.

Li, X.S., Chan, C.K., and Shen, C.K., "An Automated Triaxial Testing System," *Advanced Triaxial Testing of Soil and Rock*, ASTM STP 977, 1988, pp. 95-106.

Lindenberg, J. and Koning, H.L., "Critical Density of Sand," *Geotechnique*, 31(2), 1981, pp. 231-245.

Mohamad, R. and Dobry, R., "Undrained Monotonic and Cyclic Triaxial Strength of Sand," *J. of Geotech. Eng.*, ASCE, 112(10), Oct. 1986, pp. 941-958.

Mulilis, P.J., Chan, C.K., Seed, H.B., "The Effect of Method of Sample Preparation on the Cyclic Stress Strain Behavior of Sand," Earthquake Eng. Res. Center Rept. 75-18, UC Berkeley, 1975.

Poulos, S., "The Steady State of Deformation," *J. of the Geotech. Eng. Div.*, ASCE, 107(GT5), May 1981, pp. 553-561.

Poulos, S., Castro, G., and France, J., "Liquefaction Evaluation Procedure," *J. of Geotech. Eng.*, ASCE, 111(6), Jun. 1985, pp. 772-792.

Riemer, M.F., Seed, H.B., Nicholson, P.G. and Jong, H., "Steady State Testing of Loose Sands: Limiting Minimum Density," Technical Note, *J. of Geotech. Eng.*, ASCE, 116(2), Feb. 1990, pp. 332-337.

Riemer, M.F., "The Effects of Testing Conditions on the Constitutive Behavior of Loose, Saturated Sand Under Monotonic Loading," PhD. Thesis at UC Berkeley, *In progress*

Sladen, J.A., D'Hollander, R.D., and Krahn, J., "The Liquefaction of Sands, a Collapse Surface Approach," *Can. Geotech. Jrnl.*, Vol. 22, 1985, pp. 564-578.

Sladen, J.A., and Handford, G., "A Potential Systematic Error in Laboratory Testing of Very Loose Sands," *Can. Geotech. Jrnl.*, Vol. 24, 1987, pp. 462-466.

Vaid, Y.P., and Chern, J.C., "Cyclic and Monotonic Undrained Response of Sands," Advances in the Art of Testing Soils Under Cyclic Conditions, Proc. ASCE Convention, Detroit, 1985, pp. 120-147.

Vaid, Y.P., Chung, E.K.F., and Kuerbis, R.H., "Stress Path and Steady State," *Can. Geotech. Jrnl.*, Vol. 27, 1990, pp. 1-7.

Yapa, K.A.S., "Decomposed Granite as an Embankment Fill Material: Physical and Mechanical Properties -- A Review," UC Berkeley Geotechnical Rept., 1992, *In progress.*

Post-Liquefaction Settlement of Sand -Mechanism and in Situ Evaluation

K. Arulanandan[1] and Jesus Sybico, Jr.[2]

[1]Professor of Civil Engineering
University of California, Davis

[2]Graduate Student
University of California

ABSTRACT

The mechanism causing the substantial settlement observed during and immediately after liquefaction in a centrifuge test is studied using resistivity measurements to characterize the soil structure. The permeability value at the point of initial liquefaction is shown to increase from the value at the initial state when the tortuosities and the pore shape factors at the appropriate states are used in the Kozeny Carman equation. The mechanism causing the substantial increase in settlement is considered to be due to the increase in permeability. The higher the permeability, the higher is the rate of settlement and the larger is the incremental settlement in each time step. In addition, the increase in permeability causes the liquefaction front to propagate upwards faster and therefore, the generation and dissipation processes affect a larger depth of the soil column during shaking, and hence, produces a larger settlement.

The use of a modified permeability in a fully coupled finite element code, DYSAC2, provides a good measure of the observed settlement.

INTRODUCTION

The settlement behaviour of saturated sands under earthquake loading has led to several studies since the 1964 earthquakes in Alaska and Niigata. Historically, liquefaction has been associated with sand boils, excessive settlement and massive lateral deformation.

Field observations of earthquake induced settlements in saturated sands range from a fraction of an inch to 20 inches[21]. In the case of pipeline facilities transitioning from firm ground to liquefiable soil deposits, ground settlements on the order of several inches may become significant with respect to damage potential. Hence, an understanding of deformation behaviour and methods of evaluation during and after liquefaction are necessary.

It has been postulated that as soon as sand liquefies, the settlement of particles or sand consolidation takes place followed by the flowing out of water from the voids[11]. The boundary between settled and liquefied sand starts in the lower part of the liquefied stratum and moves up towards the surface. This process of settling, solidification and consolidation was represented[20] by considering sedimentation first followed by consolidation in the growing solidified layer as a linear function of pore water pressure diffusion. Material properties such as permeability and coefficient of consolidation during pore water dissipation were obtained. It has been suggested that the process of settlement and pore water pressure dissipation occurs after the shaking stops[12]. However, it has been observed from centrifuge model studies[12] and from studies conducted under the NSF sponsored VELACS Project[5], that substantial settlement starts immediately after initial liquefaction. Settlement actually occurs when the shaking starts, however, it is relatively small[15]. Currently, numerical procedures predict only 20 to 30% of the settlement measured in the centrifuge.

The objectives of this paper are: 1) To study the mechanism causing the substantial settlement observed during and immediately after soil liquefaction in a centrifuge test using resistivity measurements to determine the change in soil structure and permeability during initital liquefaction; and, 2) To evaluate the observed settlement by using a modified permeability in a finite element computer code DYSAC2[18].

ELECTRICAL CHARACTERIZATION OF TRANSVERSELY ISOTROPIC SANDS

An index which has been shown experimentally to depend on the porosity, particle shape and size distribution and the direction of measurement is the formation factor, F[1,4,8,9,16,23]. It is defined as the ratio of the conductivity of the electrolyte, which saturates a particulate medium consisting of non-conductive particles, to the conductivity of the mixture[1]. Formation factor measurements have seen used for determining volume changes during a pressuremeter test[22] and for evaluating the in situ porosity of non-cohesive sediments[13], and for evaluation of in situ density and fabric of soils[2].

In recent years, the formation factor measurements made in the horizontal and vertical directions, where the latter is the direction of placement of the sample, have been used to characterize the anisotropic nature of sand deposits due to particle orientation[3,4,6,8]. These electrical parameters are

Vertical Formation Factor, $$F_v = \frac{\sigma_s}{\sigma_v} \quad (1)$$

Horizontal Formation Factor, $$F_h = \frac{\sigma_s}{\sigma_h} \quad (2)$$

(where σ_s = conductivity of the solution, σ_v = conductivity of the soil in the vertical direction and σ_h = conductivity of the soil in the horizontal direction.) It was also possible to develop theoretically, on the basis of electromagnetic theory, analytical relations between the average formation factor, $\bar{F}$, the porosity, n, and parameters associated with the shape and orientation of particles for transversely isotropic sands called the average shape factor, $\bar{f}$ [3,6,8]. This relationship is

$$\bar{F} = n^{-\bar{f}} \quad (3)$$

The average formation factor, $\bar{F}$, is calculated as

$$\bar{F} = \frac{F_v + 2F_h}{3} \quad (4)$$

Using the values of the shape and orientation parameters obtained independently[8] from the results of thin section studies[17], the theoretically predicted values of F along the axis of transverse isotropy were shown to be in close agreement with the experimentally measured values[8]. This gave a sound theoretical confirmation of the experimentally known fact that F depends on the sand structure, especially on the orientation of particles which cannot be accounted by other indices like relative density.

CENTRIFUGE TEST

Centrifuge and Laminar Box

The tests were performed in a stacked rectangular ring apparatus as shown in Fig. 1. The inside dimensions of the rings are 7 in. x 14 in. and the thickness of each ring is 0.5 inches. A total of 20 rings comprise the box and adds up to a height of 10.24 inches with spacing between rings. The earthquake motions were simulated using an electro hydraulic shaker.

Electrical Resistivity Probe

Two 3 in. x 3 in. brass plates were glued on to 3/16 " plexiglass and braced so that the plates are 3 inches apart as shown in Fig. 2 and the schematic drawing in Fig. 3. The plates were hung vertically into position inside the laminar box before the sand was poured in. The plates' faces were placed parallel to the direction of shaking to minimize disturbance to the sand during shaking. Since electrical resistance is affected by the area of plate-sand contact, and consequently the depth

at which it is buried, the top of the plates were positioned at least 2 inches below the surface. At a depth of 1.25 in. or more, the readings were found not to be sensitive to changes in height. The horizontal electrical resistance between the two plates is converted into volts by an electrical circuit and is sent through the existing data acquisition system. The circuit requires a function generator, a negative and positive DC power supply as shown in Fig. 4.

With the resistance measured and the dimensions of the electrical probe known, the conductivity can be calculated using the relationship

$$\sigma = \frac{1}{R}\frac{L}{A} \tag{5}$$

where σ is the conductivity, R is the electrical resistance in ohm, L is the length of the sample in cm and A is the cross sectional area of the sample in cm^2. Since L and A are the same, the formation factor can alternatively be defined as the ratio of the $\frac{1}{R}$ readings. Thus, equations 1 and 2 can be also expressed as

$$F_v = \frac{R_{\text{soil in vert. dir.}}}{R_{\text{solution}}} \tag{6}$$

$$F_h = \frac{R_{\text{soil in hor. dir.}}}{R_{\text{solution}}} \tag{7}$$

Sample Preparation

A thin plastic bag of slightly larger size than the inside dimensions of the laminar box was first placed inside to contain the sample. After the resistivity probe was hung in its desired position, an appropriate amount of water with known conductivity was poured into the box. Fine Nevada sand was then pluviated to the appropriate height in the laminar box. As the sample increased in height, pore pressure transducers and accelerometers were placed in positions at their desired locations. Two Linear Variable Differential Transformer (LVDT) were placed on top of thin balsa wood blocks to prevent them from sinking into the liquefied soil. Balsa wood was found to prevent sinking better than aluminum square plates. This may be because the density of the wood is closer to the density of the liquefied soil than the aluminum. The weight of the LDVT's potentiometer on the balsa wood blocks prevented it from floating in the layer of water that developed at the surface after liquefaction. The method of using Balsa wood to prevent sinking was first attempted by Fiegel[10].

TEST RESULTS

Nevada sand with gradation characteristics as shown in Fig. 5 was used in this study. The measured vertical and horizontal formation factors of the sand prepared at different porosities by the pluviation method of placement are shown in Fig. 6. It can be seen that an index of anisotropy, A, defined as

$$A = \sqrt{\frac{F_v}{F_h}} \tag{8}$$

where F_v is the vertical formation factor in the direction of placement of the sample and F_h is the horizontal formation factor[4] is 1.04.

The centrifuge model at a porosity of 0.418 was accelerated to 50g and subjected to a base acceleration as shown in Fig. 7. The initial permeability at this porosity was measured to be 6.56 x 10^{-5} m/s based on permeameter tests on this sand.

An accelerometer, attached underneath the box, measured the horizontal acceleration. The formation factor plates were positioned in the middle of the box with the top of the plates 2 inches beneath the surface. Six pore water pressure transducers (Weight = 2.9 g, Diameter = 0.3 in., Length = 0.4 in) were placed inside the sample, in pairs, an inch to the left and right of the formation factor plates at depths of $\frac{1}{4}$ H, $\frac{1}{2}$ H and $\frac{3}{4}$ H from the bottom. Two LVDTs, placed at 1.15 in. on each side of centre line, measured the settlement of the surface. The measured base accelerations, generated pore water pressure ratios, horizontal formation factor and surface settlement with respect to time are shown in Figs. 7 to 10, respectively. The prepared sample, initially, had a horizontal flat surface. After liquefaction, the surface formed a curvature with radius equal to the distance from the soil surface to the axis of the centrifuge rotation. The correction due to this curvature at the location of the LVDTs is equivalent to 9.92 inches at the prototype scale as shown in Fig. 11. The total measured settlement at the end of shaking has been corrected for the above curvature of the soil surface. The settlement time history was adjusted proportionally to be consistent with the corrected settlement at the end.

Prior to shaking, after the pore water pressures stabilized at 50g, the centrifuge was stopped to observe the settlement due to curvature and it was found that the curvature did not form before shaking. It was difficult to determine at which point the curvature was formed during shaking based on the settlement time history. It is for this reason that the time history of settlement was adjusted proportionally to account for the curvature of the soil surface.

ANALYSIS

The change in the value of F_h is related to the change in the value of permeability. The Kozeny-Carman equation,

$$k = \frac{\gamma_w}{\mu} \frac{1}{k_o T^2 S_o^2} \frac{n^3}{(1-n)^2} \tag{9}$$

where k = permeability, γ_w = unit weight of water, μ = viscosity of water, k_o = pore shape factor, T = tortuosity, S_o = specific surface area and n = porosity, has been shown to be valid for the evaluation of the permeability of non-clay minerals.

The tortuosity, T, in eqn. 9 can be expressed in terms of the formation factor, F, and porosity, n, using the relationship[23]

$$n = cT^2 \tag{10}$$

where

$$c = \frac{1}{F} \tag{11}$$

and F is the formation factor measured in the same direction as the permeability measurement. Eqn 9 becomes

$$k = \frac{\gamma_w}{\mu} \frac{1}{k_o F S_o^2} \frac{n^2}{(1-n)^2} \tag{12}$$

relating permeability to the structure of the soil in terms of the formation factor, F, and the pore shape factor, k_o.

The pore shape factor, k_o, prior to shaking was estimated using the following properties: 1) permeability; 2) the vertical formation factor calculated using the measured horizontal formation factor and the anisotropy index; 3) the specific surface area, S_o, 426 cm^{-1} evaluated using the grain size distribution as shown in Fig. 5; and, 4) the constant value $\frac{\mu}{\gamma_w}$ of 1.02 x 10^{-5} cm-sec. The estimated value of k_o prior to shaking is shown in Table 1.

Table 1. Estimated Values of k_o Prior to Shaking

Test No.	Height (inches)	Porosity n	Permeability x 10^{-3} cm/s	F_h Measured	F_v A = 1.04	Estimated value of k_o
1	7.500	0.418	6.55	3.05	3.30	12.90

At the point of initial liquefaction, the soil particles lose full contact with each other. This creates an easier path for water flow. The creation of such flow paths reduces the tortuosity, T, and the pore shape factor, k_o. These two properties lead to an increase in the permeability at the point of initial liquefaction. At the point of initial liquefaction, it is assumed that there is negligible change in porosity. It is further assumed that the soil is homogeneous throughout the layer and the pore sizes become uniform as effective stresses approach zero. At this state, the pore shape factor, k_o is assessed to be 2.5 and used in the Kozeny-Carman equation to evaluate permeability.

Equation 9 may also be expressed as

$$k = C_s \frac{\gamma_w}{\mu} \frac{1}{S_o^2} \frac{n^3}{(1-n)^2} \tag{13}$$

where

$$C_s = \frac{1}{k_o T^2} \tag{14}$$

is called the shape coefficient. Since n has been assumed to be constant, the rest of the equation remains unchanged when comparing permeabilities at the initial and liquefied states. It is convenient to express the permeability value at a different state in terms of

$$k_{new} = C\, k_{initial} \tag{15}$$

where k_{new} = permeability at a new state, $k_{initial}$ = initial permeability and C is a factor. (The value of C at the initial and liquefied states are 1.0 and C_{Liq}, respectively).

The factor, C, is calculated using the values of C_s at the initial and the new states.

$$C = \frac{Cs_{new}}{Cs_{initial}} = \frac{(k_o T^2)_{initial}}{(k_o T^2)_{new}} = \frac{(k_o F_v)_{initial}}{(k_o F_v)_{new}} \tag{16}$$

To calculate C_{Liq}, use $(k_o F_v)_{liquefied}$ in eqn 16. Since the pore shape changes constantly as the particles settle down, an average factor, C_{ave} (average of the factors at the initial and liquefied states) was used to modify the permeability. The use of C_{ave} assumes that the permeability at the point of initial liquefaction and at the end of the settlement process may be represented by the average of the two permeabilities. The change in porosity after settlement contributes to the change in permeability as indicated in eqn 9 and should be included in eqn 16 if it is a post liquefaction prediction. However, it is relatively small compared to the contributions due to changes in k_o and F_v. The estimated values of C_{ave} are shown in Table 2.

Table 2. Calculation of Average Factor

Test No.	(F_v) initial A = 1.04	(F_v) liquefied A = 1.00	k_o initial Table 1	k_o liquefied	C_{Liq}	C_{ave}
1	3.30	2.68	12.90	2.50	6.35	3.67

The above analysis show that the permeability at the point of initial liquefaction increases 6-7 times due to structure change.

EVALUATION OF SETTLEMENT

The computer code, DYSAC2 (using 4 noded quadrilateral elements with pore fluid and soil skeleton displacements as variable) was used to predict the settlement of each test twice, using the initial permeability in the first prediction and the average or modified permeability in the second. The predicted settlements are compared with the measured settlements and are shown in Figs. 12. A reasonable agreement between the measured and evaluated settlements is seen to exist if the modified permeability is used in the calculations. A summary of the measured and the predicted settlements is shown in Table. 3.

Table 3. Summary of Measured and Predicted Settlements

Test No.	Measured Settlement	Initial Prediction of settlement	Modified Prediction of settlement
1	6.29	2.22	5.98

MECHANISM CAUSING SETTLEMENT DURING EARTHQUAKE SHAKING

The magnitude of the pore water pressure ratio of a layer for a given time interval during shaking is influenced by two major factors: 1) the earthquake acceleration which tends to increase it, and 2) the dissipation during consolidation which tends to reduce it. Centrifuge model studies[5,15] have shown that the initial liquefaction occurs simultaneously in all layers. At a particular layer, once the initial sedimentation is completed after initial liquefaction, the pore water pressure decreases due to consolidation and an increase in pore water pressure occurs due to the earthquake acceleration. The net effect of the two processes may be zero and the measured pore water pressure values may indicate that no dissipation/consolidation has occurred. A layer can therefore consolidate without visible change in the measured pore water pressure even when the pore water pressure is 100 percent. There will be no visible change in the measured pore water pressure until the shaking diminishes or until sufficient consolidation has taken place. It is due to this dynamic effect that an increase in permeability results in an increase in total settlement. The higher the permeability, the faster the rate of settlement and larger is the incremental settlement in a given time interval.

The height of the soil column and the duration of shaking are important factors that influence the degree of the effect of a higher permeability on the total settlement. The larger the depth of the layers where initial sedimentation is completed after initial liquefaction the larger in the increase in settlement expected.

In the static case (no shaking during dissipation), an increase in permeability does not affect the total settlement. The soil column with a lower permeability has a lower rate of settlement and will simply require a longer period to dissipate the excess pore water pressure.

CONCLUSIONS

The fabric of the soil has been characterized using electrical properties. The influence of fabric on permeability during low effective stresses is estimated in terms of k_0 the pore shape factor using the Kozeny-Carman equation for permeability. Permeability values at initial liquefaction and during the earthquake motion are necessary for the analysis of post liquefaction settlement.

The application of the above approach to predict post liquefaction vertical settlement in practice requires the evaluation of the increased permeability at the point of initial liquefaction. The porosity, the specific surface area and the initial permeability may be estimated using electrical methods. The assumed change in vertical formation factor and pore shape factor will provide an indication as to the permeability increase which is necessary for use in analytical predictions.

Three similar centrifuge tests were conducted using resistivity measurements to evaluate the post liquefaction settlements. The results of the settlements obtained in the three tests are in close agreement with the predicted values.

ACKNOWLEDGEMENTS

The support provided by the National Science Foundation - Grant No. BCS89-12074 (The VELACS Project) is gratefully acknowledged. The results presented in this paper are from a M.Sc thesis on "Post Liquefaction Settlement of Sands," submitted by the second author. The authors are grateful for the assistance given by Dr. X.S. Li in the development of the electronic systems used in this study. The authors are also grateful to Prof. Ronald F. Scott for reviewing the paper and providing valuable suggestions.

REFERENCES

1. ARCHIE, G.E. (1942) The Electrical Resistivity Log as an Aid in Determining Some Reservior Characteristic. Tran AIME, 146, pp 54-61.

2. ARULANANDAN, K. (1977) Method and Apparatus for Measuring In-Situ Density and Fabric of Soils. Patented, Regents of the University of California, 1977.

3. ARULANANDAN, K. and MURALEETHARAN, K. (1988) Level Ground Soil Liquefaction Analysis using In-Situ Properties Part I. *J. Geotech. Eng'g. Div.*, ASCE, Vol. 114, No. 7, pp 753-770.

4. ARULANANDAN, K. and KUTTER, B. (1978) A Directional Structural Index Related to Sand Liquefaction. Proceedings of a Specialty Conference on Earthquake Engineering on Soil Dynamics, ASCE, Pasadena, CA, pp 213-230, June 19-21.

5. ARULANANDAN, K. AND SCOTT, R. F.(1992) Project VELACS - Control Test Results, Submitted to ASCE.

6. ARULMOLI, K., ARULANANDAN, K. and SEED, H.B. (1985) New Method for Evaluating Liquefaction Potential. *J. Geotech. Eng'g. Div.*, ASCE, Vol. 111, No. 1, pp 95 - 114.

7. CARMAN, P.C. (1956) Flow of Gases through Porous Media, Academia New York.

8. DAFALIAS, Y. and ARULANANDAN, K. (1979) Electrical Characterization of Transversely Isotropic Sands. *Archives of Mechanics*, Warsaw.

9. De La RUE, R.E. and TOBIAS, C.W. (1959) On the Conductivity of Dispersions. J. Electrochem. Soc., 106, pp 827-833.

10. FIEGEL, G.L. (1992) Centrifuge modeling of liquefaction in layered soils, MSc. Thesis, University of California, Davis.

11. FLORIN, V. and IVANOV, P. (1961) Liquefaction of Saturated Sandy Soils. 5th International Conference, Soil Mechanics & Foundation Engineering, Paris.

12. HUSHMAND, B., CROUSE, C., MARTIN, G. and SCOTT, F. (1988) Centrifuge Liquefaction Tests in a Laminar Box. *Geotechnique* 38, No. 2, pp 253 - 262.

13. JACKSON, P.D. (1975) An Electrical Resistivity Method for Evaluating the In Situ Porosity of Non-cohesive Marine Sediments. *Geophysics.*

14. KOZENY, J. (1927) Ueber kapillare Leitung des Wassers im Boden, *Wien, Akad. Wiss.*, Vol. 136, Pt. 2a, p. 271.

15. LAMBE, P. (1981) Dynamic Centrifuge Modelling of a Horizontal Sand Stratum," Sc. D Thesis, Dept. of Civil Engineering, Mass. Inst. of Technology, Cambridge, Mass.

16. MEREDITH, R.E. and TOBIAS, C.W. (1962) Conduction in Heterogeneous systems. Adv. Electrochem, Electrochem. Engng., 2nd ed., J. Wiley and Sons Inc., New York.

17. MITCHELL, J.K., CHATOIAN, J.M. AND CARPENTER, G.C. (1976) The Influence of Fabric in the Liquefaction Behaviour of Sand, Report to U.S. Army Engineering Waterways Experiment Station, Vicksburg, Berkleley.

18. MURALEETHARAN, K.K. and ARULANANDAN, K. (1991) Dynamic Behavior of Earth Dams Containing Stratified Soils, Centrifuge 91, Proceedings of the International Conference Centrifuge 1991, Boulder, CO, June 13-14.

19. MURALEETHARAN, K., MISH, K., YOGOCHANDRAN, C. and ARULANANDAN, K. (1991) Users Manual for DYSAC2.

20. SCOTT, R. F. (1986) Soil Properties from Centrifuge Liquefaction Tests. *Mechanics of Materials*, Vol. 5, pp 199-205.

21. TOKIMATSU, K. and SEED, H.B. (1987) Evaluation of Settlements in Sand due to Earthquake Shaking. *J. Geotech. Eng'g. Div.* ASCE, Vol. 113, No. 8, August, pp 861-878.

22. WROTH, C.P. and WINDLE, D. (1975) Analysis of the Pressuremeter Test Allowing for Volume Change. *Geotechnique.*

23. WYLLIE, M.R.J. (1955) Verification of Tortuosity Equations. Bulletin of the American Association of Petroleum Geology, Vol. 30, No.2, pp 266-267

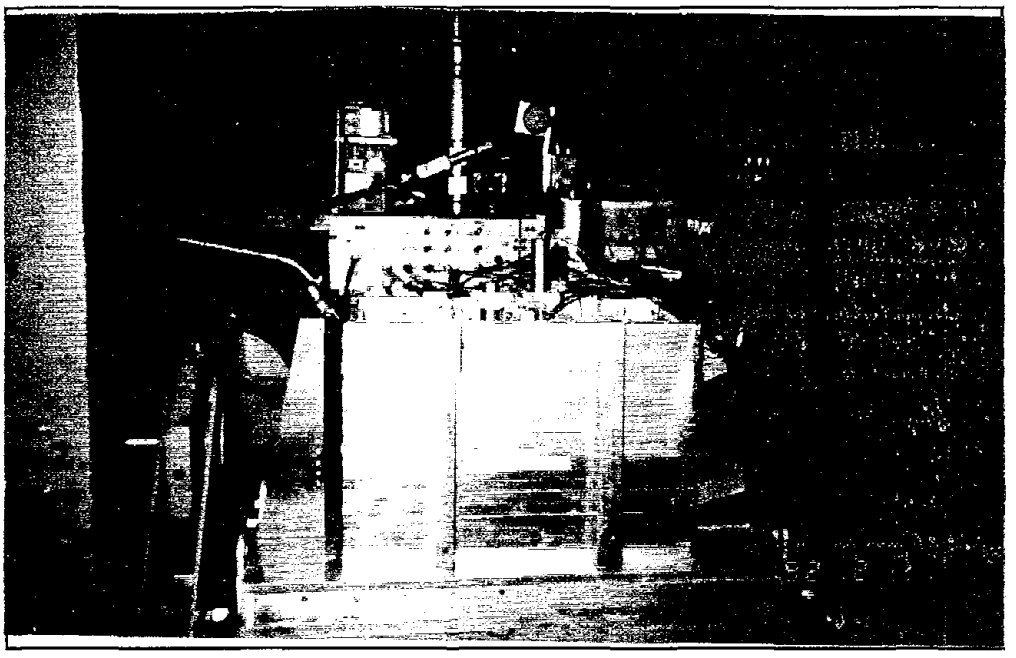

Fig. 1. Stacked Ringed Laminar Box

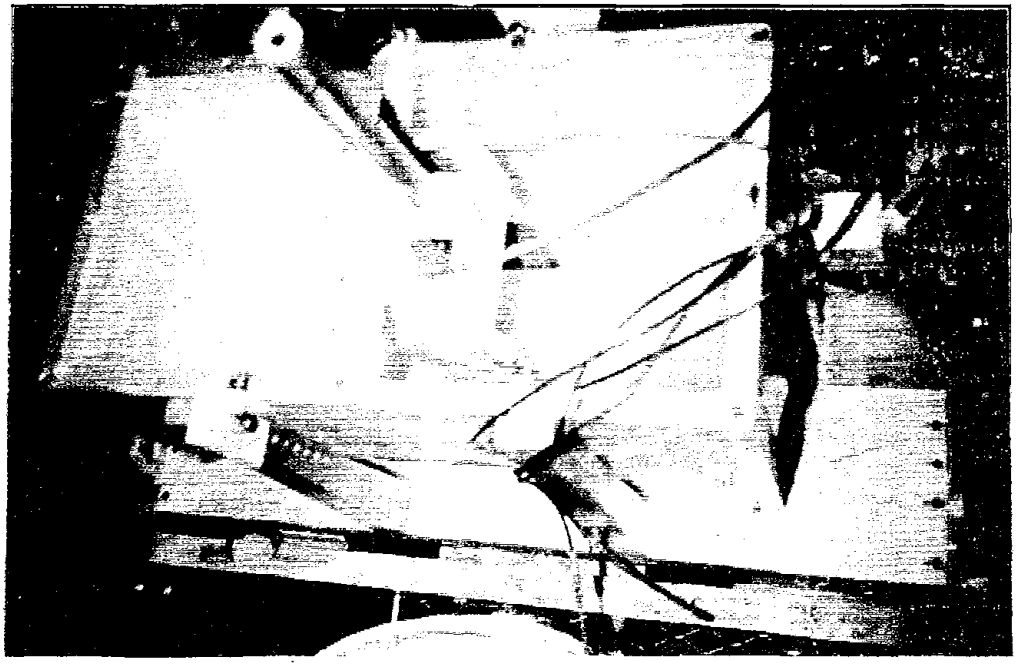

Fig. 2. Electrical Resistivity Probe Inside the Laminar Box

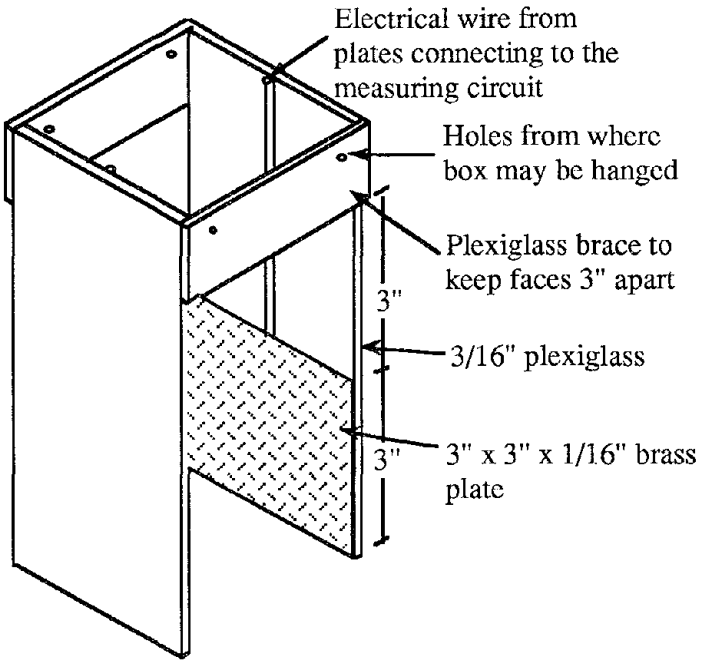

Fig. 3. Schematic Drawing of the Resistivity Probe.

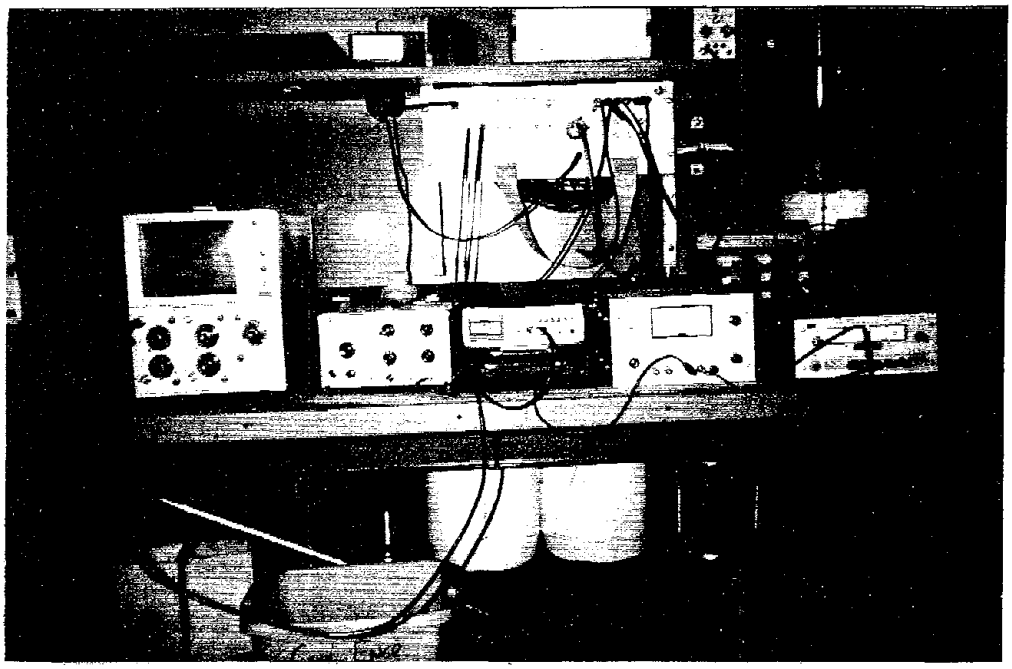

Fig. 4. Oscilloscope, Function Generator, Multi-Tester, Negative and Positive D.C. Power Supply

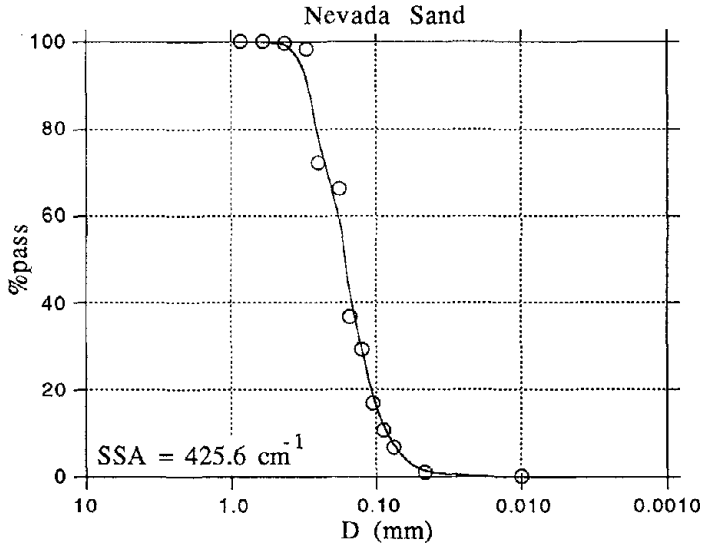

Fig. 5. Grain Size Distribution Curve

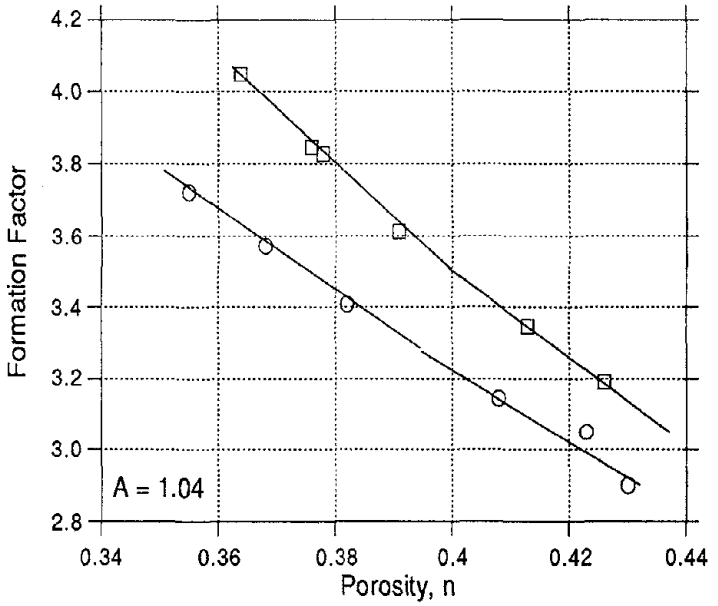

Fig. 6. Vertical and Horizontal Formation Factors of Pluviated Nevada Sand

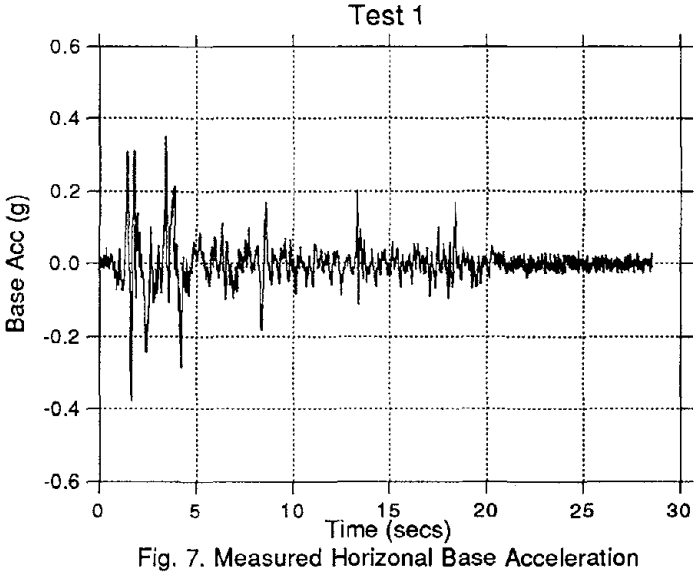

Fig. 7. Measured Horizonal Base Acceleration

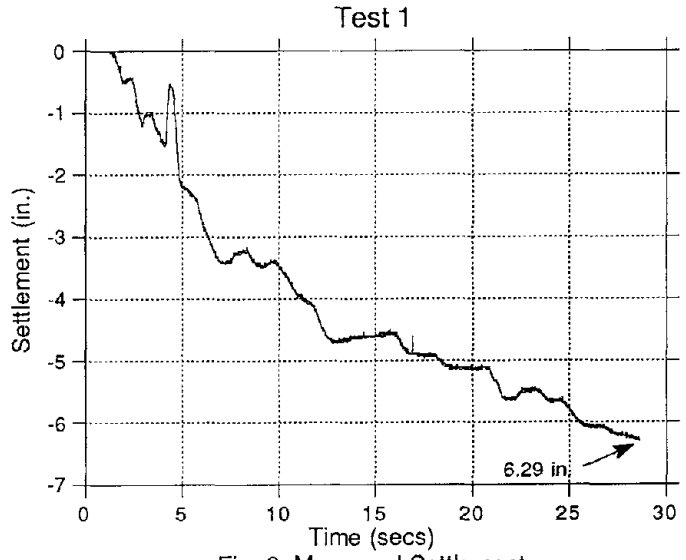

Fig. 8. Measured Settlement

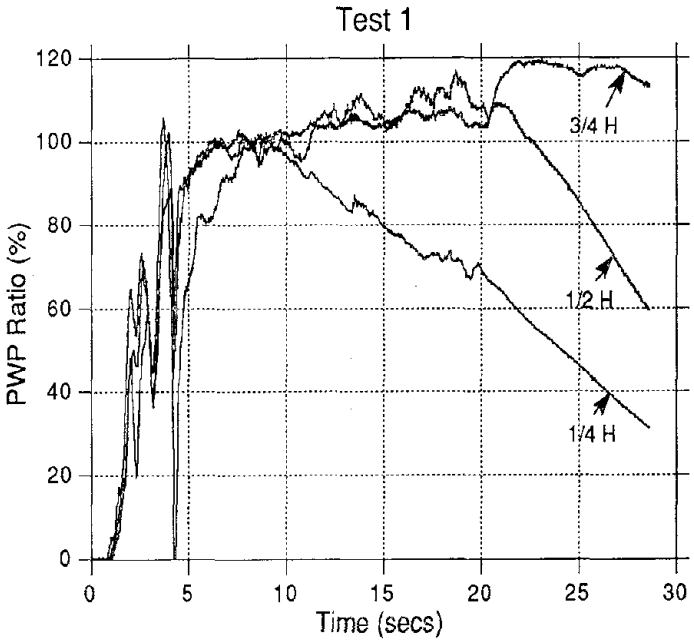

Fig. 9. Measured Excess Pore Water Pressure Ratio

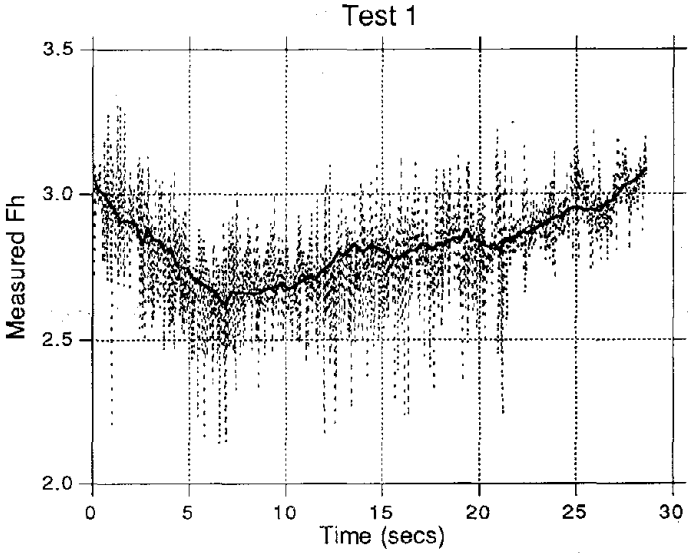

Fig. 10. Measured Horizontal Formation Factor

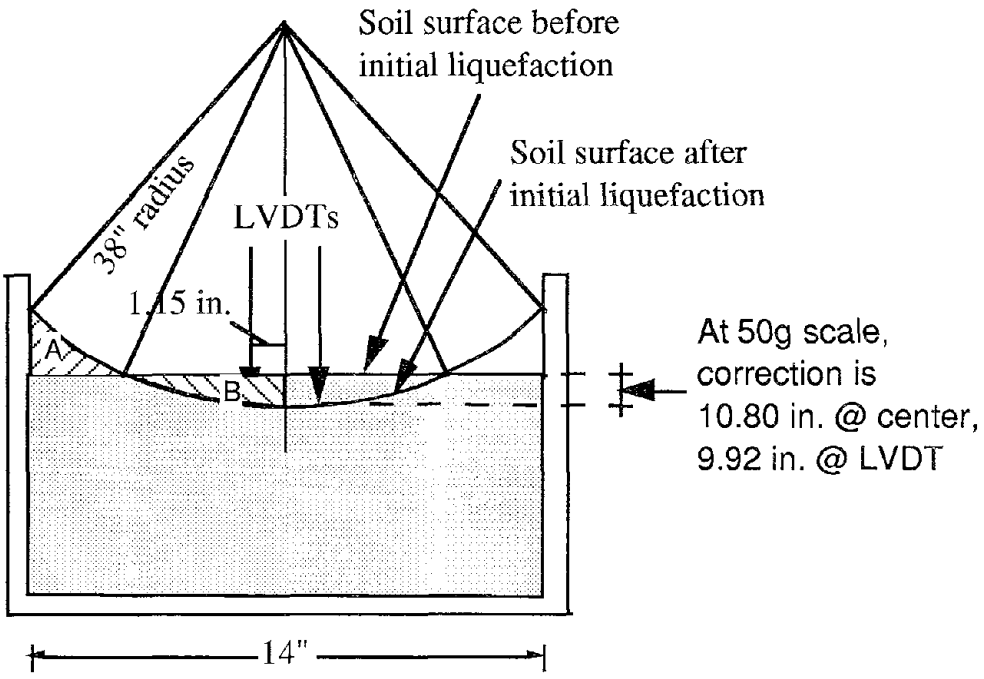

The curvature is due to radius of the centrifuge.
Area A = Area B.

Fig. 11. Correction due to Surface Curvature.

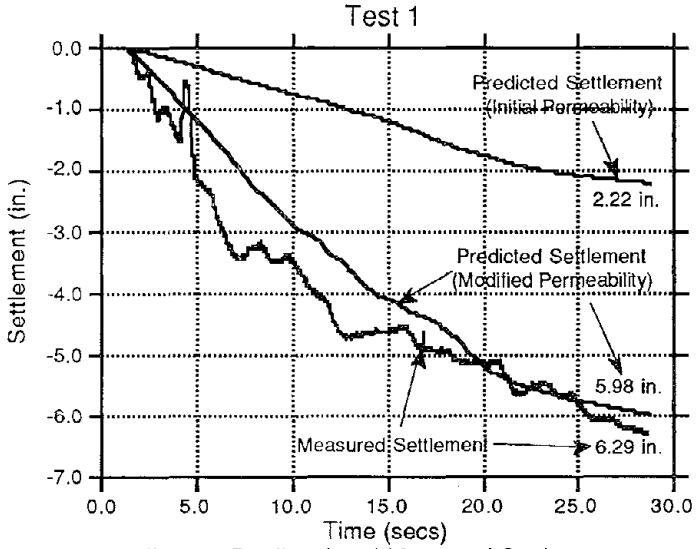

Fig. 12. Predicted and Measured Settlements

Modelling of the Stress–Strain Behavior of Liquefiable Sands

Mladen (Mike) Vucetic and Neven Matasovic

Assistant Professor and Research Assistant
University of California, Los Angeles

ABSTRACT

The concept to use the dynamic backbone curve in conjunction with the Masing criteria for the construction of unloading and reloading branches of the initial cyclic loop, and its extension to subsequent cyclic loading when the soil undergoes significant degradation due to pore water pressure buildup, is verified. To accurately describe the initial and subsequent cyclic stress-strain loops, the original Kondner and Zelasko hyperbolic model and a well known degradation model are modified. The hysteretic damping can also be described quite accurately by the same method. The investigation is based on the test results obtained on several different liquefiable sands. The modelling of one of these sands is presented in detail.

INTRODUCTION

A nonlinear seismic response of horizontally layered liquefiable saturated sand deposits is often evaluated under the assumption that the governing seismic waves are the one-dimensional shear waves which are propagating vertically upwards. In such a case, in addition to the initial vertical effective consolidation stresses, σ'_{vc}, and horizontal effective consolidation stresses, σ'_{hc}, shown in Fig. 1a, a representative soil element is subjected to shear stresses, τ, and associated shear strains, γ, as shown in Fig. 1b. The figure also shows that during the cyclic shearing the initial hydrostatic pore water pressure, u_o, increases by the residual cyclic pore water pressure, u. Typical τ vs. γ curves describing the cyclic behavior of such a sand element in the first cycle (starting at time t = 0) and a subsequent cycle (at time t) are sketched in Fig. 2. For both cyclic loops, the associated backbone curves are also constructed, i.e., for the first cycle, the initial backbone curve, and for the subsequent cycle when the soil has undergone cyclic degradation, the subsequent degraded backbone curve.

The most important aspect of the initial backbone curve is that it can be used in conjunction with the Masing criteria (Masing, 1926) to describe the first cyclic loop. The first Masing criterion postulates that the tangent shear moduli at the reversal points of the unloading and reloading branches of the loop are identical to the initial shear modulus, G_{mo}. The second Masing criteria states that the shape of the reloading branch is the same as that of the positive part of the backbone curve enlarged by a factor of two, and similarly, that the unloading branch has the shape of the negative part of the backbone curve enlarged by a factor of two. These two criteria for the conditions of no degradation under cyclic loading were originally proposed by Masing for brass. Newmark and Rosenblueth (1971) suggested that they can be used for granular materials. Later, the application of Masing criteria has been extended to clays (Idriss et al., 1978) and fully saturated sands (Finn et al., 1977) which degrade under repetitive loading.

The process of cyclic degradation, which may eventually lead to full liquefaction, is characterized in Fig. 2 by the reduction of the ordinates of subsequent cyclic stress-strain curve in relation to the ordinates of the initial stress-strain curve (see also Fig. 3d). Also, if for the subsequent cyclic loop the associated degraded backbone curve is constructed using the Masing criteria, the cyclic degradation can be simply characterized by the reduction of the ordinates of the subsequent degraded backbone curve in relation to the ordinates of the initial backbone curve. However, as indicated in Fig. 2, the tangent moduli G_{mo} and G_{mt} at the beginning of the initial and subsequent backbone curves respectively are not exactly the same as those at the tips of the corresponding cyclic loops, because significant degradation can occur in saturated sands in a single cycle.

Parameters and models for the description of the cyclic stress-strain behavior based on the concept of the backbone curve can be divided into three main groups. Those related to the stress-strain curve in the first cycle, those related to the stress-strain curve in subsequent cycles, and those describing the cyclic degradation between the first and subsequent cycles. As shown in Fig. 2, the cyclic stress-strain behavior in any cycle can be described by five main parameters. For the first cycle starting at time t = 0 these are: initial tangent shear modulus, G_{mo}; cyclic shear strain amplitude, γ_{co}; corresponding cyclic shear stress amplitude, τ_{co}, and secant shear modulus, G_{so}; and the internal damping which is inherent to the nonlinear hysteretic behavior of soils. The internal damping of soil can be conveniently represented by the equivalent viscous damping ratio, λ_o(Jacobsen, 1930):

$$\lambda_o = \frac{1}{4\pi} \frac{\Delta W_o}{\frac{1}{2} \gamma_{co} \tau_{co}} \qquad (1)$$

where ΔW_o is the area within the first closed hysteresis loop. Similarly, for the loop at time t, these five parameters are G_{mt}, γ_{ct}, τ_{ct}, G_{st}, and λ_t corresponding to ΔW_t. The cyclic degradation of soil between the first and subsequent cycles can be described by modelling the transformation of the backbone curve using an appropriate degradation parameter. In the case of fully saturated sands, a continuous reduction of the backbone curve ordinates can be modelled by using the residual excess cyclic pore water pressure, u, as a degradation parameter.

This paper describes refinement and verification of the approach to cyclic characterization of liquefiable sands which employs the concept of the initial and degraded backbone curves in conjunction with the Masing criteria. The following components of the approach are encompassed: (i) improved definition of the initial backbone curve based on the initial stress-strain curve model proposed by Kondner and Zelasko (1963), (ii) improved cyclic degradation models which are commonly used to define the degraded backbone curves (employing the residual excess cyclic pore water pressure as the degradation parameter), and (iii) examination of the applicability of Masing criteria to nondegraded and cyclically degraded sands. The conclusions put forward are based on the laboratory cyclic test results obtained on several liquefiable sands. However, only the results obtained on one sand, the Santa Monica Beach sand, abbreviated here as SMB sand, are presented and discussed in detail.

SAND ANALYZED AND TESTING PROCEDURE

The SMB sand is a uniformly graded liquefiable sand. To simulate the undrained field conditions sketched in Fig. 1, the sand was tested in the NGI-type direct simple shear (DSS) apparatus, using the constant volume equivalent undrained testing procedure (Bjerrum and Landva, 1966). The specimens had a diameter of 47.5 mm and a height of approximately 18 mm prior to consolidation. A total of 4 static and 16 cyclic tests were performed to characterize the initial stress-strain curve and subsequent cyclic behavior. During the cyclic shearing, i.e., after the consolidation, the average void ratio was, e_o = 0.56, vertical effective consolidation stress, σ'_{vc} = 196 kN/m^2, and the estimated maximum shear modulus, G_{mo} = 140 000 kN/m^2. The results of a representative cyclic test are presented in Fig. 3. The shear stress and the excess pore water pressure time histories are presented in the normalized form with respect to the vertical effective consolidation stress, σ'_{vc}, i.e., in terms of $\tau^* = \tau/\sigma'_{vc}$ and $u^* = u/\sigma'_{vc}$.

INITIAL STRESS-STRAIN CURVE AND THE BEHAVIOR IN THE FIRST CYCLE

Initial Stress-Strain Curve

As shown in Fig. 2, the positive part of the initial backbone curve is described by the initial monotonic (static) stress-strain curve, which can in turn be used to construct the complete initial backbone curve and the associated first cycle loop. It is customary to express the initial stress-strain curve in an analytical form by either using the

hyperbolic model (Kondner and Zelasko, 1963; Hardin and Drnevich, 1972; Finn et al., 1977) or the Ramberg-Osgood model and its modifications (Ramberg and Osgood, 1943; Richart, 1975; Idriss et al., 1978; Hara, 1980; Ishihara et al. 1985; Ishihara, 1986). As explained earlier, such models have been commonly used in conjunction with the Masing criteria incorporated for modelling the stress-strain behavior of soil during unloading and reloading phases, and with the empirical models for cyclic degradation, which in the case of sand relate the degrading properties to the residual excess pore water pressure.

The behavior of fully saturated sands during undrained cyclic loading can be treated in a consistent manner if it is considered that the cyclic shear strains are governing the cyclic pore pressure response and associated degradation of stiffness (Dobry et al., 1982). If such cyclic strain-controlled behavior is considered, it is convenient to use the stress-strain model which expresses the stress as an explicit function of strain. The Kondner and Zelasko (1963) hyperbolic model, abbreviated here as the K-Z model, is such a model.

The K-Z model for the initial loading stress-strain curve is described by the equation:

$$\tau = f(\gamma) = \frac{G_{mo} \cdot \gamma}{1 + \frac{G_{mo}}{\tau_{mo}} \cdot \gamma} \cdot \qquad (2)$$

In the normalized form with respect to σ'_{vc}, Eq. 2 can be rewritten as:

$$\tau^* = f^*(\gamma) = \frac{G^*_{mo} \cdot \gamma}{1 + \frac{G^*_{mo}}{\tau^*_{mo}} \cdot \gamma}, \qquad (3)$$

where $\tau^*_{mo} = \tau_{mo} / \sigma'_{vc}$ and $G^*_{mo} = G_{mo} / \sigma'_{vc}$. As shown in Fig. 2, G_{mo} in Eq. 2 is the initial tangent shear modulus at time $t = 0$. In the original Kondner and Zelasko formulation τ_{mo} is the shear strength of the soil, i.e., the maximum shear stress that can be applied to the soil. With such τ_{mo} parameter, Eq. 2 would cover a large range of strains all the way up to the strains at failure. However, the dominant shear strains in the seismic response of soil deposits are relatively small, because the large shear strains may occur only at the extreme when the soil is approaching full liquefaction. Therefore, to accurately model the initial loading curve in the dominant range of strains, τ_{mo} can be arbitrarily selected as the τ ordinate of the experimentally obtained initial loading stress-strain curve corresponding approximately to the upper boundary of this dominant shear strain range. Such an approach to the selection of τ_{mo} has been used in this study. In particular, the value of τ_{mo} corresponding to $\gamma = 1.0\%$ was selected.

It has been noticed (e.g. Ishihara et al., 1985) that the K-Z model is often incapable of describing the soil stress-strain behavior with a desired degree of accuracy. Consequently, for more accurate liquefaction response analyses it may be necessary to modify the K-Z model by increasing the number of its parameters. The results of this investigation revealed that by adding only two parameters to the original K-Z stress-strain formulation, the experimentally

obtained initial stress-strain curve can be described accurately. If these two additional parameters, called β and s, are introduced in the original hyperbolic formulation given by Eq. 3, the improved model assumes the following form:

$$\tau^* = f^*(\gamma) = \frac{G^*_{mo} \cdot \gamma}{1 + \beta\left(\frac{G^*_{mo}}{\tau^*_{mo}}\gamma\right)^s} \tag{4}$$

This modified Kondner and Zelasko model will be abbreviated here as the M-K-Z model. The proposed M-K-Z model is similar in form and number of parameters to the Ramberg-Osgood model. However, as already emphasized, in the M-K-Z model the stress is an explicit function of the strain, which is more convenient in the cyclic strain-controlled approach to the evaluation of seismic response.

The curve in Fig. 4, which was constructed on the basis of 20 tests on the SMB sand, illustrates the deficiency of the original K-Z model and justifies the proposed modification. If the value of shear modulus at very small strains, G_{mo}, is regarded as constant, the only parameter that can be varied to fit the data using the original K-Z model is τ_{mo}. As it can be seen in Fig. 4, that may not be sufficient for a satisfactory fit, while an excellent fit can be obtained by the M-K-Z model which has two additional parameters. For the SMB sand shown in Fig. 4, G_{mo} = 140 000 kN/m^2, τ_{mo} = 69 kN/m^2, β = 1.7 and s = 0.8.

Stress-Strain Behavior in the First Cycle

If the calculated M-K-Z curve in Fig. 4 is extended into the negative domain, the corresponding initial backbone curve will be obtained. If in turn this backbone curve is used in conjunction with the Masing criteria, the stress-strain curves of the first cycle can be constructed, i.e., the initial cyclic loop for a given γ_{co} can be determined analytically. Such calculated cyclic stress-strain curves can then be compared to the corresponding measured curves, thereby enabling an examination of the validity of the Masing criteria. This is presented in Fig. 5. The figure reveals that the Masing criteria are indeed suitable for cyclic characterization of the first cycle behavior of the liquefiable SMB sand.

BEHAVIOR DURING SUBSEQUENT CYCLES

Cyclic Stress-Strain Behavior

During the second and subsequent cycles, the stress-strain behavior can be characterized by the degrading backbone curves in conjunction with the Masing criteria, as mentioned in the introduction. Traditionally, this has been done for liquefiable sands by replacing the parameters G_{mo} and τ_{mo} in Eq. 2 by G_{mi} and τ_{mi} respectively, and by their continuous updating, considering the residual excess pore water pressure, u, as the degradation parameter. The corresponding degradation models are called the modulus degradation model and the stress degradation model respectively, and in normalized form they are expressed by the following equations:

$$G^*_{mt} = G^*_{mo}\sqrt{\frac{(\sigma'_{vc} - u)}{\sigma'_{vc}}} = G^*_{mo}\sqrt{1 - u^*} \tag{5}$$

and

$$\tau^*_{mt} = \tau^*_{mo}\frac{\sigma'_{vc} - u}{\sigma'_{vc}} = \tau^*_{mo}(1 - u^*), \tag{6}$$

where u^* is the normalized residual excess pore water pressure. These types of cyclic degradation models were adopted by Hardin and Drnevich (1972) and have been frequently used in cyclic effective stress analyses of the response of liquefiable sites (e.g. Finn, et all., 1977; Lee and Finn, 1978; Vucetic, 1986).

To improve the modelling of the degradation, the stress degradation model is modified here by introducing an exponential constant, v, in the following manner:

$$\tau^*_{mt} = \tau^*_{mo}\{1 - (u^*)^v\} \tag{7}$$

The effect of this modification is illustrated for the SMB sand in Figs. 6 and 7, using the results of the representative test on the SMB sand presented in Figs. 3 to 5. In Fig. 6a the families of degraded backbone curves are constructed on the basis of the models given by Eqs. 5 and 7, for $v = 3.5$ obtained by curve fitting for the SMB sand. In Fig. 6b, a family of degraded backbone curves for $v = 1.0$, corresponding to the original stress degradation model given by Eq. 6 is constructed for comparison. The difference between the two families of curves is significant. In Fig. 7 the measured cyclic stress-strain curves and the calculated stress-strain curves obtained using Eq. 7 are compared for the full range of u^*. It can be seen that the analytical description of the experimentally obtained loops in Fig. 7 is excellent for u^* up to approximately 0.8. For $u^* > 0.8$ the fit is no longer as good, because of a pronounced "S-shaping" of the unloading and reloading curves. It should be noticed, however, that $u^* = 0.8$ corresponds to a large reduction of G_{mo} and τ_{mo} to 55% and 46% of their initial values, respectively.

Internal Damping of Degraded Soils

The variation of the equivalent viscous damping ratio, λ_t, during subsequent cyclic loading is shown in Fig. 8. The data points correspond to the cyclic tests on the SMB sand. The measured values which correspond to the beginning of cyclic loading, i.e., the number of cycles $N = 2$ are denoted by squares. The measured values determined for the interval of the number of cycles, N, between 5 and 30 are denoted by crosses. The range of damping values calculated for the corresponding variation of u^* using the M-K-Z model is plotted by solid lines. The figure reveals that the predicted variation of λ_t calculated using the M-K-Z model is similar to the variation of measured values, except at larger strains (around $\gamma_c = 1.0\%$) where λ_t is decreasing with γ_c instead of increasing. Such a drop at larger strains is, again, the consequence of "S-shaping," for which the definition of the equivalent viscous damping in Eq. 1 has not been originally intended (Jacobsen, 1930). It should be noted that the values of λ_t at very small strains were not measured, and therefore the modelling of damping at small strains is not treated here.

CONCLUSIONS AND DISCUSSION

The following conclusions about the behavior of fully saturated liquefiable sands under undrained cyclic loading may be derived from this study:

1. The initial loading stress-strain curve and associated initial backbone curve can be accurately defined by a modified version of the hyperbolic Kondner and Zelasko model. The modification consists of two additional material constants which can be easily determined by fitting the test data.

2. In conjunction with the Masing criteria the modified stress-strain model can be used to accurately describe the unloading and reloading branches of the first cycle loop.

3. The cyclic stress-strain behavior during subsequent undrained cyclic loading can be successfully characterized by the concept of the degraded modified backbone curves in conjunction with the Masing criteria. Such characterization employs both modulus and stress degradation models with the normalized residual excess pore water pressure as the degradation parameter. For accurate modelling, the commonly used stress degradation model may have to be modified.

4. The cyclic test results confirmed that the equivalent viscous damping ratio can be modelled reasonably well using the proposed model. However, this has been verified here only for a limited strain range.

The above conclusions verify that the concept of the backbone curve in conjunction with the Masing criteria represents a powerful tool for accurate cyclic characterization of liquefiable sands.

ACKNOWLEDGMENTS

The research reported herein was supported by the National Science Foundation Grants No. CES - 880 8682 and MSS - 892 2170. This support is gratefully acknowledged.

REFERENCES

Bjerrum, L. and Landva, A. (1966). "Direct simple-shear test on a Norwegian quick clay." Géotechnique, Vol. 16, No. 1, 1 - 20.

Dobry, R., Ladd, R.S., Yokel, F.Y., Chung, R.M. and Powell, D., (1982). "Prediction of pore water pressure buildup and liquefaction of sands during earthquakes by the cyclic strain method." Building Science Series 183, National Bureau of Standards, U.S. Department of Commerce, U.S. Government Printing Office, Washington, D.C., 150 pp.

Finn, W.D.L., Lee, K.W. and Martin, G.R. (1977). "An effective stress model for liquefaction." Journal of the Geotechnical Engineering Division, Proc. ASCE, Vol. 103, No. GT6, pp. 517 - 533.

Hara, A. (1980). "Dynamic deformation characteristics of soils and seismic response analyses of the ground." Dissertation submitted to the University of Tokyo.

Hardin, B.O. and Drnevich, V.P. (1972). "Shear modulus and damping in soils: Design equations and curves." Journal of the Soil Mechanics and Foundations Division, Proc. ASCE, Vol. 98. No. SM7, 667 - 692.

Idriss, I.M., Dobry, R., and Singh R.D. (1978). "Nonlinear behavior of soft clays during cyclic loading." Journal of the Geotechnical Engineering Division, Proc. ASCE, Vol. 104, No. GT12, 1427 - 1447.

Ishihara, K., Yoshida, N. and Tsujino, S. (1985). "Modelling of stress-strain relations of soils in cyclic loading." Proc. 5th International Conference on Numerical Methods in Geomechanics, Nagoya, Japan, 373 - 380.

Ishihara, K. (1986). "Evaluation of soil properties for use in earthquake response analysis." *Geomechanical Modelling in Engineering Practice*, R. Dungar and J.A. Studer Eds., A.A. Balkema, Rotterdam, the Netherlands, 241 - 275.

Jacobsen, L.S. (1930). "Steady forced vibrations as influenced by damping." Transactions, ASME, Vol. 52, No. 15, 169 - 181.

Kondner, R.L. and Zelasko, J.S. (1963). "A hyperbolic stress-strain formulation of sands." Proc. 2nd Pan American Conference on Soil Mechanics and Foundation Engineering, Sao Paulo, Brasil, 289 - 324.

Masing, G. (1926). "Eigenspannungen und Verfestigung beim Messing." Proc. 2nd International Congress on Applied Mechanics, Zürich, Switzerland, 332 - 335.

Newmark, N.M. and Rosenblueth, E. (1971). "Fundamentals of Earthquake Engineering." Prentice-Hall, Inc., Englewood Cliffs, New Jersey, pp. 162-163.

Ramberg, W. and Osgood, W.R. (1943). "Description of stress-strain curves by three parameters." NACA Technical Note No. 902, Washington, DC, 26 p.

Richart, F.E., Jr. (1975). "Some effects of dynamic soil properties on soil-structure interaction." Journal of the Geotechnical Engineering Division, Proc. ASCE, Vol. 101, No. GT12, 1197 - 1240.

Vucetic, M. (1986). "Pore pressure buildup and liquefaction of level sandy sites during earthquakes." Ph.D. Thesis, Rensselaer Polytechnic Institute, Troy, New York.

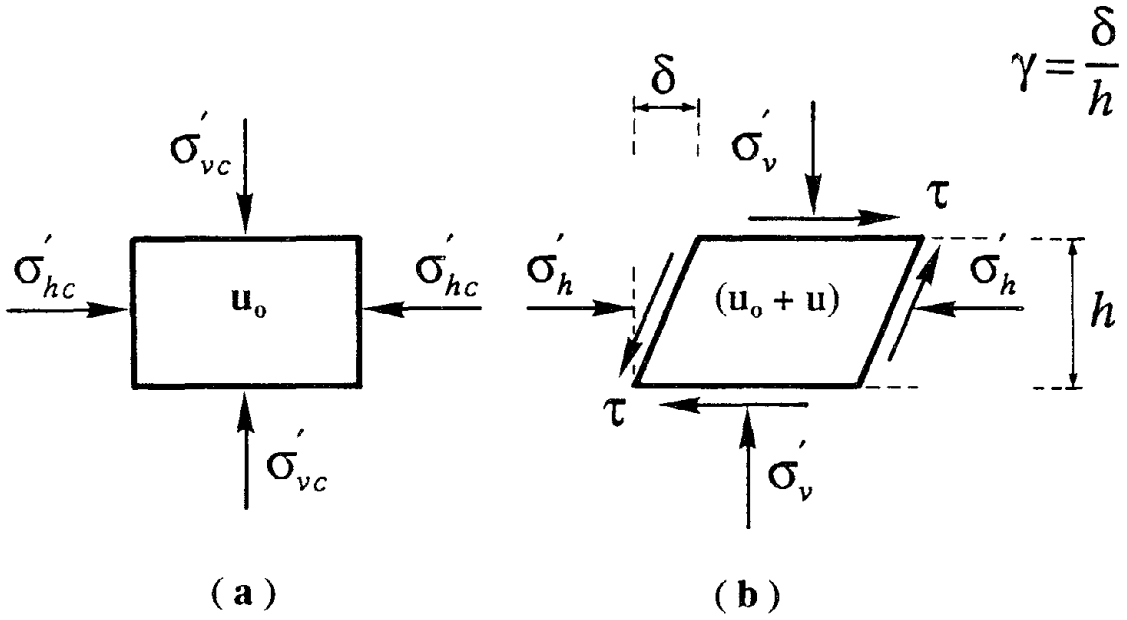

Fig. 1 **State of Stresses in a Representative Soil Element: a) Before Shaking; b) During Shaking (Note that $\sigma'_v = \sigma'_{vc} - u$ and $\sigma'_h = \sigma'_{hc} - u$)**

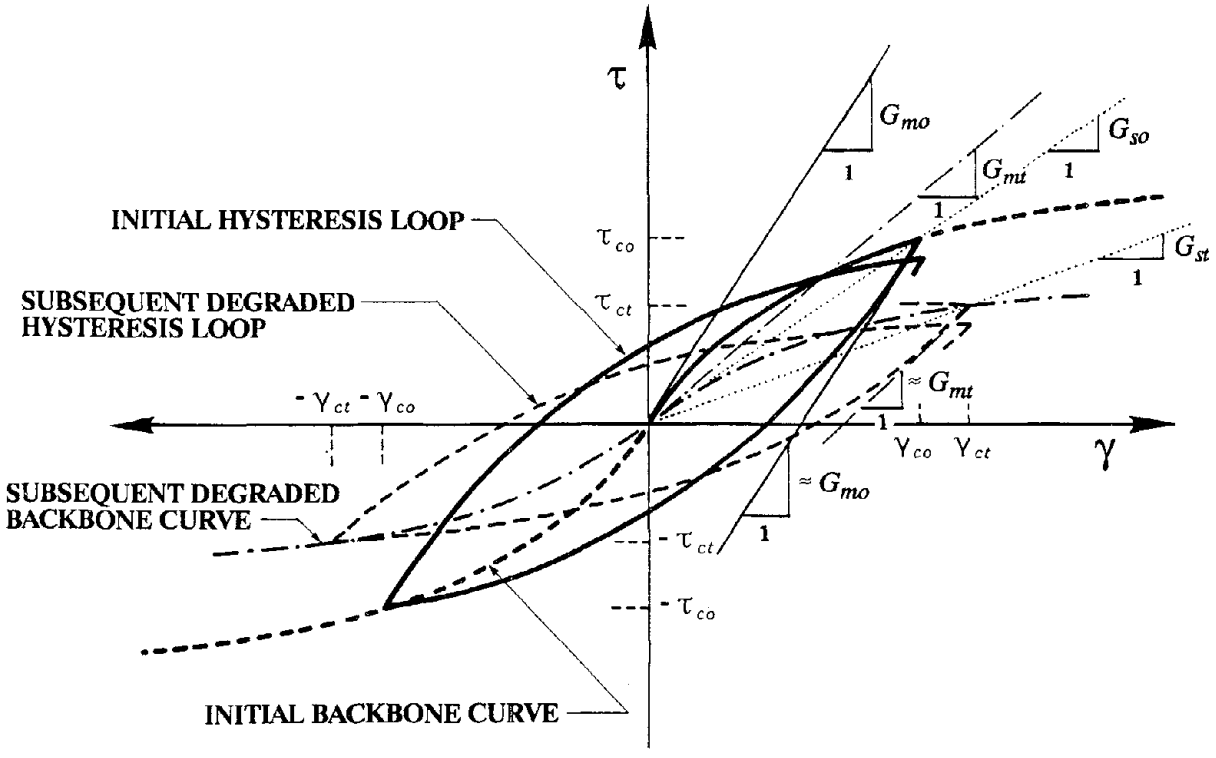

Fig. 2 **Schematic Illustration of the Stress-Strain Behavior in the First Cycle (Starting at Time t = 0) and a Subsequent Cycle (at Time t)**

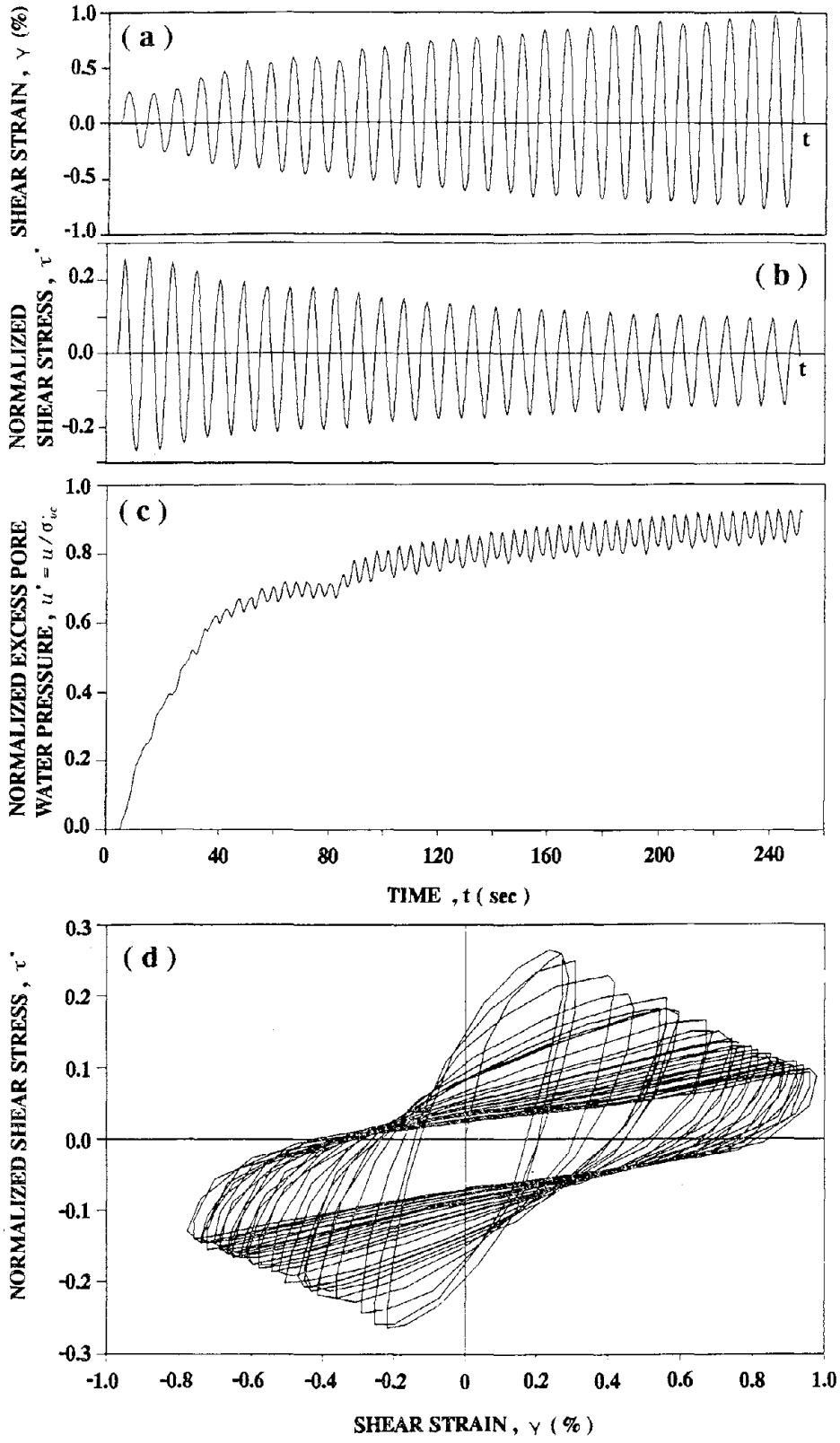

Fig. 3 Results of a Representative Cyclic Test on the Santa Monica Beach Sand

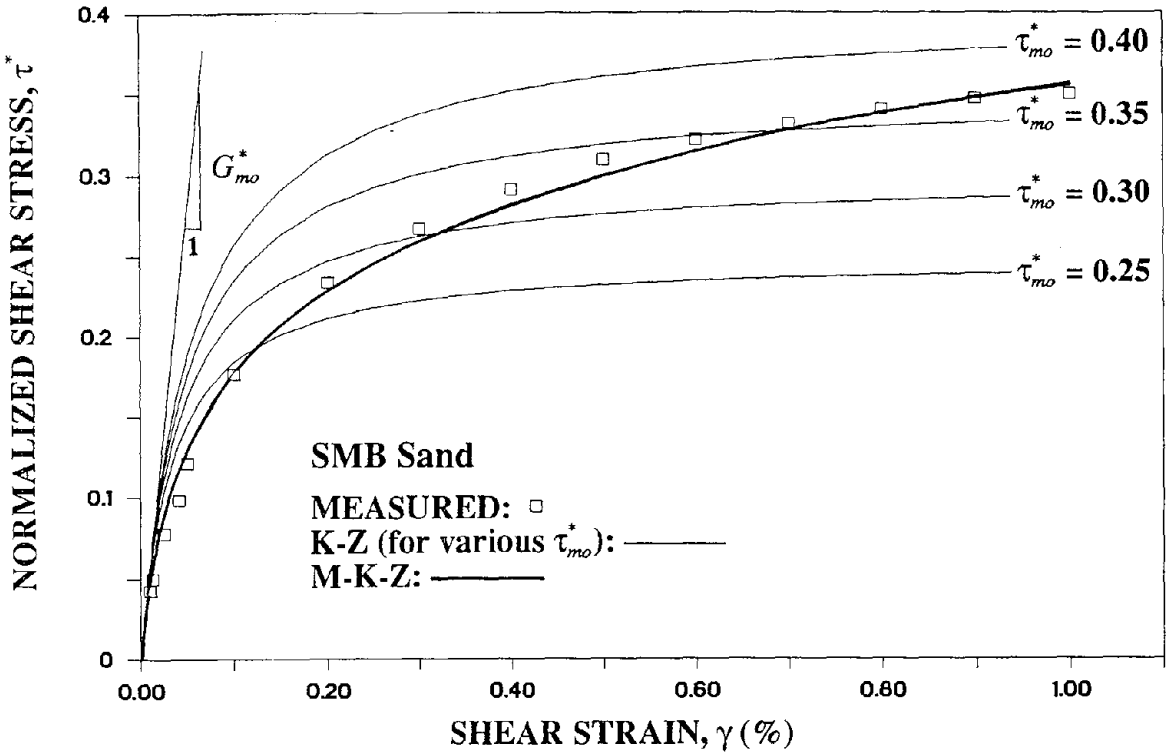

Fig. 4 Comparison between the Original and Modified Kondner and Zelasko Models

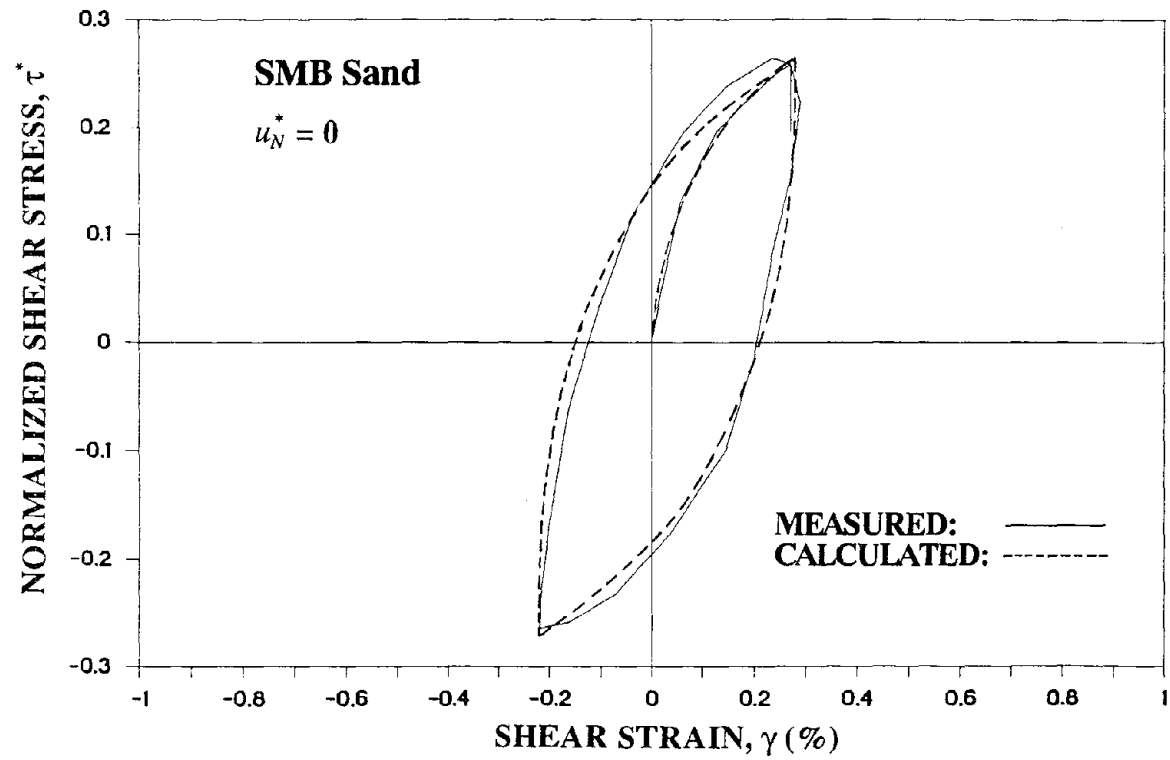

Fig. 5 Initial Cyclic Stress-Strain Behavior

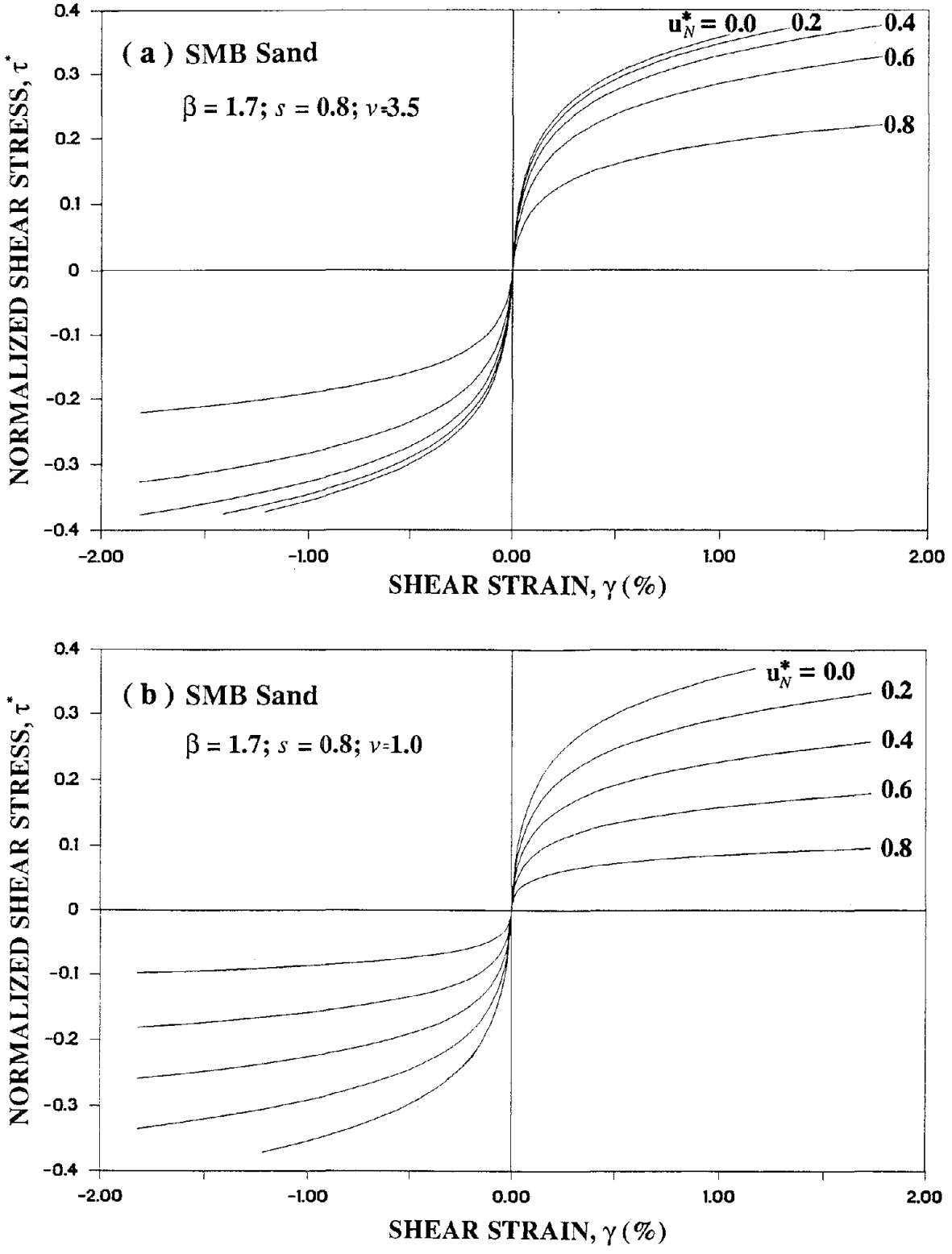

Fig. 6 Families of Degraded Backbone Curves for SMB Sand

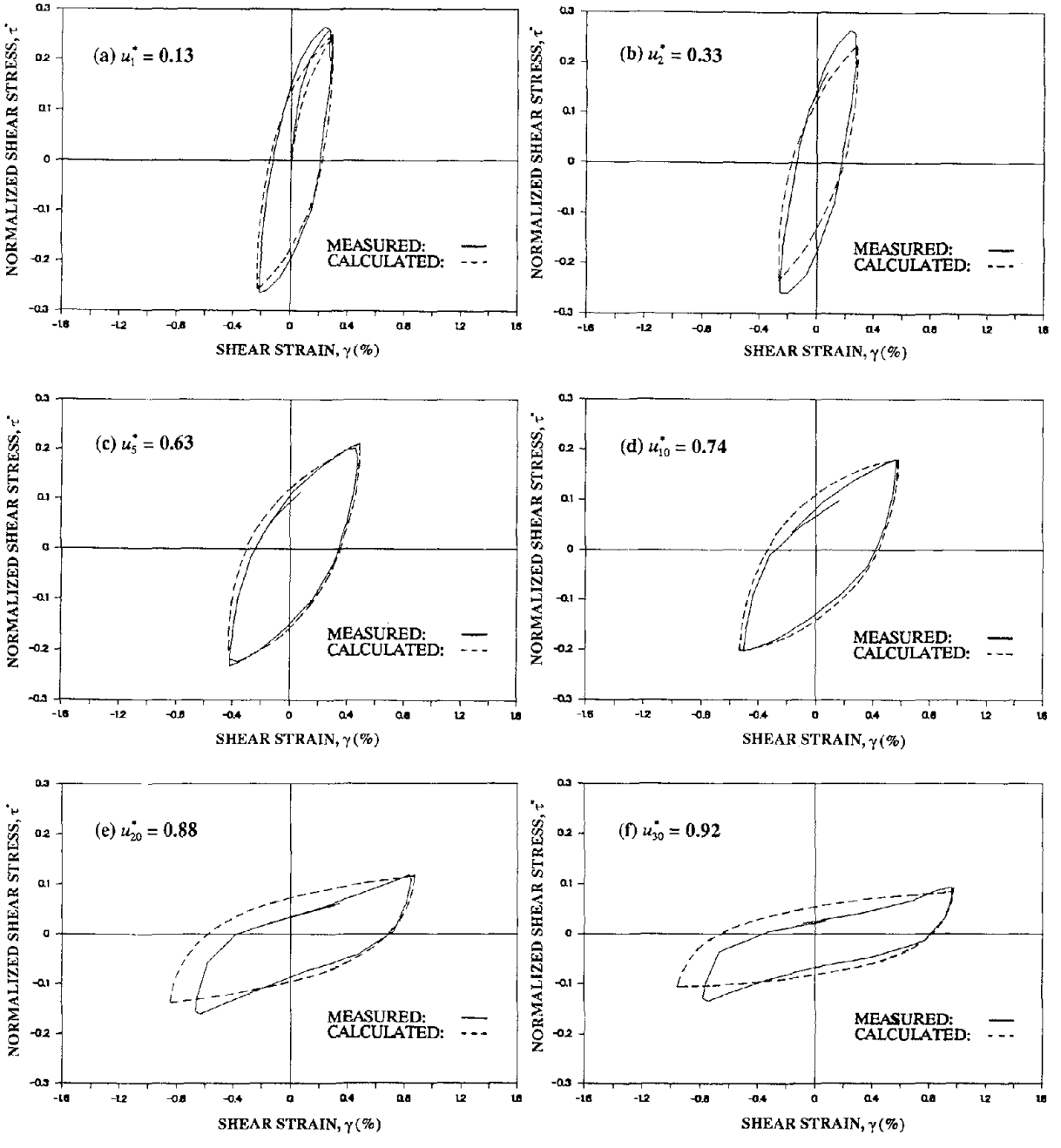

Fig. 7 Measured and Calculated Cyclic Loops for SMB Sand in Representative Test

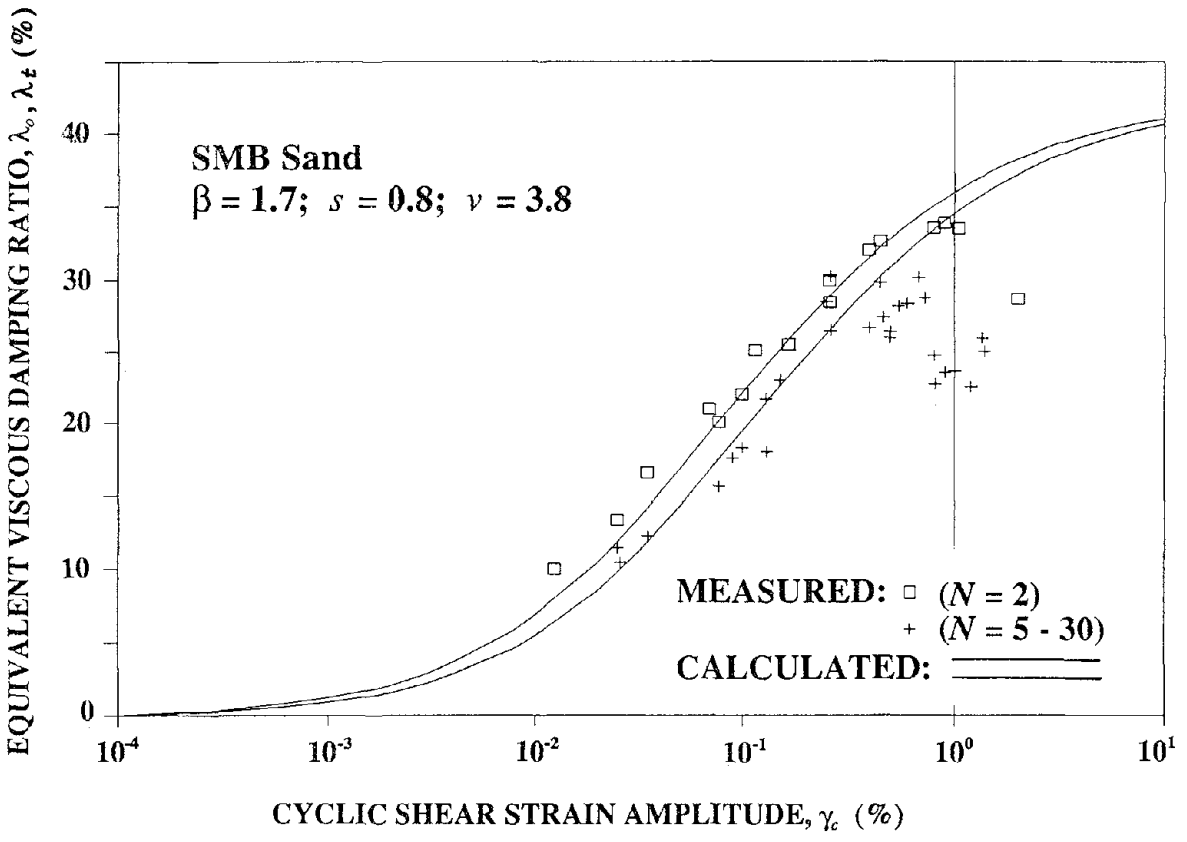

Fig. 8 Damping During Cyclic Loading

Numerical Simulations of Soil Liquefaction

Radu Popescu and Jean H. Prevost
Department of Civil Engineering and Operations Research, Princeton University
Princeton, NJ

Naoto Ohbo and Kazuo Hayashi
Kajima Technical Research Institute
Tokyo, Japan

ABSTRACT

Two dimensional finite element simulations (1) of a centrifuge test for an embankment model carried out at Cambridge University, and (2) of soil liquefaction in the area of a four story building at Kawagishi–cho during the Niigata Earthquake, were performed with the program DYNAFLOW.

The multi–yield surface model was used to predict the soil behaviour. The constitutive parameters were evaluated from data provided by the Japanese Society of Soil Mechanics and Foundations Engineering and also from an extended program of liquefaction strength analysis and parametric studies. Element tests are presented to illustrate the material behaviour under simple cyclic loading conditions.

The embankment behaviour simulation indicated large pore pressure build up in the lower third of the model. The analysis results – acceleration and pore pressure time histories – are compared to the recorded values, and a good agreement is found.

The Kawagishi–cho apartment analysis results – acceleration and pore pressure time histories, contours of pore pressure ratio and effective stress, structure displacements at the end of the shaking – clearly point out to the facts that occured during the earthquake: soil liquefaction, large tilt and settlements of the building. Several analyses were performed to examine the influence of the foundation drainage condition and of the soil improvement. It was found that soil liquefaction might occur close to the ground surface around the building for all cases, but the foundation drainage and especially the soil improvement reduce tilt and settlements of the structure.

Introduction

DYNAFLOW is a finite element computer program for nonlinear seismic site response analysis. Dry and saturated deposits can be analyzed. The solid and fluid coupled field equations (Biot, 1962) and constitutive equations proposed by Prevost (1977) and Prevost (1985) are general and applicable to multidimensional situations. The program and the multi-yield surface model implemented in DYNAFLOW were validated in the past for liquefaction analysis, using laboratory (Ohbo et.al., 1990; Hayashi et.al., 1992) and in situ (Keane and Prevost, 1989) recorded pore pressures and accelerations.

The liquefaction simulation analyses presented here are based on the information provided by the Japanese Society of Soil Mechanics and Foundations Engineering [10] – material characteristics, input motions and also experiment layout and measured accelerations and pore pressures for the centrifuge model. The paper emphasizes the capabilities of the mathematical model to simulate the recorded phenomena, providing that a proper evaluation of the constitutive parameter values is achieved. Some of the results of an extended analysis for the Kawagishi–cho apartment, to account for various drainage conditions at the base of the structure and to study the effects of the foundation soil improvement, are also presented.

Mathematical model

The multi–yield surface kinematic hardening model is based on a relatively simple plasticity theory (Prevost, 1985) and is applicable to both cohesive and cohesionless soils. A non–associative flow rule is used for the dilatational component of the plastic potential. The model has been tailored: (1) to retain the extreme versatility and accuracy of the simple multi–surface J_2–theory (Prevost, 1977) in describing observed shear nonlinear hysteretic behaviour and shear stress–induced anisotropic effects; (2) to reflect the strong dependency of the shear dilatancy on the effective stress ratio in both cohesionless and cohesive soils. Nested conical yield surfaces are used for that purpose.

The soil behaviour is analysed by incorporating the effects of the transient flow of the pore–fluid through the voids. An extension of Biot's theory into the nonlinear domain is employed to analyse the transient response of the soil deposits. The coupled field equations are presented by Prevost (1989). The time integration is accomplished by a finite difference time steping algorithm, using the "split operator method".

All the required elastic–plastic model parameters can be derived from the results of conventional laboratory (e.g. "triaxial", "simple shear") and in–situ (e.g. "wave velocity", "standard penetration") soil tests.

Material parameter evaluation

The multi-yield surface model constitutive parameters, are as follows (Prevost, 1989):

- a. State parameters (mass density, porosity, permeability)
- b. Elastic parameters (shear and bulk moduli, power exponent)
- c. Dilation parameters (dilation angle, dilation parameter)
- d. Yield surface parameters (friction angle, coefficient of earth pressure at rest, maximum deviatoric strain)

In ref. [10], some of them are provided (solid and fluid mass density), and some assumed (low strain base moduli, power exponent, porosity, friction and dilation angles, liquefaction strength). The other parameters, as well as some of those which were assumed, were subjected to careful analyses or were evaluated form previous experience. The final values are listed in Tables 1 and 2, and an explanation is provided in the following for the embankment model case.

1. **State** and **Elastic** parameter values, excepting permeability and power exponent, were taken from ref [10]

2. **The power exponent**, $n = 1.0$, resulted from parametric analyses. This value, which is not in the range of those commonly used for sands, can be explained by the presence of the silicon oil, used as pore fluid, which might modify some characteristics of the saturated sand.

3. **Maximum deviatoric strain** in compression and extension was appreciated according to the values used in a previous study by Hayashi et al. (1992).

4. **The coefficient of earth pressure at rest**, used for the plasticity parameter generation, was taken $k_0 = 0.5$. The initial effective stress ratio τ_h/σ_{v0} was taken 1.0 for the element tests and 0.5 for the finite element analyses.

5. **The friction angle** assumed in ref [10], $\phi = 39^0$, was evaluated by Dunhum's correlation formula ($\phi = \sqrt{12\,N} + 25^0$), which provides values at the upper limit. Consequently, two sets of constitutive parameter values were used: one from reference [10] – set #1 – and the other with friction and dilation angles evaluated from information provided by other analysts – set #2. These values, either reported by analists [10], or derived from element test stress paths, are as follows: Iai, S. (FLIP) – 30^0, Shinomi, T. (MuDIAN) – $30^0 \ldots 32^0$, Nishi, K. et al. (NAFSS) – $28^0 \ldots 29^0$, Tanaka, T. (NONSOLAN) – 32^0. An average value $\phi = 31^0$ was adopted for set #2.

6. **The dilation angle** for set #1 was taken $\bar{\phi} = 32^0$ – value provided in ref. [10] – and for set #2 was computed from the measured critical stress ratio provided by element tests: $\bar{\phi} = 25^0$.

7. **The dilation parameter** was evaluated from the liquefaction strength analysis:

- The Standard Penetration Resistance was appreciated from Meyerhof's correlation formula:

$$D_r = 210 \cdot \sqrt{\frac{N}{\sigma_v + 70}}$$

which gives $N \approx 8$ blows/ft for relative density $Dr = 60\%$ and effective overburden pressure $\sigma_v = 30$ KPa (the value in the lower third of the embankment, where

liquefaction is most likely to occur).

- The normalized standard penetration resistance was computed as: $N_1 = C_N \cdot N \approx 13$ blows/ft, with $C_N = 1.65$ – correction coefficient for the overburden pressure (Seed et.al., 1984).
- The value of cyclic stress ratio, corresponding to $N_1 = 13$ blows/ft for a number of 15 cycles to liquefaction (M = 7-1/2), was evaluated from the relationship between stress ratios causing liquefaction and N_1 values for clean sands (Seed et.al., 1984): $\frac{\tau_h}{\sigma_{v0}} = 0.14$ for $N_l = 15$.
- Cyclic undrained simple shear tests were simulated for the two sets of parameters. Different values for cyclic stress ratio (τ_h/σ_{v0}) and dilation parameter (X_{pp}) were used. The other material parameters were constant. The resulted numbers of cycles to liquefaction were plotted versus cyclic stress ratio (figure 1). The material liquefaction strength was plotted with large solid points and the dilation parameter values were evaluated by interpolation: $X_{pp} = 0.27$ – set #1 and $X_{pp} = 0.18$ – set #2. Some of the element test results for the final values are presented in figure 1.

8. **The permeability coefficient**, $k = 5 \times 10^{-5}$ m/s, was appreciated as for fine sand, from Creager correlation.

Finite Element model

Two dimensional plane strain analyses were performed, using two node or four node linear izoparametric elements. The sandy soil was idealized as a two phase nonlinear porous medium, with four nodal degrees of freedom (horizontal and vertical displacements for both the solid and fluid phases). The compressibility of water was considered.

The finite element discretization of the embankment model (figure 2) has 128 elements, disposed in eight layers, and 153 nodes. The boundary conditions were prescribed as follows:

- prescribed acceleration to the solid phase horizontal d.o.f. at the base nodes;
- zero vertical displacement for both solid and fluid phases at the base nodes;

The soil foundation of the Kawagishi–cho apartment was divided into 94 two–phase finite elements. The structure was modelled as a one–phase, elastic medium (figure 6). The depth of the base rock in the area is at about 70 m. The mesh is only extended down to a depth of 14 m, as recommended in [10] (the soil in that area has an N_{SPT} value of 30 blows/ft). The base node boundary conditions are similar to those assumed for the embankment model. The infinite layered soil condition was simulated by assigning the same equation number for each nodal degree of freedom (i.e. both for the solid and fluid phases) in the horizontal direction for the lateral nodes of the mesh. The undrained condition at the base of structure was considered.

The analyses were performed in two steps. First, gravity loads were applied. Next, nodal velocities and accelerations were zeroed and the input acceleration was applied in the horizontal direction to the the base nodes. The input wave for centrifuge test and the N–S component of

the Niigata Earthquake accelerogram, recorded at Akita Prefectural Office (1964), were scaled at 0.2g.

Analysis results

a. Embankment model

Only the results which can be compared to the recorded values are selected

The measured model settlement was δ_v = 8.04 cm, at the prototype scale. The predicted values are (figure 3):

- δ_v = 5.19 cm – for set #1;
- δ_v = 8.45 cm – for set #2.

Computed and recorded pore pressure time histories are compared for the locations of the pore pressure transducers, in figure 4. The analysis results point out to the fact that large pore pressure build up led to liquefaction in the lower third of the dam. A very good agreement between computed and measured values is found, excepting the PPT2335 location, were the predicted pore pressures are lower than the recorded ones.

Acceleration time histories are compared for a central location only (ACC 1225 and node #43), since the accelerometer ACC965, placed close to the top of the dam, was not properly installed. Computed accelerations show the same tendency of decreasing in amplitude as the recorded ones, but the results obtained for set #2 are closer to the real behaviour (figure 5).

b. Kawagishi–cho apartment

The computed deformation of the soil and structure movements at the end of shaking (figure 7) simulate the phenomena which occured at Kawagishi–cho site during the Niigata Earthquake: soil liquefaction and structure tilt (the inclination of the building gradually progressed to failure after the earthquake).

Effective vertical stress and excess pore pressure contours (figure 8) indicate that the structure tilt was caused by soil liquefaction in the lateral zones. According to the analysis results, the water might have been expelled from the zone underneath the structure, due to its weight, and consequently, the excess pore pressure had lower values in this region. This phenomenon is rendered evident by the effective vertical stress and pore pressure time histories at two locations – beneath the structure and laterally (figure 9): the effective stress gradually diminishes and eventually the soil liquefies in the lateral zone (element 61), while under the structure (element 63) the pore water is drained laterally and the effective stress increasses at the end of shaking.

The effects of some earthquake countermeasures are presented in figure 10. The perfect drainage at the base of the structure reduces the settlement, but the tilt is still unacceptable. A "safe" option seems to be the soil improvement (the analysed situation is for sand with N_{SPT} = 30 under the building).

Acknowledgements

This research was supported in part by a grant from the National Science Foundation under the auspices of the National Center for Earthquake Engineering Research (NSF ECE 86–07591) and by a collaborative research agreement between Kajima Corporation and Princeton University. These supports are gratefully acknowledged.

References

1. BIOT, M.A., (1962), "Mechanics of deformation and acoustic propagation in porous media", J. Appl. Phys., Vol. 33, No. 4, pp. 1482–1498.
2. KEANE, C.M. AND PREVOST, J.H., (1989), "An analysis of earthquake data observed at the Wildlife Liquefaction Array Site, Imperial County, California", Proc. 2nd U.S.–Japan Workshop on Liquefaction, Large Ground Deformation and their Effects on Lifelines, pp. 39–53.
3. OHBO, N., NOJIRI Y., HAYASHI K., UENO K., PREVOST J.H., (1990), "Liquefaction of sandy soil deposits – Analysis and experiments", Proc. 3rd U.S. – Japan Workshop on Liquefaction, Large Ground Deformation and their Effects on Lifelines, pp. 387–402.
4. PREVOST, J.H., (1977), "Mathematical modeling of monotonic and cyclic undrained clay behaviour", Int. J. Num. Meth. Geom., Vol. 1, No. 2, pp. 195–216.
5. PREVOST, J.H., (1981), "DYNAFLOW: A nonlinear transient finite element analysis program", Dept. Civil Engineering Op. Res., Princeton University, last update 1992.
6. PREVOST J.H., (1985), "A simple plasticity theory for frictional cohensionless soils", Soil Dynamics and Earthq. Eng., Vol. 4, No. 1, pp. 9 – 17.
7. PREVOST, J.H., (1989), "DYNA1D - A Computer Program for Nonlinear Seismic Site Response Analysis", Report No. NCEER–88–0025, Dept. of Civil Engineering and Op. Res., Princeton University, Princeton.
8. HAYASHI, K., OHBO, N., UENO, K., PREVOST, J.H., POPESCU, R., (1992), "Numerical simulations of sandy soil deposit liquefaction during earthquakes", 10th World Conf. on Earthq. Eng., Spain, July 19–25 (submitted).
9. SEED, H.B., TOKIMATSU, K., HARDER, L.L., CHUNG, R.M., (1984), "The influence of SPT procedures in soil liquefaction resistance evaluation", Rep. UCB/EERC – 90/05.
10. * * *, (1991), "Simultaneous simulations of liquefaction analysis", Jap. Soc. Soil Mech. Found. Eng., transl. by Kajima Inst. Tech.

Table 1 – Material parameters for the embamkment model

Property	Value
Mass density - solid, ρ_s (Kg/m^3)	2650.0
Porosity, n	0.444
Low strain base shear modulus, G_0 (MPa)	87.59
Poisson's ratio, ν	0.3
Fluid bulk modulus, λ_w (MPa)	2000.0
Reference mean normal stress, p_0 (KPa)	100.0
Power exponent, n_e	1.0
Dilation angle (compression and extension), $\bar{\phi}$	25^0 (set#1), 32^0 (set#2)
Dilation parameter, X_{pp}	0.18 (set#1), 0.27 (set#2)
Friction angle (compression and extension), ϕ	31^0 (set#1), 39^0 (set#2)
Coefficient of lateral stress, k_0	0.5
Maximum deviatoric strain, $\bar{\varepsilon}_C^{max}$, $\bar{\varepsilon}_E^{max}$ (%)	5.0, 3.0
Permeability, k (m/s)	5×10^{-5}

Table 2 – Material parameters for Kawagishi–cho apartment analysis

Property (*)	sand 0–2 m	sand 2–5 m	sand 5–8 m	sand 8–14 m	improved soil
ρ_s (Kg/m^3)	2650.0	2650.0	2650.0	2650.0	2650.0
n	0.51	0.45	0.45	0.45	0.33
G_0 (MPa)	21.78	23.00	42.75	65.03	111.1
ν	0.3	0.3	0.3	0.3	0.3
λ_w (MPa)	2000.0	2000.0	2000.0	2000.0	2000.0
p_0 (KPa)	9.45	32.34	49.98	76.44	63.37
n_e	0.5	0.5	0.5	0.5	0.5
$\bar{\phi}$ (deg)	29	29	24	20	24
X_{pp}	0.115	0.115	0.085	0.07	0.15
ϕ (deg)	31	31	32	33	37.5
k_0	0.5	0.5	0.5	0.5	0.5
$\bar{\varepsilon}_C^{max}$, $\bar{\varepsilon}_E^{max}$ (%)	5.0, 3.0	5.0, 3.0	5.0, 3.0	5.0, 3.0	5.0, 3.0
k (m/s)	5×10^{-5}	5×10^{-5}	5×10^{-5}	5×10^{-5}	5×10^{-5}

(*) The notations are explained in Table 1.

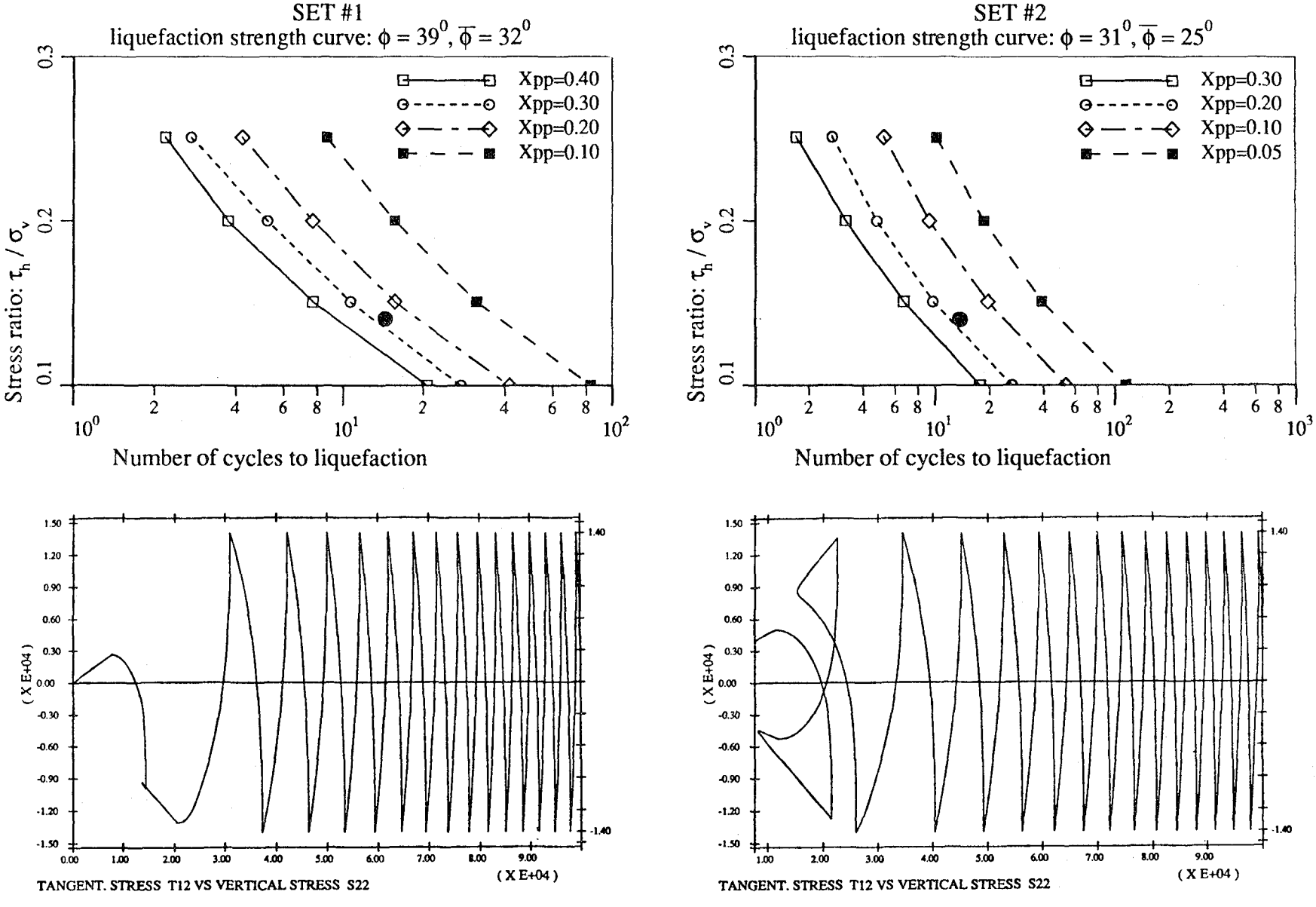

Figure 1. Embankment model – liquefaction strength analysis: *a.* liquefaction strength curves; *b.* stress paths from element tests.

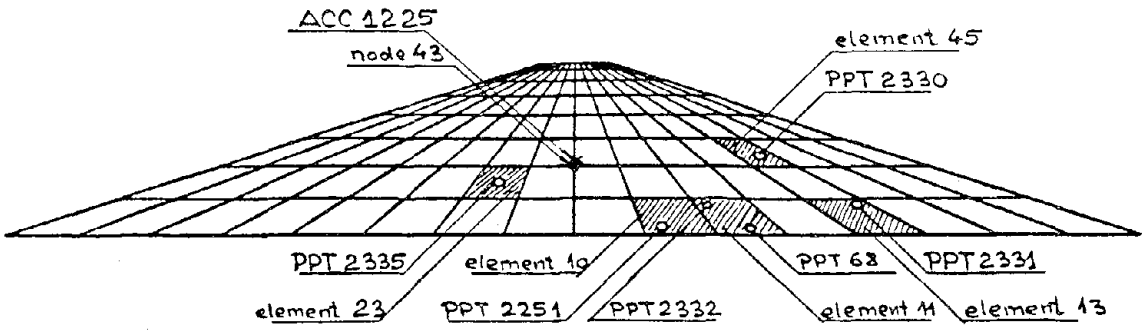

Figure 2. Embankment model – finite element mesh and transducer locations.

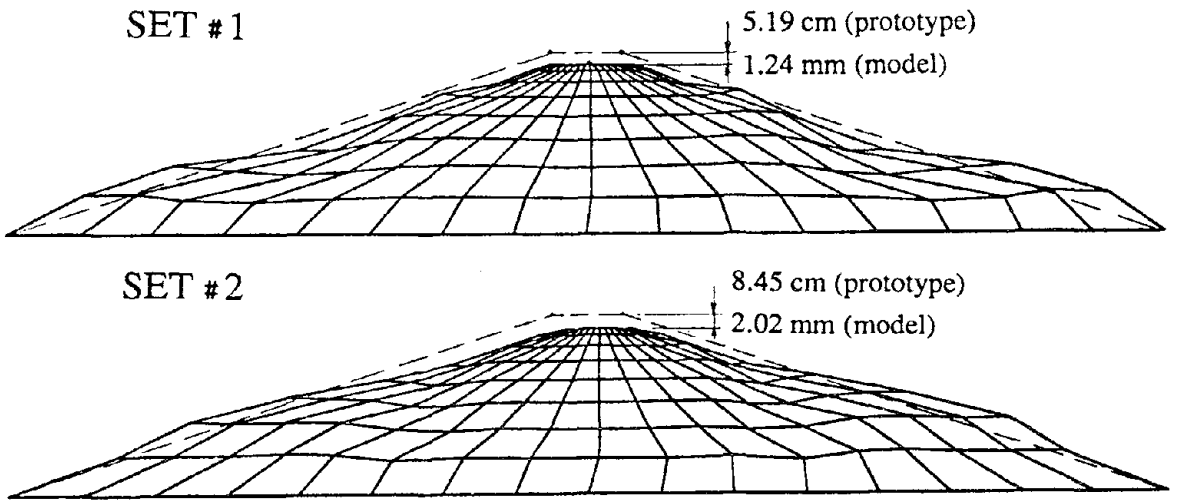

Figure 3. Deformed mesh at the end of shaking (deformation magnification factor = 5).

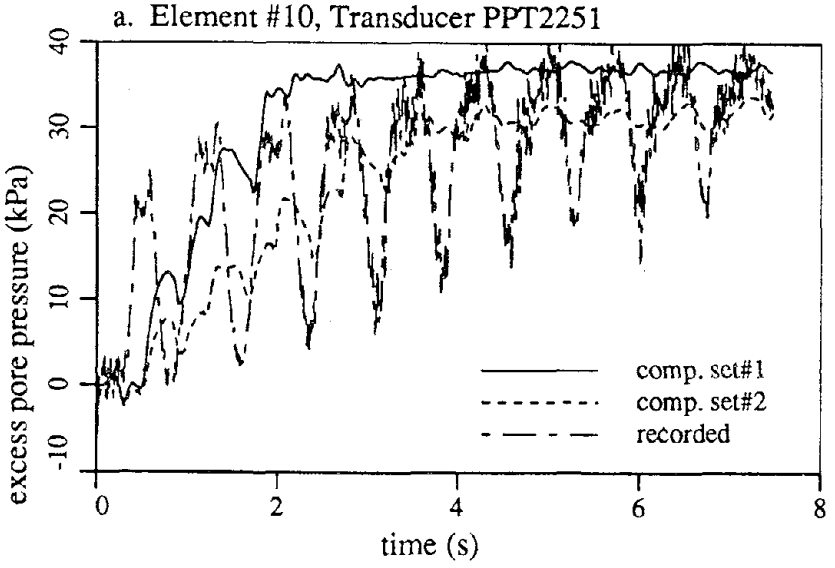

Figure 4.a. Embankment model – computed and recorded excess pore pressure time histories.

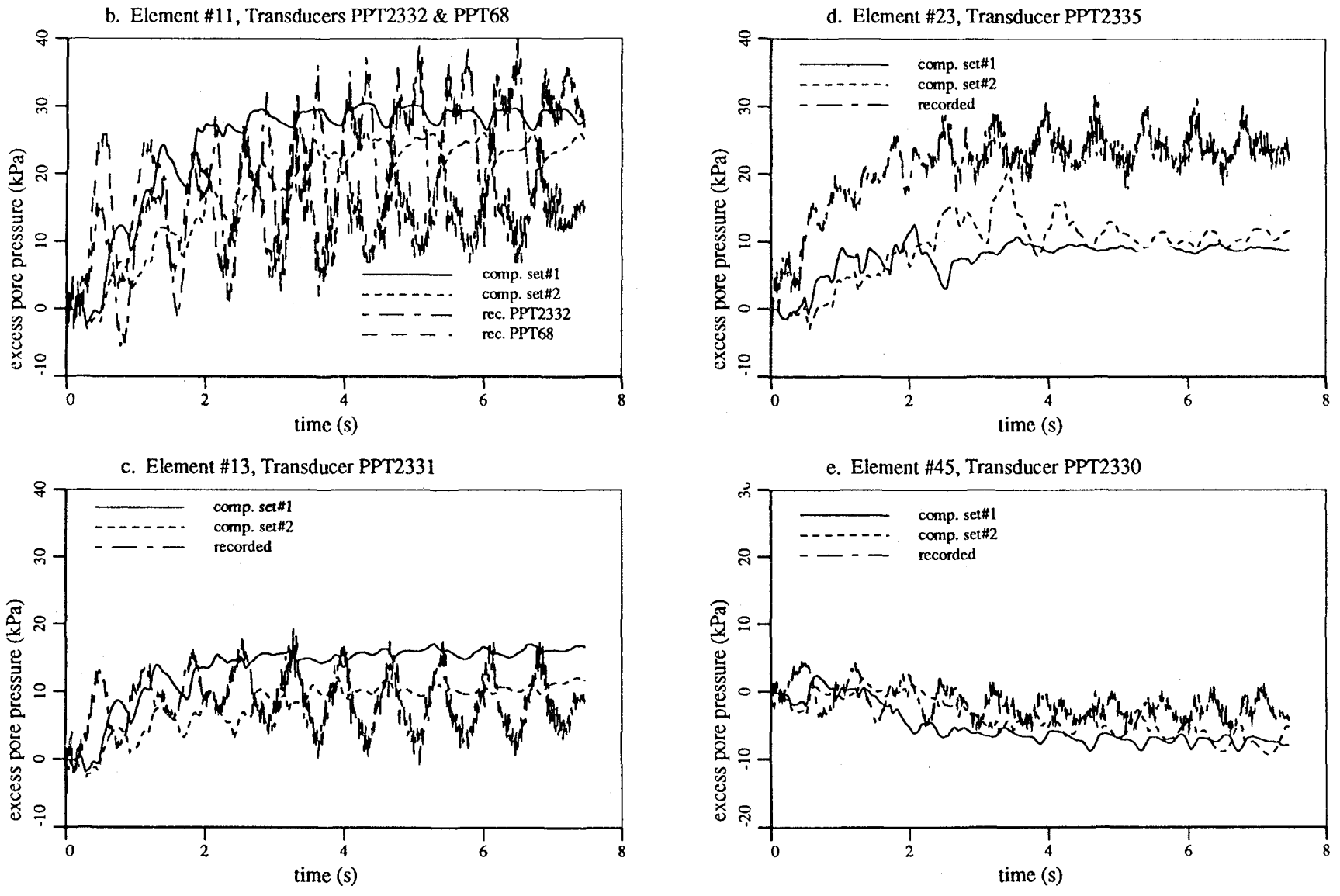

Figure 4. Embankment model – computed and recorded excess pore pressure time histories.

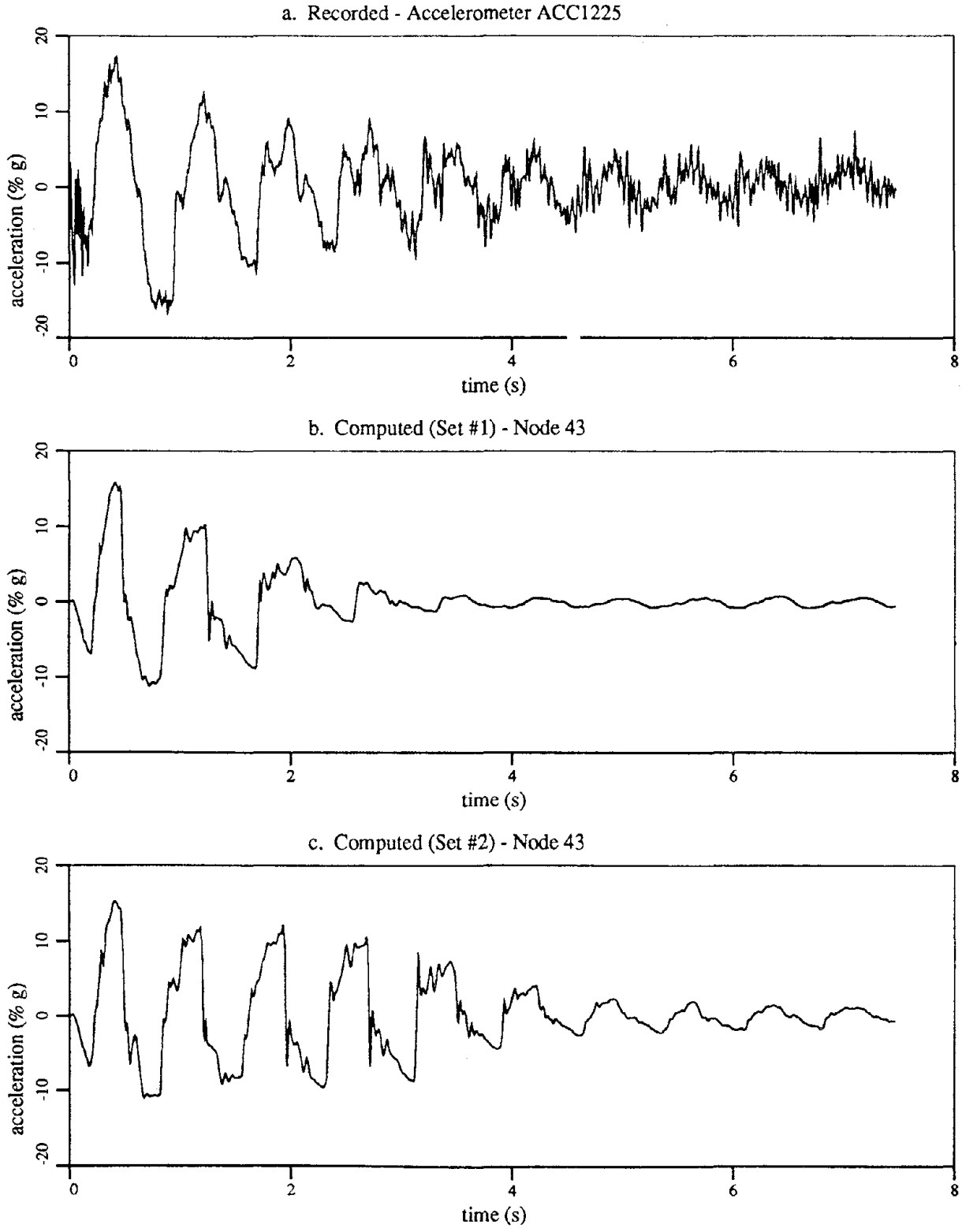

Figure 5. Embankment model – recorded and computed horizontal acceleration time histories.

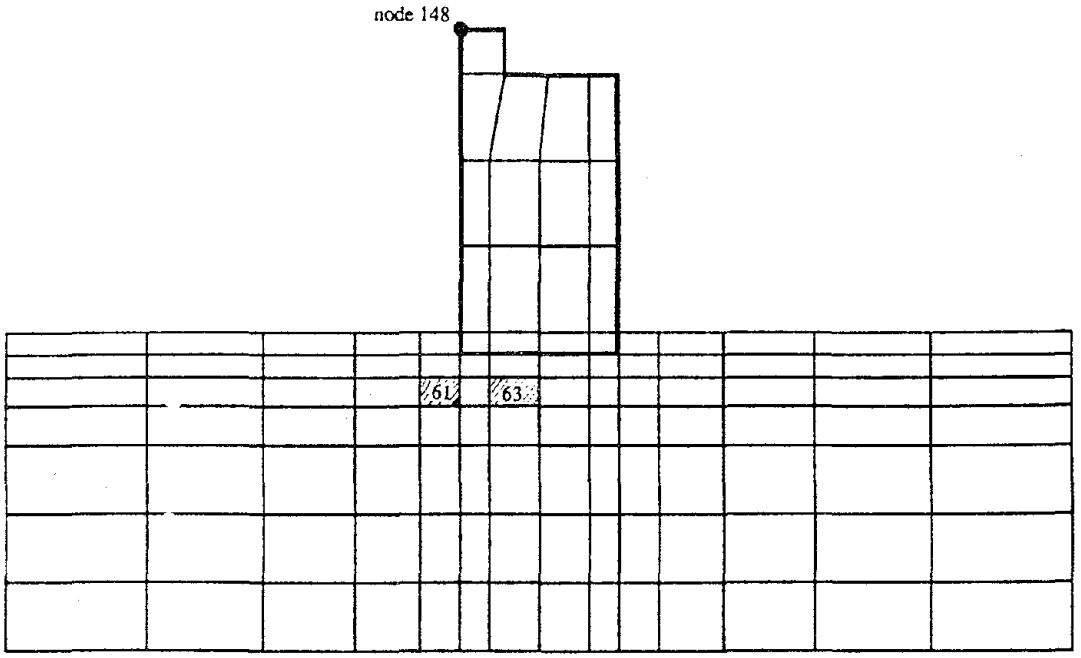

Figure 6. Finite element mesh for Kawagishi–cho apartment analysis.

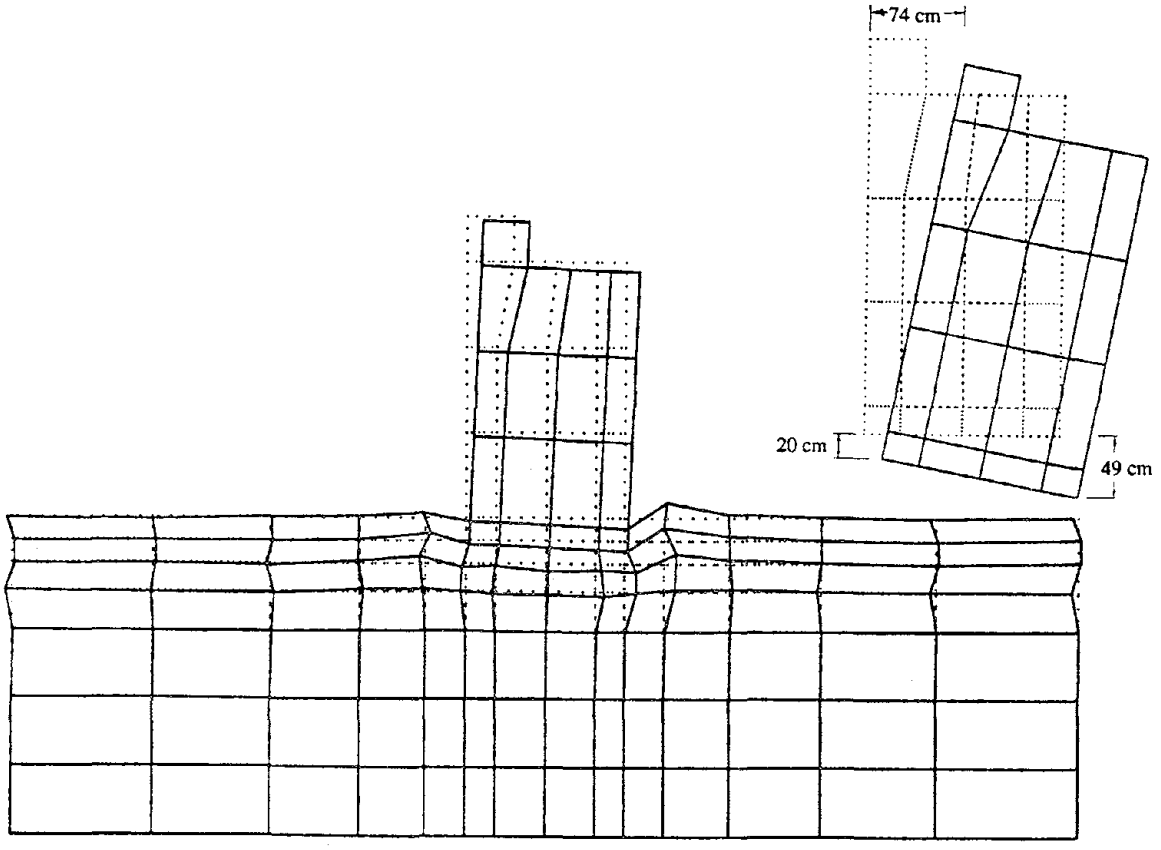

Figure 7. Deformed mesh at the end of shaking: *a.* deformation magnification factor = 1; *b.* deformation magnification factor = 5.

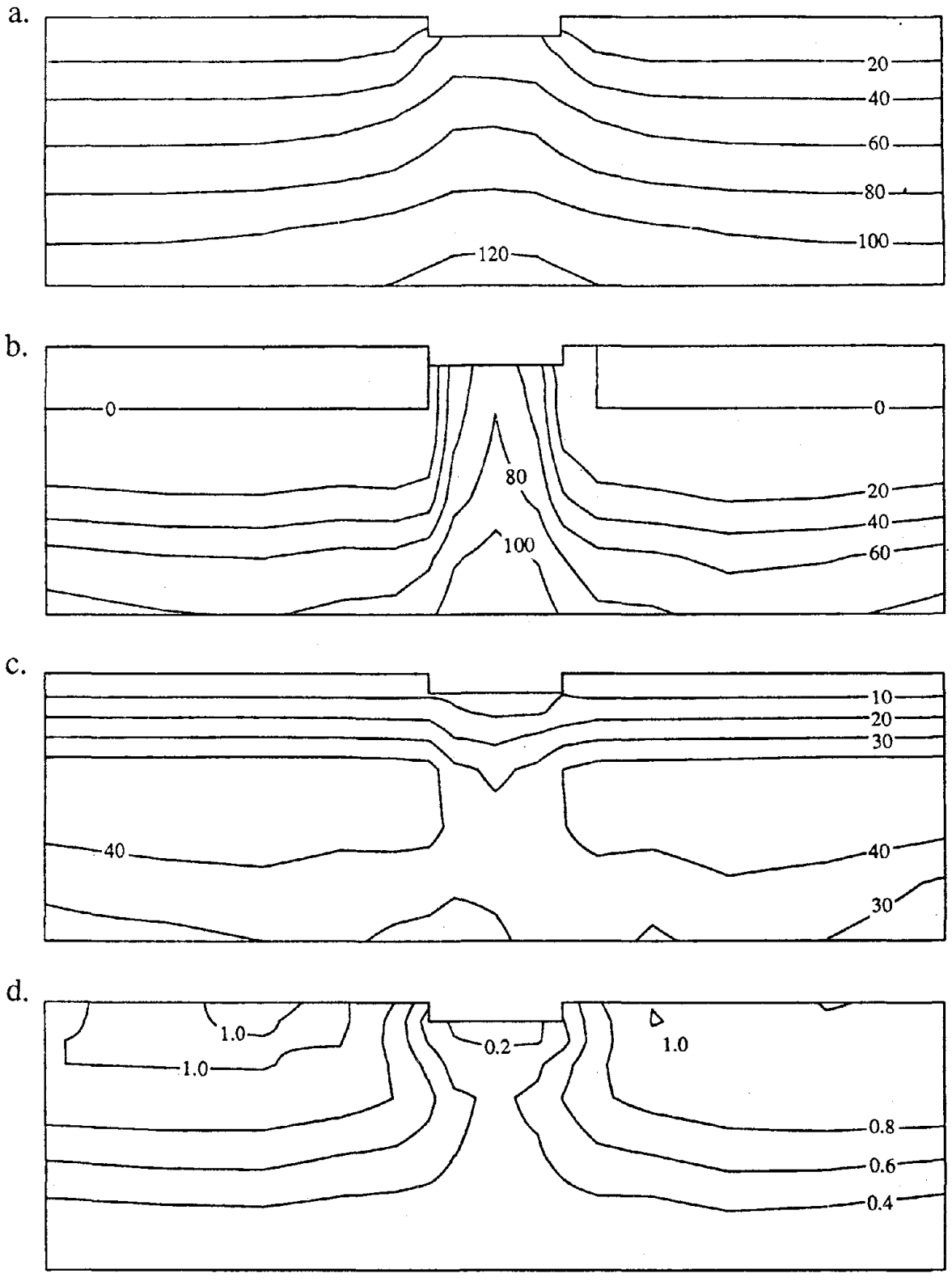

Figure 8. Kawagishi–cho apartment – effective vertical stress and excess pore pressure contours: *a.* initial effective vertical stress (σ_{v0}); *b.* effective vertical stress at the end of shaking; *c.* excess pore pressure (u) at the end of shaking; *d.* ratio u/σ_{v0} at the end of shaking.

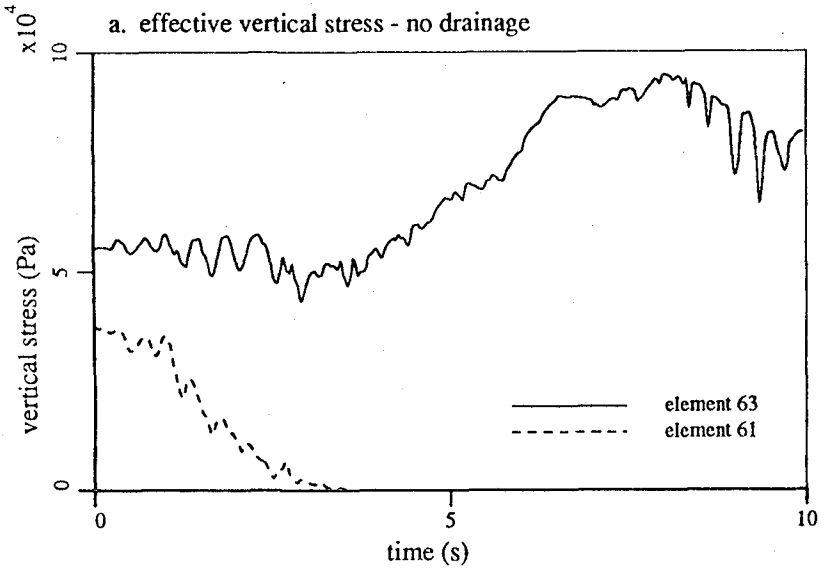

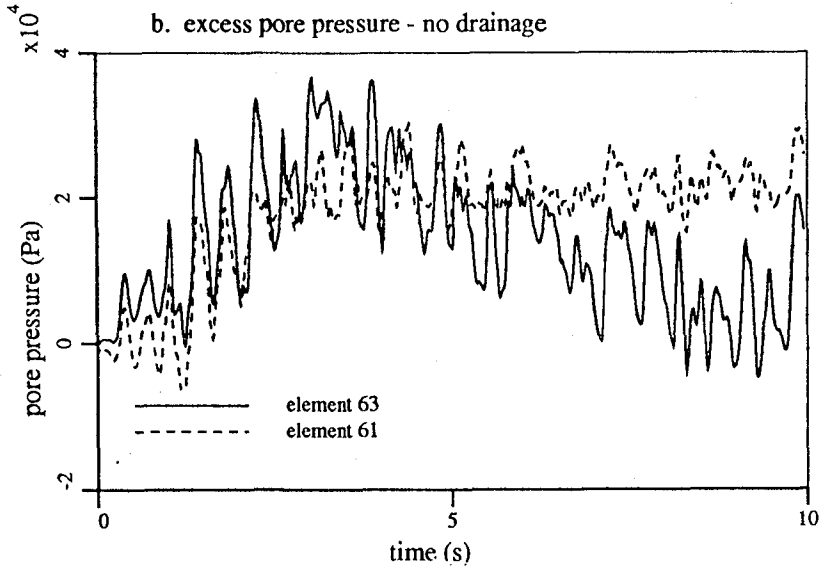

Figure 9. Effective stress and excess pore pressure evolution at two locations close to the structure.

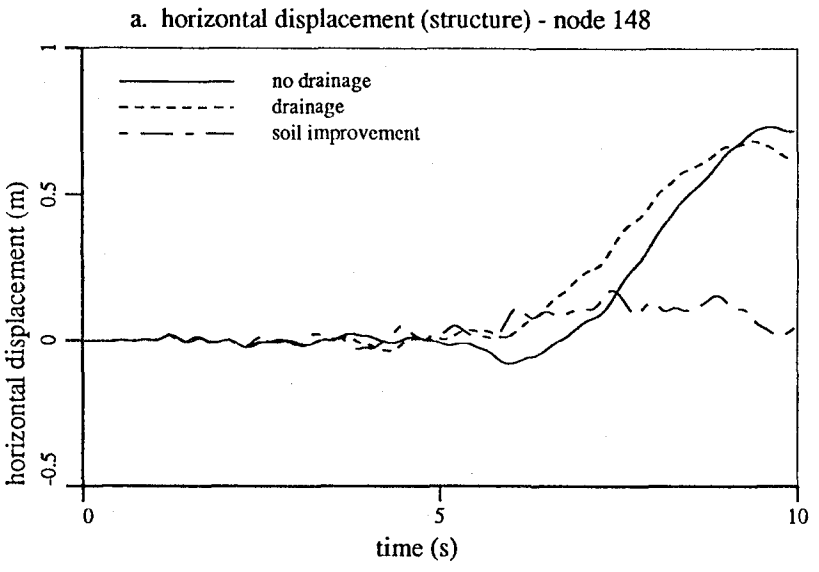

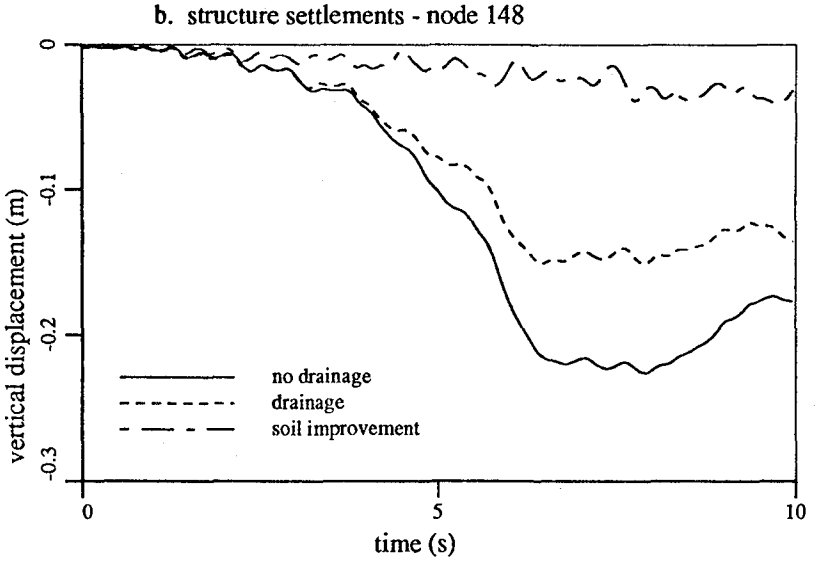

Figure 10. Kawagishi–cho apartment – structure movement time histories.

IV Modeling of Liquefaction-Induced Large Ground Displacements

Analysis on Development of Permanent Displacement with Time in Liquefied Ground

Ikuo Towhata
Associate Professor,
University of Tokyo

Hideo Matsumoto
Research Engineer,
Public Works Research Institute

ABSTRACT

A predictive method for the temporal development of permanent displacement is hereby proposed. This method considers the transient displacement as a fraction of the ultimate one which can be predicted by using the principle of the minimum potential energy. The fraction varies with time and is predicted in turn in this text by solving the Lagrangian equation of motion. Since this equation gives a simple second-order differential equation in terms of time, its closed-form solution is easily derived. Therefore, the computation time is very short. When a mechanism of energy dissipation, as suggested by a shaking table test, is combined with the analysis, the agreement between calculation and observation is satisfactory. The amount of soil data is very limited for a practical convenience.

INTRODUCTION

The authors have been studying the mechanism and the prediction of the permanent displacement of ground caused by seismic liquefaction (Towhata et al., 1991a, 1991b). It has been attempted so far to understand by means of shaking table tests the nature of liquefied ground and to predict its displacement in simple manners. Since the liquefaction-related damages to facilities are caused by an unallowable magnitude of ground distortion, it is essential to evaluate the possible extent of the ground displacement. This is particularly the case when a concerned facility is too large to prevent any liquefaction in its site by, for example, soil densification. With a reasonable reliability in the predicted ground displacement, an appropriate mitigation measure may be taken against liquefaction hazards.

The authors have emphasized a need for a simple way of prediction (Towhata et al., 1991a). Although the stress-strain behavior of liquefied sand is highly-nonlinear, a finite element analysis of nonlinear type is not very easy to run due to its computation time and cost. It is practically impossible to run a

nonlinear finite element analysis on a three-dimensional ground model, although it is very necessary when the liquefaction-induced damage to the function of a pipeline network is concerned with. For a general acceptance, a prediction measure has to be clear and easy for anybody to run. This is the major reason why a closed-form solution of ground displacement was developed by the authors. Their method is characterized by the idea that the liquefied sand behaves very similar to liquid without shear rigidity. This method has been extended to a three-dimensional case recently (Orense and Towhata, 1992).

The displacement of a liquefied ground so far predicted by the authors is the ultimate one that could occur when a liquefied ground was allowed to flow for a sufficiently long time. Generally, the ground displacement caused by earthquakes of seismic magnitude greater than, probably, 7 seems to be close to the predicted one, because the duration time of ground shaking is long enough. However, when an earthquake of a smaller magnitude occurs at a shallow depth beneath a concerned site, the extent of ground shaking is strong enough to trigger soil liquefaction but its duration time is short, inducing the ground displacement smaller than the authors' prediction. Thus, it was attempted to take into account the effects of time and to predict the temporal development of the ground displacement. The way of prediction was made as simple as possible again without sacrificing the reliability.

THEORY OF DYNAMIC ANALYSIS

The prediction of the ultimate displacement was made by using a variational principle in which the potential energy of the ground was made minimal by the exact solution of the displacement. Similarly, the temporal solution of displacement is derived in the present text by solving the Lagrangean equation of motion which is also a variational principle of dynamic type.

Fig.1 illustrates the coordinates. The horizontal one is denoted by x, while the vertical one is by z and taken positive upward. The ultimate displacement that would occur after a sufficiently long time is denoted by U in the horizontal and W in the vertical direction, respectively. Apparently, U and W are functions of x and z coordinates. Fig.1 demonstrates the positive directions of displacement. The temporal displacement, u in the horizontal and w in the vertical directions, vary with time, t.

For a convenience in analysis, the effects of t on u and w are separately considered from those of x and z;

$$u(x,z,t) = \lambda(t)U(x,z)$$
$$w(x,z,t) = \lambda(t)W(x,z) \qquad (1)$$

in which λ is a function of time that varies from zero at the initial stage of shaking upto unity after a sufficiently long time. Since the ultimate displacement, U and W, are obtained by the method of Towhata et al.(1991a), only λ is unknown yet.

The Lagrangian equation of motion is written as

$$\frac{d}{dt}\left\{\frac{\partial}{\partial\dot{\lambda}}(K-Q)\right\} - \frac{\partial}{\partial\lambda}(K-Q) = \text{Force} \qquad (2)$$

where λ is called a generalized displacement with its time derivative denoted by $\dot{\lambda}$. K and Q stand for the kinematic energy and the potential energy, respectively. It should be mentioned that Q consists of contributions by the strain energy and the gravity. Force on the right-hand side is the inertia force due to shaking in the present case, and when a potential function, I, for this force exists,

$$\text{Force} = -\frac{\partial I}{\partial\lambda} \qquad (3)$$

By using Eq.3 and choosing $\lambda(t)$ in Eq.1 as the generalized displacement in Eq.2, the Langrangian equation of motion becomes

$$\frac{d}{dt}\left\{\frac{\partial}{\partial\dot{\lambda}}(K-Q-I)\right\} - \frac{\partial}{\partial\lambda}(K-Q-I) = 0 \qquad (4)$$

The kinematic energy, K, is given by

$$K = \int \frac{\rho}{2}\left\{\left(\frac{\partial u}{\partial t}\right)^2 + \left(\frac{\partial w}{\partial t}\right)^2\right\} \text{dvol} \qquad (5)$$

where ρ is the mass density of soil and the volumetric integration is made all over the liquefied and the surface unsaturated layers where the displacement takes place. By substituting Eq.1 in Eq.5,

$$K = \frac{1}{2}\int \rho(U^2 + W^2)\,\text{dvol}\left(\frac{d\lambda}{dt}\right)^2 \qquad (6)$$

Since the ultimate displacement, U and W, are already known, the integration above is possible. Thus,

$$K = \frac{1}{2} m \left(\frac{d\lambda}{dt}\right)^2 \qquad (7)$$

where m stands for the integration in Eq.6. The potential energy, Q, at the ultimate stage of u = U and w = W was

calculated analytically by Towhata et al.(1992). Substituting in Q Eq.1 in place of U and W,

$$Q = \frac{1}{2} k \lambda^2 + f\lambda \tag{8}$$

in which

$$k = \int_0^L \left[ET\left(\frac{dF}{dx} \right)^2 + \frac{4\gamma}{\pi^2} \left\{ \frac{d(HF)}{dx} \right\}^2 \right] dx \tag{9}$$

$$f = - k \tag{10}$$

in which L stands for the length of the ground.

When a vertical component of inertia force is ruled out from the analysis, the potential function of the horizontal inertia force is given by

$$I = - \int (\text{Inertia force}) \, u \, dvol$$

$$= \int \rho \frac{d^2 u_b}{dt^2} u \, dvol \tag{11}$$

where $d^2 u_b / dt^2$ indicates the seismic acceleration at the base of the liquefied layer. When Eq.1 is substituted in Eq.11,

$$I = n \frac{d^2 u_b}{dt^2} \lambda \tag{12}$$

in which

$$n = \int \rho U \, dvol \tag{13}$$

With Eqs. 3, 7, 8, and 12 substituted in, Eq.2 becomes

$$m \frac{d^2 \lambda}{dt^2} + k\lambda = - f - n \frac{d^2 u_b}{dt^2} \tag{14}$$

When the base motion is a harmonic function of time,

$$\frac{d^2 u_b}{dt^2} = A \sin \omega t \tag{15}$$

Eq.14 becomes

$$m \frac{d^2 \lambda}{dt^2} + k\lambda = - f - nA \sin \omega t \tag{16}$$

which can be easily solved in an analytical manner.

Finally, it should be noted that the analysis developed here assumes no temporal change in the thickness of the liquefied layer. On the other hand, however, former studies on the ultimate displacement, U and W, were made on the experimental permanent displacement that was observed in shaking table tests after the pore pressure dissipation (Towhata et al., 1991a). Hence, the present analysis takes somehow into account the effects of the variation of the thickness of the liquefied layer by using the experimental formulation of U and W. Therefore, it is not known yet whether the present analysis should consider explicitly the effects of the pore pressure dissipation and reconsolidation of the ground.

MECHANISM OF ENERGY DISSIPATION

When the solution of Eq.16 was applied to the behavior of model grounds as will be seen later, two problems were observed. They are;

1) the predicted displacement developed much more rapidly than was observed in shaking table tests,
2) the predicted displacement oscillated around the ultimate one without decay of amplitude.

Apparently, these problems stem from the lack of any energy dissipation mechanism in Eq. 16. Thus, it was attempted to use two kinds of energy dissipation model.

Viscosity Model

The first type of energy loss is by means of viscosity. When an imaginary viscosity is assumed to the liquefied sand, the energy dissipation, ΔEnergy per unit time, is derived as

$$\Delta\text{Energy} = \int \eta \left\{ \frac{d}{dt} \left(\frac{\partial u}{\partial z} \right) \right\}^2 \text{dvol}$$

$$= \eta \int \left(\frac{\partial U}{\partial z} \right)^2 \text{dvol} \left(\frac{d\lambda}{dt} \right)^2 \qquad (17)$$

where η is an imaginary coefficient of viscosity of liquefied sand and the integration is made over the layer of liquefied sand (Fig.1). It is noteworthy that Eq.17 eliminates from consideration all the strain components other than the shear strain of $\partial u/\partial z$, because most strain components are much less significant than $\partial u/\partial z$. This has already been practiced in the calculation of the potential energy, Q (Towhata et al., 1992).

On the other hand, a viscous term of $2\sqrt{mk}\ h(d\lambda/dt)$ is added to Eq.16. The parameter, h, is the critical damping ratio and no

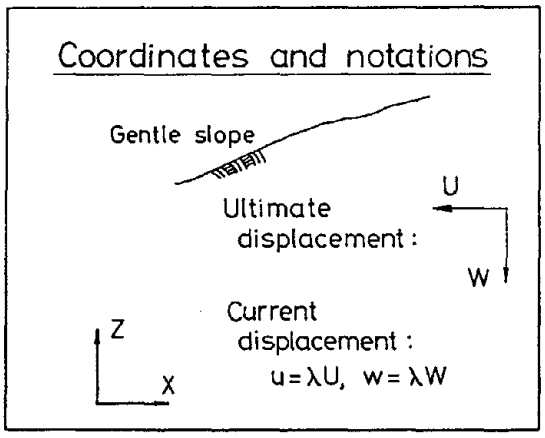

Fig.1 Coordinates and notation of displacement employed here.

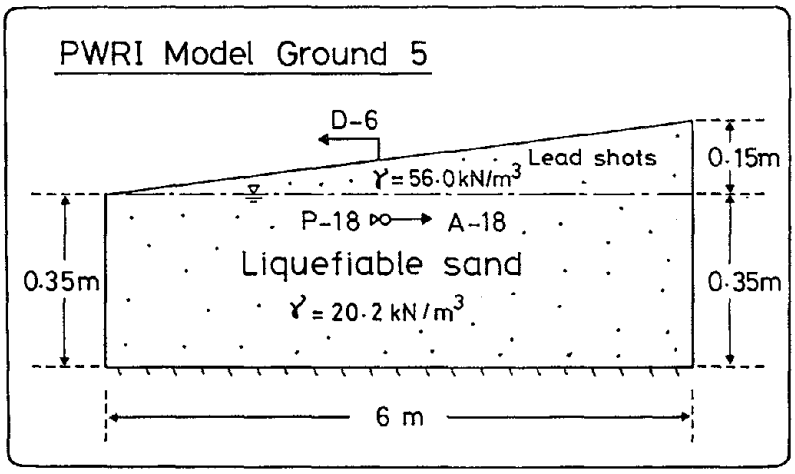

Fig.2 Model ground of shaking table test No.5 at PWRI.

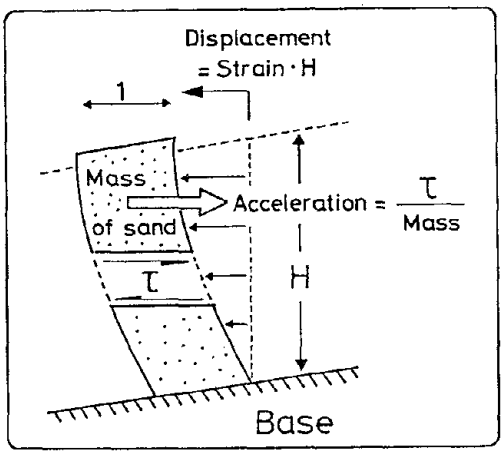

Fig.3 Evaluation of shear stress and strain in model ground by using measured records.

oscillation of λ occurs when $h > 1$ and $A = 0$. Consequently, the energy dissipation per unit time is given by

$$\Delta \text{ Energy} = 2\sqrt{mk}\, h\left(\frac{d\lambda}{dt}\right)^2 \tag{18}$$

By equating Eqs. 17 and 18,

$$h = \frac{\eta}{2\sqrt{mk}} \int \left(\frac{\partial U}{\partial z} \right)^2 \text{dvol} \tag{19}$$

It is not difficult to derive a closed-form solution of the equation of motion (Eq.16) with a viscous mechanism.

Dilatant Flow Model

The second mechanism of energy loss was developed by observing the behaviour of liquefied sand during a shaking table test. Fig.2 illustrates the configuration of a model ground which was shaken at the Public Works Research Institute. It also reveals the location of the transducers of the acceleration, the displacement, and the excess pore water pressure that will be employed in the discussion later on.

Firstly, the horizontal acceleration, A-18, of the ground near the surface was used to make a rough estimate of the shear stress, τ, in the liquefied soil. When the ground surface is not inclined significantly, the equation of motion of a soil column as illustrated in Fig.3 makes it possible to estimate the shear stress τ at the bottom of the column;

$$\tau \sim (\textit{Mass of soil column})\ (\textit{Acceleration at A-18}) \tag{20}$$

The idea of Eq.20 has been widely used in the prediction of liquefaction potential (e.g., Seed, 1976). Apparently, the shear stress thus evaluated does not include a static component of the real stress. Secondly, the measured displacement, D-6, at the ground surface in Fig.2 is the one relative to the soil container and the unliquefiable base layer. Hence, it is proportional to the shear strain of the liquefied sand. Therefore, a diagram of A-18 versus D-6 suggests a shape of a stress-strain curve of the liquefied sand. Finally, the measured excess pore water pressure in Fig.2 indicates how the effective stress varies in the ground undergoing soil liquefaction.

Fig.4 is indicative of the A-18 versus D-6 relationship and suggests the shape of a stress-strain curve. The curve in the first cycle is not discussed here because the state of liquefaction did not occur yet. In the following cycles, it may be seen that the liquefied sand exhibited a temporary shear stiffness and did not behave exactly similar to liquid, contrary to the

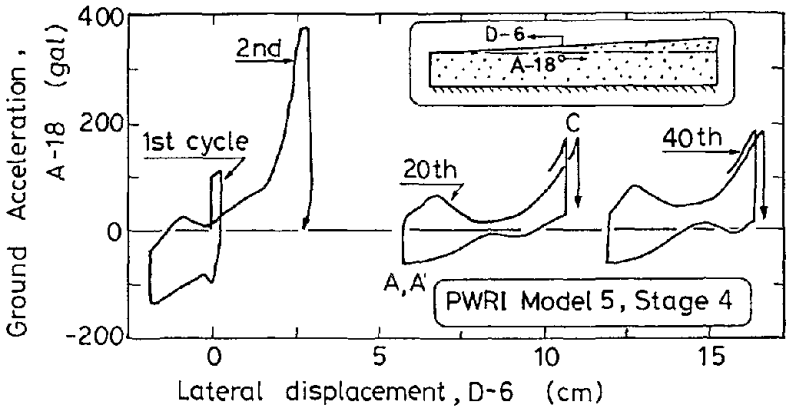

Fig.4 Estimated shape of stress-strain loop in liquefied sand.

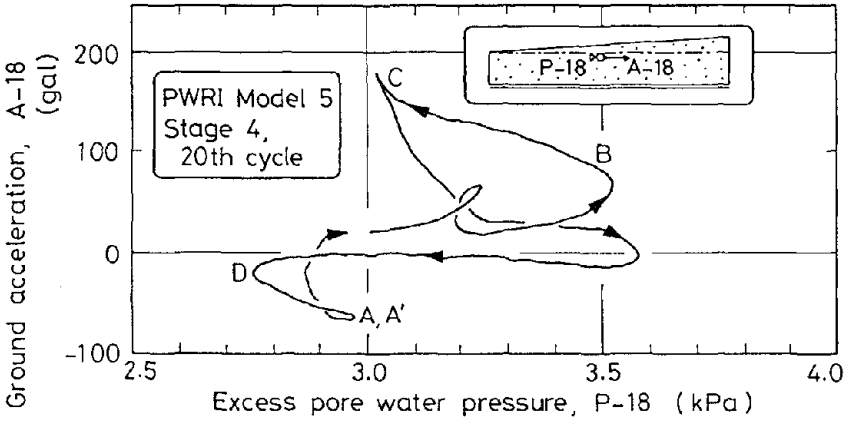

Fig.5 Estimated relation-ship of pore water pressure and shear stress in liquefied layer.

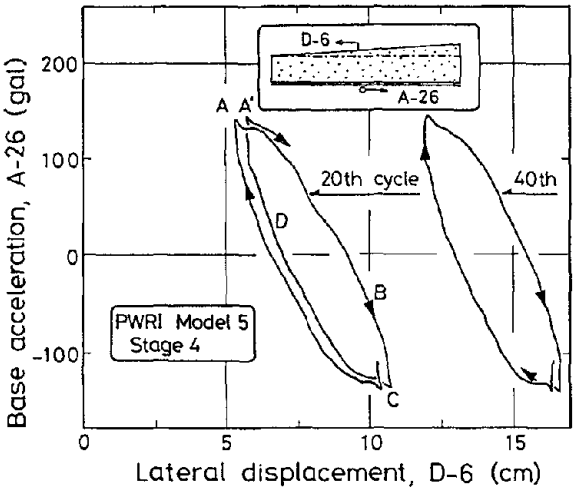

Fig.6 Observed relationship between inertia force and displacement of liquefied ground.

idea mentioned before. For a certain period after unloading of shear stress from its peak values at A and C in Fig.4, the shear stress and the tangent shear modulus are very small. Particularly, a stress softening or decrease suggests that a large distortion can develop rapidly in both positive and negative directions of displacement. After a substantial displacement of ground in both directions, the shear stress starts to develop and this increased shear modulus of soil prevents further movement of the ground. Following the peak shear stress attained at C and A', the phase of unloading and reloading in the other direction is accompanied again by a rapid development of shear distortion. Thus, a liquefied ground flows towards the location of the minimum potential energy as is predicted by the assumption of liquid ground; being associated in the meantime with a temporal development and disappearance of shear resistance of sand.

The variation in the manner of development of lateral soil movement as described above is closely related to dilatancy in sand which either increases or decreases the excess pore water pressure and thereby affects the resistance of sand against shear distortion. Fig.5 shows the relationship between the measured pore water pressure and the shear stress that was estimated from the ground acceleration in an approximate manner (Fig.3). It is seen that the excess pore water pressure drops significantly at the moment of peak shear stress, A and C; particularly at C in the positive direction. This behavior of water-saturated sand is commonly observed in undrained shear tests. Conversely, the pore water pressure rises again after the peak stress and is maintained high until the next peak stress is approached. Therefore, it is reasonable to say that the high level of the excess pore water pressure allows the liquefied sand to deform without a significant resistance against shear except after the shear distortion has occurred substantially in each half cycle of shaking and the peak shear stress is approached.

Although the soil behavior as summarized above should be modelled precisely for the purpose of dynamic analysis, this type of approach requires a step-by-step or an iterative integration of the equation of motion. This is because the change in the deformability of sand is related to either shear distortion (Fig.4) or the ground acceleration (Fig.5) both of which are not known until the equation is solved. Thus, the computation becomes much more complicated than a closed-form solution which is the goal of the present study.

Fig.6 reveals an experimental relationship between the base acceleration or the inertia force and the ground displacement, D-6. This relationship is used to make the analysis very simple.

Firstly, the ground displacement can develop rather freely after the peaks of the inertia force, A and C. This phase corresponds in Fig.4 to the stage after the peak shear stress when the excess pore water pressure is high. The rate of development of displacement decreases gradually in the following stage, until the peak inertia force occurs and the nearly vertical gradient of the curve at peaks suggests a very limited possibility of continued flow of the ground. Fig.5 already indicated that the reduced pore pressure due to dilatancy caused this change in sand behavior.

To model the ground behavior as mentioned above, a liquefied ground is allowed to move in accordance with Eq.14 without viscosity from the moment of peak inertia force, A and C in Fig.6, to the moment of null inertia force, B and D. At B and D the ground movement is ceased abruptly and no more displacement is allowed until the next peak inertia force occurs at C and A'. This model implies that a repeated loading and unloading is necessary, however small its magnitude may be, in order to keep the ground moving laterally. In other words, the ground can continue its flow as long as minor shaking is occurring with a low level of amplitude.

Eq.16 was solved with the idea in Fig.6. The value of λ at the end of each cycle of inertia loading, denoted by λ_i, is given by

$$\lambda_i - 1 = (\lambda_{i-1} - 1)\cos^2\left(\frac{\pi\sqrt{k/m}}{2\omega}\right) + \frac{nA}{m\omega^2 - k}\left[\cos\left(\frac{\pi\sqrt{k/m}}{2\omega}\right) - \cos^2\left(\frac{\pi\sqrt{k/m}}{2\omega}\right)\right] \qquad (21)$$

which is easy to be calculated with the initial condition of $\lambda_0 = 0$ at the beginning of shaking and liquefaction.

EXAMPLE CALCULATION

The results of Eq.21 is compared with an observed development of λ with time that was obtained from a small-scale shaking table test. A loose deposit of sand was created in a container by jetting pressurized water into a sand deposit. The configuration of the model ground is illustrated in Fig.7. The relative density of the ground was 38 percent. The ground was shaken horizontally with an acceleration amplitude of 200 gals and a frequency of 5 Hz. This shaking was continued for a sufficiently long time until the ultimate displacement, U and W, was attained and no more increment in soil movement was observed. The translation of the targets embeded in the ground as shown in Fig.7 was recorded by a video equipment and the

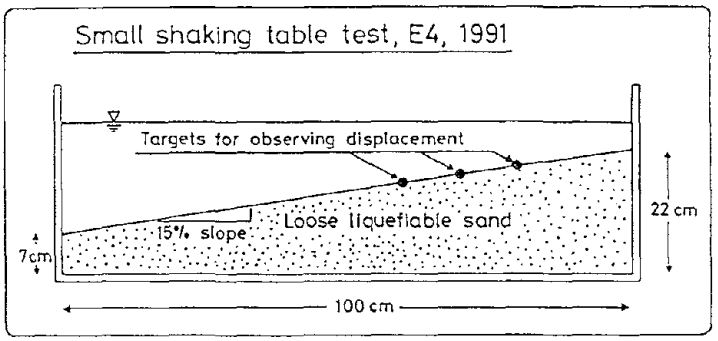

Fig.7 Configuration of model ground E4.

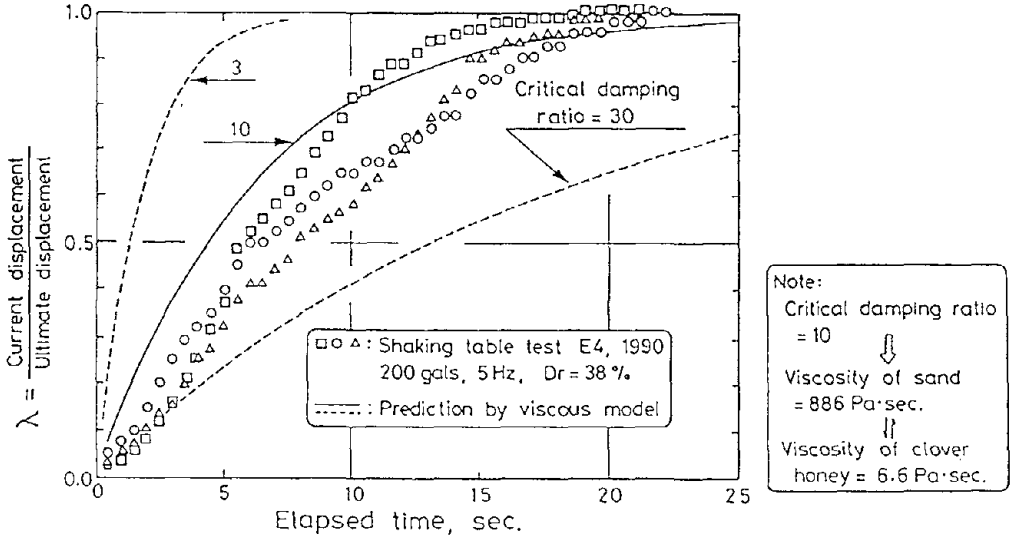

Fig.8 Observed development of λ with time in E4 and its prediction by viscous model.

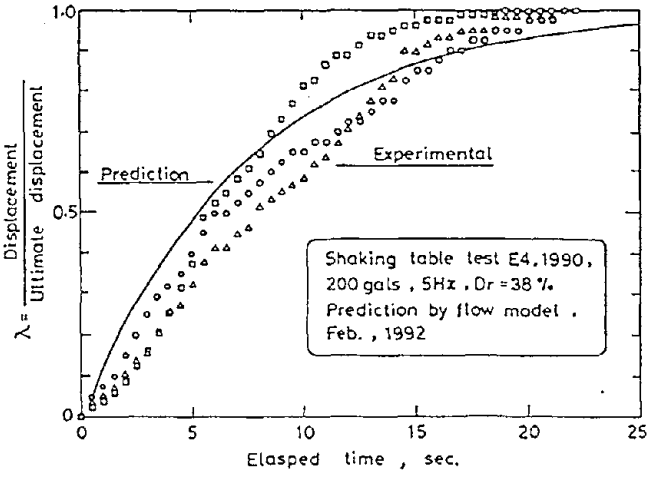

Fig.9 Development of displacement in E4 model test; both observation and calculation by dilatant flow model.

experimental values of λ were obtained;

$$\lambda = \frac{Current\ displacement\ of\ targets}{Ultimate\ displacement\ of\ targets} \qquad (22)$$

Figs.8 and 9 compare the experimental λ of the model ground in Fig.7 and the calculated value of λ that was obtained by Eq.16 combined with either the viscous mechanism (Fig.8) or the dilatant flow mechanism (Fig.9) of energy dissipation. The dilatancy model is recommendable because it agrees with the experimental data to a reasonable extent and it requires such a limited number of input data as the unit weight of soil, the elastic modulus of the surface unsaturated layer, if any, and the ground stratification.

The viscous model appears to be good as well, because the critical damping ratio equal to 10 gives a satisfactory agreement with the observation and the required amount of input data is limited. However, when the damping ratio = 10 is substituted in Eq.19, the coefficient of viscosity of liquefied sand, η, is found equal to 886 Pa•sec. Although no reliable experiment has been conducted on the viscosity of liquefied sand, this η value is much greater than the viscosity of pure water at 15 degrees Celsius (1.14×10^{-3} Pa•sec.) and even the viscosity of clover honey (6.6 Pa•sec.), that was obtained by the first author from a measured data (Mohsenin, 1986). Consequently, the idea of viscosity in a liquefied ground does not seem realistic.

Fig.9 compares the observed development of λ in the E4 model test with the calculated λ that was obtained by the dilatant flow model. The agreement seems satisfactory. It should be emphasized that this model does not need a dynamic soil property data, because the dilatancy modelling as Eq.21 takes it already into account. Moreover, the following nature of the closed form solution, Eq.21, was detected;

1) the frequency of shaking affects the calculated displacement, because the increased frequency leads to a reduced duration time of continued soil movement and the distance of soil movement in a single period of time decreases in proportion to the time squared.
2) the intensity of the base shaking hardly affects the ground displacement. This is because the effects of the positive and the negative inertia forces cancel each other and the ground moves under the effects of the gravity.

Fig.10 illustrates the calculated development of λ of a 400-meter-long ground in which the thickness of the liquefied layer is 5 meters throughout and is overlain by a one-meter-

thick surface unsaturated layer. The slope is as small as one percent. The unit weight of soil is 17.6 kN/m^3 in the liquefied layer and 15.7 kN/m^3 in the surface layer. The elastic modulus of the surface layer is 10780 kN/m^2. Thus, this model ground is exactly identical with what was called the "Control Case" ground by Towhata et al. (1992). The foot end of the slope was fixed, while an open crack was assumed at the top of the slope. The ultimate displacement took the maximum value of 5 meters at the top of the slope.

The dynamic analysis in Fig.10 with a dilatancy mechanism of energy dissipation shows that as much as 3000 seconds of shaking is needed for the loading and unloading of the inertia force to occur so that the displacement can develop to the ultimate magnitude. Apparently, the main shaking of an earthquake does not last for this long period of time, although the state of liquefaction and high pore water pressure can continue for tens of minutes. However, it seems that there are different sources of ground shaking that makes a liquefied ground continue its flow. Firstly, the main shaking of major earthquakes is accompanied by a "coda" wave and a minor excitation can keep the ground shaking for a longer time. In the meantime, loading and reloading of the inertia force is repeated and the ground displacement can develop further. Secondly, the lateral movement of the ground can in turn be the cause of a self-generated shaking as suggested by an observation of dynamic pore-pressure fluctuation in rapidly shearing granular material (Iverson and LaHusen, 1989).

Fig.11 demonstrates a viscous analysis on the same insitu control-case ground as shown in Fig.10. The particular analysis with the critical damping ratio equal to 10 shows that the ultimate displacement is attained in about 500 seconds, which seems realistic. However, this damping ratio corresponds to the viscosity coefficient of 82.8 kPa•sec. which is much greater than what was employed in the small-scale analysis (Fig.8). It is not very desirable, however, that the material property has to be changed with the ground size to get a good matching with the observation.

CONCLUSION

A closed-form solution of the temporal development of ground displacement due to seismic liquefaction was derived by using the Lagrangian equation of motion. The major conclusions drawn from this study are summarized in what follows;

1) The present analysis assumes a constant thickness of liquefied layer. It is not known yet whether the effects of

pore pressure dissipation and soil reconsolidation should be explicitly taken into account.

2) There is a mechanism of energy dissipation in a liquefied ground. However, an idea of viscosity requires unrealistically large viscosity coefficient to liquefied sand..

3) Shaking table test indicates a detailed information of the dynamic behavior of a liquefied ground undergoing lateral flow.

4) Dilatancy occurs periodically and induces a temporary development of shear resistance. Thus, the ground displacement is prevented periodically as well, followed by a reduction of shear resistance and a free movement of soil.

5) The model calculations indicates that an in-situ ground takes a long time to attain its ultimate displacement.

LIST OF REFERENCES

Iverson,R.M. and LaHusen,R.G. (1989) Dynamic Pore-Pressure Fluctuations in Rapidly Shearing Granular Materials, Science, Vol.246, pp.796-799.

Mohsenin,N. (1986) Physical Properties of Plant and Animal Materials, Gordon and Breach Science Publ., pp.320.

Orense,R. and Towhata,I. (1992) Prediction of Liquefaction-Induced Permanent Ground Displacements: a Three-Dimensional Approach, Proc. IV Japan-US Workshop on Liquefaction Countermeasures and Earthquake Resistant Design of Lifelines.

Seed,H.B. (1976) Evaluation of Soil Liquefaction Effects on Level Ground during Earthquakes, Liquefaction Problems in Geotechnical Engineering, ASCE, pp.1-104.

Towhata,I. Tokida,K., Tamari,Y., Matsumoto,H. and Yamada,K. (1991a) Shaking Table Tests and Analytical Prediction of Permanent Displacement Caused by Seismic Liquefaction, Proc. IX Pan American Conf. on Soil Mech. Found. Engg., Vol.I, pp.527-540.

Towhata,I., Sasaki,Y., Tokida,K., Matsumoto,H., and Tamari,Y. (1991b) Permanent Displacement of Liquefied Ground, Proc. IX Asian Regional Conf. on Soil Mech. Found. Engg., Vol.I, pp.437-440.

Towhata,I. Sasaki,Y., Tokida,K., Matsumoto,H., Tamari,Y., and Yamada,K. (1992) Prediction of Permanent Displacement of Liquefied Ground by Means of Minimum Energy Principle, accepted by Soils and Foundations.

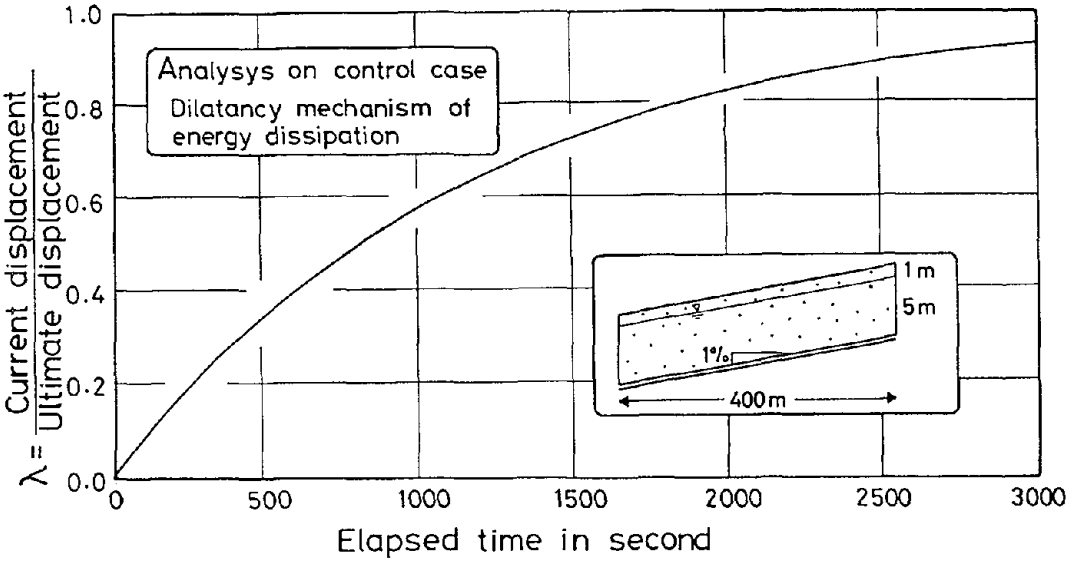

Fig.10 Displacement calculated by dilatant-flow model of a 400-meter-long ground.

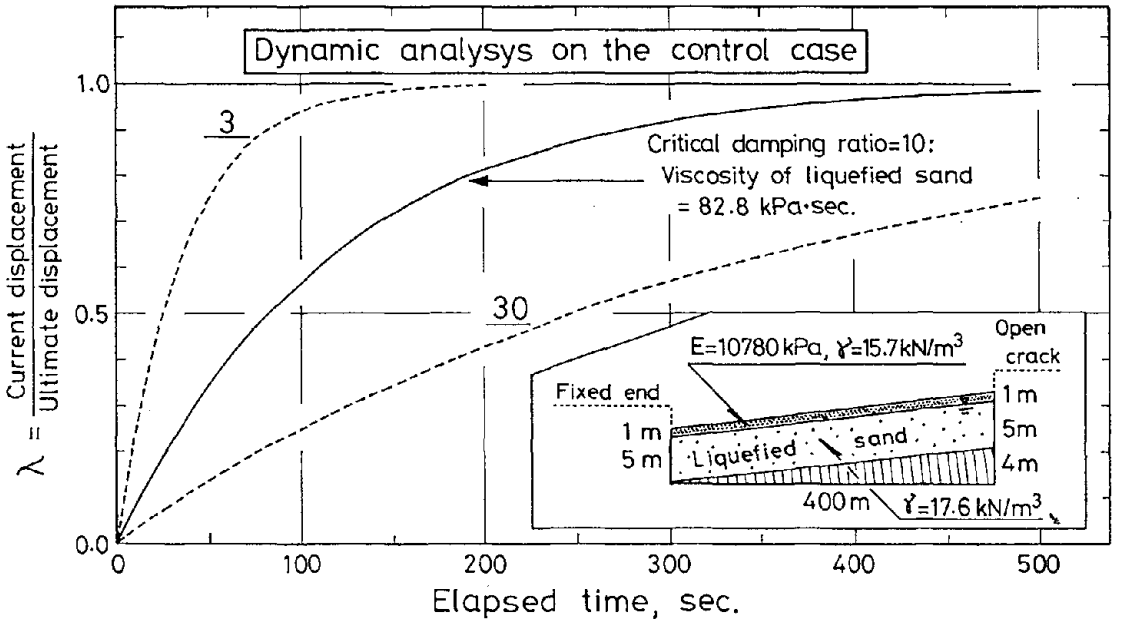

Fig.11 Displacement calculated by viscous model of a 400-meter-long ground.

Recent Work on Numerical Modelling of Flow Failure Induced by Soil Liquefaction

C. M. Famiglietti and J. H. Prevost

Department of Civil Engineering and Operations Research
Princeton University
Princeton, New Jersey 08544

ABSTRACT

The objective of this research project is to predict and simulate flow failure induced by soil liquefaction in order to quantify the possible destruction caused by such an event resulting from earthquake ground motion. Two critical aspects of the numerical treatment of this research are discussed. The first stems from the desire for the proposed methodology to allow frictional contact between different bodies. The solution of the slump test for concrete is presented to validate an explicit contact-impact element with Coulomb friction. The second aspect of the numerical treatment of this research, the inclusion of a large deformation (i.e., finite components of strain) elasto-plastic material model, is also discussed. The slump test is again used to illustrate the validity of the finite deformation Mises model.

INTRODUCTION

The ability to numerically model the flow of liquefied soil as the result of earthquake ground motion is an essential component of the prediction and/or simulation of soils due to earthquake excitation. Recent advances in this research project are included here. The ability to include frictional contact-impact between different bodies is important for the solution of general problems. The slump test for concrete is used to validate the explicit contact-impact technique. Due to the large ground deformations often associated with the flow of liquefied soil, any numerical model designed for this purpose should also incorporate a finite deformation elasto-plastic material model. The slump test is again used to illustrate the validity of a finite deformation Mises model.

An outline of the remainder of the paper is as follows. Results obtained for the slump test using a Newtonian fluid model are presented first for a variety of base conditions to validate the contact-impact element used at the base. Following this, the numerical solution of the slump test using a finite deformation Mises model is presented and compared to an analytical solution. Finally, a discussion concerning the status of the formulation of a finite deformation Drucker-Prager model is included.

Contact-impact element : Slump test

Interactions between different bodies in a finite element framework require special elements to account for contact-impact effects. Contact-impact problems are inherently nonlinear and often difficult to solve. Many implicit contact-impact elements, often combinations of Lagrange multiplier and penalty formulations, have been formulated and are presented in the literature. However, limited contributions to the literature have been made for explicit contact-impact elments. Some work on explicit elements has been performed by Hallquist (1976), Hallquist (1977), and Hallquist (1978). More recent work includes that by Belytschko and Lin (1987). Formulation and implementation of an explicit contact-impact element based on the master element - slave node approach by Belytschko and Lin (1987) has been performed and is validated here.

The slump test is regularly performed on fresh concrete to obtain an indication of its strength, or ability to flow. The test is explained fully in Tattersall and Banfill (1983). Briefly, the mold for the test specimen is filled with fresh concrete and then lifted off, allowing the concrete to slump, or flow under the action of gravity. Figure (1) shows the dimensions of the test specimen as well as the definition of the slump value.

Explicit axisymmetric simulations of the slump test have been performed in the (arbitrary) Lagrangian-Eulerian (ALE) description (see Keane and Prevost (1990)), although all nodes have been assigned Lagrangian degree of freedoms for this simulation. For these results, a compressible viscous Newtonian fluid was employed to model the concrete. Material parameters of the concrete were chosen as B = fluid bulk modulus = 1.5967×10^8 N/m^2, μ = shear viscosity = 10.0 Ns/m^2, and ρ = mass density = 2408.2 kg/m^3. Two sets of base boundary conditions have been used with the finite element mesh shown in Figure (2). Firstly, the base was treated as a frictionless boundary by putting rollers on the nodes at the base (slip condition), and secondly, the nodes of the base were fixed (no-slip condition). Deformed mesh plots for the case with rollers on the base nodes and the case with a fixed base are presented in Figures (3a) and (3b), respectively. Simulations were run until t = 0.126 sec.

The slip and no-slip results can be used as limiting cases for computations employing friction along the base. That is, results using a low friction angle along the base should approach the results of the slip base condition, whereas results using a base having a high friction angle should approach

the results of the no-slip base condition. To incorporate friction along the base, the mesh shown in Figure (4) has been employed where the surface that the concrete material is resting on is treated as a set of contact-impact elements with Coulomb friction. Computations were performed for a variety of friction angles.

Figures (5a) and (5b) contain plots of the deformed mesh for a friction angle along the base of 1° and of 50°, respectively. These plots resemble those shown in Figures (3a) and (3b), as they should. Results for a complete range of friction angles are also presented in Figure (6a) as displacement plots of node 81, and in Figure (6b) as time history plots of the slump value. Results from the two limiting cases discussed above are also plotted in Figures (6a) and (6b). Figure (6a) illustrates that the slip and no-slip cases are the limiting cases of horizontal displacement for a complete range of friction angles, as expected. The results plotted in Figure (6b) imply that the slump value is independent of the frictional contact condition along the base. Although the slump is known to be somewhat insensitive to the base boundary condition (Tanigawa and Mori (1986)), variations in the slump due to different base friction angles were expected. The discrepancy in the slump may be due to the inadequacy of the Newtonian fluid to model concrete.

Finite deformation material model : Slump test

The classical theory of infinitesimal plasticity is inappropriate for situations in which strain components are finite. Specifically, the kinematics of finite strain invalidate the usual assumption, used in infinitesimal strain analysis, that the total strain is the sum of elastic and plastic parts. For the application of interest here, finite components of strain are possible, and therefore, a finite deformation material model is necessary.

Finite strain kinematics based upon a multiplicative split of the deformation gradient were proposed by Lee and Liu (1967) and furthered by Lee (1969), among others. The fundamental idea behind this approach is that the deformation gradient, $\mathbf{F}$, can be split into the product of its elastic and plastic parts, i.e.,

$$\mathbf{F} = \mathbf{F}^e\mathbf{F}^p. \tag{1}$$

Simo (1988a) and Simo (1988b) have used this assumption at the outset to formulate a hyperelastic finite-strain elasto-plastic model valid in both the material and spatial descriptions. The formulation reduces to the usual infinitesimal theory for small strains.

Implementation of a hyperelastic finite deformation Mises model following the formulation of Simo (1988a) and Simo (1988b) has been performed. The hyperelastic free energy function with uncoupled volumetric and deviatoric parts is identical to that used by Ju (1989) for the same formulation and is written as

$$\Psi_e^0(\mathbf{g}, \mathbf{b}^e, \mathbf{F}) = B(J \ln\theta - J + 1) + \frac{1}{2}\mu(J^{-2/3}\mathbf{b}^e : \mathbf{g} - 3) \tag{2}$$

which results in

$$\mathbf{T} = BJ \ln\theta\mathbf{g} + \mu J^{-2/3} \operatorname{dev} \mathbf{b}^e \tag{3}$$

where $\mathbf{g}$ = metric tensor, $\mathbf{b}^e$ = elastic left Cauchy-Green tensor = $\mathbf{F}^e\mathbf{F}^{e^T}$, $\mathbf{F}$ = deformation gradient, B = bulk modulus, $J = \theta = \det\mathbf{F}$, μ = shear modulus, $\mathbb{T}$ = Kirchhoff stress, $\mathbf{b}^e : \mathbf{g} = \operatorname{tr}(\mathbf{b}^e\mathbf{g}) = b^e_{ij}g_{ij}$, and $\operatorname{dev}(\cdot) = (\cdot) - \frac{1}{3}\operatorname{tr}(\cdot)\mathbf{g}$.

Validation of the finite deformation Mises plasticity model is performed through the solution of the slump test. Dimensionless material parameters were taken from Christensen (1991) as $B = 1000.0$, $\mu = 1.0$, ρ = mass density = 0.1, and g = acceleration due to gravity = 0.1. The dimensionless yield value was obtained from

$$\tau_y' = \frac{\sqrt{3}}{2}\frac{c}{\rho g H} \tag{4}$$

where H = dimensionless height = 1.0 and c = cohesive coefficient from ϕ = yield function = $\sqrt{\mathbf{s} : \mathbf{s}} - \sqrt{2}\,c \leq 0$. An undeformed dimensionless axisymmetric finite element mesh consisting of 50 elements is shown in Figure (7). Implicit numerical simulations were run for a slip base condition using the mesh shown in Figure (7).

Numerical results can be validated by comparing to an analytical solution developed by Christensen (1991) for axisymmetric slumps with a slip base condition. For the analytical solution, the (dimensionless) slump value, s', is calculated from both the (dimensionless) height of unyielded material, h_0', and the (dimensionless) height of yielded material, h_1', given a (dimensionless) yield value. In other words, for a given value of τ_y' = (dimensionless) yield value, then

$$\tau_y' = \frac{1}{6}\left[(1 + h_0') - \frac{1}{(1 + h_0')^2}\right] \tag{5}$$

is solved for h_0', which is then substituted into

$$h_1' = 2\tau_y' \ln\left[\frac{7}{(1 + h_0')^3 - 1}\right] \tag{6}$$

to obtain h_1'. The (dimensionless) slump value, s', is then found from

$$s' = 1 - h_0' - h_1'. \tag{7}$$

A plot of the (dimensionless) slump value vs. (dimensionless) yield value obtained from the analytical solution (solid line) is plotted in Figure (8), as well as the numerical results obtained using the proposed methodology (dashed line). The numerical solution is unable to predict slumps below a (dimensionless) yield value of $\tau_y' = 0.05$ for the mesh used in Figure (7) due to extreme element deformation. Figure (9) is a plot of the deformed mesh for $\tau_y' = 0.05$ illustrating the situation. The numerical and analytical solutions are in good agreement over all values of τ_y', with a root mean square error (RMSE) of 0.097, computed from

$$\text{RMSE} = \sqrt{\frac{1}{N}\sum_{i=1}^{N}(s_i^{n'} - s_i^{a'})^2} \tag{8}$$

where $s_i^{n'}$ = dimensionless slump from numerical simulation at data point i, $s_i^{a'}$ = dimensionless slump from analytical solution at data point i, and N = number of data points.

CONCLUSIONS

An explicit contact-impact element allowing frictional contact at an interface has been briefly discussed. Validation is performed through the solution of the slump test by varying the friction angle at the base, and the results are as expected.

The importance of a finite deformation elasto-plastic material model for soil liquefaction flow problems has been discussed. A finite deformation hyperelastic Mises plasticity model has been implemented and is substantiated by comparing the results from the slump test to analytical results. However, the Mises plasticity model was developed for use with metals, and its applicability to the solution of soils problems is questionable. Since the pressure-dependent Drucker-Prager yield criterion is better suited for use with soils, formulation and implementation of a finite deformation Drucker-Prager plasticity model is underway. It is one of the last steps that must be performed before the proposed numerical procedure is capable of simulating and/or predicting a general problem of flow failure induced by soil liquefaction. Finally, the proposed methodology, see Keane and Prevost (1990), will be applied to the solution of a soil liquefaction flow problem to demonstrate the capabilities of the numerical procedure.

ACKNOWLEDGEMENTS

This research was supported in part by a grant from the National Science Foundation under the auspices of the National Center for Earthquake Engineering Research (NSF ECE 86-07591) and by a collaborative research agreement between Kajima Corporation and Princeton University. These supports are gratefully acknowledged.

REFERENCES

1. T. BELYTSCHKO AND J. I. LIN, (1987) "A three-dimensional impact-penetration algorithm with erosion", *Computers and Structures*, Vol. 25, No. 1, pp. 95-104.
2. G. CHRISTENSEN, (1991) "Modelling the flow of fresh concrete: the slump test", Ph. D. Dissertation, Dept. of Chemical Engineering, Princeton University, Princeton, NJ.
3. J. O. HALLQUIST, (1976) "A procedure for the solution of finite-deformation contact-impact problems by the finite element method", UCRL-52066, April 1976, Lawrence Livermore Laboratory, Livermore, CA.
4. J. O. HALLQUIST, (1977) "A numerical procedure for three dimensional impact problems", Preprint 2956, Oct. 1977, ASCE.
5. J. O. HALLQUIST, (1978) "A numerical treatment of sliding interfaces and impact", in K. C. Park and D. K. Gartling, eds., Computational Techniques for Interface Problems, AMD Vol. 30, (ASME, New York).
6. J. W. JU, (1989) "Energy-based coupled elastoplastic damage models at finite strains", *J. of Engrg. Mechs.*, Vol. 115, No. 11, pp. 2507-2525.
7. C. M. KEANE AND J. H. PREVOST, (1990) "Preliminary results of a numerical technique to model flow failure induced by soil liquefaction", Proc. of the 3rd Japan-U.S. Workshop on Earthquake Resistant Design of Lifeline Facilities and Countermeasures for Soil Liquefaction, San Francisco, CA, U.S.A., December 17-19, Technical Report NCEER-91-0001, pp. 253-267.

8. E. H. LEE, (1969) "Elastic-plastic deformation of finite strains", *J. of Appl. Mechs.*, Vol. 36, pp. 1-6.

9. E. H. LEE AND D. T. LIU, (1967) "Finite-strain elastic-plastic theory with application to plane-wave analysis", *J. of Appl. Physics*, Vol. 38, No. 1, pp. 19-27.

10. J. C. SIMO, (1988a) "A framework for finite strain elastoplasticity based on maximum plastic dissipation and the multiplicative decomposition: Part I. continuum formulation", *Comput. Meths. Appl. Mech. Engrg.*, Vol. 66, pp. 199-219.

11. J. C. SIMO, (1988b) "A framework for finite strain elastoplasticity based on maximum plastic dissipation and the multiplicative decomposition: Part II. computational aspects", *Comput. Meths. Appl. Mech. Engrg.*, Vol. 68, pp. 1-31.

12. Y. TANIGAWA AND H. MORI, (1986) "Rheological analysis of slumping behavior of fresh concrete", Proc. of the 29th Japan Congress of Materials Research, pp. 129-136.

13. G. H. TATTERSALL AND P. F. G. BANFILL, (1983) The Rheology of Fresh Concrete, (The Universities Press Ltd., Belfast, Northern Ireland).

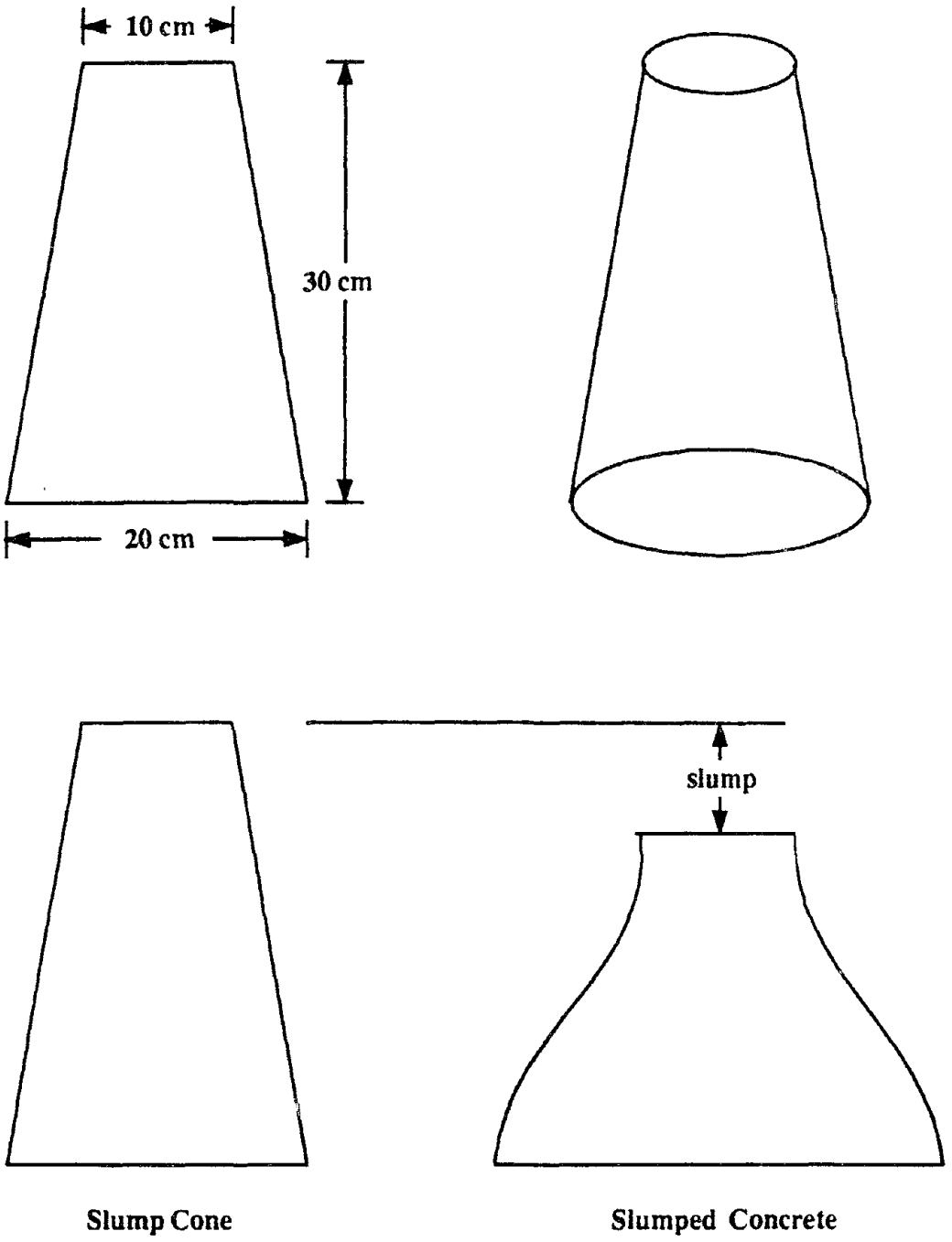

Figure 1: Dimensions of slump test specimen and explanation of slump value

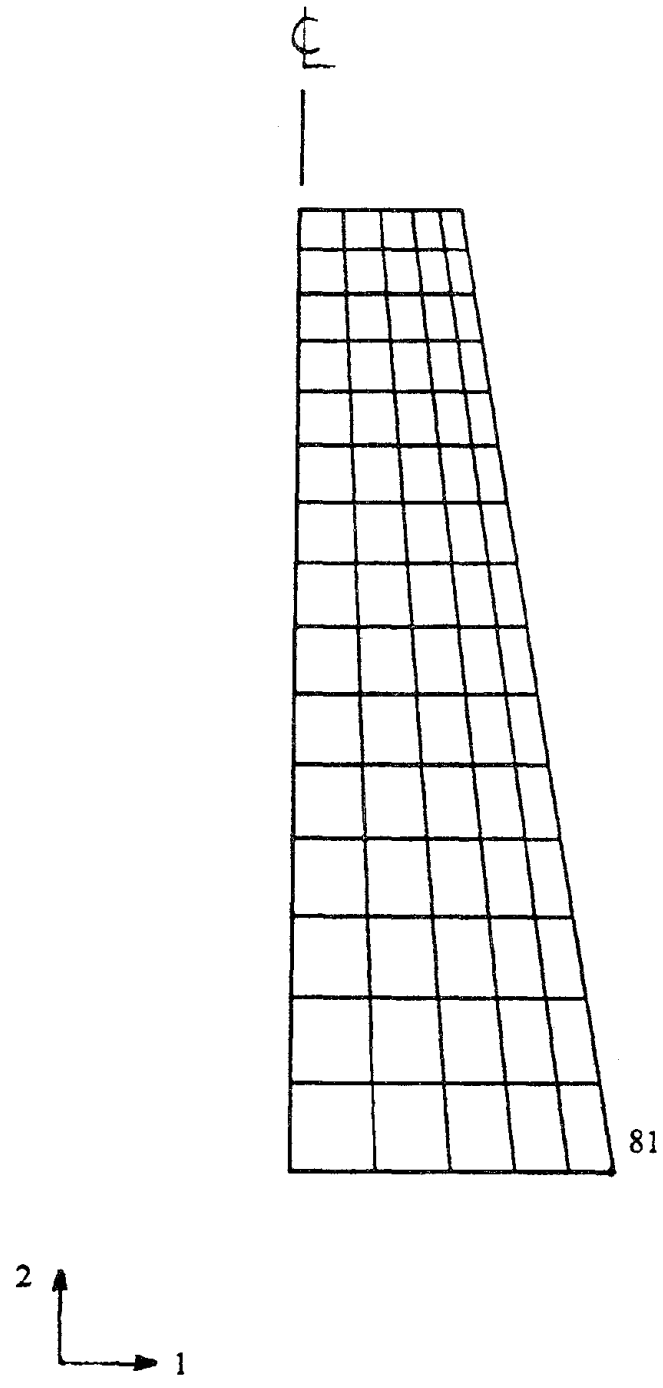

Figure 2: Finite element mesh used for slump test; slip and no-slip cases

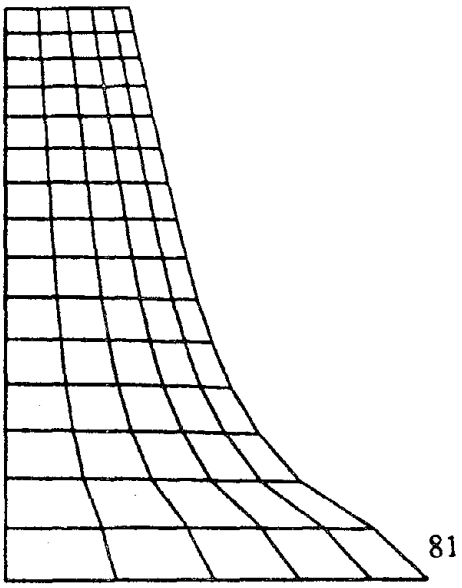

Figure 3a: Results - deformed mesh plot for slump test with slip base, $t = 0.12$ sec

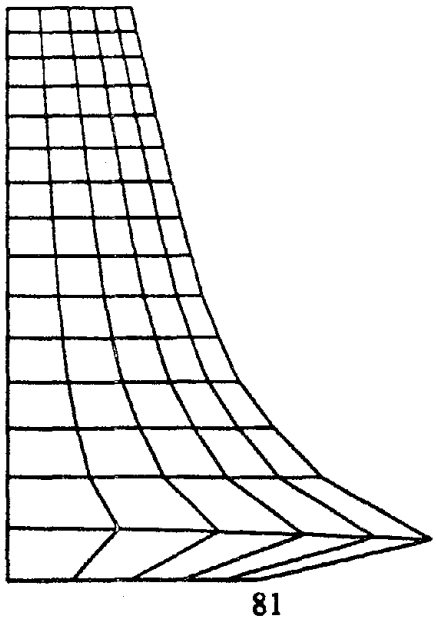

Figure 3b: Results - deformed mesh plot for slump test with no-slip base, $t = 0.12$ sec

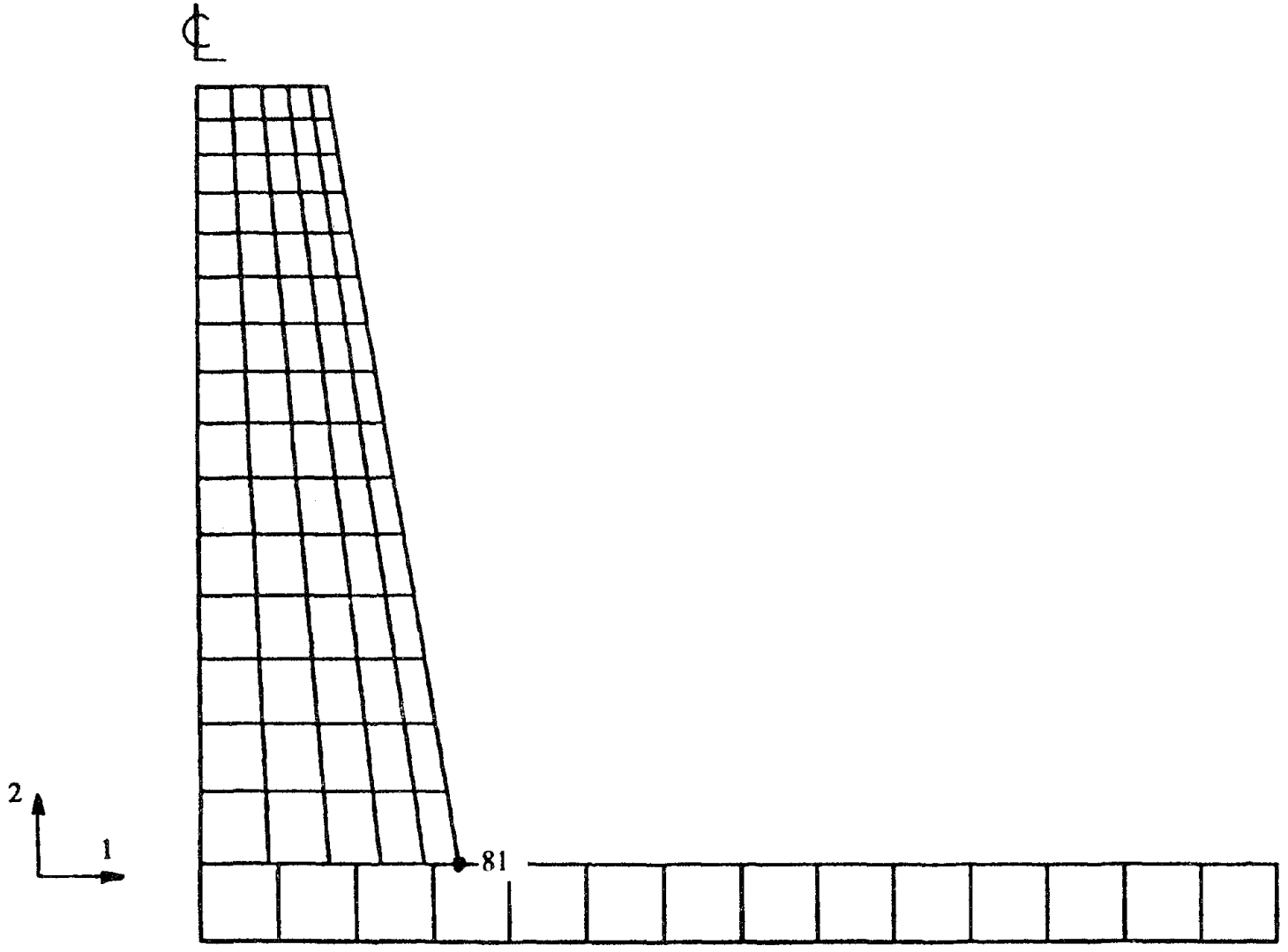

Figure 4: Finite element mesh used for slump test; frictional contact surface cases

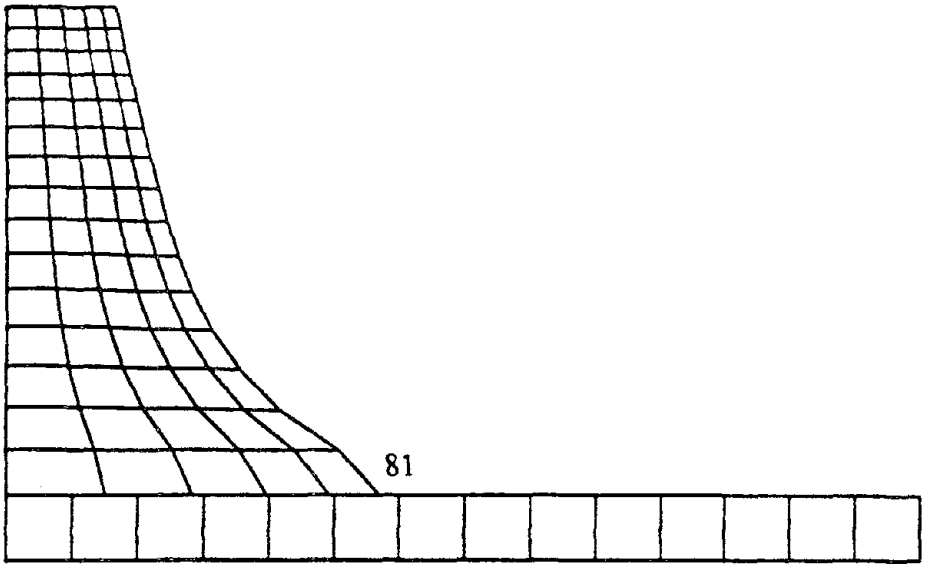

Figure 5a: Results - deformed mesh plot for slump test with friction angle at base, $\phi = 1°, t = 0.12$ sec

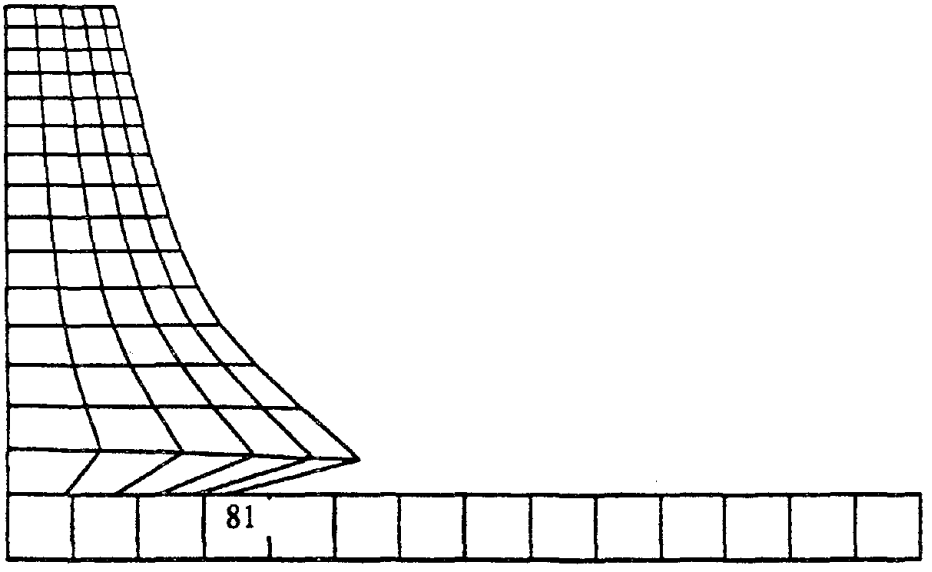

Figure 5b: Results - deformed mesh plot for slump test with friction angle at base, $\phi = 50°, t = 0.12$ sec

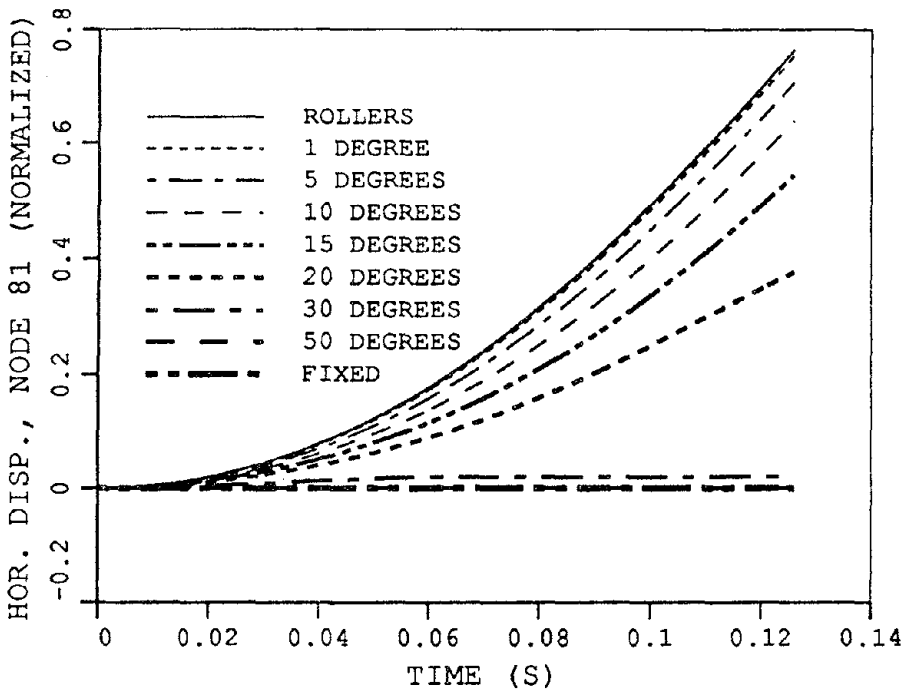

Figure 6a: Results - horizontal displacement time history plot of node 81; slip, no-slip, and frictional contact surface cases

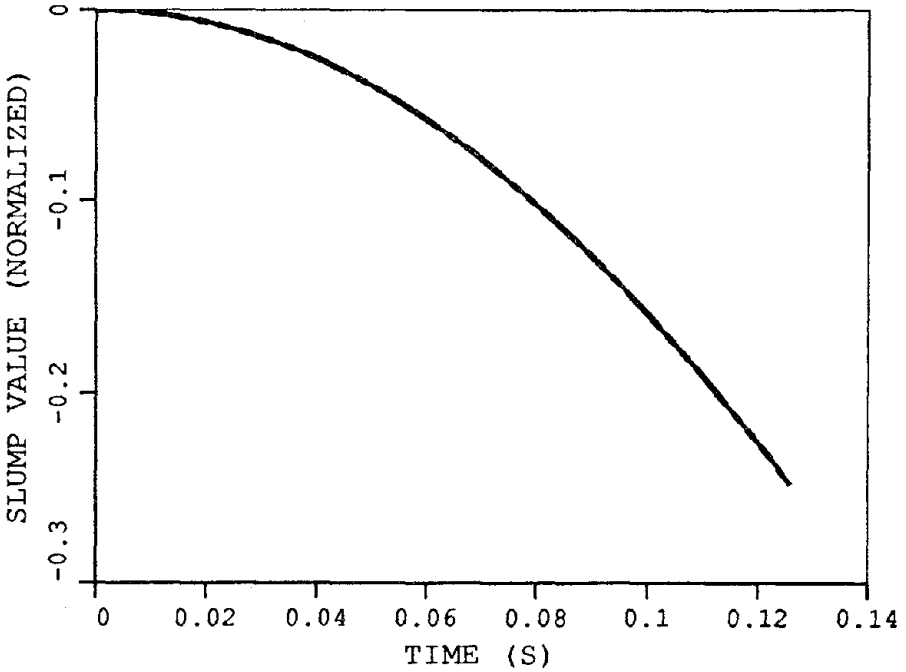

Figure 6b: Results - slump time history plot; slip, no-slip, and frictional contact surface cases

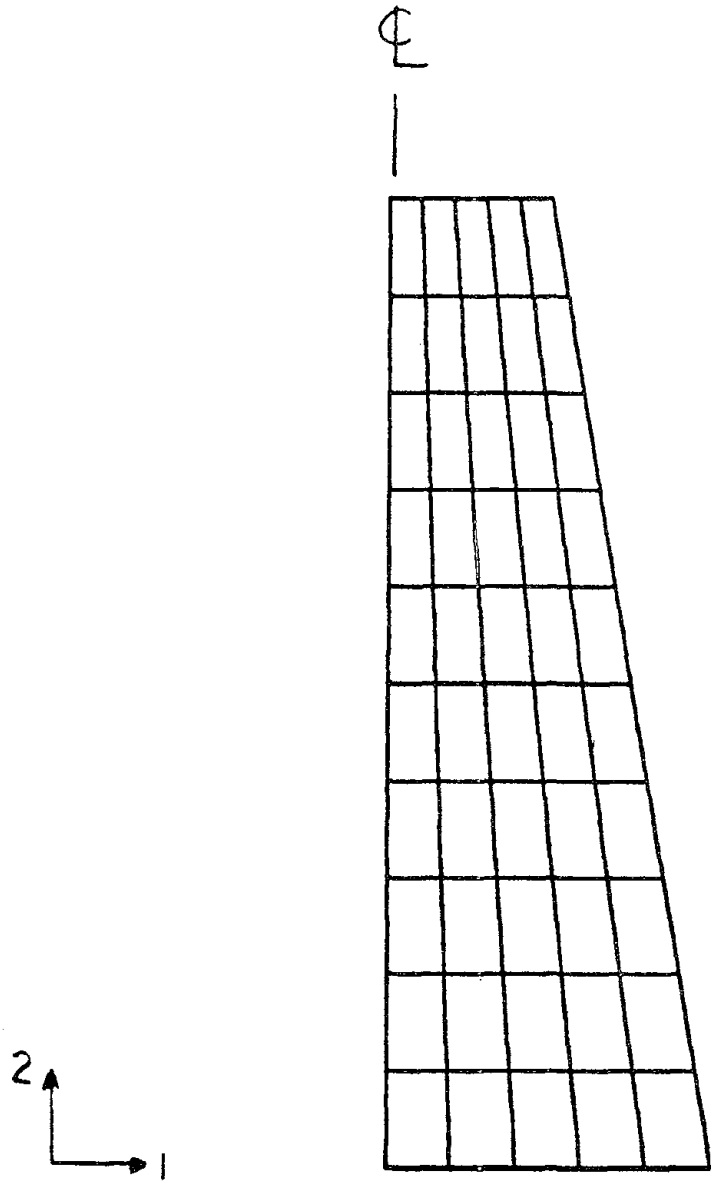

Figure 7: Finite element mesh used for slump test

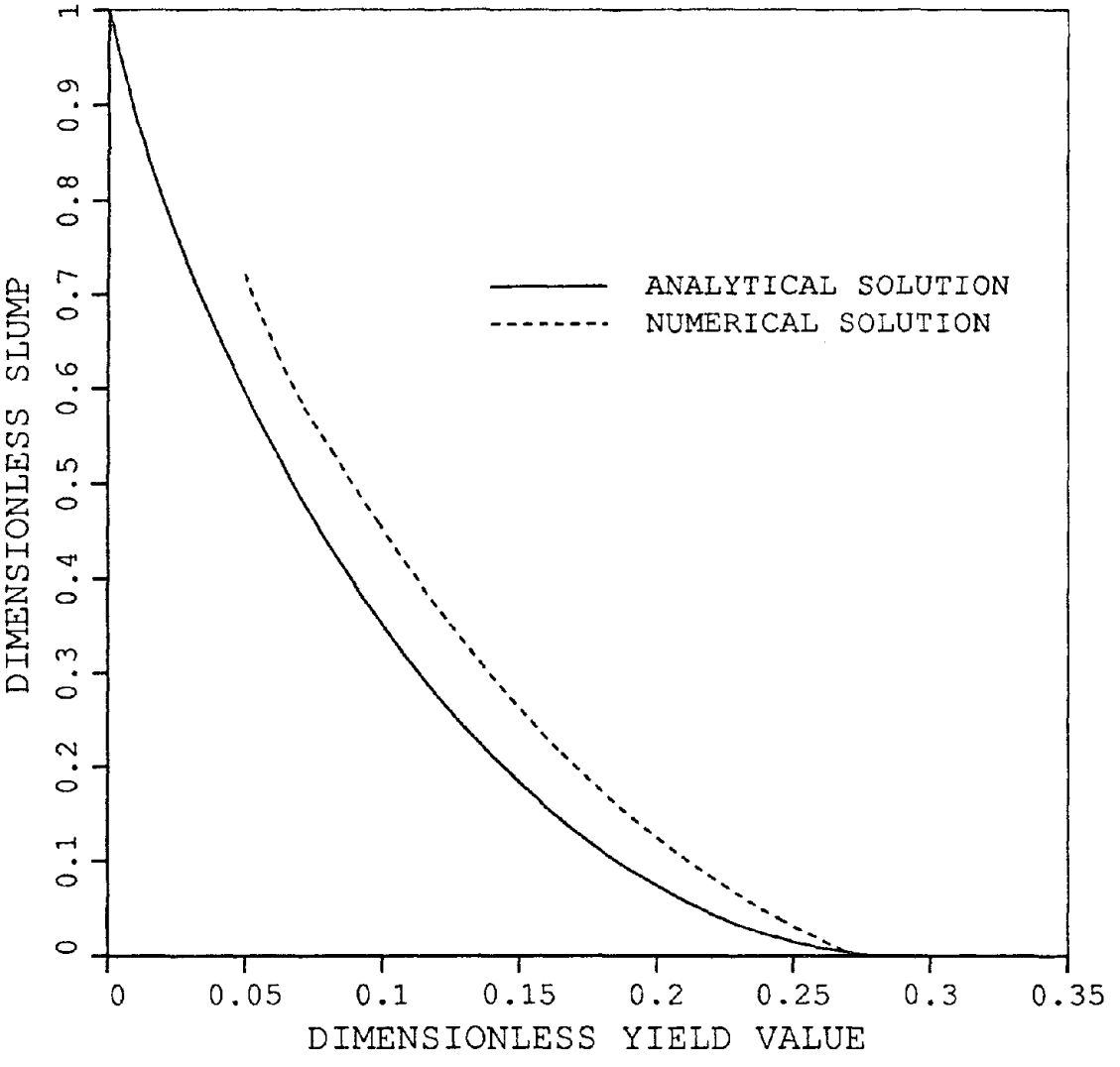

Figure 8: Results - comparison between analytical solution and numerical solution for slump test

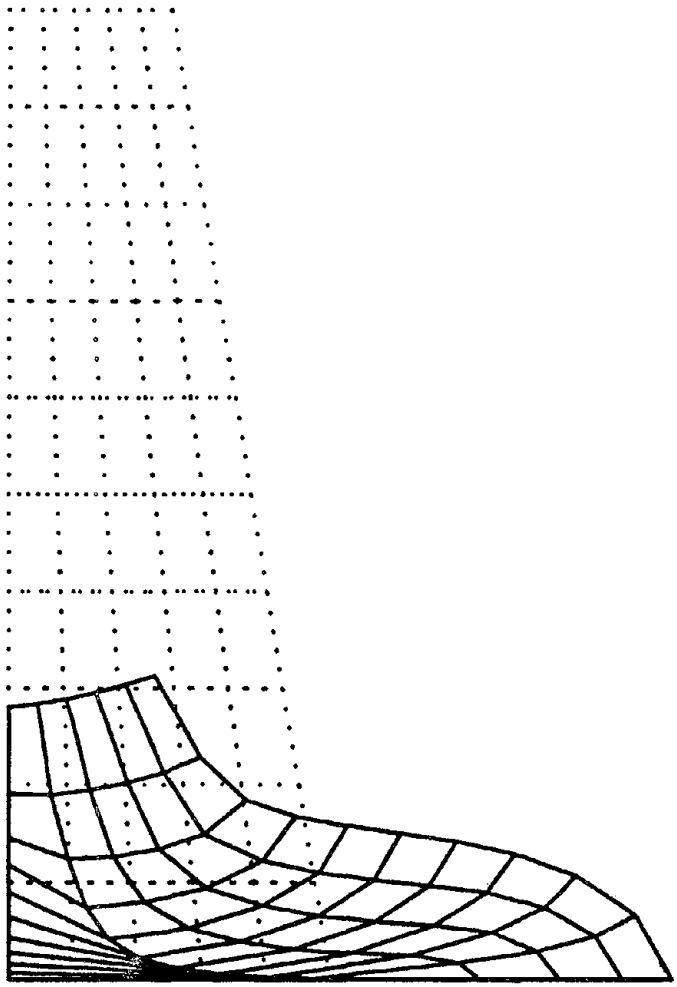

Figure 9: Results - deformed mesh plot for slump test

Utility Performance Aspects, Liquefaction Study, Marina and Sullivan Marsh Areas, San Francisco, California

Charles Scawthorn, Keith Porter and Mahmoud Khater
EQE International
San Francisco, CA 94104

Dan Seidel, Don Ballantyne
Kennedy/Jenks/Chilton
San Francisco, CA 94105

Henry T. Taylor
HLA
San Francisco, CA 94105

Robert D. Darragh
Dames & Moore
San Francisco, CA 94105

Charles Ng
Department of Public Works
San Francisco, CA

ABSTRACT

Motivated by water and sewer system failures in the Marina in the 1989 Loma Prieta earthquake, and the recognition that greater damage had occurred in the 1906 earthquake and could be expected again, the city of San Francisco retained an engineering team to estimate the amount and extent of large ground displacements, and their effect on water and sewer utilities. Geotechnical aspects are discussed in an accompanying paper while this paper reviews the utility aspects of the project. The Marina area contains 39,000 ft of potable water (MWSS) pipe, which was estimated to sustain about 80 breaks in an event similar to 1906, while a special aseismic firefighting system (AWSS) is estimated to sustain 11 breaks in 8,150 ft. of pipe. For 62,000 ft of MWSS pipe in the Sullivan Marsh area, 200 breaks are found, while the AWSS is estimated to sustain 84 breaks in 27,000 ft of pipe. Total repair costs for water and sewers are estimated at about $49 million. Geotechnical, structural, operational and systemic mitigation options were developed and prioritized.

INTRODUCTION

This paper summarizes utility aspects of a project performed for the City of San Francisco, concerning estimation of earthquake induced large permanent ground deformations and their effects on underground water supply and sewer utilities. An accompanying paper[1] summarizes geotechnical aspects of the project, while this paper presents the estimation of the effects of the estimated deformations on the underground utilities, and the range of measures considered to mitigate these effects.

The project, termed the *Liquefaction Study*, was motivated by the occurrence of widespread water supply and sewer system damage and failures in the Marina section of San Francisco in the October 17, 1989 Loma Prieta earthquake[2], and the recognition that even greater damage had occurred in the 1906 San Francisco earthquake and could be expected again in a similar event. Further increasing the hazard to San Francisco is the estimation by the U.S. Geological Survey of a 67% probability of a magnitude 7 event in the San Francisco Bay Area in the next 30 years, driven primarily by the high likelihood of a large earthquake on the Hayward fault (note that downtown San Francisco is equidistant from the San Andreas and the Hayward faults, each about 10 miles distant).

The vulnerability of buried water supply pipe due to earthquake is of critical significance, both for post-earthquake fire as well as for continued potable water supply. This criticality was overwhelmingly demonstrated in the 1906 San Francisco and 1923 Tokyo earthquakes and ensuing fires. The 1989 Loma Prieta earthquake damage in the Marina, including a large fire[3], served as a reminder. Beyond the immediate post-earthquake fire problem, continued performance of underground potable water and sewer utilities is vital to urban recovery. Given these needs, the city of San Francisco determined that an examination of the potential performance of these utilities was necessary, and retained an engineering team consisting of: Harding Lawson Associates, Dames & Moore, Kennedy/Jenks/Chilton, and EQE International.

This paper reports on vulnerability measures of underground piping subjected to area-wide deformations, and the spectrum of mitigation measures developed as part of this project. Due to limitations of space, only two of the areas studied, the Marina and Sullivan Marsh areas, are discussed. In order to do this, we next describe the underground utility systems considered as part of this project, summarize our evaluation of utility damage, and review the mitigation options developed for the project.

UNDERGROUND UTILITY SYSTEMS

The project considered two water supply systems dedicated to firefighting: the truck-borne Portable Water Supply System (PWSS), and the underground Auxiliary Water Supply System (AWSS), as well as the potable Municipal Water Supply System (MWSS), and the sewer system.

AWSS The San Francisco AWSS is a water supply system intended solely for adequate water supply for firefighting. It is separate and redundant from the MWSS, and is owned and operated by the SFFD. It was built in the decade following the 1906 San Francisco earthquake and fire, primarily in the north-east quadrant of the city (Figure 1, the urbanized portion of San Francisco in 1906 and still the central business district), and has been

gradually extended into other parts of the city. The AWSS supplies water by a special pipe network with a total length of approximately 129 miles of cast iron and ductile iron pipe serving approximately 1,500 dedicated street large capacity hydrants. The pipe is bell and spigot, originally extra heavy cast iron (e.g., 1" wall thickness for 12" diameter), and extensions are now Schedule 56 ductile iron (e.g., .625" wall thickness for 12" diameter). Restraining rods connect pipe lengths across joints at all turns, tee joints, hills and other points of likely stress. The network as originally designed and constructed was divided into two independent sections, north and south of Market Street, increasing reliability should one section fail. In the 1906 earthquake, San Francisco had sustained major ground failures (leading to water main breaks) in zones generally corresponding to filled-in land and thus fairly well defined. Because it was anticipated these ground failures could occur again, these zones (termed "Infirm Areas") were mapped and the pipe network was specially valved where it entered these Infirm Areas.

PWSS Though the above-ground PWSS was not a subject of analysis in this study, a brief description would be valuable. While the AWSS (described above) provides high assurance of firefighting water supply in the northeast quadrant of San Francisco, major fires can and do occur at large distances from the AWSS pipe network. In recognition of this, and to provide additional flexibility in deployment and to further extend the "reach" of the AWSS, the SFFD has developed in recent years the PWSS. Its basic components are (i) hose tenders with large diameter hose, (ii) hose ramps, (iii) gated inlet wye, (iv) Gleeson valve, a pressure reducing valve, and (v) portable hydrants.

MWSS The San Francisco Water District provides domestic water to the City of San Francisco. Reservoirs serve 23 distinct zones, called pressure districts - only the University Mound District and College Hill District (Figure 2) intersect the study areas. MWSS piping is of diverse vintage, the newest being welded steel pipe; the oldest, cast iron pipe dating back to the late 1850's. In the study areas, the majority of mains are of cast iron segmented bell and spigot lead/oakum-jointed construction, installed in the three decades prior to the turn of the century. Larger, older pipe is of steel. Pre-1930 pipe larger than 24-inch diameter is of riveted steel construction. Longitudinal joints were shop riveted; circumferential joints were riveted in the field. Between about 1930 and 1960, pipe larger than 24-inch diameter was of welded steel construction. Gas welding was used until about 1940, after which arc welding became common. After about 1960, welded steel construction was also used for pipe as small as 20-inch diameter. Joints were bell and spigot, welded outside for 20-inch to 24-inch diameter, and welded inside and outside for 36-inch and larger diameters. Welding for 30 inch diameter mains varied -- sometimes inside and out, sometimes only outside.

The Marina currently contains approximately 40,000 feet of 6 inch to 12 inch diameter mains; 75% is of cast iron construction installed primarily in 1924 and 1925; 3% is of ductile iron with caulked joints, and the remaining 22% is of ductile iron installed primarily in 1990, following the 1989 earthquake.

Sullivan Marsh is estimated to contain approximately 62,300 feet of pipe, of which approximately 44,000 feet is 4 inch to 16 inch diameter cast iron and 13,000 feet of 4 inch to 16 inch ductile iron pipe. Perhaps 3/4 of all MWSS pipe in the study areas was installed between 1860 and 1900. Much of the remainder was installed in the 1930s, although every decade since 1900 saw installation of some length of pipe in the study areas.

Sewer City records indicate that sewers were first constructed in the 1870s in the Sullivan Marsh Study Area. Many of the existing sewers in the Sullivan Marsh area were constructed in the ten-year period following the 1906 earthquake, and many others were built during the 1930s. Records indicate that the sewers in the Marina District Study area were first constructed in the ten-year period preceding the 1915 Exposition.

Based on discussions with Clean Water Program personnel and a review of city records, it was concluded that most city sewers can be divided into the following seven categories:

1. Vitrified Clay Pipe, Old Style VCP - iron or salt glazed pipe with rigid (mortared) joints. This pipe was installed up until about 1945. It is generally very weak structurally. Also included in this category is VCP installed between 1945 and 1960 with rigid joints.

2. Vitrified Clay Pipe, Modern Style VCP - Installed since 1960. This pipe has good structural integrity and has polyethylene gaskets giving it joint flexibility.

3. Brick - This pipe is egg-shaped, with the egg standing on the small end. The predominant size is 3 feet wide by 5 feet high, with a 9-inch wall consisting of two courses of brick with mortared joints. Some are pile-supported.

4. Precast Concrete Pipe, Old Style - Installed between 1900 and 1920 with mortared rigid joints. It is usually less than 24 inches in diameter. This pipe apparently has a low cement content and is not very structurally sound. There is not a significant amount of this type of pipe in the study area.

5. Precast Concrete Pipe, New Style - Installed since 1960 with elastomeric joints. There is very little of this pipe in the study area.

6. Cast-in-Place Concrete Box Structures, Non-Pile-Supported - Includes both modern (excluding the transport system) and old installations.

7. Cast-in-Place Concrete Box Structures, Pile-Supported - Includes both modern (excluding the transport system) and old installations.

UTILITY BREAKS CAUSED BY 1906 AND 1989 EARTHQUAKES

Marina District

Behavior of Marina District soil and utilities in 1906 cannot be discussed, as the Marina District was created by land fill following the 1906 earthquake.

AWSS The AWSS was not structurally damaged in the Marina District during the 1989 Loma Prieta earthquake. Despite the survival of Marina AWSS mains and hydrants, damage elsewhere in the system caused the loss of water pressure in high pressure hydrants, rendering them useless for firefighting immediately after the earthquake.

MWSS Most of the damage sustained by the MWSS in the 1989 earthquake occurred within the Marina Study Area, where approximately 120 main and service breaks were attributed to the earthquake. Approximately two-thirds of these were main breaks. Damage was concentrated in the land filled after 1895. Outside of the Marina District, fewer than 40 breaks were attributed to the earthquake. Figure 2 shows the locations of main and service breaks within the Marina District.

It is worthwhile comparing the performance of AWSS and MWSS pipe breakage in the Marina District during the 1989 earthquake. While MWSS experienced approximately 80 main breaks, AWSS experienced none. This can be explained by comparing three factors of each system: quantity, strength, and location. MWSS is far more extensive than AWSS; approximately 5 times as much MWSS pipe exists in the Marina District as AWSS pipe. AWSS pipe is also stronger and lacks services, and could therefore be expected to experience fewer breaks per length of pipe than MWSS pipe experiencing similar ground deformation. Finally, AWSS pipe in the Marina District is mostly located outside of that region of the Marina District most strongly affected, whereas MWSS pipe exists under every Marina District street.

Sewer Extensive damage resulting from the 1989 Loma Prieta earthquake was incurred by sewers in the Marina District. Most of the damage was incurred by "Old Style VCP," but there was some damage to brick sewers. Considerable damage occurred at the connections between buried sewers and those on pile supports. Minor damage in the form of joint separation was noted for cast-in-place sewers. The Clean Water Program is replacing nearly 6,500 feet of sewers in the Marina at a cost of nearly $1,700,000. Figure 2 shows sewers that were damaged in the Marina in 1989. The criteria used by the City of San Francisco for sewer replacement in the Marina District was to replace the whole run if two or more repairs were required within a single sewer run between manholes, which is a very economical approach.

Sullivan Marsh Area

AWSS SFFD personnel indicate that in the 1989 Loma Prieta earthquake, a 6-inch by 18-inch window break occurred in the 12-inch main on 7th and Natoma streets, apparently caused by settlement of the AWSS onto a sewer line below. Northeast of Sullivan Marsh, a hydrant at Fremont and Mission streets struck by falling masonry from an adjacent building sustained a break at the buried elbow. Similar hydrant elbow breaks occurred at 6th and Bluxome streets, and at 5th Street between Harrison and Bryant streets. The former may have resulted from building collapse (Nielsen, 1991). The latter break has been attributed to settlement of the hydrant branch, which crossed over a pile-supported sewer which did not settle.

The break in the 7th Street main, combined with hydrant branch breaks in the South of Market Area, drained the lower zone within 30 minutes. Following identification and isolation of these breaks, the lower zone was fully pressurized within about four hours of the earthquake.

MWSS At the time of the 1906 earthquake, Spring Valley Water Company owned and operated San Francisco's water system. Three months after the earthquake, Hermann Schussler, SVWC's chief engineer, recorded over 23,000 service breaks and approximately 300 main breaks in MWSS pipe. Schussler considered the damage relatively light, attributing the system's good performance to the high standards he had imposed since the

1860s. He wrote, *"The breaks in the main pipes (considering our great length of distributing system of 441-1/2 miles) were comparatively few, and these were, in the large majority of cases, principally confined to and caused by the sudden sinking of the streets over the old swamps, which movement... tore the pipe over the swamp away from the pipe on terra firma."* (Schussler, 1906).

Approximately 50 of the 300 main breaks were located within the Sullivan Marsh area. These were especially concentrated in the sloping region bounded by Mission, Folsom, 8th and 6th streets, where extensive lateral spreading apparently took place. The record is probably incomplete; the 1906 earthquake reportedly overwhelmed Spring Valley Water's repair crews, and accurate records could not be kept during the months following the earthquake. Breaks discovered in the late summer and fall of 1906 may have gone unreported.

Sewer Initial inspection of the sewers near the Sullivan Marsh Study Area revealed less extensive damage than in the Marina District following the Loma Prieta earthquake. This disparity may be attributed to the smaller inventory of vulnerable rigid joint VCP pipe in Sullivan Marsh. Most of the damage was to this type of pipe, although a 215-foot-long brick sewer on Seventh Street between Mission and Minna streets was damaged just outside the Study Area on 9th Street between Harrison and Division streets. Approximately 900 feet of sewer was initially identified as requiring replacement at a cost of nearly $400,000. More recent TV inspection of sewers in Sullivan Marsh indicates that earthquake damage may have been more extensive than previously thought.

Reports of sewer damage following the 1906 Earthquake are sketchy. ASCE (1907) reports that in areas of significant ground deformation south of Market, sewers were completely destroyed.

EVALUATION OF UTILITY DAMAGE

Water Pipelines

A number of previous studies provide relevant data on the vulnerability of buried water pipelines in earthquakes[5,7]. For this study, past performance of San Francisco water systems in the 1906 and 1989 earthquake was analyzed to develop breakage estimates for AWSS and MWSS water pipe by relating movement (amount of vertical settlement and lateral spreading) and break rate (number of breaks per 1000 feet of pipe), based on pipe material and construction characteristics. Break rates were compared with relevant empirical data found in the literature. Mechanics of materials analyses for pipe damage were considered but not employed, since such analyses required detailed input of ground strain fields, which was beyond the scope of the geotechnical portion of this study.

Breakage in pre-1940 MWSS cast iron pipe was correlated with amount of ground movement. These relationships were then factored to produce damage functions for other classes of pipe. Damage resulting from interaction with other buried facilities was also estimated. Three modes of damage were identified: differential settlement, vertical settlement, and lateral spreading. Differential settlement was particularly associated with pile-supported sewers. Experience in the Loma Prieta Earthquake indicates that high relative settlements can be expected at sewers supported on piles. Pipes crossing over or through

these sewers are supported at the sewer and pushed down on either side by surrounding soil settlement. The consequent bending can fracture the pipe. Break rate functions were developed for each material, as a function of permanent ground displacement, shown in Figure 3.

Sewer

Initially, it was hypothesized that the pipe damage rate would show positive correlation with average ground strain, the rate of change of absolute permanent ground deformation. Microzone plots of strain versus damage rates, however, did not verify this. It is assumed, however, that higher damage rates would occur at ground movement interfaces, such as 4th Street and Brannan Street in Sullivan Marsh, as was experienced with water mains in 1906. Next, it was hypothesized that the pipe damage rate would correlate positively with absolute permanent ground deformation. The premise was that local ground strains were much higher than average strains. Local strains would correlate to absolute deformation. Pipe damage rates would then correlate to absolute deformation. The sewer repair and replacement map, Figure 2, was laid over the estimate ground settlement, for the Marina District. Total sewer lengths of repairs and replaced Old Style VCP were measured for each settlement range zone, and damage rates were calculated. A plot of these results is shown on Figure 4.

It is worthwhile to compare the resulting curve with information from another source to assess its validity. In Santa Cruz, the most extensive damage due to the 1989 Loma Prieta Earthquake occurred in liquefiable areas, particularly along the San Lorenzo River. The City of Santa Cruz televised 40,000 feet of sewer pipe in those high water pipe damage areas. Of that total, 5,000 feet were identified as needed to be replaced. Consideration is being given to replacing 10,000 feet to avoid replacing small sections of pipe. The resulting necessary replacement rate is 12.5 percent. Those replacements are plotted on Figure 4, showing similar repair rates to those encountered in the Marina District.

Valuation of Utility Breaks

Using the procedures discussed above, repair and replacement costs were estimated and are detailed in Tables 1 through 4. As a result of the breaks estimated in this study, it was estimated that both AWSS and MWSS (i.e., high and low pressure systems) would lose pressure in the Marina and Sullivan Marsh areas.

MITIGATION OPTIONS

For extended networks, such as San Francisco's water supply or sewer systems, options for the mitigation of earthquake damage or the enhancement of functional reliability can be broadly categorized into four approaches:

- **Geotechnical**, consisting of densification, improvement, replacement or other remediation of the soils,

- **Structural**, consisting of strengthening of the pipe or joints, or other improvements to the connections, such as introduction of special flexible connections, avoidance of contact with neighboring utilities, etc,

- **Systemic**, consisting of changes to the system layout, such as enhanced redundancy via additional piping, avoidance of poor soil areas, etc, and

- **Operational**, whereby the above approaches are not employed in advance of the earthquake but rather the potential for damage is recognized and emergency preparedness measures are put in place whereby system reconfiguration and/or immediate equipment and personnel deployment permit attainment of system functionality.

Each of the above approaches has costs and benefits, including differing levels of reliability and, in some cases, deferment of capital expenditures. In some cases, mitigation options may combine several of these approaches. This section presents a summary of options for reducing improving San Francisco utility performance following a major earthquake.

Water Systems

Table 5 summarizes the above mitigation options for the AWSS. The MWSS pressure district most at risk to liquefaction damage is University Mound. As shown in Figure 5, all University Mound Pressure District feeder mains pass through Mission Creek, Sullivan Marsh, and Embarcadero Study Areas in series. As a consequence, if all mains crossing result any one of these study areas were broken, no University Mound water could be delivered farther north in the pressure district. Though several parallel mains cross through each zone of high liquefaction potential, it is possible that widespread liquefaction in any one of these study areas could damage all feeder mains crossing through it. Each of these study areas, therefore, represent a choke point in the system. Three approaches can mitigate this hazard: (1) Plan to supply water to isolated regions from adjacent, undamaged pressure districts; (2) Reroute feeder mains around these regions of high liquefaction potential; or (3) Strengthen or otherwise reduce the vulnerability of feeder mains passing through regions of high liquefaction potential. Into this last class fall soil remediation, pipe replacement, addition of pipe flexibility, and hydrant replacement. Table 6 summarizes the above mitigation options for the MWSS.

Sewer

Operational Procedures In general, sewer pipelines will function to some extent, even though they have been damaged. Some sewers may collapse, causing overflows to the streets. The overflows will travel overland in the streets to the next available operating sewer. However, some ponding will occur due to damaged streets and gutters. Following an earthquake, there is an increased probability of toxic, flammable, and explosive chemical and gasses in sewers. Toxic chemicals may spill as a result of the earthquake and drain into the sewers, such as occurred in the EBMUD system in the Loma Prieta earthquake (according to personal communication with EBMUD staff). If there is blockage or partial blockage of sewers, sewage may become septic, releasing methane and hydrogen sulfide.

In view of these conditions, the following steps could be taken, many of which are normally a part of sewer operations.

a. Sufficient testing equipment should by available, staff should be trained in its use, and it should be used in all instances upon entering any sewer. Portable ventilation equipment and breathing apparatus should also be readily available.

b. Operations should not rely on reduction in sewage flow because of water system failure. Maintain an inventory or access to large capacity portable sewage pumps and hose to bypass collapsed sections of sewers. Maintain an inventory of sewer repair materials, including cement, sand, sand bags, and earth moving equipment.

c. Inventory all pump stations for overflows and add emergency overflows, if they do not currently exist, so that the overflow would be into a storm system or other water body.

Structural Modifications New vitrified clay pipe (VCP) sewers with polyethylene gaskets have performed well to the extent that deformation can be accommodated in the joint. Because of the brittle nature of the VCP, joint restraint of VCP is not feasible. Therefore, in liquefaction areas, where the deformation exceeds VCP capabilities, pipe systems with restrained joints should be considered. The ductile iron pipe systems with restrained joints, discussed for application to the AWSS and MWSS, would be applicable for sewers. The estimated construction costs for ductile iron pipe and VCP are similar, and since sewer corrosion has not been a problem in San Francisco, ductile iron pipe should serve well. Another pipe system alternative recommended for consideration is polyethylene (PE). PE is highly ductile and would move with almost any deformation expected in the liquefaction areas. It has been used extensively for slip-lining of both sewers and natural gas systems, and it has also worked well for sewage forcemains.

A long-term program to replace Old Style VCP and concrete pipe in liquefiable soil areas should be developed. Earthquake vulnerability should be one replacement criteria in the overall pipe replacement program, in addition to considering physical condition, grade, maintenance history, and infiltration factors. Slip-lining with polyethylene pipe should be considered as an alternative to pipeline replacement. Polyethylene sections can be extruded to match nonround cross sections such as the brick sewers, and result in negligible capacity loss. Flexibility should be provided to accommodate differential movement between pile-supported to non-pile-supported pipeline and conduit structures. For small and medium diameter pipelines, this can be accomplished using rubber bellows type, Dresser type, or combination ball joint/expansion sleeve flexible joints. Provide a minimum of two flexible joints in series with a design distance separating them to allow the required design differential movement.

Continue the design of sewage collection systems for grids in selected areas so that if one pipeline fails, sewage backs up and flows through an adjoining drainage basin, rather than onto city streets or into basements.

Rerouting Relocation or paralleling of key interceptors is typically not an alternative because of grade requirement.

CONCLUDING REMARKS

The foregoing summary presents a brief overview of a major study intended to identify critical earthquake-related failures of the water and sewer lifelines in a large city, due to large ground deformations. A number of key issues and research needs emerged from the study, including:

(i) current techniques for the estimation of large permanent ground deformation are geotechnically data-intensive, precluding use of available techniques and resulting in major approximations. Increasing use of GIS-based geotechnical databases may improve this situation.

(ii) current techniques for the estimation of pipe breaks due to large permanent ground deformation are only approximate in nature, with considerable uncertainty. Data collection is vitally needed, of both the pipe performance as well as the associated ground deformations.

(iii) selection of mitigation options is usually conducted within a cost-benefit framework - both aspects require additional work. That is, we found in this study that considerable uncertainty existed regarding the costs of repair, even though recent data was available from the 1989 Loma Prieta earthquake. The benefit aspect was not considered in this study (i.e., the benefits of reduced losses due to disrupted water and sewer service, such as the reduced losses due to fire following earthquake) - considerable data and methodological work is required before this can be cost-effectively incorporated in studies such as this.

(iv) San Francisco is about to acquire a Supervisory Control and Data Acquisition (SCADA) system for the MWSS - use of SCADA systems for rapid damage data collection and reconfiguration should be considered.

(v) the numerous pipe breaks, as well as many service breaks, will clearly lead to rapid loss of pressure at fire hydrants, exacerbating the fire following earthquake problem. Reliable techniques for rapid identification and isolation of damaged areas are needed.

The main finding of the study was that water supply was likely to be disrupted within areas of large permanent ground deformation, and that cost-effective mitigation for existing systems is extremely difficult. The most effective mitigation options for existing systems generally appeared to be those accepting widespread damage, but with plans and preparedness resources to cope with and quickly restore the loss of service. Mitigation of damage for new construction can be much more cost-effectively accomplished.

ACKNOWLEDGMENTS

The authors wish to express their gratitude to Professor Thomas O'Rourke of Cornell University for his consulting assistance. We also wish to thank the blue ribbon panel of experts, consisting of Professor James Mitchell of the University of California, Berkeley, Professor I.M. Idriss of the University of California, Davis, Mr. Maurice Power of Geomatrix Consultants, Mr. Frank Rollo of Treadwell Rollo and Associates, and Mr. Daniel Shapiro of SOHA.

REFERENCES

1. Darragh, R.D. et al, 1992, "Liquefaction Study Sullivan Marsh and Mission Creek, San Francisco CA", (this volume).

2. O'Rourke. T.D., T.E. Gowdy, H.E. Stewart, and J.W. Pease, 1990, "Lifeline Performance and Ground Deformation in the Marina During 1989 Loma Prieta Earthquake," Proceedings of the Third Japan-U.S. Workshop on Earthquake Resistant Design of Lifeline Facilities and Countermeasures for Soil Liquefaction, NCEER.

3. Scawthorn, C.R., T.D. O'Rourke, M.M. Khater, and F. Blackburn, 1990, "Loma Prieta Earthquake and the San Francisco AWSS: Analysis and Observed Performance", EQE Engineering.

4. Schussler, H., 1906, "The Water Supply of San Francisco, California, Before, During and After the Earthquake of April 18, 1906 and the Subsequent Conflagration," Spring Valley Water Company.

5. Eguchi, R. T., 1983a, "Seismic Risk and Decision Analysis of Lifeline Systems," Lifeline Earthquake Engineering: Performance, Design and Construction, Am. Soc. Civil Engrs., New York.

6. O'Rourke, T.D., Grigoriu, M. and Khater, M., 1985, Seismic Response of Buried Pipelines, *Pressure Vessel and Piping Technology 1985 - A Decade of Progress,* ed. by C. Sundararajan, Pressure Vessels and Piping Division, Am. Soc. Mech. Engrs., New York.

7. Porter, K.A., Scawthorn, C., Honegger, D.G., O'Rourke, T.D., and Blackburn, F., 1991, "Performance of Water Supply Pipelines in Liquefied Soil", Proc. 4th U.S.-Japan Workshop on Earthquake Disaster Prevention for Lifeline Systems, Los Angeles CA.

Table 1
MARINA BREAK AND DAMAGE ESTIMATE FOR WATER PIPES

Horizontal Ground Displacement Vertical Ground Displacement	6"-12" 6"-12"	3"-6" 3"-6"	0"-3" 0"-3"	Totals
Estimated Ground Displacement (in.)	10.8	5.4	1.8	
Pipe Lengths - Current (feet)				
CI Pre-1940	9,550	6,450	13,650	29,650
CI 1941-1960	0	0	0	0
DI 1961-1988	400	150	800	1,350
DI 1989-1991	4,850	2,500	1,100	8,450
RS/WS Pre-1940	0	0	0	0
WS 1941-1991	0	0	0	0
Total MWSS	14,800	9,100	15,550	39,450
AWSS	2,600	1,100	4,450	8,150
Breakage Estimate				
CI Pre-1940	32	20	15	66
CI 1941-1960	0	0	0	0
DI 1961-1988	0	0	0	1
DI 1989-1991	2	1	0	3
RS/WS Pre-1940	0	0	0	0
WS 1941-1991	0	0	0	0
Total MWSS	34	21	15	70
AWSS	4	2	2	8
Sewer Crossings				
MWSS	12	0	0	12
AWSS	3	0	0	3
Total Breaks				
MWSS	46	21	15	82
AWSS	7	2	2	11
Net Break Rate, Breaks/1000 lf				
MWSS	3.12	2.27	0.98	
AWSS	2.82	1.52	0.54	
Repair/Replace?				
MWSS	Replace	Replace	Repair	
AWSS	Repair	Repair	Repair	
Damage Cost, $1000				
MWSS	$4,400	$2,730	$87	$7,257
AWSS	$733	$167	$242	$1,142

Table 3
SULLIVAN MARSH BREAK AND DAMAGE ESTIMATE FOR WATER PIPES

Horizontal Ground Displacement Vertical Ground Displacement	<2' 2'-5'	6"-2' 1'-2'	<6" 6"-18"	<3" <3"	Totals
Estimated Ground Displacement (in.)	59.4	23.4	12.4	2.1	
Pipe Lengths - Current (feet)					
CI Pre-1940	9,300	4,050	21,500	6,900	41,750
CI 1941-1960	0	1,000	0	1,100	2,100
DI 1961-1988	2,550	1,550	5,300	1,750	11,150
DI 1989-1991	1,300	0	0	900	2,200
RS/WS Pre-1940	0	0	0	0	0
WS 1941-1991	1,600	850	850	1,800	5,100
Total MWSS	14,750	7,450	27,650	12,450	62,300
AWSS	5,600	2,700	14,250	4,450	
Breakage Estimate					
CI Pre-1940	55	16	73	9	153
CI 1941-1960	0	4	0	1	5
DI 1961-1988	4	2	5	1	12
DI 1989-1991	1	0	0	0	1
RS/WS Pre-1940	0	0	0	0	0
WS 1941-1991	1	0	0	0	1
Total MWSS	61	22	78	11	172
AWSS	17	5	24	3	49
Sewer Crossings					
MWSS	10	6	12	2	30
AWSS	8	3	23	1	35
Total Breaks					
MWSS	71	28	90	13	202
AWSS	25	8	47	4	84
Net Break Rate, Breaks/1000 lf					
MWSS	4.84	3.79	3.27	1.06	
AWSS	4.41	3.12	3.32	0.87	
Repair/Replace?					
MWSS	Replace	Replace	Replace	Repair	
AWSS	Repair	Repair	Repair	Repair	
Damage Cost, $1000					
MWSS	$4,425	$2,235	$8,295	$75	$15,030
AWSS	$2,471	$842	$4,735	$385	$8,433

Table 2
DAMAGE ESTIMATES FOR MARINA SEWERS

Ground Displacement and Pipe Type	Replacement Cost/Foot	Pipe Length (feet)	Percent Replacement	Replacement (feet)	Replacement Cost
Zone of Vertical Settlement - Less than 3"					
1.8 inch Displacement:					
VCP - Rigid Joints	$225	7,605	20%	1,521	$342,225
VCP - Elastomeric Joints	$225	2,385	11%	262	59,029
Brick	$700	360	11%	40	27,720
Concrete - Pile Supported	$1,720	333	7%	23	40,093
Concrete - No Pile Supports	$1,170	4,095	7%	287	335,381
TOTAL		14,778		2,133	$804,448
Zone of Vertical Settlement - 3" to 6"					
5.4 Inch Displacement:					
VCP - Rigid Joints	$225	5,436	48%	2,609	$587,088
VCP - Elastomeric Joints	$225	1,332	26%	346	77,922
Brick	$700	0	26%	0	0
Concrete - Pile Supported	$1,720	450	17%	77	131,580
Concrete - No Pile Supports	$1,170	1,665	17%	283	331,169
TOTAL		8,883		3,315	$1,127,759
Zone of Vertical Settlement - 6" to 12"					
10.8 Inch Displacement:					
VCP - Rigid Joints	$225	6,714	91%	6,110	$1,374,692
VCP - Elastomeric Joints	$225	3,843	47%	1,806	406,397
Brick	$700	0	47%	0	0
Concrete - Pile Supported	$1,720	1,260	31%	391	671,832
Concrete - No Pile Supports	$1,170	2,565	31%	795	930,326
TOTAL		14,382		9,102	$3,383,247
				TOTAL DAMAGE	$5,315,454
				SAY	$5,320,000

Table 4
DAMAGE ESTIMATES FOR SULLIVAN MARSH SEWERS

Ground Displacement and Pipe Type	Replacement Cost/Foot	Pipe Length (feet)	Percent Replacement	Replacement (feet)	Replacement Cost
Zone of Vertical Settlement - Less than 3"					
2 inch Displacement:					
VCP - Rigid Joints	$225	143	22%	31	$ 7,079
Brick	$700	1,881	12%	226	158,004
Concrete - Pile Supported	$1,720	1,111	7%	78	133,764
Concrete - No Pile Supports	$1,170	957	7%	67	78,378
TOTAL		4,092		402	$377,225
Zone of Vertical Settlement - 0.5' to 1.5'					
12 Inch Displacement:					
VCP - Rigid Joints	$225	4,917	100%	4,917	$1,106,325
Brick	$700	1,298	52%	675	472,472
Concrete - Pile Supported	$1,720	3,883	35%	1,359	2,337,566
Concrete - No Pile Supports	$1,170	1,518	35%	531	621,621
TOTAL		11,616		7,482	$4,537,984
Zone of Vertical Settlement - 1' to 2'					
24 Inch Displacement:					
VCP - Rigid Joints	$225	0	100%	0	$ 0
Brick	$700	1,705	100%	1,705	1,193,500
Concrete - Pile Supported	$1,720	594	67%	398	684,526
Concrete - No Pile Supports	$1,170	0	67%	0	0
TOTAL		2,299		2,103	$1,878,026
Zone of Vertical Settlement - 2' to 5'					
59 Inch Displacement:					
VCP - Rigid Joints	$225	1,430	100%	1,430	$ 321,750
Brick	$700	209	100%	209	146,300
Concrete - Pile Supported	$1,720	1,815	100%	1,815	3,121,800
Concrete - No Pile Supports	$1,170	1,100	100%	1,100	1,287,000
TOTAL		4,554		4,554	$4,876,850
				TOTAL DAMAGE	$11,670,085
				SAY	$11,670,000

Table 5

MITIGATION OPTIONS, AWSS

	Option	Cost ($ millions)
1	Flexible Joints at Mains Crossing Pile-Supported Sewer	$ 0.5 - 1*
2	Infirm Area Hydrant Foundation and Connection Improvement	0.2*
3	Subdivide Upper and Lower Zones North/South	0.3**
4	Replace Corroded Tie Rods	?
5	Increase Size of SFFD Portable Water Supply System	2**
6	Fireboat Supply of the AWSS	1**
7	Hardening of Fireboat Manifold Corridors	10**
8	Standing Order to Start Pumps Following Earthquake	-**
9	Designate a Water Supply Officer	-**
10	Automated AWSS Leak Detection and Isolation	2**
11	CI Main Replacement	17*
12	Installation of Flexible Joints at all Hydrant Branches	4*

Table 6

MITIGATION OPTIONS, MWSS

	Option	Cost ($ millions)*
1	Supply Water From Adjacent Pressure Districts	$ 0.1
2	Route University Mound Around Liquefaction Zones	6.7
3	Strengthen Mains in Zones of High Liquefaction Potential	30.0
4	Flexible Joints at Mains Crossing Pile-Supported Sewers	1.0

* Costs indicated for Marina and Sullivan Marsh study areas only
** Costs indicated would benefit all study areas

Figure 1
SAN FRANCISCO AWSS

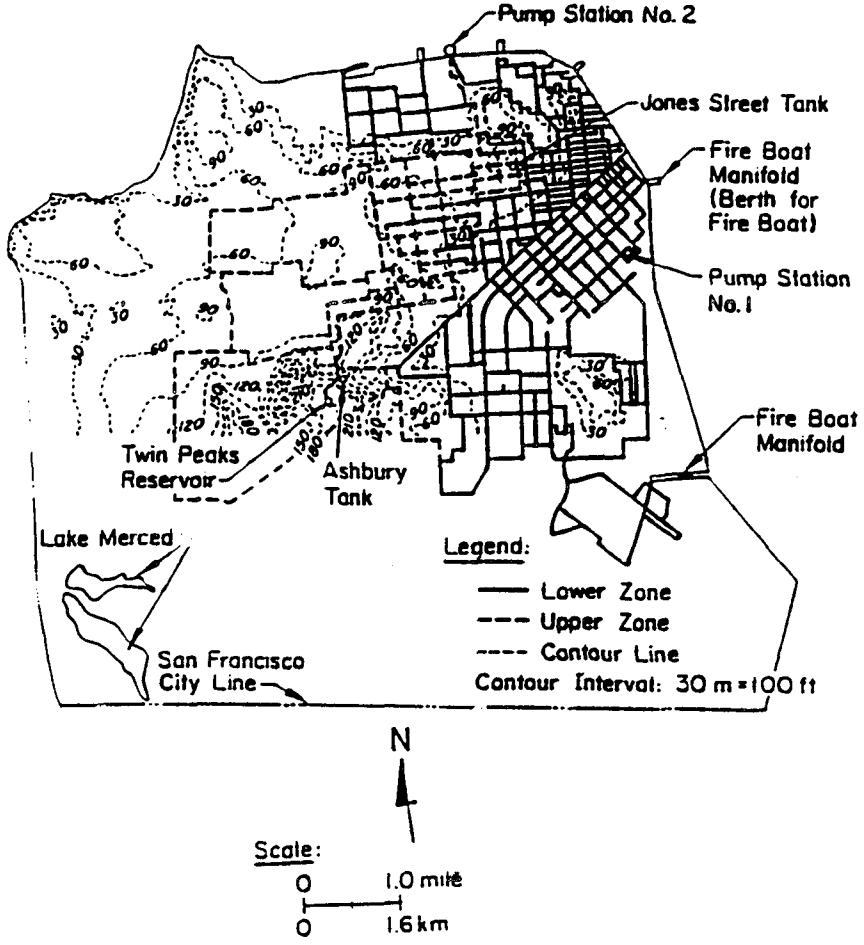

Figure 2
DAMAGED AND REPLACED SEWERS IN THE MARINA FOLLOWING LOMA PRIETA

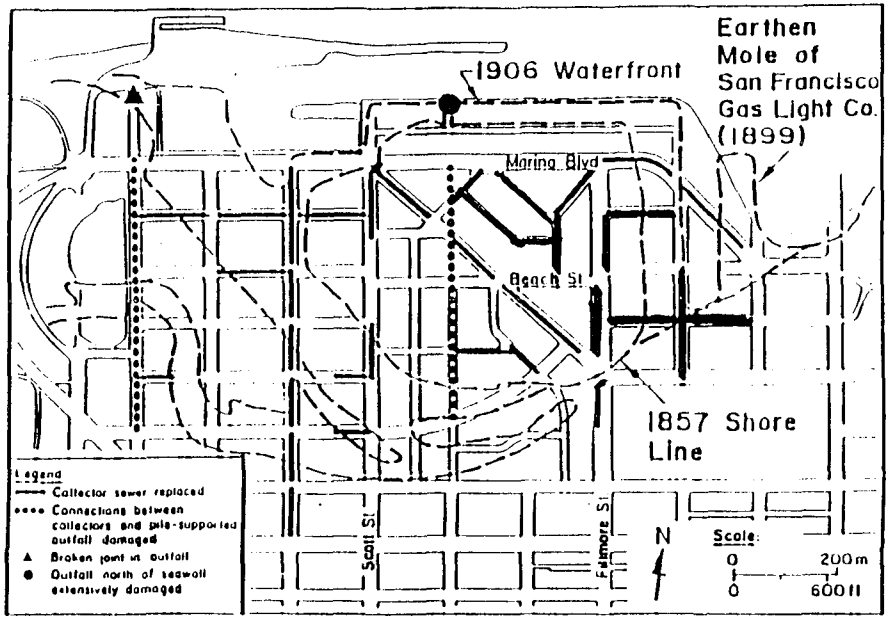

Figure 3
ESTIMATED UNDERGROUND PIPE DAMAGE FUNCTIONS

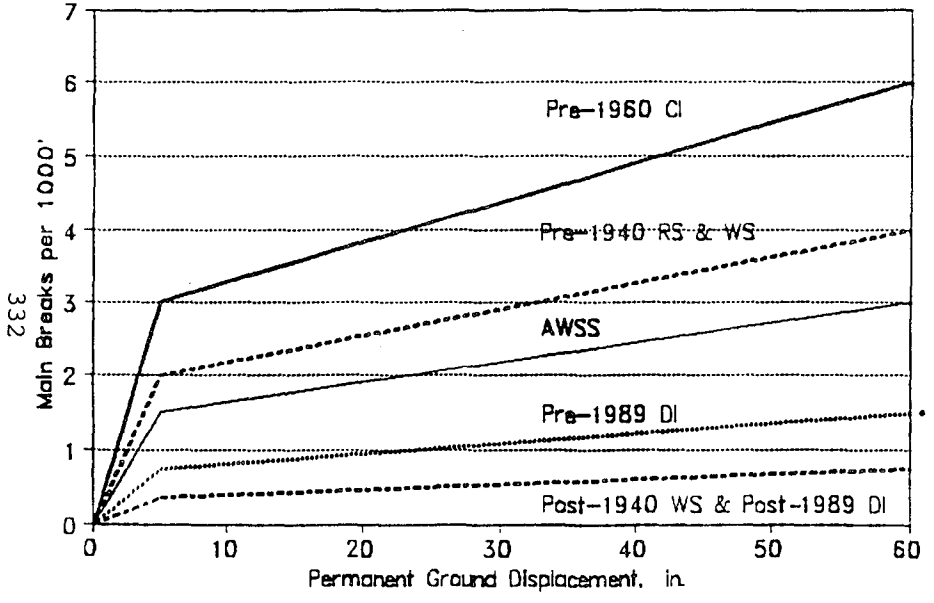

Figure 4
COMPARISON OF MARINA DISTRICT VCP DAMAGE WITH SANTA CRUZ

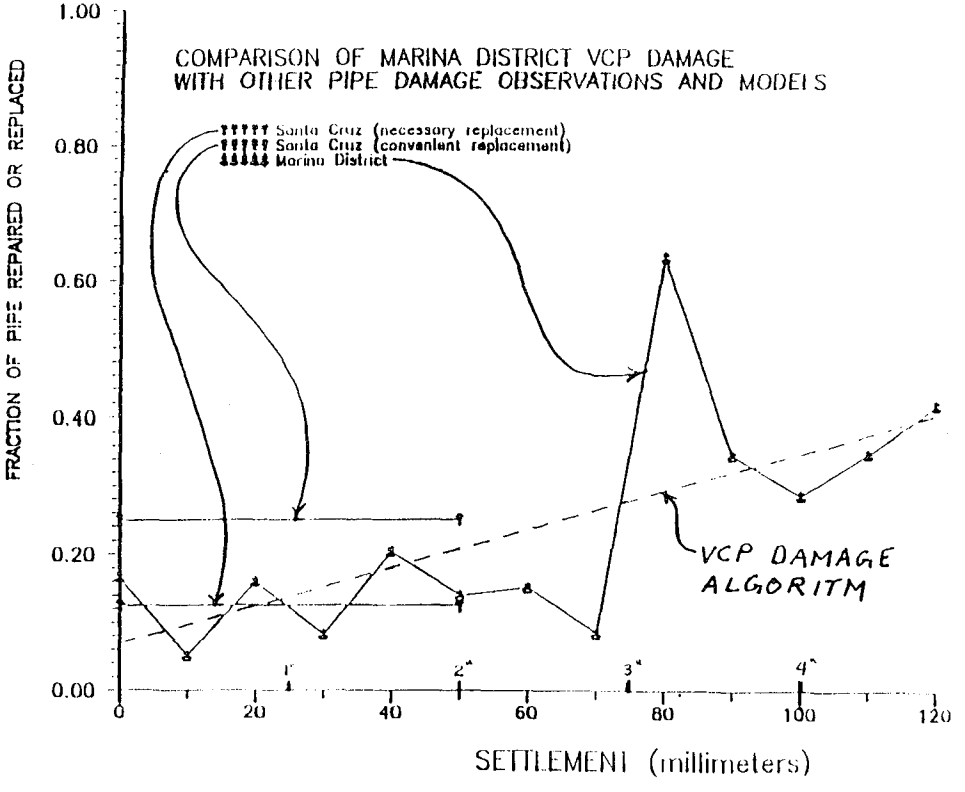

Figure 5
MWSS MITIGATION OPTION 2

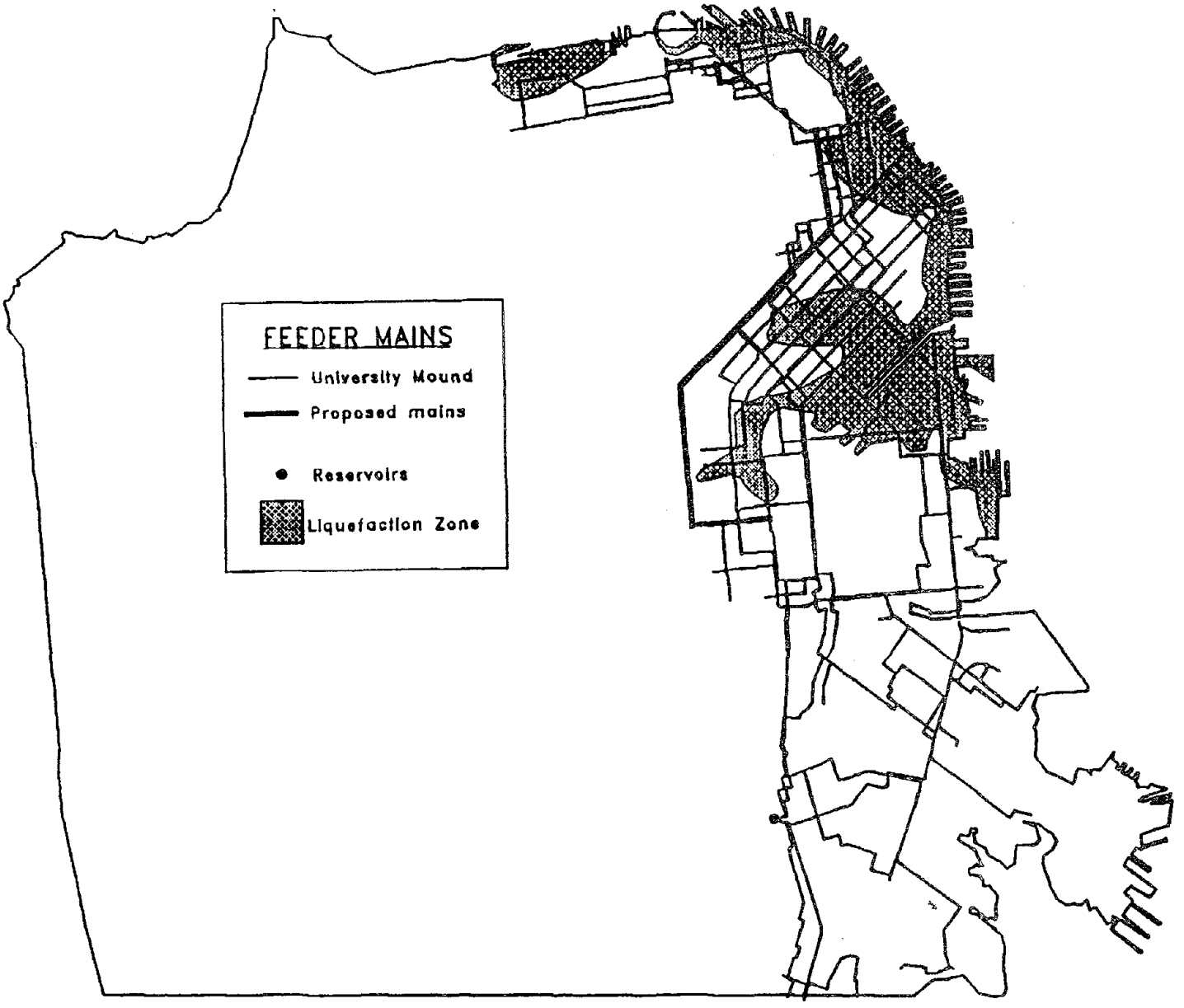

Prediction of Liquefaction-Induced Permanent Ground Displacements: A Three-Dimensional Approach

Rolando Orense
Department of Civil Engineering
University of Tokyo, Japan

Ikuo Towhata
Department of Civil Engineering
University of Tokyo, Japan

ABSTRACT

A three-dimensional model for predicting the pattern of ultimate permanent ground displacements induced by seismic liquefaction is presented. The method is based on the principle of minimum potential energy and the direct effect of seismic force on lateral displacement is removed from the analysis. In the application of the model, the ground surface area is subdivided into two-dimensional finite elements as seen from the sky. Lateral displacements are approximated by sinusoidal distributions along a vertical section and vertical displacements are calculated based on constant volume condition. The energy of each element is formulated and expressed in terms of the unknown nodal surface displacements. The total energy of the whole ground is minimized and Rayleigh-Ritz method is employed to obtain the solution. In the application of the model, surface irregularity and ground heterogeneity are considered while tensile behavior of sandy soil is eliminated. Analyses are made on both laboratory and actual field cases and the results obtained are in good agreement with the measured data.

INTRODUCTION

As observed from past earthquakes, liquefaction and the associated permanent ground displacements have caused significant damage to various civil engineering structures and lifeline networks. Clearly, engineering measures to control the effects of liquefaction at a site must include an evaluation of the susceptibility of the area to liquefaction and an assessment of the pattern of ground movement and soil failure resulting from liquefaction. Evaluation of liquefaction potential has progressed quite significantly during the past few years, and current research is now focused on liquefaction-induced permanent ground displacements.

Several techniques have been developed by various researchers to predict ground displacements induced by seismic liquefaction. Most of these methods employ non-linear stress-strain models which require complex soil properties as input parameters. However, considering the large extent of areas to be analyzed for mitigation purposes, such procedures are impractical, especially for three-dimensional problems. In view of this, an alternative procedure is required for a more economical solution to the problem.

Towhata et al. (1992) derived a closed-form solution to predict displacements in two-dimensional ground induced by liquefaction. In this model, the distribution of ground displacements was derived so that the potential energy of the ground would take minimum value.

This paper deals with the three-dimensional extension of the above model for predicting the magnitude and spatial distribution of ground displacements caused by liquefaction.

CHARACTERISTICS OF PERMANENT DISPLACEMENTS

Sasaki et al. (1992) conducted shaking table tests and reviewed field experiences during past earthquakes to study the nature of permanent displacements of ground caused by seismic liquefaction. Their observations are summarized as follows:

1. Many tension cracks are detected near the top of liquefied slopes in the field after movement. They are oriented normal to the direction of ground displacement.

2. The permanent displacement is oriented in the downward direction of a slope, suggesting the influence of gravity.

3. Displacements at the top of the slope are greater than those at the foot of the slope.

4. As for the vertical movement, subsidence is predominant near the top of a slope, while heaving is the case in the lower portion. However, the magnitude of the vertical displacement is much smaller that that of the horizontal one.

5. Liquefied ground behaves very similar to liquid; hence, its movement is highly affected by the total head gradient which is defined in terms of the total overburden stress and the elevation heads.

6. The magnitude of the lateral displacement in a liquefied sandy layer is minimum at the base and increases towards the surface.

7. There is no slip between the unsaturated surface layer and the liquefied subsoil.

8. Permanent displacement is caused by the gravity force; cyclic acceleration influences the movement only indirectly.

9. The soil movement depends not only on the slope and stratification local to the point of concern but on the overall topography of the study area.

Based on the above observations, it can be concluded that liquefaction-induced ground displacements depend on geological and topographical conditions. Seismic loads affect displacements only indirectly by triggering liquefaction and in determining the extent of liquefaction. This is reasonable, since shear wave, which causes horizontal displacements, hardly propagate through liquefied layer when the liquefied subsoil behaves as liquid.

Thus, in the formulation of the model, the effect of earthquake motion is removed from the analysis. With the idea that the principle of minimum potential energy governs the motion of the liquefied ground, a static approach to the problem is attempted. It should be noted that the present model is concerned with the maximum possible displacement that would occur when the state of soil liquefaction continues for a sufficiently long period of time. Hence, transient displacement is beyond the scope.

DESCRIPTION OF THE MODEL

In the application of the model, the ground surface area is subdivided into several two-dimensional finite elements as seen from the top; see Fig. 1(a). A typical finite element employed in the model is presented in Fig. 1(b). Each element consists of the following layers in z-direction: (1) an unliquefiable base, with elevation B; (2) a liquefiable layer with thickness H; (3) a surface unsaturated layer with thickness T; and (4) the surcharge, P, which includes the weight of the surface layer and any additional loading. The ground configuration varies linearly with the x and y coordinates, i.e.,

$$\begin{aligned} B &= B_o + a_1 x + b_1 y \qquad & H &= H_o + a_2 x + b_2 y \\ T &= T_o + a_3 x + b_3 y \qquad & P &= P_o + a_4 x + b_4 y \end{aligned} \tag{1}$$

The constants B_o, a_1, b_1, H_o, ... , a_4, b_4 can be determined from the known elevations at the nodal points.

From observation (6), the lateral displacement in a vertical cross section of a liquefied ground is maximum at the top and zero at the bottom. Thus, at any point (x, y, z) in the liquefied layer, the lateral displacements in the directions of x- and y-axes (denoted by u and v, respectively), are approximated by sinusoidal distributions in z-direction:

$$\begin{aligned} u(x,y,z) &= F(x,y) \sin \frac{\pi[z - (B_o + a_1 x + b_1 y)]}{2(H_o + a_2 x + b_2 y)} \\ v(x,y,z) &= J(x,y) \sin \frac{\pi[z - (B_o + a_1 x + b_1 y)]}{2(H_o + a_2 x + b_2 y)} \end{aligned} \tag{2}$$

In addition, observation (7) implies that the functions $F(x,y)$ and $J(x,y)$ actually represent the displacements at the ground surface ($z = B + H$).

The surface unsaturated layer behaves like an elastic plate which resists against the lateral flow of the slope. It has an elastic modulus E and Poisson's ratio ν and is subjected to in-plane stresses. On the other hand, the stress-strain ($\tau - \gamma$) relation of the liquefiable portion is modeled by

$$\tau = G\gamma + \tau_r \tag{3}$$

where G is the shear modulus and τ_r is the residual strength. Note that this relation combines both linear-elastic and rigid-plastic behaviors; this is adopted for analytical convenience.

The vertical displacement $w(x,y,z)$ at any point is related to the lateral displacements $u(x,y,z)$ and $v(x,y,z)$ by the equation

$$\frac{\partial u}{\partial x} + \frac{\partial v}{\partial y} + \frac{\partial w}{\partial z} = 0 \tag{4}$$

Note that since constant-volume condition is assumed, the settlement resulting from consolidation is excluded and should be considered separately. Upon substitution of Eqtns. (2) into Eqtn. (4), the vertical displacement is expressed in terms of $F(x,y)$ and $J(x,y)$ as follows:

$$\begin{aligned} w(x,y,z) &= -\frac{2}{\pi}\left[H\left(\frac{\partial F}{\partial x} + \frac{\partial J}{\partial y}\right) + a_2 F + b_2 J\right]\left[1 - \cos\frac{\pi(z-B)}{2H}\right] \\ &\quad + \sin\frac{\pi(z-B)}{2H}\left[(a_1 F + b_1 J) + (a_2 F + b_2 J)\frac{(z-B)}{H}\right] \end{aligned} \tag{5}$$

At $z = B + H$, the vertical displacement at the surface of the liquefied layer is given by

$$w(x,y)|_{z=B+H} = -\frac{2}{\pi}\left[H\left(\frac{\partial F}{\partial x} + \frac{\partial J}{\partial y}\right) + a_2 F + b_2 J\right] + (a_1 + a_2)F + (b_1 + b_2)J \tag{6}$$

Since there is no slip between the surface layer and the liquefied subsoil, the above equation also represents the vertical displacement of the ground surface. In addition, the change in the surface elevation, δH, at a given location (x,y) due to the lateral soil flow is derived from the difference of the flux of ground movement as shown in Fig. 2 and is given by

$$\delta H = \frac{2}{\pi}\left[H\left(\frac{\partial F}{\partial x} + \frac{\partial J}{\partial z}\right) + a_2 F + b_2 J\right] \tag{7}$$

The present model is based on the principle of minimum potential energy, which states that among all admissible displacements u, v, and w which satisfy the prescribed boundary conditions, the actual displacements make the total potential energy an absolute minimum. Thus, the potential energy of the ground is formulated and then minimized to obtain the desired displacements.

ENERGY CONSIDERATION

The energy of each ground element is formulated by considering the strain and gravity components of the liquefied and surface unsaturated layers. The unliquefied base is stable and is not involved in the flow. In the calculation of the strain energy, only the predominant components of the strain tensor are taken into account. Hence, for the liquefied layer, only the shear strains associated with $\partial u/\partial z$ and $\partial v/\partial z$ are considered as the contributions of the other strain components are negligible (Towhata et al., 1992). For the surface layer, the strain energy is calculated from plane stress condition. Thus, the total energy consists of the following:

1. Strain energy in the liquefied layer

$$E_1 = \int_B^{B+H} \left\{ \frac{G}{2} \left[\left(\frac{\partial u}{\partial z} \right)^2 + \left(\frac{\partial v}{\partial z} \right)^2 \right] + \tau_r \left[\frac{\partial u}{\partial z} + \frac{\partial v}{\partial z} \right] \right\} dz \tag{8}$$

2. Potential energy increment of the liquefied layer

$$E_2 = \frac{\gamma_l}{2} \left[(B + H + \delta H)^2 - (B + H)^2 \right] \tag{9}$$

3. Strain energy in the surface unsaturated layer

$$E_3 = \frac{ET}{2(1-\nu^2)} \left[\left(\frac{\partial F}{\partial x} \right)^2 + \left(\frac{\partial J}{\partial y} \right)^2 + 2\nu \left(\frac{\partial F}{\partial x} \frac{\partial J}{\partial y} \right) + \frac{1-\nu}{2} \left(\frac{\partial F}{\partial y} + \frac{\partial J}{\partial x} \right)^2 \right] \tag{10}$$

4. Potential energy increment of the surcharge

$$E_4 = -P \times w|_{z=B+H} \tag{11}$$

Eqtns. (8) $\sim$ (11) represent the energy components for a soil column located at coordinate (x, y). To get the total energy of the element, the equations should be integrated throughout the area of the element.

In Eqtn. (9), the energy is formulated with the assumption that the liquefied soil (with unit weight denoted by γ_l) behaves as liquid and remains in the space bounded by the boundary of the element. However, since liquefied soil can flow beyond this boundary, a correction is required to take into account the increment in the potential energy of the displaced volume of soil. This is given by

$$E_{b1} = \int_S \int_B^{B+H} (\gamma_l \times \delta_n \times z)\, dz\, dS \tag{12}$$

where δ_n is the component of the lateral displacement at any point normal to the element boundary and S is the perimeter of the element.

Based on observation (1), tension cracks can occur near the top of liquefied slopes. The presence of such cracks are incorporated by assuming that a cracked boundary is filled with sand-water mixture which exerts hydrostatic pressure on the side of the element. This energy contribution is given by

$$E_{b2} = \int_L \int_B^{B+H} \{[P + \gamma_l(B + H - z)] \times \delta_n\}\, dz\, dL \tag{13}$$

where the quantity inside the bracket is the hydrostatic pressure distribution, and L is the length of the appropriate side (cracked boundary) of the element.

It should be mentioned at this point that in the evaluation of the functions E_{b1} and E_{b2}, the integrands are positive if the boundary of the element is oriented such that the potential energy is increased; otherwise, the integrands are negative.

Therefore, the total energy in each element, represented by the functional Π, is given by

$$\Pi = \int_{Area} (E_1 + E_2 + E_3 + E_4)\, dxdy + E_{b1} + E_{b2} \tag{14}$$

From the above equations, it can be seen that Π is a function of the unknown surface displacements $F(x, y)$ and $J(x, y)$, their first-order derivatives, and the coordinates x and y. Thus, the problem is, in effect, reduced to a two-dimensional one involving only the surface lateral displacements. These unknown displacements can be calculated by applying variational principle on the the functional Π. Due to the complicated nature of the expressions involved, a closed-form solution is not attempted; instead, a two-dimensional (x, y) finite element-based formulation is employed.

FINITE ELEMENT FORMULATION

In the finite element formulation, Rayleigh-Ritz method is employed by representing the surface displacements within an element by the linear interpolating functions

$$\begin{aligned} F(x, y) &= \alpha_1 + \alpha_2 x + \alpha_3 y \\ J(x, y) &= \beta_1 + \beta_2 x + \beta_3 y \end{aligned} \tag{15}$$

The above interpolating function, which implies constant strain condition within the element, can be rewritten in the form

$$\begin{aligned} F(x,y) &= N_1F_1 + N_2F_2 + N_3F_3 \\ J(x,y) &= N_1J_1 + N_2J_2 + N_3J_3 \end{aligned} \tag{16}$$

where N_1, N_2 and N_3 are the shape functions which are expressed in terms of the coordinates x and y, while $F_1, \ldots, J_3$ are the unknown displacements at the nodes of the element.

Eqtn. (16) is then substituted into the energy functional Π. The total energy of the whole system, which is equal to the sum of the energy of each element, is minimized by taking its variation with respect to the unknown nodal displacements F_i and J_i and setting it to zero, i.e.,

$$\delta \sum_{k=1}^{m} \Pi_k = \sum_{k=1}^{m} \frac{\partial \Pi_k}{\partial F_i}\delta F_i + \frac{\partial \Pi_k}{\partial J_i}\delta J_i = 0 \tag{17}$$

where i=1 to n, n=number of nodal points, while k=1 to m, m=number of elements. The above equation can be solved by setting

$$\frac{\partial \Pi_k}{\partial F_i} = 0 \quad \text{and} \quad \frac{\partial \Pi_k}{\partial J_i} = 0 \tag{18}$$

Eqtns. (18) represent $2n$ equations and, by rearranging these set of equations, they can be written in a more familiar form

$$\{\mathbf{P}\} = [\mathbf{K}]\{\mathbf{U}\} \tag{19}$$

where $[\mathbf{K}]$ is the stiffness matrix and $\{\mathbf{P}\}$ is the equivalent load vector. Thus, the equation becomes a typical finite element problem where the displacement vector $\{\mathbf{U}\}$ is required.

In the application of the method, two boundary conditions are considered. Fixed ends correspond to boundaries where liquefaction does not occur or where displacements are negligibly small (usually at the bottom of slopes). On the other hand, cracks occurring on top of slopes are modeled as free boundaries, where Eqtn. (13) is applicable.

It should be noted that tensile stresses may develop in the surface unsaturated layer as a result of lateral movement of the ground. Since sandy soil cannot sustain tensile stresses, special consideration is needed in order to exclude the tensile behavior. In this model, the familiar "no tension" approach commonly used in general finite element analysis is employed.

The stresses which developed due to subsoil liquefaction as calculated from the above analysis are added to the average static stress in the surface soil given by

$$S_o = 1/2\, K_o \gamma_s t \tag{20}$$

where K_o is the coefficient of earth pressure at rest (assumed to be equal to 0.5 in this study), γ_s is the unit weight of the soil and t is the average thickness of the surface layer. This total stress represents the actual state of stress in the surface layer during the liquefaction of the subsoil.

Elements which show tensile principal stresses are picked out and elastic moduli in the direction indicated by the tension are reduced to one percent of the initial value. The original problem is then re-analyzed on the basis of the new, now anisotropic properties until "no-tension" state is reached. To avoid unnecessarily large number of iterations, the computation is terminated when the percentage difference in the nodal displacements obtained in two successive iterations is less than ten percent.

EXAMPLE CALCULATIONS

To examine the capability of the proposed method, it is used to simulate the ground displacements observed in shaking table tests conducted at the Public Works Research Institute (PWRI) and those measured in Noshiro City during the 1983 Nihonkai-Chubu earthquake. Due to the complexity involved in determining the soil parameters for case history studies, the present study makes use of a common set of soil properties for each analysis. The values employed are shown in Table 1. In addition, the liquefied soil is assumed to behave like liquid, as indicated by observation (5); thus, $G = 0$ and $\tau_r = 0$. For the surface unsaturated layer, $\nu = 0.30$ is used.

Shaking Table Tests

A series of large scale shaking table tests on model soil deposits were conducted at PWRI (Sasaki et al., 1991) to study the mechanism of lateral ground flow induced by soil liquefaction during earthquakes. The proposed method is used to simulate the displacements observed in two of the tests in the series.

In the first case (Model 6), a gently sloped gravel surcharge was placed over one half the length of the loose saturated deposit, as shown in Fig. 3(a). The width of the box was 0.8 m. Shaking was then applied in four stages with the acceleration increasing in each subsequent stage.

The resulting cumulative lateral deformation of the ground surface after each step is shown in Fig. 3(b), where it can be seen that the displacements are largest at the middle of the slope. Also plotted in the same figure are the calculated permanent surface displacements using the proposed method. In the calculation, the ends of the test box are assumed as fixed boundaries. It can be seen that the calculated displacements agree well with the observed values.

In the second case (Model 8), a semi-circular liquefiable deposit of 2 m in radius and 0.25 m in height was overlain by a cone-shaped gravel embankment with radius of 1 m and a height of 0.15 m at the center. This model ground was shaken in the longitudinal direction in three stages to determine the effect of the direction of excitation on the lateral movement. Fig. 4(a) shows the direction of ground flow after the first two stages. From this figure, it is

noted that the surface of the semi cone-shaped embankment and the neighboring horizontal ground seem to move almost radially, i.e., in the direction of slope.

Fig. 4(b), on the other hand, illustrates the spatial distribution of the ground displacement obtained by the proposed model. Although the calculated maximum displacement of 3.2 cm exceeds the maximum observed value of 2.7 cm, comparison of the two figures reveals that the calculated distribution conforms with those obtained from the shaking table test and the ground displacements occurred in the radial directions.

Noshiro City

Studies conducted by Hamada et al. (1986) reveal that permanent lateral displacements in the order of several meters occurred in Noshiro City after it was hit by an earthquake of magnitude 7.7. Fig. 5 shows the permanent displacements in the southern part of the city as measured from aerial photographs taken before and after the earthquake. It can be seen from the figure that the displacements are larger at high elevations while negligibly small at low places, and that the displacement vectors are directed downslope around the hilltop. These phenomena are indicated in observations (3) and (2), respectively.

The proposed method is employed to simulate the observed displacements. The top of the hill, being surrounded by cracks, is replaced by a hollow space in the finite element model, and the cracks are treated as free boundaries. Another free end is located in the north boundary of the element mesh along Highway Route No. 7, where cracks were also detected. On the other hand, fixed boundaries are assumed on lowland areas where the non-occurrence of liquefaction was observed.

The calculated ground displacements are shown in Fig. 6. The maximum predicted displacement as seen in the north slope of the hill is 6.4 m, which is larger than the measured value of 5 m. Although the analysis slightly overestimates, the method shows good agreement with the measured data. Moreover, the spatial distributions are also consistent with those observed, i.e., displacements are large at high elevations and small at low elevations.

Since the liquefied soil is assumed to behave like liquid with zero residual strength, the calculated displacements can be considered as the upper-bound solutions, i.e., these displacements are the maximum possible displacements that would occur if soil liquefaction continues for a sufficient period of time.

It is noted that the proposed method, being static in nature, does not require complicated soil properties as input data. Information on topography, location of liquefied layer, unit weight of the soil, and the elastic properties of the surface unsaturated layer are the only required parameters. The heterogeneity of the ground can be considered by allowing different values of soil properties to various elements, if necessary. Surface irregularity can be taken into account by varying the thickness of the appropriate layers. Furthermore, since the liquefiable layer and surface unsaturated layer are assumed as elastic material and liquid, respectively, the computation is relatively straight forward and is not time consuming. For example, the analysis of Noshiro City, wherein the area was divided into 314 finite elements, took only 6 minutes of CPU time per iteration in an ordinary personal computer.

CONCLUSION

A numerical procedure based on the principle of minimum potential energy is developed to predict the magnitude and spatial distribution of the ultimate ground displacements induced by liquefaction. By subdividing the study area into several finite elements and assuming sinusoidal distributions of lateral displacements of liquefied soil, the three-dimensional problem is reduced to effectively two-dimensional one. The unknown displacements are easily calculated by employing Rayleigh-Ritz method.

Inspite of its simplicity, the example calculations made on both experimental and field conditions proved the validity of the model. Hence, the proposed method can serve as a practical and economical tool to predict the potential seismic hazards to urban facilities and lifeline networks induced by the lateral flow of liquefied soil.

ACKNOWLEDGMENT

The authors would like to thank Dr. Yasushi Sasaki of PWRI for the information and data used in the present study. The financial support provided by the Ministry of Education, Science and Culture (Monbusho) is gratefully acknowledged.

REFERENCES

Hamada, M., Yasuda, S., Isoyama, R. and Emoto, K. 1986. *Study on Liquefaction-Induced Permanent Ground Displacements.* Report of Association for the Development of Earthquake Prediction, Tokyo.

Sasaki, Y., Tokida, K., Matsumoto, H. and Saya S. 1991. Experimental Study on Lateral Flow of Ground due to Soil Liquefaction, *Proceedings, Second International Conference on Recent Advances in Geotechnical Earthquake Engineering and Soil Dynamics.* St. Louis.

Sasaki, Y., Towhata, I., Tokida, K., Yamada, K., Matsumoto, H., Tamari, Y., and Saya, S. 1992. Mechanism of Permanent Displacement of Ground Caused by Seismic Liquefaction, *Soils and Foundations* (accepted for publication).

Towhata, I., Sasaki, Y., Tokida, K., Matsumoto, H., Tamari, Y., and Yamada, K. 1992. Prediction of Permanent Displacement of Liquefied Ground by Means of Minimum Energy Principle, *Soils and Foundations* (accepted for publication).

SOIL PARAMETER	MODEL 6	MODEL 8	NOSHIRO CITY
Modulus of Elasticity E (kN/m^2)	98	294	10780
Unit Weight of Surface Layer γ_s (kN/m^3)	14.5	13.3	15.7
Unit Weight of Liquefied Layer γ_l (kN/m^3)	19.6	18.0	17.6

Table 1: Soil parameters used in the analyses

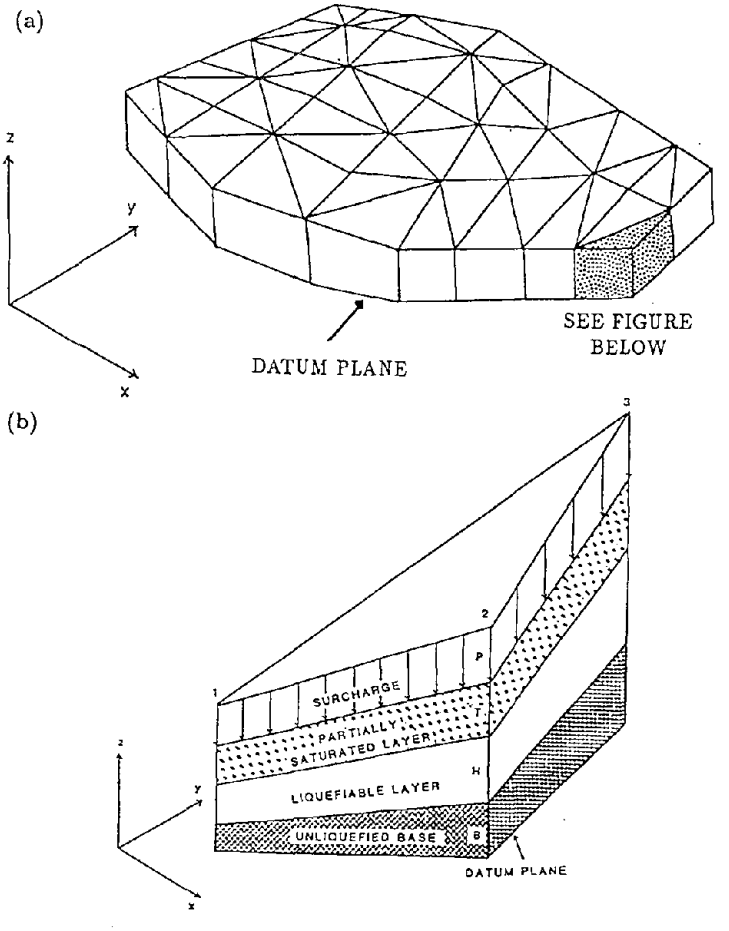

Figure 1: (a) Finite element mesh; (b) A finite element of the model ground

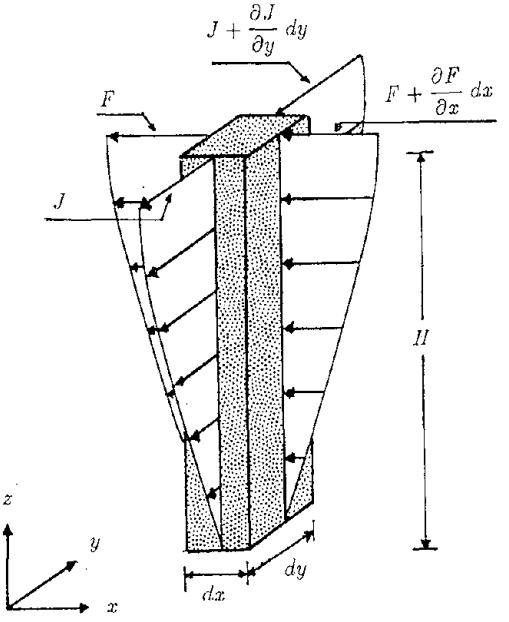

$$\delta H(dxdy) = \mathrm{Vol}_{in} - \mathrm{Vol}_{out}$$

Figure 2: Volume flux in a column of liquefied soil

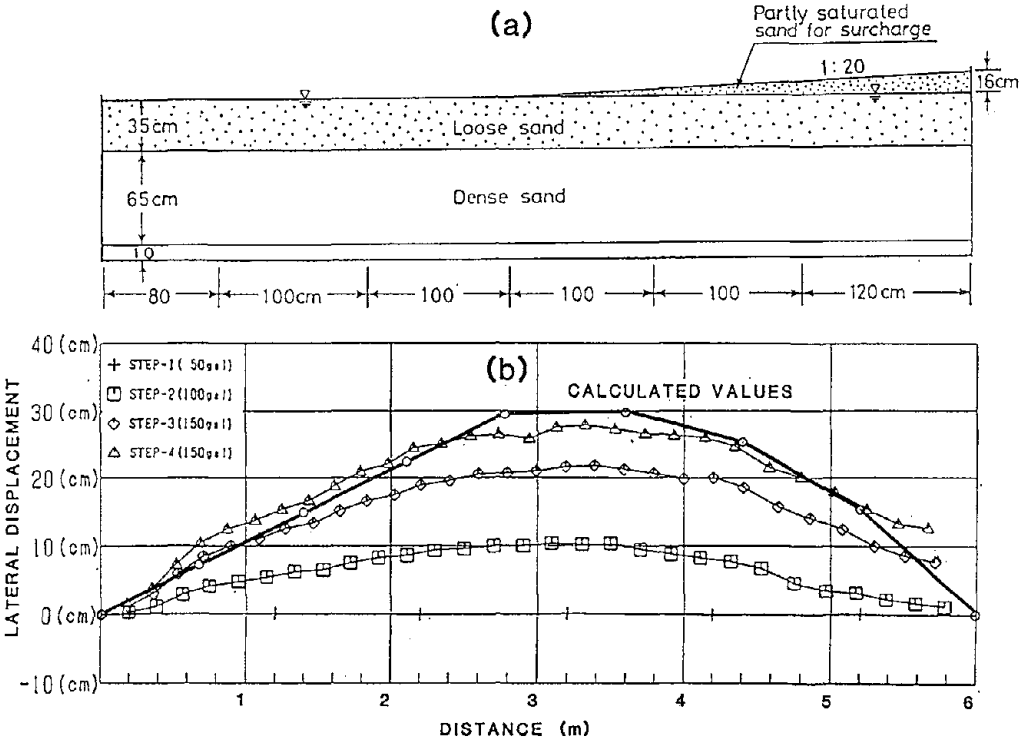

Figure 3: Model 6 Test of PWRI: (a) Ground model; (b) Observed and calculated permanent ground displacements (From Sasaki et al., 1991)

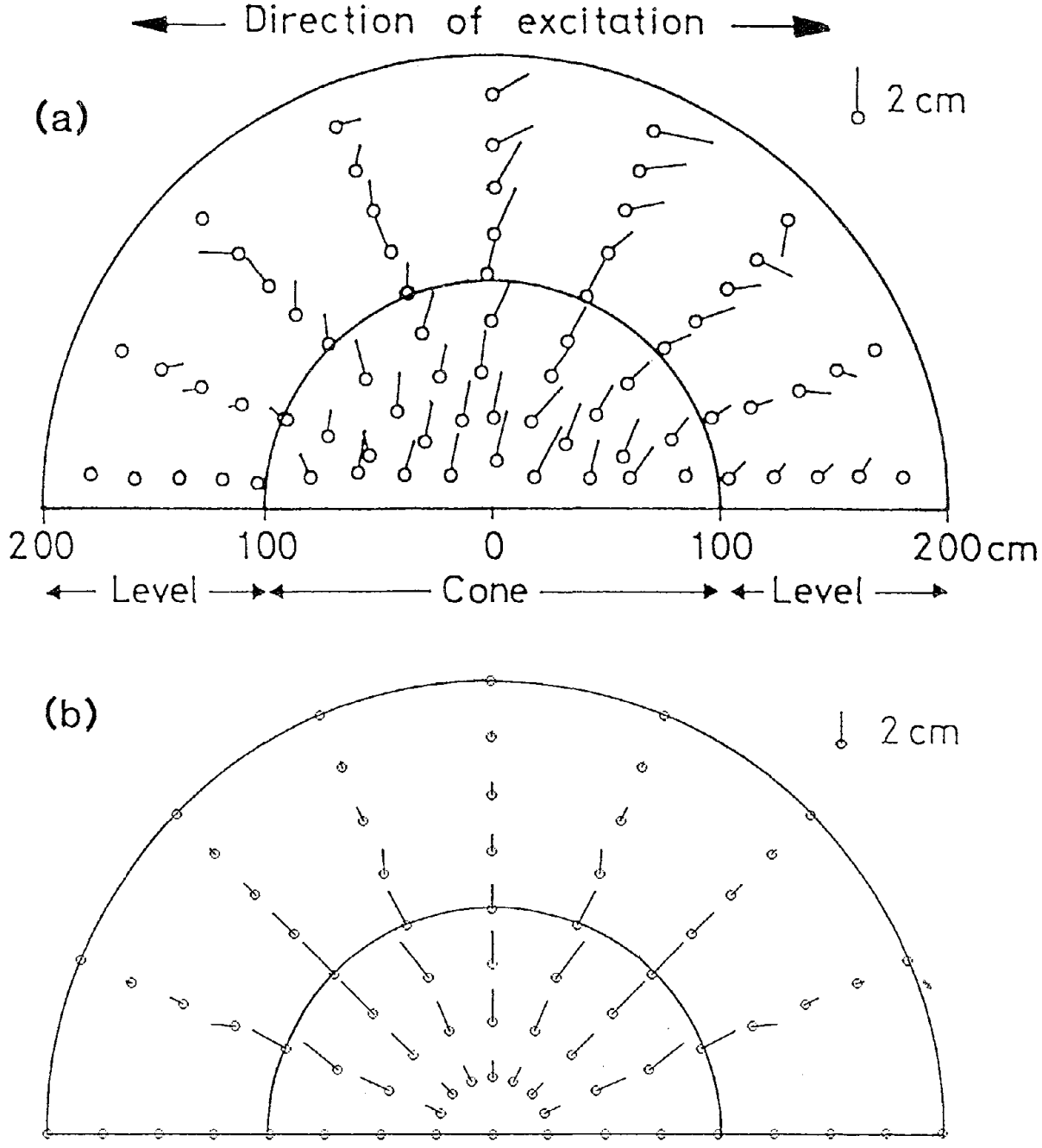

Figure 4: Model 8 Test Results of PWRI: (a) Observed direction of ground flow (From Sasaki et al., 1991); (b) Calculated permanent ground displacements

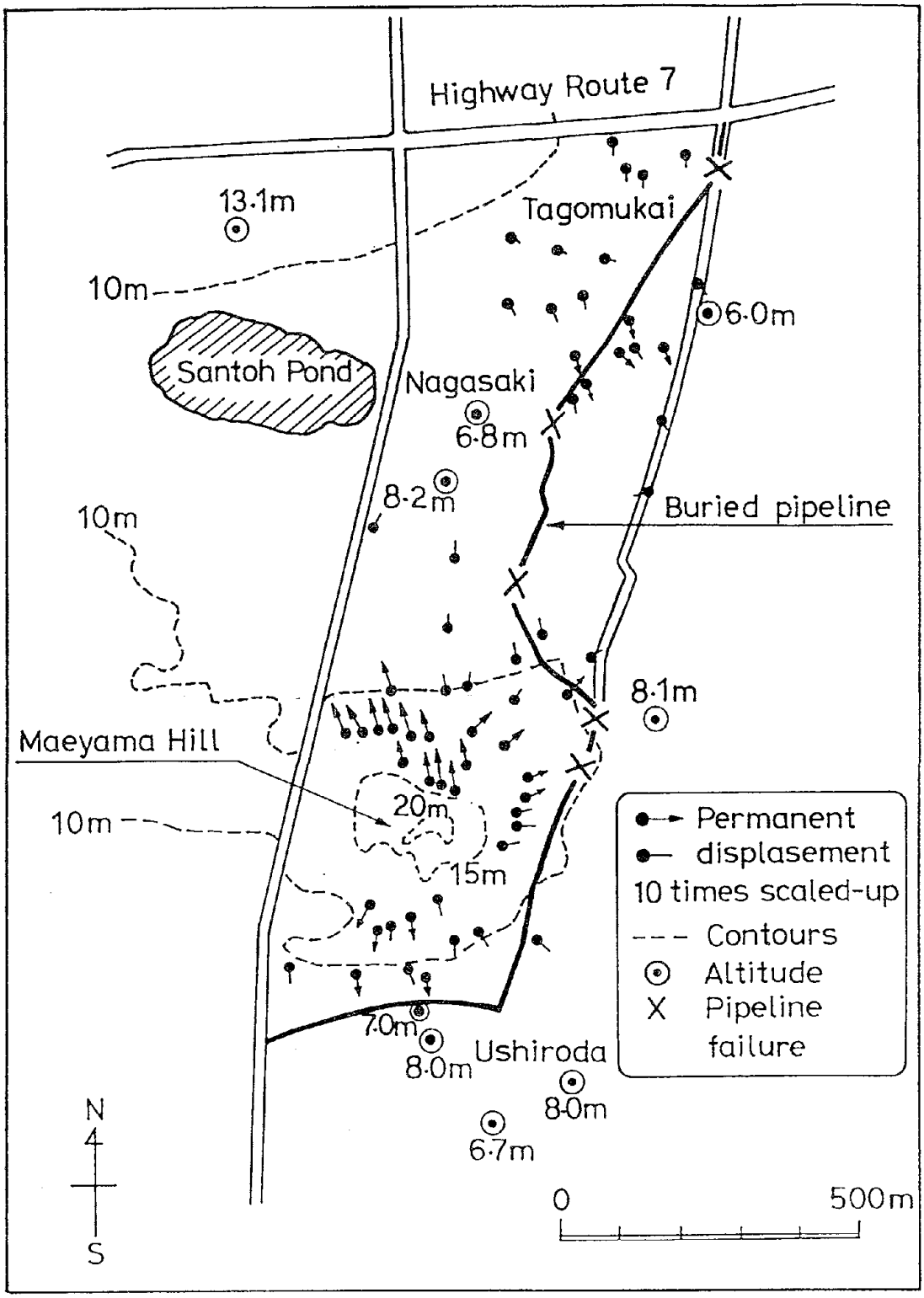

Figure 5: Observed permanent ground displacements in Noshiro City

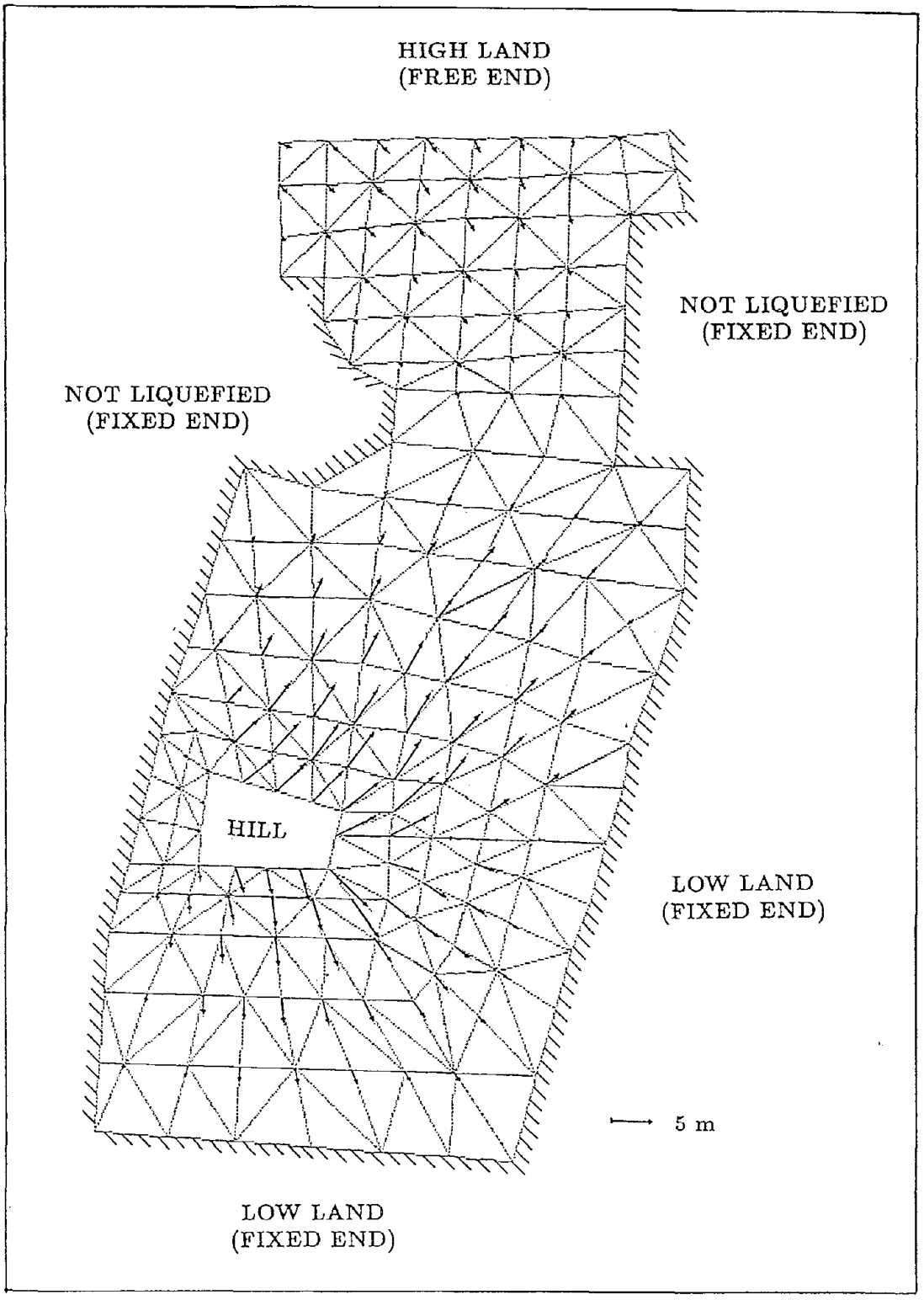

Figure 6: Calculated permanent ground displacements in Noshiro City

Empirical Prediction of Lateral Spread Displacement

Steven F. Bartlett
Research Assistant
Brigham Young University

T. Leslie Youd
Professor of Civil Engineering
Brigham Young University

ABSTRACT

Data compiled from case histories of liquefaction-induced lateral spread are used to develop an empirical model for predicting the amount of horizontal ground displacement at potentially liquefiable sites. Earthquake, topographical, geological, and soil factors associated with lateral spreads from eight major earthquakes are analyzed. Multiple linear regression (MLR) is used to determine which factors are most strongly correlated with horizontal ground displacement and an empirical model is developed from those factors. The performance of the MLR model is evaluated by comparing the displacements measured at the case history sites with those predicted by the model.

INTRODUCTION

Lateral spread on gently sloping ground is the most pervasive and damaging type of liquefaction-induced ground failure (NRC, 1985). Lateral spreads during the 1906 San Francisco earthquake damaged several buildings, bridges, roads, and pipelines (Youd and Hoose, 1978). Most notably, lateral spread along Valencia Street, between 17th and 18th Street, severed water lines to downtown San Francisco. The resulting loss of water greatly hampered fire fighting efforts during the ensuing fire. Lateral spreads spawned by the 1964 Alaska earthquake caused $80 million damage (1964 value) to 266 bridges and numerous sections of embankment along the Alaska Railroad and Highway (McCulloch and Bonilla, 1970; Kachadoorian, 1968). Lateral spreads also disrupted many buildings, pipelines, and other lifelines in southern Alaska. Lateral spreads also caused widespread damage during the 1964 Niigata, Japan earthquake (Hamada et al., 1986). Liquefaction of loosely-compacted channel deposits in Niigata allowed the banks of the Shinano River to move as much as 10 meters toward the channel.

This paper gives the results of a multiple linear regression (MLR) analysis of liquefaction-induced, horizontal ground displacement resulting from lateral spread (Bartlett and Youd, 1992). Earthquake, surface, and subsurface data are analyzed for several lateral spreads generated by the following earthquakes: 1906 San Francisco, 1964 Alaska, 1964 Niigata, Japan, 1971 San Fernando, 1979 Imperial Valley, 1983 Nihonkai-Chubu, Japan, 1983 Borah Peak, Idaho, and 1986 Superstition Hills. Stepwise, multiple linear regression is used to develop an empirical model from the earthquake, topographical, geological, and soil factors that are most strongly correlated with displacement. The empirical model proposed herein provides a basis for estimating the amount of horizontal ground displacement at potentially liquefiable sites in earthquake prone regions.

PREVIOUS EMPIRICAL MODELS

Using pre- and post-earthquake aerial photographs, Hamada et al. (1986) developed liquefaction-induced, horizontal ground displacement vector maps for Niigata and Noshiro, Japan (i.e., 1964 Niigata (M = 7.5) and 1983 Nihonkai-Chubu (M = 7.7) earthquakes, respectively). Based on the ground deformation pattern and changes in the surface topography, Hamada et al. divided the failed zones into segments or blocks that appeared to have displaced as a discrete unit. The individual displacement vectors, thickness of the liquefied layer(s), and the slope were averaged within each block. These averages were used to develop the following empirical model:

$$D = 0.75\ H^{0.50}\ \theta^{0.33} \qquad (1)$$

where D is the horizontal ground displacement, in meters, H is the thickness of the liquefied layer, in meters, and θ is the maximum of the ground slope or slope at the base of the liquefied layer, in percent. Although Hamada et al. (1986) used this equation to predict lateral spread displacements in Niigata and Noshiro, Japan within a factor of about 2, the data from which their equation was derived came from a rather narrow range of soil (mostly clean, medium-grained sands) and earthquake (M = 7.5 - 7.7) conditions. Thus, this equation has not been verified for a wide range of seismic and sediment conditions.

Youd and Perkins (1987) introduced the "Liquefaction Severity Index" or LSI as a convenient index for estimating the general maximum horizontal ground displacement at liquefaction sites. The LSI study was limited to lateral spreads that occurred in moderately to highly liquefiable sediments having standard penetration resistances ranging from 2 to 10 blows per foot. Also, only failures on gently sloping ground or into river channels with widths greater than 10 meters were considered. Sites where the amount of ground displacement had exceeded 2.5 m were also excluded from their study. These large displacements were so damaging and erratic in nature that extending the LSI beyond 2.5 m was not meaningful.

For the specific geological setting considered, Youd and Perkins postulated that horizontal ground displacement is primarily a function of the amplitude and duration of strong ground motion. Because strong motion records were not available for most sites, they chose to express LSI in terms of earthquake magnitude (M) and the log of the distance from the seismic energy source, R, in kilometers. Ordinary least squares regression was used to fit the following equation:

$$\text{LOG LSI} = -3.49 - 1.86\ \text{LOG R} + 0.98\ M_w \qquad (2)$$

where LSI is the maximum permanent horizontal displacement in inches (millimeters divided by 25). This equation is valid only for predicting the maximum ground displacement that would likely occur at sites characterized by the specified site conditions. Also, the equation has only been verified for sites in the western U.S.

Ambraseys (1988) compiled values of moment magnitude, M_w, and the distance to the farthest observed liquefaction effects, R_f (in kilometers), for several earthquakes and bounded these data with the equation:

$$M_w = 0.18 + 9.2 \times 10^{-8}\ R_f + 0.90\ \text{LOG}\ R_f. \qquad (3)$$

Although Ambraseys' equation was not developed for estimating ground displacement, it does indicate that there is a maximum distance beyond which liquefaction and ground displacement should not occur. The functional form of the equation also suggests that displacement should attenuate in a non-linear fashion as a function of M, LOG R_f, and R_f.

TOWARDS A MORE COMPREHENSIVE MODEL

The Hamada et al. thickness-slope model, the Youd-Perkins LSI model, and Ambraseys' R_f bound suggest that a more comprehensive, predictive model should include earthquake, topographical, geological, and soil factors. In this study, we postulate that the dependent variable, horizontal ground displacement, D_H, is a function of the independent variables listed in Table 1. Prior to performing multiple linear regression analysis, we compiled a database of 448 horizontal displacement vectors and 270 boreholes with SPT measurements from the lateral spread sites listed in Table 2. We also incorporated 19 observations from Ambraseys' (1988) study into our database to improve the performance of the model for sites where lateral spread was at its inception (Bartlett and Youd, 1992).

For many lateral spread sites, several boreholes were drilled within the failure area. For these sites, we used an inverse-distance, linearly-weighted average to interpolate all geological and soil independent variables between boreholes. This scheme assigns greater weight to boreholes located nearest to D_H.

$$X_{AVG} = W_1*X_1 + W_2*X_2 + \ldots + W_n*X_n \quad (4)$$

where X_{AVG} is the weighted average, $X_1,\ldots,X_n$ are the respective values of the independent variable to be averaged, and $W_1,\ldots,W_n$ are the weights. The weights were calculated from:

$$W_i = 1/d_i/\Sigma(1/d_i) \quad (5)$$

where $\Sigma(1/d_i)$ is summed for n number of boreholes and d_i is the distance from i^{th} borehole to the displacement vector of interest. The averages from Equation 4 were assigned to individual displacement vectors prior to performing regression analysis (Bartlett and Youd, 1992).

STRATEGY FOR MODEL DEVELOPMENT

We used a modified, stepwise regression procedure to guide us in the development of our models (Draper and Smith, 1981). In short, this procedure begins by searching the set of independent variables (i.e., the X's) for the X that has the highest correlation with horizontal displacement, D_H, and this X enters the model. The remaining X's are then re-examined to find the next X yielding the highest improvement in R^2, and this X is added to the model. This process of adding X's to the model continues in a stepwise fashion until no additional X's can be found that significantly improve the performance of the model.

Because the earthquakes that generated lateral spreads in Niigata and Noshiro, Japan were seismically similar (M = 7.5 and 7.7, respectively), we were able to ignore the effects of earthquake factors in developing our preliminary MLR models for Japan. Also, the extensive displacement and subsurface measurements from these localities provided a large database amenable to MLR regression analysis.

We observed two types of lateral spreads in Niigata and Noshiro: (1) lateral spread towards a free face (free face failure), and (2) lateral spread down gentle, ground slopes (ground slope failure). For example, Figure 1 shows displacement vectors measured along the banks of the Shinano River near the northern abutment of the Echigo Railway Bridge in Niigata, Japan. The large and erratic displacements near the river were in part a consequence of the lack of lateral resistance created by the incised channel. In contrast, lateral spread displacements in the area north of the railroad embankment were smaller (a maximum displacement of 2 m), more uniform, and moved down a gentle grade of approximately 0.2 percent that slopes away from the Shinano River.

TABLE 1
SUMMARY OF INDEPENDENT VARIABLES CONSIDERED IN MLR ANALYSIS

Earthquake Variables	Description
M*	Earthquake moment magnitude, M_w.
R*	Horizontal distance to nearest seismic energy source or to nearest fault rupture, (km).
A	Peak horizontal ground acceleration, (g).
D	Duration of strong ground motion (>0.05 g), (s).

Topographical Variables	Description
S*	Ground slope, (%).
L	Distance to the free face from the point of displacement, (m).
H	Height of free face, (m).
W*	Free face ratio, (%), (i.e., 100 H/L).

Geological Variables	Description
T	Cumulative thickness of liquefied zone,(m).
T_{10}	Thickness of saturated cohesionless soils with $(N1)_{60} \leq 10$, (m).
T_{15}*	Thickness of saturated cohesionless soils with $(N1)_{60} \leq 15$, (m).
T_{20}	Thickness of saturated cohesionless soils with $(N1)_{60} \leq 20$, (m).
I	Index of Liquefaction Potential, (Hamada et al., 1986).
C	Depth to top of liquefied zone, (m).
B	Depth to bottom of liquefied zone, (m).
Z	Depth to lowest factor of safety against liquefaction, (m).
E	Depth to lowest SPT N value in saturated cohesionless soil, (m).
G	Depth to lowest SPT $(N1)_{60}$ value in saturated cohesionless soil, (m).
N	Lowest SPT N value in saturated cohesionless sediments.
N_a	Lowest SPT $(N1)_{60}$ value in saturated cohesionless sediments.
J	Lowest factor of safety against liquefaction below water table.
$(N1)_{60FS}$	$(N1)_{60}$ value corresponding to J.
K	Average factor of safety in T_S.
O	Average $(N1)_{60}$ in T_S.

Soil Variables	Description
$D50_S$	Average D_{50} in T_S, (mm).
$D50_L$	Average D_{50} in T_L, (mm).
$D50_{10}$	Average D_{50} in T_{10}, (mm).
$D50_{15}$*	Average D_{50} in T_{15}, (mm).
$D50_{20}$	Average D_{50} IN T_{20}, (mm).
F	Average fines content (<0.075 mm) in T, (%).
F_{10}	Average fines content (<0.075 mm) in T_{10}, (%).
F_{15}*	Average fines content (<0.075 mm) in T_{15}, (%).
F_{20}	Average fines content (<0.075 mm) in T_{20}, (%).

* Indicates independent variables used in final MLR models.

TABLE 2
EARTHQUAKES AND LATERAL SPREAD SITES INCLUDED IN STUDY

1906 San Francisco Earthquake (Youd and Hoose, 1978)
Coyote Creek Bridge near Milpitas, California
Mission Creek Zone in San Francisco, California
Salinas River Bridge near Salinas, California
South of Market Street Zone in San Francisco, California

1964 Alaska Earthquake (Bartlett & Youd, 1991; McCulloch & Bonilla 1970)
Bridges 141.1, 147.4, 147.5, 148.3, Matanuska River, Alaska
Bridges 63.0, 63.5, Portage Creek, Portage, Alaska
Highway Bridge 629, Placer River, Alaska (Ross et al., 1973)
Snow River Bridge 605A, Snow River, Alaska (Ross et al., 1973)
Bridges 3.0, 3.2, 3.3, Resurrection River, Alaska

1964 Niigata, Japan, Earthquake (Hamada et al., 1986)
Numerous lateral spreads in Niigata, Japan

1971 San Fernando, California Earthquake
Jensen Filtration Plant, (O'Rourke et al., 1990)
Juvenile Hall, (Bennett, 1989; Youd, 1973)

1979 Imperial Valley, California Earthquake (Bennett et al., 1981, 1984)
Heber Road near El Centro, California
River Park near Brawley, California

1983 Borah Peak Idaho, Earthquake
Whiskey Springs near Mackay, Idaho (Andrus and Youd, 1987)
Pence Ranch near Mackay, Idaho (Andrus et al., 1991)

1983 Nihonkai-Chubu Earthquake (Hamada et al., 1986)
Lateral spreads in the Northern Sector of Noshiro, Japan

1987 Superstition Hills Earthquake (Holzer et al., 1988, 1989)
Wildlife Instrument Array, Brawley, CA, (Youd and Bartlett, 1988)

In analyzing the lateral spreads in Niigata, we found that regression coefficients fitted for free face failures differed significantly from those fitted for ground slope failures. Thus, we developed separate MLR models for each type of failure. We first develop a free face model using data exclusively from Niigata. We then develop a ground slope model using data from both Niigata and Noshiro. Finally, we develop a comprehensive model by including the U.S. case histories in the analyses and by adjusting the site-specific model(s) for a wider range of seismic and site conditions.

DEVELOPMENT OF FREE FACE MODEL FOR NIIGATA, JAPAN

Stepwise regression indicated that distance, L, from the channel is the most important site factor affecting ground displacement for free face failures along the Shinano River in Niigata. For example, Figure 1 shows that displacement south of the Echigo Railway generally decrease with increasing L. The analysis also shows that the height, H, of the free face (depth of the channel) also influenced displacement. To normalize L for the effect of H, we combined these two measures into one independent variable called the free face ratio, W, where W = 100 H/L (in percent). The relationship between these two variables is

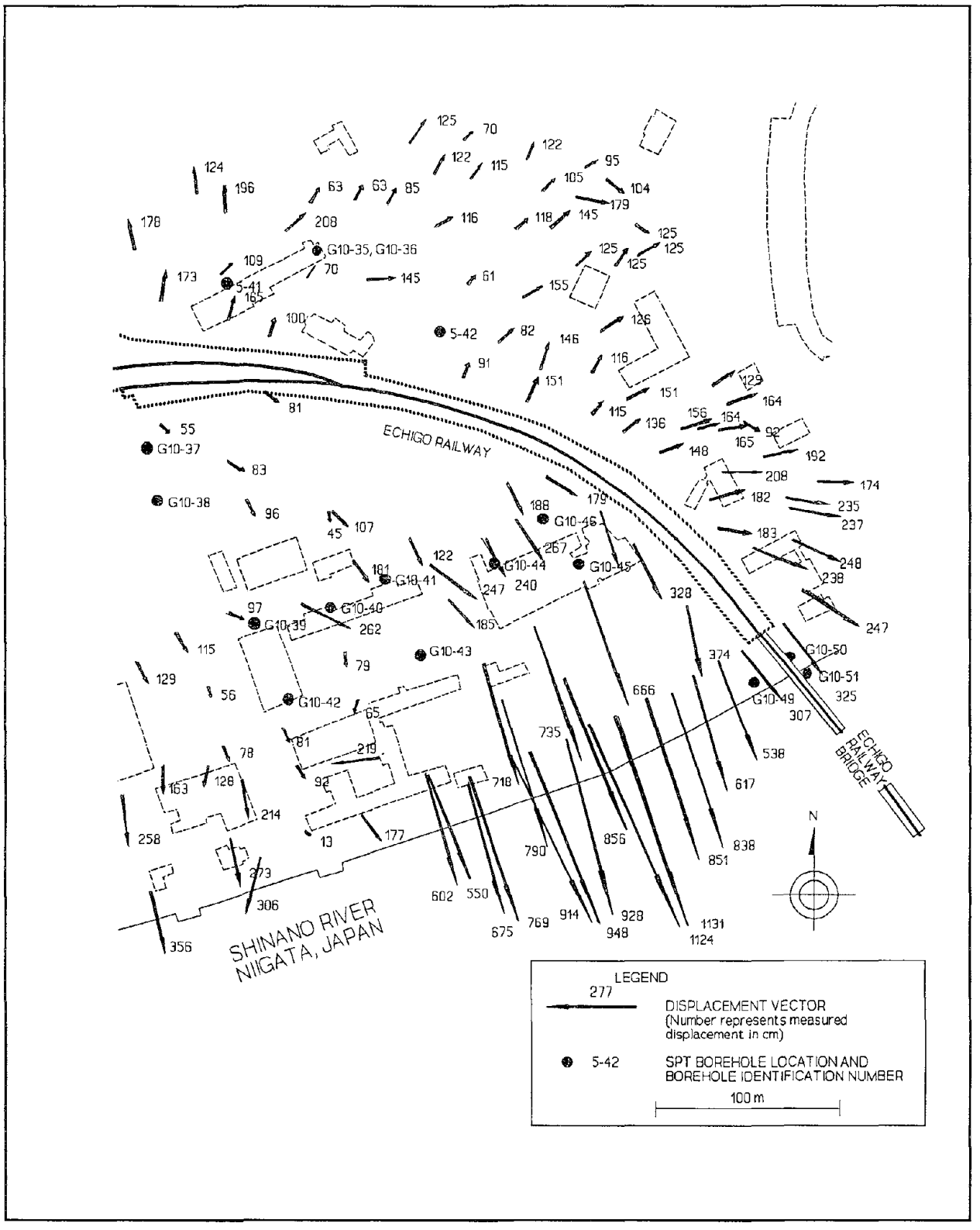

Figure 1 Map showing displacement vectors and SPT boreholes for part of Niigata, Japan (adapted from an unpublished working map courtesy of M. Hamada)

approximately log linear; thus, we formed the model:

$$\text{LOG } D_H = b_0 + b_1 \text{ LOG } W \quad (6)$$

Approximately 40 percent of the variability in D_H is explained by this simple model (i.e., R^2 = 40 percent).

In addition to W, we postulated that ground slope near the river could have influenced displacement, and we defined a second variable, S, to represent that influence. We assigned a positive value to S for ground that sloped toward the channel and a negative value to S for ground that sloped away. The inclusion of S in the free face model did not significantly improve its performance, probably because S does not vary over a wide range in the area near the Shinano River.

Stepwise regression suggested that thickness of the liquefied layer, T, in meters, is the next variable that should enter the free face model. Some modelers have calculated T using empirical liquefaction analyses. However, these procedures require the input of earthquake magnitude, M, and peak acceleration, A, to estimate T, thus introducing correlation between T, M, and A. To eliminate this undesired correlation, we tested three thickness measures that are determined without performing liquefaction analysis. These variables, T_{10}, T_{15}, and T_{20}, are defined as the cumulative thickness, in meters, of saturated cohesionless sediments with $(N1)_{60}$ values $\leq$ 10, 15, and 20, respectively. Soils with a clay content $\geq$ 15 percent were not included in these thicknesses. Also, T_{10}, T_{15}, and T_{20} were accumulated only in the upper 20 m of the profile. Each of these estimates of T were substituted into the following model:

$$\text{LOG } D_H = b_0 + b_1 \text{ LOG } W + b_2 \text{ T} \quad (7)$$

The calculated R^2 values were 50.9, 62.4, and 63.8 percent, respectively. We ultimately chose T_{15} rather than T_{20} for subsequent models because our analyses suggest that lateral spreads is generally restricted to saturated deposits with $(N1)_{60} \leq 15$ for $M \leq 8$ earthquakes.

After adjusting for W and T_{15}, stepwise regression indicated that the average percentage of fines, F_{15} (particle size $\leq$ 0.075 mm in layer T_{15}) is the next variable that should enter the model:

$$\text{LOG } D_H = b_0 + b_1 \text{ LOG } W + b_2 \, T_{15} - b_3 \, F_{15} \quad (8)$$

The R^2 for this model is 66.0 percent.

In addition to F_{15}, the average mean grain size, $D50_{15}$ (mm) in the T_{15} layer, also contributes to predicting D_H. Incorporating this factor yields the model:

$$\text{LOG } D_H = b_0 + b_1 \text{ LOG } W + b_2 \, T_{15} - b_3 \, F_{15} - b_4 \, D50_{15} \quad (9)$$

The R^2 for this model is 70.0 percent.

In addition to $D50_{15}$, the $(N1)_{60}$ corresponding with the lowest factor of safety against liquefaction in the soil profile makes a minor improvement to R^2. The factor of safety, FS, against liquefaction was calculated for each $(N1)_{60}$ value in the profile by applying the "simplified procedure" for liquefaction analysis (Seed and Idriss, 1971; Seed et al., 1983; 1985):

$$\text{FS} = \text{CSRL/CSRE} \quad (10)$$

where CSRL is the cyclic stress ratio required to generate liquefaction in the soil, and CSRE is the cyclic stress ratio induced by the earthquake. The $(N1)_{60}$ corresponding to the lowest FS in granular materials was denoted by $(N1)_{60FS}$ and added to the model:

$$\text{LOG } D_H = 0.608 + 0.574 \text{ LOG } W + 0.0249\ T_{15} - 0.0279\ F_{15} - 1.61\ D50_{15} - 0.0317\ (N1)_{60FS}. \quad (11)$$

Other possible geological and soil independent variables did not appreciably improve the performance of Equation 11 thus it was adopted as the final site-specific free face model for Niigata.. The R^2 for this model is 72.4 percent and all regression coefficients are significant at 99.9 percent confidence level.

DEVELOPMENT OF A GROUND SLOPE MODEL FOR NIIGATA AND NOSHIRO, JAPAN

The evaluation of lateral spreads in Niigata and Noshiro indicates that ground slope, S (in percent), has a high correlation with horizontal displacement in the absence of a free face. Thus, the following model was hypothesized and tested:

$$\text{LOG } D_H = b_0 + b_1 \text{ LOG } S \quad (12)$$

The R^2 for this model is 42.1 percent.

Like the free face model, the addition of the variables T_{15}, $D50_{15}$, and F_{15} significantly improve the performance of the ground slope model. Our preliminary analysis suggested that the relationship between LOG D_H and T_{15}, $D50_{15}$, and F_{15} is approximately linear:

$$\text{LOG } D_H = 0.698 + 0.378 \text{ LOG } S + 0.0362\ T_{15} - 0.0326\ F_{15} + 0.929\ D50_{15} \quad (13)$$

Other possible independent variables made only minor contributions to R^2. Thus, Equation 13 was adopted as the final model for ground slope failures in Niigata and Noshiro. The R^2 for this model is 54.2 percent and all regression coefficients are significant at the 99.9 percent confidence level.

COMBINED MLR MODEL DEVELOPED FROM U.S. AND JAPANESE CASE HISTORIES

The free face and ground slope models for Niigata and Noshiro, Japan were modified for a wider range of earthquake and soil conditions by including the U.S. case histories and adjusting the models for the effects of earthquake factors. The U.S. data include earthquakes with magnitudes (M_w) ranging from 6.5 to 9.2 and estimated peak accelerations ranging from 0.1 to 0.6 g (Bartlett and Youd, 1992). Also, in contrast to the homogeneous, clean, medium-grained sands found in Niigata and Noshiro, the U.S. sites include a wide range of soil types (e.g., silt, sandy silt, silty sand, sand, and fine gravel).

Based on the studies of Youd and Perkins (1987) and Ambraseys (1988), we postulated that:

$$D_H = f(A, D) \quad (14)$$
$$D_H = f(M, \text{LOG } R) \quad (15)$$
$$D_H = f(M, \text{LOG } R, R). \quad (16)$$

Our analyses of the combined U.S. and Japanese database indicate that models based on Equation 16, yield R^2 values approximately 20 percent higher than models based on Equation 14, and 10 percent higher than models based on Equation 15. Thus, we chose Equation 16 to formulate the earthquake component of our final MLR model. We do not imply, however, that M and R are better measures of seismic energy than instrumentally obtained values of A and D. Models based on A and D should be superior in that these factors are more fundamental measures of seismic energy delivered to a given site. Unfortunately, strong motion records are not available for most sites in the database. For these non-instrumented sites, we estimated A and D from empirical relationships based on M and LOG R. The poorer

performance of the A-D models may have been due in large part to our inability to accurately estimate A and D.

Because the U.S. database does not contain a sufficient number of ground slope failures to independently adjust for M, LOG R and R, we combined the free face and ground slope databases and fitted the common earthquake parameters while retaining separate topographical, geological, and soil parameters for each type of failure:

$$D_H = f(M, \text{LOG } R, R, \text{LOG } W_{ff}, T_{15ff}, F_{15ff}, D50_{15ff}, (N1)60FS_{ff}, \text{LOG } S_{gs}, T_{15gs}, F_{15gs}, D50_{15gs} \quad (17)$$

The subscripts ff and gs in Equation 17 indicate variables that are assigned to the free face and ground slope components of the model, respectively. Inherent in this approach is the assumption that M, LOG R, and R equally influence both types of failure. This assumption seems reasonable given that the amount of seismic energy delivered to a particular site should be independent of the type of failure. Based on the form expressed in Equation 17, we formulated the following model:

$$\begin{aligned} \text{LOG}(D_H+0.01) = {} & b_0 + b_{0ff} + b_1 M + b_2 \text{ LOG } R + b_3 R + b_4 \text{ LOG } W_{ff} + b_5 T_{15ff} + b_6 F_{15ff} + b_7 D50_{15ff} \\ & + b_8 (N1)_{60FSff} + b_9 \text{ LOG } S_{gs} + b_{10} T_{15gs} + b_{11} F_{15gs} + b_{12} D50_{15gs} \end{aligned} \quad (18)$$

The regression coefficient b_0 is the intercept for the combined equation. The coefficient b_{0ff} is used to adjust b_0 for any difference between b_0 and the intercept of the free face component of the model (i.e., the intercept for the free face component of the model is calculated by adding b_0 and b_{0ff}). Also, because the LOG(0) is undefined, we expediently added 0.01 m to all values of D_H. This expediency enabled calculation of LOG D_H for zero displacement observations in the database.

A least squares fit of Equation 18 yields a R^2 of 83.8 percent. All regression coefficients, except for b_8, are significant at the 99.9 percent confidence level. The regression coefficient b_8 is significant only at the 82 percent confidence level, so $N1_{60FSff}$ was dropped from the model. Also, this analysis showed that $b_5 \approx b_{10}$, and $b_6 \approx b_{11}$, and $b_7 \approx b_{12}$, suggesting that common parameters can be fitted for T_{15ff} and T_{15gs}, and for F_{15ff} and F_{15gs}, and for $D50_{15ff}$ and $D50_{gs}$. Hence, we formed the model:

$$\text{LOG}(D_H+0.01) = b_0 + b_{0ff} + b_1 M + b_2 \text{ LOG } R + b_3 R + b_4 \text{ LOG } W_{ff} + b_5 \text{ LOG } S_{gs} + b_6 T_{15} + b_7 F_{15} + b_8 D50_{15} \quad (19)$$

The R^2 for Equation 19 is 83.4 and all regression coefficients are significant at the 99.9 percent confidence level.

After fitting Equation 19, we reexamined all of the variables listed in Table 1 for any trends that might enhance the performance of the model and found none. We also performed a sensitivity analysis on this equation and found that the transformation of T_{15} to LOG T_{15} and the transformation of F_{15} to LOG $(100-F_{15})$ yielded predicted displacements that are more credible for small values of T_{15} and F_{15}. Thus, we slightly modified the model:

$$\begin{aligned} \text{LOG}(D_H+0.01) = {} & b_0 + b_{0ff} + b_1 M + b_2 \text{ LOG } R + b_3 R + b_4 \text{ LOG } W_{ff} + b_5 \text{ LOG } S_{gs} \\ & + b_6 \text{ LOG } T_{15} + b_7 \text{ LOG}(100-F_{15}) + b_8 D50_{15} \end{aligned} \quad (20)^1$$

A least squares fit of Equation 20 yields the following regression coefficients: $b_0 = -15.787$, $b_{0ff} = -0.579$, $b_1 = 1.178$, $b_2 = -0.927$, $b_3 = -0.013$, $b_4 = 0.657$, $b_5 = 0.429$, $b_6 = 0.348$, $b_7 = 4.527$, $b_8 = -0.922$. All coefficients are significant at the 99.9 percent confidence level and the R^2 for Equation 20 is 82.6 percent. This is our final MLR model.

[1] This analysis was done after the Fourth U.S.-Japan Workshop and this equation is slightly different from the equation given at the Workshop.

The free face component of Equation 20 is:

$$\text{LOG}(D_H+0.01) = -16.366 + 1.178\,M - 0.927\,\text{LOG}\,R - 0.013\,R + 0.657\,\text{LOG}\,W + 0.348\,\text{LOG}\,T_{15} + 4.527\,\text{LOG}(100-F_{15}) - 0.922\,D50_{15} \quad (20a)$$

and the ground slope component is:

$$\text{LOG}(D_H+0.01) = -15.787 + 1.178\,M - 0.927\,\text{LOG}\,R - 0.013\,R + 0.429\,\text{LOG}\,S + 0.348\,\text{LOG}\,T_{15} + 4.527\,\text{LOG}(100-F_{15}) - 0.922\,D50_{15} \quad (20b)$$

APPLICATION OF THE MLR MODEL

Because D_H may be strongly nonlinear outside the range of the independent variables used to develop the model, caution should be applied when extrapolating Equation 20. However, we believe that extrapolation may be warranted in some cases. For example, an important problem for engineers is the estimation of lateral displacements at sites underlain by layers with T_{15} less than 0.3 m. Because the literature is devoid of guidance for estimating such displacements, extrapolation of Equation 20 may be useful. Estimates from Equation 20 appear to be conservative for such cases (i.e., Equation 20 tends to over predict measured displacements). Also, if T_{15} is allowed to go to zero, Equation 20 yields non-zero displacements, which are unlikely to occur. Similarly, extrapolation to earthquake magnitudes less than 6.0 appears to give plausible predictions.

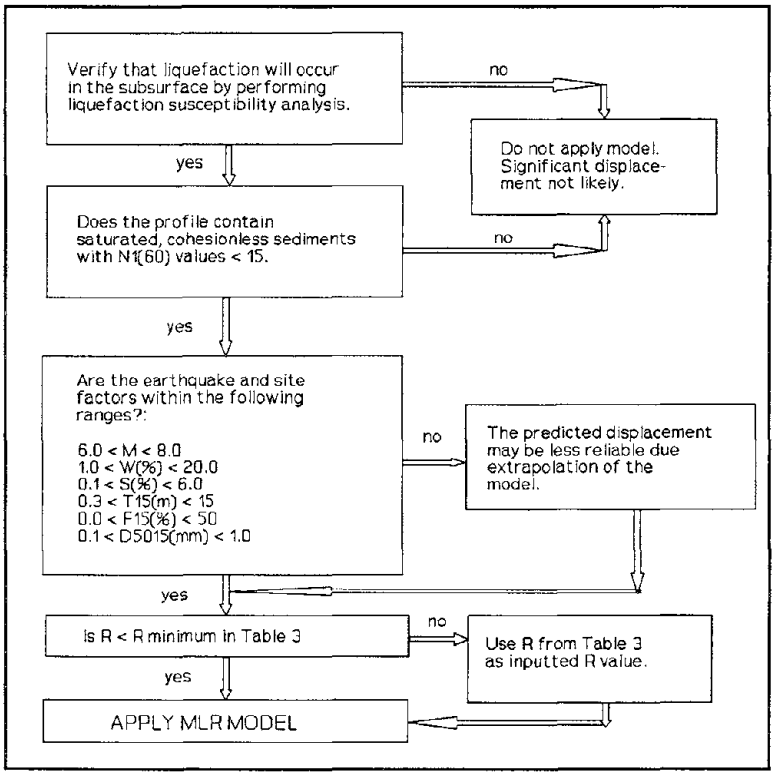

Figure 2 Flow chart for the application of Equation 20.

Given some allowances for extrapolation as noted above, Figure 2 summarizes the procedure we recommend for applying Equation 20. In short, the model yields reasonable predictions for displacements generated by magnitude 6.0 to 8.0 earthquakes at sites underlain by shallow ($Z < 15$ m), widespread layers of sand or silty sand ($F_{15} < 50\%$) with $(N1)_{60}$ values less than 15. Also, because the model was developed primarily from western U.S. and Japanese data, it is most applicable to regions having high to moderate ground motion attenuation.

To further show the predictive performance of the model, displacements measured from the dataset are plotted versus the predicted displacements on Figure 3. The solid diagonal line on that figure represents perfect prediction, i.e., predicted displacements equal measured displacements. The lower dashed line represents 100 percent overprediction and the upper dashed line represents 50 percent underprediction. Approximately ninety percent of the points on this plot lie between these two dashed bounds. This grouping indicates that predicted

displacements are generally valid within a factor of 2 and that doubling of the predicted displacement provides an estimate with a high probability of not being greatly exceeded.

At some sites, it may be difficult to decide whether to apply the free face or ground slope model. An analysis of the compiled displacement vectors indicates that displacements are not significantly influenced by a free face for W < 1 percent; thus, for these cases the ground slope model should apply. For 1 ≤ W ≤ 5 percent, we suggest estimating displacement using both Equations 20a and 20b and applying the larger value. For 5 < W ≤ 20 percent, the free face model should be used. The data set is devoid of case histories for W > 20 percent; thus, the model should not be extrapolated too close to a free face where slumps or even flow may be the primary mode of failure. Similarly, liquefaction beneath slopes with S > 5 percent may produce very large displacements or even flow failure and Equation 20b should not be extrapolated into that range.

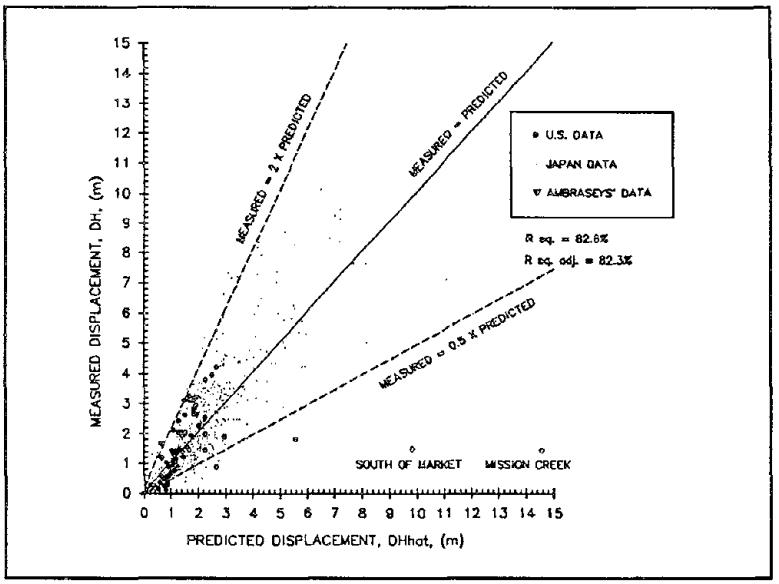

Figure 3 Measured displacements versus displacements predicted using Equation 20 for U.S., Japan, and Ambraseys' data.

Although the bulk of the case history data are from M = 6.0 to 8.0 earthquakes, seven observations are from the 1964 Alaska earthquake (M = 9.2). The standardized residuals for Alaskan observations show no unusual behavior indicating that Equation 20 appears to perform reasonably well for M > 8.0. More data are needed, however, to strengthen the MLR model for M > 8.0 earthquakes.

Equation 20 attenuates D_H with increasing R in a manner that is consistent with both the case history data and Ambraseys' R_f bound (Ambraseys, 1988), and it yields reasonable predictions at large R. However, if R is allowed to decrease to a small value, the predicted displacements appear to become unacceptably large. To overcome this problem, we suggest that the inputted R not be allowed to decrease below the minimum values listed in Table 3.

During preliminary development, we noted that our models yielded poor results for gravelly sites. Because of the number of outliers for predicted values of D_H, it appears that gravelly soils may behave differently than sandy or silty soils. For example, our preliminary models performed poorly in predicting displacements measured at gravelly sites following the 1983 Borah Peak, Idaho, earthquake. Because we do not have enough observations to adequately adjust the model for gravelly soils, we removed the observations from gravelly sites prior to fitting Equation 20. Hence, we do not recommend the use of Equation 20 for $D50_{15}$ greater than 1 mm.

TABLE 3
MINIMUM VALUES OF R FOR VARIOUS EARTHQUAKE MAGNITUDES

M	R (km)	M	R (km)	M	R (km)
6.5	0.25	7.4	2.4	8.3	17
6.6	0.3	7.5	3	8.4	20
6.7	0.4	7.6	4	8.5	24
6.8	0.5	7.7	5	8.6	28
6.9	0.7	7.8	6	8.7	33
7.0	0.9	7.9	8	8.8	38
7.1	1.1	8.0	9	8.9	43
7.2	1.4	8.1	12	9.0	50
7.3	1.8	8.2	14		

Ground displacements compiled in the dataset were restricted, with few exceptions, to saturated cohesionless soils with $(N1)_{60} \leq 15$. The few exceptions were from lateral spreads at gravelly sites generated by the very large 1964 Alaska earthquake (M_w 9.2). These data indicate that large earthquakes may generate displacements in sediments with $(N1)_{60} > 15$. However, the $(N1)_{60}$ values from these Alaskan sites may have been flawed because they were measured in gravels with a non-standard hammer. Conversely, the data set also includes several sites where the minimum $(N1)_{60}$ were greater than 15 but horizontal displacement did not develop. Hence, we suggest that cohesionless materials with $(N1)_{60}$ values > 15 appear to be immune to lateral spread for earthquakes with magnitudes less than 8. In summary, Equation 20 may be used to predict displacements at sites underlain by saturated, non-gravelly, cohesionless soils with $(N1)_{60}$ values ≤ 15. For sites with higher $(N1)_{60}$ values and $M < 8$, lateral spread displacement should not occur.

In the collected case histories, the depth to the lowest factor of safety against liquefaction, Z, was invariably less than 15 m for sites where significant lateral displacement occurred. Also, the depth to the top of the liquefied layer was generally within a few meters of ground surface. Thus, Equation 20 should restricted to liquefiable sediments no deeper than 15 m.

The points that plot below the lower dashed line on Figure 3 indicate an overprediction of D_H by a factor greater than 2. Most of these points are for U.S. sites where the measured displacements were less than 1 m. These measurements generally were taken near the margins of lateral spreads where lateral boundary effects may have hampered displacement. Because our model is heavily dependent on Japanese case history data, where liquefiable sediments were widespread and lateral boundary effects were relatively minor, Equation 20 may significantly overpredict displacements near the margins of lateral spreads. Equation 20 also greatly overpredicts the 1.5 m ground displacements reported from the Mission Creek and South of Market zones following the 1906 San Francisco earthquake (Youd and Hoose, 1978; O'Rourke et al., 1991). As shown on Figure 3, predicted values for those two zones are approximately 10 m and 14.5 m, respectively. We believe this poor predictive performance was also due to lateral boundary effects, although the poor quality of SPT and grain-size data reported from these zones also may have added uncertainty to the predicted values. The Mission Creek failure migrated down the sinuous course of an old creek channel causing the lateral spread to change directions at several locales. Similarly, the South of Market failure developed in a rather narrow zone where boundary effects could have inhibited movement. These observations indicate that lateral boundary effects are not properly considered in Equation 20; more research is required to incorporate this influence.

CONCLUSIONS

We used information from an extensive database, derived from Japanese and U.S. case histories of liquefaction and lateral spread, to formulate a comprehensive, empirical model for predicting horizontal ground displacement. The model was developed using multiple linear regression procedures with stepwise addition of influential factors. The analysis indicated that models with different parameters are required to predict lateral spread displacements for free face and ground slope conditions, respectively. Models (Equation 20) with the best fit of the observed data are:

for free face conditions,

$$\begin{aligned} LOG(D_H+0.01) = &- 16.366 + 1.178\ M - 0.927\ LOG\ R - 0.013\ R \\ &+ 0.657\ LOG\ W + 0.348\ LOG\ T_{15} + 4.527\ LOG(100-F_{15}) - 0.922\ D50_{15} \end{aligned} \quad (20a)$$

and for ground slope conditions,

$$\begin{aligned} LOG(D_H+0.01) = &- 15.787 + 1.178\ M - 0.927\ LOG\ R - 0.013\ R \\ &+ 0.429\ LOG\ S + 0.348\ LOG\ T_{15} + 4.527\ LOG(100-F_{15}) - 0.922\ D50_{15} \end{aligned} \quad (20b)$$

where:

M = Earthquake magnitude (moment magnitude).
R = Horizontal distance from the seismic energy source, (km).
W = 100 * (height (H) of the free face / distance (L) from the free face).
S = Ground slope (%).
T_{15} = Cumulative thickness of saturated granular layers with $N1_{60} \leq 15$, (m).
F_{15} = Average fines content of saturated granular layers included in T_{15}, (%).
$D50_{15}$ = Average mean grain size in layers included in T_{15}, (mm).

This model is applicable for earthquakes with magnitudes between 6.0 and 8.0 affecting sites underlain by continuous layers of sandy materials with $T_{15} > 0.3$ m, $Z_S < 15$ m, $F_{15} < 50\%$) and $(N1)_{60} \leq 15$. Because the model was developed from Japanese and western U.S. data, it is most applicable to regions that have high to moderate ground motion attenuation. Extrapolation to lower T_{15} and M may be warranted for engineering analyses. Such extrapolation should yield conservative (overly-predicted) displacements.

REFERENCES

Ambraseys, N. N., 1988, "Engineering Seismology," Earthquake Engineering and Structural Dynamics, Volume 17, pp. 1-105.

Andrus, R. D., Stokoe, K. H., and Roesset, J. M., 1991, in press, "Liquefaction of Gravelly Soil at Pence Ranch During the 1983 Borah Peak, Idaho Earthquake," Preprint of Proceedings of the Fifth International Conference on Soil Dynamics and Earthquake Engineering, Karlsruhe, Germany, Sept. 1991.

Andrus, R. D., and Youd, T. L., 1987, "Subsurface Investigation of Liquefaction-Induced Lateral Spread Thousand Springs Valley, Idaho," U. S. Army Corp of Engineers, Miscellaneous Paper GL-87-8, 106 p.

Bartlett, S. F., and Youd, T. L., 1991, in press, "Case Histories of Lateral Spreads Caused by the 1964 Alaska Earthquake," Case History Volume, US-Japan Workshop on Liquefaction, Large Ground Deformation, and Their Effects on Lifelines, National Center for Earthquake Engineering Research, State University of New York at Buffalo, Red Jacket Quadrangle, Buffalo, NY, 127 p.

Bartlett, S. F., and Youd, T. L., 1992, "Empirical Analysis of Horizontal Ground Displacement Generated by Liquefaction-Induced Lateral Spreads," Brigham Young University, Department of Civil Engineering Technical Report CEG-92-01, 129 p.

Bennett, M. J., 1989, "Liquefaction Analysis of the 1971 Ground Failure at the San Fernando Valley Juvenile Hall, California," Bulletin of the Association of Engineering Geologists, Vol. XXVI, No. 2, pp. 209-226.

Bennett, M. J., Youd, T. L., Harp, E. L., and Wieczorek, G. F., 1981, "Subsurface Investigation of Liquefaction, Imperial Valley Earthquake, California, Oct. 15, 1979," U.S. Geological Survey Open File Report 81-502, 83 p.

Bennett, M. J., McLaughlin, P. V., Sarimento, J. S., and Youd, T. L., 1984, "Geotechnical Investigation of Liquefaction Sites, Imperial Valley, California," U.S. Geol. Survey Open File Report 84-252, 103 p.

Draper, N. R., and Smith, H., 1981, Applied Regression Analysis, Second Edition, John Wiley and Sons, New York, New York, 709 p.

Hamada, M., Yasuda, S., Isoyama, R., and Emoto, K., 1986, "Study on Liquefaction Induced Permanent Ground Displacements," Published by the Association for the Development of Earthquake Prediction in Japan, 87 p.

Holzer, T. L., Youd, T. L., Bennett, M. J., 1988, "In Situ Measurement of Pore-Pressure Build-Up During Liquefaction," 20th Joint UJNR Panel on Wind and Seismic Effects, 17 p.

Holzer, T. L., Youd, T. L, Hanks, T. C., 1989, "Dynamics of Liquefaction During the 1987 Superstition Hills, California, Earthquake," Science, Vol. 244, pp. 56-59.

Kachadoorian, R., 1968, "Effects of the Earthquake of March 27, 1964, on the Alaska Highway System," U. S. Geological Survey Professional Paper 545-C, 66 p.

McCulloch, D. S., Bonilla, M. G., 1970, "Effects of the Earthquake of March 27, 1964, on the Alaska railroad," U. S. Geological Survey Professional Paper 545-D, 161 p.

National Research Council (NRC), 1985, Liquefaction of Soils During Earthquakes, National Academy Press, Washington D. C., 240 p.

O'Rourke, T. D., Roth, B. L., and Hamada, M., 1990, in press, "Large Ground Deformations and Their Effects on Lifeline Facilities: 1971 San Fernando Earthquake," Technical Report, National Center for Earthquake Engineering Research, State University of New York at Buffalo, Red Jacket Quadrangle, Buffalo, N.Y., 14261, 71 p.

O'Rourke, T, D., Beaujon, P. A., and Scawthorn, C. R., 1991, in press, "Large Ground Deformations and Their Effects on Lifelines Facilities: 1906 San Francisco Earthquake," Technical Report, National Center for Earthquake Engineering Research, State University of New York at Buffalo, Red Jacket Quadrangle, Buffalo, N.Y., 14261, 65 p.

Ross, G. A., Seed, H. B., and Migliaccio, R. R., 1973, "Performance of Highway Bridge Foundations," The Great Alaska Earthquake of 1964, Engineering Volume, National Academy of Sciences, Washington D. C., pp. 190-242.

Seed, H. B., and Idriss, I. M., 1971, "Simplified Procedure for Evaluation of Soil Liquefaction Potential," Journal of Soil Mechanics and Foundations Division, ASCE, Vol. 97, No. SM9, pp. 1249-1273.

Seed, H. B., Idriss, I. M., Arrango, I., 1983, "Evaluation of Liquefaction Potential Using Field Performance Data," Journal of Geotechnical Engineering, ASCE, Vol. 109(3), pp. 458-482.

Seed, H. B., Tokimatsu, L. F., Harder, L. F., and Riley, M. C., 1985, "Influence on SPT Procedures in Soil Liquefaction Resistance Evaluations." Journal of Geotechnical Engineering, ASCE, Vol. 3, No. 12, pp. 1425-1446.

Youd, T. L., 1973, "Ground Movements in Van Norman Lake Vicinity During San Fernando Earthquake," The San Fernando, California Earthquake of February 9, 1971, Vol. 3, U.S. Department of Commerce, National Oceanic and Atmospheric Administration, Washington D.C., 1973, pp. 197-206.

Youd, T. L., and Hoose, S. N., 1978, "Historic Ground Failures in Northern California Triggered by Earthquakes," U. S. Geological Survey Professional Paper 993, 177 p.

Youd, T. L., and Perkins, D. M., 1987, "Mapping of Liquefaction Severity Index," Journal of Geotechnical Engineering, Vol. 113, No. 11, pp. 1374-1392.

Youd, T. L., and Bartlett, S. F., 1988, "U.S. Case Histories of Liquefaction-Induced Ground Displacement," Proceeding, First Japan -U.S. Workshop on Liquefaction, Large Ground Deformation and Their Effects on Lifeline Facilities, pp. 22-31.

Shaking Table Tests on Countermeasures against Large Ground Displacement due to Liquefaction

Susumu YASUDA[1], Hideo NAGASE[1], Hiroyoshi KIKU[2], Yutaka UCHIDA[3] and Masato KIYOTA[2]

1) Associate Professor, Department of Civil Engineering, Kyushu Institute of Technology
2) Graduate Student, ditto
3) Engineer, Daiichifukken, Co., Ltd.

ABSTRACT

Large ground displacements due to liquefaction are classified into two groups : (1) permanent ground displacement along a gentle slope, and (2) lateral flow near banks or seashore. Against the first group, following three categories of countermeasures are seemed to be effective: (1-A) improving the ground in all area by densification to prevent liquefaction, (1-B) strengthening structures to prevent damage, and (1-C) strengthening the ground with walls or steel piles, densification at narrow bands. And, two categories of countermeasures: (2-A) improving the ground and (2-B) strengthening quay walls or retaining walls, are seemed to be effective against the second group. Shaking table tests and some analyses were conducted to study the effectiveness of (1-C) and (2-B) methods. Based on these tests and analyses, several appropriate methods are proposed.

INTRODUCTION

Large ground displacements due to liquefaction during past several earthquakes have been clarified by arerial photo surveys, soil investigations and etc. (Hamada et al. 1986, Hamada et al. 1989, Wakamatsu et al. 1989, O'Rourke et al. 1989, Yasuda et al. 1989). According to the results, extremely large ground displacements up to several meters occurred in the ground liquefied at several areas.

The authors conducted shaking table tests, vane tests and cyclic shear tests to study the mechanism of the permanent ground displacement and to ascertain the rate of decrease of the shear modulus and the shear strength (Yasuda et al.1992). Based on these tests, a simplified procedure for forecasting permanent ground displacement was proposed.

In the next step, appropriate countermeasures against the permanent ground displacement were studied based on shaking table tests and analyses. In case of the large displacement along a gentle slope, countermeasures by strengthening the ground with sand piles, steel piles, densification at a narrow band or continuous walls were studied. The effectiveness and the limitation were clarified. Moreover, effectiveness of the countermeasure in the full scale ground was studied by some analyses. In case of the lateral flow, increasing of earth pressure due to liquefaction were studied.

IDEAS OF COUNTERMEASURES AGAINST LARGE GROUND DISPLACEMENTS

According to the studies on large ground displacements during past earthquakes, the large ground displacements due to liquefaction seem to be classified into two groups : ① large ground displacement along a gentle slope, and ② lateral flow near banks or seashores. Permanent ground displacements induced at Noshiro City and near Niigata Station during the 1983 Nihonkai-chubu Earthquake and the 1964 Niigata Earthquake, respectively, belong to the first group. Lateral flow induced along the Shinano River and the Furutone River during the 1964 Niigata Earthquake and the 1923 Kanto Earthquake, respectively, are typical example of the second group.

It is not clear what kind of countermeasures are effective against the permanent ground displacement due to liquefaction on a gentle slope, because no countermeasures have been applied. However, the following three categories of countermeasures, as shown in Fig.1, seem to be effective : (1) improving the ground in all area by densification to prevent liquefaction, (2) strengthening structures to prevent damage, and (3) strengthening the ground with walls or steel piles, sand piles, densification at narrow bands, to prevent large ground displacement if liquefaction occurs.

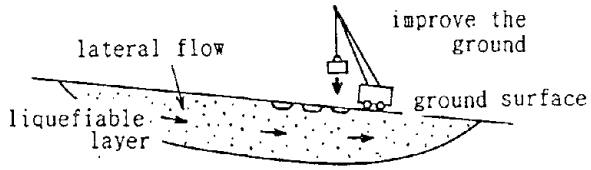

(a) Improving the ground in all area by densification to prevent liquefaction

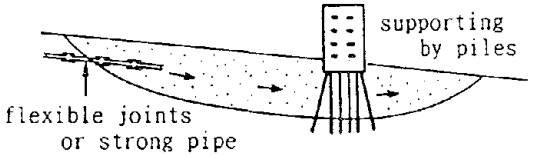

(b) Strengthening structures to prevent damage

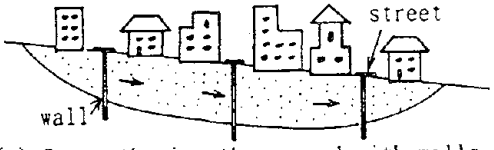

(c) Strengthening the ground with walls or steel piles, sand piles, densification at narrow bands, to prevent large ground displacement

Fig. 1 Three Categolies of Countermeasures against Permanent Ground Displacement on Gentle Slope

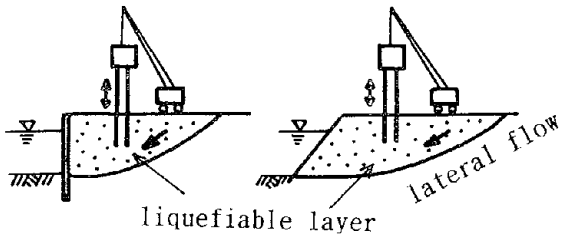

(a) Improving the ground behind quay walls or shores

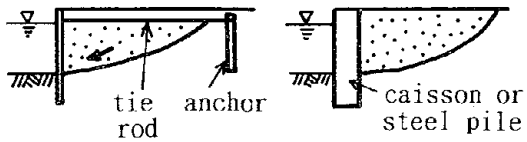

(b) Strengthening the quay walls

Fig. 2 Two Categories of Countermeasures against Lateral Flow near Banks or Seashores

Ground densification in all area is generally considered uneconomical, because it must be applied to a wide area. Different methods must be used to strengthen different structures making this approach somewhat impractical. Therefore, strengthening the ground by walls or steel piles, sand piles, densification through a narrow band was studied by shaking table tests and analyses.

In case of the lateral flow near banks or seashores, the following two categories of countermeasures, as shown in Fig.2, seems to be effective: (1) improving the ground behind quay walls or shores, and (2) strengthening quay walls to prevent damage. In the second method, earth pressure during liquefaction must be considered into the design of the quay wall. Therefore, increment of earth pressure acting on a quay wall due to liquefaction was studied by shaking table tests.

SHAKING TABLE TESTS ON COUNTERMEASURES AGAINST PERMANENT GROUND DISPLACEMENT ON GENTLE SLOPES

Shaking table tests to ascertain effective countermeasures against permanent ground displacement due to liquefaction on gentle slopes were carried out by using a soil container shown in Fig.3. Sand used was Toyoura Sand, which is

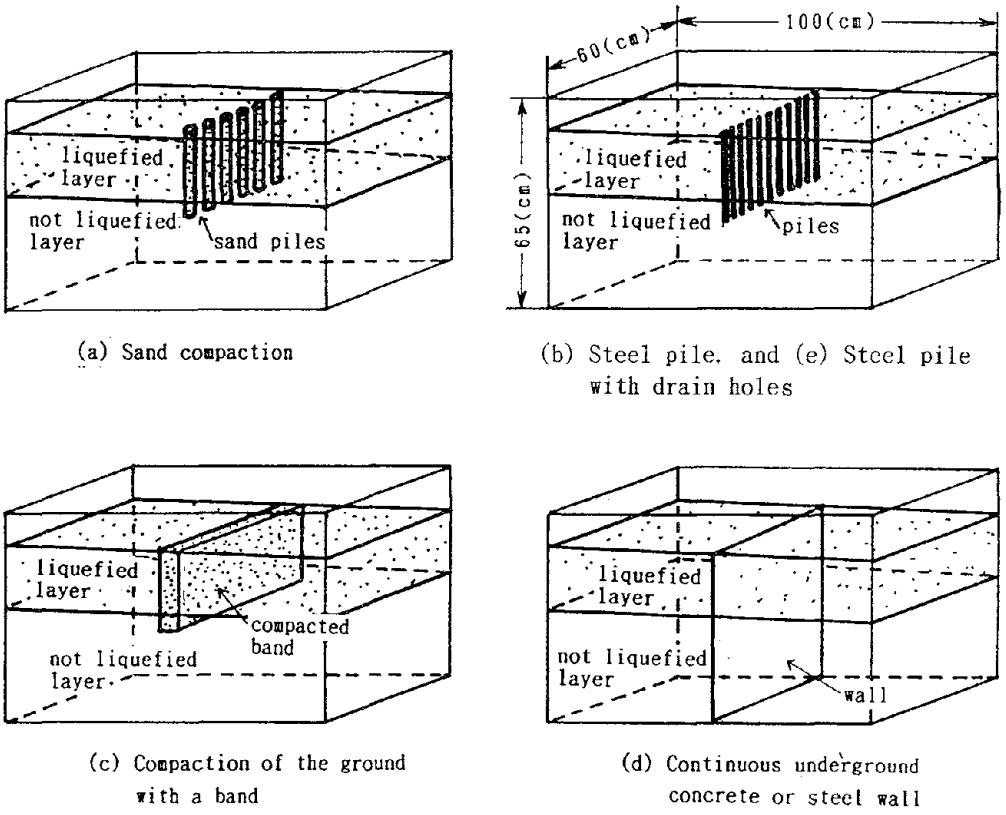

(a) Sand compaction

(b) Steel pile, and (e) Steel pile with drain holes

(c) Compaction of the ground with a band

(d) Continuous underground concrete or steel wall

Fig. 3 Models of Countermeasures in Shaking Table Tests

a clean sand, and the relative density of the loose layer, which is the liquefied layer, was arranged as 30% in cases of (a), (b), (c) and (d), and 50% in case of (e). Five types of countermeasures were applied to the model ground, (1) sand compaction, (2) steel piles, (3) compaction of the ground with a band, (4) continuous underground concrete or steel wall, and (5) steel piles with drain holes. The following models were used for the five types of countermeasures in considering scale effects:

(1) In the sand compaction method, aluminum piles of 2 cm in outer diameter were stood in the dense layer, which is the not-liquefied layer, with a depth of 5 cm. Then the loose layer, which is the liquefied layer, was filled with the pipes erect. After filling the loose layer, the pipes were pulled out and some Toyoura Sand was poured into the holes. The sand in the holes was compacted by pushing a rod to a relative density of almost 90 % to 100 %. Tests were conducted under three conditions. The number of the compacted sand piles and rate of replacement in each case is shown in Table 1(a).

(2) In the steel pile method, vinyl chloride piles of 1.8 cm in outer diameter and 2.5 mm in thickness were used. The method of erecting the piles and of filling the loose layer were also the same as in the sand compaction method. Young's modulus of the piles was 32,000 kgf/cm^2. In this method, piles were stood in one row or in two rows with triangle

Table 1 Test Conditions of Countermeasures

(a) Sand Compaction

Case No.	Number of piles	Rate of replacement As (%)
S-1	6	3.1
S-2	8	5.6
S-3	10	8.7

(b) Steel pile

Case No.	Number of piles	Pitch of piles(cm)	Number of rows
P -1	10	6	1
P -2	12	5	1
P -3	15	4	1
P -4	20	3	1
PT-1	15	7.5	2
PT-2	20	5.8	2

(c) Compaction of the ground with a band

Case No.	Thickness of the compacted band (cm)
W-1	0.5
W-2	1.0
W-3	1.5
W-4	2.0

(d) Continuous underground concrete or steel wall

Case No.	Thickness of the wall (cm)
A-1	0.2
A-2	0.3

(e) Steel pile with drain holes

Case No.	Drain	No. of piles	Pitch (cm)	No. of rows
D-1	with	10	6	1
D-2	with	15	4	1
D-3	with	5	12	1
P-1	without	10	6	1
P-2	without	15	4	1
DT-1	with	10	12	2
DT-2	with	15	7.5	2

alignment. Test conditions are shown in Table 1(b).

(3) Instead of vinyl chloride pipes, two sheets of walls made of aluminum, with a thickness of 2 mm, were used in the ground compaction with a band method. The depth of installation of the walls, method of filling loose layer, and method of compacting the sand in the trench after pulling out the walls were the same as in the sand compaction method. Four thicknesses of the compaction band were tested, as shown in Table 1(c).

(4) In the continuous underground concrete or steel wall method, an acrylic wall of 2 mm or 3 mm in thickness was used, as shown in Table 1(d). The wall was stood on the bottom surface of the soil container. Eight pieces of strain gauges were pasted on the wall to measure the bending strain of the wall due to earth pressure. Installation of the wall and method of filling loose layer were the same as in the steel pile method.

(5) In the steel pile with drain holes method, polycarbonate piles of 2.2 cm in outer diameter and 1 mm in thickness were used. The piles have many

holes of 5 mm in diameter and covered with screens, for drainage. The areal ratio of holes to the surface of a pile was 5.6%. Young's modulus of the piles was 20,000 kgf/cm^2. The method of erecting the piles and of filling the loose layer, and the alignment of the piles were the same as the steel pile method. Tests of polycarbonate piles under closing the holes were also conducted to make clear the effect of drainage. Test conditions are shown in Table 1(e).

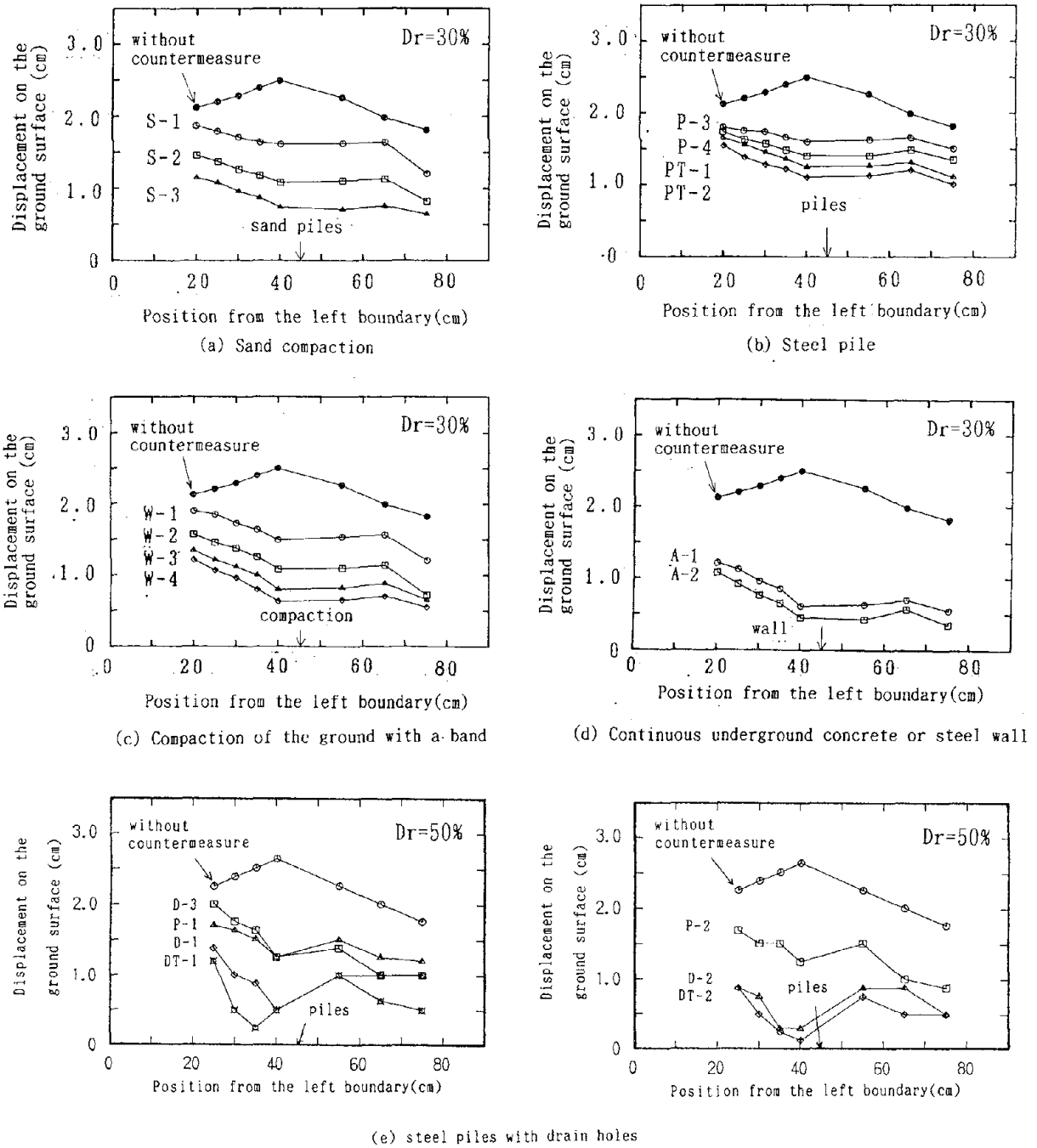

Fig. 4 Measured Displacement in Shaking Table Tests

In all tests, the thickness of the loose layer was 20 cm, and slopes of the ground surface and bottom surface of the loose layer were 3 %. Models were shaken in the perpendicular direction to the horizontal axis in cases of (a), (b), (c) and (d), and parallell direction in case of (e), according to a 3 Hz sine wave up to 10 seconds after the occurrence of liquefaction.

Fig.4 shows the measured displacements on the ground surface after stopping the shaking. Without countermeasures, displacements of 2 to 2.5 cm occurred on the ground surface, with the maximum value at the center. In contrast, displacements with countermeasures decreased to 2 cm to 2 mm, with the minimum value on the upper side, on the left side in the figure of the countermeasures. Fig.5 compares the displacements with rate of replacement, pitch of the steel piles, thickness of the compacted band, and thickness of the wall, in four types of countermeasures. It can be seen that displacements changed with these factors. In the steel pile method and the steel pile with drain holes method, an alignment with two rows was more effective than an alignment with one row if the numbers of piles were the same. In case of the continuous underground wall method, the distribution

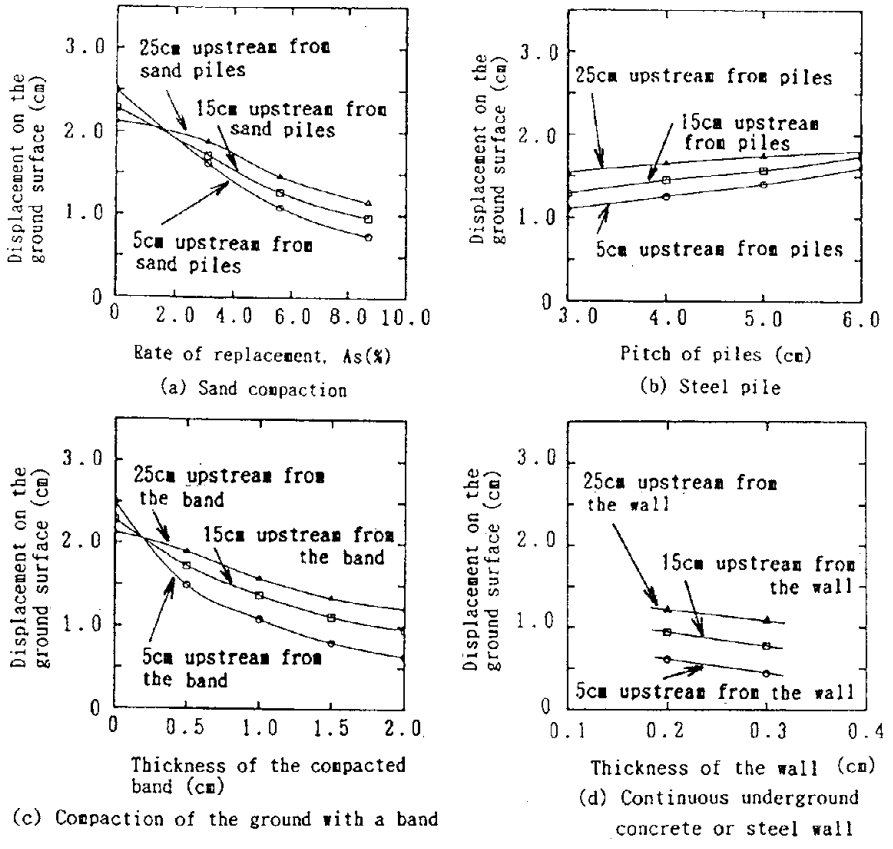

Fig. 5 Effect of Countermeasures in Shaking Table Tests

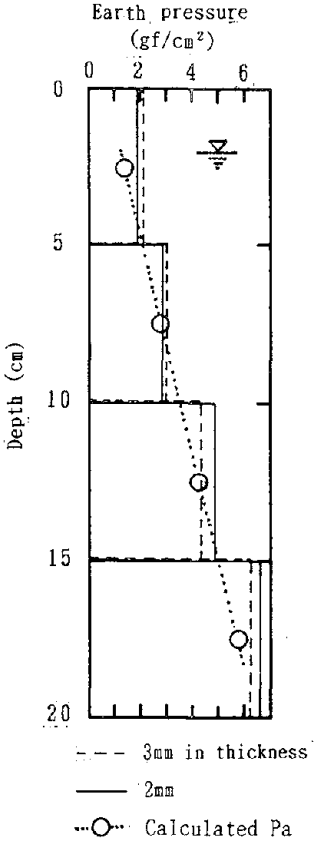

Fig. 6 Distribution of Earth Pressure

of earth pressure acting on the wall was estimated as shown in Fig.6 based on the measured strain and Young's modulus of the wall. The distribution curve was almost triangular. Open circles in the Fig.6 show calculated active earth pressures in static condition. As the open circles are close to the solid and broken lines, it can be said that the earth pressure acting on the wall due to liquefaction-induced ground deformation, is not so large, and the pressure approximates to the active earth pressure in static condition. However, the earth pressure due to liquefaction-induced ground deformation may change with deformation of the wall. In case of the steel pile with drain holes method, displacements decreased with the effect of drainage.

Displacements with an underground wall were the smallest among the four types of countermeasures, as shown in Fig.4. In the sand compaction method or steel pile method, some soil-flow through the piles was induced. And, in the ground compaction with a band, some bending of the compacted band occurred due to inadequate stiffness of the compacted band. Therefore, it can be said that the continuous wall method is the most effective among the four methods. However, stress induced in the wall must be evaluated during the design of the wall.

ANALYSES FOR THE EFFECTIVENESS OF COUNTERMEASURES IN THE GROUND

To know the effectiveness of the countermeasures, mentioned above, in the ground, several analyses were performed based on a simple method proposed by the authors (Yasuda et al. 1992), assuming different countermeasure parameters, on a ground model of 100 m in length, with a liquefied layer 10 m in thickness and a 3 % slope of the ground surface. Among the five types of countermeasures by the compaction of the ground with bands and the continuous underground concrete or steel wall were selected for the analyses. The SPT-N values of liquefied layer and the non-liquefied layer were assumed as 3 and 30, respectively. The rate of decrease of the elastic modulus due to liquefaction and Poisson's ratio were supposed as 1/1000 and 0.499, respectively according to the previous study (Yasuda et al. 1992).

In the case of the compaction of the ground with bands, the analyses were conducted under the following conditions: (1) number of compacted band was one and depth of the band was varied from 0 m to 10 m with a constant width of 4 m, (2) number of compacted band was one and width of the band was varied from 0 m to 16 m with a constant depth of 10 m, and (3) numbers of compacted bands were varied from 1 to 7 with a constant width and depth of 4 m and 10 m, respectively. In the case of the continuous underground concrete or steel wall, Young's modulus of the wall was varied from 100 kgf/cm^2 to 1,000,000 kgf/cm^2 with a constant width of 0.4 m.

Fig.7 shows typical analyzed deformations of the compaction of the ground with bands. Deformations close to the compacted bands on the upstream side were decreased due to the countermeasure. Displacements at points P and Q

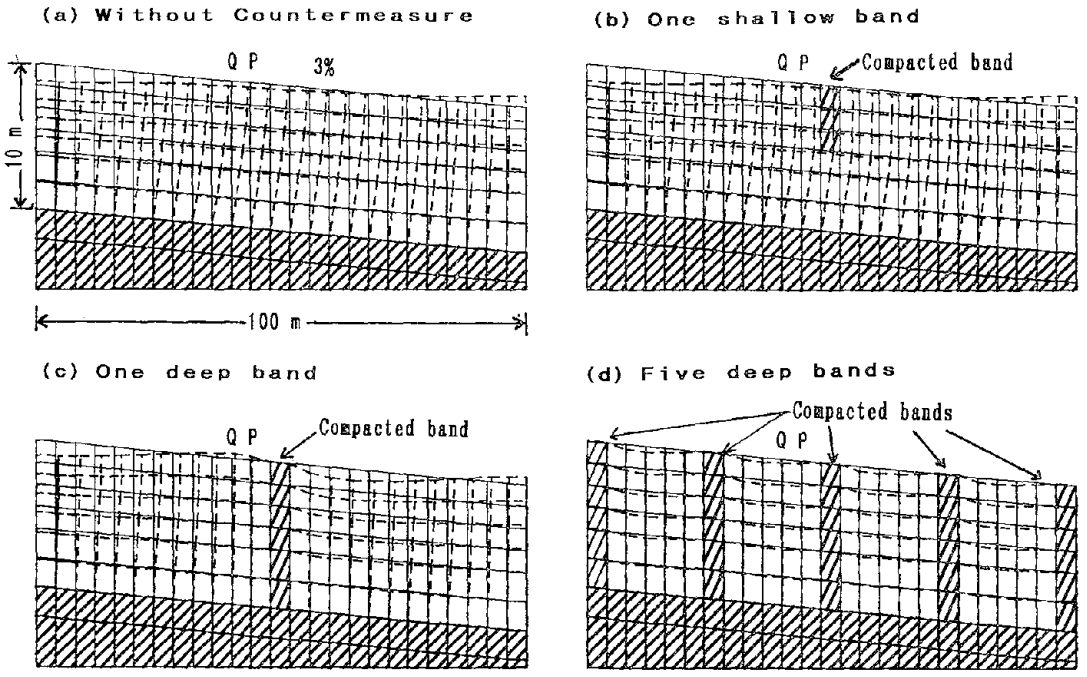

Fig. 7 Typical Analyzed Deformations of the Compaction with Bands

which are 4 m and 8 m apart from the compacted band as shown in Fig.7, were plotted against the depth of the band, the width of the band and the numbers of bands in Fig.8, Fig.9 and Fig.10, respectively. Effectiveness of the countermeasure decreased if the compacted zone did not reach the bottom of the liquefied layer as shown in Fig.8. Effectiveness of the countermeasure was no more change if the width of the compacted band beyonded about four meters as shown in Fig.9. Displacements at points P and Q decreased with the pitch of the compacted bands as shown in Fig.10.

Fig.11 shows three analyzed deformations of the continuous underground concrete or steel wall. Deformations close to the wall on the upstream side were decreased due to the countermeasure. Fig.12 shows relationships between displacements at points P and Q, which are 4 m and 8 m apart from the wall, respectively, and Young's modulus of the wall. The displacements decreased with stiffness of the wall.

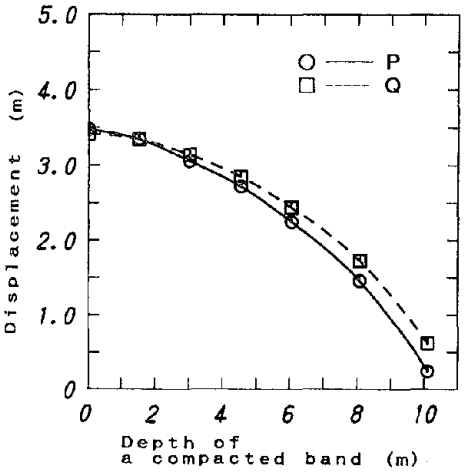

Fig. 8 Relationships between Displacements and Depth of a Compacted Band

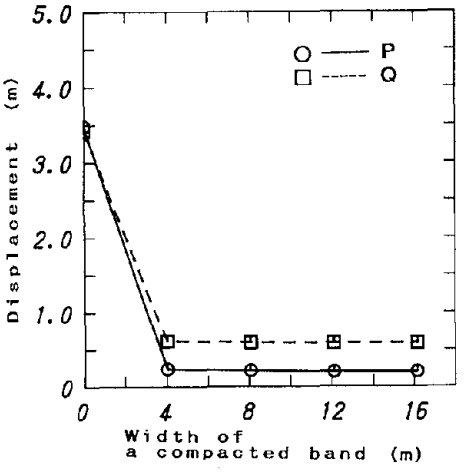

Fig. 9 Relationships between Displacements and Width of a Compacted Band

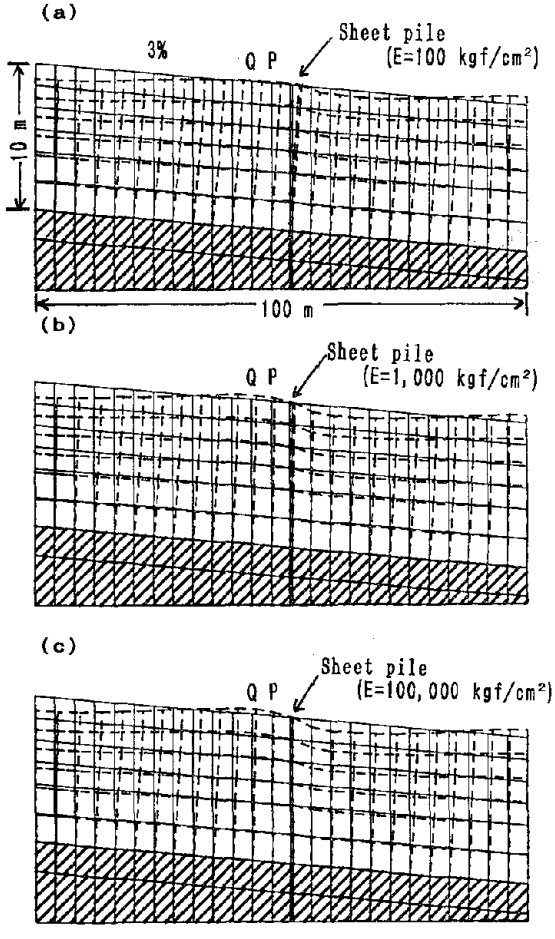

Fig. 11 Analyzed Deformations of Continuous Underground Concrete or Steel Wall

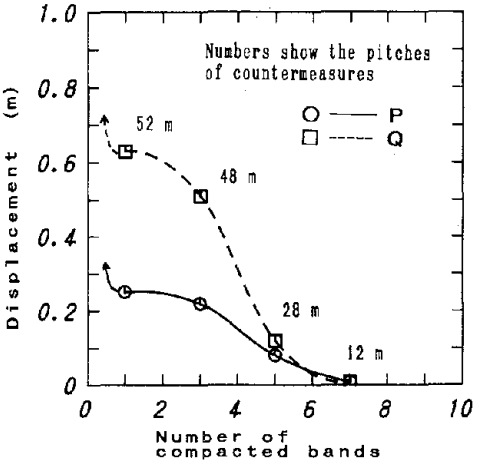

Fig. 10 Relationships between Displacements and Number of a Compacted Bands

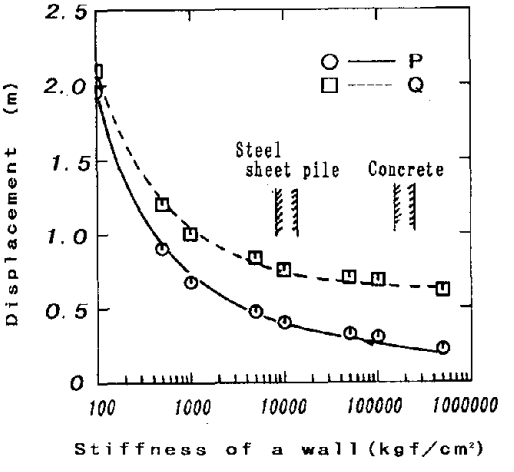

Fig. 12 Relationships between Displacement and Stiffness of the Wall

SHAKING TABLE TESTS ON EARTH PRESSURE

According to Tsuchida (1968), the coefficient of earth pressure acting on a quay wall increases to about 1.0 if the ground behind the quay wall is liquefied.

In view of the findings of displacements at oil storage district of Akita Port during the 1983 Nihonkai-chubu Earthquake (Hamada, et al., 1988), if the bottom surface of the liquefied layer behind the quay wall is sloped toward the sea or river with an angle of θ_b, as shown in Fig.13(a), it is supposed that the earth pressure acting on the quay wall as a result of liquefaction is greater than the earth pressure when $\theta_b = 0$: On the contrary, if the bottom surface is sloped in the opposite direction, as shown in Fig.13(b), the earth pressure is assumed to be smaller than the pressure when $\theta_b = 0$: In general, the slope of the bottom surface of the liquefied layer toward the sea or river is considered to be more common in-situ than the opposite case, because most of the ground in the vicinity of quay walls is reclaimed land. However, it is considered possible that the bottom surface of the liquefied layer may slope away from the sea or river if the quay wall is constructed at a site with different ground conditions, such as the oil storage district of Akita Port. Therefore, shaking table tests were conducted using both patterns.

In the tests, a container, of 80 cm in length, 70 cm in depth and 50 cm in width shown in Fig.14 was used. In the container, a retaining wall of aluminum plate was installed with reinforcement.

Total earth pressure was measured using a loadcell, assuming that the retaining wall of the model is hard enough to resist deformation by earth pressure. In this case, it was supposed that the earth pressure was distributed in the shape of a right angled triangle with depth. This assumption is absolutely valid. Therefore, two series of tests were performed; one was conducted with the hinge connection at the bottom edge and the load cell at the top edge; the other was the opposite case. In these tests, the slope of the bottom of the liquefied layer θ_b was varied from -10 % to 10 %. The soils used for the tests were clean sand and sand with 6 % of fines.

The coefficient of earth pressure was measured at three points during the test: (1) after the dry sand was poured into the soil container through a sieve in air, (2) at the time the ground water level was raised to a depth of 4 cm from the ground surface, (3) during shaking.

The earth pressure increased as the excess pore water pressure builds up, and it reaches a maximum value at the onset of initial liquefaction. After the shaking, the earth pressure decreased as the excess pore water pressure dissipates.

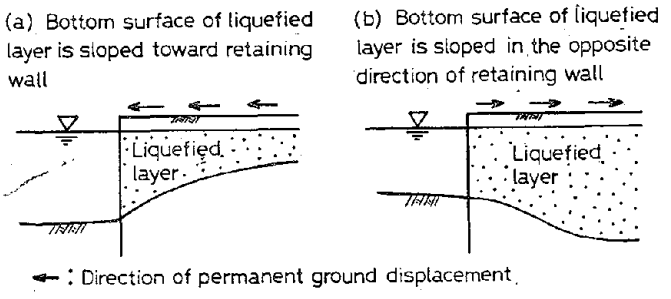

Fig. 13 Schematic Illustrations of Two Types of the Liquefied Layer

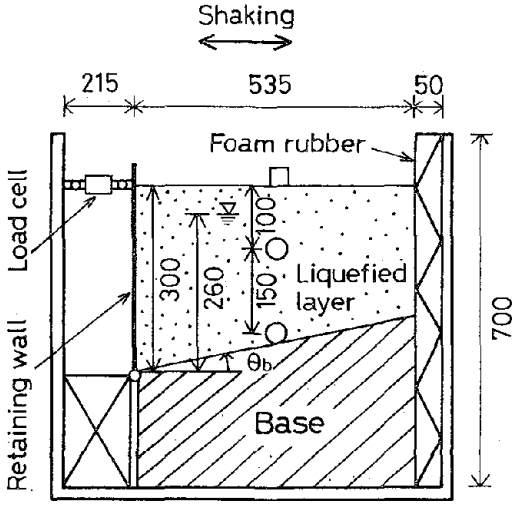

Fig. 14 Soil Containers and Models of Shaking Table Test

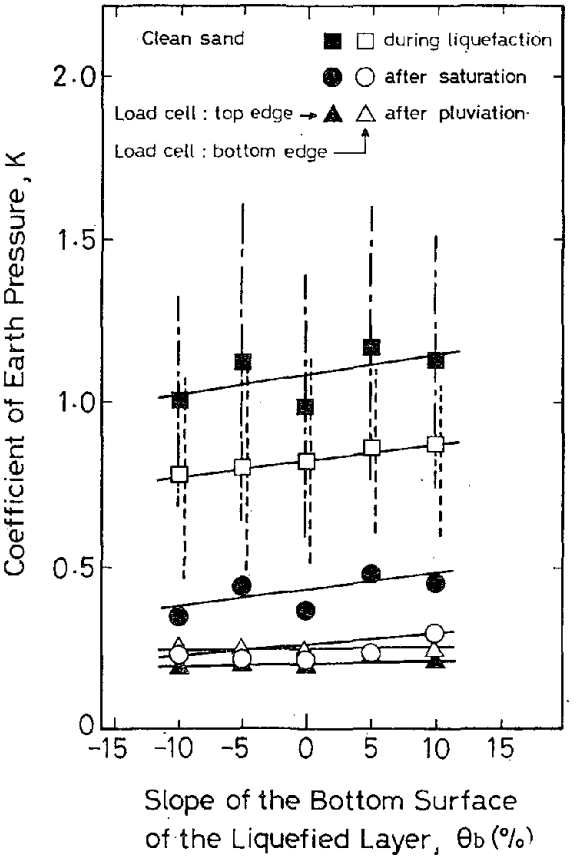

Fig. 15 Relationships between K and θ_b of Clean Sand

Fig.15 indicates the coefficient of the earth pressure, K, obtained by assuming that the earth pressure is distributed in the shape of a right-angled triangle with depth, as described above. After the dry sand was poured into the soil container, the value of the coefficient K was 0.2 to 0.3, irrespective of the slope of the bottom of the liquefied layer θ_b. When the sand layer was saturated by raising the ground water level to a desired depth, the value of K was nearly 0.4 and varies with θ_b. At the onset of liquefaction, K reached about 1.0 and varies with θ_b. The coefficient of earth pressure measured by a loadcell at the top edge differed slightly from the coefficient measured at the bottom edge. The distribution of the earth pressure was not precisely in the shape of a right-angled triangle. The dashed lines and the chain lines in Fig.15 denote amplitudes of the dynamic component of the earth pressure. Averages of the maximum and minimum value of these amplitude are plotted in Fig.15 using the marks □ and ■.

CONCLUSIONS

Large ground displacement due to soil liquefaction brings severe damages to many structures. To study the effectiveness of countermeasures on a gentle slope by strengthening the ground, several shaking table tests and analyses were conducted. Five type of strengthening method were selected: (1) sand compaction, (2) steel pile, (3) compaction of the ground with a band, (4) continuous underground concrete or steel wall, and (5) steel piles with drain holes. In all shaking table tests, the amount of the ground displacement of some area close to the countermeasures was decreased. The most effective method was the continuous wall method. Analyses on a ground model of 100 m in length also showed that the amount of the displacement was decreased by installing the continuous wall, or by compacting the ground with bands. Moreover, increment of earth pressure acting on a quay wall was studied by shaking table tests. Test results showed that the coefficient of the earth pressure reached to about 1.0 at the onset of liquefaction, and the coefficient increased slightly with the slope of the bottom surface of the liquefied layer.

REFERENCES

1) Hamada,M., Yasuda,S., Isoyama,R. and Emoto,K. : Study on Liquefaction Induced Permanent Ground Displacements: Association for the Development of Earthquake Prediction, 1986.
2) Hamada,M., Wakamatsu,K. and Yasuda,S. : Liquefaction-Induced Ground Displacement During the 1948 Fukui Earthquake, Proc. from the 2nd U.S.-Japan Workshop on liquefaction, Large Ground Deformation and Their Effects on Lifelines, pp.6-15, 1989.
3) Wakamatsu,K., Hamada,M., Yasuda,S. and Morimoto,I.: Liquefaction Induced Ground Displacement During the 1923 Kanto Earthquake, ditto, pp.36-49, 1989.
4) O'Rourke,T.D., Roth,B.L. and Hamada,M. : A Case Study of Large Ground Deformation During the 1971 San Fernando Earthquake, ditto, pp.50-66, 1989.
5) Yasuda,S., Hamada,M., Wakamatsu,K. and Morimoto,I. : Liquefaction Induced Permanent Ground Displacements in Niigata City, ditto, pp.67-81, 1989.
6) Yasuda,S., Nagase,H., Kiku,H. and Uchida,Y. : The Mechanism and a Simplified Procedure for the Analysis of Permanent Ground Displacement due to Liquefaction: Soils and Foundations, Vol.32, No.1, pp.149-160, 1992.
7) Tsuchida,H. : Study on Lateral Earth Pressure and Dynamic Pore Water Pressure of Water Saturated Sand during Vibration: Tsuchi-to-kiso, JSSMFE, Vol.16, No.5, pp.3-10 (in Japanese), 1968.
8) Hamada,M., Yasuda,S. and Wakamatsu,K. : Case Study on Liquefaction-

Induced Ground Failures during Earthquakes in Japan, 1st Japan-US Workshop on Liquefaction, Large Ground Deformation and Their Effects on Lifelines, pp.3-21, 1988.
9) Yasuda,S., Nagase,H., Kiku,H. and Uchida,Y. : Effect of Permanent Ground Displacement on the Damage to Quay walls : Proc. of the International Conference on Geotechnical Engineering for Coastal Development, pp.525 -530, 1991.

Small Scale Tests on Countermeasures against Liquefaction for Pipelines Using Gravel Drain System

Masakatsu MIYAJIMA

Associate Professor
Kanazawa University, Kanazawa, JAPAN

Masaho YOSHIDA

Research Associate
Fukui National College of Technology, Sabae, JAPAN

Masaru KITAURA

Professor
Kanazawa University, Kanazawa, JAPAN

ABSTRACT

The present paper deals with small scale tests on application of gravel drain system to buried pipelines as a countermeasure against soil liquefaction. Construction of gavel drain system has no great vibration and noise, therefore it can be applicable to sites in urban areas and near buildings. This system has constructed at many sites as a countermeasures for buildings . The purposes of the paper are to investigate the effects of gravel drain system to performance of pipelines during an earthquake and to clarify the problems which should be solved before gravel drain system is designed for buried pipelines. Two types of gravel drain system are focused in this paper; one is gravel wall and the other is gravel pile. The following conclusions are obtained. The effect of gravel drain system is to reduce the maximum excess pore water pressure and duration of liquefaction. Therefore, the settlement of ground around pipelines can be reduced and the duration of vibration strains of the pipeline also can be reduced. The effect of the system is, however, sensitive to the distance between piles.

INTRODUCTION

Countermeasures for pipelines against liquefaction could be classified into two categories as follows. One is a countermeasure for pipelines themselves and the other is that for the surrounding soil. The countermeasure for surrounding soil is focused in this paper, because it can be applicable to not only pipelines to be newly constructed but also existing pipelines. According to the results of a questionnaire survey for construction companies in Japan, a sand compaction method was the most popular countermeasure and a drain system was more for five and a half years (1985-1990) [1]. The drain system includes not only gravel but also steel and polyethylene as the materials in this survey. Construction of gravel drains produces no great vibration and noise in comparison with the sand compaction, therefore they can be applicable to sites in urban areas and near buildings. The number of construction of drain system was 102 sites for the five and half years but only six cases for underground structures, that is, pipelines, common ducts and foundations of steel tower [1].

The purposes of the present paper are to study the effects of gravel drain system to performance of pipelines during an earthquake and to clarify the problems which should be solved before the gravel drain system is designed for pipelines. Two types of gravel drain system are focused in this paper; one is gravel wall and the other is gravel pile as shown in Fig. 1. Small scale vibration tests were conducted and the performance of a model ground and pipe were measured.

GRAVEL WALL TYPE

Test Procedure

The general view of test apparatus is shown in Fig. 2. The size of a sand box is 500 mm in width, 1500 mm in length and 350 mm in height. Loose and densified saturated sand layers, whose thickness was 200 mm, were made in it. The model buried pipe was simulated by a rubber rod with 20 mm in diameter and 1000 mm in length. Its elastic modulus was 810 kgf/cm^2 (79.4 MPa). Strain gauges were utilized on it. Gravel drain system was constructed by stuffing No. 5 crushed stone and it was covered by nylon mesh and wire mesh in order to stabilize the walls and to prevent sand transferring into gravel, respectively. The width of the gravel wall was 50 mm and its height was 100 mm. The physical properties of the sand, gravel and model pipe are listed in Table 1 and physical properties of model ground are listed in Table 2. The model sand layer was vibrated by a harmonic wave with 5 Hz. Target acceleration of the table was 100 gal and it took about 5 seconds for the table to reach the given acceleration. The duration of the test was 30 seconds. Pore pressure transducers were installed in the saturated sand layer to measure the excess pore water pressure during excitation. After excitation, settlements of the ground and residual displacement of the pipe were measured. The test without the gravel drain was also conducted in order to compare the results with each other.

Tests Results and Discussion

Test results using improved and unimproved ground are illustrated in Figs. 3 and 4, respectively. These figures indicate the time histories of the input acceleration, excess pore water pressure and axial pipe strains. The time histories of the excess pore water pressure suggest that the model ground with gravel drain system also reached complete liquefaction but the gravel drain system reduced the duration of complete liquefaction. In case of unimproved ground (Fig. 4), the axial vibration strain at the boundary between the liquefied and non-liquefied ground (SG5 and SG6)

was great . Residual strains were greater than vibration strains at the other parts. This can be explained by the pipe floating at the center of liquefied ground. In case of improved ground (Fig. 3), the duration time of greater vibration strains became short due to the short duration of complete liquefaction, however the value of vibration strains was not reduced. The time when the greater vibration strains occurred coincided with the time of complete liquefaction of the ground under the gravel wall. Therefore, it is conceivable that preventing liquefaction of the ground under the gravel wall could be needed in order to reduce vibration strains. The height of gravel wall is one of the key parameters.

GRAVEL PILE TYPE

Test Procedure

The general view of test apparatus is shown in Fig. 5. The gravel pile is 50 mm in diameter and 200 mm in height, that is, the same height of the model sand layer. Gravel piles were constructed by stuffing No. 5 crushed stone and it was covered by nylon mesh and wire mesh in order to stabilize the piles and to prevent sand transferring into gravel, respectively. Seven series of shaking table tests were conducted under the conditions listed in Table 3. There were basically two groups of tests; one group was the tests in variety of the distance between piles in parallel to the pipe axis (Variation-I), the other was the tests in variety of that in perpendicular to the pipe axis (Variation-W). Moreover, the test without the gravel pile was conducted in order to compare the results of these groups with each other. The target acceleration of the shaking table was 200 gal in these series of tests.

Test Results and Discussion

The time histories of excess pore water pressure ratio are illustrated in Fig. 6. The excess pore water pressure was measured at the same depth of the model pipe. These figures indicate that the duration time of liquefaction of the ground with gravel piles was shorter than that of the ground without gravel piles. The shorter the distance between piles were, the smaller the maximum excess pore water pressure ratio. Fig. 7 shows the settlement of the model ground surrounded by gravel piles. The shorter the distance between the piles became, the smaller the settlements of ground. This indicates that the gravel piles reduced the excess pore water pressure, thus the ground settlement was also reduced. On the other hand, difference of settlement between the inner and outer ground of the gravel piles occurred. As the settlements of the outer ground had not much difference in each case, the differences of the settlement between the inner and outer ground increased with a decrease in the distance between the piles as shown in Fig. 8.

Vertical displacement of the model pipe is shown in Fig. 9. The vertical displacement means that the variety of the average thickness of soil above the model pipe after excitation. Therefore it includes the amount of pipe floating and settlement of the ground above the pipe. The vertical displacement of the pipe at the ground with gravel piles was smaller than that without gravel piles and it was more sensitive to the distance between piles in parallel to the pipe axis (Variation-I) rather than that in perpendicular to the pipe axis (Variation-W). When the distance between piles in parallel to the pipe axis decreases, number of gravel piles increase, thus, effects of gravel piles increase. Therefore, the distance between piles affects the vertical displacement of pipe directly. The optimum distance between piles should be given from the point of economical aspects in design.

Fig. 10 shows the relationship between the excess pore water pressure ratio and vibration strains at the strain gauge SG2 (See Fig. 5). The interval between two points indicates a time lapse of

0.5 sec. This figure suggests that the period when the vibration strains become great coincides with that when the excess pore water pressure ratio is 0.7 to 0.95, that is, when the model ground incompletely liquefies. These results confirm that the longer the period of the incomplete liquefaction of the ground, the longer the period of great vibration strains. It has good agreement with the another test results obtained by authors [2]. Therefore, the target excess pore water pressure ratio should be set under 0.7 or less in design. According to Fig. 10, the vibration strain took the maximum value in case of the greatest distance between piles in parallel to the pipe axis. When the distance in parallel to the pipe axis is great, the area where the effect of gravel piles does not reach exists along the model pipe.. Variety of the soil behavior along the model pipe occurs and, thus, the vibration strains become great. The distance between piles should be determined from this point of view.

CONCLUSIONS

The present paper experimentally investigated the application of gravel drain system to buried pipelines as a countermeasure against soil liquefaction. Findings in the paper can be summarized as follows;

(1) The effects of gravel drain system is to reduce the maximum excess pore water pressure and duration of liquefaction.

(2) The settlement of ground around pipe can be reduced and duration of vibration pipe strains also can be reduced.

(3) The time when greater vibration strains occurred coincided with the time of complete liquefaction of the ground under the gravel wall. Therefore, it is conceivable that preventing liquefaction of the ground under gravel wall could be needed in order to reduce vibration strains.

(4) The effects of gravel piles is sensitive to the distance between piles. The settlement of the ground surrounded by gravel piles decreased with a decrease in the distance between the piles. On the other hand, the vibration pipe strains became great when the distance in parallel to the pipe axis was great. Therefore, the distance between piles should be determined from these points of view.

ACKNOWLEDGEMENTS

A part of expense of this study defrayed by the Grant-in-Aid for scientific research from the Ministry of Education, Science and Culture of Japan. The authors also wish to thank the research grant from NKK Corporation.

REFERENCES

1) Tanaka, Y., Nakajima, Y. and Tsuboi, H.: Countermeasures, Proc. of Symposium on Countermeasures on Soil Liquefaction, JSSMFE, pp. 15-40, 1992.

2) Kitaura, M., Miyajima, M. and Yoshioka, M.: Dynamic Behavior of Buried Model Pipe During Incomplete Liquefaction, Journal of Structural Engineering, JSCE, Vol. 31A, pp. 421-426, 1985.

Table 1 Physical properties of sand, gravel and model pipe.

Sand		
Specific gravity	2.67	
Uniformity coefficient	2.96	
Maximum void Ratio	1.030	
Minimum void Ratio	0.721	
50 Percent diameter	0.2	(mm)
Coefficient of permeability	1.92×10^{-2}	(cm/s)
Gravel		
Specific gravity	2.69	
Maximum grain size	25	(mm)
Coefficient of permeability	8.24	(cm/s)
Model pipe		
Young's modulus	810	(kgf/cm^2)
Unit weight	1.65	(gf/cm^3)
Length	1000	(mm)
Diameter	20	(mm)

Table 2 Physical properties of model ground.

Loose sand layer		
Wet unit weight	1.84	(gf/cm^3)
Void ratio	0.95	
Water content	34.2	(%)
Relative density	25.9	(%)
Dense sand layer		
Wet unit weight	1.90	(gf/cm^3)
Void ratio	0.87	
Water content	32.9	(%)
Relative density	51.8	(%)

Table 3 Test conditions of gravel pile type.

Case name	Code number	Interval of piles l (cm)	Width of piles W (cm)	Number of piles
Variation-I	I05	5	10	30
	I10	10	10	20
	I15	15	10	15
Variation-W	W05	10	5	20
	W10	10	10	20
	W15	10	15	20
No-countermeasure	NC	---	---	0

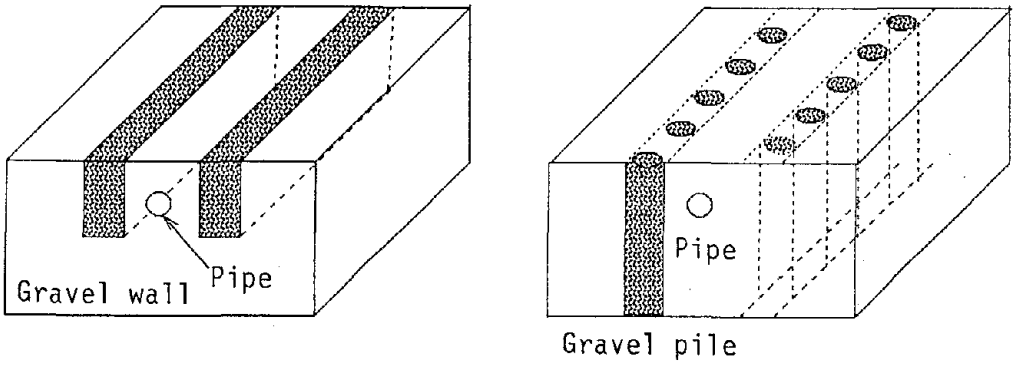

Fig. 1 Two types of gravel drain system.

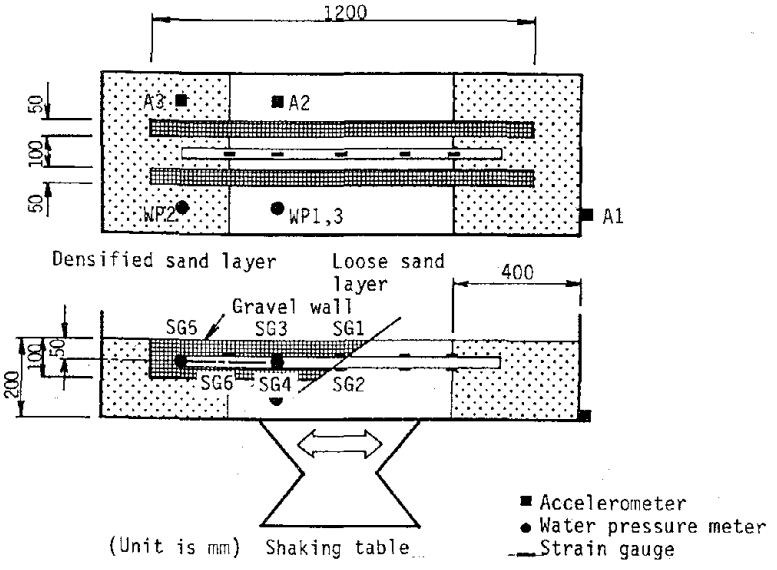

Fig. 2 Test apparatus of gravel wall type.

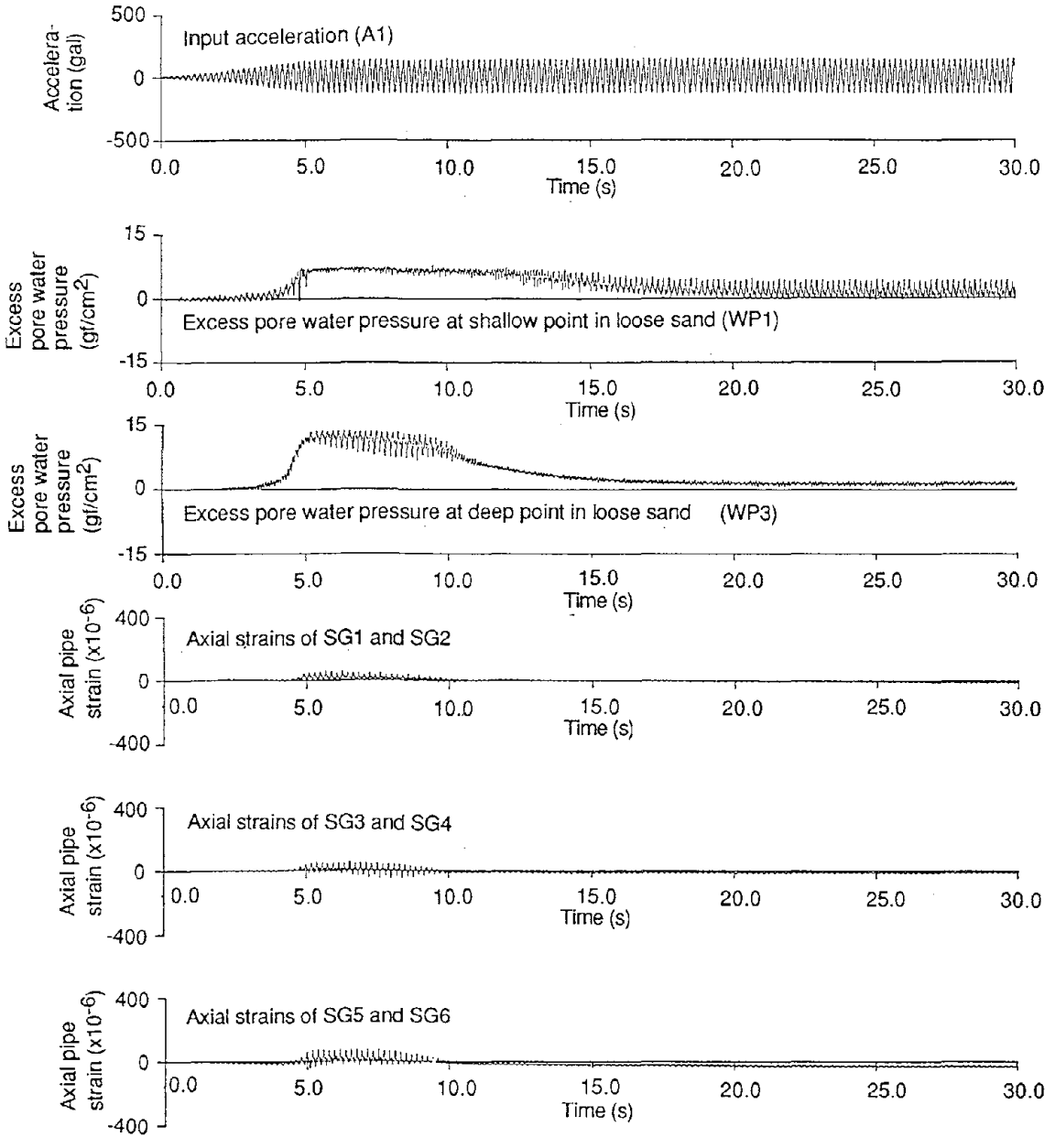

Fig. 3 Time histories of input acceleration, excess pore water pressure and axial pipe strain of improved ground.

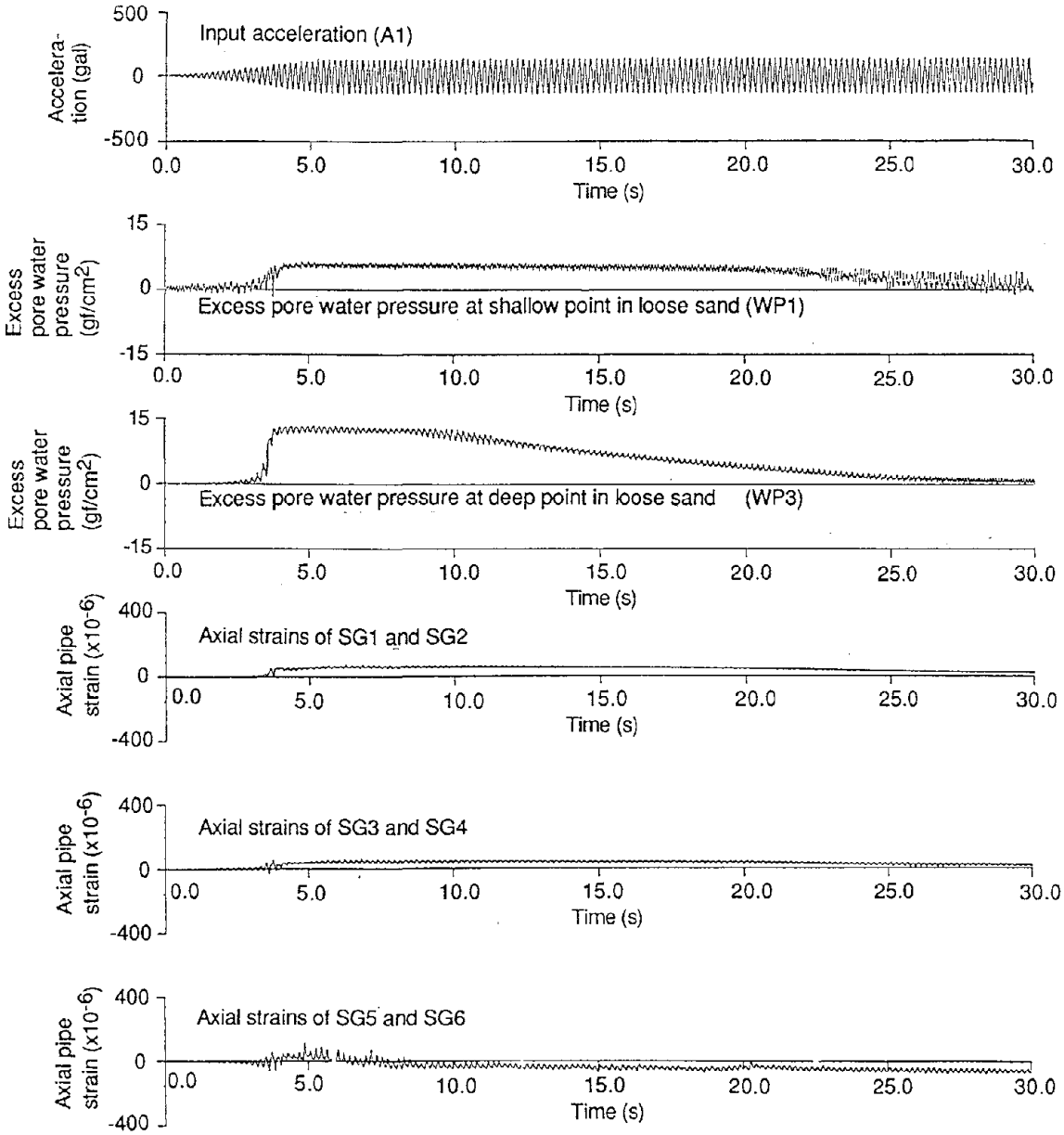

Fig. 4 Time histories of input acceleration, excess pore water pressure and axial pipe strain of unimproved ground.

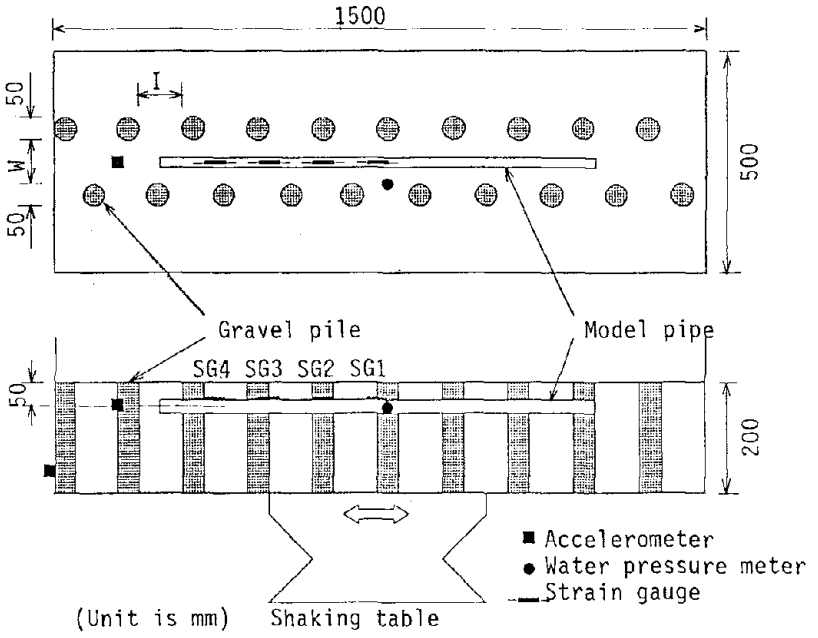

Fig. 5 Test apparatus of gravel pile type.

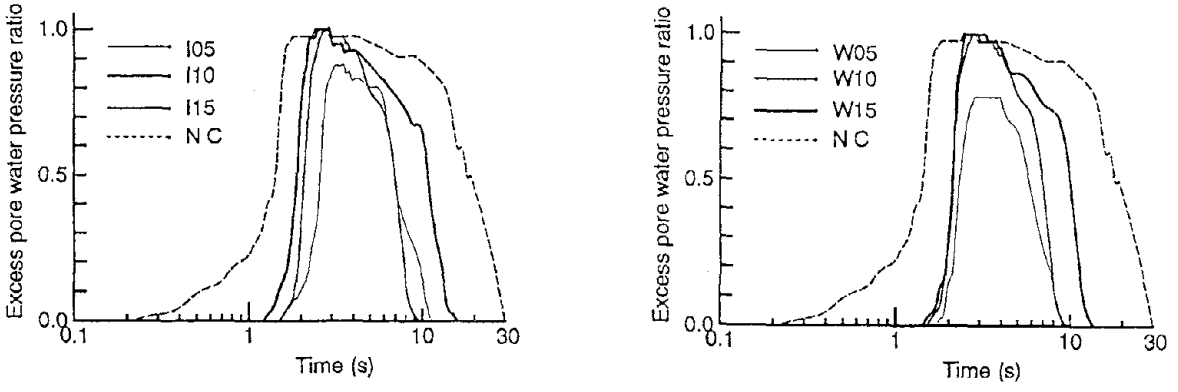

(a) Variation-I

(b) Variation-W

Fig. 6 Time histories of excess pore water pressure ratio.

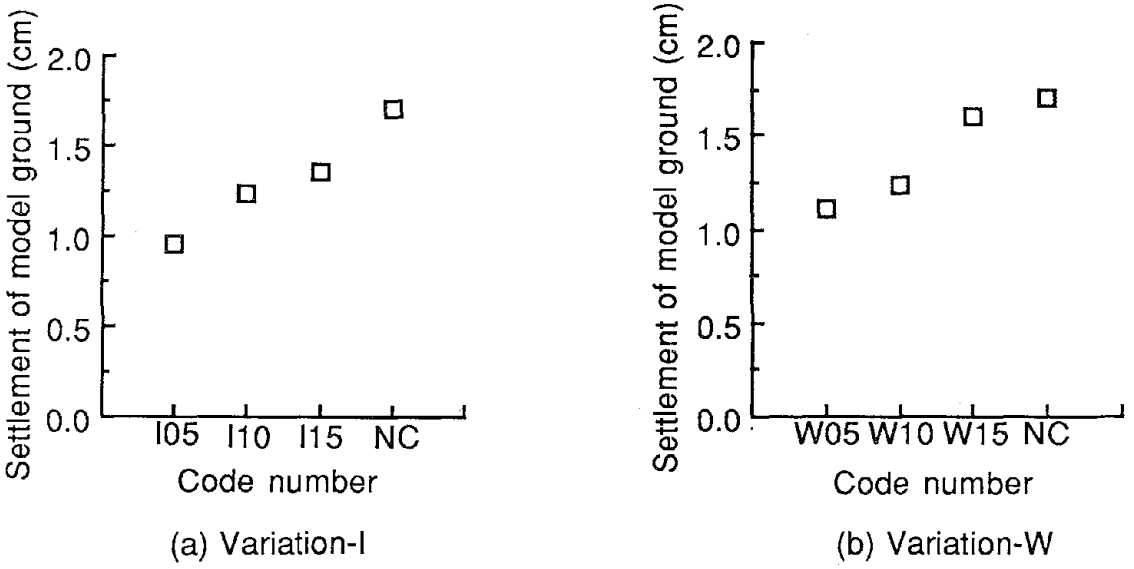

Fig. 7 Settlement of model ground surrounded by gravel piles.

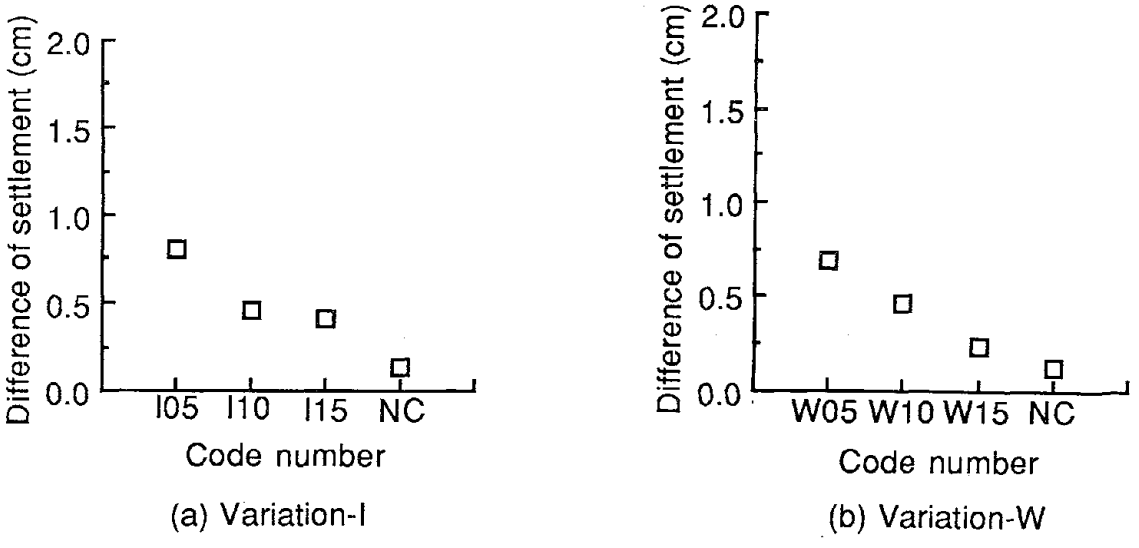

Fig. 8 Difference of settlement between inner and outer ground.

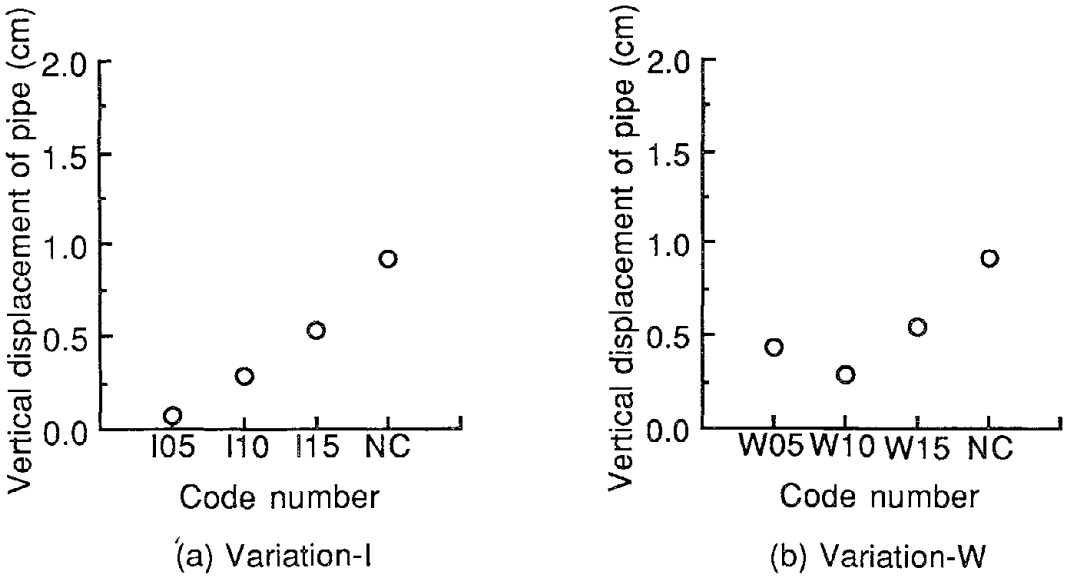

Fig. 9 Vertical displacement of model pipe.

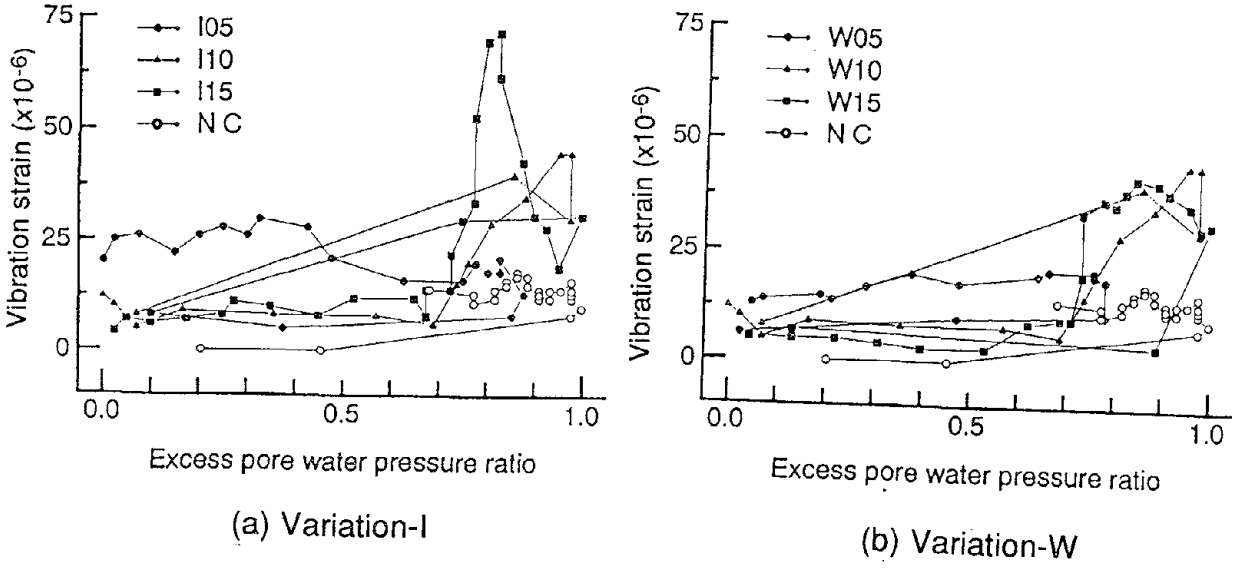

Fig. 10 Vibration strain of pipe in relation to excess pore water pressure ratio.

V Performance of Lifeline Facilities and Foundations During Liquefaction

Post-Liquefaction Consolidation and Lifeline Damage in the Marina District after the 1989 Loma Prieta Earthquake

J.W. Pease[1], T.D. O'Rourke[2], and H.E. Stewart[3]

ABSTRACT

The relationship between settlements caused by post-liquefaction consolidation and damage to buried lifeline systems is discussed. Settlement strains of submerged fill are used to evaluate the pattern of observed settlements. Vertical strains predicted with existing simplified procedures show good general agreement with observations, provided that the presence of non-liquefiable soils are accounted for properly. It appears that the post-liquefaction consolidation of hydraulic fill in the Marina was influenced by layers of fine-grained sediments. The resolution in delineating subsurface conditions with cone penetration test (CPT) measurements is shown to be an important factor in estimating the magnitude and extent of post-liquefaction consolidation in the hydraulic fill.

1, 2, 3 - Graduate Student, Professor, and Associate Professor, respectively, Cornell University, School of Civil and Environmental Engineering, Ithaca, NY 14853-3501

POST-LIQUEFACTION CONSOLIDATION AND LIFELINE DAMAGE IN THE MARINA DISTRICT AFTER THE 1989 LOMA PRIETA EARTHQUAKE

J.W. Pease, T.D. O'Rourke, and H.E. Stewart

INTRODUCTION

Post-liquefaction consolidation is the volume loss and settlement that result as soils densify during the dissipation of excess porewater pressures triggered by an earthquake. Post-liquefaction consolidation often develops in loose, saturated sands and silty sands, and thus represents a major hazard for the loose, sandy fills which comprise a substantial part of the waterfront properties in the San Francisco Bay region. Post-liquefaction settlement can damage structures founded on or within the soil mass.

After the 1989 Loma Prieta earthquake, water supply pipelines were damaged at several locations in San Francisco where soil liquefaction was observed. Pipeline damage in the Marina has been described by O'Rourke, et al. (1991a, 1991b), who have shown that loss of water in both the Municipal and Auxiliary Water Supply Systems of San Francisco was related directly to liquefaction-induced ground deformation.

This paper focuses on post-liquefaction consolidation and its effect on buried pipelines. The paper begins by reviewing the settlements in the Marina caused by post-liquefaction consolidation after the Loma Prieta earthquake, and explores the relationship between settlement and pipeline damage. Different types of soil are identified in the Marina. The average settlement and vertical strain associated with each type of soil are summarized. Comparisons are made between observed vertical strains and those given by the simplified prediction models of Tokimatsu and Seed (1987) and Ishihara and Yoshimine (1992). Special attention is given to the use of cone penetration tests (CPT) in conjunction with the Ishihara and Yoshimine model to predict vertical strains and settlements.

PATTERN OF SETTLEMENT AND PIPELINE DAMAGE

Settlement contours associated with post-liquefaction consolidation caused by the Loma Prieta earthquake are shown in Figure 1. They are superimposed on a map showing the current Marina street system, as well as the 1906 and 1857 shorelines (O'Rourke, et al., 1991a). Placement of fill and development in the Marina may be simplified as having occurred in two prominent stages. The first stage was associated with the placement of land-tipped, or end-dumped, fills until about 1900 adjacent to both the original shoreline and a previous sand spit, known as Strawberry Island. Some land-tipped fills were also placed as part of the seawall construction. The second major stage of filling occurred in 1912, when sandy sediments were dredged and pumped into the lagoon bounded by the old seawall. The expansion of land from 1857 to 1906 and from 1906 to current conditions represents the approximate locations of land-tipped and hydraulic fills, respectively.

To represent the distribution of damage in the Municipal Water Supply System (MWSS), the Marina was divided into a grid of approximately 40 cells, and the number of repairs per length of pipeline in each cell was counted (O'Rourke, et al., 1991a). Contours of equal repairs per 300 m reference length of pipeline were superimposed on the street system and previous shorelines, as illustrated in Figure 2. Inspection of Figures 1 and 2 shows that concentrations of repairs often are closely related to high settlement gradients represented by the close spacings of settlement contours.

To explore further the relationship between pipeline damage and settlement pattern, MWSS repair rates were correlated with both the magnitude of settlement and the slope of the local settlement profile. The MWSS pipeline repairs within half a block in all street directions from each intersection were divided by the total length of pipe within this area and correlated with settlement at each intersection. Furthermore, the MWSS pipeline repairs along each block were divided by total length of pipeline along the block and correlated with the differential settlement across each block divided by the block length. This latter measure is the local slope of the settlement profile and is referred to as angular distortion.

In developing the correlations, the pipelines on Rico Way and Pierce St. were deleted from the data base. The main on Rico Way had been laid along a relatively sharp curve in the street, and is believed to have been especially vulnerable to damage because of installation stresses and constraints imposed by such construction. The main along Pierce St. was underlain by a pile-supported sewer.

Regressions were developed for each diameter of cast iron main. Only a weak correlation was found between repair rate and the magnitude of settlement. Relatively good correlations were found between repair rate and angular distortion. Figure 3 shows the MWSS repair rate, expressed as repairs per 300 m of pipe, plotted relative to angular distortion. It should be understood that the data plotted in Figure 3 do not include service lines and connections, and involve only damage to mains. An equation and coefficient of determination, r^2, are given for each regression in the figure. The linear regression slopes increase in inverse proportion to nominal diameter. For the 200-mm mains, a bilinear plot also conforms with the data. The bilinear trend is shown by dashed lines in the figure.

The pattern of damage in Figure 2 and its close relationship with the pattern of settlement in Figure 1 shows a strong link between pipeline damage and differential movement. This relationship is corroborated further by the correlations in Figure 3.

NATURAL SANDS AND FILLS

Extensive subsurface explorations have been performed in the Marina both before and after the 1989 Loma Prieta earthquake. Figure 4 shows 180 conventional borings and 14 cone penetration test (CPT) soundings. On the basis of historical development and the soil explorations, three general types of granular soil can be distinguished in the Marina: 1) natural sands associated primarily with beach and spit deposits, 2) land-tipped fills, and 3) hydraulic

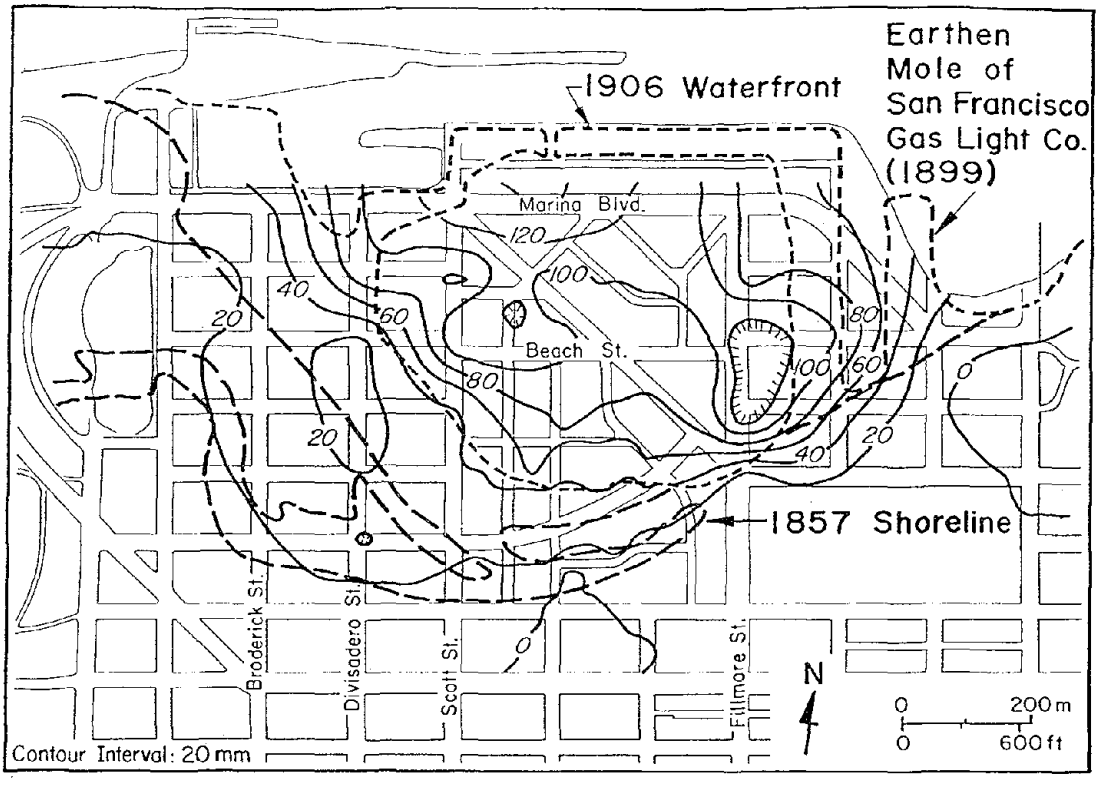

Figure 1. Settlement Contours from Post Liquefaction Consolidation in the Marina

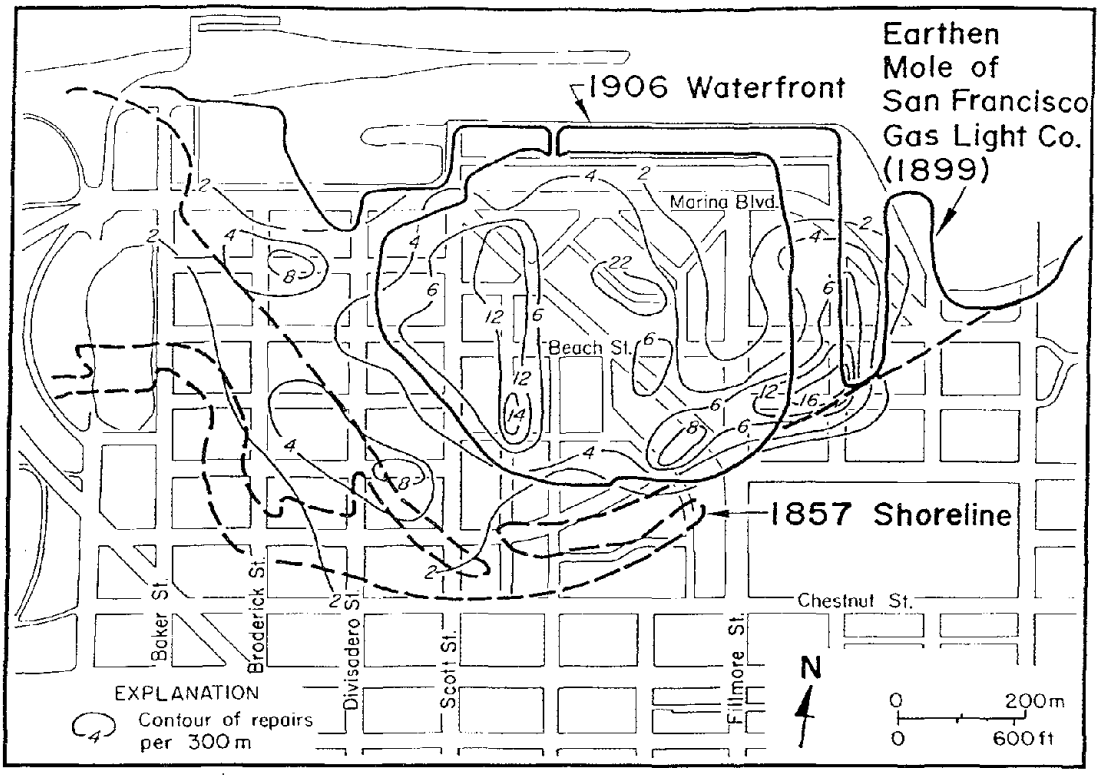

Figure 2. Contours of Repair per 300 m of MWSS Pipelines in the Marina

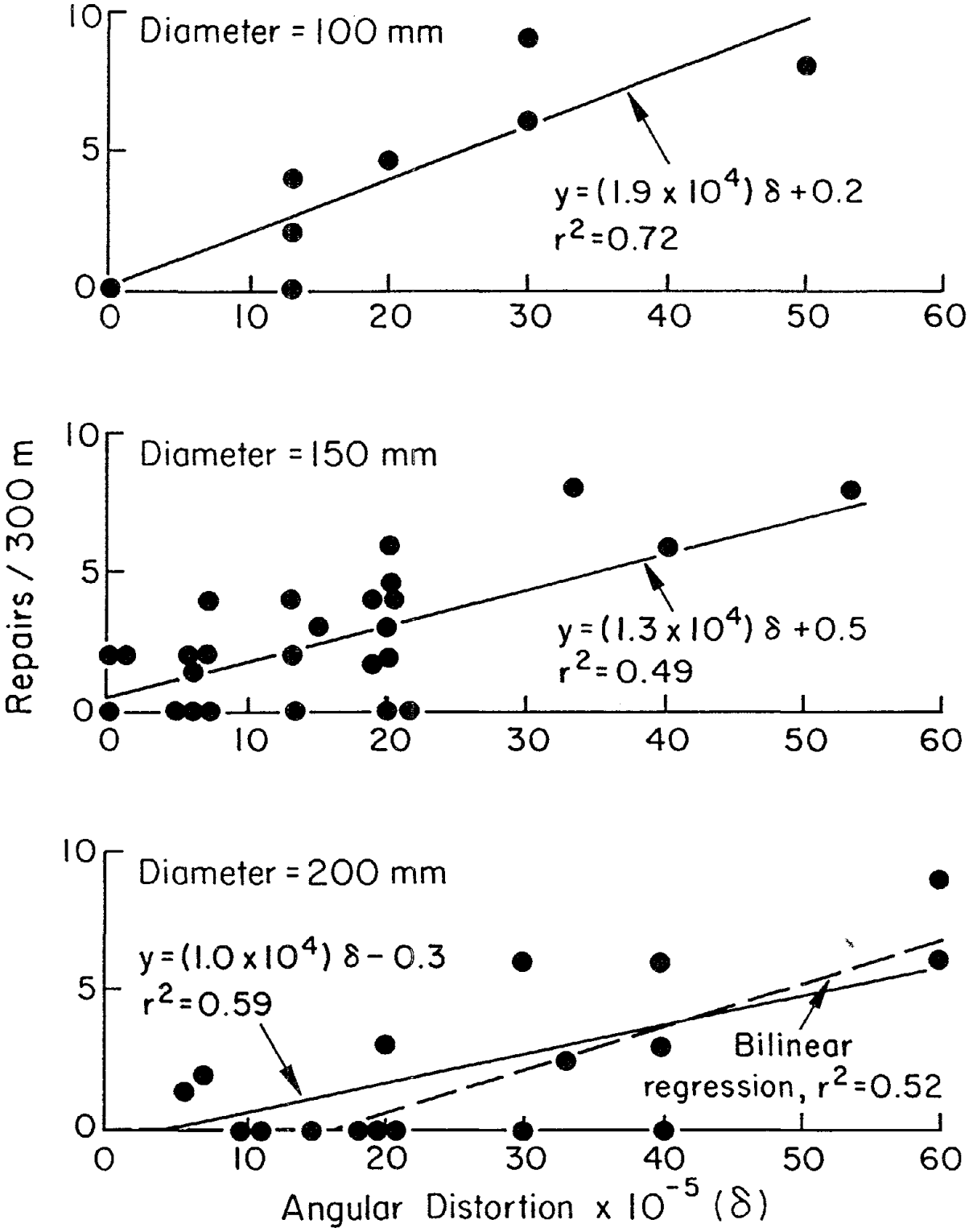

Figure 3. MWSS Pipeline Repair Rate vs. Angular Distortion

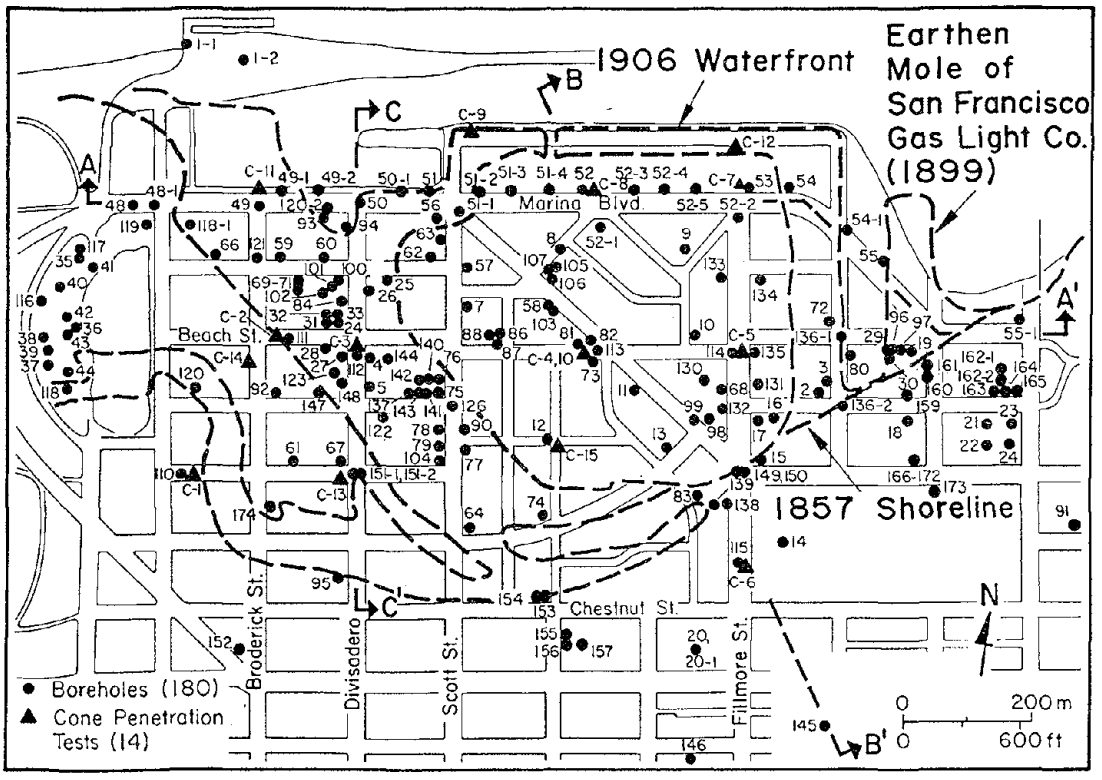

Figure 4. Plan View of Soil Borings and CPT Soundings in the Marina

fill. The natural sands described in this paper are located above the Holocene bay mud and are confined primarily to the location of the old Strawberry Island. The exploration data provide information on stratigraphy, variation in soil properties, and areal extent of the three types of soil.

The natural sands and land-tipped fills have a relatively consistent composition with depth. The percentage of fines and mean grain size typically are less than 5% and 0.2 to 0.4 mm, respectively, for these soils. Soil investigations (Bennett, 1990; Bardet and Karpuskar, 1991) indicate considerable stratification exists in the hydraulic fill, with varying thicknesses of interbedded sands and cohesive soils. Soil samples show the coarsest layers consist of fine sand (mean grain size 0.2 mm or less) with an average 10% silt or clay by weight.

Liquefaction potential analyses were performed for each soil type using the empirical relationship between cyclic stress ratio and corrected normalized standard penetration test (SPT) values developed by Seed, et al. (1983). The cyclic stress ratios for various depths were calculated assuming a peak horizontal acceleration of 0.2 g, which is consistent with a nearby seismic recording in the Presidio (EERI 1990), and also with values reported by other authors in this volume (e.g., Bardet and Martin, 1992). This acceleration level is believed to be consistent with accelerations of the soil deposits north of Chestnut Street.

Figure 5 shows the cyclic stress ratio plots for the three soil types. In each figure, empirical dividing lines are plotted for various fines contents

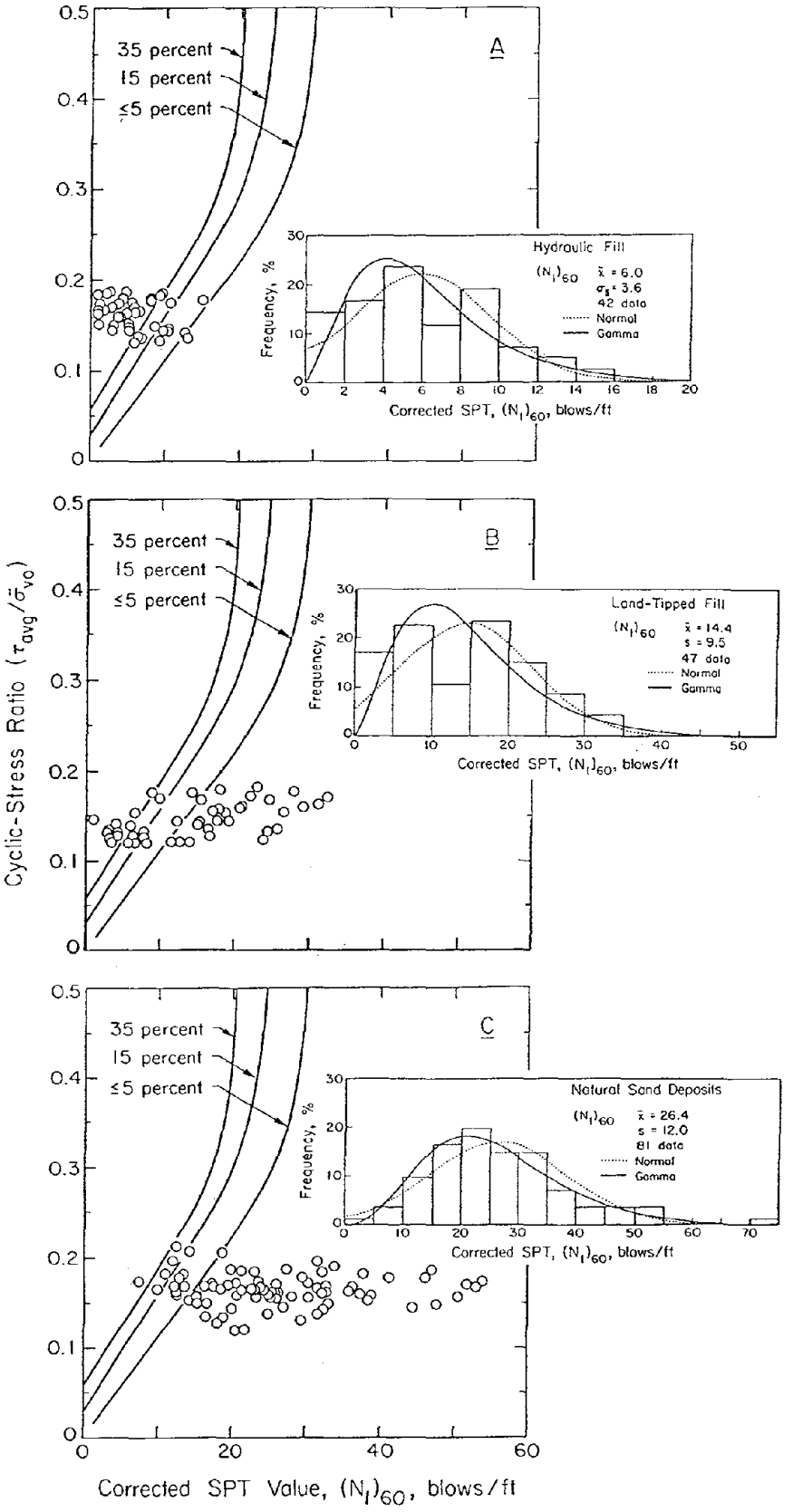

Figure 5. Cyclic Stress Ratio vs. Corrected SPT for Marina Granular Soils

between liquefiable (left side) and non-liquefiable soils. The cyclic stress ratios were adjusted for a 7.1 M earthquake based on recommendations by Seed, et al. (1983). In each figure, a histogram shows the frequency distribution of corrected SPT values $(N_1)_{60}$. Normal and gamma probability density functions are fitted to the data. The mean, x, and standard deviation, s, and the number of data in each sample are listed.

The most striking feature of the plots is the apparently high susceptibility to liquefaction displayed by the hydraulic fill. The corrected SPT values for at least half of the measurements in the sample are less than six. This implies a low factor of safety with respect to liquefaction and a high tendency towards settlement. In contrast, both the land-tipped fill and natural soils show increasing resistance to liquefaction. These soils also show successively larger ranges of in-situ densities. Roughly 50% of the land-tipped fill data plot to the left of the liquefaction curve for 5% fines, whereas only about 15% of the natural sand data plot in the same zone. The high variability of SPT values for the land-tipped fills means that data correspond to both liquefiable and non-liquefiable densities, so that moderate average settlement should result.

As illustrated in Figure 4, 14 CPT soundings were used in this study. The CPT soundings can resolve subsurface conditions in considerably more detail than SPT measurements, and therefore provide a more accurate picture of variations of in-situ density and soil type.

Liquefaction potential analyses were performed for all CPT soundings in hydraulic fill areas using the empirical correlations between cyclic stress ratio and modified cone tip resistance, q_{c1}, proposed by Seed and DeAlba (1986). The cyclic stress ratios for various depths were calculated in a manner similar to those for the SPT evaluations by assuming a peak acceleration of 0.2 g. The CPT data for each sounding also were analyzed to identify the soil type at each depth according to the recommendations of Robertson and Campenella (1983). The soil identification was used to evaluate whether the soil at a given depth was susceptible to liquefaction.

LIQUEFIABLE THICKNESS AND OBSERVED VERTICAL STRAIN

The term *liquefiable thickness* is used to describe the thickness of sands and gravels which are clean to moderately silty (fines content less than about 20 to 35% by weight) and fully saturated or submerged. Liquefiable thickness is intended to identify cohesionless materials which have the potential to densify in response to the application of dynamic shear strains. Nagase and Ishihara (1988) and Ishihara and Yoshimine (1992) have shown that volumetric strains will develop even in relatively dense sands, provided that dynamic shear strains and associated stresses are of sufficient magnitude. In this paper, therefore, liquefiable thickness is defined solely on the basis of soil composition and is independent of in-situ density.

Table 1 summarizes the observed settlements, fill thicknesses below water table, liquefiable thicknesses, and vertical strains near the CPT soundings in the hydraulic fill. The CPT data were used to evaluate the liquefiable thickness as a percent of the total submerged thickness of the hydraulic fill. On average,

Table 1. Observed Settlements at CPT Soundings in Hydraulic Fill

CPT Sounding	Settlement, mm	Fill Thickness below Water Table, m	Percentage of Liquefiable Soil, %	Observed Vertical Strain, %
C4	95	4.5	53-71	3.0-4.0
C7	80	5.3	45	3.3
C8	135	5.0	58	4.7
C10	95	4.5	53-87	2.4-4.0
C15	60	5.1	40	3.0
		Averages	55	3.5

45% of the hydraulic fill consists of clay or plastic silt which are not considered to be liquefiable. In some cases there was uncertainty regarding the soil composition at a particular level, so the percentages of liquefiable soil were calculated as upper and lower bounds. The liquefiable thickness is given by the product of the percentage of liquefiable soil and the fill thickness below the water table. The vertical strain was calculated as the ratio of settlement to liquefiable thickness.

Vertical strains also were determined on a global basis by evaluating the settlement data, represented in Figure 1, with respect to the liquefiable thickness at each settlement location for the three soil types. Each boring in Figure 4 was examined for changes in soil type, color, penetration resistance, and presence of debris to evaluate the most probable change in strata from fill to underlying natural soil. On the basis of interpreted borehole data, the fill thickness at each borehole location was determined and used to generate contours of fill thickness, as illustrated in Figure 6. The contours in Figure 6 were generated with the computer program "Surfer" by Golden Software (1985). The software employs a procedure known as kriging to perform a statistical evaluation of randomly spaced input data and develop an evenly spaced grid of data with minimal estimation variance (Ripley, 1987). A similar procedure was followed to evaluate the depth of the water table.

Contours of the submerged fill thickness are shown in Figure 7. The thickness of fill below the water table was computed by subtracting the water table depth from the fill thickness, using "Surfer" grid data. The submerged thickness is equivalent to the liquefiable thickness where the fills have substantially no silty or clayey layers. Comparing Figures 1 and 7, we see that contours of settlement and fill are frequently parallel, and submerged thickness helps to explain the pattern of regional settlement. Where there is no submerged fill, settlement is less than 10 mm. Submerged land-tipped fills are relatively

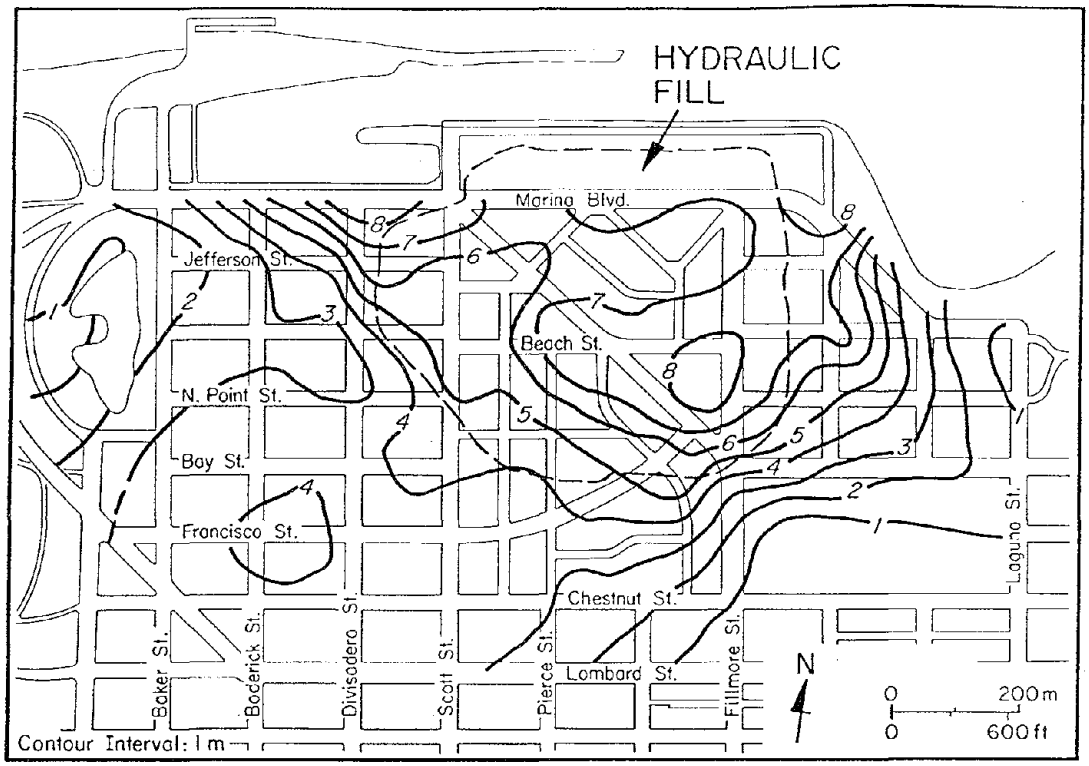

Figure 6. Contours of Fill Thickness in the Marina

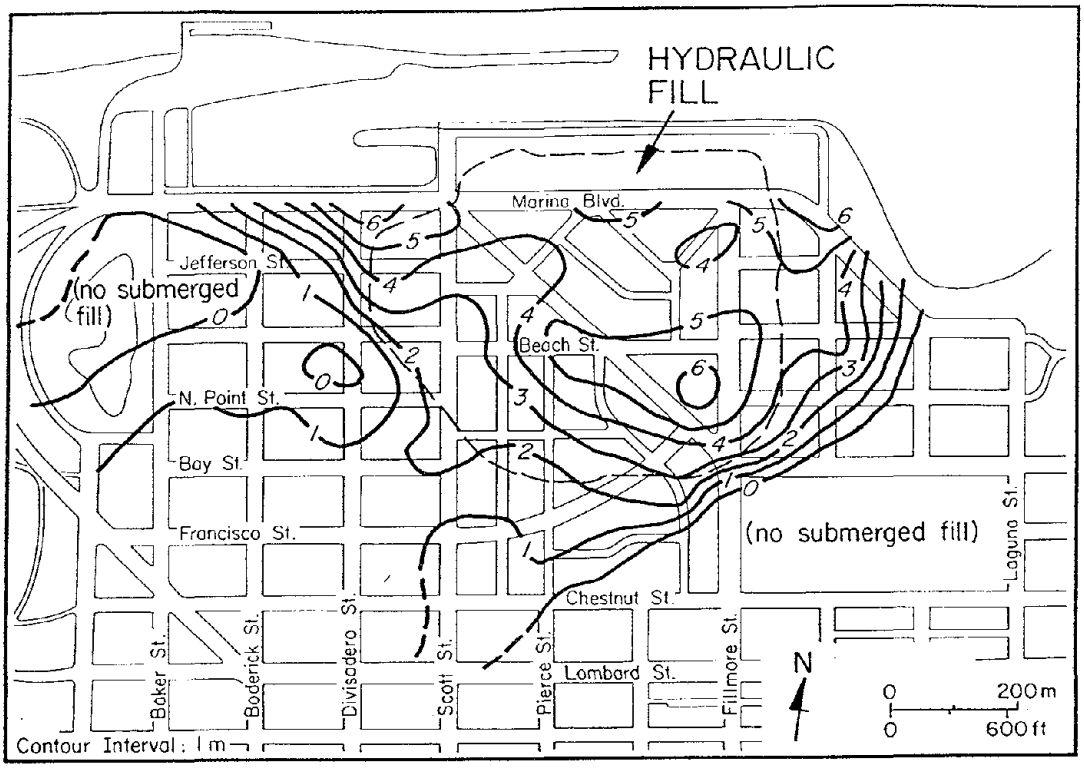

Figure 7. Contours of Submerged Fill Thickness in the Marina

Table 2. Observed Vertical Strains

Deposit Type	Percent Liquefiable, %	Settlement Strain, %
Recent Natural Sand (Strawberry Island)	100	0.2
Land-Tipped Fill	100	1.5
Hydraulic Fill	55	3.7

shallow and therefore produce less settlement. Hydraulic fills occupy the deepest portion of the basin and have the largest submerged thickness, resulting in the largest settlement.

As mentioned previously, the natural sands and land-tipped fills are generally clean, with less than 5% by weight of fines. Accordingly, the full submerged thicknesses of these deposits were assumed to be liquefiable. To obtain the liquefiable thickness for the hydraulic fill, the average value of 55% from Table 1 was used as the percentage of liquefiable soil.

Data from Figures 1 and 7 were plotted and regressed linearly through zero to compute observed settlement strains for the fills. Natural sand settlement strain was evaluated in a similar manner, based on mapping submerged thickness. By regressing settlement against submerged thickness, an average slope was determined which represents the average vertical strain for a given soil type. Because this strain is based on submerged thickness, an adjustment for the average 55% liquefiable soil was made for the hydraulic fill. Table 2 summarizes the observed vertical strains determined in this manner. Note that the average vertical strains for the hydraulic fill in Tables 1 and 2 are in close agreement.

PREDICTION OF VERTICAL STRAIN

Settlement was predicted for the recent natural sands, land-tipped fills, and hydraulic fills using predictive methods developed by Tokimatsu and Seed (1987) and Ishihara and Yoshimine (1992). These methods utilize laboratory results which show that vertical strain is controlled by the maximum shear strain, which can be related either to: 1) in-situ density and cyclic stress ratio, as proposed by Tokimatsu and Seed, or 2) in-situ density and factor of safety against liquefaction, as proposed by Ishihara and Yoshimine. The Ishihara and Yoshimine method is the more flexible of the two, but it is also subject to variations in interpretation by the user. In this paper, special attention is given to the Ishihara and Yoshimine method.

Vertical strains were determined by using Figure 8, which provides a relationship among vertical strain, factor of safety for liquefaction (FS_L), and density as referenced with respect to relative density (D_r), SPT value (N_1), and

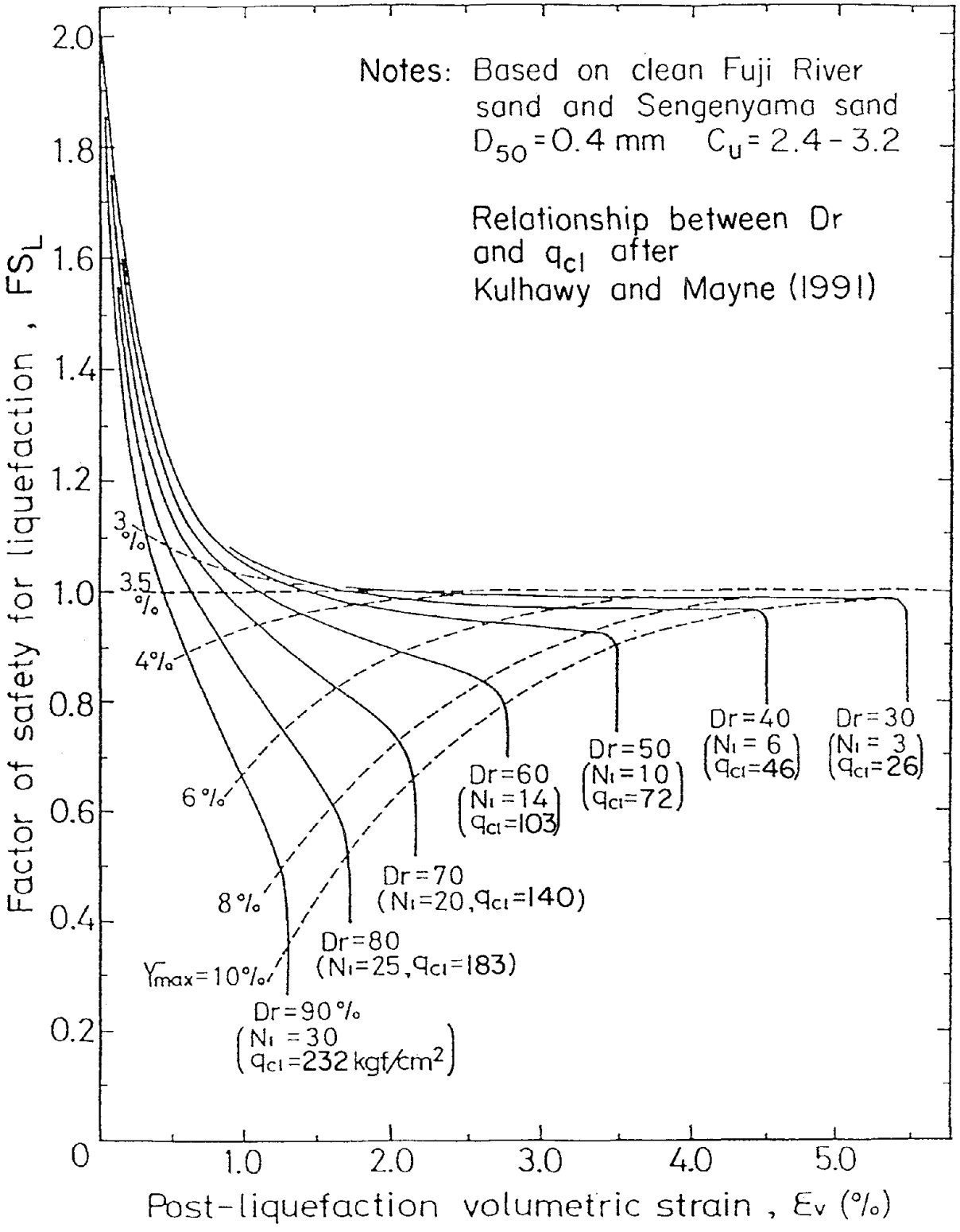

Figure 8. Relationship Among Volumetric Strain, Factor of Safety for Liquefaction, and In-situ Density (after Ishihara and Yoshimine, 1992)

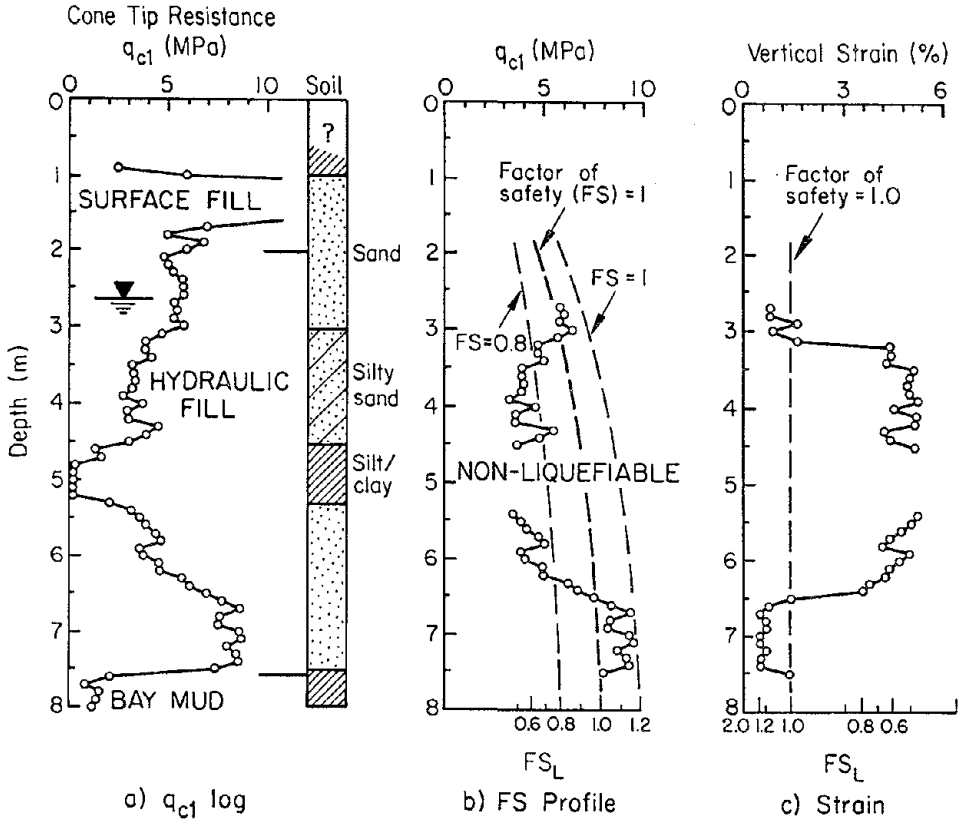

Figure 9. Determination of Vertical Strain from CPT Profile

modified cone tip resistance, (q_{c1}). The cone penetration values in the figure have been revised from those proposed by Ishihara and Yoshimine (1992) to account for the relationship between relative density and q_{c1}, based on data and interpretation provided by Kulhawy and Mayne (1991) for high to medium compressibility sands. All other aspects of the figure remain the same as originally proposed.

The factor of safety is defined in this work as the ratio of cyclic stress at incipient or initial liquefaction (CSR_L) to the cyclic stress ratio (CSR) representative of the ground stresses at a peak acceleration of 0.2 g [$FS_L = (CSR_L/CSR)$]. In Figure 5, for example, the cyclic stress ratio at incipient liquefaction (CSR_L) is the cyclic stress ratio for a given $(N_1)_{60}$ corresponding to the intercept of the liquefaction envelope. A similar cyclic stress ratio plot can be developed for q_{c1} according to the recommendations of Seed and DeAlba (1986). Once the penetration value and factor of safety have been determined, the two values are located on Figure 8 and volumetric, or vertical, strain is read from the horizontal axis beneath the data point.

Figure 9 illustrates the procedure to determine hydraulic fill settlement for sounding C8 located on Marina Green. Figure 9a shows modified cone tip resistance (q_{c1}) with depth. Figures 9b and 9c include q_{c1} and predicted settlement strain results, respectively, plotted against depth. Factor of safety against liquefaction is shown relative to q_{c1} and predicted settlement strain on a parallel horizontal axis. A line corresponding to a factor of safety of unity is plotted on each graph, which shows that the factor of safety varies

with depth. Soil above the water table and nonliquefiable layers are eliminated from the analysis.

An important feature of the liquefaction settlement prediction is that settlement response is highly nonlinear, so strains must be determined from individual penetration values and factors of safety, not average values. In Figure 9c, a critical jump in settlement occurs at a factor of safety of unity. If an entire deposit is represented statistically by an average penetration and Figure 8 is used, the results will be highly varied and sensitive to small changes when the factor of safety is near unity. Computing settlement strains individually and then averaging gives a much more stable answer.

COMPARISON OF OBSERVED AND PREDICTED STRAINS

The prediction models of Tokimatsu and Seed (1987) and Ishihara and Yoshimine (1992) were used to estimate the vertical strains associated with post-liquefaction consolidation in the natural sands, land-tipped fill, and hydraulic fill. The results are compared with the observed vertical strains in Tables 3 and 4. Table 3 summarizes the predicted vertical strains, using SPT data. Table 4 summarizes the predicted values for hydraulic fill using the Ishihara and Yoshimine method with both CPT and SPT data.

As indicated in Table 3, the vertical strains in the land-tipped fills have been evaluated for two zones. One zone includes soils with a liquefiable thickness less than 3.5 m. The other zone includes soils below a liquefiable thickness greater than 3.5 m. Data from SPT borings show a considerable increase in $(N_1)_{60}$ below a liquefiable thickness of 3.5 m, which results in a lower estimate of strain for this zone.

In general, the agreement between observed and predicted vertical strains is good. It is important, however, to recognize some of the variations and limitations inherent in both the database and assumptions pertaining to application of the simplified prediction methods. The observed vertical strains represent average values which were obtained by regressing settlement against liquefiable thickness. Although a detailed discussion of the database and interpretive procedures is not possible within the length restrictions of this paper, it should be recognized that there is variation about these average values. Roughly 90% of the observed strains fall within $\pm$ 90% of the average values for land-tipped fill, whereas 90% of the observed strains fall within $\pm$ 30% of the average values for hydraulic fill. The predictive techniques require an estimate of the peak ground acceleration, which was assumed to be 0.2 g in this paper. Both methods, near cyclic stresses or factors of safety associated with the onset of liquefaction, are sensitive to variations in the input acceleration. Finally, the vertical strains predicted for hydraulic fill from CPT measurements are based on only five soundings (see Table 1). Although the average predicted strain is close to the observed strain, there is considerable scatter about the average predicted value, with high and low estimates of 1.0% and 5.4%, respectively.

It should be recognized that the observed vertical strains for the hydraulic fill would have been roughly half the values listed in Table 3 if liquefiable thicknesses had not been reduced by subtracting the cumulative

Table 3. Comparison of Observed and Predicted Vertical Strains

Soil Type	Observed		Predicted Vertical Strain SPT-Based	
	Liquefiable %	Vertical Strain, %	Tokimatsu & Seed (1987)	Ishihara & Yoshimine (1992)
Natural Sands	100	0.2	0.3	0.2
Land-Tipped Fill[a]				
< 3.5 m thick	100	1.5	2.2	2.7
> 3.5 m thick	100	1.5	1.3	1.8
Hydraulic Fill	55	3.5-3.7	3.7	4.5

a - refers to two zones above and below a liquefiable thickness of 3.5 m.

Table 4. Comparison of Observed and Predicted Settlement Strains for Hydraulic Fill

Observed Vertical Strain, %	Predicted Vertical Strain, % Ishihara and Yoshimine (1992)	
	SPT	CPT
3.5 - 3.7	4.5	3.2

thicknesses of silt and clay from the total depths of submerged fill. These adjustments could not be made with SPT data. The relatively thin layers of silt and clay in the hydraulic fill required a more sensitive and continuous profiling technique. Accordingly, CPT soundings were needed for proper characterization of the fill and accurate assessment of vertical strain.

CONCLUDING REMARKS

Pipeline damage in the Marina was related directly to liquefaction-induced ground deformation. There is a close relationship between the distribution of pipeline damage and the pattern of surface settlement caused by post-liquefaction consolidation. The damage rate for each diameter of pipeline is shown to correlate with angular distortion, which is a measure of the local slope of the settlement profile.

The settlement pattern in the Marina is related closely to the variation of liquefiable thickness, which is defined as the submerged thickness of clean to moderately silty sands and gravels. Liquefiable thickness is relatively simple to evaluate and shows promise as a parameter that can be mapped and used to estimate patterns of potential settlement caused by post-liquefaction consolidation.

The average vertical strains predicted with simplified procedures proposed by Tokimatsu and Seed (1987) and Ishihara and Yoshimine (1992) compare favorably with those observed in natural sands, land-tipped fill, and hydraulic fill. The Ishihara and Yoshimine procedure is more versatile than the Tokimatsu and Seed approach, but it is also subject to variations in interpretation by the user. An important feature of liquefaction settlement prediction with the Ishihara and Yoshimine approach is that settlement response is highly nonlinear, so that strains from individual penetration values and factors of safety must be integrated to predict settlement.

The resolution in delineating subsurface conditions with cone penetration test (CPT) measurements is an important factor in estimating the magnitude and extent of post-liquefaction consolidation in the hydraulic fill. Hydraulic fills, because they may be stratified with fine grained soils, are likely to require a more detailed evaluation for assessing post-liquefaction settlement than can be supplied by the widely used methods of the SPT and split spoon sampling.

ACKNOWLEDGMENTS

The research supported in this paper was supported by the National Science Foundation under Award No. BCS-9011458. Thanks are extended to L. Mayes and A. Avcisoy, who prepared the manuscript and figures, respectively, for their skills and contributions.

REFERENCES

Bardet, J.P. and M. Kapuskar, "Site Investigation of the Marina District of San Francisco in September 1990," Report to the National Science Foundation, Civil Engineering Department, University of Southern California, Los Angeles, CA, Feb. 1991.

Bardet, J.P. and G.R. Martin, "An Assessment of Two-Dimensional and Wave-Propagation Effects on the Site Response of the Marina District of San Francisco During the 1989 Loma Prieta Earthquake," this volume.

Bennett, M.J., "Ground Deformation and Liquefaction of Soil in the Marina District," Open File Report 90-253, USGS, Menlo Park, CA, Effects of the Loma Prieta Earthquake on the Marina District, San Francisco, CA, Apr. 1990, pp. D-1 - D-36.

Earthquake Engineering Research Institute, "Loma Prieta Earthquake Reconnaissance Report," L. Benuska, Tech. Ed., Earthquake Spectra, Supplement to Vol. 6, May 1990.

Golden Software, Inc., "Surfer," Golden, CO, 1985.

Ishihara, K. and M. Yoshimine, "Evaluation of Settlements in Sand Deposits Following Liquefaction During Earthquakes," Soils and Foundations, Vol. 32, No. 1, Mar. 1992, pp. 173-188.

Kulhawy, F.H. and P.W. Mayne, "Relative Density, SPT, and CPT Interrelationships," Proceedings, First International Symposium on Calibration Chamber Testing, A-B Huang, Ed., Elsevier Scientific Publishing Co., Inc., New York, NY, 1991, pp. 197-211.

Nagase, H. and K. Ishihara, "Liquefaction-Induced Compaction and Settlement of Sand During Earthquakes," Soils and Foundations, Vol. 28, No. 1, Mar. 1988, pp. 65-78.

O'Rourke, T.D., T.E. Gowdy, H.E. Stewart, and J.W. Pease, "Lifeline Performance and Ground Deformation in the Marina During 1989 Loma Prieta Earthquake," Proceedings, 3rd Japan-U.S. Workshop on Earthquake-Resistant Design of Lifeline Facilities and Countermeasures for Soil Liquefaction, NCEER-91-0001, National Center for Earthquake Engineering Research, Buffalo, NY, Feb. 1991a, pp. 129-146.

O'Rourke, T.D., T.E. Gowdy, H.E. Stewart, and J.W. Pease, "Lifeline and Geotechnical Aspects of the 1989 Loma Prieta Earthquake," Proceedings, 2nd International Conference on Recent Advances in Geotechnical Earthquake Engineering and Soil Dynamics, St. Louis, MO, Mar. 1991b, Vol. II, pp. 1601-1612.

Ripley, B.D., Spatial Statistics, John Wiley and Sons, New York, NY, 1981.

Robertson, P.K. and R.G. Campanella, "Interpretation of Cone Penetration Tests. Part I: Sand," Canadian Geotechnical Journal, Vol. 20, No. 4, Nov. 1983, pp. 718-733.

Seed, H.B. and P. DeAlba, "Use of SPT and CPT Tests for Evaluating the Liquefaction Resistance of Sands," Use of In-Situ Tests in Geotechnical Engineering, S.P. Clemence, Ed., Geotechnical Special Publication No. 6, ASCE, New York, NY, 1986, pp. 281-302.

Seed, H.B., I.M. Idriss, and I. Arango, "Evaluation of Liquefaction Potential Using Field Performance Data," Journal of Geotechnical Engineering, ASCE, New York, NY, Vol. 109, No. 3, Mar. 1983, pp. 458-482.

Tokimatsu, K. and H.B. Seed, "Evaluation of Settlements in Sands Due to Earthquake Shaking," Journal of Geotechnical Engineering, ASCE, Vol. 113, No. 8, Aug. 1987, pp. 861-878.

Experimental Study on the Uplift Deformation of Underground Structures Induced by Soil Liquefaction

by

Ken-ichi Tokida[1] and Yoshio Ninomiya[2]

ABSTRACT

Earthquake-induced soil liquefaction causes uplift deformation of lifeline facilities buried in saturated sand layers. This paper presents results of shaking table tests carried out to evaluate the uplift deformation of an underground structure with a rectangular section buried in liquefiable layers. In these tests, the thickness of a liquefiable layer below an underground structure and the size of a structure section are varied. The excess pore water pressures and the accelerations in liquefied ground models are measured. Furthermore, the deformation of liquefied sand layers surrounding the underground structure model is observed.

---

1)Head, Ground Vibration Division, Earthquake Disaster Prevention Department, Public works Research Institute(PWRI), Ministry of Construction, Japan.
2)Senior Research Engineer, ditto.

INTRODUCTION

Uplift deformation caused by soil liquefaction is a very important problem for the earthquake resistant design of lifeline facilities buried in liquefiable ground. Such lifeline facilities as common utility ducts are designed estimating a safety factor of uplift at present in Japan[1]. However, for establishing a reasonable earthquake resistant design method and an earthquake disaster prevention one, uplift deformation of underground structures should be discussed considering the deformation of liquefied sand.

Forces acting on an underground structure with a rectangular section in liquefied sand are body weight of the structure, an overburden load on the top plate of the structure, frictions of the side surfaces of the structure, static water pressure and excess pore water pressure at the bottom plate of the structure. The purpose of this study is especially to investigate the occurrence of excess pore water pressure which relates to the deformation characteristics of the underground structure and the surrounding ground induced by soil liquefaction. The unit weight of an underground structure are smaller than that of the surrounding ground. Thus, an effective overburden pressure at the bottom face of the underground structure is smaller than that in the surrounding layer at the same depth as the bottom plate of the structure, in other words, the maximum excess pore water pressure on the bottom plate of the structure is smaller than the that in surrounding ground at the same depth. Thus, the distribution of the excess pore water pressure around the underground structure should be investigated as one of factors relating to the uplift of the underground structure.

Furthermore, it should be noticed that the flow/movement of soils and pore water are necessary to occur uplift of a structure. It is important to investigate the mechanism of the flow/movement of soils and pore water to evaluating uplift deformation.

METHOD OF EXPERIMENTS

The conditions of ground models and measurements are shown in Figure 1 and table 1. The ground models are made in a square container placed on a shaking table. This container is 600mm wide, 1,800mm long and 1,100 mm high. the front and back plates of it are made of acrylic resin. The ground model consists of a liquefiable sand layer and a non-liquefiable sand layer. The total

thickness of these two layers and the one of a layer above the underground structure model are set to be constant in each test, and the thickness of liquefiable sand layer below the structure model is varied in three cases.

The material of the ground model is a clean sand called as Toyoura Sand. These characteristics of the material is shown in Table 2. The liquefiable sand layer is constructed by the underwater drop method. The non-liquefiable sand layer is firstly compacted enough in the container not to liquefy during exiting. These characteristics of liquefiable sand in each test is shown in Table 3.

The underground structure model is buried in the liquefiable sand layer in each test. In this study, two types of underground structure models:150mm wide, 590mm long and 150mm high and 450mm wide,590mm long and 150mm high are used as shown in table 4. These are made of aluminum and hollow models with a rectangular section. Sponge is stuck on the front and back surfaces of the structure models to reduce a friction force between the container and the structure model.

In each test, constant sinusoidal acceleration with a frequency of 3Hz was employed for 20 seconds(60cycles). Several levels of maximum acceleration (80 ~ 230gals) are applied stepwise to the shaking tables as an input motion. The conditions of the input maximum acceleration are shown in Table 5.

As shown in Figure 1, pore water pressure meters, accelerometers and bench mark points are installed in or on the ground models to measure the time history of excess pore water pressure, acceleration and displacement of ground surface. Furthermore, at the surface of the underground structure models, pore water pressure meters, accelerometers, slide wire displacement meters, earth pressure meters and a friction meter are installed to measure the time history of excess pore water pressures, an acceleration, uplift displacements, earth pressures, a friction between sand and the underground structure model.

RESULTS OF EXPERIMENTS

Because a main factor causing the uplift of the underground structure is the rise of excess pore water pressure on the bottom plate of the structure. the difference between excess pore water pressure on the bottom plate of the underground structure and that in the surrounding ground at the same depth is investigated in this study. The relation between these excess pore water pressure and the uplift deformation of the underground structure is also studied based on the test results.

Figure 2 (a) shows the time histories of vertical displacement of the underground structure model in Model 1-3. Figure 2 (b), (c) show the relation between excess pore water pressure or excess pore water pressure ratio at the point P1 and P5 in Figure 1 and the vertical displacement, respectively. The excess pore water pressure at the bottom plate of the underground structure in Figures 2 (b), (c) and 4 is calculated from the measured excess pore water pressure corrected / added by the quantity of decrease of static water pressure caused by uplift deformation of the underground structure. It can be noticed from Figure 2 (a) that the thicker the liquefiable layer (Hb) below the underground structure model is, the more early and rapidly the underground structure uplifts. Figure 2 (b) indicate that the rise of excess pore water pressure at the point P1 is smaller than that of excess pore water pressure at the point P5. On the other hand, as Figure 2 (c) indicates at the initial stage of uplifting, the excess pore water pressure ratio at the point P1 is larger than that at the point P5; the former is 0.8-1.0 and the latter is 0.7-0.8.

Figures 3 (a) and (b) show the time histories of input base acceleration and ground acceleration at the point P5, respectively. Figures 3 (c) and (d) show that excess pore water pressure at the point P5 and P1, respectively. Based on the Figure 3, the following can be indicated; the excess pore water pressure at the point P5 is increasing rapidly and the excess pore water ratio is about 0.7 at the elapsed time of about 3.5 seconds: ① in Figure 3 (c). On the other hand, the excess pore water pressure at the point P1 becomes about 1.0 at the elapsed time of about 3.5 seconds: ① in Figure 3 (d). Afterward, the underground structure keeps uplifting and excess pore water pressure at the point P1 decreases once and increases again and becomes over 1.0 until the elapsed time of about 8 seconds when the ground is liquefied completely. The decrease and increase of pore water pressure can be explained by the decrease of static water pressure caused by uplifting of the structure model and the seepage pressure from the surrounding liquefied ground, respectively.

Figure 4 shows the distribution of excess pore water pressure. As indicated in Figure 2, the excess pore water pressure under the structure model is larger than that at the surrounding ground at the same depth.

Photograph 1 shows the deformation of the liquefied ground and the underground structure model, when the underground structure is uplifted at 5cm in Model 1-6. The vertical black belts in the ground models are black colored sands, which consist of the same sands as the surrounding ground. Because the vertical white lines show the initial position of the black colored

sand, it can be noticed that liquefied sands are flowed from the surrounding ground toward the bottom of the underground structure and the flow of liquefied soils cause the uplift of the structure model. Thus it can be indicated that one of the factors relating to the magnitude of uplift deformation and its progress of underground structures is the difficulty or ease of the flow of liquefied soils toward the bottom of underground structures.

CONCLUSION AND FUTURE REMARKS

Based on the experimental study using the shaking table on the uplift of an underground structure model caused by soil liquefaction the following can be concluded;

(1) When the excess pore water pressure ratio at the center point on the bottom plate of the underground structure model increases to 0.8-1.0, the underground structure model begins to be uplifted rapidly, although the excess pore water pressure ratio at the surrounding ground of the underground structure is 0.7-0.8.

(2) The flow of liquefied soils from the surrounding ground toward the bottom of an underground structure model can be observed experimentally, when the underground structure model is uplifted.

(3) The magnitude of the uplift deformation of an underground structure relates to the difficulty or ease of the flow of liquefied soils from the surrounding ground toward the bottom of the underground structure. In this study, the thickness of the liquefiable layer below the underground structure and the width of the section of the structure are investigated as factors relating to uplift deformation of the structure. It can be indicated that the thicker the liquefiable ground below the underground structure is, the more easily the underground structure is uplifted.

Future subjects on the uplift deformation of an underground structure can be considered as follows:

(1) Further evaluation of the difficulty of the flow of liquefied soils from the surrounding ground toward the bottom of an underground structure.

(2) Investigation of other factors relating to the uplift deformation of an underground structure, for example, an overburden load on the top plate of

that.

(3)Establishment of a simplified procedure to evaluate the liquefaction potential considering the magnitude of the uplift deformation of an underground structure.

(4) Establishment of the reasonable countermeasures to prevent or decrease the uplift deformation of an underground structure applying the results of this study.

ACKNOWLEDGEMENTS

The authors wish to express their sincere gratitude to Mr. H. Matsumoto, Research Engineer of PWRI for his helpful comments to conduct shaking table tests and to Mr. T. Azuma of PWRI for his assistance in presenting this paper.

REFERENCE

1)Japan Road Association, "Design Guidelines for Common Utility Ducts", March, 1986(in Japanese)

Table 1 Conditions of ground models

Model No.	layer thickness (mm)						width
	Ha	Hm	Hb	H_L	h_{NL}	H	W
1	200	150	50	400	550	950	150
2	200	150	100	450	500	950	150
3	200	150	150	500	450	950	150
4	200	150	75	425	525	950	450
5	200	150	150	500	450	950	450
6	200	150	300	650	300	950	450

Table 2 Characteristics of sand used for the experiments
(Toyoura Sand)

Specific gravitiy of soil particle Gs	2.648
Maximum void ratio e_{max}	0.940
Minimum void ratio e_{min}	0.621
Coefficient of uniformity Uc	1.6
Maximum size (mm)	0.85

Table 3 Characteristics of ground models(befor shaking)

Model No.	Dry density ρ_t (tf/m^3)	Saturated density ρ_{sat}(tf/m^3)	Relative density Dr(%)
1	1.426	1.887	26.0
2	1.441	1.897	32.0
3	1.434	1.892	29.2
4	1.469	1.914	43.0
5	1.444	1.899	33.2
6	1.443	1.898	32.8

Table 4 Conditions of underground structure models

Model No.	Width (mm)	Length (mm)	Height (mm)	Specific gravity
1	150	590	150	0.94
2	450	590	150	0.85

Table 5 Conditions of input motion

Model No.	Maximum acceleration of input motion (gal)	frequency and duration
1	80	3 Hz 20 sec
	110	
	170	
2	80	
	110	
	140	
3	80	
	110	
4	80	
	110	
	170	
	230	
5	80	
	110	
6	140	

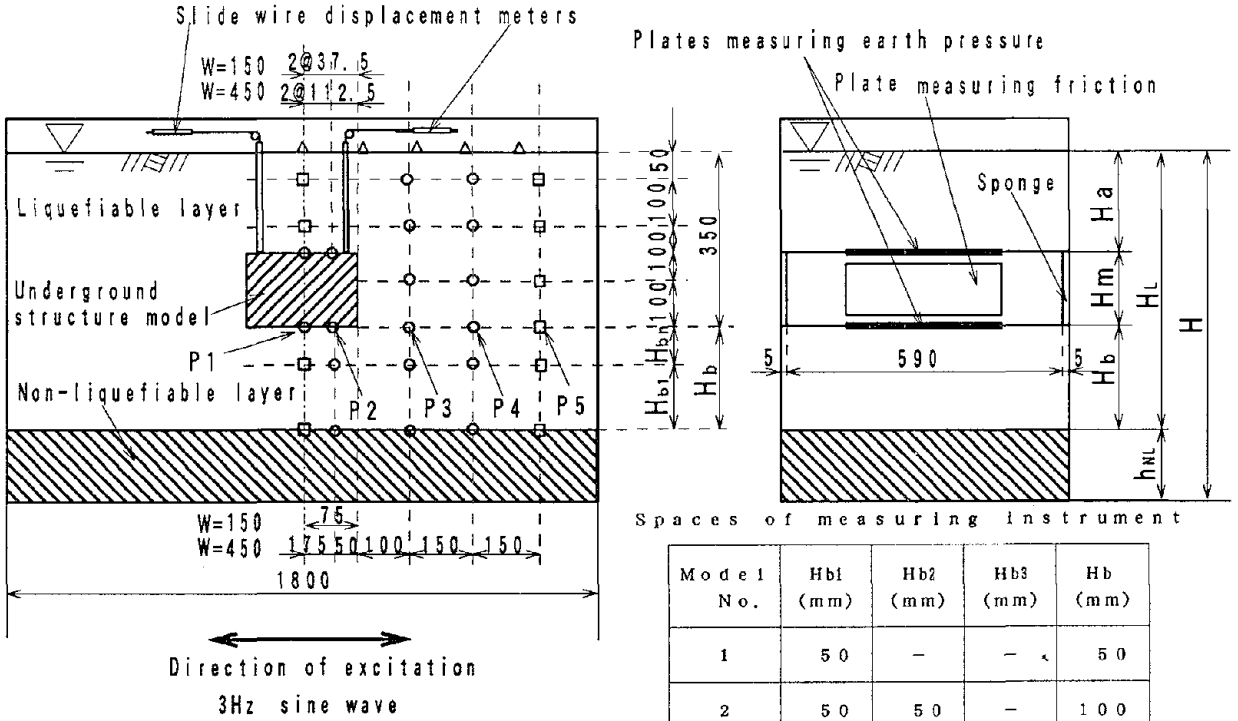

O Pore water pressure meter
□ Accelerometer
△ Bench mark point

Unit: mm

Model No.	Hb1 (mm)	Hb2 (mm)	Hb3 (mm)	Hb (mm)
1	50	–	–	50
2	50	50	–	100
3	100	50	–	150
4	37.5	37.5	–	75
5	100	50	–	150
6	150	100	50	300

Figure 1 Models of ground and underground structure, and measurements

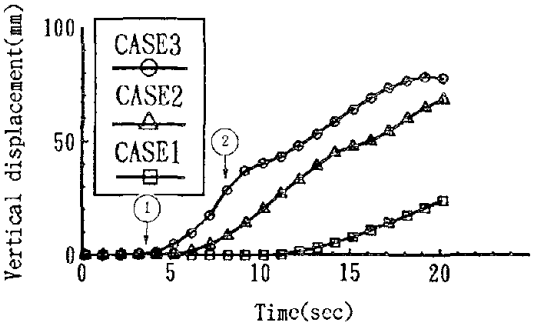

(a) Time history of vertical displacement

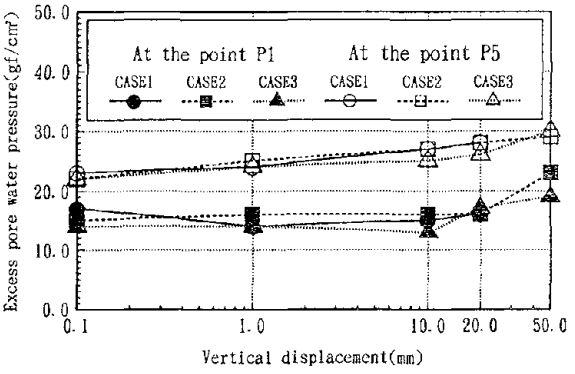

(b) Relation between excess pore water pressure and vertical displacement

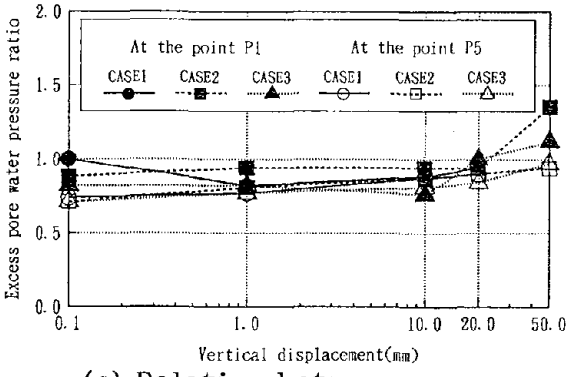

(c) Relation between excess pore water pressure ratio and vertical displacement

Figure 2 Comparison of excess pore water pressure and vertical displacement (Model 1-3)

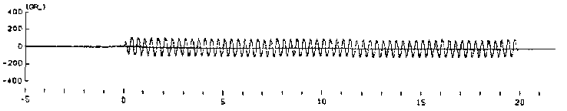

Elapsed time (sec)

(a) Input base acceleration

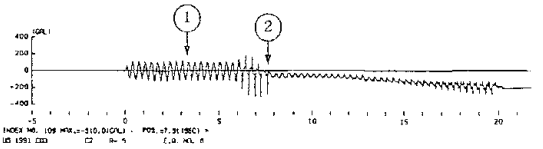

Elapsed time (sec)

(b) Ground acceleration (P5) (P2 in Figure 1)

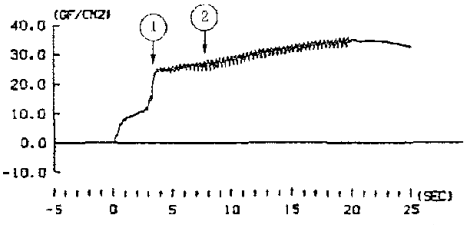

Elapsed time (sec)

(c) Excess pore water pressure (P5)

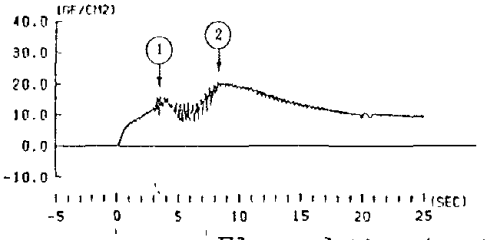

Elapsed time (sec)

(d) Excess pore water pressure (P1)

Figure 3 Example of time histories (Model 3)

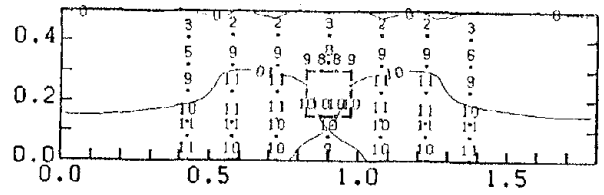

(a) D= 0.0mm

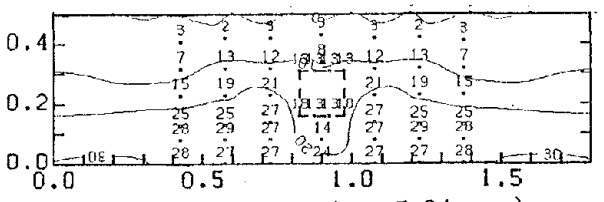

(d) D= 1.0cm

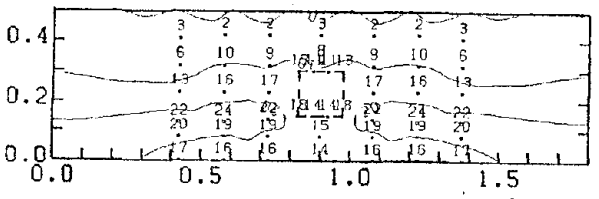

(b) D= 0.1mm

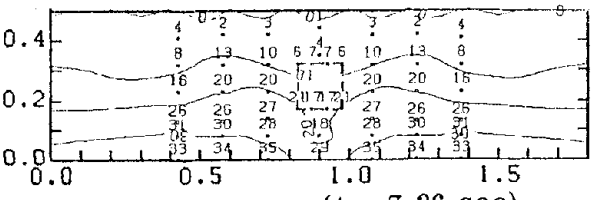

(e) D= 2.0cm

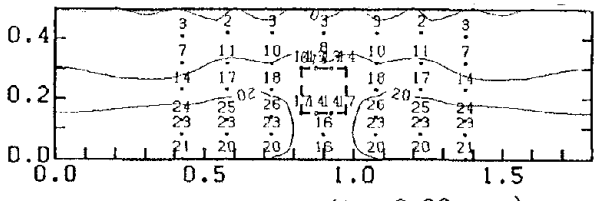

(c) D= 1.0mm

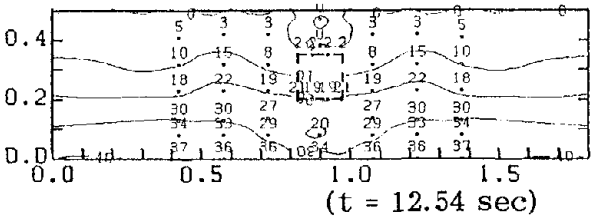

(f) D= 5.0cm

Note : D=Vertical displacement of underground structure model
t = Elapsed time
Input Maximum Acceleration 110gal

Figure 4 Time history of distribution of excess pore water pressure in the cross section of ground model (Model 3)

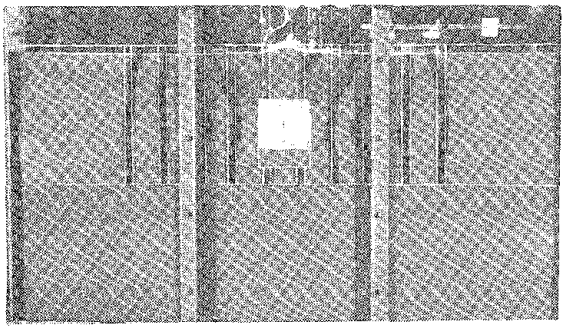

(a) Model 1 W=15cm, Hb=5cm

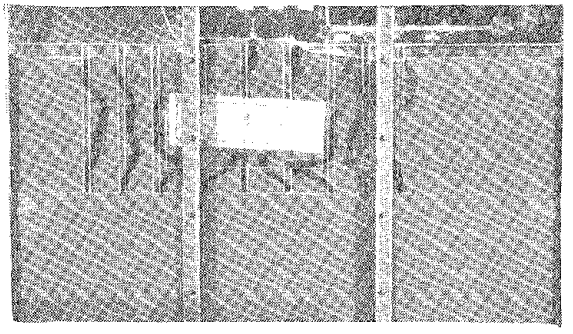

(d) Model 4 W=45cm, Hb=7.5cm

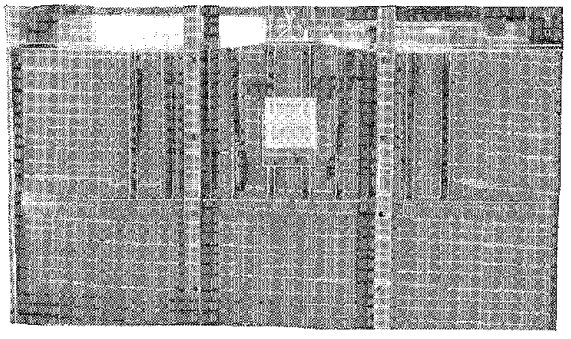

(b) Model 2 W=15cm, Hb=10cm

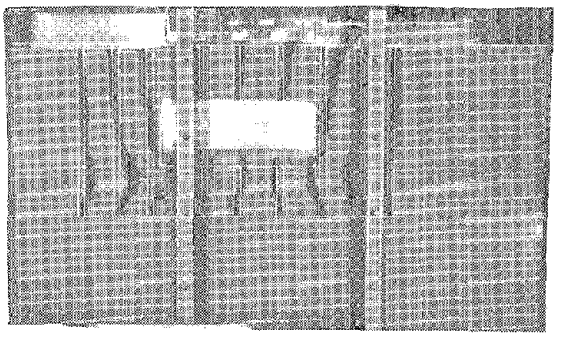

(e) Model 5 W=45cm, Hb=15cm

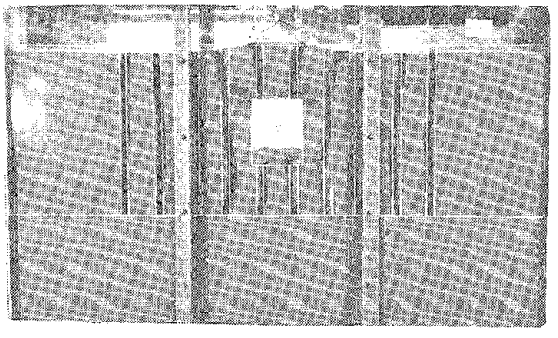

(c) Model 3 W=15cm, Hb=15cm

(f) Model 6 W=45cm, Hb=30cm

W (Width of the underground structure)
Hb (Thickness of liquefied sand below the underground structure)

Photo. 1 Deformation of liquefied ground model and underground structure model, when vertical displacement of structure model is 5cm.

Analysis of Liquefaction Induced Uplift of Underground Structures

Susumu IAI and Yasuo MATSUNAGA

Port and Harbour Research Institute
Ministry of Transport, JAPAN

ABSTRACT

Uplift of underground structures associated with soil liquefaction is currently explained with the force balance between buoyancy and gravity. This explanation is not adequate when the soil partially liquefies and retains some amount of shear resistance nor will it be useful when one intends to estimate amount of uplift due to soil liquefaction.

In order to obtain a reasonable understanding on the mechanism of the uplift and a reasonable estimation procedure of the amount of uplift, an effective stress analysis is conducted on a submerged tunnel in a loosely deposited sand. Results of the analysis indicate that a fundamental mechanism in producing deformation of soil and structure is the existence of static stress due to gravity and its release in accordance with deformation. In particular, the most important mechanism which governs the amount of the uplift of underground structures is the extension shear deformation of the soil below the structures.

INTRODUCTION

When soil liquefies during earthquakes, underground structures generally "float" in the liquefied soil and thereby exhibit uplift. The mechanism in this phenomenon is currently interpreted in terms of force balance between buoyancy and gravity. This is obviously adequate when the soil completely liquefies. The buoyancy is easily calculated from the unit weight of saturated soil.

A problem arises when the soil partially liquefies and retains some amount of shear resistance. The soil no longer behaves like liquid but does like solid. Even in this case, buoyancy could be defined as a resultant force of the total stresses acting on the entire surface of structures. It should be noted, however, that the total stress is determined by not only pore water pressure but also the effective stress of the soil. Such an assumption that effective stress be zero obviously simplifies a procedure for estimating the buoyancy but it leads to an unconservative error.

Another problem arises when one intends to estimate amount of uplift due to liquefaction. The amount of uplift is governed by deformation of soil surrounding the structures. In order to estimate the amount of uplift, a full understanding on the behavior of soil is necessary.

Recent studies on the uplift of the underground structures are being done along such simplified approaches as a sliding block approach and a linear elastic analysis with use of reduced moduli [1] but a full understanding on the mechanism of uplift has not yet been obtained. In the present study, an effective stress analysis is conducted on a submerged tunnel in a loose sand deposit. A close look is directed into stress and strain of soil surrounding the tunnel in order to understand the mechanism of the uplift.

OUTLINE OF EFFECTIVE STRESS MODEL

The effective stress model of sands to be used in this study consists of a multiple shear mechanism in the plane strain condition [2 & 3]. With the effective stress and strain vectors written by

$$\{\sigma'\}^T = \{ \sigma_x' \ \sigma_y' \ \tau_{xy} \} \tag{1}$$

$$\{\epsilon\}^T = \{ \epsilon_x \ \epsilon_y \ \gamma_{xy} \} \tag{2}$$

the basic form of the constitutive relation is given by

$$\{d\sigma'\} = [D](\{d\epsilon\} - \{d\epsilon_p\}) \tag{3}$$

in which

$$[\mathbf{D}] = K\{\mathbf{n}^{(0)}\}\{\mathbf{n}^{(0)}\}^T + \sum_{i=1}^{I} R_{L/U}^{(i)}\{\mathbf{n}^{(i)}\}\{\mathbf{n}^{(i)}\}^T \quad (4)$$

In this relation, the term $\{d\epsilon_p\}$ in Eq.(3) represents the additional strain increment vector to take the dilatancy into account and is given from the volumetric strain increment due to the dilatancy ϵ_p as

$$\{d\epsilon_p\}^T = \{\ \epsilon_p/2\ \ \epsilon_p/2\ \ 0\ \} \quad (5)$$

The first term in Eq.(4) represents the volumetric mechanism with rebound modulus K and the direction vector is given by

$$\{\mathbf{n}^{(0)}\}^T = \{\ 1\ 1\ 0\ \} \quad (6)$$

The second term in Eq.(4) represents the multiple shear mechanism. Each mechanism i = 1,...,I represents a virtual simple shear mechanism, with each simple shear plane oriented at an angle $\theta_i/2 + \pi/4$ relative to the x axis. The tangential shear modulus $R_{L/U}^{(i)}$ represents the hyperbolic stress strain relationship with hysteresis characteristics. The direction vectors for the multiple shear mechanism in Eq.(4) are given by

$$\{\mathbf{n}^{(i)}\}^T = \{\ \cos\theta_i\ -\cos\theta_i\ \sin\theta_i\ \} \quad (\text{for } i = 1,\ldots, I) \quad (7)$$

in which

$$\theta_i = (i-1)\Delta\theta \quad (\text{for } i = 1,\ldots,I) \quad (8)$$
$$\Delta\theta = \pi/I \quad (9)$$

The loading and unloading for shear mechanism are separately defined for each mechanism by the sign of $\{\mathbf{n}^{(i)}\}^T\{d\epsilon\}$.

The multiple shear mechanism takes into account the effect of rotation of principal stress axis directions, the effect of which is known to play an important role in the cyclic behavior of the anisotropically consolidated sand [4]. The model has 10 parameters; two of which specify elastic properties of soil, other two specify plastic shear behavior, and the rest specify dilatancy.

ANALYSIS OF SUBMERGED TUNNEL

Cross Section and Input Motion

The ground and structure system to be analyzed in the present study has a cross section shown in Figure 1. The cross section is a simplified version of one of the tentative sections of the tunnel to be constructed at Niigata City in Japan. The effect of the

liquefaction is one of major concerns in the design of the structures to be constructed in this area because of its history in the liquefaction during the Niigata Earthquake in 1964. The tunnel structure has a dimension of 20 meters in width and 7.5 meters in height. The ground consists of a loosely deposited sand layer of 19 meters in thickness, below which lies a dense sand layer down to 48 meter deep and alternating clay and sand layer down to 128 meter deep.

Soil parameters for the effective stress model were determined based on the results of the undrained cyclic triaxial tests and other laboratory tests. Unit weight of the loosely deposited sand averaged 1.8 tf/m^3 whereas apparent unit weight of the submerged tunnel was about 1.0 tf/m^3. Before conducting the dynamic analysis, a simple one step static analysis was conducted by assigning the gravity for computing initial stress.

The input motion used for the analysis, shown in Figure 2(b), was obtained from a record at Hachinohe Port during 1968 Tokachi-Oki Earthquake of magnitude 7.9 [5]. The maximum acceleration of the input motion was scaled to be 225 Gals for the analysis. Computation was done in the undrained condition using a time step of 0.01 seconds for the duration of 20 seconds. The rigid boundary was imposed at the base whereas transmitting boundaries were considered on both sides of the analyzed domain for taking into account the transmitting waves. Full bonding between the soil and the structure was assumed.

Results of the Analysis

When the shaking starts, the ground and tunnel system at point A in Figure 1 responded to the input motion as shown in Figure 2(a), the maximum acceleration being about half of the input motion possibly due to the liquefaction of loosely deposited sand. In accordance with this response, the tunnel gradually displaced upward as shown in Figure 3(a) and exhibited uplift of about 55 cm at the end of the computation without inducing any significant residual displacement in the horizontal direction as shown in Figure 3(b).

The gradual uplift of the tunnel, shown in Figures 4 and 5, was associated with significant deformation of soil in the vicinity of the tunnel. Because the soil layers at a depth of 19 meters consisted of dense sand and clay as mentioned earlier, the deformation in these layers was much smaller than that in the loosely deposited soil layer above 19 meters. The loosely deposited soil deformed as if they flew into the central part of the soil between the tunnel and the dense sand layer at 25 meters in depth.

The general pattern of the computed soil deformation is consistent

with the one observed during the shaking table tests conducted by Koseki and Koga [1], whose model test result is reproduced in Figure 6. In the analysis as well as in the model test result, the most easily recognized pattern of soil deformation is the one below the structure where extension shear mode is predominant. Axial strains in the soil (indicated by B in Figure 1) are gradually increased as shown in Figure 7. These results clearly indicate that, though the behavior of buried structures is the primary concern, a close look should be directed to the behavior of soil around the structures if one intends to fully understand the mechanism of uplift of the buried structures.

MECHANISM OF UPLIFT

Stress and Strain of Soil below the Structure

The soil element below the structure (element B in Figure 1) underwent gradual extension shear deformation associated with cyclic shear in the horizontal direction as shown in Figure 8. This element initially underwent a deviatoric stress $\tau = \sqrt{[(\sigma_x'-\sigma_y')/2]^2 + \tau_{xy}^2}$ as shown in Figure 9. It was in the compression shear mode as shown in Figure 10, in which stress and strain in extension are defined positive. The compression shear mode before shaking may be the result of the single step static analysis with the gravity, in which soil tended to drag down the structure during consolidation. More realistic initial stress distribution associated with the actual construction procedures may likely be the one in extension shear mode.

When the shaking started, however, the initial stress in the compression shear mode, as seen in Figure 10, was very rapidly released without involving large amount of shear deformation and stabilized at a certain value in the extension shear mode. From then on, axial strain difference in extension shear mode gradually increased up to as much as ten percent as the shaking continued. When this behavior of soil is re-evaluated in the stress space in Figure 9, the stress path rapidly converges to a certain loop in the vicinity of the failure line, at which major deformation of the soil presumably was induced.

Whereas the axial stress difference $(\sigma_y'-\sigma_x')/2$ ranged from 5 to 10 kPa after shaking, the value of $(\sigma_y'-\sigma_x')/2$ to be given by the buoyancy of the structure was 30 kPa. The difference between these values indicates that, though the soil exhibited significant reduction in the effective confining pressure as well as large deformation as much as ten percent in strain, a certain amount of shear resistance was always retained owing to positive dilatancy of sand. It is considered that this resistance tended to drag the structure undergoing uplift, reducing the effect of the buoyancy.

Stress and Strain of Soil at the Side of the Structure

This type of dragging was seen in the soil at the side of the tunnel (soil element D in Figure 1). This soil element, as shown in Figure 11, mainly underwent a simple shear deformation along the vertical plane. Gradual growth in shear deformation, as shown in Figure 12, was induced in accordance with the shaking but a certain amount of shear stress was always recoverable whenever there was an increase in the shear stress.

Stress and Strain of Soil at the Corner of the Structure

At the corner of the structure where the soil apparently turns into below the structure (soil element C in Figure 1), the axial strain difference and the simple shear strain is about the same magnitude as shown in Figure 13. These strains are gradually induced in accordance with the shaking as shown in Figure 14.

DISCUSSIONS

The results seen above indicate that the primary mechanism in producing the uplift of buried structures is the extension shear deformation of soil below the structures. The amount of uplift of the structure, however, is also affected by the dragging effect of soil at the side of the structures. In the present analysis, a full bonding between the structure and the soil was assumed. In reality, this might not be fully satisfied when the water spouting along the sides of the structure occurs. In this regard, some additional work may be necessary. This work may be, in the analysis, simply accomplished by introducing the slip elements in the analysis. This, however, poses somewhat a difficult problem when the stress and the strain concentration in the soil elements at the corners of the structure has to be realistically analyzed. There are simple approaches to handle the stress concentration but one has to take care of the large strain situation as well. This may be an analogous situation to the analysis of the progressive formation of shear band. A lot of attention is being paid to this issue but this seems not very easy to be accomplished with the currently available analytical or computational tools.

Though a complex stress strain relation is seen in each soil element, a trend is recognized which indicates overall gradual reduction in the shear stiffness of soil. In this context, a simple elastic analysis with reduced moduli might be an efficient tool for estimating amount of uplift if a reasonable procedure is obtained for estimating the reduction factor. In view of the complex stress system in the soil around buried structures, the reduction factor

should be obtained through such an effective stress analysis as seen in this study or appropriately conducted model tests of buried structures.

CONCLUSIONS

An effective stress analysis was conducted on a buried structure in a loosely deposited sand. Results of the analysis lead to the following conclusions on the mechanism of uplift of buried structures.

(1) A fundamental mechanism in producing deformation of soil and structure is the existence of static stress due to gravity and its release in accordance with deformation.
(2) The primary mechanism which governs the amount of the uplift of underground structures is the extension shear deformation of the soil below the structures.
(3) A trend is recognized which indicates overall gradual reduction in the shear stiffness of soil.

REFERENCES

[1] Koseki J. and Koga Y. (1990) : "Uplift of Semi-buried Structures in Liquefiable Sands during Earthquake," Proceedings of 8th Japan Earthquake Engineering Symposium, Vol. 1, pp.933-938

[2] Iai, S. and Kameoka, T. (1989) : "Initial stress and residual deformation - effective stress analysis of anchored sheet pile quaywall -," Proceedings from the Second U.S.-Japan Workshop on Liquefaction, Large Ground Deformation and Their Effects on Lifelines, Technical Report NCEER-89-0032, pp.161-175

[3] Iai, S., Matsunaga, Y. and Kameoka, T. (1992a) : "Strain space plasticity model for cyclic mobility," Soils and Foundations, Vol.32, No.2 (in print)

[4] Iai, S., Matsunaga, Y. and Kameoka, T. (1992b) : "Analysis of undrained cyclic behavior of sand under anisotropic consolidation," Soils and Foundations, Vol.32, No.2 (in print)

[5] Tsuchida, H., Kurata, E. and Sudo, K. (1969) : "Strong-motion earthquake records on the 1968 Tokachi-Oki Earthquake and its aftershocks," Technical Note of the Port and Harbour Research Institute, No.80, pp.1-476

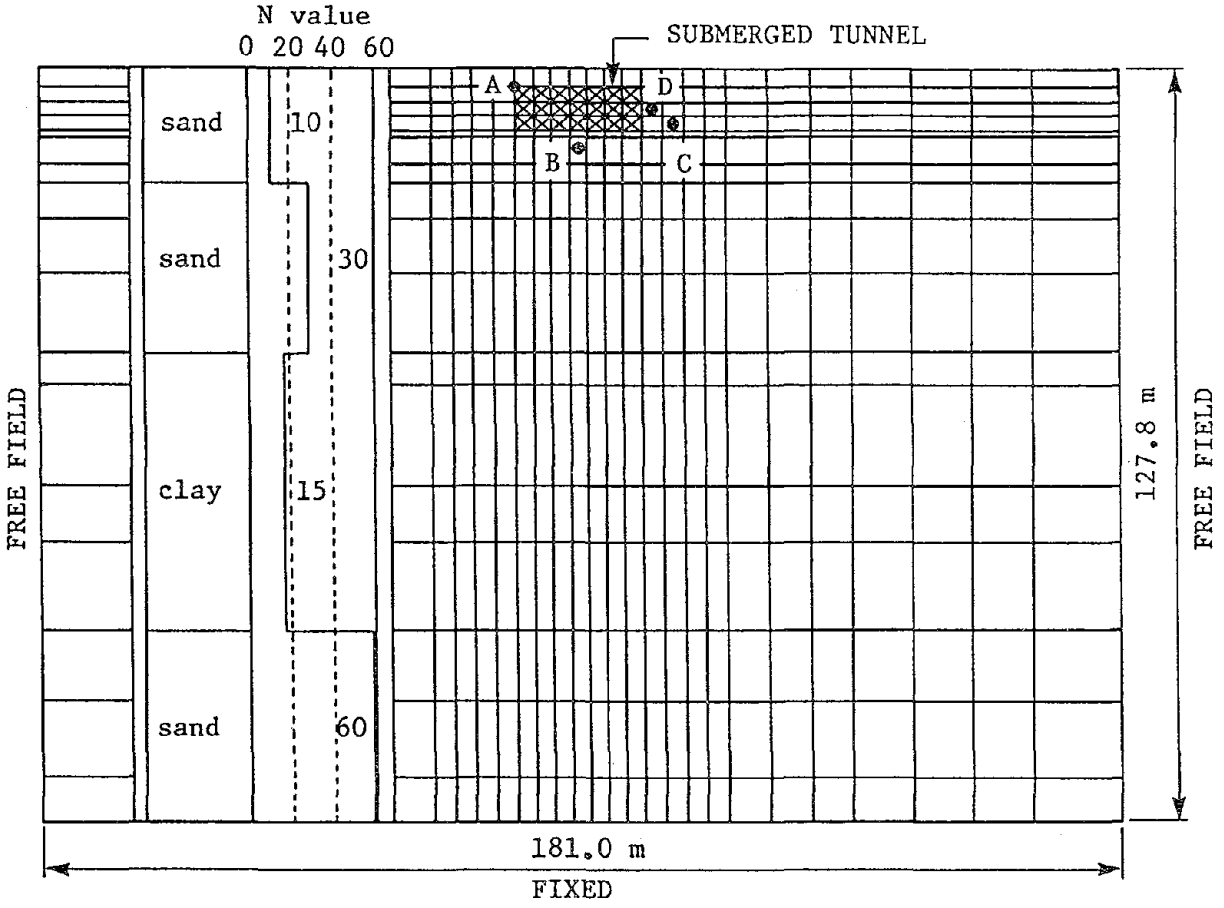

Figure 1 Cross Section of Submerged Tunnel and Soil Profile

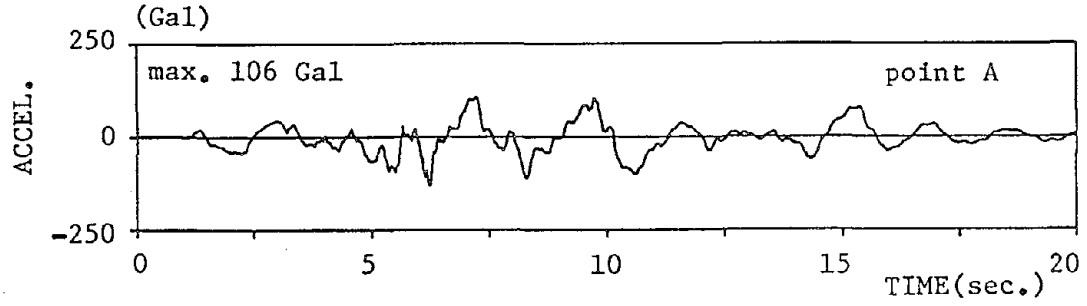

(a) Response Acceleration at Submerged Tunnel

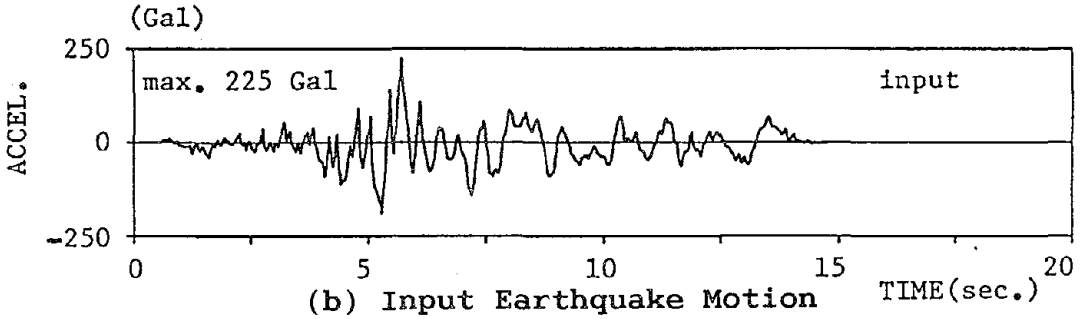

(b) Input Earthquake Motion

Figure 2 Acceleration Response of Ground Structure System

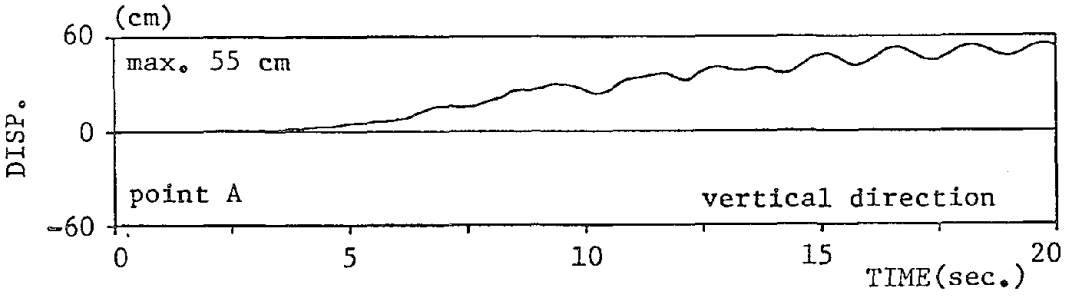

(a) Vertical Component

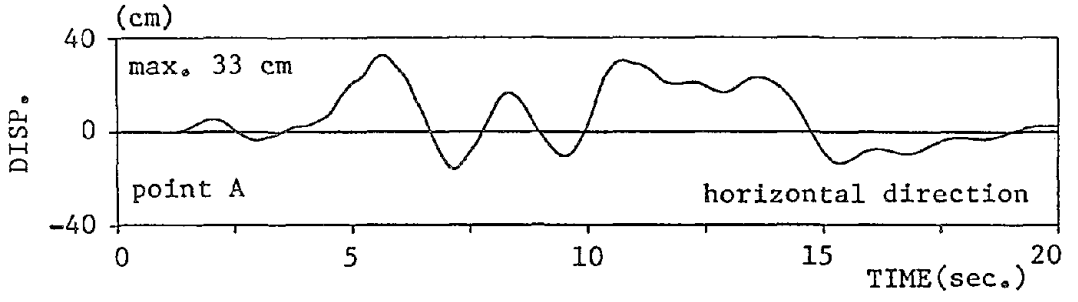

(b) Horizontal Component

Figure 3 Displacement of Submerged Tunnel due to Shaking

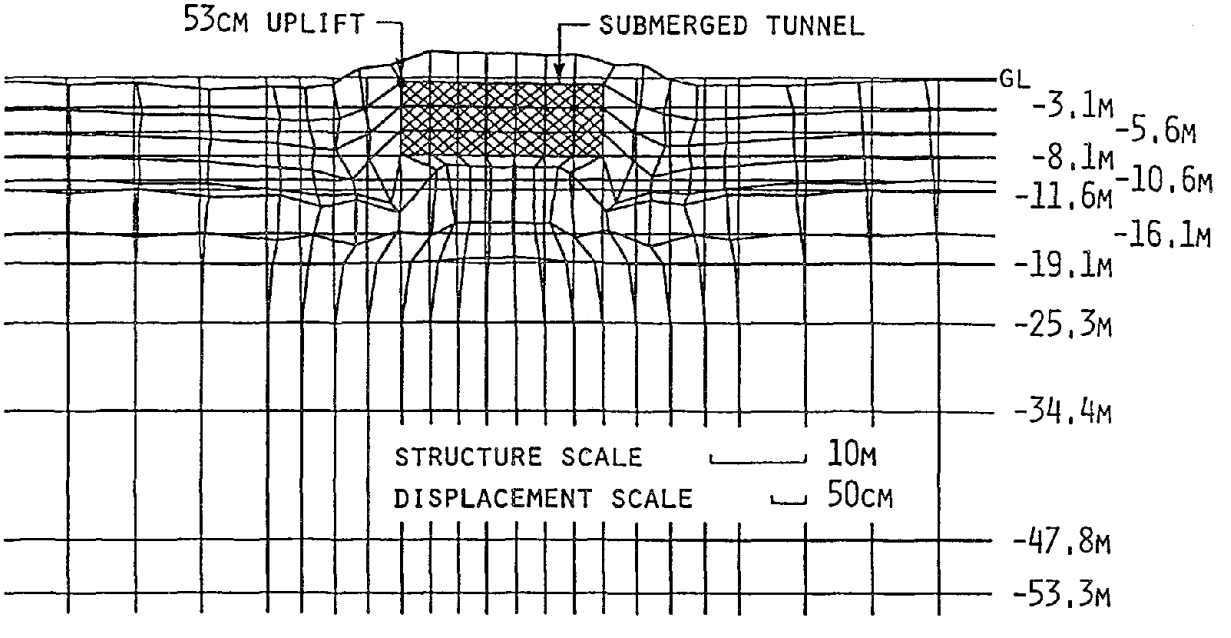

Figure 4 Uplift of Submerged Tunnel and Deformation of Soil

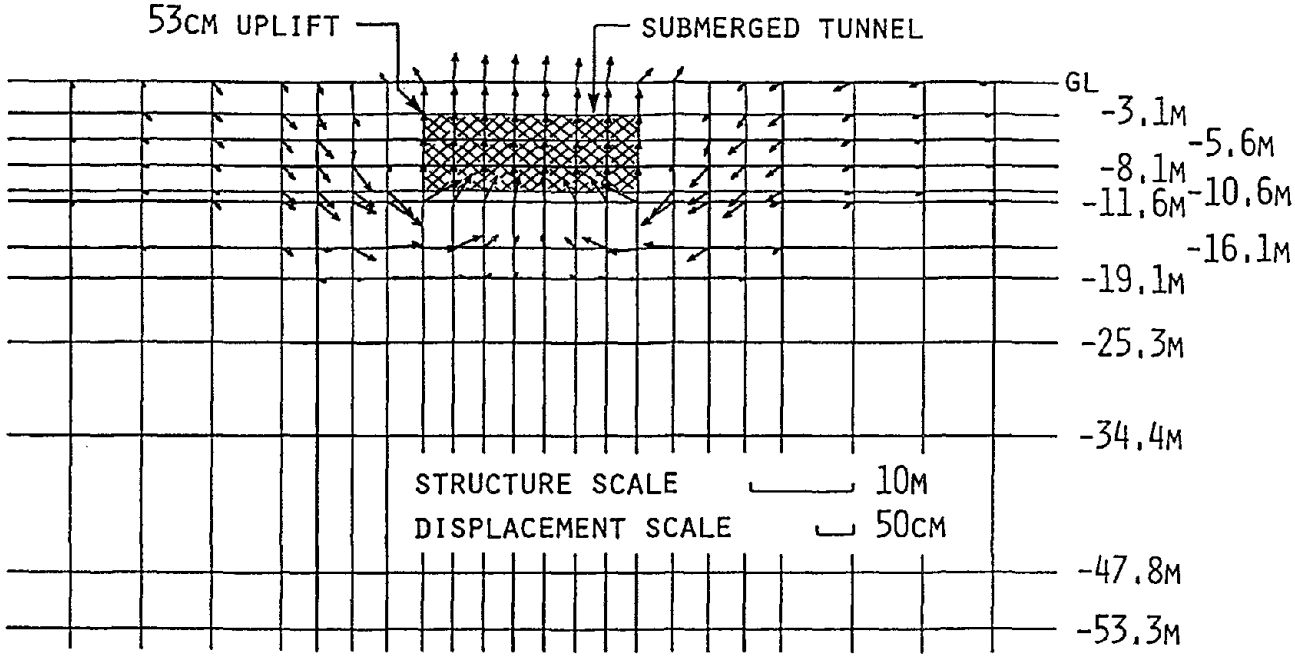

Figure 5 Representation by Arrows of Soil Structure Deformation

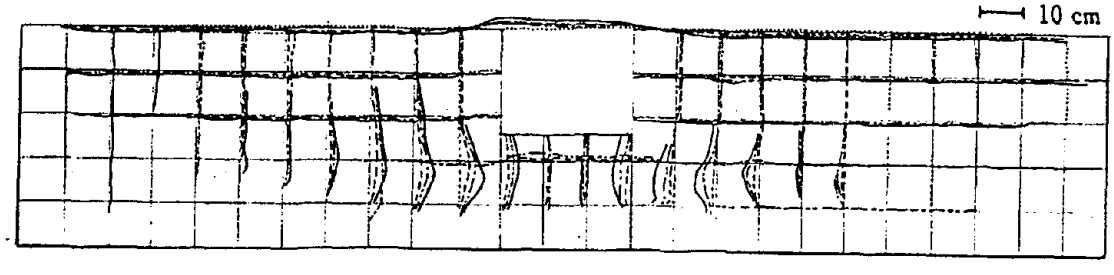

(a) Overall Deformation Pattern

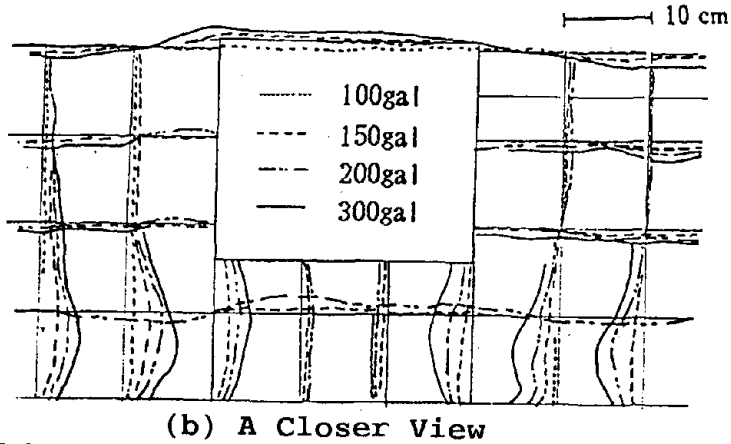

(b) A Closer View

Figure 6 Shaking Table Test Results of a Model Underground Structure (after Koseki and Koga, 1990)

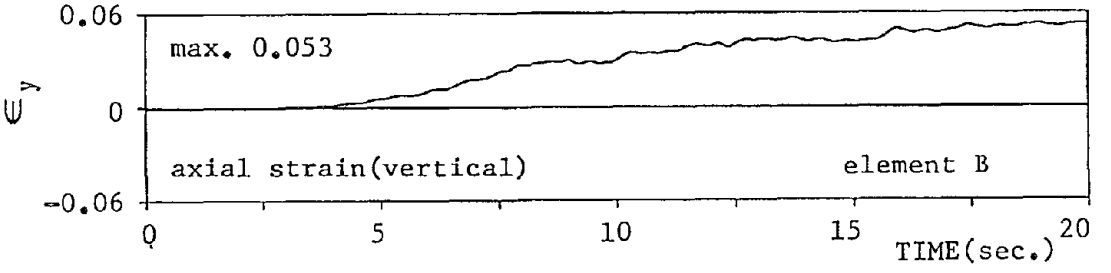

(a) Vertical Normal Strain

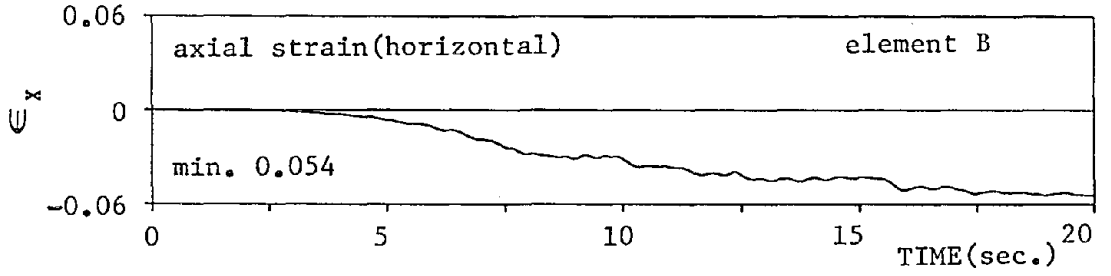

(b) Horizontal Normal Strain

Figure 7 Normal Strains at Soil below Submerged Tunnel (Soil Element B)

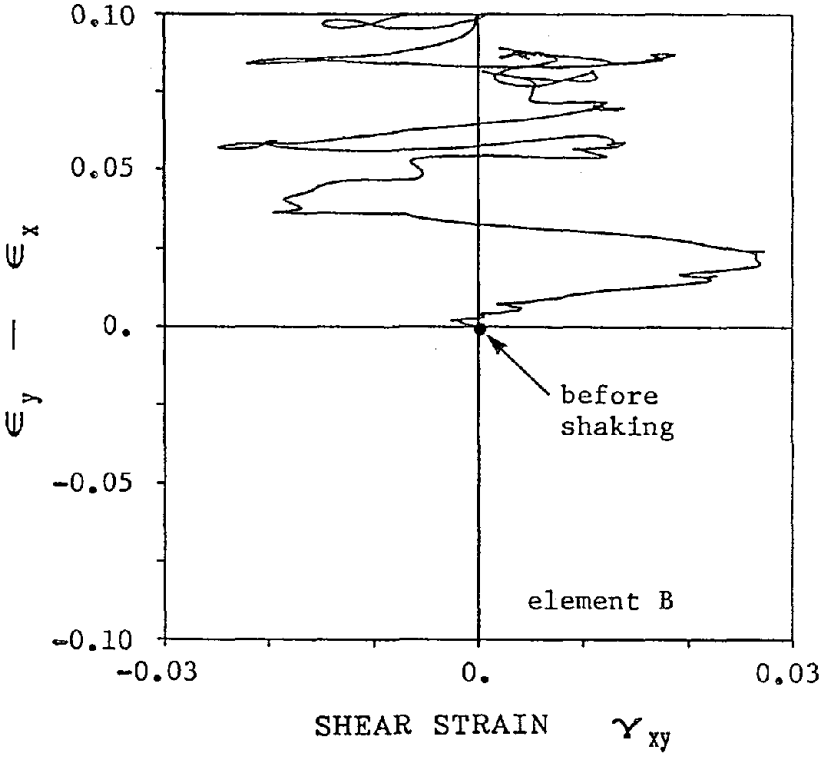

Figure 8 Relation between Axial Strain Difference and Shear Strain at Soil below Submerged Tunnel (Soil Element B)

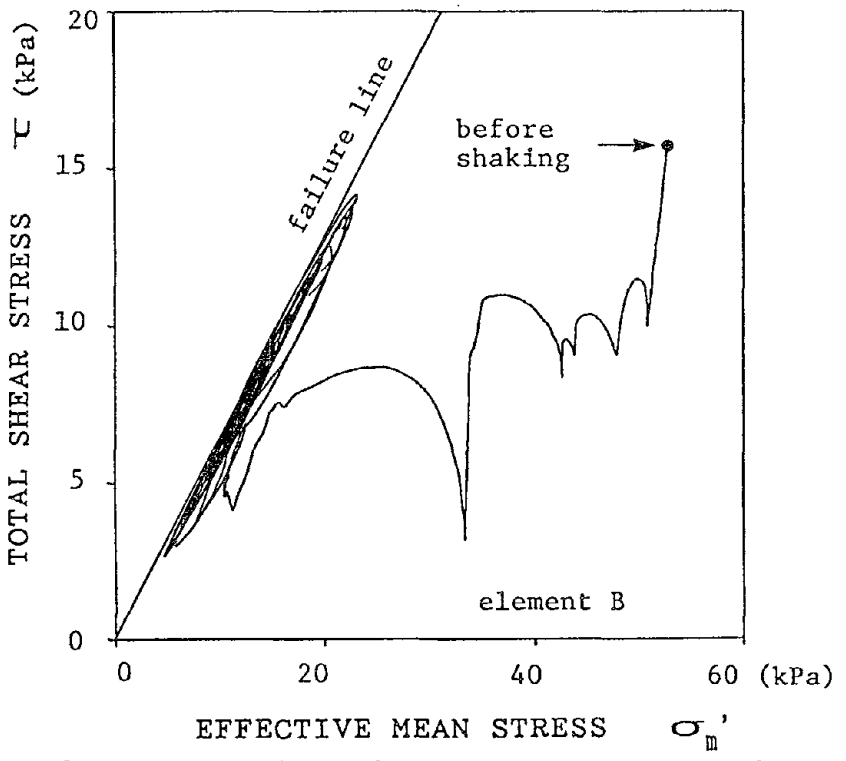

Fig. 9 Relation between Deviatoric Stress and Effective Mean Stress at Soil below Submerged Tunnel(Soil Element B)

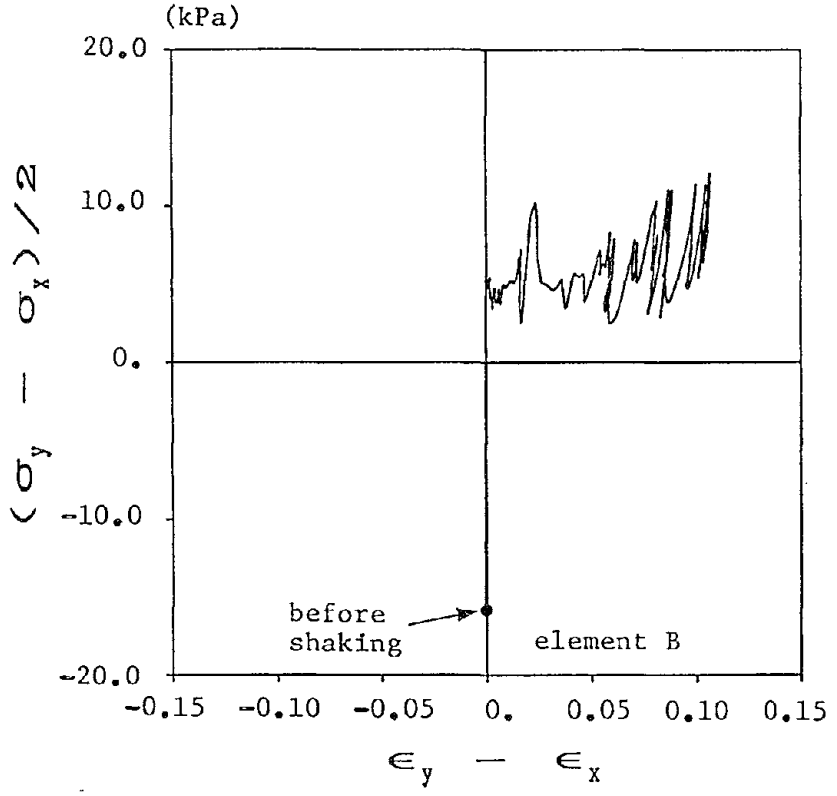

Fig. 10 Relation between Axial Stress Difference and Axial Strain Difference at Soil below Submerged Tunnel (Soil Element B)

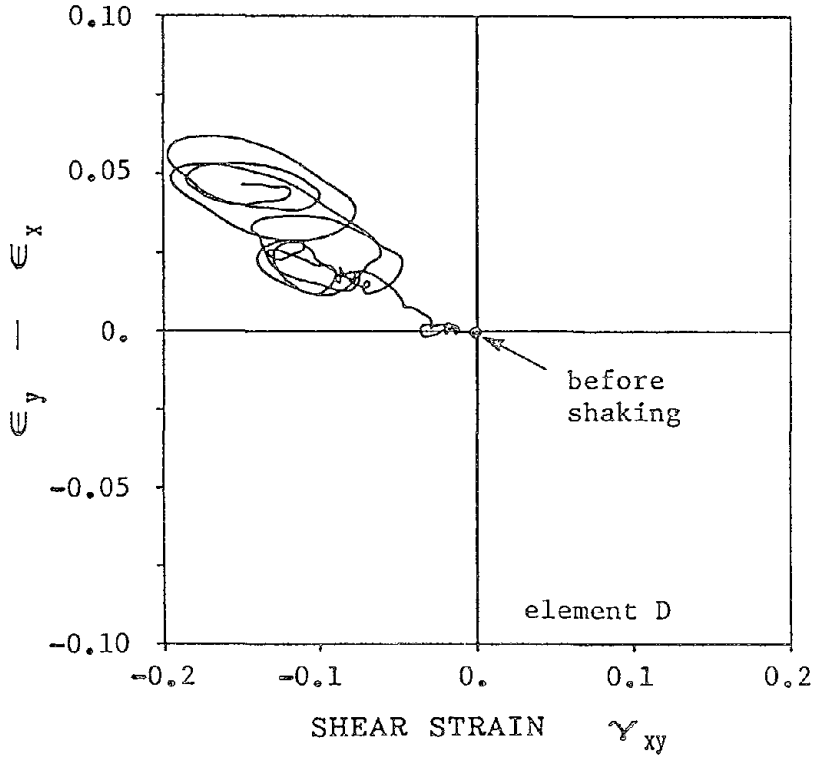

Fig. 11 Relation between Axial Strain Difference and Shear Strain at Soil on the Side of Submerged Tunnel (Soil Element D)

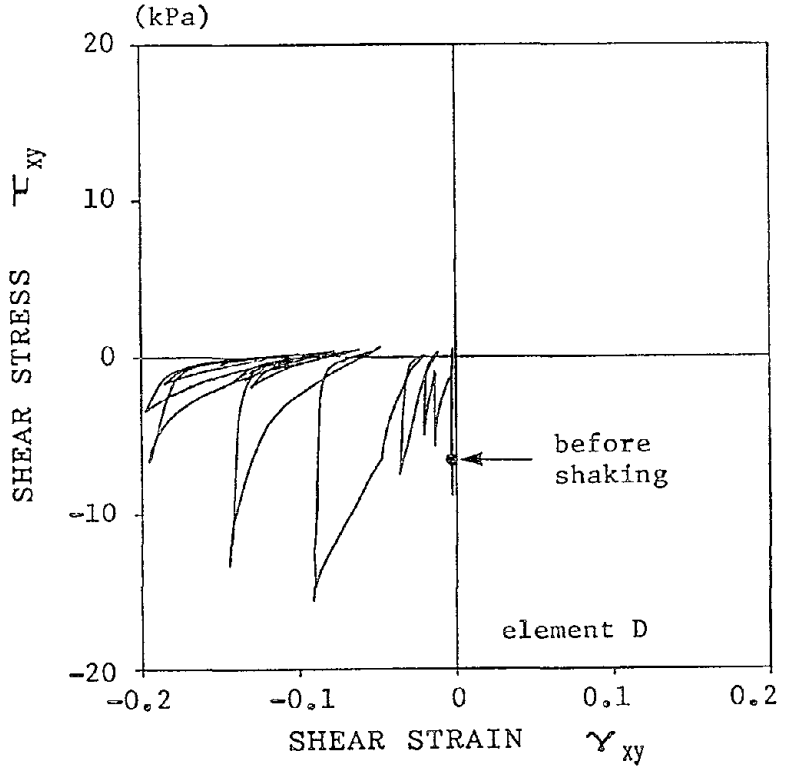

Fig. 12 Relation between Shear Stress and Shear Strain at Soil on the Side of Submerged Tunnel (Soil Element D)

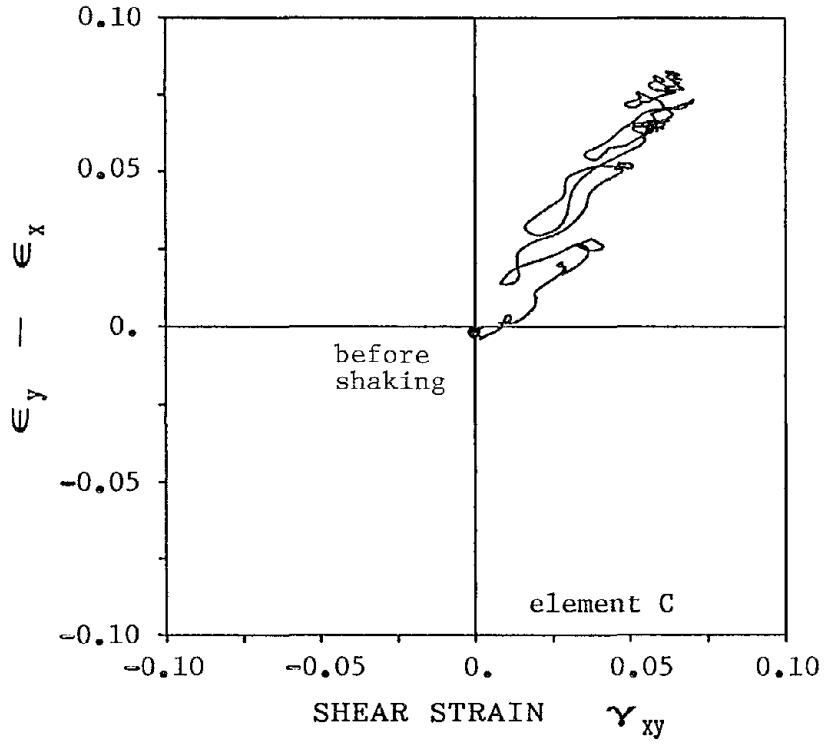

Fig. 13 Relation between Axial Strain Difference and Shear Strain in Soil at the Corner of Submerged Tunnel (Soil Element C)

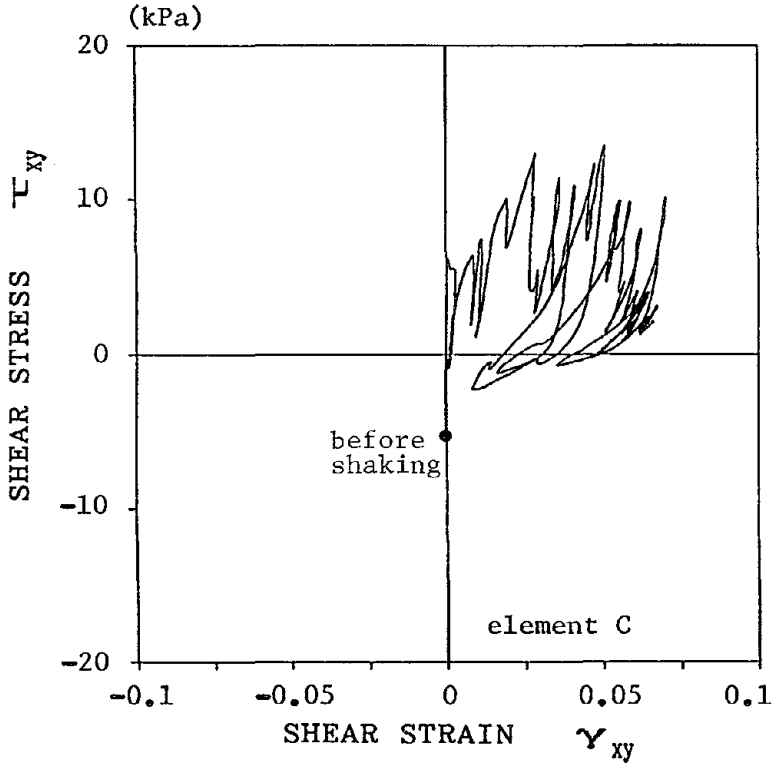

Fig. 14 Relation between Shear Stress and Shear Strain in Soil at the Corner of Submerged Tunnel (Soil Element C)

A New Method to Estimate Earthquake Liquefaction Damage to Buried Lifelines

Dr. Phillip A. Lowe, President
INTECH Inc.
11316 Rouen Dr.
Potomac, MD 20854-3126

Mr. William Bivins
Federal Emergency Management Agency
500 C St.
Washington DC, 20472

Dr. T.D. O'Rourke
Professor of Civil Engineering
Cornell University
Ithaca, NY 14853-3501

ABSTRACT

A new method that relates soil movement to buried lifeline damage state has been developed and applied during a Federal Emergency Management Agency-sponsored study to evaluate the impacts of lifeline proximity during earthquakes. The method considers landslides and liquefaction as a continuum of ground displacement; it uses similar analysis methods for estimating the impacts of such motions on buried lifelines. For landslides, a critical acceleration parameter is used to estimate the lifeline damage state, which is also related to a displacement scaling parameter. Similarly, a Liquefaction Severity Index (LSI) parameter is used to estimate the lifeline damage state for lateral spread or liquefactions conditions. The LSI can also be related to a displacement scaling parameter. The relationship of the LSI parameter to the earthquake intensity and lifeline damage state is new and is based on empirical data and expert judgement.

INTRODUCTION

The Federal Emergency Management Agency (FEMA) sponsored the development of an engineering methodology to classify California facilities and to assess their potential damage, economic losses, and restoration times from earthquake events. The methodology is described in a document referred to as ATC-13 (Applied Technology Council, 1985). In work recently completed under FEMA sponsorship (Rojahn et. al, 1991), the ATC-13 methodology was used to evaluate lifeline vulnerability and potential service disruptions for seven scenario earthquakes representative of the principal seismic regions of the coterminous U.S. (Applied Technology Council, 1991).

The early work of ATC-13 proposed using the methods of Wieczorek et. al. (1985) as modified by Legg et. al. (1982). Using the local lithology, a critical acceleration parameter was calculated. The critical acceleration was related to a slope failure state scale, which can be expressed either as a relative failure

condition or as a predicted ground displacement, using the Modified Mercalli Intensity (MMI) index (Wood and Newmann, 1931) as a scaling parameter. Any lifeline in a region where a landslide is predicted is assumed to incur a percent damage, based on the value of the predicted ground displacement or the relative failure condition. This single approach does not differentiate between modern high strength buried lifelines and older, less rugged lifelines. That is, the methodology predicts the same failure level in either lifeline.

Buried pipeline damage from permanent ground deformation caused by soil liquefaction is accounted for indirectly by means of an empirical factor derived from pipeline repair statistics associated with the 1906 San Francisco earthquake. Specifically, the procedure for calculating damage caused by liquefaction/poor ground involves multiplying the damage estimate for seismic shaking by the product of the probability of ground failure intensity and a factor of 10. The factor of 10 is intended to magnify the damage estimate for shaking alone so that the resulting estimate is consistent with the observation of Wood (1908) from the 1906 earthquake that "damage on poor ground was 5 to 10 times greater than on firm ground" (ATC-13, 1985). For above ground lifelines, the ATC-13 methodology used a multiplying factor of 5. Thus, under some conditions, buried modern, high strength steel pipelines would be estimated to fail during liquefaction conditions which would only cause partial damage to masonry, surface buildings.

In other work sponsored by FEMA (Lowe et. al, 1992), a methodology has been developed for evaluating the risk and potential losses for collocated lifelines, with application to the Cajon Pass, CA, where many lifeline facilities cross the San Andreas fault in order to provide services for the Los Angeles area. This methodology improved the ATC-13 methodology for both bridges and for buried lifelines. In that collocation study, a different approach was adopted for estimating buried lifeline damage from liquefaction to allow differentiation between rugged, modern lifeline construction and older more fragile construction techniques. The new method makes use of measures for liquefaction severity developed by Youd and Perkins (1978, 1987). The category of buried pipelines adopted in ATC-13 was expanded into three separate categories of buried pipelines and conduits to reflect better the different levels of vulnerability associated with various types and composition of underground utilities. Empirical data were used to relate the Liquefaction Severity Index (LSI) (Youd and Perkins, 1978, 1987) to the MMI value. The LSI was also related to physical lateral ground movement, lifeline damage condition, and lifeline damage state. The probability-damage state matrix developed for landslide-induced damage (which is really a description of soil movement-induced damage) could then be related to the probability of liquefaction-induced damage for the buried lifelines. This paper describes the methodology adopted in the collocation study for evaluating liquefaction intensity and its effects on buried lifelines.

GROUND FAILURES

Three principal modes of ground failure were emphasized in ATC-13: liquefaction, landslides, and surface faulting. These categories were preserved in the collocation study, and the methodologies for assessing landslide and surface faulting

effects were adopted as provided in ATC-13.

It was recognized that liquefaction can cause lateral spreading, flow failure, differential settlement, loss of bearing, and buoyancy effects. Of these, lateral spreading and flow failure cause the most severe ground deformation and subsequent damage to buried piping and conduits. Previous earthquake experience has shown that lateral spreads tend to be more widespread and frequent in occurrence than flow failures. Accordingly, lateral spreads were selected as the most appropriate type of severe ground movement caused by liquefaction, and as being a suitable failure state for evaluating liquefaction-induced damage.

A lateral spread involves the horizontal movement of surface soil layers over a liquefied layer. Because the earth pressures and deformation conveyed to a buried lifeline from lateral spreading generally occur through the intact surface soils, the effects of lateral spreads and landslides should be identical for similar magnitudes of displacement and areal dimensions for the unstable ground. As far as the mechanical effects on a buried lifeline are concerned, there is no practical difference between the consequences of a lateral spread and a landslide with similar magnitudes and patterns of displacement. Hence, the procedure for assessing the potential buried lifeline damage from a lateral spread should be consistent with that used for landslide analysis.

As stated above, the ATC-13 method for evaluating landslide effects was derived from slope and failure intensity matrices developed originally by Wieczorek et. al. (1985) and Legg, et. al. (1982). The method characterizes the potential stability of a slope according to its critical acceleration, a_c, which is defined according to the dynamic stability models and field assessment procedures summarized by Wilson and Keefer (1985). Table 1 shows the slope failure probability matrix in ATC-13 for a slope of low stability, for which $0.01\ g \leq a_c < 0.1\ g$. Five failure states are defined according to the qualitative descriptions and quantitative ranges of displacements given in the table. The probabilities of all failure states for a given MMI result in a cumulative probability of 100%. The stability of the slope is assessed by calculating a_c and estimating the horizontal component of acceleration at the location of interest on the basis of earthquake magnitude, epicentral distance, and appropriate attenuation relationships.

The relationship between Lifeline Damage State and Percent Damage, for both pipeline and non pipeline lifelines is taken from ATC-13 and is shown in Table 2. The definitions which were used by the ATC-13 panel of experts to develop the relationships were: percent damage meant the estimate of the dollar value of the earthquake damage divided by the dollar cost to replace the entire lifeline. However, for pipelines they were asked to think in terms of breaks in a pipeline per kilometer of pipeline length.

Lateral Spread Assessment

The Liquefaction Severity Index (LSI) parameter is defined as the amount of differential movement in inches of lateral spreads in active flood plains, deltas, and other areas of gently-sloping late Holocene fluvial deposits. The

LSI is the "general maximum" value of differential movement, excluding single high displacements that may have resulted from unusual soil or hydrological conditions. LSI represents a relatively large estimate of potential movement that will exceed the values observed in the majority of sites susceptible to liquefaction. Lifeline damage will depend not only on the presence of liquefiable soil deposits, but also on the location of the lifeline on or within liquefiable soils. Accordingly, LSI is a conservative estimate of the deformation imposed on a particular lifeline or lifeline system because it is biased to large values of movement, and is dependent on the collocation of lifeline and liquefiable deposit.

As proposed by Youd and Perkins (1987), LSI can be estimated on the basis of attenuation relationships involving earthquake magnitude and distance from the seismic energy source. Because damage probability matrices, such as the one for landslides in Table 1, are defined for various levels of MMI, it is convenient to express LSI as a function of MMI. This type of relationship can be developed from the records of observed lateral spreads in previous U.S. earthquakes.

Table 3 summarizes the data from liquefaction-induced lateral spreads or differential lateral movement expressed as LSI and MMI values. It is based on interpreting the narrative discussion reported for the 1906 San Francisco, 1964 Alaska, 1971 San Fernando, and 1979 Imperial Valley earthquakes. The pertinent references also are listed in the Table. Figure 1 is a plot of the data of Table 3. The best fit linear regression and its associated regression equation are shown in the figure. The coefficient of determination, r^2, for the regression is 0.68, which implies a reasonably good fit of the linear trend.

In a manner similar to using the landslide critical acceleration as a scaling parameter to relate landslide effects to damage states, Table 4 relates the LSI to damage states and damage conditions. Using the equation of Figure 1 and Table 4 relationships, Figure 2 can be constructed to visually show the relationship between LSI and damage state.

The data in Table 2 and regression analysis of Figure 1 also can be used to develop the Liquefaction-Induced Lateral Spread Probability Matrix in Table 5. In choosing the distribution of lateral spread probabilities for a given MMI, it was assumed that LSI corresponds to the 90-percentile deformation in a given liquefaction-prone environment. This assumption is consistent with the definition given by Youd and Perkins (1987) that LSI equals the "general maximum" lateral displacement. The predicted LSI from the regression equation was used to fix the Liquefaction Failure State for a given MMI that corresponds to the 90-percentile value; i.e., the sum of probabilities within the failure state and at all failure states less severe equals approximately 90%. The distributions were structured to be skewed to the lower and higher ends of the Liquefaction Failure State for lower and higher MMIs, respectively. This skewing of the distributions reflects the preponderance of large deformation likely to prevail for very high MMI and the relative absence of significant displacement likely to be characteristic of relatively low MMI. More symmetric distributions were assumed for MMI = VIII to X.

As a final check, the probability matrix for lateral spreads should be similar to that for landslides on slopes with a_c equivalent to the a_c which best

represents the lateral spreads. Recent analytical studies (Harding Lawson Associates, et al., 1991) suggest that lateral spreads similar in magnitude to those triggered at MMI = X by the 1906 earthquake in San Francisco were characterized by 0.05 g < a_c ≤ 0.15 g. Accordingly, the distribution of probabilities for lateral spreads at MMI = X should be similar to those for landslides at MMI = X with 0.01 g ≤ a_c < 0.1 g. By comparison of Tables 1 and 5, the similarity can be verified. This general similarity is preserved for all other values of MMI.

Unlike LSI, the lateral spread probability matrix in Table 5 accounts for various ranges of displacement, and thus, is more consistent with the actual variation of lateral displacement that would occur in the field. As indicated in the footnote of Table 5, the probability matrix applies not only to late Holocene fluvial deposits, but to loose sandy fill placed either by end dumping or hydraulic dredging and pumping.

DAMAGE FACTORS

Pipelines and underground conduits comprise many different materials, standards of workmanship, ages, stress histories, and degrees of maintenance. In ATC-13, all lifelines were accounted for under a single category. Given the diversity of pipelines and conduits used in practice, as well as the varying degrees of vulnerability exhibited by them, it is important to establish several different categories to account properly for the different levels of expected loss associated with stronger and weaker facilities.

Three categories, or groups, of underground lifelines were defined as shown in Table 6. Damage factors were assigned to each group in accordance with the severity of the ground failure state defined for either landslides (Table 1) or liquefaction (Table 5). The damage factor is represented as both the percentage loss for a particular portion or segment of a lifeline system or as a damage state. This facilitates use of the Table 6 values for calculating expected damage or lifeline restoration times, as those items are typically related to either damage state or damage factor.

EXAMPLE CALCULATIONS

The mean damage factor for ground failure, MDF_{GF}, for a given category of underground lifelines is calculated by summing the products of the damage factor (a central damage factor which is expressed as a fraction) from Table 5 times the probability that the damage occurred taken from Table 6 (also expressed as a fraction. This is given in equation 1:

$$MDF_{GF} = \Sigma\ P_{GFI} \times CDF_{GFI}; \quad (1)$$

MDF_{GF} = the ground failure caused by either landslide or liquefaction,

P_{GFI} = the probability of a given failure intensity associated with either

landslide or liquefaction from Table 1 or 6,

and CDF_{GFI} = the central damage factor, as given in Table 5.

Consider, for example, modern gas and petroleum pipelines located in the toe area of saturated, late Holocene alluvial fan deposits where MMI = X is predicted. Using Tables 5 and 6, the MDF_{GF} is computed as follows:

$$MDF_{GF} = (0)(0) + (0.15)(0) + (0.35)(0.15) + (0.35)(0.5) + (0.15)(1.0) = 0.3775 \quad (2)$$

The MDF_{GF} implies that there is a 1 in 3 to 2 in 5 chance of failure. During the 1971 San Fernando earthquake, five modern steel gas and petroleum pipelines were subjected to lateral spreads in a MMI = X area on the western side of the Upper Van Norman Reservoir (O'Rourke, et al., 1992). One of these lines failed, thereby indicating a 1 out of 5 failure ratio, which compares reasonably with the estimate of MDF_{GF}.

As a second example, consider a cast iron water distribution system in an area of liquefiable soil for which MMI = IX is predicted. The MDF_{GF} is computed as follows:

$$MDF_{GF} = (0.10)(0) + (0.25)(0.3) + (0.40)(0.6) + (0.20)(0.9) + (0.05)(1.0) = 0.55 \quad (3)$$

The MDF_{GF} implies that there is over a 50% chance of failure in the local water supply system. During the 1989 Loma Prieta earthquake, cast iron distribution water mains were subjected to soil liquefaction at an intensity level of MMI = IX in the Marina District (O'Rourke, et al., 1992). There were 69 repairs to broken water mains, 54 repairs to services, and 20% of the mains eventually were replaced. No water was available locally from this system after the earthquake. In terms of water disruption, restoration time, hours of personnel activity, and repair and replacement cost, this loss compares reasonably with the MDF_{GF} estimate.

CONCLUSIONS

This methodology has been successfully applied to lifelines in the Cajon Pass, CA, (Lowe et. al., 1992). It provides more definition for the liquefaction-induced damage that can result to buried lifelines during earthquake conditions than was previously. In the application to the Cajon Pass, the methodology was used to develop a screening approach that could identify the high risk locations where lifelines in proximity or collocation conditions would be subjected to earthquakes. Since most of the data used for the development of the present methodology to examine buried lifelines subjected to liquefaction conditions and all of the related data taken from ATC-13 were based on information from California, it is now important to apply the methodology to additional U.S. regions to establish its general applicability. The Cajon Pass study was sponsored by the Federal Emergency Management Agency, and they are now in the process of implementing a program to further examine collocated lifelines at other U.S. regions.

ACKNOWLEDGEMENT

The authors wish to acknowledge the support received from FEMA for the development of the information presented in this paper.

REFERENCES

American Petroleum Institute, "Standard for Welding Pipelines and Related Facilities," API Standard 1104, 15th ed., Washington, D.C., September 1980.

Applied Technology Council, "Earthquake Damage Evaluation Data for California," ATC-13, Redwood City, CA, 1985.

Bartlett, S.F. and T.L. Youd, "Case Histories of Lateral Spreads Caused by the 1964 Alaska Earthquake", Case Studies of Liquefaction and Lifeline Performance During Past Earthquakes, Vol. 2: United States Case Studies, T.D. O'Rourke and M. Hamada, Eds., NCEER-92-0002, National Center for Earthquake Engineering Research, Buffalo, NY, 1992.

Harding Lawson Associates, Dames & Moore, Kennedy/Jenks/Chilton, and EQE Engineering, "Liquefaction Study of Marina District and Sullivan Marsh Area, San Francisco, California", report prepared for City and County of San Francisco, August 1991.

Lawson, A.C., et. al.,The California Earthquake of April 18, 1906: Report of the California State Earthquake Investigation Commission, Pub. No. 87, Carnegie Institute, Washington, D.C., 1908.

Legg, M., G. Slosson, and R. Eguchi, "Seismic Hazard for Lifeline Vulnerability Analyses", Proceedings, 3rd International Conference on Microzonation, Seattle, WA, 1982.

Lowe, P.A., C.F. Scheffey, and P. Lam, "Collocation Impacts on the Vulnerability of Lifelines During Earthquakes with Application to the Cajon Pass, California", FEMA 226, February 1992.

McCulloch, D.S. and M.G. Bonilla, "Effects of the Earthquake of March 27, 1964 on the Alaska Railroad", USGS Professional Paper 545-D, U.S. Government Printing Office, Washington, D.C., 1970.

O'Rourke, T.D., P.A. Beaujon, and C.R. Scawthorn, "Large Ground Deformations and Their Effects on Lifeline Facilities: 1906 San Francisco Earthquake", Case Studies of Liquefaction and Lifeline Performance During Past Earthquakes, Vol. 2: United States Case Studies, T.D. O'Rourke and M. Hamada, Eds., NCEER-92-0002, National Center for Earthquake Engineering Research, Buffalo, NY, 1992a, pp. 1-1 to 1-143.

O'Rourke, T.D., B.L. Roth, and M. Hamada, "Large Ground Deformations and Their

Effects on Lifeline Facilities: 1971 San Fernando Earthquake", Case Studies of Liquefaction and Lifeline Performance During Past Earthquakes, Vol. 2: United States Case Studies, T.D. O'Rourke and M. Hamada, Eds., NCEER-92-0002, National Center for Earthquake Engineering Research, Buffalo, NY, 1992b.

O'Rourke, T.D. and J.W. Pease, "Large Ground Deformations and Their Effects on Lifeline Facilities: 1989 Loma Prieta Earthquake", Case Studies of Liquefaction and Lifeline Performance During Past Earthquakes: Vol. 2: United States Case Studies, T.D. O'Rourke and M. Hamada, Eds., NCEER-92-0002, National Center for Earthquake Engineering Research, Buffalo, NY, 1992c.

Reagor, B.G., et al., "Preliminary Evaluation of the Distribution of Seismic Intensities", The Imperial Valley, California Earthquake of October 25, 1979, USGS Professional Paper 1254, U.S. Government Printing Office, Washington, D.C., 1982.

Rojahn, C., et. al., "Seismic Vulnerability and Impact of Disruption of Lifelines in the Conterminous United States", FEMA 224, September 1991.

Steinbrugge, K.V., "Earthquakes, Volcanoes, and Tsunamis", Scandia America Group, New York, NY, 1982.

Wieczorek, C., et. al., "Seismic Slope Stability Map of San Mateo County, California", U.S. Geological survey, Menlo Park, CA, 1985.

Wilson, R.C. and D.K. Keefer, "Predicting the Limits of Earthquake-Induced Landsliding", in Evaluating Earthquake Hazards in the Los Angeles Region - An Earth-Science Perspective, J.I. Ziony, Ed., USGS Professional Paper 1360, Washington, D.C., 1985.

Wood, H., "Isoseismals: Distribution of Apparent Intensity", The California Earthquake of April 18, 1906, Report of the State Investigation Commission, Carnegie Institution of Washington, 1908.

Wood, H.O. and F. Newmann, "Modified Mercalli Intensity Scale of 1931", Seismological Society of America Bulletin, Vol. 21, No. 4, 1931.

Youd, T.L. and G.F. Wieczorek, "Liquefaction and Secondary Ground Failure in the Imperial Valley, California Earthquake of October 25, 1979", The Imperial Valley, California Earthquake of October 25, 1979, USGS Professional Paper 1254, 1982.

Youd, T.L. and D.M. Perkins, "Mapping Liquefaction Induced Ground Failure Potential", Journal of the Geotechnical Engineering Division, ASCE, Vol. 104, GT4, 1978.

Youd, T.L. and D.M. Perkins, "Mapping Liquefaction Severity Index", Journal of the Geotechnical Division, ASCE, Vol. 113, No. GT11, 1987.

Table 1
LANDSLIDE SLOPE FAILURE PROBABILITY MATRIX
(after Applied Technology Council, 1985)

Slope Failure State	Slope Stability: Low, .01 g < a_c < 0.1 g			MMI			
	VI	VII	VIII	IX	X	XI	XII
3 - Light	40	25	15	10	5	0	0
4 - Moderate	30	30	35	30	20	10	0
5 - Heavy	25	35	40	40	35	35	30
6 - Severe	5	10	10	15	30	35	40
7 - Catastrophic	0	0	0	5	10	20	30
Σ_p	100%	100%	100%	100%	100%	100%	100%

SLOPE FAILURE STATE SCALE

Light - Insignificant ground movement, no apparent potential for landslide failure, ground shaking only effect. Predicted displacement less than 0.5 cm.

Moderate - Moderate ground failure, small cracks likely to form (having effects similar to lurch phenomena). Predicted displacement between 0.5 cm and 5.0 cm.

Heavy - Major ground failure, moderate cracks and landslide displacements likely. Predicted displacement between 5.0 cm and 50 cm.

Severe - Extreme ground failure, large cracks and landslide displacements likely. Predicted displacement between 50 cm and 500 cm.

Catastrophic - Landslide moves large distances. Predicted displacement greater than or equal to 500 cm.

Table 2
DEFINITIONS FOR RELATING LIFELINE DAMAGE STATE TO PERCENT DAMAGE

Lifeline Damage State		For Non Pipeline Lifelines	For Pipeline Lifelines	
Number	Description	% Damage	Breaks/kilometer	% Damage
1	None	0	0	0
2	Slight	0.5	0.25	0.6
3	Light	5	0.75	2
4	Moderate	20	5.5	14
5	Heavy	45	15	38
6	Major	80	30	75
7	Destroyed	100	40	100

Table 4
RELATIONSHIP BETWEEN LIQUEFACTION SEVERITY INDEX (LSI) AND DAMAGE STATE

Physical Lateral Ground Movement	Equivalent LSI	Damage State	Damage Condition
< 0.5 inch	< 1	3	light
0.5 to 5.0 inches	1-5	4	moderate
5 to 30 inches	5-30	5	heavy
30 to 90 inches	30-90	6	severe
> 90 inches	> 90	7	catastrophic

Table 3
SUMMARY OF LIQUEFACTION SEVERITY INDEX AND MODIFIED MERCALLI INTENSITY FOR SEVERAL U.S. EARTHQUAKES

Earthquake	Location	LSI	MMI	Reference
1906 San Francisco	San Ardo	5	V	Youd and Perkins (1987)
	Gonzales Bridge	20	VII	
	Salinas Bridge	70	IX	
	Neponsat Bridge	100	IX	Youd and Hoose (1978)
	Moss Landing	100	IX	
	McGowan Ranch	100	IX	
	Whitcomb Ranch	70	IX	Lawson, et al. (1908)
	Duncan's Mill	100	IX	
	Healdsburg	25	IX	
	Alexander Valley	15	VIII	Steinbrugge (1982)
	Eel River Delta	30	IX	
	Foot of Market	50	X	O'Rourke, et al. (1992a)
	South of Market	80	X	
	Mission Creek	80	X	
1964 Alaska	Matanuska River	25	IX	Bartlett and Youd (1991)
	Portage Area	70	X	
	Snow River	100	X	McCulloch and Bonilla (1970)
	Resurrection River	30	X	
1971 San Fernando	East Side of Upper Van Norman Reservoir	90	X	O'Rourke, et al. (1992b)
	West Side of Upper Van Norman Reservoir	70	X	
1979 Imperial Valley	Wiest Lake	7	VI	Youd and Wieczorek (1982)
	Hwy. 2, Mexico	5	VII	Reagor, et al. (1982)

Table 5
LIQUEFACTION-INDUCED LATERAL SPREAD PROBABILITY MATRIX[1]
(after Lowe et. al., 1992)

Liquefaction Failure State	MMI VI	VII	VIII	IX	X	XI	XII
Light	75	50	20	10	0	0	0
Moderate	20	30	40	25	15	10	0
Heavy	5	20	30	40	35	25	20
Severe	0	0	10	20	35	40	30
Catastrophic	0	0	0	5	15	25	50
P_{Σ}	100%	100%	100%	100%	100%	100%	100%

[1]MMI and corresponding probabilities of lateral spreads are defined relative to soil environments in which liquefaction is likely to occur under strong earthquake shaking. These environments include active flood plains, deltas, and other areas of gently-sloping late Holocene fluvial deposits [as defined by Youd and Perkins (1987)] and loose sandy fill below the water table, generally placed by end dumping or hydraulic fill methods. For liquefaction-susceptible environments, the water table generally should be within 3 to 5 m of the ground surface.

LIQUEFACTION FAILURE STATE SCALE

Light - General maximum differential movement: $\leq$ 1 cm; equivalent LSI < 1.

Moderate - General maximum differential movement: 1 to 10 cm; equivalent LSI: 1 - 5.

Heavy - General maximum differential movement: 10 to 75 cm; equivalent LSI: 5 - 30.

Severe - General maximum differential movement: 75 to 230 cm; equivalent LSI: 30 - 90.

Catastrophic - General maximum differential movement > 230 cm; equivalent LSI > 90.

Table 6
CONVERSION OF LIQUEFACTION FAILURE STATE TO DAMAGE STATE
Damage State and % Damage

Failure State	ATC-13 Values for all Lifelines		New Values Determine During This Study: High Strength Lifelines		Low Strength Lifelines	
	Damage State	Percent Damage	Damage State	Percent Damage	Damage State	Percent Damage
Light	0-3	0%	0-2	0%	0-3	0%
Moderate	4	15%	3	0%	4	30%
Heavy	5	50%	4	15%	5	60%
Severe	6	80%	5	50%	6	90%
Catastrophic	7	100%	7	100%	7	100%

The definition of High Strength buried lifelines used to determine the damage state is: continuous steel pipelines constructed according to modern quality control standards with full penetration girth welds; welds and inspection performed according to API 1104 or equivalent.

The definition of the buried lifelines which should be represented by the original ATC-13 definitions is: pipelines and conduits constructed according to modern standards with average to good workmanship, other than the high strength lifelines defined above. Lifelines in this category are expected to include electric cables, steel pipelines with welded slip joints, ductile iron pipelines, telecommunication conduits, reinforced concrete pipe including concrete steel cylinder pipe, and plastic pipelines and conduits. Also, if the high strength lifelines are oriented so that the landslide motion is expected to place them into compression, they should be analyzed in this category. Also, lifelines not included in either the High Strength or Low Strength definitions should be evaluated using the ATC-13 column.

The definition of Low Strength buried lifelines is: pipelines and conduits sensitive to ground deformation because of age, brittle materials, corrosion, and potentially weak and defective welds. Lifelines in this category include cast iron, rivetted steel, asbestos cement, and unreinforced concrete pipelines; pipelines with oxyacetylene welds; and pipelines and conduits with corrosion problems. If other non high strength buried lifelines (e.g., lifelines that would normally be analyzed using the column for ATC-13 lifelines) are oriented so that they are perpendicular to the expected landslide motion (e.g., their orientation is such that they will be put into compression by the landslide), then they should be analyzed as a Low Strength lifeline rather than with the ATC-13 column.

Several Simulations of Buried Pipelines During Liquefaction

Hayao Yanagimoto,* Toshitaka Ono,* Susumu Yasuda,** Hiroyoshi Kiku**

*Nippon Steel Corporation, Technical Planning & Development Div.,
Civil Engineering & Marine Construction Dept.,
**Kyushu Institute of Technology

ABSTRACT

In Japan, everyday life would be seriously affected by damage to the infrastructure resulting from an earthquake, since most lifeline facilities are buried. Given those circumstances, studies of the damage caused to underground structures due to liquefaction have began over the past few years. However, most studies have concentrated on the behavior of buried structures in liquefied ground, with few taking into consideration the process by which the ground is liquefied or the large permanent displacements produced by liquefaction. Accordingly, we have traced the mechanism of damage to lifeline facilities, specifically buried pipelines, with the lapse of time, based on knowledge obtained from past experimental results. We carried out stress analysis on buried pipelines during the liquefaction process and looked for correspondence between the analytical results and the temporally equivalent results of effective stress analysis.

INTRODUCTION

During the Niigata earthquake, which had an epicenter under the central Japan Sea, liquefaction and large-scale ground movements resulted in permanent ground displacements, and this caused serious damage to underground structures and buried pipelines.

A consideration of the stress on buried pipelines during liquefaction shows that large forces result from these ground disturbances, and in evaluating the response of pipelines it is also necessary to take into account the fact that the restraining force of the ground itself is reduced due to the liquefaction.

The authors[1)] have carried out restraining-force experiments on PL steel piping, using a vibration table to simulate ground liquefaction. The results indicate that the restraining force abruptly decreases as liquefaction progresses. Based on a review of past experimental results, this study estimates the changes in the ground's spring constant as liquefaction proceeds and offers a stress analysis of buried pipes during liquefaction. Also, by combining the results of effective stress analysis of the ground and stress analysis of buried pipes, we trace the changing stress on pipes with time as the ground is liquefied during an earthquake.

ANALYSIS PROCEDURE

To calculate the stress on buried pipes moment by moment during an earthquake, the basic requirement is to establish an algorithm that considers three processes simultaneously: the seismic response, which is analyzed using the effective stress method; the reduction in ground spring constant during liquefaction; and the stress on the buried pipe. Specifically, by solving the vibration equation and the permeability equation for a buried pipeline system in the time domain, obtain the yield of excess pore water pressure from shearing strain of each ground and the member stress from deformation amount of pipelines. And for renewing the relationship between ground rigidity and stress-strain of buried pipelines according to the decrease in the effective stress due to occurrence of the excess pore water pressure, move to the next step.

Although changes in the stress on buried pipelines with time can be clarified through repeated application of this procedure, we decided in this study to separate the response analysis of the ground and the stress analysis of the buried pipes, tying them together through a model which evaluates the reduction in ground spring constant. This decision was made since a method that considers the effective stress in a dynamic analysis of the ground-structure has yet to be established, and knowledge of pipe movement, restitutive force characteristics, and equivalent ground spring at the time of an earthquake is inadequate. The overall analysis procedure is shown in Fig. 1.

By following the procedure below, the process of liquefaction from the

beginning of the earthquake until collapse of the pipeline can be traced temporally.

(1) From the time-resolved results obtained through the analysis of effective stress, the maximum response is extracted for each time increment.
(2) From the value of porewater pressure at that time, the ratio of excess pore water pressure is obtained.
(3) Using the model of ground spring constant reduction, the ground spring constant at that step is determined.
(4) By using the maximum response obtained from (1) and the ground spring constant obtained from (3) in the stress analysis program, the stress on the buried pipeline at each step is evaluated.

DETERMINATION OF GROUND SPRING CONSTANT DURING LIQUEFACTION

Determination of Ground Spring Constant in the Direction of the Pipeline Axis

Figure 2 shows a conceptual drawing of the ground spring characteristics. In the Guidelines for Aseismic Design of Gas Pipelines, the relationship $\tau_{cr}=\eta \cdot \tau_s$ (η is a constant determined by the exterior characteristics of the pipeline) is proposed as a method of obtaining the critical shear force from the maximum shear resistance. Accordingly, we decided to obtain the ground spring constant k_l during liquefaction by calculating the critical shear force τ_{cr} between the pipeline and the ground from the maximum shear resistance of the soil directly below the buried pipeline, and then multiplying the resulting value by the reduction in critical shear force at each excess pore water pressure ratio obtained through the ground restraint force experiment, as shown in Fig. 3. The yield relative displacement was fixed at $\Delta_{lc}=0.17$ cm, corresponding to the ground spring coefficient (0.6 kgf/cm^2) as provided for in the Guidelines for Aseismic Design of Gas Pipelines.

In Direction at Right Angles to the Pipeline Axis

Although the Guidelines for Aseismic Design of Gas Pipelines take the ground spring characteristics at right angles to the pipeline axis as linear, this might lead to underestimating the safety of pipelines in cases where the relative displacement between ground and pipeline is large. Since the ground restraint force at right angles to the pipeline axis can be considered to peak as the displacement increases, a general model should make the ground spring characteristics bi-linear in the direction at right angles to pipelines axis, as shown in Fig. 4, and the yield load (maximum ground reaction force) decrease with the progress of liquefaction. The ground spring constant during the liquefaction process is obtained by multiplying the restraint force in the non-liquefied state by the reduction in yield load, P_y, at each increment in pore water pressure obtained through the vibration table test (Fig. 5). Also, the yield relative displacement was made $\Delta_{he}=1.0$ (cm) due to the reasons in the selection of the yield relative desplacement in the direction at right angles to the pipelines axis, and in these studies it was assumed not to vary as

liquefaction progressed.

GROUND RESTRAINT FORCE MODEL

Since there is no established way of handling the value of ground restraint force, the model shown in Fig. 6 was adopted. That is, assuming the sliding along the passive collapse plane as the ground restraint force when buried pipes move in the horizontal direction, the shearing resistance force along this sliding plane was considered. Specifically, the shear strength along the slip plane at a certain point on the plane (h in the depth direction) was obtained and the restraint force acting on the pipe is obtained by integrating this throughout the slip plane.

ANALYSIS MODEL

As shown in Fig. 7, two models are used; a straight pipe model and a bent pipe model with 22.5° bend. The pipes assumed to be embedded 3.0 m below the ground (distance to the center of pipe). The pipes themselves was 100 A steel pipes of 114.3 mm outside diameter and 6.0 mm in thickness.

The ground at Kawagishi town in Niigata, of which detailed analysis parameters have been published by Ishihara and Tohata[2)] and which is shown in Fig. 8, was adopted as the basis of analysis. The input seismic forces were that of the East Chiba earthquake (as a representative of the short period type) and the Tokachi earthquake (as a representative of the long period type) with the maximum input acceleration adjusted to 140 gal. Also, it is assumed that the earthquake ground motion was uniform over the liquefied layer in the direction at right angles to the pipeline axis.

The time-step is one second and the stress acting on the pipe body is traced temporally by obtaining the maximum response displacement and excess pore water pressure at each step, then determining the ground spring constant and ground displacement which are used in the stress analysis of the buried pipe.

ANALYSIS RESULTS

Figures 9 and 10 show changes in ground displacement and in excess pore water pressure ratio resulting from the input of seismic forces in correspondence to temporally changes in axial force and bending stress that act on pipeline body from time to time and moment by moment.

The East Chiba Earthquake (Fig. 9)

The earthquake was of the short period type and its duration was also short

at about 18 seconds. As a result, the rise in excess pore water pressure was small and the response displacement was not very large either, at 2.2 cm. The excess pore water pressure ratio at the end of the earthquake was $\Delta_u/\sigma_v'=0.45$, and the ground was not completely liquefied.

In the case of the straight pipe model, no axial force occurs when the ground displacement is at right angles to the pipeline axis. The maximum bending stress occurs at the point where the ground abruptly changes (A, C) from soft to hard or vice versa. The bending stress increases near points where more displacement occurs as the excess pore water pressure rises; and at the point in time when the maximum displacement occurs, it reaches a maximum. However, in the analysis carried out this time, the bending stress is not extreme because the displacement is relatively small.

In the case of the bent pipe model, both axial force and bending stress are manifest because the ground displacement includes a component in the direction of the pipeline axis. Although it is assumed that the maximum value of axial force differs depending on the magnitude of the applied displacement, the bending stress is concentrated on the elbow portion.

As in the case of the straight pipe model, both the axial force and the bending stress increase as the displacement becomes larger. Though the axial force reaches a maximum value before the ground displacement peaks, the timing of maximum bending stress and maximum ground displacement is the same.

In the case of the bent pipe model, while the displacement is small, the ground restraining force is large. As a result, considerable axial force and bending stress occurs. In particular, the axial force comes extremely close to the yield stress, and may be considered dangerous for the pipeline. However, since the maximum values of axial force and bending stress arise at different locations, the combined stress does not exceed the breaking stress, although this cannot be read from the figure.

The Tokachi Earthquake Seismic Input (Fig. 10)

In the Tokachi Earthquake Seismic input (Fig. 10), the long period component is predominant and the vibration lasts longer, so the ground is completely liquefied. With the relatively large vibrations continuing for about 10 seconds after the earthquake, the excess pore water pressure ratio rises to near 0.5 and the response displacement begins to increase. Immediately after the ground is completely liquefied due to the principal earthquake motion, the displacement amplitude registers the highest value. However, even after that point, the ground displacement continues to increase and yawing occurs.

The bending stress calculated by the straight pipe model increases as the ground displacement becomes greater, and it exceeds the yield stress at around 30 seconds. Even thereafter, it continues to increase.

The axial force reaches a peak immediately before the ground liquefies. Its value has already exceeded the fracture stress of the pipelines at this point,

because although the ground restraint force is reduced, the displacement is large. While the bending stress rises in proportion to the degree of displacement, the axial force becomes relatively stable as the displacement rises above the designated value.

Since the stress analysis of buried pipelines is affected greatly by the response displacement, it is probable that the relationship between the ground's natural period and the period of the seismic input has a large effect. Therefore, it cannot be said without qualification that buried pipelines would be fractured even when the acceleration is large.

CONCLUSIONS

By combining the stress analysis and the effective stress analysis, an attempt was made to trace the stress on buried pipes during an earthquake in the time domain. Generally, it was discovered that an earthquake with a long period, such as the Tokachi earthquake, causes a larger response displacement in the ground and leads to a greater possibility of fractures. This is attributable to the large displacement which occurs while the earthquake motion continues. On the other hand, even when the earthquake has a short period, the possibility of pipe breaking during the earthquake motion increases at higher input accelerations, and it is assumed that the pipeline is also be in danger if permanent displacement occurs. However, these are considered to occur as factors, such as ground conditions (liquefaction characteristic, vibration characteristics, etc.), ground spring, maximum acceleration of seismic wave, period, etc., affect each other.

It can be stated that this study successfully applies stress analysis to buried pipelines for the period between the initial occurrence of an earthquake and the time when the pore water pressure ratio reaches 1.0. Confirmation of the reduction in ground spring when the permanent displacement occurs thereafter has not been made. Accordingly, it will in future be necessary to evaluate the reduction in ground restraint force when permanent displacement occurs through permanent displacement experiments on a larger vibration table or by carrying out repeated tri-axial tests and torsional shear tests, etc. It will then be possible to determine the ground spring constant while the permanent displacement is occurring.

REFERENCES

1) Kiku, Yasuda, and Yoshida: Relationship Between Ground Restraint Force and Liquefaction As Regards Buried Pipelines, the 20th Presentation Conference of Research Papers on Earthquake Engineering, 1989.

2) Ishihara, K. and Touhata, I.: One-dimensional Soil Response Analysis During Earthquakes Based on Effective Stress Method, Journal of the Faculty of Eng., University of Tokyo (B), Vol. 35, No. 4, 1980.

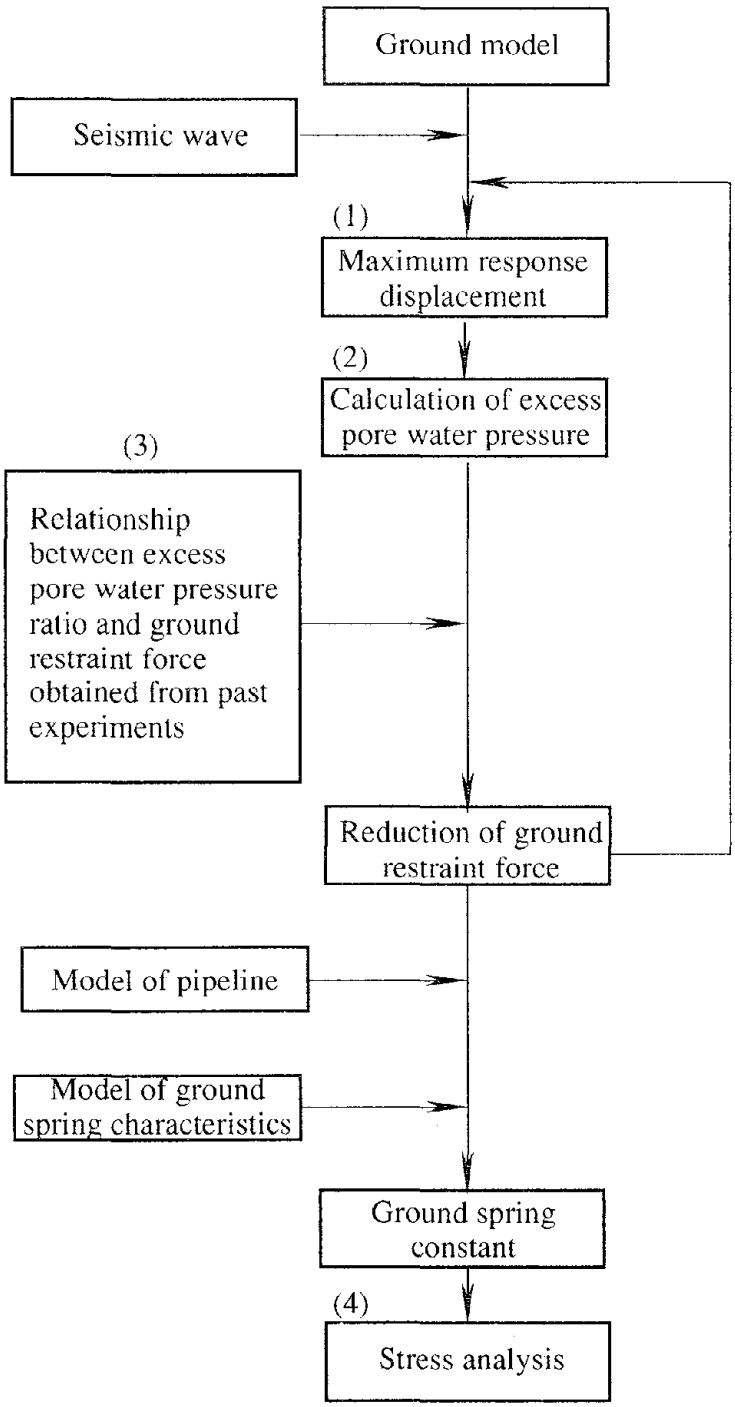

Fig. 1 Overall analysis procedure

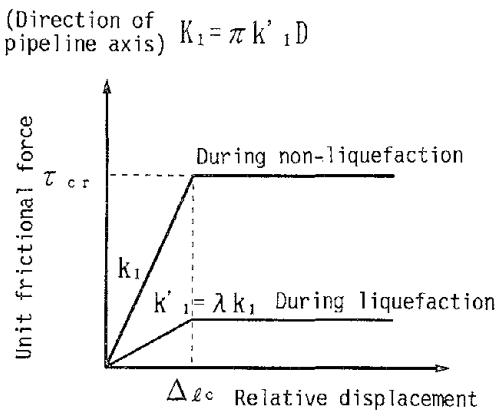

Fig. 2 Conceptual drawing of ground spring characteristics in the direction of pipeline axis

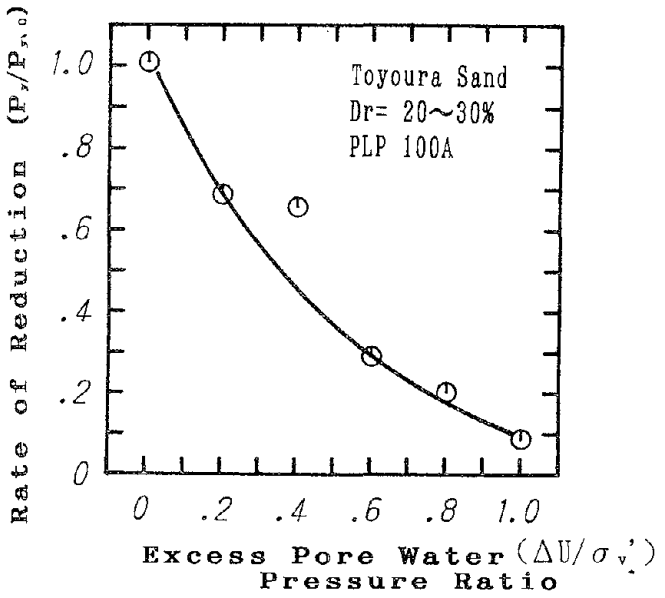

Fig. 3 Relationship between excess pore water pressure and critical shear force

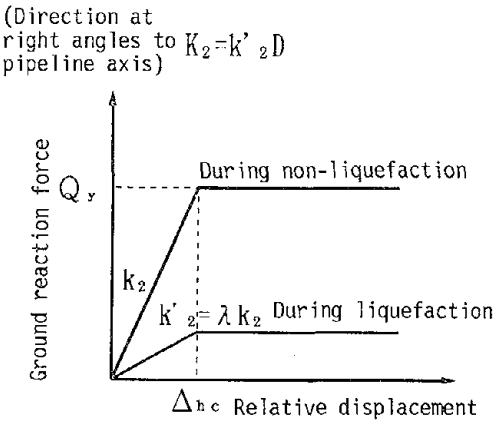

Fig. 4 Conceptual drawing of ground spring characteristics at right angles to pipeline axis

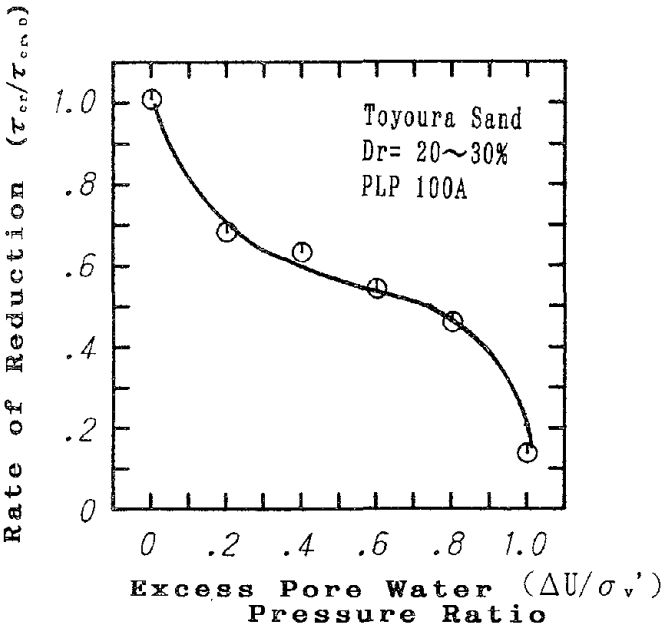

Fig. 5 Relationship between excess pore water pressure and yield load at right angles to to pipeline axis

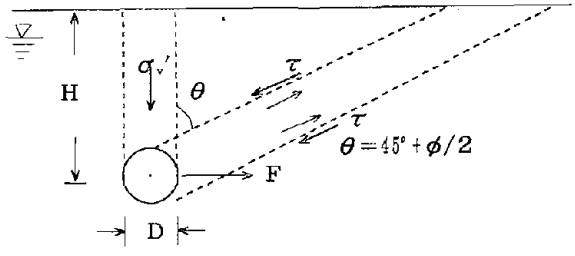

Fig. 6 Ground restraint force model

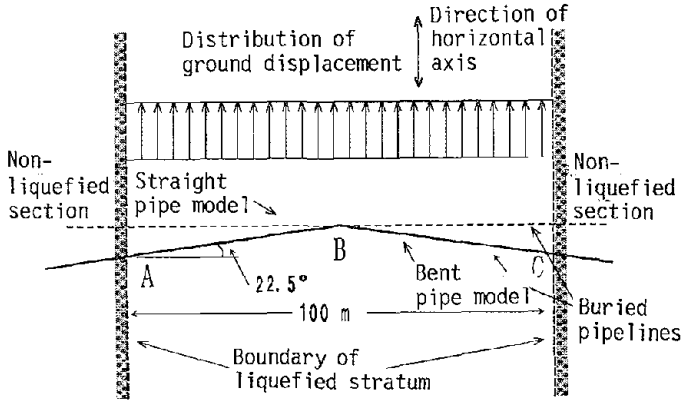

Fig. 7 Buried pipeline displacement distribution model

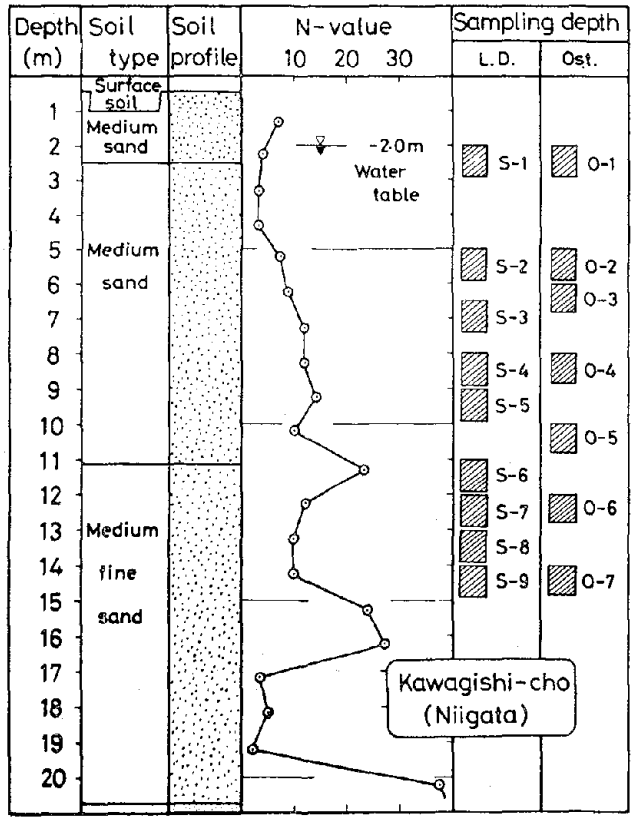

Fig. 8 Ground model

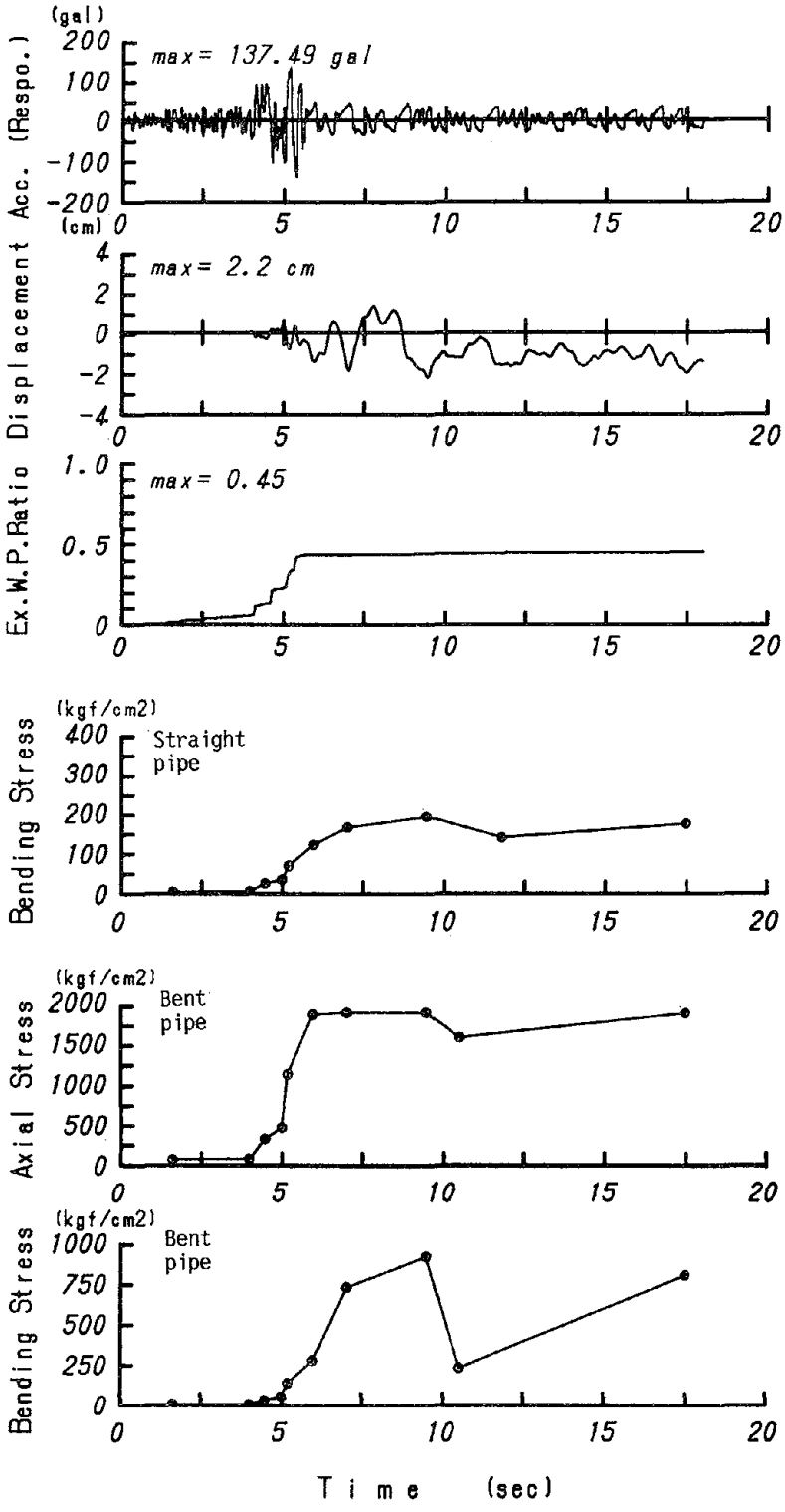

Fig. 9 Analysis results
(East Chiba earthquake)

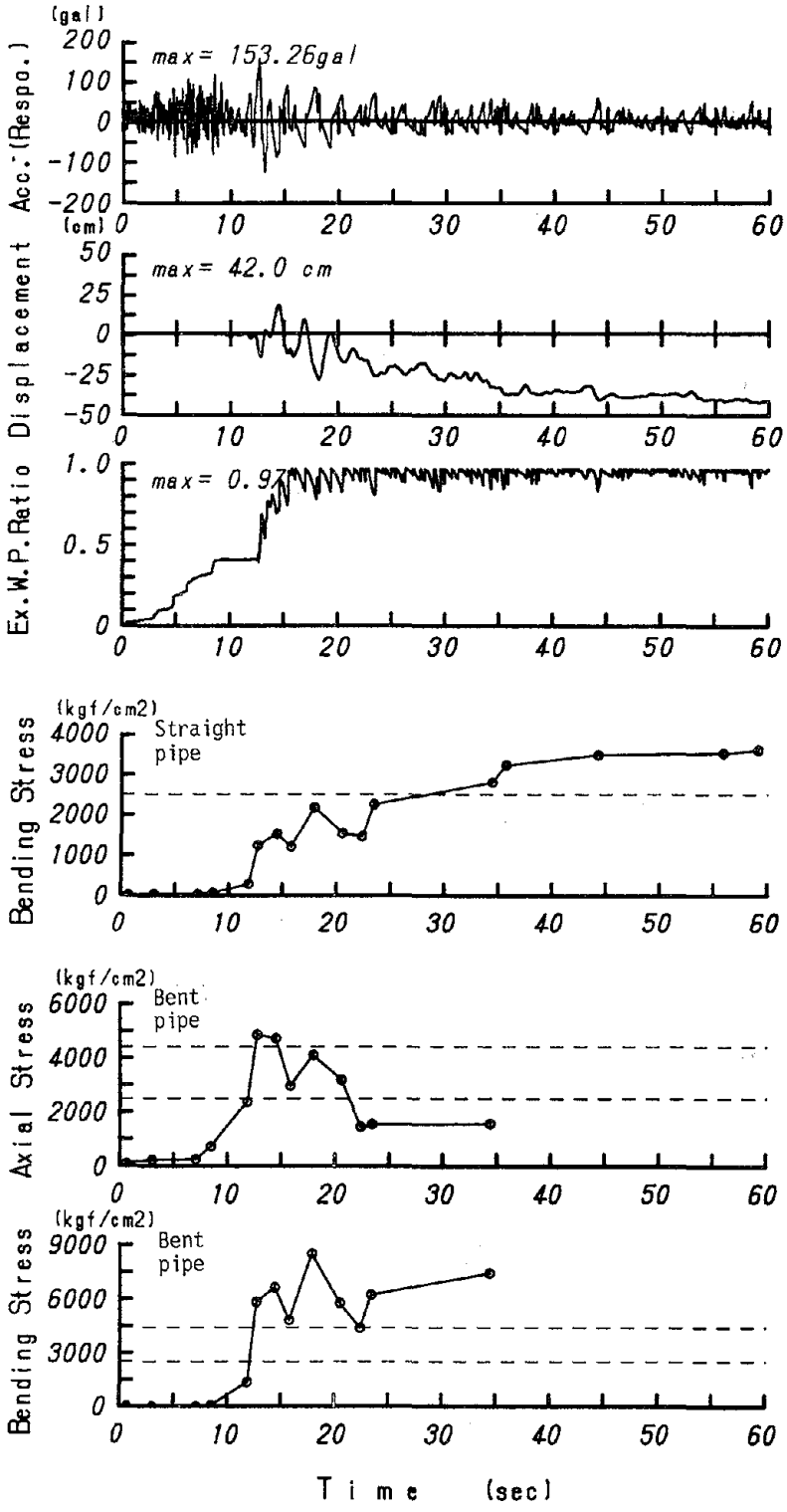

Fig. 10 Analysis results
(Tokachi earthquake)

Seismic Effects On Underground Pipelines due to Permanent Longitudinal Ground Deformations

Raul Flores–Berrones and Michael O'Rourke

Visiting Research Professor and Professor
Civil & Environmental Engineering Department
Rensselaer Polytechnic Institute
Troy, New York 12180–3590

ABSTRACT

The behavior of buried, welded steel pipelines subjected to longitudinal permanent deformations (PGD) is considered. Longitudinal PGD refers to soil movements which are parallel to the pipelines axis. The induced axial strain in the pipe is shown to theoretically be a function of the length of the PGD zone, the spatial distribution of the ground movement and the pipes embedment length. The embedment length for the pipe is similar to a development length for a reinforcing bar in concrete design.

Analytical expressions and graphs are developed for evaluating pipe strain due to five idealized patterns of longitudinal PGD. These expressions are then used to determine axial strain in three hypothetical pipeline due to 27 PGD patterns observed by Japanese investigators.

INTRODUCTION

Seismic damage to buried welded steel pipelines is usually attributed to either seismic wave propagation or permanent ground deformation effects (O'Rourke et al, 1985). The analysis of damage produced by seismic wave propagation has been studied by O'Rourke and his co–workers (O'Rourke and ElHmadi, 1988, and O'Rourke and Ayala, 1990). In this paper particular attention is given to the seismic effect created by permanent ground deformation (PGD).

PGD damage to pipelines has been reported by several researchers. For example O'Rourke and Tawfik (1983) describe damage to welded steel pipelines occasioned by the 1971 San Fernando Earthquake, while Hamada et al. (1986) describe damage to a buried gas pipeline occasioned by the 1983 Nihonkai–Chubu earthquake. These soil deformations might be caused by lateral ground displacements, liquefaction or cycle compaction of sandy soils. For the general case, a buried pipeline would be subject to some combination of transverse (ground movement perpendicular to the pipeline axis) and longitudinal (ground movement parallel to the pipelines axis) PGD. However, O'Rourke & Nordberg (1991), have demonstrated that the strains in straight buried pipelines due to longitudinal PGD is typically more than an order of magnitude larger than that due to transverse PGD.

In this paper the effect of longitudinal PGD on straight (ie no bends or elbows) steel pipe with constant burial depth is considered. Five idealized longitudinal PGD patterns based on observed patterns from previous earthquakes are used and analytical relations for the axial strain in the pipe are developed.

LATERAL SPREAD GEOMETRY

Although there are different kinds of permanent soil deformation (active geological faults, consolidation or densification of compressible soils, landslides, etc.), the only ones that are considered in this analysis are those caused by soil liquefaction and subsequent lateral spreading. Estimation of the magnitude of such deformations has been addressed by several authors. For example, Hamada et al (1986) suggests the following empirical formula to predict the magnitude of horizontal PGD δ, in meters:

$$\delta = 0.75 \sqrt{h} \cdot \sqrt[3]{\phi_g} \tag{1}$$

where h is the thickness of the liquefied layer (m), and ϕ_g is the slope, in percent, of the lower boundary of the liquefied layer or the ground surface, whichever is larger. The above formula was deducted after quantitatively analyzing data from the 1964 Niigata and 1983 Nihonkai–Chubu earthquakes in Japan, and the 1971 San Fernando earthquake in the US. In these earthquakes, horizontal PGD in the order of 1 to 5 meters were observed. Youd and Perkins (1987) developed an empirical relation for their measure of PGD magnitude, the Liquefaction Severity Index (LSI). Using data from Western US earthquakes, LSI is given as a function of earthquake magnitude and site–source distance. More recently Baziar (1991) and Towhata et al (1991) have developed analytical relations for the amount of horizontal PGD.

PGD often also results in a vertical component of ground movement. However, the vertical component is typically smaller than the horizontal component, and the vertical component of PGD is disregarded herein.

SOIL – PIPE INTERACTION

Strain in a continuous buried pipeline subject to longitudinal PGD is due to friction–like forces at the soil pipe interface. The elasto–plastic model shown in Fig. 1 is often adopted (ASCE, 1984). This model is fully defined by two parameters; the maximum force per unit per length at the soil pipe interface, f_m, and D_s, the relative displacement at which slippage between pipe and soil occurs. The axial stiffness of the soil spring is f_m/D_s.

The maximum axial force per unit of length f_m depends on the type of soil surrounding the pipe and the method of pipe installation (i.e. the compaction control of the backfill). For cohesionless soils f_m depends on the effective normal stress at the soil–pipe interface, the coefficient of friction between the soil and the pipe material, and the pipe diameter ϕ. Considering that we are in a plain strain problem, and that the coefficient of lateral pressure k_o for compacted soils is approximately equal to unity, the effective normal stress

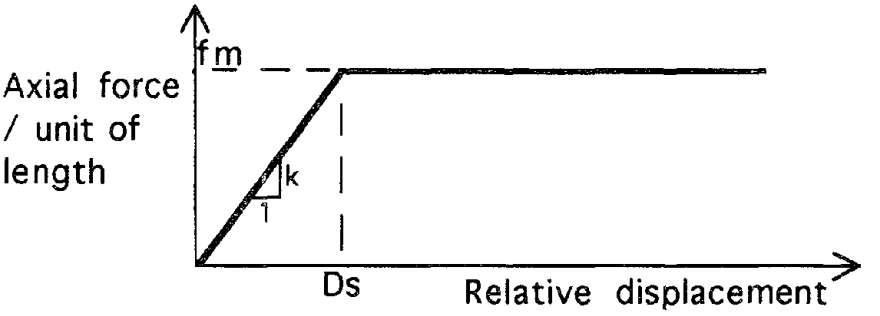

Figure 1 Elasto–plastic Model of Soil Pipeline Interface

will be simply equal to the product of the effective unit weight of soil γ, and the depth H to the pipe center line. We assume herein that H is constant in and around the PGD zone.

For the case of a steel pipeline, the coefficient of friction of the soil pipeline interface, based upon experimental results, is $\mu = 0.9 \tan \phi_s$ where ϕ_s is the angle of shearing resistance of the soil. Hence for cohesionless backfill, the friction force per unit length becomes

$$f_m = \mu \cdot \gamma H \cdot \pi\phi \tag{2}$$

For cohesive soils, f_m depends on the undrain shear strength S_u of the soil. For normally consolidated clays, S_u gives a good estimation of the adhesion to the pipe. For overconsolidated soils, the observed adhesion is generally less than the undrain strength. For overconsolidated soils Lambe & Whitman (1969) recommended to use as adhesion the undrain shear strength of an equivalent normally consolidated soil. So for cohesive soils, $f_m = S_u \cdot \pi\phi$. For the most general soil condition, when the soil surroundings the pipe has both friction and cohesive characteristics, f_m will be given by:

$$f_m = (c + \mu\gamma H)\pi\phi \tag{3}$$

where c is the shear strength of the soil corresponding to zero effective vertical stress on the shear strength curve.

The relative axial displacement for slippage, D_s in cohesionless soils is shown in Fig. 2 as a function of pipe diameter and coefficient of friction μ, for a pipe burial depth H = 6 ft. Note that the relative axial displacement for slippage at the soil pipeline interface is quite small. O'Rourke and Nordberg, (1991) have shown that a simplified model of the soil pipe interface in which D_s is taken as zero, yields maximum pipe strain within 4% of those using the model in Figure 1. Hence the simplified model (ie $D_s = 0$) will be used herein to evaluate response to longitudinal PGD.

SIMPLIFIED PGD PATTERNS

O'Rourke and Nordberg (1991) determined the response of straight continuous welded steel pipelines with constant buried depth to three idealized patterns of longitudinal PGD. The three patterns considered were Block, Ramp, and Ridge patterns. The Block pattern, for example, corresponds to a mass of soil having a length L moving horizontally as a rigid block. A ground crack or gap occurs at the head of the slide and a compression mound at

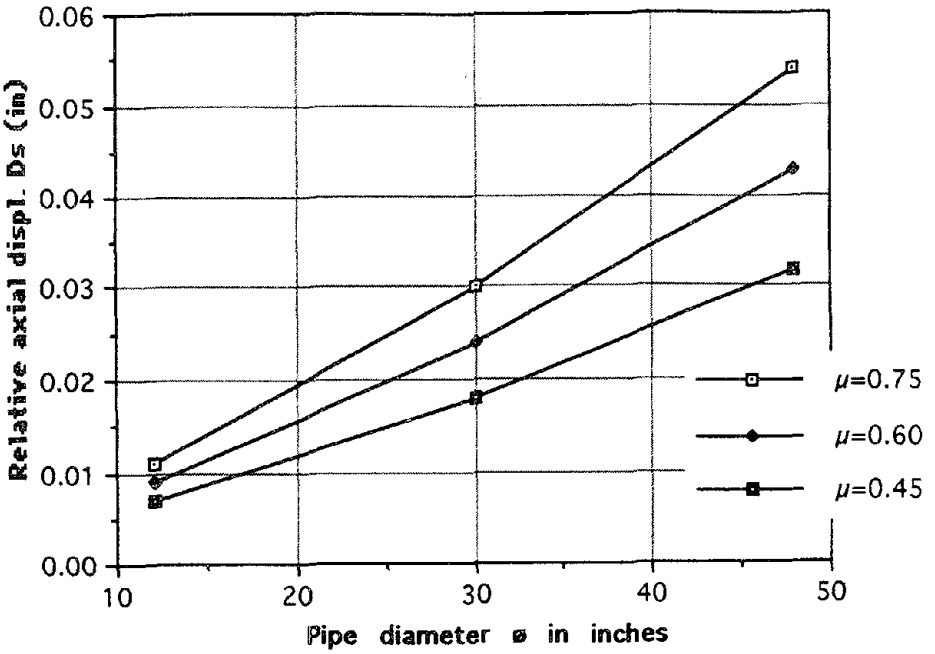

Figure 2 Relative Axial Displacement for Slippage at the Soil Pipeline Interface, D_S, for H = 5 ft.

the toe. This pattern is an approximation to horizontal PGD observed by Hamada et al. (1986) and shown in Figure 3. In Figure 3, the height of the vertical line corresponds to the amount of observed horizontal PGD. The Block pattern approximation, shown as a dashed line, is 1.8m of uniform horizontal movement δ over a length L of 150 m.

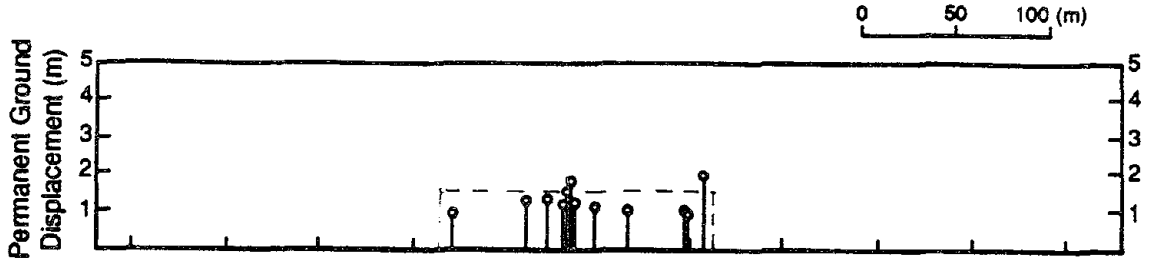

Figure 3 Horizontal PGD observed at Secton S–10 in Noshiro City after the 1983 Nohonkai–Chubu Earthquake

Using a simplified model of the soil pipeline interface with D_s taken as zero, and defining an equivalent ground strain for the Block pattern as $\alpha = \delta/L$, O'Rourke and Nordberg (1991) show that the axial strain induced in a continuous buried pipeline due to a Block pattern of longitudinal PGD is

$$\epsilon = \begin{cases} \dfrac{\alpha L}{2L_{em}} & L < 4L_{em} \\ \alpha\sqrt{L/L_{em}} & L > 4\ L_{em} \end{cases} \tag{4}$$

where L_{em} is an embedment length defined as the length over which the constant slippage force f_m must act to induce a pipe strain ϵ equal to the ground strain α

$$L_{em} = \frac{\alpha EA}{f_m} \tag{5}$$

Figure 4 plots the embedment length L_{em} for a steel pipe in cohesionless soil with unit weight 100 pcf (1600 kg/m^3) as a function of ground strain α. Curves are shown for three combinations of the buried depth H, pipe wall thickness t, and the coefficient of friction at the soil pipe interface μ.

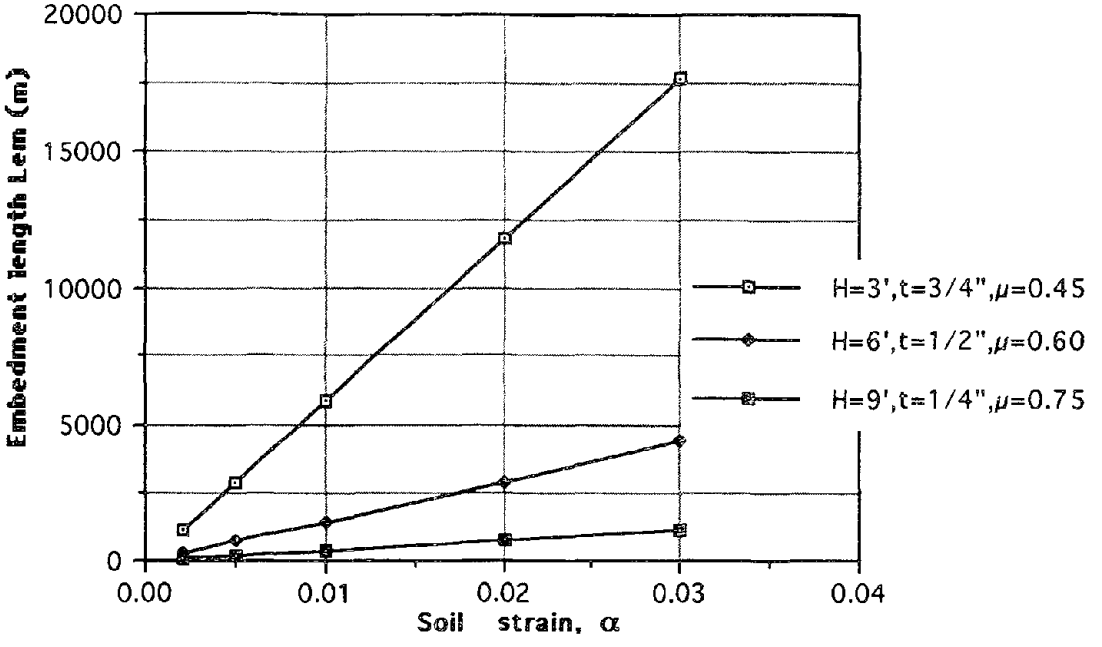

Figure 4 Embedment Length L_{em} for Steel Pipe in Cohesionless Soil with Unit Weight 100 pcf.

For a Ramp pattern of longitudinal PGD, the pipe strain is given by

$$\epsilon = \begin{cases} \alpha\left[\sqrt{4 + 2L/L_{em}} - 2\right] & L < 2.5\ L_{em} \\ \dfrac{\alpha}{2}\left[\sqrt{4L/L_{em}} - 1\right] & L > 2.5\ L_{em} \end{cases} \tag{6}$$

while for a Ridge pattern

$$\epsilon = \begin{cases} \alpha\left[\sqrt{1 + L/L_{em}} - 1\right] & L < 3L_{em} \\ \alpha & L > 3L_{em} \end{cases} \tag{7}$$

The axial strain ϵ in the pipe, normalized by the ground strain α is plotted in Figure 5 as a function of the normalized length of the PGD zone, for the Block, Ramp, and Ridge patterns considered by O'Rourke and Nordberg (1991).

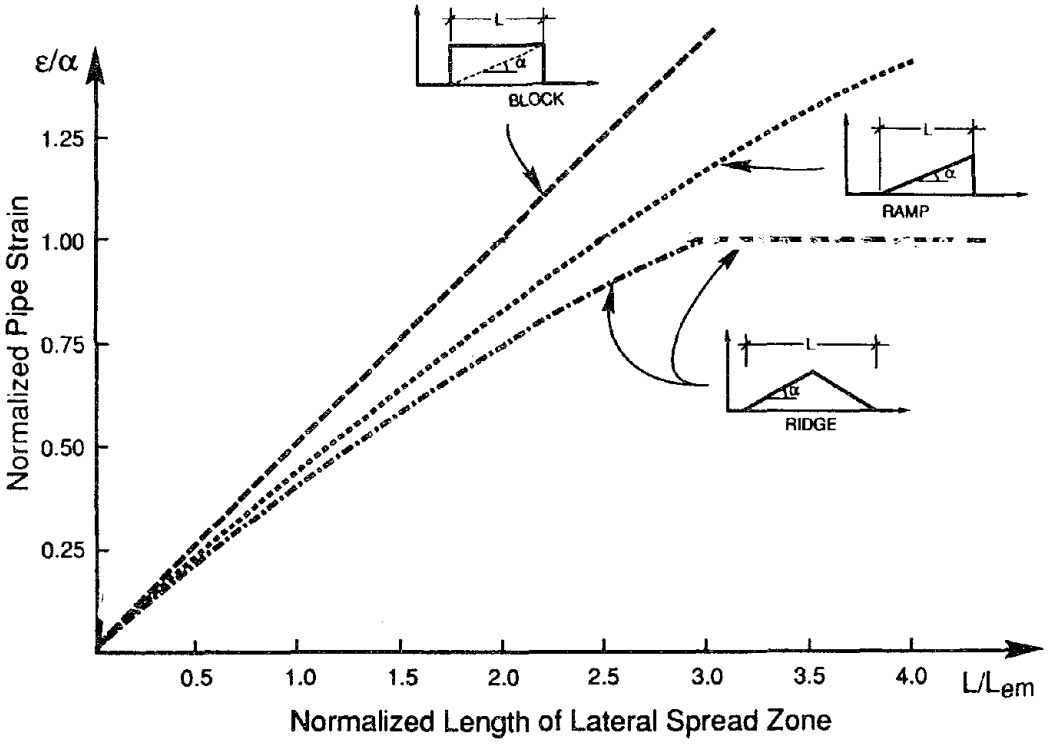

Figure 5 Normalized Pipe Strain as Function of Normalized Length of PGD Zone for Three Simplified Patterns

COMPLEX PGD PATTERNS

The three simplified longitudinal PGD patterns shown in Figure 5 are realistic approximation to a number of PGD patterns observed by Hamada et al (1986). However, there are other observed PGD patterns, such as shown in Figure 6 which are more complex than the three given in Figure 5. Herein we will evaluate the strain in a straight continuous steel pipeline with constant burial depth, subject to a Ramp Block and a Asymmetrical Ridge pattern of longitudinal PGD.

Ramp/Block Pattern

The idealized Ramp/Block pattern is shown in Figure 7. Establishing a coordinate system with an origin at the toe of the ramp, the assured horizontal soil displacements are:

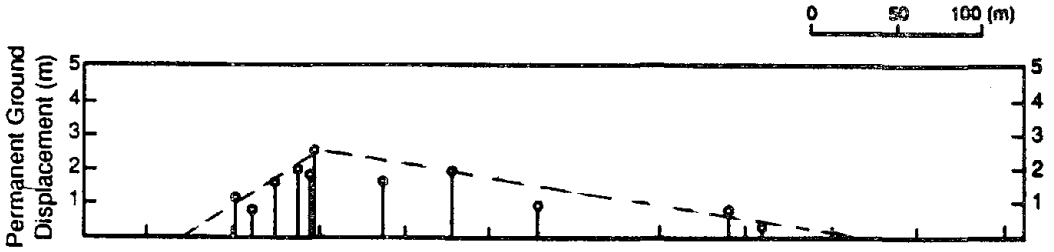

Figure 6 Horizontal PGD Observed at Section S–19 and Asymmetric Ridge Approximation

$$U_g(x) = \begin{cases} 0 & x < 0 \\ \frac{\alpha}{\beta}x & 0 < x < \beta L \\ \alpha L & \beta L < x < L \\ 0 & x > L \end{cases} \tag{8}$$

One possible pipe configuration is also shown in Fig. 7. For this configuration the tensile pipe strain is less than the ground strain α/β and the maximum pipe displacement $u_p(x_c)$, is less than the maximum soil displacement αL. The strain in the pipe is zero at points A, C and E, while the maximum pipe strain occurs at point B (tension) and point D (compression). Since the force per unit length at the soil pipe interface f_m is a constant, the distance AB, BC, etc. are all equal to L_e.

By geometry we have:

$$L_a = 3L_e - L \tag{9}$$

At point B the ground and pipe displacements match, therefore

$$U_p(x_b) = U_g(x_b) = \frac{\alpha}{\beta}(L_e - L_a) \tag{10}$$

and

$$U_p(x_b) = \frac{\alpha}{\beta}(L - 2L_e) \tag{11}$$

Since there is a constant force per unit length between points A and B, and the pipes horizontal displacement and strain at point A are zero, we have

$$U_p(x_b) = \int_0^{L_e} \frac{f_m s}{AE} ds = \frac{f_m L_e^2}{2AE} \tag{12}$$

Equaling the two last equations, we obtain:

$$\frac{f_m L_e^2}{2AE} + 2\frac{\alpha}{\beta}L_e - \frac{\alpha}{\beta}L = 0 \tag{13}$$

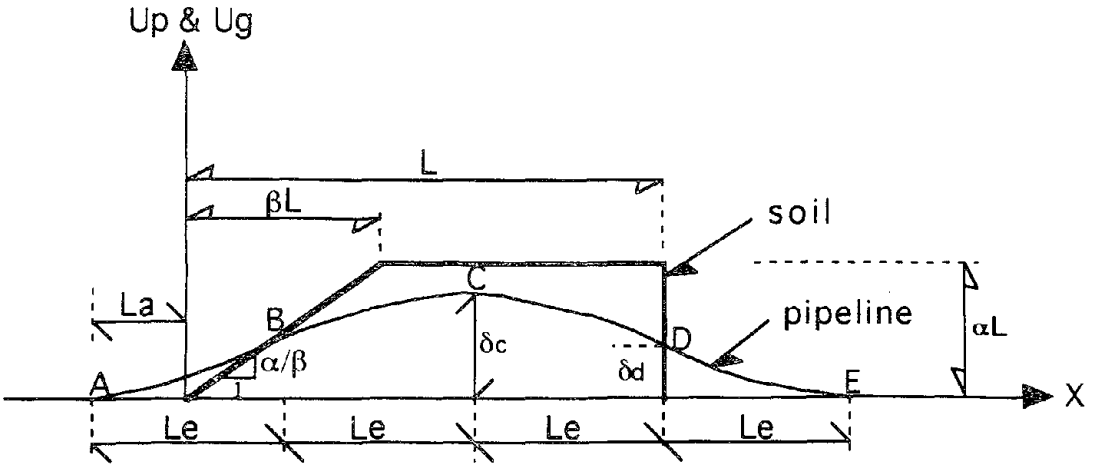

Figure 7 Ramp–Block Pattern of Longitudinal PGD with Pipe Displacement

from which L_e is calculated:

$$L_e = L_{em}\left\{\sqrt{\frac{4}{\beta^2} + \frac{2L}{\beta L_{em}}} - \frac{2}{\beta}\right\} \tag{14}$$

where L_{em} is given by Equation 5. The maximum pipe strain, tension at B, and compression at D, is given by:

$$\epsilon = \frac{f_m L_e}{AE} = \alpha\frac{L_e}{L_{em}} = \alpha\left\{\sqrt{\frac{4}{\beta^2} + \frac{2L}{\beta L_{em}}} - \frac{2}{\beta}\right\} \tag{15}$$

or

$$\epsilon = \frac{\alpha}{\beta}\left\{\sqrt{4 + 2\beta\frac{L}{L_{em}}} - 2\right\} \tag{16}$$

Equation 16 applies as long as the pipe strain is less than the ground strain α/β, and the maximum pipe displacement is less than the maximum ground displacement αL. It can be shown that those conditions apply for

$$\frac{L}{L_{em}} \leq \frac{16}{4-4\beta+\beta^2} \qquad \text{for } 0 \leq \beta \leq 0.4$$

and

$$\frac{L}{L_{em}} \leq \frac{5}{2\beta} \qquad \text{for } 0.4 \leq \beta \leq 1.0$$

However, as it will be shown later, the length of the PGD zone is typically less than twice the pipes embedment length, hence equation 16 is considered adequate for most situations of a Ramp/Block pattern of longitudinal PGD. The pipe strain from equation 16, normalized by α is plotted against the normalized length of the PGD zone in Figure 8. Note that for $\beta = 1$, the Ramp/Block pattern yield the same results as the Ramp pattern in Equation 6 and Figure 5. Also we get the Block results for $\beta = 0$, as expected.

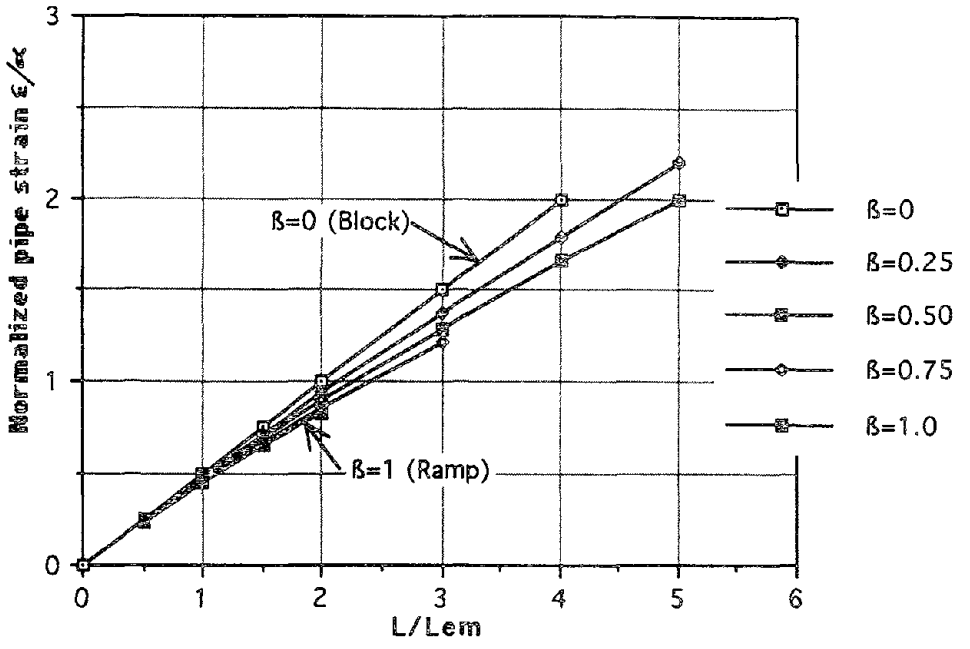

Figure 8 Normalized Pipe Strain for a Ramp/Block Pattern of Longitudinal PGD

Asymmetrical Ridge Pattern

The idealized asymmetric Ridge pattern of longitudinal PGD is shown in Figure 9 It approximates an actual PGD pattern shown in Figure 6. Establishing a coordinate system as before, the assumed horizontal soil displacement is given by:

$$U_g(x) = \begin{cases} 0 & x < 0 \\ \alpha x & 0 < x < \beta L \\ \dfrac{\alpha\beta(L - x)}{1 - \beta} & \beta L < x < L \\ 0 & x > 0 \end{cases} \qquad (17)$$

where $0.5 \leq \beta \leq 1$.

One possible configuration for pipe behavior is also shown in Figure 9. This corresponds to the situation where the pipe strain is less than α. As in Figure 7, the pipe strain is zero at Points A, C and E, and the distance AB, BC etc. are equal to L_e. The pipe and soil displacements at point B are equal hence

$$U_p(x_b) = U_g(x_b) = (L_e - L_a)\alpha \tag{18}$$

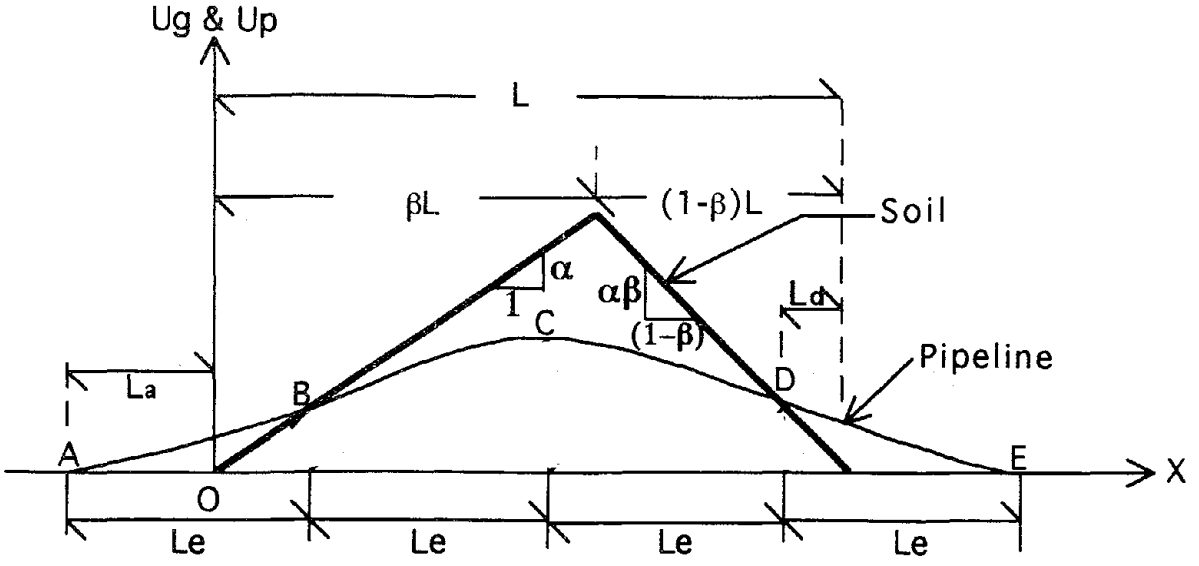

Figure 9 Unsymmetric Ridge pattern of Longitudinal PGD Showing Soil and Pipe Displacement

where L_a is the distance from point A to the start of the lateral PGD zone (point O). By geometry, the distance from the end of the PGD zone to point D is:

$$L_d = L + L_a - 3L_e \tag{19}$$

The pipe and soil displacement are equal at point D and

$$U_p(x_d) = U_g(x_d) = L_d\left(\frac{\alpha\beta}{1-\beta}\right) \tag{20}$$

Since the pipe strain and displacement are zero at points A and E, the pipe displacements at points B and D are both due to f_m acting over a distance L_e. Hence from Equation (12)

$$U_p(x_b) = U_p(x_d) = \frac{f_m L_e^2}{2AE} \tag{21}$$

By combining Eqs. 18 through 21, the value of L_e is found.

$$L_e = \beta L_{em}\left(\sqrt{4 + \frac{2L}{\beta L_{em}}} - 2\right) \tag{22}$$

The maximum pipe strain, tension at point B and compression at point D, becomes

$$\epsilon = \frac{f_m L_e}{AE} = \alpha\beta\left(\sqrt{4 + \frac{2L}{\beta L_{em}}} - 2\right) \tag{23}$$

Equation 23 applies for $\epsilon < \alpha$. It can be shown that this condition is satisfied for

$$L \leq L_{em}\,(2 + \frac{1}{2\beta})$$

However, as mentioned previously, the length of the PGD zone is typically less than twice L_{em}. Hence equation 23 is considered adequate for most situation of an Asymmetric Ridge pattern of longitudinal PGD. Note that for $\beta = 0.5$ we get the same results as the Ridge pattern in Equation 7 while for $\beta = 1.0$ we get the Ramp results in Equation 6, as expected.

PIPE STRAIN

Hamada et al (1986) present 27 observed patterns of horizontal PGD in Noshiro City which resulted from the 1983 Nohonkai Chubu Earthquake. Idealized longitudinal PGD patterns, Block, Ramp, Ridge, Ramp/Block or Asymmetrical Ridge which best approximate the observed patterns, were determined. For example, the observed PGD at Section S–19 which is shown in Figure 6 is approximated by an idealized Asymmetrical Ridge pattern with $L = 390$ m, $\delta = 2.5$ m, $\alpha = 0.0081$ and $\beta = 0.79$.

The axial strains in three hypothetical pipelines were determined for each of the 27 PGD pattern. Each pipeline is assured to be buried in cohesionless soil with unit weight of 100 pcf (1600 kg/m^3). The water table is assumed to be located below the pipeline hence the pipeline is contained in a nonliquefied layer which overrides a liquefied layer below. The wall thickness t, burial depth H, and coefficient of friction for the three hypothetical pipeline are presented in Table 1. The pipes were chosen to represent what is felt to be a reasonable range of actual pipe burial conditions. Pipe #3 is the most vulnerable to seismic damage due to its small wall thickness, large burial depth and high coefficient of friction corresponding to a soil with an angle of shearing resistance of 40°. On the other hand, Pipe #1 is the least vulnerable with low μ corresponding to an angle of shearing resistance of 27°. Axial strain induced in each of the three hypothetical pipes due to the 27 patterns of longitudinal PGD were determined. As expected, the axial strains are smallest in the first hypothetical pipe (Pipe #1). Since the pipeline is assumed to be linear elastic, the computed pipe strain is correct if it is below the pipe yield strain ϵ_y. If $\epsilon > \epsilon_y$ the actual strain in the hypothetical pipeline is unknown, but is at least equal to the yield strain. Except for section S–12 and S–15 (L=35m and 140 m respectively) the axial stress is pipe #3 is always larger than the yield stress for X–52 grade steel. The axial strain in pipe #2 is always less than the yield stress for X–52 grade steel, except for section S–7 N–3, N–4 and N–6 (L = 615 m, 590 m, 720 m and 740 m respectively). Figure 10 plots for each of the 27 patterns of longitudinal PGD, the computed axial strain in hypothetical pipes #1 and #2 versus the PGD amplitudes δ. Note that the pipe strain is poorly correlated with δ. Figure 11 plots pipe strain versus the length of the PGD zone L. This figure suggests that the length of the PGD zone is the key parameter in determining axial strain in straight continuous pipe with constant burial depth subject to longitudinal PGD. That is, although pipe strain is theoretically a function of the pattern or spatial distribution of the PGD, the lengths of the PGD zone are small enough with respect to the

Table 1 Parameters for three hypothetical steel pipeline

Pipe No.	t (in)	H (ft)	μ
1	3/4	3	0.45
2	1/2	6	0.60
3	1/4	9	0.75

embankment length L_{em} that variations between different patterns is a second order effect.

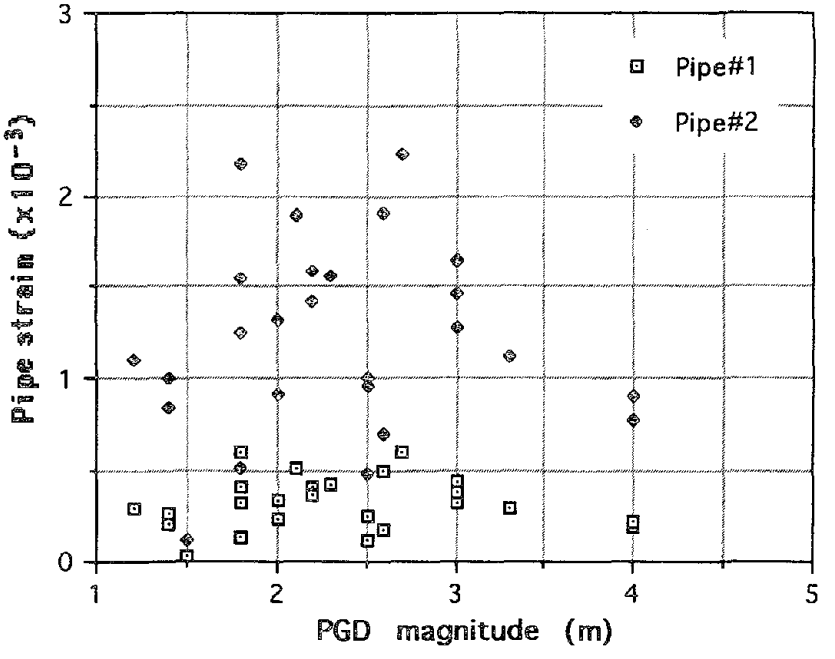

Figure 10 Pipe Strain Versus PGD Magnitude

That is, as a first approximation, at least for the 27 patterns of longitudinal PGD considered herein, the pipe strain corresponds to a Block pattern where $L < 4L_{em}$ and

$$\epsilon \simeq \frac{f_m L}{2AE} \tag{24}$$

SUMMARY AND CONCLUSIONS

A method for estimating the strain in a straight continuous pipeline subjected to various patterns of longitudinal permanent ground deformations (PGD) is presented in this paper. The method takes into account the shear strength characteristics of the soil surrounding the pipeline. It is based in a simplified force–displacement model for the soil pipe interface which for practical purposes gives the same results than those obtained using a more elaborate elasto–plastic model. Five patterns of idelaized longitudinal PGD, based on observations by Japanese investigators in previous earthquakes, are considered.

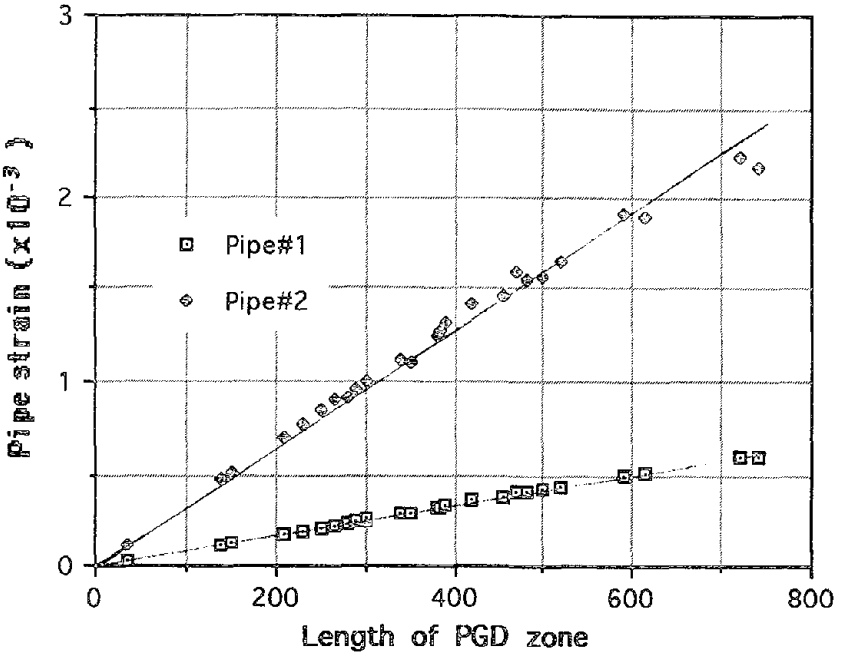

Figure 11 Pipe Strain Versus Length of PGD Zone

The pipe strain ϵ is presented in terms of the length L of the PGD zone, a characteristic ground strain α (peak horizontal ground displacement divided by a characteristic length of the PGD zone) and an embedment length L_{em}. L_{em} is defined as the distance over which the soil–pipe friction force per unit length f_m must act to induce a pipe strain equal to the characteristics ground strain α. L_{em} is similar in concept to the "development length" in reinforced concrete design.

Three hypothetical pipeline, having various wall thickness, burial depths and friction coefficients at the soil pipeline interests were analyzed for 27 patterns of longitudinal PGD observed by Japanese investigators. This analysis indicates the following:

1) The key parameters influencing the pipeline axial strain is the length L of the PGD zone. The amount of PGD, δ, and the spatial distribution or pattern of longitudinal PGD are second order effects.

2) Pipeline axial strain due to longitudinal PGD is reduced by increasing the pipe wall thickness, reducing the pipe burial depth, and reducing the angle of shearing resistance of the landfill material. Pipeline axial strain is not influenced by pipe diameter.

The authors believe that the following items should be considered for future research in this area; (a) Analytical or empirical relations for the length or spatial extent of PGD zones should be established; (b) The response of buried pipelines to the vertical component of PGD (neglected herein) should be investigated; (c) The influence of pipeline bends and elbows in both horizontal and vertical planes should be determined. This is particularly important in light of the fact that PGD often occurs near river banks where, by necessity, the pipeline profile contains bends, elbows or other stress raisers.

ACKNOWLEDGEMENTS

The work presented in this paper was sponsored by the National Center for Earthquake Engineering Research under project number NCEER–91–3331. However, the finding and conclusions are the authors alone and do not necessarily reflect the views of NCEER nor the US National Science Foundation.

REFERENCES

American Society of Civil Engineers (1984), "Guidelines for the Seismic Design of Oil and Gas Pipeline Systems", Committee on Gas and Liquid Fuel Lifelines, ASCE, New York, NY.

Baziar, M., (1991), "Engineering Evaluation of Permanent Ground Deformation Due to Seismically–Induced Liquefaction", dissertation for Ph.D. in Civil Engineering, Rensselaer Polytechnic Institute, August.

Hamada, M., Yasuda, S., Isoyama, R., and Emoto, K., (1986), "Study of Liquefaction Induced Permanent Ground Displacements", Association for the Development of Earthquake Prediction, Japan, November.

Lambe, W., and Whitman, R., (1969), "Soil Mechanics" John Wiley & Sons, pp. 452 & 502.

O'Rourke, M., and Ayala, G., (1990), "Seismic Damage to Pipeline: Case Study", Journal of Transportation Engineering, ASCE, Vol. 116, No.2, March/April.

O'Rourke, M., and ElHamadi, K., (1988), "Analysis of Continuous Buried Pipelines for Seismic Wave Effects", Int. J. of Earthquake Engr. and Struct. Dyn., Vol. 16, No. 6, pp. 917–929.

O'Rourke, M., and Nordberg, C., (1991), "Longitudinal Permanent Ground Deformation Effects on Buried Continuous Pipelines", Technical Report No. NCEER–91–XXXX, National Center for Earthquake Engineering Research, State University of New York at Buffalo, November.

O'Rourke, T., and Tawfic, M., (1983), "Effects of Lateral Spreading on Buried Pipelines During the 1971 San Fernando Earthquake", Earthquake Behavior and Safety of Oil and Gas Storage Facilities Buried Pipelines and Equipment, PVP–Vol. 77, ASME, New York, N.Y.

O'Rourke, T., Grigoriu, M., and Khather, M., (1985) "Seismic Response of Buried Pipelines", Pressure Vessels and Piping Technology, A Decade of Progress, Edited by C. Sundararajan, ASME, N.Y., pp. 281–323.

Towhata, I., Tokida, K., Tamari, Y., Matsumoto, H., and Yamada, K., (1991), "Prediction of Permanent Lateral Displacement of Liquefied Ground by Means of Variational Principle," Technical Report NCEER–91–0001, Proc. 3rd Japan – US Workshop on Earthquake Resistant Design of Lifeline Facilities and Countermeasures for Soil Liquefaction, San Francisco, CA, pp. 237–251.

Youd, T., and Perkins, D., (1987) "Mapping of Liquefaction Severity Index", Journal of Geotechnical Engineering, ASCE, Vol. 113, No. 11, pp. 1374–1392, November.

Experimental Study of Effects of Liquefaction-Induced Ground Displacement on In-Ground Structures

Masanori Hamada,* Keizo Ohtomo,** Hiroshi Sato,*** and Takahiro Iwatate****

*Professor, **Senior Research Engineer,
***Senior Research Engineer, ****Section Manager

*Tokai University, School of Marine Science and Technology,
**Central Research Institute of the Electric Power Industry,
***Tokyo Electric Power Company,
****Central Research Institute of the Electric Power Industry

ABSTRACT

The authors have conducted the following experiments to investigate the fundamental characteristics of the effect that liquefaction-induced ground displacements have on in-ground structures:

(i) Experiments to measure the pressure of liquefied soil on a rigid in-ground wall
(ii) Experiments to measure the effects of liquefaction-induced ground displacements on a pile
(iii) Experiments on the load acting on spheres moving in liquefied soil

From these experiments it was concluded that the pressure exerted by liquefied soil on a rigid in-ground wall was approximately equal to the pressure of a liquid with an equivalent specific gravity. The force due to laterally flowing ground on in-ground structures did not depend on the magnitude of the ground displacement, but was greatly affected by the flow velocity.

INTRODUCTION

It was reported in case studies into the 1964 Niigata and 1983 Nihohkai-Chubu earthquakes that a large number of in-ground structures such as buried pipes and foundation piles were severely damaged as a result of liquefaction-induced ground displacements.[1),2)] The earthquake resistance of in-ground structures is formulated using the so-called "Seismic response displacement method" in Japanese design codes,[3)] where the magnitude of the ground displacement is considered the major factor in the design. When the ground does not liquefy, the propriety of this method has been verified by earthquakes observations of buried pipes, submerged tunnels, and in-ground tanks, as well as by shaking model tests. However, the effectiveness of the seismic response displacement method has not been adequately examined in the case of ground which liquefies.

The authors have conducted three kinds of shaking table tests to study the fundamental characteristics of the effect that liquefaction-induced ground displacements have on in-ground structures. The first series of experiments investigated the pressure exerted on a rigid in-ground wall by liquefied soil on an inclined surface. The second and the third sets of tests, where an acrylic pile and a steel sphere were used to represent in-ground structures, respectively, were conducted to examine the fundamental characteristics of the external forces exerted by laterally flowing ground.

PRESSURE OF LIQUEFIED SOIL ON A RIGID WALL

Figure 1 shows the soil box and the rigid wall used in these experiments. The model ground has a length of 3 m, a width of 0.8 m, a depth of 0.70-0.64 m and a surface gradient of 2%. The grain size distribution of the sand making up the model ground is given in (A) in Figure 2, and the relative density of the ground is 52%. The rigid wall, constructed of steel framing and steel plates, is located in the center of the model, and the earth pressure was measured on both the upstream and downstream surfaces of the wall during liquefaction.

Liquefaction of the model ground was induced by shaking the rigid soil box in the direction of its shorter side. Sinusoidal waves with a frequency of 5.0 cycles/second and a duration of 2.6 seconds were used. The effects of the inertia of the liquefied soil on earth pressure can be ignored, since the direction of shaking is perpendicular to the direction of flow.

Figure 3 shows the time histories of changes in earth pressure and pore water pressure. The earth pressure increases simultaneously with increasing pore water pressure, remains constant for a while and then gradually decreased, as the pore water pressure falls.

Figure 4 shows the maximum earth pressure, which was obtained by adding the maximum increment in earth pressure to the pressure before shaking. The maximum earth pressures on each side is mostly equal to the static liquid pressure. However, the earth pressure is a little higher than liquid

pressure on the upstream side, but somewhat smaller on the downstream side. This is a result of the heaving of the ground surface on the upstream side due to lateral flowing of the liquefied soil as well as settlement of the ground surface on the downstream side.

As shown in Figure 4, the earth pressure on the two sides of the wall is almost equal, and is roughly the same magnitude as the liquid pressure. This means that the total external force acting on the wall is not large even in liquefied ground with a great potential for lateral displacement; only the difference in earth pressure between the two sides, which is caused by the heaving and subsidence of the ground, is shouldered by the wall. This experimental result suggests that in-ground walls, even though they are low in strength and stiffness, are a possible measure to prevent liquefaction-induced ground displacement.

EFFECTS OF LIQUEFACTION-INDUCED GROUND DISPLACEMENT ON PILES

Figure 5 shows the model ground and the foundation pile used in the experiments on the effects of liquefaction-induced ground displacement on piles. The model ground has a length of 3.0 m, a width of 1.0 m, a depth of 25-31 cm, and a surface gradient of 2%. The grain size distribution of the sand making up the model ground is given in (B) in Figure 2, and the relative density of the ground is 54%. The model foundation pile consists of an an acryle pipe with a length of 28 cm, and a diameter of 21.5 mm. It is placed in the center of the soil box. The lower end of the model pile was fixed to the floor of the soil box.

Liquefaction was induced by shaking the soil box in the direction of its shorter side using sinusoidal waves with a frequency of 5.0 cycles/second and a duration of about 10 secconds. Consequently, the ground moved downward because of the inclination of the surface. The effects of the liquefied soil's inertial forces on ground movement can be eliminated, since the shaking is perpendicular to the direction of the ground movement. During ground movement, the bending strain on the model pile, pore water pressure, acceleration, and displacement of the ground were measured.

Knowledge of the time history of ground displacement is essential in order to quantitatively examine the relationship between the load, acting on the pile due to the liquefied ground and the displacement, velocity, and acceleration of the ground. The ground displacement history was measured by the method shown in Figure 6. Target plates with the same apparent specific gravity as the liquefied soil were buried in the ground, and the movement of these plates was recorded using a roll-type displacement meter. The accuracy of displacement measurement was verified by a comparison between the maximum values measured by this method and the displacements measured by colored sand columns.

Figure 7 shows the input acceleration, the pore water pressure, the bending strain on the model pile, and the displacement of the ground. Ground displacements began when the pore water pressure reached the effective overburden stress. Maximum displacements were reached 4-5 second later.

These displacements remained, as permanent ground displacements, after liquefaction ceased. The strain on the model pile also began when the pore water pressure peaked, and reached a maximum 2-3 seconds later while the ground displacements were still increasing. After recording a peak value, the strains on the pile gradually decreased. The results, shown in Figure 7, demonstrate that ground displacement had no direct effect on the deformation of the pile in the laterally flowing ground.

The bending strain on the model pile was measured at six depths. From these strain records, the force acting on the pile was estimated according to the following procedure:

The four coefficients a_0-a_3 in the formula below for the distributed load $q(x)$ on the pile were calculated from the six strain records by the least squares method. The coefficients a_0-a_3 are functions of time.

$$q(x) = a_0(t) + a_1(t)\, x + a_2(t)\, x^2 + a_3(t)\, x^3 \qquad (1)$$

On the other hand, the velocity and acceleration of ground movement was calculated from the measured displacements. Figure 8 shows the estimated external force at each depth along with the displacement, velocity and acceleration of the ground at that depth. It can be concluded from this figure that the load imposed on the pile by the laterally flowing ground has a close correlation with the velocity of the ground movement. This suggests that liquefied ground behaves as a liquid and that pile deformation is a result of viscous forces caused by the flowing liquid.

LOAD ON SPHERES MOVING IN LIQUEFIED SOIL

Figure 9 shows the experimental arrangement used to investigate the fundamental characteristics of the load on spheres moving in liquefied soil. The soil box is cylindrical, with a diameter of 30 cm and a depth of 30 cm. Steel spheres with diameters of 3, 4 and 5 cm sink into the liquefied soil under their own weight and by the action of counterweights. Their speed can be varied by changing the counterweights. Liquefaction was induced by shaking the soil box using sinusoidal waves with a frequency of 5 cycles/second. The load placed on each sphere by the liquefied soil can be estimated by subtracting the sum of the tensile force on the wire and the buoyancy of the liquefied soil from the total weight of the sphere and counterweight.

Figure 10 shows the relationship between the load on moving spheres and the velocity of the soil movement. Even though the experimental results are widely scattered, a proportional relationship can be seen between the load and the velocity of a sphere. If the liquefied soil is assumed to be a viscous liquid, the load on a sphere moving with a uniform velocity can be expressed as follows:

$$F_V = 6 \eta \pi r v \quad (2)$$

where F_V, r, v are the load, radius of the sphere, and the velocity, respectively, and η is the coefficient of viscosity.

Figure 11 shows the coefficient of viscosity for the liquefied soil calculated from the results in Figure 10. It can be seen that the coefficient of viscosity appears to vary with the size of the sphere, suggesting that the liquefied soil can not be simply treated as a viscous liquid.

CONCLUSION

Three shaking model ground experiments were conducted to investigate the fundamental characteristics of liquefied soil and its effect on in-ground structures. The following notable results were obtained:

(i) The pressure exerted by liquefied soil on a rigid in-ground wall is almost equal to the pressure which would be applied by a liquid with the same specific gravity as the ground. The pressures on the upstream and downstream surfaces of the wall is roughly equal. The latter result suggests that the total force acting on the in-ground wall is small even in ground with a great potential for lateral flow.

(ii) The force acting on a model pile in laterally flowing ground is not directly related to the ground displacement, but to the ground velocity.

(iii) The load on a moving sphere in liquefied soil has a proportional relationship with the velocity of the sphere. However, the coefficient of the viscosity is not constant with respect to the size of the sphere. This suggests that liquefied soil cannot be treated as a simple viscous liquid.

REFERENCES

1) M. Hamada, Large Ground Deformation and Their Effects on Lifelines: The 1964 Niigata Earthquake, Technical Report, National Center for Earthquake Engineering Research, pp. 2-001, 3-1 to 3-119, 1992.

2) M. Hamada, Large Ground Deformations and Their Effects on Lifelines: 1983 Nihonkai-Chubu Earthquake, National Center for Earthquake Engineering Research, pp. 1-001, 4-1 to 4-85, 1992.

3) Earthquake Engineering Committee, Japan Society of Civil Engineers, Earthquake Resistant Design Features of Submerged Tunnels in Japan, Earthquake Resistant Design for Civil Engineering Structures in Japan, pp. 189-260, 1988.

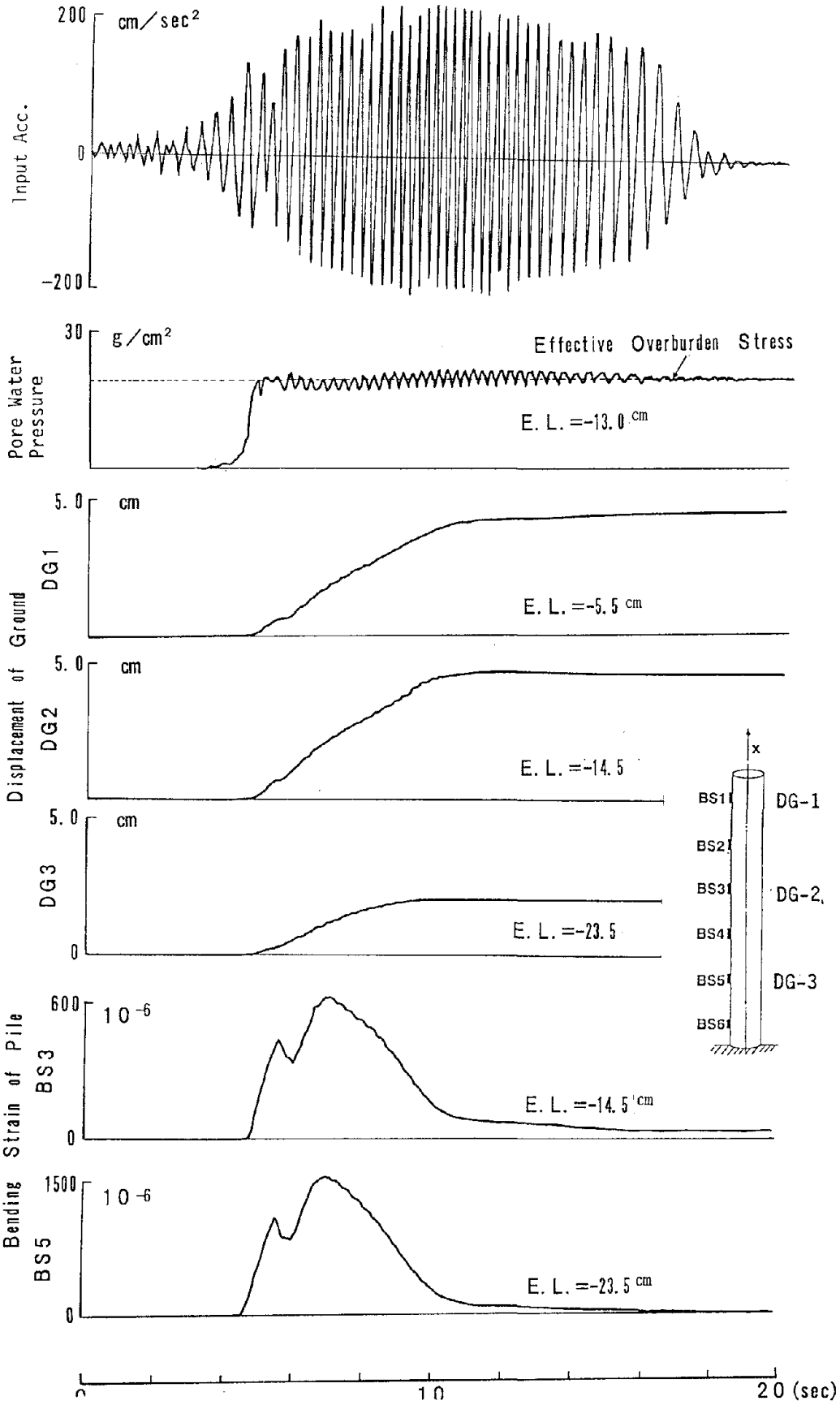

Figure 7 Records of Pore Water Pressure, Ground Displacement and Bending Strain of Pile

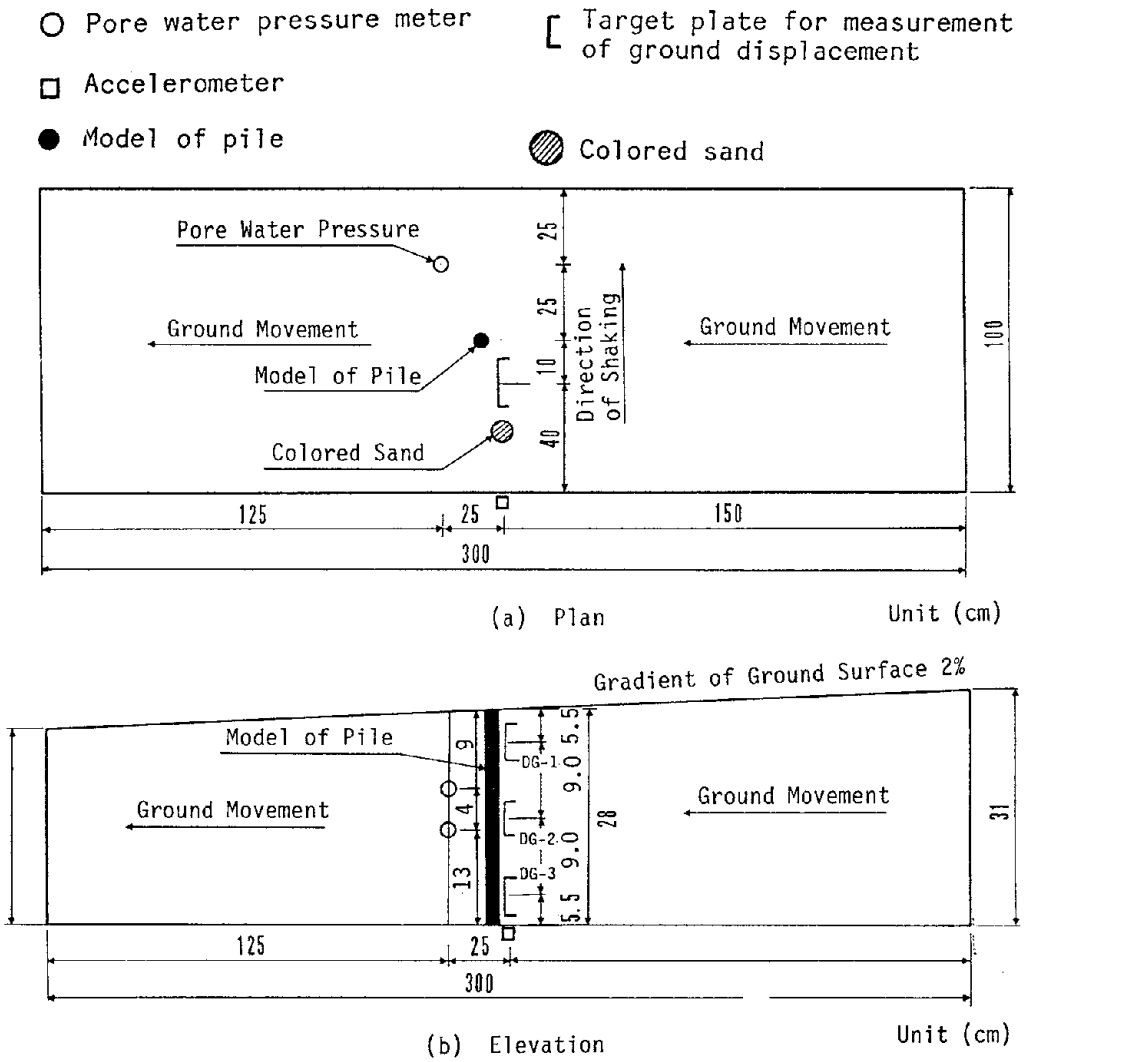

Figure 5 Model of Ground and Foundation Pile

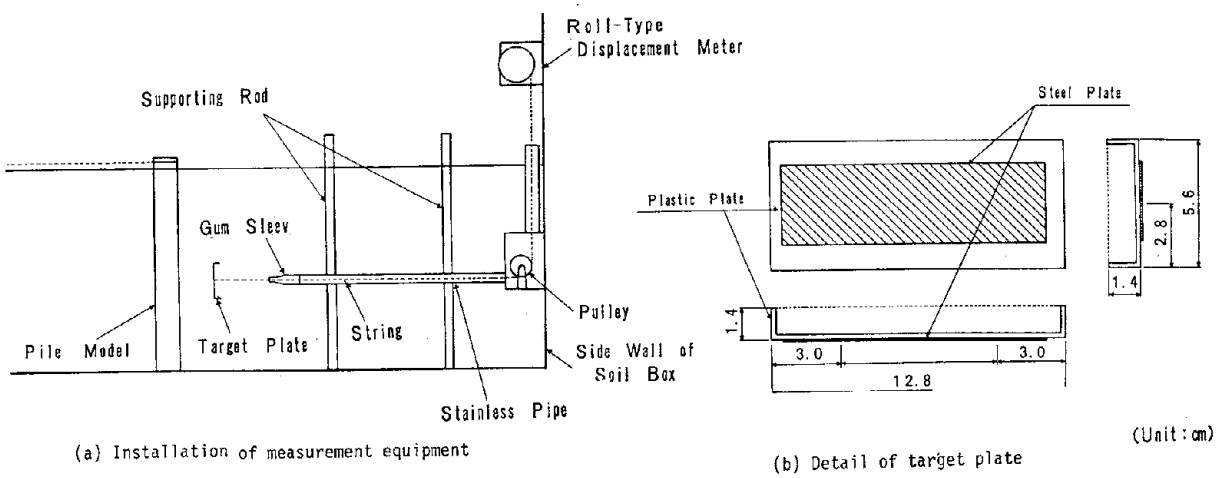

Figure 6 Method of Measurement of Time History of Ground Displacement

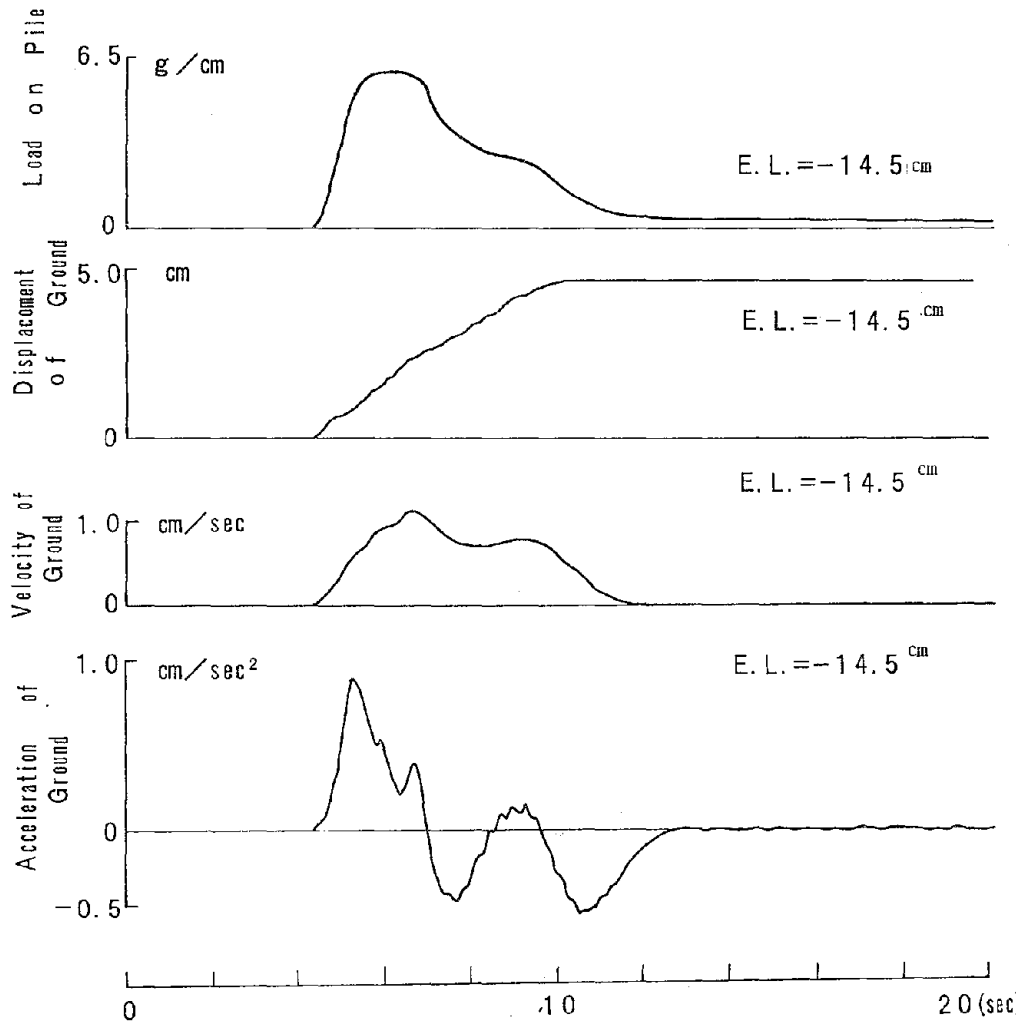

Figure 8 Load of Pile, Displacement, Velocity and Acceleration of Ground, and Relative Displacement between Ground and Pile

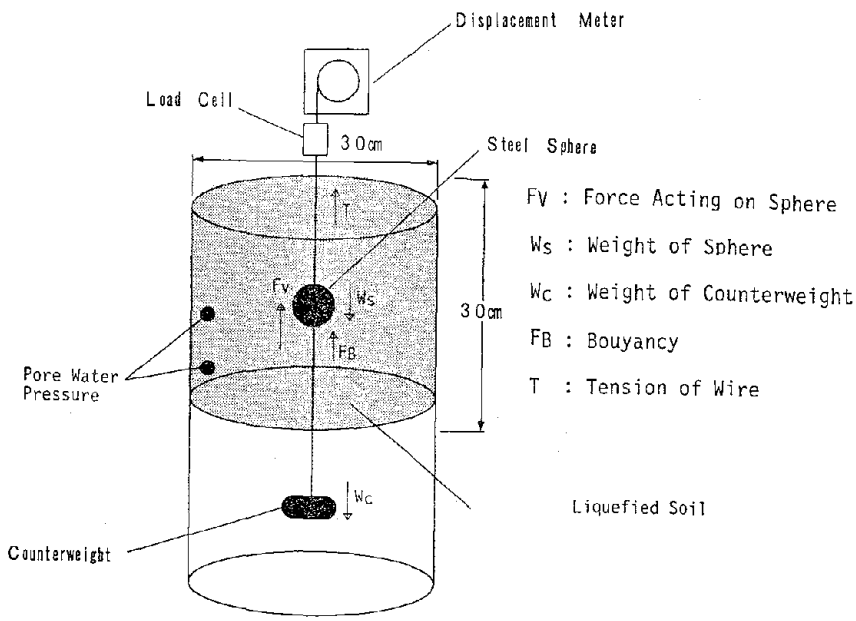

Figure 9 Experimental Equipment of Spheres Moving in Liquefied Soil

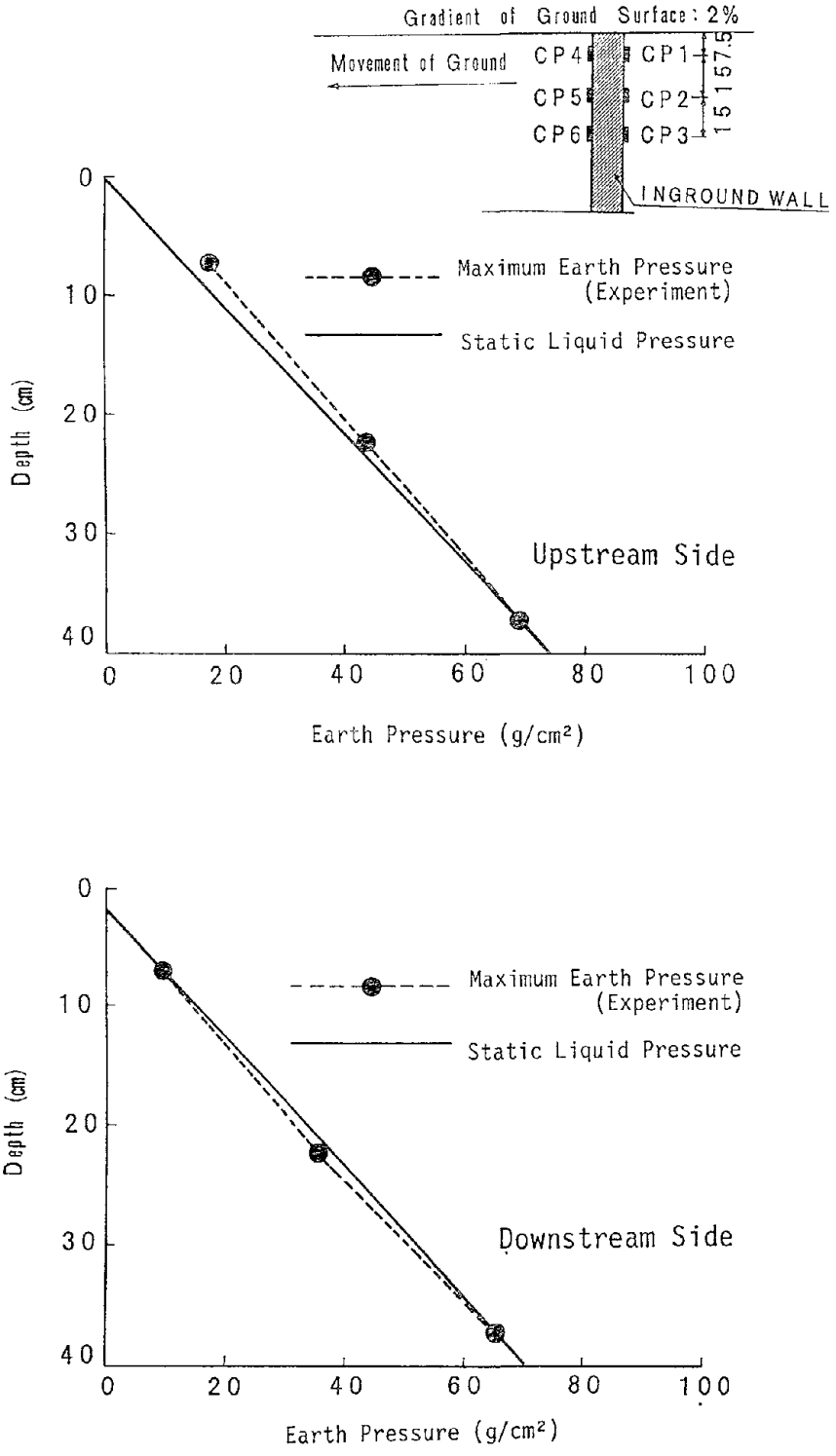

Figure 4 Maximum Earth Pressure on Rigid In-Ground Wall

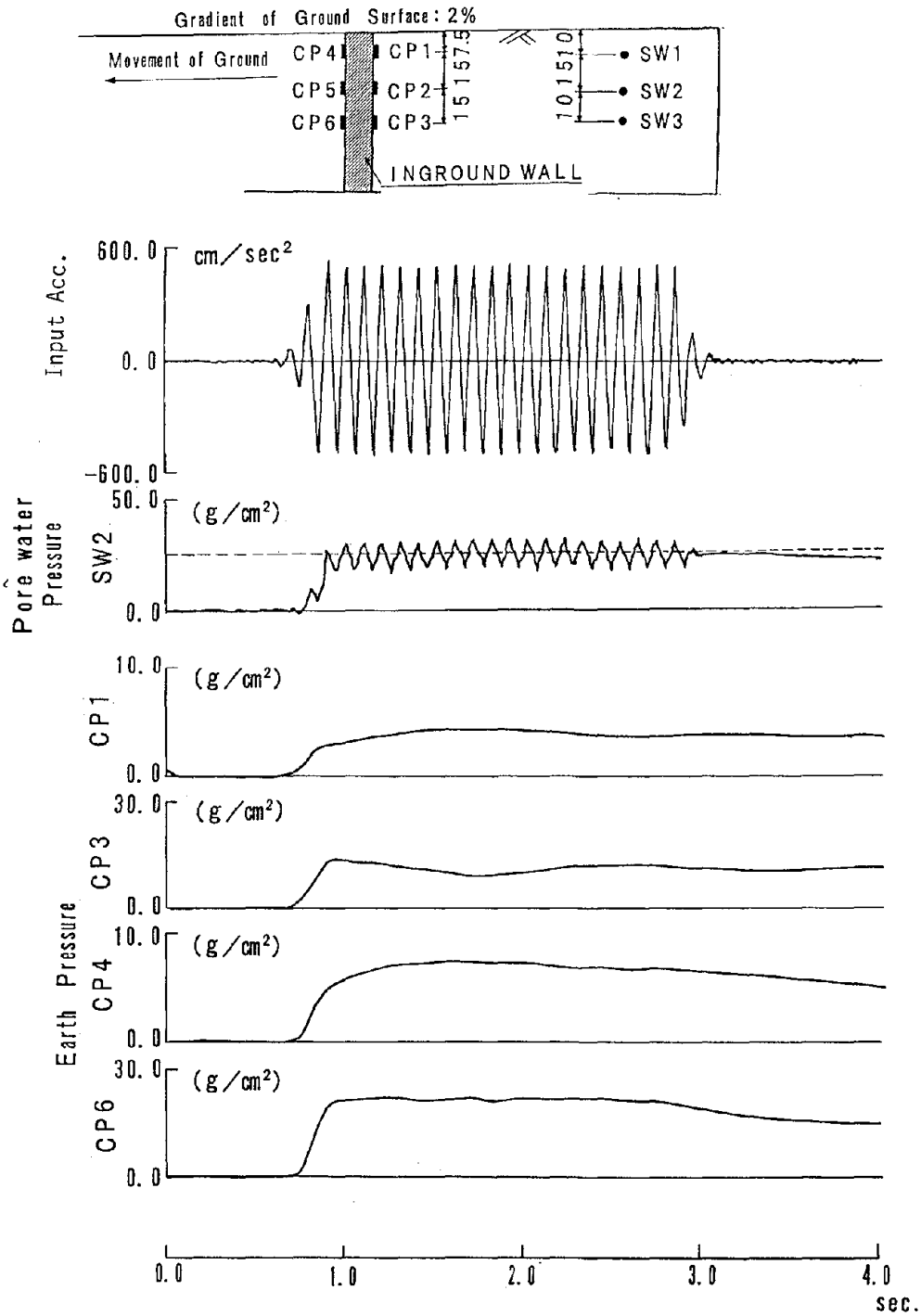

Figure 3 Record of Earth Pressure and Pore Water Pressure

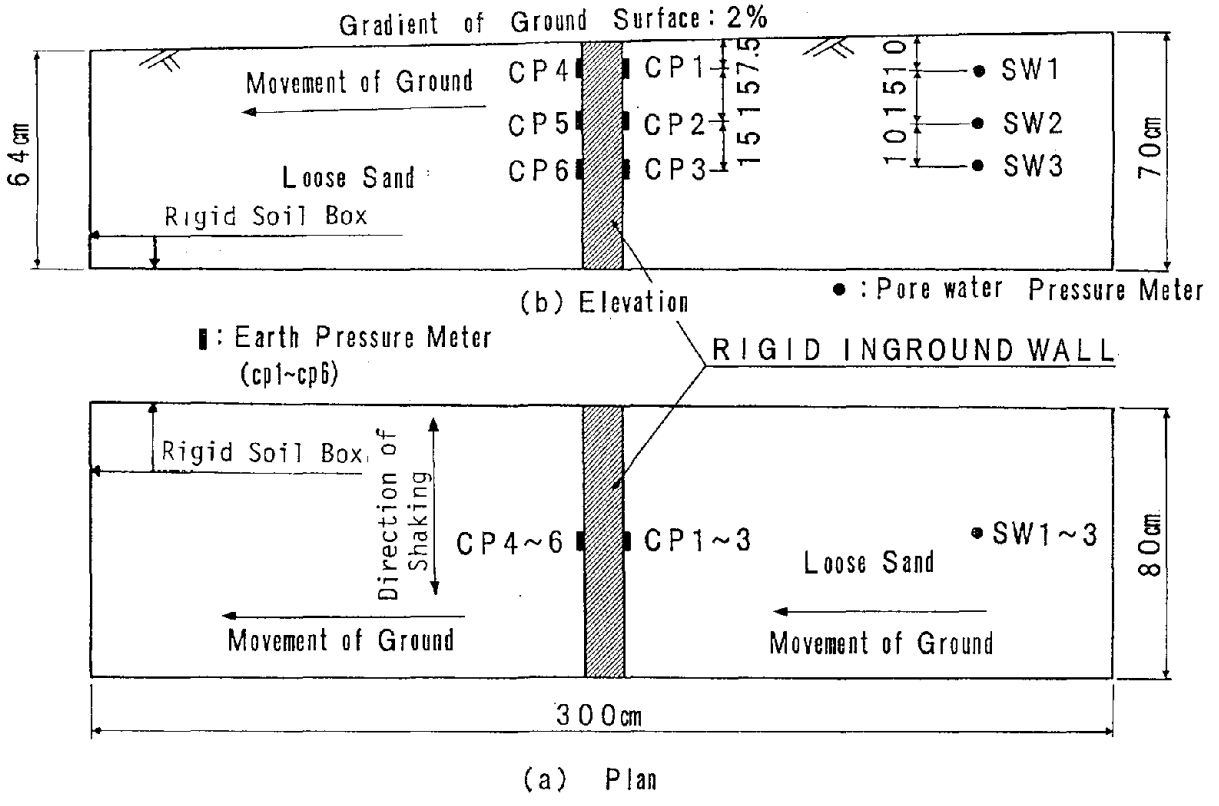

Figure 1 Model of Ground and In-Ground Wall

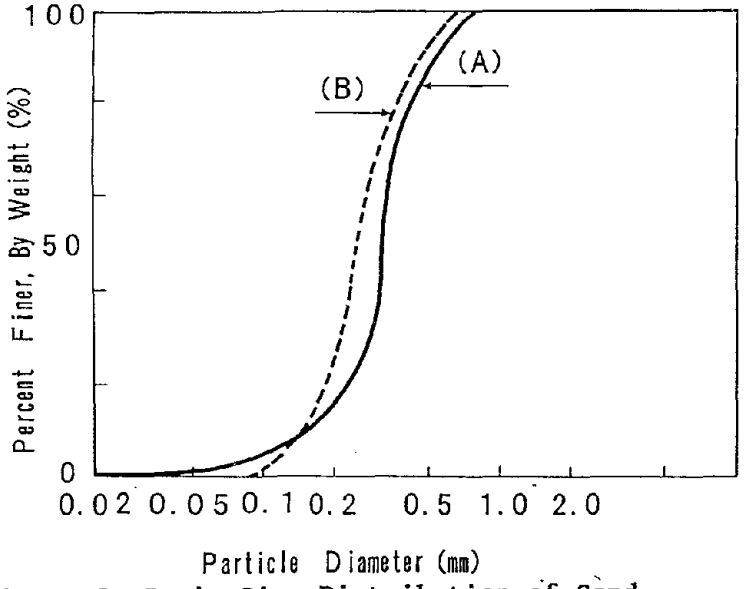

Figure 2 Grain Size Distribution of Sand
((A): Experiment on Pressure of Liquefied Soil on Rigid Wall, (B): Experiment on Effect of Liquefaction-Induced Ground Displacement on Pipe)

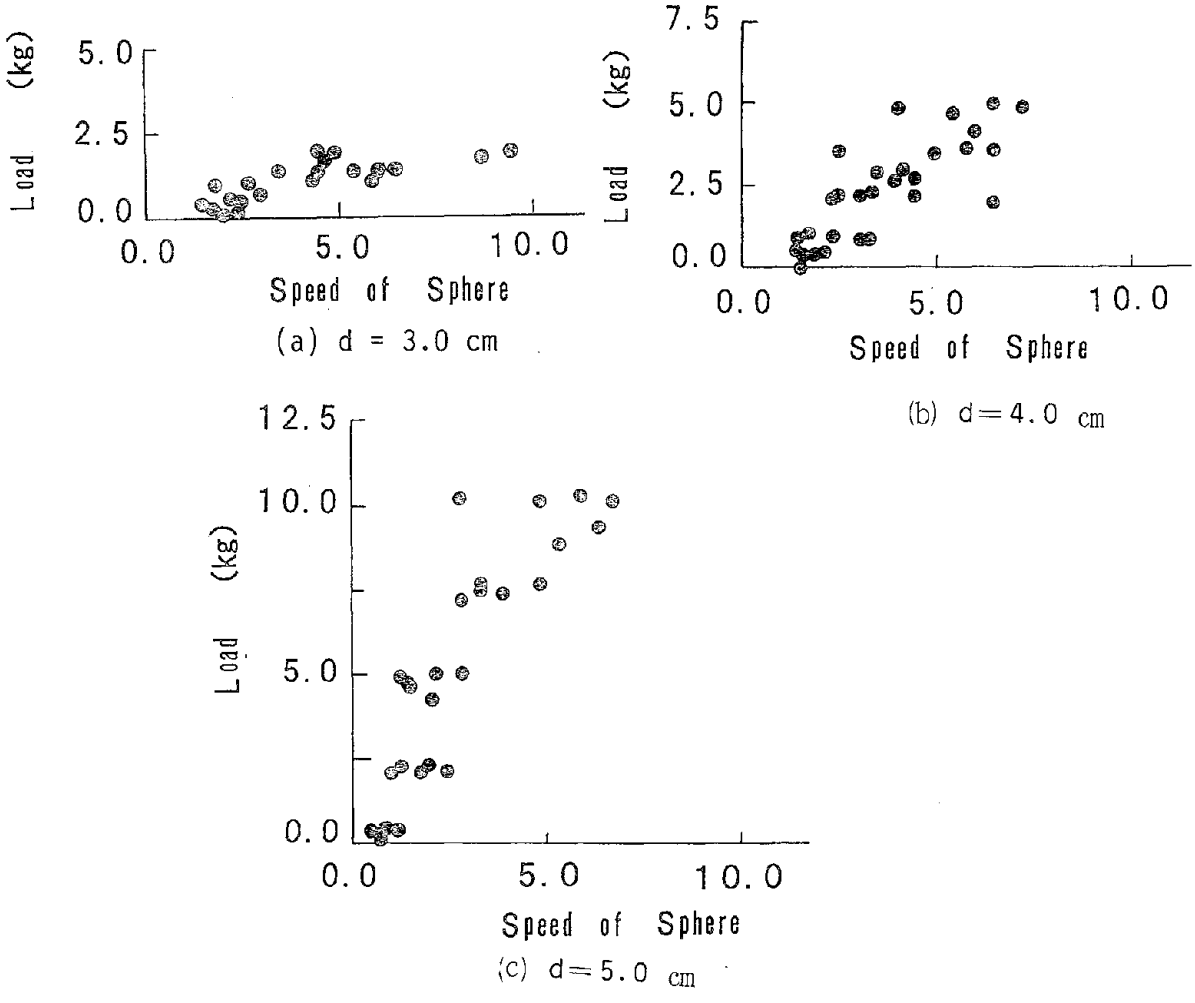

Figure 10 Relationship between Load on Moving Spheres and Velocity

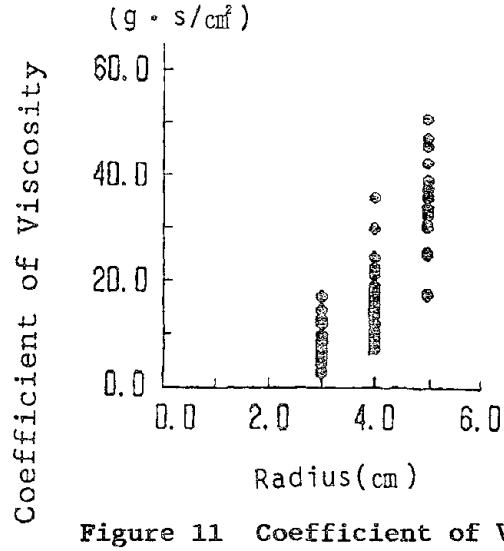

Figure 11 Coefficient of Viscosity

Centrifuge Study of Shallow Foundation on Saturated Sand During Earthquakes

Li Liu[1] and Ricardo Dobry[2]

[1] Graduate Student [2] Professor of Civil Engineering
Rensselaer Polytechnic Institute

ABSTRACT

A series of centrifuge model tests with earthquake shaking simulations were performed on the RPI 100 g-ton geotechnical centrifuge to clarify various aspects of the behavior of shallow foundations on liquefiable soil. The tests were conducted with saturated sand of various densities and permeabilities, with and without a fine–grained soil layer on top, and with and without a surface foundation model at the ground surface. Parameters measured included accelerations of soil and structure, excess pore pressures, and settlements of soil and structure. The results indicate a complex interaction between the different aspects of the problem, including formation of a soil water interlayer under the fine–grained soil, and redistribution of total foundation stresses within the sand mass after shaking.

INTRODUCTION

Large scale liquefaction-induced bearing capacity failures affecting hundreds of buildings occurred during the 1964 Niigata earthquake, with the structures sinking up to 3.8 m and tilting as much as 80° (Seed and Idriss, 1967; Yoshimi and Tokimatsu, 1977). Kishida (1966) classified the damages to foundations into four categories and correlated building settlement and tilt, as shown on Table 1. The most severe damage occurred on soil deposits with low standard penetration N-values (Fig. 1), suggesting that sand density played a key role in the settlement and tilting of the damaged buildings.

The post-earthquake investigations revealed that many of the sands involved were relatively clean and uniform, extending to more than 15 m in depth. The bearing capacity failures were observed to occur typically several minutes after the end of the shaking, suggesting that the effective stresses in the foundation soil reached their minimum values rather slowly. Most likely this reduction of effective stresses in the foundation soil, which was responsible for the bearing capacity failures, was not caused directly by shaking, but rather by migration of water toward the foundation from areas of high excess pore pressure located at some distance.

Although the 1964 Niigata experience is the most dramatic example, sinking and tilting of building foundations due to liquefaction has been reported in many earthquakes. The response of such saturated sand-foundation systems to base excitation has been experimentally studied by both 1g shaking tests and centrifuge model tests, with emphasis on the behavior of shallow footings. Yoshimi and Tokimatsu (1977) investigated the factors influencing structure settlement during earthquakes by means of shaking table tests. They found that the excess pore pressures developed under the center of the footing were smaller than those in the free field, and that the structure settlement increased rapidly if a significant fraction of the soil mass directly under the foundation reached a pore pressure ratio of about 60%. Liu and Qiao (1984) observed the formation of water interlayers in their stratified sand models during shaking table tests, with these interlayers eventually leading to sand boils at the ground surface (Fig. 11b). Liu and Qiao also reported that the excess pore pressures under the foundation were lower than those in the free field, with surface manifestation of liquefaction occurring first near the structure where the earlier sand boils appeared, and then in the free field. In the centrifuge model tests conducted by Whitman and Lambe (1982, 1988), the excess pore pressures measured under the foundation were also lower than those away from the structure, both for axisymmetric tests conducted in a cylindrical stacked ring device (Fig. 2a), and for plane strain tests done in a rigid rectangular box container (Fig. 2b).

This paper reports some preliminary results from a series of centrifuge tests including earthquake simulations conducted at a 50 g centrifugal acceleration in the RPI centrifuge. The RPI 100 g-ton centrifuge, an electro-hydraulic shaker and a dedicated data acquisition system are used in the experiments. An important objective of the investigation is to understand better the dynamic response and key aspects of the behavior of this complex saturated sand-shallow footing system. The emphasis is on the distribution pattern and magnitudes of the excess pore pressures under and near the foundation, as well as on the settlement of the foundation and free field soil. Factors studied include sand density, soil permeability and soil configuration (homogeneous versus layered deposit). Throughout the paper the earthquake accelerations measured in the model are consistently divided by a factor of 50 before plotting, and the model times and settlements are multiplied by 50, while the values of measured excess pore pressures are plotted without change. Therefore, it can be said that these plotted accelerations, times, settlements, and excess pore pressures

correspond to the prototype being modeled. However, due to the different time scaling laws for dynamic response and groundwater flow, this statement must be tempered by some caution. Depending on the viscosity of the pore fluid used in the centrifuge tests, the prototype soil in question may have a permeability similar to that of the model soil at 1 g, or as much as 50 times that permeability. This aspect is further discussed later herein.

CENTRIFUGE TEST SERIES AND SETUP

All centrifuge tests were conducted using a 12 cm thick model soil investigated at a 50 g centrifugal acceleration (Fig. 3), simulating a 6 m thick prototype soil deposit. The model container is a rigid rectangular box 43.2 × 19.3 cm in plan dimensions and 28.6 cm high. The experiments included both uniform fine sand and layered silt-sand or clay-sand deposits, with or without a circular model surface foundation on top. The model footing used in all cases was a flat steel cylinder 10 cm in diameter, simulating a 5 m diameter prototype. The seismic simulations were run by applying to the model a horizontal base excitation with a peak acceleration between 8.5 g and 18 g (see Fig. 3), corresponding to $8.5/50 = 0.17$ g and $18/50 = 0.36$ g in the prototype.

Four test series are reported here as listed in Table 2. In Series A (Fig. 3a), a uniform sand deposit saturated with water was tested with and without foundation; both the bearing foundation pressure q_{av} and the sand relative density D_r were varied between tests, as listed in the table. In Series B, some of Series A tests, with a model foundation and $D_r \simeq 50\%$ were repeated, but now with different water-glycerine fluid mixtures used as pore fluid to examine the influence of soil permeability. In free field test Series C, a thin fine-grained layer (silt) was placed on a sand layer of D_r ranging between 40% and 60%; water was used as pore fluid. Finally, in Series D the shallow foundation model was placed on top of the fine-grained layer (silty clay), which in turn overlaid sand with $D_r \simeq 50\%$; water was again used as pore fluid (Fig. 3b). The shift from silt to clay between Series C and D was done for an easier monitoring of some phenomena observed in this layered system. Table 3 lists some relevant properties of the soils used in the tests.

In all model experiments, the sand layer was placed by dry pluviation followed by application of one hour of vacuum at -14.8 psi to eliminate the air within the sample. Then deaired water (or the glycerine solution in Series B tests) was supplied slowly into the sample from the bottom while keeping the vacuum on top. For the two-layer models, the upper layer was constructed by pouring a thick silt (or silty clay) slurry very gently on top of the sand. The uniform sand-water models were consolidated by spinning the model to the 50 g centrifugal acceleration and keeping this acceleration for 20 minutes. In the uniform sand-glycerine solution models and silty clay-sand models, more consolidation time and steps were used. At the end of consolidation, the specified horizontal seismic shaking was applied to the base of the model.

Three types of miniature transducers were employed to measure the earthquake accelerations during shaking, the soil surface and foundation settlements, and the excess pore pressures within the soil. The general transducer layouts for Series A, B and D are shown in Fig. 3. Three piezometer sets were generally installed. Piezometers PC1, PC2, and PC3 were located at different depths along the centerline. Piezometers PF1, PF2, and PF3 were installed away from the foundation and represent approximately the response in the free field. The third set, consisting of one piezometer, PE, was installed at a shallow

depth under the edge of the footing.

TEST RESULTS

Selected records from Test A3, conducted with uniform sand and using water as pore fluid are included in Fig. 4. The relative density of the sand in this test is 53%. The base input acceleration in prototype units is a 10-cycle, 2-Hz uniform sinusoidal signal with an average amplitude of 0.35 g. The behavior exhibited by these records is typical of the soil-foundation tests done by the authors. The excess pore pressure records away from the foundation (PF1, PF2, and PF3 in Fig. 4) are similar to those obtained in the corresponding test without a foundation model (not shown), and they indicate that a pore pressure buildup of 100% ("initial liquefaction") occurred away from the footing during shaking. The pore pressures under the footing were lower than in the free field during shaking (PC1, PC2, and PC3 in Fig. 4), and they increased and reached a maximum shortly after the end of the shaking. During shaking, negative pore pressures were developed under the foundation at shallow depths ($\lesssim$ diameter of foundation). It is believed that as the pore pressure under the circular footing was much lower than in the free field at the same elevation, horizontal migration of excess pore water took place from the free field toward the foundation soil.

The excess pore pressure measured under the edge of the foundation, PE, exhibited a significant fluctuation and a simultaneous monotonic increase during shaking (Fig. 4). The phase angle between the PE pore pressure record and the horizontal acceleration measured at the foundation is about 180° (Fig. 5). Therefore, these fluctuations in pore pressure were caused by the large cyclic mean total stresses induced in the soil under the edge of the footing due to foundation rocking.

Maximum excess pore pressures at various depths are compared in Fig. 6 for the three Series A tests conducted with different sand densities. The tests with $D_r = 53\%$ and 76% had model foundations with average contact static pressures of 125 kPa (at 50 g), and an input base acceleration amplitude of 0.35 g. The model with $D_r = 34\%$ had an average contact pressure of 80 kPa, as it could not carry a much heavier load without static bearing capacity failure, and the input acceleration intensity was correspondingly reduced to 0.17 g.

The maximum excess pore pressures in the free field were essentially the same independently of sand density (Fig. 6a); that is, initial liquefaction was reached in all three tests. On the other hand, the maximum pore pressures under the foundation were different for models having different sand densities (Fig. 6b). As expected, the excess pore pressure under the footing decreases as the sand density increases. All these maximum pore pressures under the foundation occurred after shaking, and were undoubtedly influenced by water migration from other zones of the sand mass. Two explanations are advanced for the influence of D_r on excess pore pressure shown by Fig. 6b. One is that the amount of water expelled from the surrounding liquefied soil was larger for the loose sand, which made more water available to migrate into the central sand zone under the foundation. The other is that the loose sand under the footing had less potential for volume expansion due to dilatancy, and thus needed to absorb less water to reach significant positive excess pore pressures.

In centrifuge simulations involving saturated soil the time scaling factor is N for dynamic response (N is the centrifuge acceleration of the test in g; N = 50 in our case), but it is N^2 (= 2500) for diffusion phenomena including consolidation and pore fluid flow. Therefore, when the model times are multiplied by a factor N (= 50) as done in this paper, the diffusion behavior of the soil in the model actually corresponds to a comparable prototype soil having a permeability N times higher. In the tests reported herein where water was used, the prototype soil would have 50 times the permeability of the soil in the model. One way to solve this problem is to use a pore fluid having a viscosity N times higher, thus adjusting the permeability of the soil also by a factor N. This was done in Series B to investigate the impact of soil permeability on the behavior of the foundation model tests. A glycerine solution was used, and the soil permeabilities were adjusted by varying the glycerine content (GC) in the pore fluid. Both from theory and experiment, GC = 55% and 85% reduce the soil permeability by factors of 10 and 100, respectively, thus bracketing the desired value N = 50.

The excess pore pressure ratios in the free field in Test A3 (GC = 0) and in Test B1 (GC = 55%) are compared in Fig. 7a and b, while the locations of the transducers are included in Fig. 3a. The soil density, average contact pressure, and intensity of input acceleration are similar in both model tests, and they are also comparable to Test B2 (GC = 85%). In both tests A3 and B1 the excess pore pressure ratios in the free field reached 100% within 2-3 cycles of shaking. The two records have similar patterns and magnitudes except that the pore pressures in Test A3 dissipate faster than in Test B1, as expected. The pore pressure ratios under the footing at a depth of about 3 m are plotted in Fig. 7c and d. Figure 7e includes the pore pressure ratio at a depth of about 4.5 m under the foundation for Test A3; as this record was not available for Test B1 because of transducer malfunction, Fig. 7f shows the corresponding plot for Test B2. In all these plots the pore pressure ratio is defined as the excess pore pressure divided by the initial effective overburden stress from the soil alone (effective overburden pressure in the free field). At depths of about 3 and 4.5 m under the footing, the pore pressures in Test A3 (GC = 0), B1 (GC = 55), and B2 (GC = 85) show a similar pattern, with the pore pressure ratios becoming smaller as the GC decrease. That is, in Tests B1 and B2, the pore pressures of both signs (positive and negative) are larger than in Test A3. This shows that a lower soil permeability reduces the rate of pore pressure equalization and enhances the pore pressure differences between different parts of the soil mass. It also means that the use of water as pore fluid in these centrifuge tests tend to make the fine sand behave like coarse sand or even gravel 50 times more pervious, thus seriously masking the real picture of pore pressure generation and spatial distribution as it occurs in field prototype conditions.

In almost all soil-foundation model tests, the excess pore pressures under the footing reached their maximum values after the shaking had ended. In some cases these maximum pore pressures were higher than those simultaneously monitored away from the foundation at the same elevation. For example, in Test B2 shown in Fig. 7f, the maximum pore pressure ratio for PC3 is in excess of 170%, which was the highest excess pore pressure anywhere in the sand mass at that time. Similarly, in Test D5, the excess pore pressure under the foundation, PC1, reached its maximum of 25 kPa about 5 minutes after shaking (not shown), and that was also the highest excess pore pressure in the entire model at the time. Therefore, when these excess pore pressures under the footing were approaching their maximum values, the shaking had already stopped and all hydraulic gradients pointed outward from the foundation, and thus these pore pressure increases below the footing were not caused by dynamic loading or by water migration from other zones. A possible explanation for this phenomenon is that a total stress redistribution was taking place, associated with the development and redistribution of pore pressures near the

foundation. In this redistribution, the static stresses caused by the weight of the footing were being transferred from soil that had liquefied to the soil under the foundation. The authors plan to repeat some of the tests in this series with total stress measurements in the soil to verify this explanation.

Series C tests were done without foundation to investigate the behavior of layered soil during and following shaking. Figure 8 shows the input base acceleration and excess pore pressures measured in the middle of the sand layer in Test C1. This model has two layers 6 cm thick each, simulating a saturated sand 3 m thick under a 3 m thick surface silt layer. The input acceleration in prototype units is a 10-cycle, 2-Hz sinusoidal signal with various amplitudes generated randomly by computer. It can be seen that after the sand liquefies by the end of shaking (the calculated initial effective stress at mid-sand is 36 kPa), the pore pressures in the sand decay quickly as a result of sedimentation of the liquefied sand particles (from about 6 sec to 10 sec). However, because the upward water flow from the liquefied sand cannot dissipate through the surface silt stratum fast enough, water accumulates along the lower boundary of this surface layer, forming a thin water film or water interlayer. The plateau in the pore pressure history of the sand from about 10 sec to almost 2 minutes in Fig. 8c demonstrates this phenomenon. The excess pore pressure in this plateau equals the buoyant weight of the surface layer (25 kPa) and is independent of the depth of the piezometer within the sand, clearly indicating the presence of the water interlayer along the interface. It has been reasonably speculated by the authors and others, that such water interlayers may be major contributors to important liquefaction field phenomena observed at the ground surface in earthquakes, including lateral spreading, bearing capacity failures, and sand boils.

In Series D tests, done with a shallow footing on top of the layered soil deposit, similar measurements were obtained from the piezometers installed away from the foundation. Figure 9a shows the excess pore pressure isochrones away from the footing in Test D6 (see Fig. 3b for transducer locations). At 5 seconds, corresponding to the end of shaking, the maximum excess pore pressure ratios for the entire sand deposit are almost 100%. The sedimentation and consolidation of the sand layer under its own buoyant weight was completed about 20 sec after the end of shaking, at which time essentially there were no hydraulic gradients or water flow within the sand. Afterwards, the constant excess pore pressure in the sand due to the weight of the clay on the water interlayer stayed for more than 60 sec, indicating that this interlayer was present at the interface sand-clay during all that time. Figure 9b shows the maximum excess pore pressures under the foundation in the same Test D6, all of which occur some time after shaking and not necessarily at the same time in all records. The initial effective overburden pressure under the foundation sketched in Fig. 9b was estimated from elastic theory. It can be seen that the maximum excess pore pressures under the foundation were far below the total effective overburden pressure (including the weight of the footing), thus suggesting that no water interlayer was formed under the foundation.

Therefore, the authors speculate that the water film in Test D6 developed as shown in Fig. 10a. The water interlayer did form along the soil interface in the free field due to the strong shaking, but did not exist under the foundation. Even the water expelled by the sand under the footing must have found its way toward the water interlayer away from the foundation, contributing to its total thickness there. The water interlayer pattern observed in the shaking table tests by Liu and Qiao (1984) is also sketched in Fig. 10b for comparison. These two plots provide a general picture of the pattern of water interlayering in a layered soil-shallow foundation system, and may help explain the abundance of sand boils typically found near buildings after earthquakes.

The total prototype settlements S measured in the free field in Series A, B, and D fell in the range between 4.8 and 9.5 cm, corresponding to volumetric strains $\epsilon_v = 0.8$ to 1.6% of the soil thickness, with the exception of Test A3, which had 20 cm, or $\epsilon_v =$ 3.4%. The measured foundation settlements in Series A, B, and D were much larger, in the range from 17 to 53 cm, corresponding to a ratio of settlement over footing diameter S/D = 3.4 to 10.6%. These are very substantial settlements, similar to those associated with slight and intermediate damage and tilting of buildings in the 1964 Niigata earthquake (Table 1). Some of these measured settlements are summarized in Table 4 for several tests having similar input accelerations and static bearing stresses but different relative densities and permeabilities. The comparison between tests A2 and A3 shows the influence of D_r on S, with S being three times larger for the looser soil in Test A3. More than 90% of the total foundation settlement occurred during shaking for GC = 0 models (Series A and D), while for the low permeability models in Series B, the increase of glycerine content tended to decrease the foundation settlement during shaking and to increase it after shaking (Table 4, tests A3, B1, and B2).

DISCUSSIONS AND CONCLUSIONS

Several effects were observed in these preliminary results, which are consistent with 1g and centrifuge model tests reported by other authors:

1. The excess pore pressures due to earthquake shaking under the foundation are smaller than those occurring in the free field, due to sand dilatancy associated with the static shear stresses. Negative pore pressures are observed under the foundation when dense or medium dense sand is used. This dilatancy effect decreases with depth under the footing. An important consequence is that groundwater flow develops from the free field toward the soil beneath the foundation with a tendency toward pore pressure equalization.

2. As the sand liquefies in the free field, there seems to be a redistribution of the static stresses due to the weight of the footing, from the free field toward the soil directly under the foundation, near the end of shaking and after it. As a result, typically the excess pore pressures under the foundation continued to increase after the shaking had ended, reaching values significantly higher than those in the free field.

3. Both effects just discussed in Conclusions 1 and 2 tend to increase the excess pore pressures under the footing with time, and in fact in most tests these excess pore pressures reached their maximum values after the shaking had ended. This suggests that the greatest danger of bearing capacity failure may well occur after shaking.

4. The maximum excess pore pressures under the footing increase when the sand is looser, due to a decrease in the dilatancy effect and an increase in the excess pore water available from the liquefied soil in the free field.

5. Large cyclic fluctuations of pore pressure tend to occur due to rocking under the edge of the foundation.

6. The permeability of the granular soil plays a key role in the actual distribution of excess pore pressures during and after shaking. As the permeability of the soil

increases, all excess pore pressures (positive and negative) are decreased. Also, all pore pressure differences (under the footing versus the free field, during shaking versus after shaking) are decreased. One consequence is that the use of water as pore fluid in centrifuge earthquake modelling can give erroneous results by masking the real picture of pore pressure distribution in the vicinity of the prototype foundation.

7. The conclusions above relate mostly to a shallow footing on uniform sand or other granular soil. When the liquefiable soil lies under a fine–grained stratum of lower permeability, a water interlayer may form along the interface between the two layers in the free field. This water interlayer may stay for some time after the shaking. However, the weight of the foundation will tend to prevent the development of such water film under it.

8. The total prototype foundation settlements measured in the centrifuge tests are in the range between 17 and 53 cm, corresponding to a settlement/diameter ratio S/D = 3.4 to 10.6 %. For a given base input shaking and contact pressure, the value of S increases significantly as the sand becomes looser. A larger soil permeability does not change much the total value of S, but it increases the fraction of S which occur during the shaking.

ACKNOWLEDGMENTS

The equipment development and the research reported here were supported by Grants NCEER 90–1507 and BCS–9016880 (VELACS) of the National Center for Earthquake Engineering Research and National Science Foundation, respectively. The authors also want to thank Mr. Paul Van Laak for his help in performing the centrifuge model tests.

REFERENCES

Arulanandan, K., C. Yogachandran, and K. K. Muraleetharan, B. L. Kutter, and G. S. Chang (1988) "Laboratory Flow Slide During Earthquake Simulation," pp. 539-544, In: *Centrifuge 88*, Paris, J.-F. Corte (ed.), Balkema, Rotterdam, The Netherlands, April.

Bouckovalas, G., C. Stamatopoulos, and R. V. Whitman (1991) "Analysis of Seismic Settlements and Pore Pressures in Centrifuge Tests," ASCE JGE Vol 117(10):1492-2508, October.

Dobry, R. (1989) "Some Basic Aspects of Soil Liquefaction During Earthquakes," pp. 172-182, In: *Earthquake Hazards and the Design of Constructed Facilities in the Eastern United States*, Annals of the New York Academy of Sciences, Vol. 558, K. H. Jacob and C. J. Turkstra (eds.), The New York Academy of Sciences, New York.

Kishida, H. (1966) "Damage to Reinforced Concrete Buildings in Niigata City with Special Reference to Foundation Engineering," Soils & Foundations VI(1):71-88, January.

Liu, H., and T. P. Qiao (1984) "Liquefaction Potential of Saturated Sand Deposits Underlying Foundation of Structure," pp. 199-206, In: *Proc. 8th World Conference on Earthquake Engineering*, Vol. III, San Francisco, CA, July.

Seed, H. B., and I. M. Idriss (1967) "Analysis of Soil Liquefaction: Niigata Earthquake," JSMF ASCE Vol. 93(SM3):83-108, May.

Whitman, R. V., and P. C. Lambe (1982) "Liquefaction: Consequences for a structure," pp. 941-949, In: *Proc. Conf. Soil Dynamics and Earthquake Engineering*, Southampton Univ., Balkema Rotterdam.

Whitman, R. V., and P. C. Lambe (1988) "Earthquake Like Shaking of a Structure Foundation on Saturated Sand," pp. 529-538, In: *Proc. Centrifuge 88*, Paris, J.-F. Corte (ed.), Balkema, Rotterdam, The Netherlands, April 25-27.

Yoshimi, Y., and K. Tokimatsu (1977) "Settlement of Buildings on Saturated Sand During Earthquakes," *Soils & Foundations*, 17(1):23-38, March.

Table 1. Classification of damage to building foundations, maximum settlement and building tilt, 1964 Niigata earthquake (Kishida, 1966)

Classification	Max Settlement (cm)	Tilting Angle	Damage to Foundation Structure
I	$0 \leq 20$	$0 \leq 20'$	None
II	$20 \leq 50$	$20' \leq 1.°$	Slight
III	$50 \leq 100$	$1° \leq 2.3°$	Intermediate
IV	$100 -$	$2.3° -$	Heavy (needs extensive repair)

Table 2. Centrifuge Test Series

Series	Soil layering	Dr(%)	GC(%)	q_{av}(kpa)
A	Sand	34–76	0	0/80/125
B	Sand	$\simeq 50$	55/85	$\simeq 120$
C	Silt over sand	40–60	0	0
D	Clay over sand	$\simeq 50$	0	125

D_r: relative density of sand

GC: glycerine content of pore fluid by weight

q_{av}: average contact pressure of model foundation

Table 3. Soil Properties

Soil	G_s	d_{50}	e_{max}	e_{min}	k(cm/s)
Nevada No. 120 sand	2.68	0.13	0.894	0.516	2.3×10^{-3}
Ottawa No. 106 silt	2.65	–	–	–	1×10^{-5}
Silty clay	2.69	–	(PI=9.1)	–	8×10^{-7}

G_s: specific gravity

d_{50}(mm): median particle size (in weight)

e_{max}, e_{min}: maximum, minimum void ratio

k: permeability (using water, tested at 1g)

Table 4. Foundation Settlement

Test No.	D_r (%)	GC (%)	a_{av} (g)	q_{av} (kpa)	Foundation settlement S (cm)		
					during shaking	after shaking	total
A2	76	0	0.35	125	16.5	0.5	17
A3	53	0	0.35	125	48	5	53
B1	51	55	0.36	122	27	7	34
B2	45	85	0.39	119	24	12	36

D_r: relative density of sand

GC: glycerine content of pore fluid by weight

a_{av}: model average peak acceleration divided by 50

q_{av}: average contact pressure of model foundation

S: measured model settlement multiplied by 50

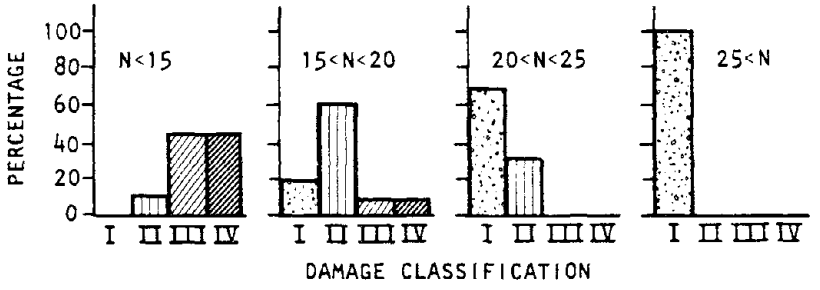

Figure 1. Shallow foundation damage referred to SPT N–values in Niigata earthquake (after Kishida, 1966)

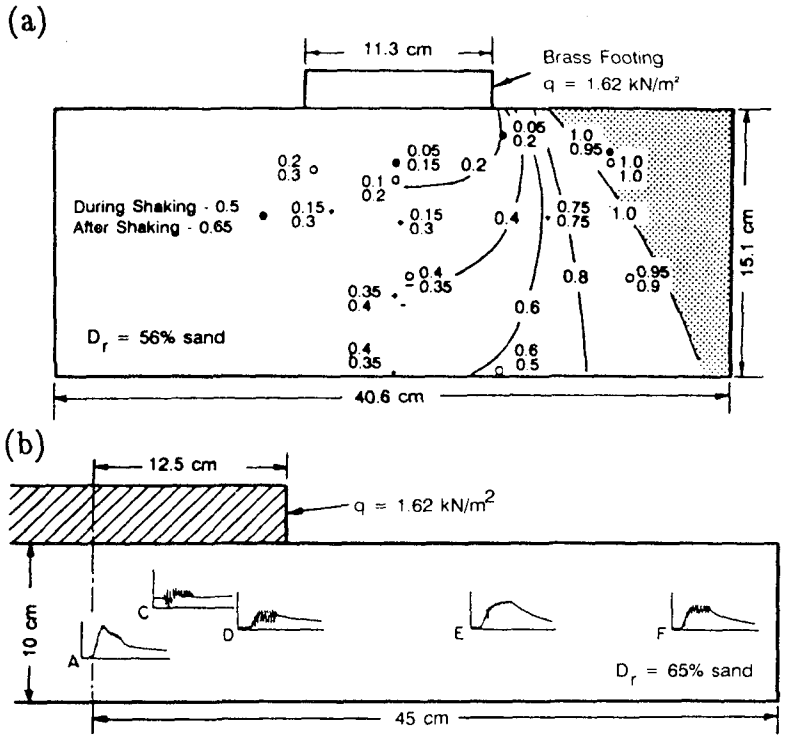

Figure 2. (a) Pore pressure contours in centrifuge test using stacked–ring device; (b) pore pressure histories in plane–strain centrifuge model test (after Whitman and Lambe, 1982 and 1988)

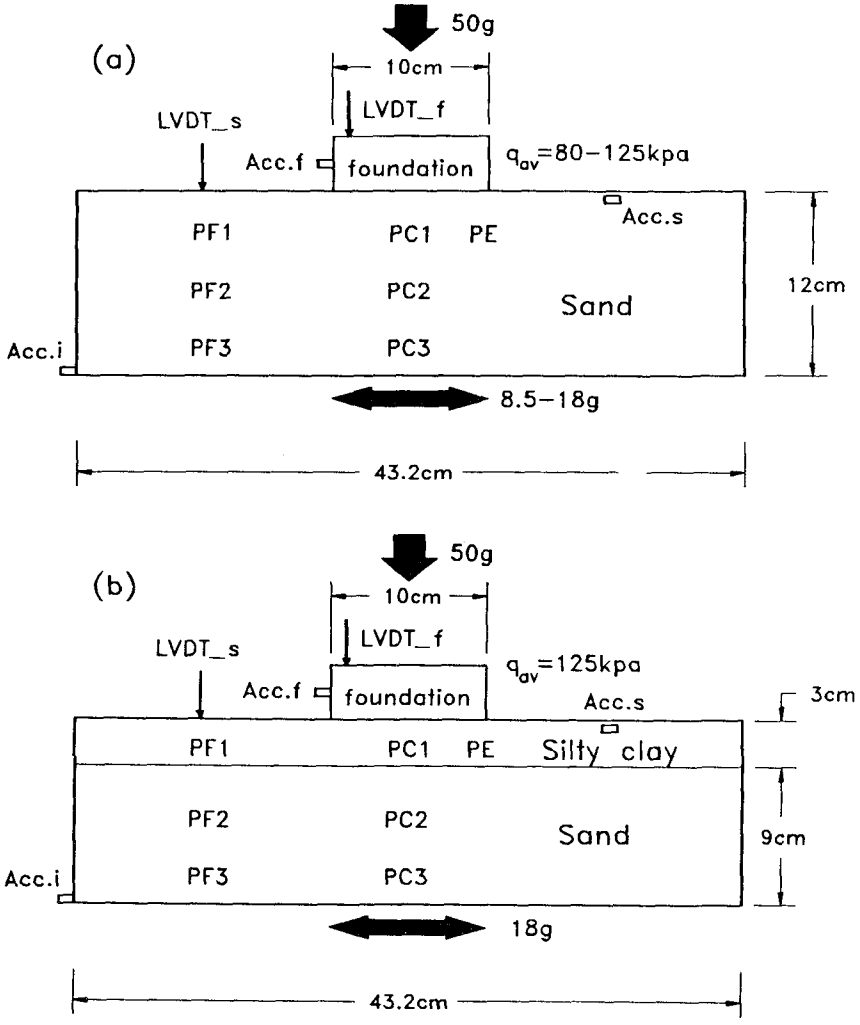

Figure 3. General model configurations for: (a) test Series A and B; and (b) Series D

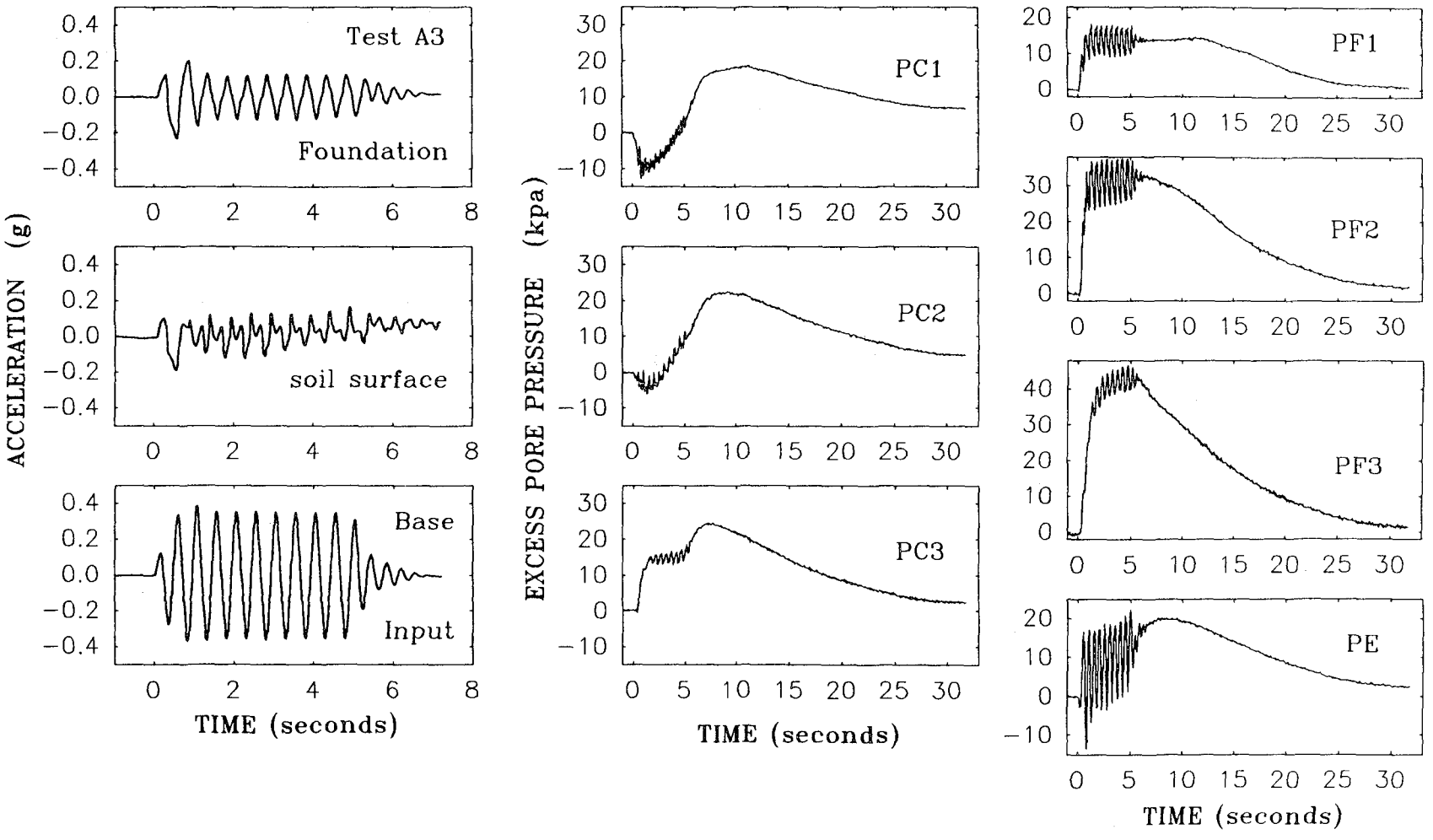

Figure 4. Input, soil surface and foundation horizontal accelerations and excess pore pressures recorded in Test A3 (D_r = 53%, GC = 0)

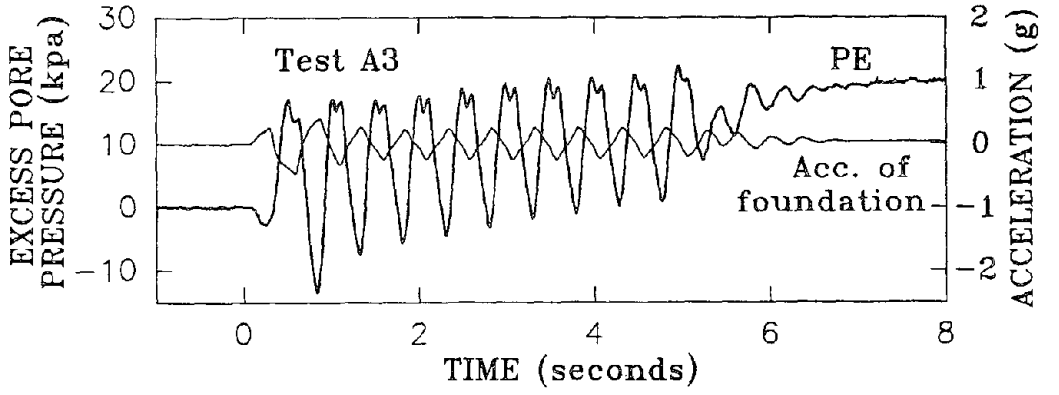

Figure 5. Phase difference between foundation acceleration and excess pore pressure under footing edge in Test A3 (D_r = 53%, GC = 0)

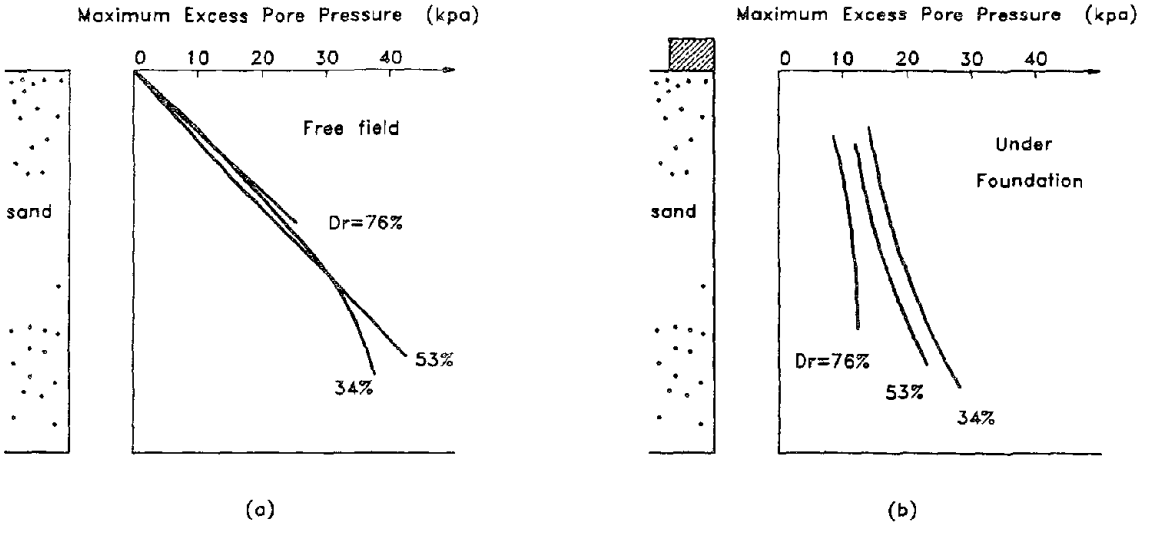

Figure 6. Maximum excess pore pressures in test Series A: (a) free field; and (b) under the center of footing (GC = 0 in all cases)

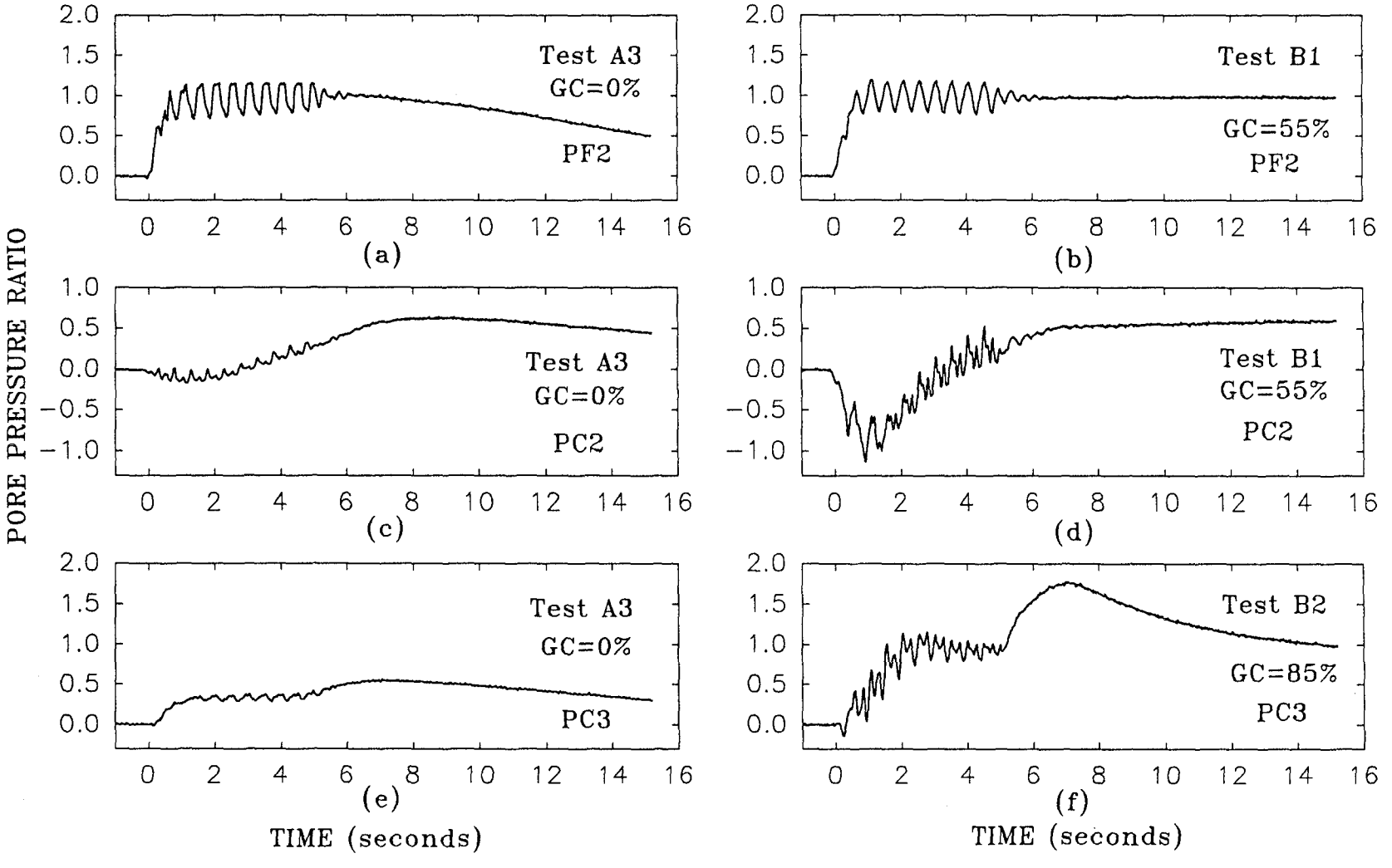

Figure 7. Pore pressure ratios measured in: (a),(c),(e) high permeability model (GC=0%); and (b),(d),(f) low permeability models (GC=55%, 85%); the transducer locations refer to Fig. 3 ($D_r \simeq 50\%$ in all cases)

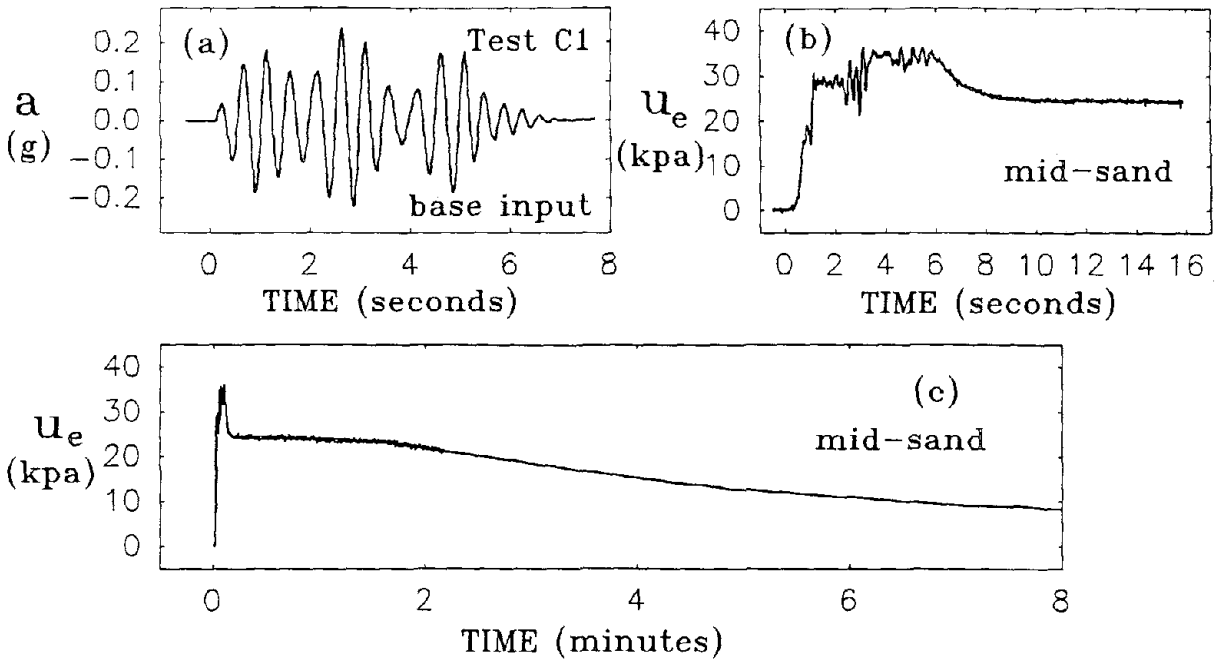

Figure 8. Input base acceleration and excess pore pressure histories in 2–layer Test C1 (D_r = 54%, GC = 0)

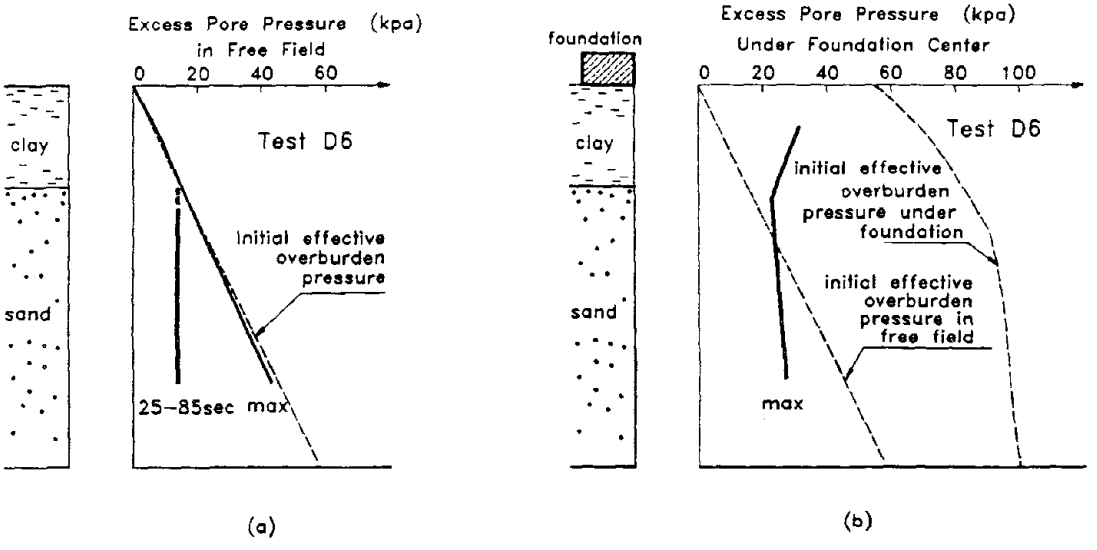

Figure 9. Measured excess pore pressure isochrones in Test D6 with D_r = 50%, GC=0: (a) free field, and (b) under the footing

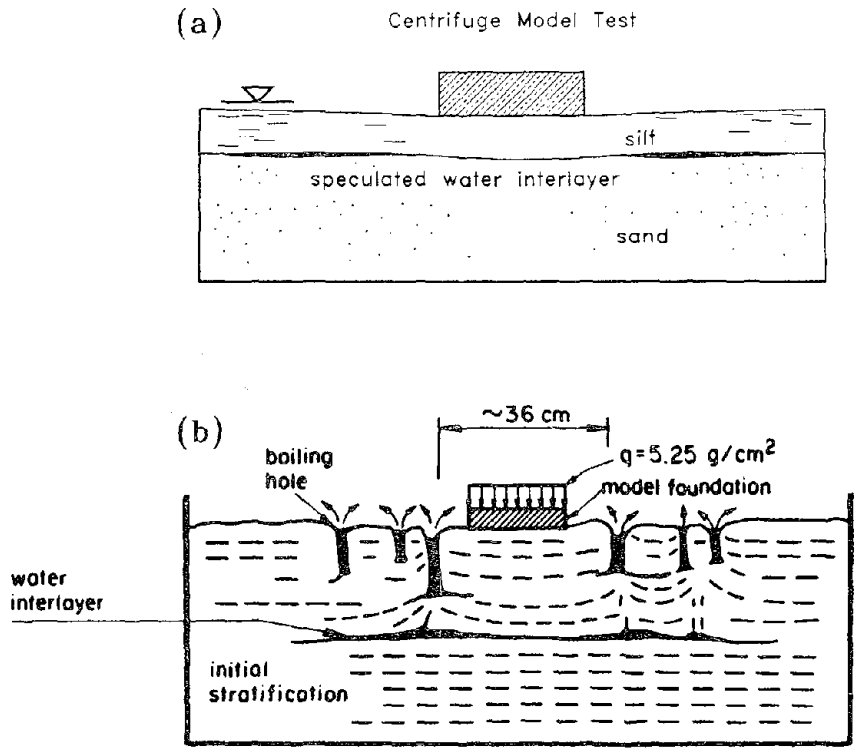

Figure 10. (a) Probable pattern of water interlayer suggested by the measurements in centrifuge Test D6; (b) observed water interlayer in 1g shaking table test of stratified sand deposit (after Liu and Qiao, 1984)